ISSN 0304-4289

Volume 21 Number 1 July 1983

Pramāṇa

a journal of physics

published by
THE INDIAN ACADEMY OF SCIENCES
in collaboration with
THE INDIAN PHYSICS ASSOCIATION
and
THE INDIAN NATIONAL SCIENCE ACADEMY

Pramāṇa

A journal of physics

Annual subscription rates

Foreign:

Institutions & Libraries	$ 30 or £ 12
Individuals	$ 20 or £ 8

Domestic:

Institutions & Libraries	Rs. 75
Individuals	Rs. 25

Pramāṇa is not sold as single issues. Cheques should be made out to the Indian Academy of Sciences.

Editorial Office:

Indian Academy of Sciences, P. B. No. 8005, Bangalore 560 080, India

Pramāṇa is published monthly by the Indian Academy of Sciences, in collaboration with the Indian Physics Association and the Indian National Science Academy. There will be two volumes of six issues each in a year.

Notes on the preparation of papers

Authors wishing to have papers published in Pramāṇa should send them to

The Editor, *Pramāṇa*, Indian Academy of Sciences
P. B. No. 8005, Bangalore 560 080, India.

Three copies of the paper must be submitted.
The submission of a paper will be held to imply that it represents the results of original research not previously published; that it is not under consideration for publication elsewhere; and that if accepted for Pramāṇa it will not be published elsewhere. Papers should not normally exceed 8000 words.

Typescript:

Papers must be written clearly and concisely in English, the preferred spelling being that of the Concise Oxford Dictionary. They must be typed double spaced with ample margin on all sides on white bond paper, 292 × 210 mm. This also applies to the abstract, tables, figure captions, and the list of references which are to be typed on separate sheets.

Title page:

The first page must bear (*a*) the title of the paper; (*b*) the initials and names of the authors; (*c*) the name and address of the institution where the work was carried out; (*d*) the permanent or present addresses of the authors, if different from (*c*); and (*e*) the American Physical Society classification number for the manuscript. A copy of the APS classification scheme can be obtained from the Academy. Authors should suggest an abbreviated running title of not more than 50 letters and spaces. Title must be specific and should contain words useful for indexing.

Continued on the inside back cover

Regd. No. KRN-A 64

Pramāṇa

a journal of physics Vol. 21, No. 1, July 1983

CONTENTS

Indexed in CURRENT CONTENTS

Edited and published by C N R Rao for the Indian Academy of Sciences, Bangalore 560 080, and printed by him at Macmillan India Press, Madras 600 041.

Notes for authors continued from the inside front cover

Abstract:

All papers must have an abstract of not more than 200 words of the significant results reported in the paper.

Keywords:

Between 3 and 6 keywords must be provided for indexing and information retrieval services.

List of Symbols:

Authors should attach to the manuscript a complete list of symbols identified typographically, not mathematically. This list will not appear in print, but it is essential in order to avoid costly corrections at the proof stage.

The Text:

The paper must be divided into sections starting preferably with 'Introduction' and ending with 'Conclusions'. The main sections should be numbered 1, 2, 3, etc. and the subsections 2.1., 2.2., etc.

References:

References should be cited in the text by author and year, not by number. If there are more than two authors, reference should be to the first author followed by *et al* in the text, but names of all authors must be given in the list of references at the end. References at the end of the paper should be listed alphabetically by authors' names, followed by initials, year of publication, name of the journal (abbreviated in the standard form, as in *Chemical Abstracts*), volume number, and number of the first page. References to book should include: name(s) of author(s), initials, year of publication, title of the book, edition if not the first, initials and name(s) of editor(s) if any, preceded by ed(s), place of publication, publisher, and chapter or pages referred to. References to theses must include the year, the title of the thesis, the degree for which submitted and the university.

Mathematical Material:

Equations must be clearly written, each on its own line, well away from the text. All equations must be numbered consecutively in arabic numerals with the number in parentheses near the right hand margin. Indices or superscripts must be indicated in pencil with a $\surd$ sign and subscripts with a $\wedge$ sign; 'oh' and 'zero', K, *k*, and kappa, 'ell' and one, etc., must be clearly distinguished. Authors must indicate wherever special characters (Greek, German, script, scalar vector, tensor, matrix, etc.) are required. All other letters will be set in italic types. Vectors must be underlined by a wavy line and tensors by two wavy lines. The SI system of units and symbols is recommended.

Figures:

All figures, including photographs which must be glossy prints, should be numbered consecutively in arabic numerals in the order of occurrence in the text. Figure captions must be typed on a separate sheet.

Line drawings must be in Indian ink on good quality tracing paper or white card of the same size as the text paper or smaller. Curves should be drawn sufficiently thick to permit reduction to one half or even one third of the original size. The axes must be about 0.3 mm thick and the curves 0.6 mm thick.

Tables:

All tables must be numbered consecutively in arabic numerals in the order of appearance in the text. The tables should be self-contained and have a descriptive title. Column headings of tables should be brief. Extensive tables will be reproduced photographically and should therefore be typed carefully and in the exact format desired. Footnotes to the tables, if any, should be identified by superscript letters and placed at the bottom of the page containing the table.

Footnotes:

Footnotes to the text should be avoided if possible but when necessary should be numbered consecutively, and typed on a separate sheet.

Appendices:

All appendices should be numbered consecutively in arabic numerals.

Proofs:

Authors are requested to prepare the manuscript carefully before submitting it for publication to minimise corrections and alterations in the proof stage which increase publication costs. Galley proofs sent to the author together with a reprint order form must be returned to the editorial office within two days of their receipt.

Reprints:

50 reprints of each article will be supplied free of charge.

Regd. No. KRN-A 64

Pramāṇa

a journal of physics

Vol. 21, No. 2, August 1983

CONTENTS

Indexed in CURRENT CONTENTS

Edited and published by C N R Rao for the Indian Academy of Sciences, Bangalore 560 080, and printed by him at Macmillan India Press, Madras 600 041.

Notes for authors continued from the inside front cover

Abstract:

All papers must have an abstract of not more than 200 words of the significant results reported in the paper.

Keywords:

Between 3 and 6 keywords must be provided for indexing and information retrieval services.

List of Symbols:

Authors should attach to the manuscript a complete list of symbols identified typographically, not mathematically. This list will not appear in print, but it is essential in order to avoid costly corrections at the proof stage.

The Text:

The paper must be divided into sections starting preferably with 'Introduction' and ending with 'Conclusions'. The main sections should be numbered 1, 2, 3, etc. and the subsections 2.1., 2.2., etc.

References:

References should be cited in the text by author and year, not by number. If there are more than two authors, reference should be to the first author followed by *et al* in the text, but names of all authors must be given in the list of references at the end. References at the end of the paper should be listed alphabetically by authors' names, followed by initials, year of publication, name of the journal (abbreviated in the standard form, as in *Chemical Abstracts*), volume number, and number of the first page. References to book should include: name(s) of author(s), initials, year of publication, title of the book, edition if not the first, initials and name(s) of editor(s) if any, preceded by ed(s), place of publication, publisher, and chapter or pages referred to. References to theses must include the year, the title of the thesis, the degree for which submitted and the university.

Mathematical Material:

Equations must be clearly written, each on its own line, well away from the text. All equations must be numbered consecutively in arabic numerals with the number in parentheses near the right hand margin. Indices or superscripts must be indicated in pencil with a $\surd$ sign and subscripts with a $\wedge$ sign; 'oh' and 'zero', K, *k*, and kappa, 'ell' and one, etc., must be clearly distinguished. Authors must indicate wherever special characters (Greek, German, script, scalar vector, tensor, matrix, etc.) are required. All other letters will be set in italic types. Vectors must be underlined by a wavy line and tensors by two wavy lines. The SI system of units and symbols is recommended.

Figures:

All figures, including photographs which must be glossy prints, should be numbered consecutively in arabic numerals in the order of occurrence in the text. Figure captions must be typed on a separate sheet.

Line drawings must be in Indian ink on good quality tracing paper or white card of the same size as the text paper or smaller. Curves should be drawn sufficiently thick to permit reduction to one half or even one third of the original size. The axes must be about 0.3 mm thick and the curves 0.6 mm thick.

Tables:

All tables must be numbered consecutively in arabic numerals in the order of appearance in the text. The tables should be self-contained and have a descriptive title. Column headings of tables should be brief. Extensive tables will be reproduced photographically and should therefore be typed carefully and in the exact format desired. Footnotes to the tables, if any, should be identified by superscript letters and placed at the bottom of the page containing the table.

Footnotes:

Footnotes to the text should be avoided if possible but when necessary should be numbered consecutively, and typed on a separate sheet.

Appendices:

All appendices should be numbered consecutively in arabic numerals.

Proofs:

Authors are requested to prepare the manuscript carefully before submitting it for publication to minimise corrections and alterations in the proof stage which increase publication costs. Galley proofs sent to the author together with a reprint order form must be returned to the editorial office within two days of their receipt.

Reprints:

50 reprints of each article will be supplied free of charge.

Regd. No. KRN-A 64

Pramāṇa

a journal of physics Vol. 21, No. 3, September 1983

CONTENTS

Indexed in CURRENT CONTENTS

Edited and published by C N R Rao for the Indian Academy of Sciences, Bangalore 560 080, and printed by him at Macmillan India Press, Madras 600 041.

Notes for authors continued from the inside front cover

Abstract:

All papers must have an abstract of not more than 200 words of the significant results reported in the paper.

Keywords:

Between 3 and 6 keywords must be provided for indexing and information retrieval services.

List of Symbols:

Authors should attach to the manuscript a complete list of symbols identified typographically, not mathematically. This list will not appear in print, but it is essential in order to avoid costly corrections at the proof stage.

The Text:

The paper must be divided into sections starting preferably with 'Introduction' and ending with 'Conclusions'. The main sections should be numbered 1, 2, 3, etc. and the subsections 2.1., 2.2., etc.

References:

References should be cited in the text by author and year, not by number. If there are more than two authors, reference should be to the first author followed by *et al* in the text, but names of all authors must be given in the list of references at the end. References at the end of the paper should be listed alphabetically by authors' names, followed by initials, year of publication, name of the journal (abbreviated in the standard form, as in *Chemical Abstracts*), volume number, and number of the first page. References to book should include: name(s) of author(s), initials, year of publication, title of the book, edition if not the first, initials and name(s) of editor(s) if any, preceded by ed(s), place of publication, publisher, and chapter or pages referred to. References to theses must include the year, the title of the thesis, the degree for which submitted and the university.

Mathematical Material:

Equations must be clearly written, each on its own line, well away from the text. All equations must be numbered consecutively in arabic numerals with the number in parentheses near the right hand margin. Indices or superscripts must be indicated in pencil with a $\surd$ sign and subscripts with a $\wedge$ sign; 'oh' and 'zero', K, *k*, and kappa, 'ell' and one, etc., must be clearly distinguished. Authors must indicate wherever special characters (Greek, German, script, scalar vector, tensor, matrix, etc.) are required. All other letters will be set in italic types. Vectors must be underlined by a wavy line and tensors by two wavy lines. The SI system of units and symbols is recommended.

Figures:

All figures, including photographs which must be glossy prints, should be numbered consecutively in arabic numerals in the order of occurrence in the text. Figure captions must be typed on a separate sheet.

Line drawings must be in Indian ink on good quality tracing paper or white card of the same size as the text paper or smaller. Curves should be drawn sufficiently thick to permit reduction to one half or even one third of the original size. The axes must be about 0.3 mm thick and the curves 0.6 mm thick.

Tables:

All tables must be numbered consecutively in arabic numerals in the order of appearance in the text. The tables should be self-contained and have a descriptive title. Column headings of tables should be brief. Extensive tables will be reproduced photographically and should therefore be typed carefully and in the exact format desired. Footnotes to the tables, if any, should be identified by superscript letters and placed at the bottom of the page containing the table.

Footnotes:

Footnotes to the text should be avoided if possible but when necessary should be numbered consecutively, and typed on a separate sheet.

Appendices:

All appendices should be numbered consecutively in arabic numerals.

Proofs:

Authors are requested to prepare the manuscript carefully before submitting it for publication to minimise corrections and alterations in the proof stage which increase publication costs. Galley proofs sent to the author together with a reprint order form must be returned to the editorial office within two days of their receipt.

Reprints:

50 reprints of each article will be supplied free of charge.

Regd. No. KRN-A 64

Pramāṇa

a journal of physics Vol. 21, No. 4, October 1983

CONTENTS

Indexed in CURRENT CONTENTS

Edited and published by C N R Rao for the Indian Academy of Sciences, Bangalore 560 080 and printed by him at Macmillan India Press, Madras 600 041.

Notes for authors continued from the inside front cover

Abstract:

All papers must have an abstract of not more than 200 words of the significant results reported in the paper.

Keywords:

Between 3 and 6 keywords must be provided for indexing and information retrieval services.

List of Symbols:

Authors should attach to the manuscript a complete list of symbols identified typographically, not mathematically. This list will not appear in print, but it is essential in order to avoid costly corrections at the proof stage.

The Text:

The paper must be divided into sections starting preferably with 'Introduction' and ending with 'Conclusions'. The main sections should be numbered 1, 2, 3, etc. and the subsections 2.1., 2.2., etc.

References:

References should be cited in the text by author and year, not by number. If there are more than two authors, reference should be to the first author followed by *et al* in the text, but names of all authors must be given in the list of references at the end. References at the end of the paper should be listed alphabetically by authors' names, followed by initials, year of publication, name of the journal (abbreviated in the standard form, as in *Chemical Abstracts*), volume number, and number of the first page. References to book should include: name(s) of author(s), initials, year of publication, title of the book, edition if not the first, initials and name(s) of editor(s) if any, preceded by ed(s), place of publication, publisher, and chapter or pages referred to. References to theses must include the year, the title of the thesis, the degree for which submitted and the university.

Mathematical Material:

Equations must be clearly written, each on its own line, well away from the text. All equations must be numbered consecutively in arabic numerals with the number in parentheses near the right hand margin. Indices or superscripts must be indicated in pencil with a $\surd$ sign and subscripts with a $\wedge$ sign; 'oh' and 'zero', K, *k*, and kappa, 'ell' and one, etc., must be clearly distinguished. Authors must indicate wherever special characters (Greek, German, script, scalar vector, tensor, matrix, etc.) are required. All other letters will be set in italic types. Vectors must be underlined by a wavy line and tensors by two wavy lines. The SI system of units and symbols is recommended.

Figures:

All figures, including photographs which must be glossy prints, should be numbered consecutively in arabic numerals in the order of occurrence in the text. Figure captions must be typed on a separate sheet.

Line drawings must be in Indian ink on good quality tracing paper or white card of the same size as the text paper or smaller. Curves should be drawn sufficiently thick to permit reduction to one half or even one third of the original size. The axes must be about 0.3 mm thick and the curves 0.6 mm thick.

Tables:

All tables must be numbered consecutively in arabic numerals in the order of appearance in the text. The tables should be self-contained and have a descriptive title. Column headings of tables should be brief. Extensive tables will be reproduced photographically and should therefore be typed carefully and in the exact format desired. Footnotes to the tables, if any, should be identified by superscript letters and placed at the bottom of the page containing the table.

Footnotes:

Footnotes to the text should be avoided if possible but when necessary should be numbered consecutively, and typed on a separate sheet.

Appendices:

All appendices should be numbered consecutively in arabic numerals.

Proofs:

Authors are requested to prepare the manuscript carefully before submitting it for publication to minimise corrections and alterations in the proof stage which increase publication costs. Galley proofs sent to the author together with a reprint order form must be returned to the editorial office within two days of their receipt.

Reprints:

50 reprints of each article will be supplied free of charge.

Regd. No. KRN-A 64

Pramāṇa

a journal of physics

Vol. 21, No. 5, November 1983

CONTENTS

Indexed in CURRENT CONTENTS

Edited and published by G N R Rao for the Indian Academy of Sciences, Bangalore 560 080, and printed by him at Macmillan India Press, Madras 600 041.

Notes for authors continued from the inside front cover

Abstract:

All papers must have an abstract of not more than 200 words of the significant results reported in the paper.

Keywords:

Between 3 and 6 keywords must be provided for indexing and information retrieval services.

List of Symbols:

Authors should attach to the manuscript a complete list of symbols identified typographically, not mathematically. This list will not appear in print, but it is essential in order to avoid costly corrections at the proof stage.

The Text:

The paper must be divided into sections starting preferably with 'Introduction' and ending with 'Conclusions'. The main sections should be numbered 1, 2, 3, etc. and the subsections 2.1., 2.2., etc.

References:

References should be cited in the text by author and year, not by number. If there are more than two authors, reference should be to the first author followed by *et al* in the text, but names of all authors must be given in the list of references at the end. References at the end of the paper should be listed alphabetically by authors' names, followed by initials, year of publication, name of the journal (abbreviated in the standard form, as in *Chemical Abstracts*), volume number, and number of the first page. References to book should include: name(s) of author(s), initials, year of publication, title of the book, edition if not the first, initials and name(s) of editor(s) if any, preceded by ed(s), place of publication, publisher, and chapter or pages referred to. References to theses must include the year, the title of the thesis, the degree for which submitted and the university.

Mathematical Material:

Equations must be clearly written, each on its own line, well away from the text. All equations must be numbered consecutively in arabic numerals with the number in parentheses near the right hand margin. Indices or superscripts must be indicated in pencil with a $\surd$ sign and subscripts with a $\wedge$ sign; 'oh' and 'zero', K, *k*, and kappa, 'ell' and one, etc., must be clearly distinguished. Authors must indicate wherever special characters (Greek, German, script, scalar vector, tensor, matrix, etc.) are required. All other letters will be set in italic types. Vectors must be underlined by a wavy line and tensors by two wavy lines. The SI system of units and symbols is recommended.

Figures:

All figures, including photographs which must be glossy prints, should be numbered consecutively in arabic numerals in the order of occurrence in the text. Figure captions must be typed on a separate sheet.

Line drawings must be in Indian ink on good quality tracing paper or white card of the same size as the text paper or smaller. Curves should be drawn sufficiently thick to permit reduction to one half or even one third of the original size. The axes must be about 0.3 mm thick and the curves 0.6 mm thick.

Tables:

All tables must be numbered consecutively in arabic numerals in the order of appearance in the text. The tables should be self-contained and have a descriptive title. Column headings of tables should be brief. Extensive tables will be reproduced photographically and should therefore be typed carefully and in the exact format desired. Footnotes to the tables, if any, should be identified by superscript letters and placed at the bottom of the page containing the table.

Footnotes:

Footnotes to the text should be avoided if possible but when necessary should be numbered consecutively, and typed on a separate sheet.

Appendices:

All appendices should be numbered consecutively in arabic numerals.

Proofs:

Authors are requested to prepare the manuscript carefully before submitting it for publication to minimise corrections and alterations in the proof stage which increase publication costs. Galley proofs sent to the author together with a reprint order form must be returned to the editorial office within two days of their receipt.

Reprints:

50 reprints of each article will be supplied free of charge.

Regd. No. KRN-A 64

Pramāṇa

a journal of physics Vol. 21, No. 6, December 1983

CONTENTS

Indexed in CURRENT CONTENTS

Edited and published by C N R Rao for the Indian Academy of Sciences, Bangalore 560 080, and printed by him at Macmillan India Press, Madras 600 041.

Notes for authors continued from the inside front cover

Abstract:

All papers must have an abstract of not more than 200 words of the significant results reported in the paper.

Keywords:

Between 3 and 6 keywords must be provided for indexing and information retrieval services.

List of Symbols:

Authors should attach to the manuscript a complete list of symbols identified typographically, not mathematically. This list will not appear in print, but it is essential in order to avoid costly corrections at the proof stage.

The Text:

The paper must be divided into sections starting preferably with 'Introduction' and ending with 'Conclusions'. The main sections should be numbered 1, 2, 3, etc. and the subsections 2.1., 2.2., etc.

References:

References should be cited in the text by author and year, not by number. If there are more than two authors, reference should be to the first author followed by *et al* in the text, but names of all authors must be given in the list of references at the end. References at the end of the paper should be listed alphabetically by authors' names, followed by initials, year of publication, name of the journal (abbreviated in the standard form, as in *Chemical Abstracts*), volume number, and number of the first page. References to book should include: name(s) of author(s), initials, year of publication, title of the book, edition if not the first, initials and name(s) of editor(s) if any, preceded by ed(s), place of publication, publisher, and chapter or pages referred to. References to theses must include the year, the title of the thesis, the degree for which submitted and the university.

Mathematical Material:

Equations must be clearly written, each on its own line, well away from the text. All equations must be numbered consecutively in arabic numerals with the number in parentheses near the right hand margin. Indices or superscripts must be indicated in pencil with a $\vee$ sign and subscripts with a $\wedge$ sign; 'oh' and 'zero' K, k, and kappa, 'ell' and one, etc., must be clearly distinguished. Authors must indicate wherever special characters (Greek, German, script, scalar vector, tensor, matrix, etc.) are required. All other letters will be set in italic types. Vectors must be underlined by a wavy line and tensors by two wavy lines. The SI system of units and symbols is recommended.

Figures:

All figures, including photographs which must be glossy prints, should be numbered consecutively in arabic numerals in the order of occurrence in the text. Figure captions must be typed on a separate sheet.

Line drawings must be in Indian ink on good quality tracing paper or white card of the same size as the text paper or smaller. Curves should be drawn sufficiently thick to permit reduction to one half or even one third of the original size. The axes must be about 0.3 mm thick and the curves 0.6 mm thick.

Tables:

All tables must be numbered consecutively in arabic numerals in the order of appearance in the text. The tables should be self-contained and have a descriptive title. Column headings of tables should be brief. Extensive tables will be reproduced photographically and should therefore be typed carefully and in the exact format desired. Footnotes to the tables, if any, should be identified by superscript letters and placed at the bottom of the page containing the table.

Footnotes:

Footnotes to the text should be avoided if possible but when necessary should be numbered consecutively, and typed on a separate sheet.

Appendices:

All appendices should be numbered consecutively in arabic numerals.

Proofs:

Authors are requested to prepare the manuscript carefully before submitting it for publication to minimise corrections and alterations in the proof stage which increase publication costs. Galley proofs sent to the author together with a reprint order form must be returned to the editorial office within two days of their receipt.

Reprints:

50 reprints of each article will be supplied free of charge.

Pramāṇa

a journal of physics

Volume 21, July–December 1983

CONTENTS

Letter

Nuclear and Particle Physics

Plasma Physics

Quantum Mechanics

Solid State Physics

Statistical Physics

Ultrasonics

Pramāṇa, Vol. 21, No. 1, July 1983, pp. 1–10. © Printed in India.

Propagation of the electromagnetic ion-cyclotron wave in a fusion plasma

CHANDU VENUGOPAL
Department of Physics, University of Kerala, Kariyavattom, Trivandrum 695 581, India

MS received 27 July 1982; revised 11 May 1983

Abstract. The propagation of the electromagnetic ion-cyclotron wave in a fusion plasma described by a loss-cone structure is discussed. The wavelength is assumed to be much larger than the ion Larmour radius and the ion plasma frequency $\gg$ the ion-cyclotron frequency. The two modes that propagate in the plasma interact strongly and fuse together under certain conditions making the plasma unstable. The coalescence of the modes is found to decrease with an increase in electron temperature.

Keywords. Dispersion relation; ion-cyclotron wave; fusion plasma; loss-cone structure.

1. Introduction

The instabilities produced by generalised loss-cone distributions play an important role in mirror-magnetic configurations. For example, the electrostatic ion-cyclotron instability causes anomalous end-losses in mirror-machines (Baldwin 1977). Several aspects of the instabilities which occur in loss-cone plasmas have already been considered: the case of warm plasmas (Harris 1961; Dory *et al* 1965; Rosenbluth and Post 1965), the case of mixed warm-cold plasmas (Pearlstein *et al* 1966; Farr and Budwine 1968; Gomberoff and Cuperman 1976, 1981) and the correction due to electromagnetic effects (Callen and Guest 1971, 1973). The dispersion relations using loss-cone distributions are very complex and hence past analyses were essentially numerical (Himmell 1971; Cordey and Farr 1972).

We have derived in a simple form the dispersion relation for the near perpendicular propagation of the electromagnetic ion-cyclotron wave for wavelengths larger than the ion-Larmour radius γ_L and large ion plasma frequencies ($\omega_{p+}^2 \gg \Omega_+^2$). Our analysis shows that two modes can propagate in the plasma. These modes interact strongly fusing together in a number of cases and making the plasma unstable. This coalescence between the modes is found to decrease with an increase in electron temperature.

2. Dielectric tensor

Consider a plasma of uniform density N, in a uniform magnetic field $\mathbf{B}_{oz}$, directed along the z-axis. The Vlasov equations can be solved and a dispersion equation

obtained if a Fourier-Laplace transform exists for the perturbed distribution function f, electric field **E** and magnetic field **B** (Montgomery and Tidman 1964). Setting $k_y = 0$ ($k_x \equiv k_\perp$; $k_z \equiv k_\parallel$), we get (Stix 1962)

$$\begin{vmatrix} -n_\parallel^2 + K_{xx} & K_{xy} & n_\perp n_\parallel + K_{xz} \\ K_{yx} & -n_\parallel^2 - n_\perp^2 + K_{yy} & K_{yz} \\ n_\perp n_\parallel + K_{zx} & K_{zy} & -n_\perp^2 + K_{zz} \end{vmatrix} = 0. \tag{1}$$

In (1) $n_\parallel$ and $n_\perp$ are the refractive indices parallel and perpendicular to the magnetic field respectively and K_{ik} ($i, k = x, y, z$) are the elements of the dielectric tensor.

In this paper we assume that the equilibrium distribution function f_0 has a loss-cone structure given by

$$f_0 = \frac{1}{j!\,\pi^{3/2}\,W^{2j+2}\,U}\,[v_\perp]^{2J} \exp\left[-\frac{v_\parallel^2}{U^2} - \frac{v_\perp^2}{W^2}\right] \tag{2}$$

where $W^2 = 2\,T_\perp/[m\,(j+1)]$,

$U^2 = 2\,T_\parallel/m$,

j is the loss-cone index. A loss-cone structure is assumed for both electrons and ions to simplify the algebra.

Substituting (2) into the elements of the dielectric tensor (Landau and Cuperman 1971; hereinafter referred to as I), carrying out the $dv_\perp$ (Chandu Venugopal and Viswanathan 1982) and $dv_\parallel$ (Appendix A of I) integrations gives us the following expressions for K_{ik}:

$$\begin{matrix} K_{xx} - 1 \\ K_{xy} \\ K_{yy} - 1 \end{matrix} = \sum_{'+','-'} C \sum_{n=-\infty}^{+\infty} \begin{matrix} n^2/a^2 \\ in/a \\ 1 \end{matrix} \left\{ \begin{matrix} I_P^{(j)} & & I_P^{(j-1)} \\ I_{aP}^{(j)} \left[\frac{1-E}{n-z} - \frac{AE}{z}\right] & -j\left[\frac{1-E}{n-z} - \frac{E}{z}\right] & I_{aP}^{(j-1)} \\ Q_P^{(j)} & & Q_P^{(j-1)} \end{matrix} \right\}$$

$$\begin{matrix} K_{zx} \\ K_{zy} \end{matrix} = \sum_{'+','-'} C \sum_{n=-\infty}^{+\infty} \begin{matrix} n/\theta a^2 \\ i/\theta a \end{matrix} \left\{ \begin{matrix} I_P^{(j)} \left[E + \frac{A\,(n-z)\,E}{z}\right] & -j\left[E + \frac{(n-z)\,E}{z}\right] & I_P^{(j-1)} \\ I_{aP}^{(j)} & & I_{aP}^{(j-1)} \end{matrix} \right\}$$

$$K_{zz} - 1 = \sum_{'+','-'} C \sum_{n=-\infty}^{+\infty} 1/\theta^2\,a^2 \left\{ I_p^{(j)} \left[\frac{nA}{z} + \frac{W^2}{U^2}\right](z-n)\,E - j\left[\frac{n(z-n)E}{z}\right] \cdot I_p^{(j-1)} \right\}$$

with $K_{xz} = K_{zx}$ and $K_{yz} = -K_{zy}$. (3)

In (3) '+' refers to ions and is assumed on all quantities and, in general, should be understood, as added when not specifically stated and '—' refers to electrons. Also

$$\Omega = eB_0/(mc),\ \omega_p^2 = 4\pi Ne^2/m,\ \bar{\omega}_p^2 = \omega_p^2/\Omega^2,$$

$$z = \omega/\Omega,\quad \theta = k_\parallel/k_\perp,\quad a = k_\perp/\Omega \text{ and } A = 1 - \frac{W^2}{U^2} \tag{4a}$$

$$C = 4\,[j!\ W^{2j+2}]^{-1}\,\bar{\omega}_p^2/z. \tag{4b}$$

$$I_p^{(j)} = \frac{(-1)^j}{W^2}\frac{d^j I}{dp^j};\ I_p^{(j-1)} = (-1)^{j-1}\frac{d^{j-1} I}{dp^{j-1}}. \tag{4c}$$

$$I_{ap}^{(j)} = \frac{(-1)^j}{2W^2}\frac{d}{da}\left(\frac{d^j I}{dp^j}\right);\ I_{ap}^{(j-1)} = \frac{(-1)^{j-1}}{2}\frac{d}{da}\left(\frac{d^{j-1} I}{dp^{j-1}}\right). \tag{4d}$$

$$Q_p^{(j)} = \frac{(-1)^j}{W^2}\frac{d^j Q}{dp^j};\ Q_p^{(j-1)} = (-1)^{j-1}\frac{d^{j-1} Q}{dp^{j-1}}. \tag{4e}$$

where $$p = 1/W^2 \text{ and } Q = \left.\frac{d^2 I(a, \beta)}{da\, d\beta}\right|_{a=\beta}. \tag{4f}$$

$I = I(\alpha, \beta)$ arises from integrals of the type (Gradshteyn and Ryzhik 1965)

$$\int_0^\infty \exp(-\Delta^2 x^2)\, J_n(\alpha x)\, J_n(\beta x)\, x\, dx = I(\alpha, \beta)$$

$$= \frac{1}{2\Delta^2}\exp\left[-\frac{(\alpha^2+\beta^2)}{4\Delta^2}\right] I_n(\alpha\beta/2\Delta^2). \tag{5}$$

In our case $1/\Delta^2 = W^2$. In (4c) we have $a=\beta$ in $I(a, \beta)$, in (4d) we differentiate $I(a, a)$ with respect to a and in (4e) we differentiate $I(a, \beta)$ with respct to a and β and finally set $a=\beta$. They are then differentiated j or $(j-1)$ times with respect to p. The arguments of the Bessel functions are $I_n = I_n(l_\perp)$ where

$$l_\perp = \frac{2k_\perp^2 T_\perp}{\Omega^2 m (j+1)} = \frac{2}{(j+1)}\, l_\perp'. \tag{6}$$

The E-function is defined as

$$E(S') = -\tfrac{1}{2}Z'(s'/\sqrt{2}),$$

where $$S' = (z-n)/(\theta\sqrt{l_\parallel}),$$

and $$l_\parallel = k_\perp^2 T_\parallel/(\Omega^2 m). \tag{7}$$

Z' is the derivative of the plasma dispersion function of Fried and Conte.

3. The approximation scheme

We choose an ordering scheme (in terms of a small parameter ϵ) that reduces the electron contribution to a minimum as we are interested only in the ion-cyclotron wave propagating with a small range of frequencies around its first harmonic. We thus choose

$$\gamma = 1 - z_+^2 \sim \epsilon; \quad l_\perp,\ l_\parallel,\ \theta \text{ and } 1/\bar{\omega}_p^2 \sim \epsilon,$$

$$T_+/T_- \text{ and } W^2/U^2 \sim 1 \text{ and } m_-/m_+ \sim \epsilon^2. \tag{8}$$

Since $l_\perp \ll 1$ we can use relations (4c) to (4e) combined with a series expansion of both terms in (5) to get expressions for

$$I_p^{j,(j-1)}, \quad I_{ap}^{j,(j-1)} \text{ and } Q_p^{j,(j-1)}.$$

These are given in Appendix 1.

From (8), $s' \gg 1$ for all n. The asymptotic expansion of Z, in terms of the E-function, thus needed is given by (I)

$$E(S') = -\frac{\theta^2 l_\parallel}{(n-z)^2} - 3\frac{(\theta^2 l_\parallel)^2}{(n-z)^4} \ldots + 2i(z-n)\, e_n$$

where $$e_n = \left(\frac{\pi}{8\theta^2 l_\parallel}\right)^{1/2} \exp\left[-(z-n)^2/2\theta^2 l_\parallel\right], \tag{9}$$

e_n for $n = 0$, 1 and $2 \ll 1$ and hence will be neglected.

4. Explicit evaluation of the tensor elements

We calculate the dielectric tensor elements retaining terms of the order of $1/\epsilon$, 1 and ϵ. Only the n=0, 1, 2 ion terms and the n=0 electron terms contribute; all electron terms are written down in terms of the ion terms.

We demonstrate the calculation of the element K_{xx}. Expanding the first square bracket of (3) using (9) and summing over n, we get

$$\sum_{n=-\infty}^{\infty} n^2\left[\frac{1-E}{n-z} - \frac{AE}{z}\right] = 2\sum_{n=1}^{\infty} n^2 \left\{\frac{z}{n^2-z^2} + (\theta^2 l_\parallel)\frac{z(3n^2+z^2)}{(n^2-z^2)^3}\right.$$

$$\left. + 3(\theta^2 l_\parallel)^2 \frac{z(5n^4 + \text{ion}^2 z^2 + z^4)}{(n^2-z^2)^5} + \frac{A}{z}(\theta^2 l_\parallel)\frac{n^2+z^2}{(n^2-z^2)^2}\right\}. \tag{10}$$

The other sum (labelled 10a), for the square bracket multiplying j in (3), can be got from (10) by putting A=1. The sums (10) and (10a) are then multiplied by the

appropriate expressions for $I_p^{(j)}$ and $I_p^{(j-1)}$ for $n=1$ and 2 and then added. The resultant expression for K_{xx} can be further simplified by using (A3). We finally get

$$\frac{K_{xx}}{\bar{\omega}_p^2} = \frac{1 - l'_\perp}{\gamma} + 4\frac{\theta^2 l_\parallel}{\gamma^3} + \frac{\theta^2 l_\parallel}{\gamma^2}[(2A-1)(j+1) - j]$$

$$+ 48\frac{\theta^4 l_\parallel^2}{\gamma^5} - 4\frac{\theta^2 l_\parallel l'_\perp}{\gamma^3} + \frac{5}{16}\frac{l'^2_\perp}{\gamma}\frac{(j+2)}{(j+1)} + \frac{l'_\perp}{3} + \frac{1}{\bar{\omega}_p^2}. \tag{11a}$$

The other elements can be derived in a similar manner. The expressions are:

$$K_{yy}\frac{z_+^2}{\bar{\omega}_p^2} = \frac{1 - 3l'_\perp}{\gamma} + 4\frac{\theta^2 l_\parallel}{\gamma^3} - 1 + \frac{\theta^2 l_\parallel}{\gamma^2}[(2A-5)(j+1) + 3j]$$

$$+ 48\frac{\theta^4 l_\parallel^2}{\gamma^5} - 12\frac{\theta^2 l_\parallel l'_\perp}{\gamma^3} + \frac{37}{16}\frac{l'^2_\perp}{\gamma}\frac{(j+2)}{(j+1)} + 2\left[\frac{2}{3} - \frac{T_{\perp,-}}{T_{\perp,+}}\right] l'_\perp + \frac{1}{\bar{\omega}_p^2}. \tag{11b}$$

$$\frac{K_{xy}}{i}\frac{z_+}{\bar{\omega}_p^2} = \frac{1 - 2l'_\perp}{\gamma} + 4\frac{\theta^2 l_\parallel}{\gamma^3} - 1 + \frac{\theta^2 l_\parallel}{\gamma^2}[(2A-3)(j+1) + j]$$

$$+ 48\frac{\theta^4 l_\parallel^2}{\gamma^5} - 8\frac{\theta^2 l_\parallel l'_\perp}{\gamma^3} + \frac{15}{16}\frac{l'^2_\perp}{\gamma}\frac{(j+2)}{(j+1)} + \frac{2}{3}l'_\perp. \tag{11c}$$

$$\frac{K_{xz}}{\bar{\omega}_p^2} = -2\frac{\theta l_\parallel}{\gamma^2} + 2\frac{\theta l_\parallel l'_\perp}{\gamma^2} - 24\frac{\theta^3 l_\parallel^2}{\gamma^4} - \frac{\theta l_\parallel}{\gamma}[A(j+1) - j] \tag{11d}$$

$$\frac{K_{zy}}{i}\frac{z_+}{\bar{\omega}_p^2} = -2\frac{\theta l_\parallel}{\gamma^2} - \theta l_\parallel\frac{m_+}{m_-}\frac{T_{\perp,-}}{T_{\parallel,+}} + 4\frac{\theta l_\parallel l'_\perp}{\gamma^2}$$

$$- 24\frac{\theta^3 l_\parallel^2}{\gamma^4} - \frac{\theta l_\parallel}{\gamma}[(A-1)(j+1)] \tag{11e}$$

and $$K_{zz}(z_+^2/\bar{\omega}_p^2) = -(m_+/m_-). \tag{11f}$$

Only the $1/\epsilon^2$ term has been retained for K_{zz}. The next term is ~ 1.

5. The dispersion relation

The tensor elements (11a) to (11f) will now be used to derive the dispersion relation for the propagation of the electromagnetic ion cyclotron wave. We propose to

retain terms only ~ 1. Starting from the basic definition of $n_\perp$ $(= k_\perp C/\omega)$ we can easily show that

$$n_\perp^2 = \frac{l'_\perp}{\beta_\perp}\,\frac{\bar{\omega}_p^2}{z_+^2} \text{ and } n_\parallel^2 = \theta^2\, n_\perp^2,$$

where $$\beta_\perp = 4\pi N T_{\perp,+}/B_0^2. \tag{12}$$

Assuming that, at most, $(l'_\perp/\beta_\perp) \sim 1$, we find from (12) that $(n_\parallel^2/\bar{\omega}_p^2) \sim \epsilon^2$ and thus

$$\frac{K_{xx}}{\bar{\omega}_p^2} + \frac{n_\parallel^2}{\bar{\omega}_p^2} \approx \frac{K_{xx}}{\bar{\omega}_p}$$

and $$K_{yy}\frac{z_+^2}{\bar{\omega}_p^2} + \frac{n_\parallel^2}{\bar{\omega}_p^2} \approx K_{yy}\frac{z_+^2}{\bar{\omega}_p^2}$$

as the least significant terms retained in $K_{xx}/\bar{\omega}_p^2$ and $(K_{yy}\, Z_+^2/\bar{\omega}_p^2)$ are $\sim \epsilon$.

Expanding the determinant (1) in factors of the last column, dividing by $(-n_\perp^2 + K_{zz})$ and multiplying by $z_+^2/\bar{\omega}_p^4$ we get

$$\frac{K_{xx}}{\bar{\omega}_p^2}\left[-\frac{l'_\perp}{\beta_\perp} + K_{yy}\frac{z_+^2}{\bar{\omega}_p^2}\right] + \left[K_{xy}\frac{z_+}{\bar{\omega}_p^2}\right]^2$$

$$+ \left\{\frac{n_\perp\, n_\parallel + K_{xz}}{-n_\perp^2 + K_{zz}}\left[K_{xy}\frac{z_+}{\bar{\omega}_p^2}\, K_{yz}\frac{z_+}{\bar{\omega}_p^2} + \left(\frac{\theta}{z_+^2}\,\frac{l'_\perp}{\beta_\perp} + \frac{K_{xz}}{\bar{\omega}_p^2}\right)\right.\right.$$

$$\left.\left(\frac{l'_\perp}{\beta_\perp} - K_{yy}\frac{z_+^2}{\bar{\omega}_p^2}\right)\right] + \frac{K_{yz}\, z_+}{-n_\perp^2 + K_{zz}}\left[\frac{K_{xx}}{\bar{\omega}_p^2}\, K_{yz}\frac{z_+}{\bar{\omega}_p^2}\right.$$

$$\left.\left. + K_{xy}\frac{z_+}{\bar{\omega}_p^2}\left(\frac{\theta}{z_+^2}\,\frac{l'_\perp}{\beta_\perp} + \frac{K_{xz}}{\bar{\omega}_p^2}\right)\right]\right\} = 0. \tag{13}$$

We shall now show that the curly-bracketed terms of (13) do not contribute to the dispersion relation. An examination of the tensor elements (11a) to (11f) reveals that

$$K_{xy} = i\, K_{yy} = i\, K_{xx},$$

and $$K_{yz} \approx -\, i\, K_{xz},$$

for the most significant term. Thus

$$K_{xy}\, K_{yz} - K_{yy}\, K_{xz} = 0$$

and $$K_{xx} K_{yz} + K_{xy} K_{xz} = 0$$

Also $$\frac{n_\perp n_\parallel + K_{xz}}{-n_\perp^2 + K_{zz}} \text{ and } \frac{K_{yz} z_+}{-n_\perp^2 + K_{zz}} \text{ are } \sim \epsilon^2.$$

Their product with the square-bracketed terms would be at most $\sim \epsilon$ and since we retain only terms ~ 1 the curly-bracketed terms do not contribute to the dispersion relation. Substituting from (11a) to (11c) for the tensor elements, simplifying and finally multiplying by $-\gamma^2$ we get the dispersion relation as

$$\gamma^2 - \gamma\left[1 - \frac{l'_\perp}{\beta_\perp} - \delta\right] + \frac{l'^2_\perp}{4}\frac{(j-2)}{(j+1)} - 4\frac{\theta^2 l_\parallel}{\gamma}\left[1 - \frac{l'_\perp}{\beta_\perp}\right] = 0, \tag{14}$$

where $$\delta = \left[\frac{8}{3} + 2\frac{T_{\perp,-}}{T_{\perp,+}} - \frac{l'_\perp}{\beta_\perp}\right] l'_\perp - \frac{2}{\bar{\omega}_p^2}.$$

If we let $[1-(l'_\perp/\beta_\perp)]$ be ~ 1 we get $\gamma=0$ for the ϵ order term and this is much greater than the other ϵ^2 terms. This result is inconsistent with our ordering as θ^2 cannot now be $\sim \epsilon^2$. Thus to get a consistent ordering we need to set $[1-(l'_\perp/\beta_\perp)] \sim \epsilon$. But the θ^2 term is now of order $\sim \epsilon^3$ and thus does not contribute to the dispersion relation as the other terms are of the order ϵ^2. Thus the dispersion relation reduces to the first three terms.

Due to the tediousness of differentiating (5) previous numerical computations considered only low values of j. For example Cordey and Farr (1972) considered the ion cyclotron instability for $j=0$ and 1 while Himmell (1971) considered it for $j=1$ to 4. In contrast our dispersion relation (14) is a very general one and j can take on any value upwards of zero. As a check on our result we note that for $j=0$ the dispersion relation (14) reduces to that in I which was derived using anisotropic Maxwellian distribution function (the loss-cone distribution function reduces to the anisotropic Maxwellian for $j=0$).

6. Applications

We now plot the dispersion relation (14) for typical fusion conditions (Cap 1976)

$$N = 10^{16}\ \text{Cm}^{-3},\ T_+ = 10^8\ ^\circ\text{K and } B_0 = 10^5\text{G}.$$

With these parameters $\beta_\perp = 0{\cdot}17343$.

The plot given in figure 1 is the dispersion relation for $j=0$ and 8 and shows that two modes, one with a constant frequency and another with an increasing frequency, can propagate in the plasma. They interact strongly and mode conversion takes place at $k_\perp \gamma_L = 0{\cdot}5$, beyond this point the former mode increases in frequency while the latter mode exhibits a constant frequency. Such mode conversion mechanisms are of interest in fusion plasmas; one of the methods suggested for the electron cylotron resonance heating of plasmas in tokomaks is by the mode conversion of the ordinary

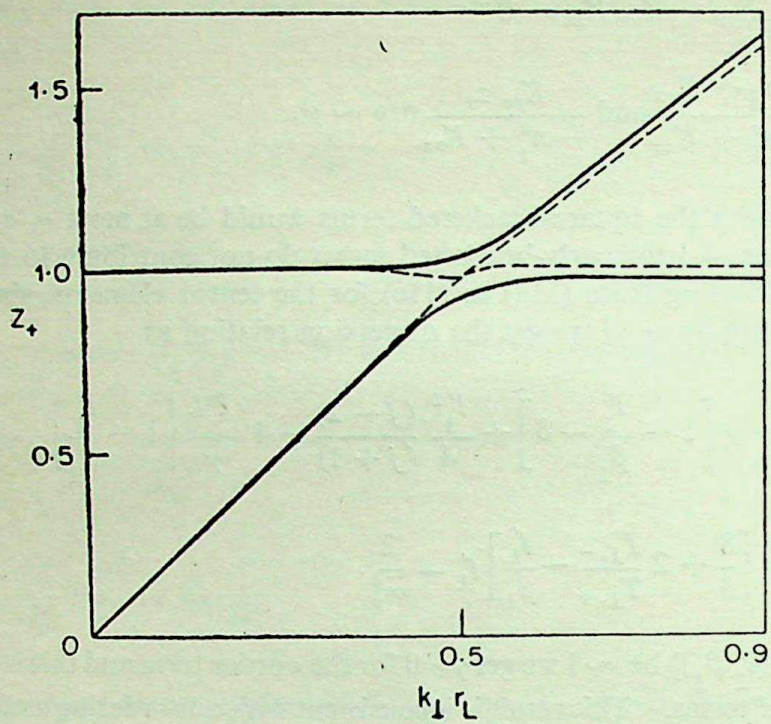

Figure 1. Plot of the dispersion relation for $\beta_\perp = 0{\cdot}17343$ and $T_{\perp,-}/T_{\perp,+} = 1$. The dotted lines are for $j = 8$ and the solid lines for $j = 0$.

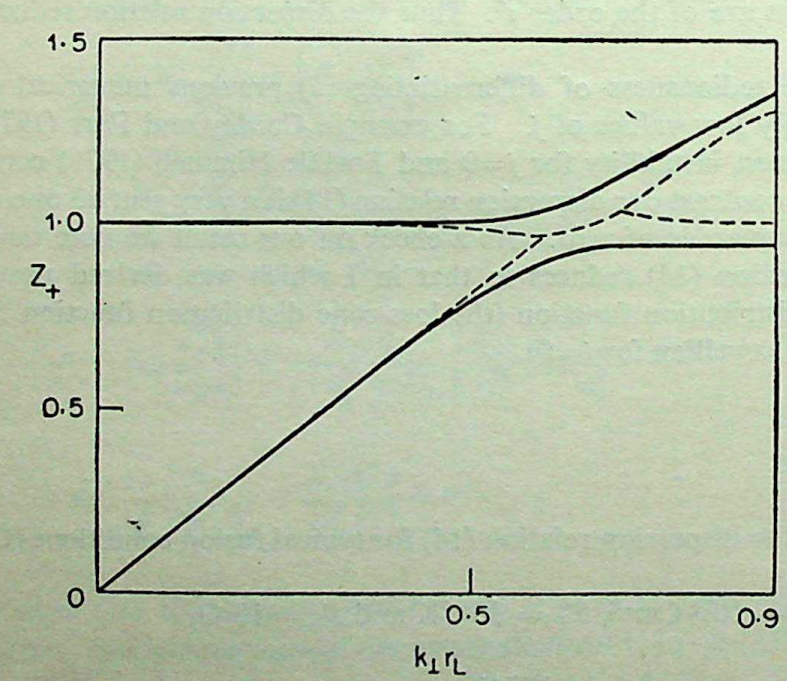

Figure 2. Plot of the dispersion relation for $\beta_\perp = 0{\cdot}17343$ and $T_{\perp,-}/T_{\perp,+} \sim \epsilon$. The dotted lines for $j = 7$ and the solid lines for $j = 0$.

wave into a cyclotron harmonic wave (Cairns and Lashmore-Davies 1982). For $j \geqslant 8$ the two modes coalesce at $k_\perp \gamma_L = 0{\cdot}5$ resulting in a pair of complex conjugate roots for the dispersion relation. This indicates that the plasma is unstable (Cordey and Farr 1972); the values of the imaginary part of z_+ are $\sim 10^{-2}$.

Table 1. Propagation characteristics of the modes.

$\beta_\perp$	$T_{\perp,-}/T_{\perp,+}$	Characteristics
0·17343	2	Modes do not coalesce upto $j = 10$
	1	Modes coalesce for $j \geqslant 8$ at $k_\perp \gamma_l = 0{\cdot}5$
		Real $z_+ = 0{\cdot}974$
	0·1	Modes coalesce for $j \geqslant 3$ at $k_\perp \gamma_l = 0{\cdot}6$
		Real $z_+ = 0{\cdot}985$.
	$\sim \epsilon$	Modes coalesce for $j \geqslant 4$ at $k_\perp \gamma_l = 0{\cdot}6$
		Real $z_+ = 0{\cdot}976$. For $j \geqslant 7$ they
		fuse from $k_\perp \gamma_l = 0{\cdot}6$ to 0·7.
		Real $z_+ = 0{\cdot}976$ to 1·045 (figure 2).
1·7343	2	Modes do not coalesce upto $j = 10$.
	1	Modes coalesce for $j \geqslant 5$ at $k_\perp \gamma_l = 0{\cdot}6$.
		Real $z_+ = 0{\cdot}97$.
		For $j \geqslant 8$ they fuse from $k_\perp \gamma_l = 0.6$ to 0·7.
		Real $z_+ = 0{\cdot}97$ to 1·048.
	0·1	Modes coalesce for $j \geqslant 3$ at $k_\perp \gamma_l = 0{\cdot}8$.
		Real $z_+ = 0{\cdot}996$.
		For $j \geqslant 4$ they fuse from $k_\perp \gamma_l = 0{\cdot}8$ to 0·9.
		Real $z_+ = 0{\cdot}996$ to 1·056.
	$\sim \epsilon$	Modes coalesce for $j \geqslant 3$ in the region
		$k_\perp \gamma_l = 0{\cdot}8$ to 0·9.
		Real $z_+ = 0{\cdot}979$ to 1·037.

Table 1 depicts the characteristics of the roots of the dispersion relation when the parameters are altered.

The table shows that the two modes tend to coalesce over a larger frequency range as the electron temperature tends to zero. Also the modes are unstable around $\omega \approx \Omega_+$ in agreement with the results of Cordey and Farr (1972).

7. Conclusion

The dispersion relation for the near perpendicular propagation of the electromagnetic ion cyclotron wave has been derived. Two modes, which interact strongly, can propagate in the plasma. These modes coalesce under certain conditions making the plasma unstable. A possible method of stabilisation is to increase the electron temperature as the modes do not coalesce for electron to ion temperature ratios greater than 2.

Appendix 1

The expressions for $I_p^{(j)} \cdot I_{ap}^{(j)}$ and $Q_p^{(j)}$ derived as indicated earlier are:

where $\quad j_{(x)} = (j + x)!/[j!\, x!] \quad x = 1, 2, 3, \ldots$ (A1)

n	$\frac{4}{j!\,W^{2j+2}\,\alpha^2}\,I_p^{(j)}$	$\frac{4}{j!\,W^{2j+2}\,\alpha}\,I_{\alpha p}^{(j)}$	$\frac{4}{j!\,W^{2j+2}}\,Q_p^{(j)}$
0	$\frac{2}{l_\perp} - j_{(1)} + \frac{3}{8}\,l_\perp\,j_{(2)}$	$-j_{(1)} + \frac{3}{4}\,l_\perp j_{(2)} - \frac{5}{16}\,l_\perp^2\,j_{(3)}$	$l_\perp\,j_{(2)} - \frac{3}{4}\,l_\perp^2\,j_{(3)}$
1	$\frac{j_{(1)}}{2} - \frac{l_\perp}{4}\,j_{(2)} + \frac{5}{64}\,l_\perp^2\,j_{(3)}$	$\frac{j_{(1)}}{2} - \frac{l_\perp}{2}\,j_{(2)} + \frac{15}{64}\,l_\perp^2\,j_{(3)}$	$\frac{j_{(1)}}{2} - \frac{3}{4}\,l_\perp\,j_{(2)} + \frac{37}{64}\,l_\perp^2\,j_{(3)}$
2	$\frac{l_\perp}{16}\,j_{(2)} - \frac{l_\perp^2}{32}\,j_{(3)}$	$\frac{l_\perp}{8}\,j_{(2)} - \frac{3}{32}\,l_\perp^2\,j_{(3)}$	$\frac{l_\perp}{4}\,j_{(2)} - \frac{l_\perp^2}{4}\,j_{(3)}$

Expressions for

$$I_p^{(J-1)},\ I_{\alpha p}^{(J-1)} \text{ and } Q_p^{(J-1)}$$

(labelled A-2) can be derived from the above by dividing the quantities by W^2 and replacing the j-factors by g-factors, these being defined by

$$g_{(y)} = (j+y)!\,/\,[j!\,(y+1)!] \quad y = 0, 1, 2, \ldots$$

We also have the relations

$$\begin{aligned} j_{(1)} - j\,g_{(0)} &= 1, \\ j_{(2)} - j\,g_{(1)} &= (j+1), \\ j_{(3)} - j\,g_{(2)} &= \frac{(j+1)\,(j+2)}{2}. \end{aligned} \tag{A3}$$

References

Baldwin D E 1977 *Rev. Mod. Phys.* **49** 317
Cairns R A and Lashmore-Davies C N 1982 *Phys. Fluids* **25** 1605
Callen J D and Guest G E 1971 *Phys. Fluids* **14** 1588
Callen J D and Guest G E 1973 *Nucl. Fusion* **13** 87
Cap F F 1976 *Handbook on plasma instabilities* (New York: Academic Press) Vol. 1, p. 27
Chandu Venugopal and Viswanathan K S 1982 *Planet. Space Sci.* **30** 687
Cordey J G and Farr W M 1972 *Plasma Phys.* **14** 1109
Dory R A Guest G E and Harris E G 1965 *Phys. Rev. Lett.* **14** 131
Farr W M and Budwine R E 1968 *Phys. Fluids* **11** 883
Gomberoff L and Cuperman S 1976 *J. Plasma Phys.* **15** 325
Gomberoff L and Cuperman S 1981 *J. Plasma Phys.* **25** 103
Gradshteyn I S and Ryzhik I M 1965 Tables of integrals series and products (New York: Academic Press)
Harris E G 1961 *J. Nucl. Energy* **C2** 138
Himmell L C 1971 *Phys. Fluids* **14** 1419
Landau R W and Cuperman S 1971 *J. Plasma Phys.* **6** 495
Montgomery D C and Tidman D A 1964 *Plasma kinetic theory* (New York: McGraw-Hill)
Pearlstein L D, Rosenbluth M N and Chang D B 1966 *Phys. Fluids* **9** 953
Rosenbluth M N and Post R F 1965 *Phys. Fluids* **8** 547
Stix T H 1962 *The theory of plasma waves* (New York: McGraw-Hill).

Pramāṇa, Vol. 21, No. 1, July 1983, pp. 11–27. © Printed in India.

Spin structure of nucleon

R RAMACHANDRAN
Department of Physics, Indian Institute of Technology, Kanpur 208 016, India

MS received 11 March 1983

Abstract. The quark spin content of the nucleons is subjected to constraints implied by sum rules due to global approximate chiral symmetries and perturbative QCD effects. The model, so obtained, has a large polarisation residing in the flavour singlet constituents of hadron. Predictions for the expected longitudinal and transverse spin asymmetries in deep inelastic lepton-nucleon scattering are made on the basis of the standard form of the electromagnetic and charged weak currents.

Keywords. Perturbative QCD; spin structure; partons; sea and gluon polarisation; longitudinal and transverse spin asymmetries.

1. Introduction

The main experimental support for quantum chromodynamics comes from the study of nucleon structure function, revealed in deep inelastic lepton-nucleon scattering. (For a review see Buras 1980). The Q^2-dependances of $F_2^{em}(x, Q^2)$, $F_2^{\nu}(x, Q^2)$ and $F_3^{\nu}(x, Q^2)$ have confirmed the leading order predictions. The next to leading order, however, depends on the details of the renormalisation prescription and for every process there is an optimum scheme for which the prediction is unique and agrees with the experimental values. This state of affairs encourages one to expect that the spin dependant structure functions of nucleon $G_1(x, Q^2)$ and $G_2(x, Q^2)$, studied by observing the polarisation asymmetries, will satisfy the expected scaling properties and appropriate scaling violations, further confirming QCD.

The quark distribution and the internal spin structure of the nucleons are, *per se*, non-perturbative aspects of QCD and, as of now, there exists no procedure for calculating them from first principles. Nevertheless, we should expect that they are governed by the constraints imposed by the flavour symmetries (such as isospin, SU (3) etc., the origins of which can be traced to the small symmetry breaking quark masses, compared to the intrinsic scale Λ of QCD), current algebra (such as Björken sum rule, which is a consequence of the approximate chiral symmetry (Björken 1970)) and such other dynamical restrictions as implied by general principles like Regge behaviour etc. In this paper, we use the various constraints and clues to arrive at the form of the spin structure of the nucleon and translate the same into expected asymmetries in the lepton-nucleon scattering. In particular we will emphasize the constraints implicit in the leading order (Q^2) evolution of the structure functions (Bajpai and Ramachandran 1980) and the experimental signals in which the effects may become observable.

2. Basic model

The spin-dependant part of the electroproduction ($e + p \to e + X$) may be expressed in terms of the antisymmetric tensor

$$W_{\mu\nu}^{(\text{spindep.})} = (1/2\pi) \int d^4\, \zeta \exp(iq.\zeta) \langle p, s \mid [J_\mu(\zeta), J_\nu(0)] \mid p, s \rangle$$

$$= \epsilon_{\mu\nu\lambda\sigma} \frac{q^\lambda}{(p.q)} \{ s^\sigma G_1(x, Q^2) + [1/(p.q)]\, s^\sigma (p.q)$$

$$- (q.s)\, p^\sigma]\, G_2(x, Q^2) \} \tag{1}$$

where x is the scaling variable $Q^2/2(q.p)$ and $Q^2 = -q^2$. Since in longitudinally polarised spin-dependent experiments s is parallel to p, $G_2(x, Q^2)$ does not contribute. Thus $G_2(x, Q^2)$ will arise only in the transverse polarisation measurements. In quark-parton model, we expect scaling and the scaled function ($M^2 \nu G_1(x, Q^2) \xrightarrow[Q^2 \to \infty]{} g_1(x)$) measures the spin structure of the quarks that make up the hadron. It is possible to identify $g_1(x)$ with spin structure through

$$2 g_1(x) = \sum_i e_i^2 (\Delta q_i + \Delta \bar{q}_i) \tag{2}$$

where the subscript refers to the various flavours of quarks and $\Delta q_i \equiv q_i^+(-q_i^-), q_i^\pm(x)$ is the probability of finding a quark with flavour i of $\pm$ helicity in the positive helicity hadron (here proton) carrying a longitudinal momentum fraction x of the hadron, when measured in an infinite momentum frame. The Q^2 -dependance of $g_1(x, Q^2)$ (and hence that of $\Delta q_i(x, Q^2)$) is determined by the use of an operator product expansion and the renormalisation of the relevant operators introduces appropriate $\ln Q^2/Q_0^2$ dependance determined by the anomalous dimensions of the operators thereof (Politzer 1974). More intuitively Altarelli-Parisi equations (Altarelli and Parisi 1977) can be set up to give a set of coupled integro-differential equations. The role of anomalous dimensions is played here by the convolution of the probability $p(z)$ of finding a parton (quark or gluon) within another carrying a definite momentum fraction (z) of the former per unit interval of t ($\equiv \ln Q^2/Q_0^2$). These coefficients can be read off from the basic vertices of QCD in the leading order and in principle to any order.

It is convenient to split $\Delta q_i(x, Q^2)$ into a valence part and a sea part and work with the moments, defined through

$$\Delta q_i^{v,n} \equiv \int_0^1 dx\, x^{n-1} [\Delta q_i(x, Q^2) - \Delta \bar{q}_i(x, Q^2)], \tag{3}$$

$$\Delta q_i = \Delta q_i^v + \Delta q_{i0}. \tag{4}$$

The moments of the valence part satisfies a first order equation in t:

$$\frac{\mathrm{d}}{\mathrm{d}t}\Delta q_i^{v,n} = (\alpha_s(t)/2\pi)\ \tilde{A}_{qq}^n\ \Delta q_i^{v,n};\quad \alpha_s(t) = \alpha_s(0)/(1+b\ \alpha_s(0)\ t) \tag{5}$$

which can be solved to give

$$\Delta q_i^{v,n}(t) = \Delta q_i^{v,n}(0)\ [\alpha_s(0)/\alpha_s(t)]^{\tilde{A}_{qq}^n/2\pi b} \tag{6}$$

The $n = 1$ moment, which measures the net difference in the number of quarks with $+$ and $-$ helicities in a positive helicity hadron, is t-independent, since $\tilde{A}_{qq}^1 = 0$ in the leading order. In proton, $\Delta q_u^{v,1}$ and $\Delta q_d^{v,1}$ will be some fixed number. To determine this value, we appeal to various aspects of flavour symmetry. If the proton is described by an SU(6) wave function for its constituent valence quarks (Kuti and Weisskopf 1971) then we will have

$$\Delta q_u^{v,1} = 4/3,\quad \Delta q_d^{v,1} = -1/3. \tag{7}$$

together with the unwanted consequence of $(G_A/G_V)_{p\to n} = 5/3$ Sehgal (1974) uses, instead, Björken sum rule for G_A/G_V:

$$\Delta q_u^{v,1} - \Delta q_d^{v,1} = (G_A/G_V)_{p\to n}. \tag{8}$$

and the experimental value for G_A/G_V ($\simeq 1{\cdot}25$), together with a similar relation for $(\Xi^- \to \Xi^0)$ β decay transition connected by the flavour SU(3) symmetry to give

$$\Delta q_u^{v,1} = 0{\cdot}97,\quad \Delta q_d^{v,1} = -0{\cdot}28. \tag{9}$$

In contrast, Carlitz and Kaur (1977) propose that the valence quark spin is governed by Feynman's leading quark hypothesis and most of the momentum and helicity is carried by the 'leading quark' in the hadron (Kaur 1977). Accordingly

$$\Delta q_u^v(x) = \cos 2\,\Theta(x)\ [q_u^v(x) - 2/3\ q_d^v(x)], \tag{10}$$

$$\Delta q_d^v(x) = -(1/3)\cos 2\,\Theta(x)\ q_d^v(x), \tag{11}$$

with
$$\cos 2\,\Theta(x) = [1 + 0{\cdot}052\ (1-x^2)/\sqrt{x}]^{-1} \xrightarrow[x\to 1]{} 1. \tag{12}$$

This parametrisation implies, since $\cos 2\,\Theta(x)$ rapidly approaches unity (as $x \to 1$) and $q_u^v(x)$ dominates over $q_d^v(x)$ at large x, that the valence u-quarks in this region of x, have their spins aligned almost fully along the proton spin. The first moment—the net number of valence spin—is, however, not very different from the values in (7) or (9). Typically they are $\Delta q_u^{v,1} = 1{\cdot}01$ and $\Delta q_d^{v,1} = -0{\cdot}25$. Since this model

appears to be in general agreement with the phenomenology at large x, we will henceforth treat the valence spin to be given by (10)–(12) in our analysis.

We now turn to the analysis of the flavour singlet parts, which includes $\sum_{i=1}^{2f} \Delta q_i$, the combination that sums over the valence and the sea quarks of all flavours and $\Delta G \equiv G^+(x, Q^2) - G^-(x, Q^2)$ where $G^{\pm}(x, Q^2)$ denote the gluon distribution in the proton. The QCD evolution equations for them are given by:

$$\frac{\mathrm{d}}{\mathrm{d}t}\sum_i \Delta q_i^n(t) = (\alpha_s(t)/2\pi)\left[\tilde{\mathrm{A}}_{qq}^n \sum_i \Delta q_i^n(t) + 2f\,\tilde{\mathrm{A}}_{qG}^n\,\Delta G^n(t)\right] \tag{13}$$

$$\frac{\mathrm{d}}{\mathrm{d}t}\Delta G^n(t) = (\alpha_s(t)/2\pi)\left[\tilde{\mathrm{A}}_{Gq}^n \sum_i \Delta q_i^n(t) + \tilde{\mathrm{A}}_{GG}^n\,\Delta G^n(t)\right] \tag{14}$$

Since the anomalous dimensions $(\tilde{A}^n/2\pi b)$ are known constants in QCD to any desired order, the above equations are solved easily to give the Q^2 dependance of the moments and hence that of the structure functions. For $n = 1$, since $\tilde{A}_{qq}^n = 0$ and $\tilde{A}_{qG}^n = 0$ in the leading order, this suggests Δq_i^1 for each i is constant independent of Q^2. This then means that the net difference of quarks with either helicity for each flavour is constant. When this equation is taken together with the conservation of angular momentum (*i.e.* the proton spin $\frac{1}{2}$ is made up of the quark and gluon spin, together with the negligible orbital angular momentum), we are led to the equation (Bajpai and Ramachandran 1980)

$$\sum_i \Delta q_i^1 + \Delta G^1 = \tfrac{1}{2}, \tag{15}$$

the Q^2 independence of which leads to, using (14)

$$\tilde{A}_{Gq}^1 \sum_i \Delta q_i^1 + \tilde{A}_{GG}^1\,\Delta G^1 = 0. \tag{16}$$

Solving these equations, we obtain (with $\tilde{A}_{Gq}^1 = 2$ and $\tilde{A}_{GG}^1 = (33 - 2f)/6$ where f is the number of flavours)

$$\sum_i \Delta q_i^1 = (33 - 2f)/(9 - 2f) \text{ and } \Delta G^1 = -12/(9 - 2f) \tag{17}$$

We notice two features of these equations: (i) They are rather large ($f = 3$, 4 or 5 for example) compared to the valence spin, obtained in the various models (ii) As one crosses the flavour thresholds, there is an accompanying large jump in the value of net quark spin (which resides mostly among the sea quarks) and gluon spin. These conclusions are not altered even if we consider some moderate contributions of orbital

angular momentum*. We should expect, therefore, observable experimental signals, related to these effects.

3. Longitudinal asymmetries

The longitudinal asymmetries in $\vec{e}\,\vec{p}$ scattering (the arrow on top of e and p imply polarisation of the same), measuring

$$A = \frac{d\sigma(\uparrow\downarrow) - d\sigma(\uparrow\uparrow)}{d\sigma(\uparrow\downarrow) + d\sigma(\uparrow\uparrow)}$$

is related to the function $g_1(x, Q^2)$ through

$$A(x, Q^2) = \frac{2x g_1(x, Q^2)}{F_2(x, Q^2)} A_{eq}, \tag{18}$$

where A_{eq} is some known kinematical factor. $A(x, Q^2)/A_{eq}$ is referred to as the longitudinal asymmetry function, $A_{LL}(x, Q^2)$ in the literature. Thus, explicitly

$$A_{LL}(x, Q^2) = \sum_i e_i^2 (\Delta q_i + \Delta \bar{q}_i) \Big/ \sum_i e_i^2 (q_i + \bar{q}_i) \tag{19}$$

For $\vec{e}\,\vec{p}$ longitudinal asymmetry

$$A_{LL}^p(x, Q^2) = \frac{\frac{4}{9}\Delta q_u^v + \frac{1}{9}\Delta q_d^v + \sum e_i^2 \Delta q_{i0}}{\frac{4}{9} q_u^v + \frac{1}{9} q_d^v + \sum e_i^2 q_{i0}} \tag{20}$$

The parametrisations used to obtain the plot for A_{LL}^p given in figure 1 are summarised in table 1. We use the CDHS analysis of the unpolarised deep inelastic muon scattering data (de Groot *et al* 1979; Falciano 1981). For the spin structure, the valence spin is given by Carlitz-Kaur model (equations (10) to (12)) and the

*If the orbital angular momentum is considered, the essential conclusions of large singlet polarisation persists with a modulating factor

$$\left[1 - 2\langle L_z\rangle + \frac{24\pi}{\alpha_s}\frac{1}{(33-2f)}\langle \dot{L}_z\rangle\right]$$

for $\sum_i \Delta q_i^1$ and a factor

$$[1 - 2\langle L_z\rangle + (\pi/\alpha_s)\langle \dot{L}_z\rangle]$$

for ΔG^1. It is not possible to determine these factors from first principles. However we may estimate it as follows: We may expect $\langle L_z\rangle \sim \langle \vec{r} \times \vec{p}\rangle_z$ to be of order $\langle p_T\rangle$, primordial average transverse momentum and from the leading 2nd order QCD $\langle p_T\rangle \sim (\alpha_s Q^2)^{1/2} = \sqrt{\alpha_s}\, Q_0\, e^{t/2}$ and thus $\langle dL_z/dt\rangle \sim \frac{1}{2}\langle L_z\rangle$. It is observed that $\langle dL_z/dt\rangle$ and $\langle L_z\rangle$ are of the same sign and hence tend to neutralise each other in the modulating factors. Even for a substantial magnitude of $\langle L_z\rangle \sim 0{\cdot}1$ (which is 20% the angular momentum of proton) the modulating factor is about 1·5, implying an enhancement of our conservative values. In summary, it is unlikely that these factor will so conspire as to nullify the large polarisation structure implied here.

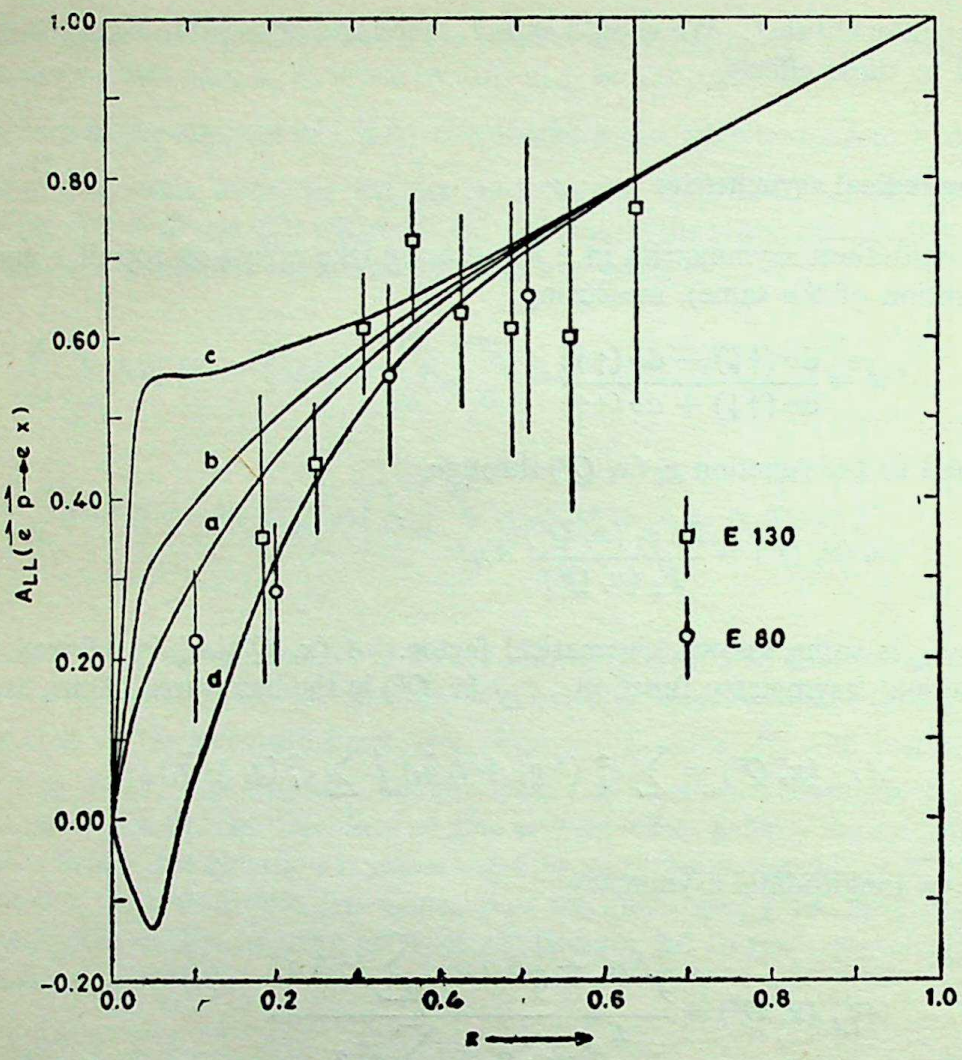

Figure 1. Longitudinal asymmetry $A_{LL}(\vec{e} + \vec{p} \to e + X)$ vs $x(= Q^2/2M\nu)$ the scaling variable. Theoretical predictions give the curve marked **a** when sea polarisation is negligible, and the curves **b d** when 3, 4 and 5 flavours are excitedrespectively. Parametrisation used are as given in table 1 for the unpolarised structure functions and as in equations (10), (11) and (22) with ϵ chosen as 0·05 in all computations. Data refer to the only available results from SLAC-Yale experiments (Alguard *et al* 1976, 1978 (E-80) and Baum *et* al 1982 (E-130).

Table 1. CDHS parametrisation of unpolarised structure functions.

Structure functions	CDHS parametrisation
$q_u^v(x, Q_0^2)$	$2{\cdot}13\,(1-x)^{2.8}/x^{1/2}$
$q_d^v(x, Q_0^2)$	$1{\cdot}21\,(1-x)^{3.8}/x^{1/2}$
$\sum_i q_{0i}(x, Q_0^2)$	$0{\cdot}27\,(1-x)^8/x$

flavour singlet sea quarks must satisfy constraints implied by (17). If the sea polarisation derives equal contribution from u, d and s flavours, then we have

$$\Delta q_0^1 = [(33 - 2f)/(9 - 2f - 0{\cdot}76)]/6. \tag{21}$$

For the x-dependance, while the sea quarks distribution $q_0(x)$ has the form $(1-x)^8/x$ indicating the presence of wee partons (peaking for small x), we may expect the spin structure to be given by

$$\Delta q_0(x, Q^2) = c\, x^\epsilon\, q_0(x);\ \epsilon > 0, \tag{22}$$

where for a given ϵ, c is obtained by the constraint (21). Further, since for all values of x, $|\Delta q_0(x)|/q_0(x) \leqslant 1$ and hence all moments satisfy $|\Delta q_0^n|/q_0^n \leqslant 1$ we find that $\epsilon <$ (0·14, 0·07 and 0·07) for 3, 4 and 5 flavours respectively for the parameters employed*.

Shown in figure 1 are the predicted curves for longitudinal asymmetry A_{LL}, demonstrating the effect of sea polarisation at small x region, when 3, 4 or 5 flavours are excited. The magnitude and the sign of the deviation from the 'no sea' parametrisation may be observed as also the comparison with results from E80 and E130 Yale-SLAC polarised $\vec{e}\ \vec{p}$ scattering experiments (Alguard *et al* 1976, 1978; Baum *et al* 1980; Oppenheim 1982). Our predictions may also be compared with those of other existing model (not shown in the figure), such as (i) SU(6) prediction (Kuti and Weisskopf 1971) (ii) various different parametrisation of valence quark spin structure (Close 1974; Look and Fishbach 1977; Sehgal 1974; Carlitz and Kaur 1977; Jaffe 1975) and (iii) other unorthodox models like source theory (Schwinger 1977) and Fire strings (Preparata 1981). For a recent summary see Bjorken 1982.

3.1 A_{LL}^N, *longitudinal asymmetry in* $\vec{e}\ \vec{N} \to e\ X$

There are, as of now, no measurements of asymmetry for scattering off neutron. However, such information is needed in order to verify Björken sum rule, which has been an ingredient in our parametrisation. To determine the neutron spin structure, it will be appropriate to measure the asymmetry parameters off an isoscalar target. There is currently a proposal (E = 138, SLAC) which aims to achieve this. The asymmetry, expected is

$$A_{LL}^N(x, Q^2) = \frac{(5/18)(\Delta q_u^v + \Delta q_d^v) + \sum_i e_i^2\, \Delta q_{0i}}{(5/18)(q_u^v + q_d^v) + \sum e_i^2\, q_{0i}}. \tag{24}$$

Figure 2 gives the plot for $A_{LL}^N(x)$, using the same set of parameters, as employed to predict A_{LL}^p. From this it is straightforward to extract the structure functions $g_1^p(x)$

*Alternatively the spin structure may behave similar to the valence quark structure near $x = 0$ as dictated by the usual Regge behaviour of the spin flip amplitudes. (Recall as $x \to 0$, $\nu \to \infty$ implies finite Q^2 Regge kinematical region; $1/\sqrt{x}$ form is related to $\nu^{\alpha(0)}$, with Regge intercept $\alpha(0) = \frac{1}{2}$. We then, may make an ansatz

$$\Delta q_0 \simeq c'\,(1-x)^p/\sqrt{x} \tag{23}$$

In order that (21) is satisfied and at the same time $|\Delta q_0^n|/q_0^n \leqslant 1$ is maintained, we find $p > 66$ for $f = 4$. This implies a sharply falling function for Δq_0 and because of the kinematical zero present in the asymmetry function at $x = 0$, experimentally this parametrisation is indistinguishable from $\Delta q_0 = 0$. (*i.e.* no polarisation in the sea).

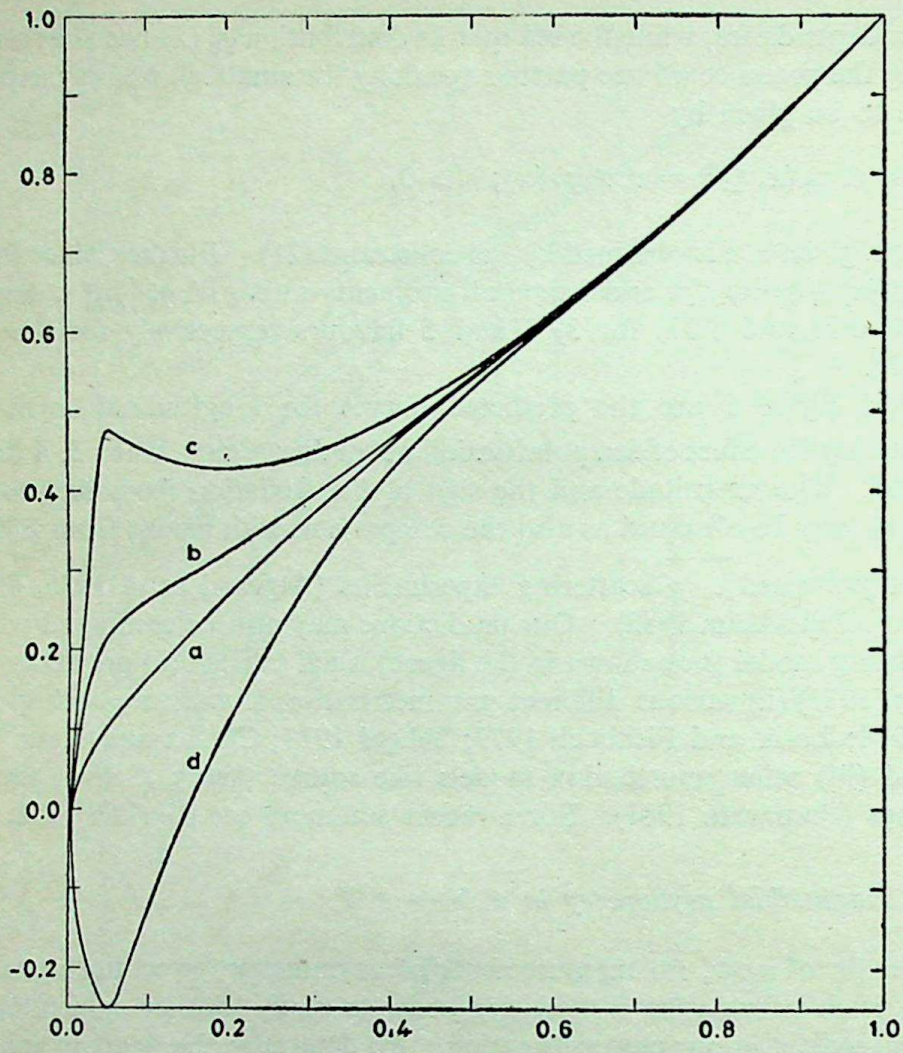

Figure 2. A_{LL} $(\vec{e} + \vec{N} \to e + X)$ vs x. **a-d.** refer to the same set of parameters as in figure 1.

and $g_1^n(x)$ and verify the Björken sum rule, which is a consequence of chiral symmetry, implicit in QCD, to the extent we may ignore quark masses:

$$\int_0^1 [g_1^p(x) - g_1^n(x)] = \frac{1}{6}(\Delta q_u^{v,1} - \Delta q_d^{v,1}) = \frac{1}{6}(G_A/G_V)_{p \to n} \tag{25}$$

Carlitz-Kaur parametrisation for the valence spin structure ensures that the sum rule is satisfied and thus any deviation of the experimental evaluation of the sum rule is attributable to the QCD non-leading correction, for which there is now an estimate. It is, however, more significant to test the sum rule of $g_1^p(x)$ and $g_1^n(x)$ separately. In our model, we expect

$$\int_0^1 g_1^p(x)\,dx = \tfrac{1}{2}\,[4/9\,\Delta q_u^{v,1} + 1/9\,\Delta q_d^{v,1} + \Sigma\, e_i^2\,\Delta q_{i0}^1]$$

$$= 0{\cdot}21 + \begin{Bmatrix} 1{\cdot}26 & 3 \text{ flavours} \\ 3{\cdot}36 & 4 \text{ flavours} \end{Bmatrix}, \tag{26}$$

and $$\int_0^1 g_1^n(x)\,dx = \tfrac{1}{2}\,[4/9\,\Delta q_d^{v,1} + 1/9\,\Delta q_u^{v,1} + \Sigma e_i^2\,\Delta q_{i0}^1]$$

$$= 0{\cdot}001 + \left\{\begin{matrix} 1{\cdot}26 & 3 \text{ flavours} \\ 3{\cdot}36 & 4 \text{ flavours}\end{matrix}\right\}. \tag{27}$$

The terms in the curly brackets arise from the large sea polarisation, coming mostly from the experimentally insensitive small x-region. While a direct experimental confirmation of the presence of large values of the integrals should be the main evidence for large sea polarisation effects, it should be recognized that this is concentrated in a kinematical region, hard to reach and the structure function extracted is expected to have large uncertainties in this region.

4. Transverse spin in nucleon

Transverse polarisation of the electron and proton in $\vec{e}\,\vec{p} \to e + X$ measures in addition to $g_1(x)$ the function $g_2(x)$ $(= \underset{Q^2\to\infty}{\text{Lt}}\ M\nu^2\, G_2\,(x, Q^2))$. In parton model the combination $g_1(x) + g_2(x)$ is equal to $k_+(x) - k_-(x)$, where $k_\pm(x)$ is the probability (weighted by the (charge)^2 of the quark) of finding a quark of spin up (down), with a momentum function x in the infinite momentum frame in a proton or neutron spinning up (perpendicular to the infinite momentum). When the quark is moving rapidly ($x \gg 0$), then we expect it to be spinning along the direction of momentum, which implies that $k_+(x) \simeq k_-(x)$. Thus

$$g_1(x) + g_2(x) = 0,\ x \gg 0. \tag{28}$$

The longitudinal asymmetry, we have already seen, is governed by the function $g_1(x)$ and its magnitude and the ln Q^2 dependance are governed by the relevant twist-2 operator of the symmetry type (bilinear in quark) $O^{\lambda,\,\mu_1,\,\mu_2,\ldots,\,\mu_{n-1}}$ (traceless symmetric in all indices). It can be shown that the operator of the symmetry type $O^{[\lambda,\,\sigma],\,\mu_1,\,\mu_2,\ldots,\,\mu_{n-1}}$ (symmetric in μ's and antisymmetric in λ and σ) dictates the dynamics of the moments:

$$\int_0^1 dx\, x^{n-1}\left\{\frac{n-1}{n} g_1\,(x, Q^2) + g_2\,(x, Q^2)\right\} = M_n\,(Q^2) \tag{29}$$

In contrast to the similar moments of $g_1(x, Q^2)$ which were discussed in §2, the numerical magnitudes of the moments in (29) have been argued to be very small, that we may assume $M_n(Q^2)=0$. (See Wandzura and Wilczek 1977 for the relevant arguments). For large n this is simply the reaffirmation of (28). Further, notice that

$$g_1(x) + g_2(x) = \int_x^1 \frac{dx'}{x'} g_1(x'), \tag{30}$$

solves (29) and thus in terms of the quarks spin distributions

$$\Delta q_i^T(x, Q^2) = \int_x^1 \frac{dx'}{x'} \Delta q_i^L(x)(Q^2). \tag{31}$$

The transverse asymmetries are thus given by

$$A_{NN}(x) = \frac{\int_x^1 dx'/x' \; \Sigma e_i^2 \, \Delta q_i^L(x')}{\int \sum_i e_i^2 \, q_i(x)}. \tag{32}$$

It may be observed that $A_{NN}(x) \to 0$ as $x \to 1$, consistent with the expectation that the transverse polarisation of the hard quarks inside a nucleon should be vanishing. The transverse asymmetries are much smaller than the longitudinal asymmetries and should show sizable enhancements due to large sea polarisation effects at small values of x. Figures 3 and 4 indicate the expected values for $\vec{e}\,\vec{p} \to eX$ and $\vec{e}\,\vec{N} \to eX$ respectively. (For earlier analysis see Hidaka *et al* 1979). These measurements are expected to be made in (E-138) SLAC experiment during 1983.

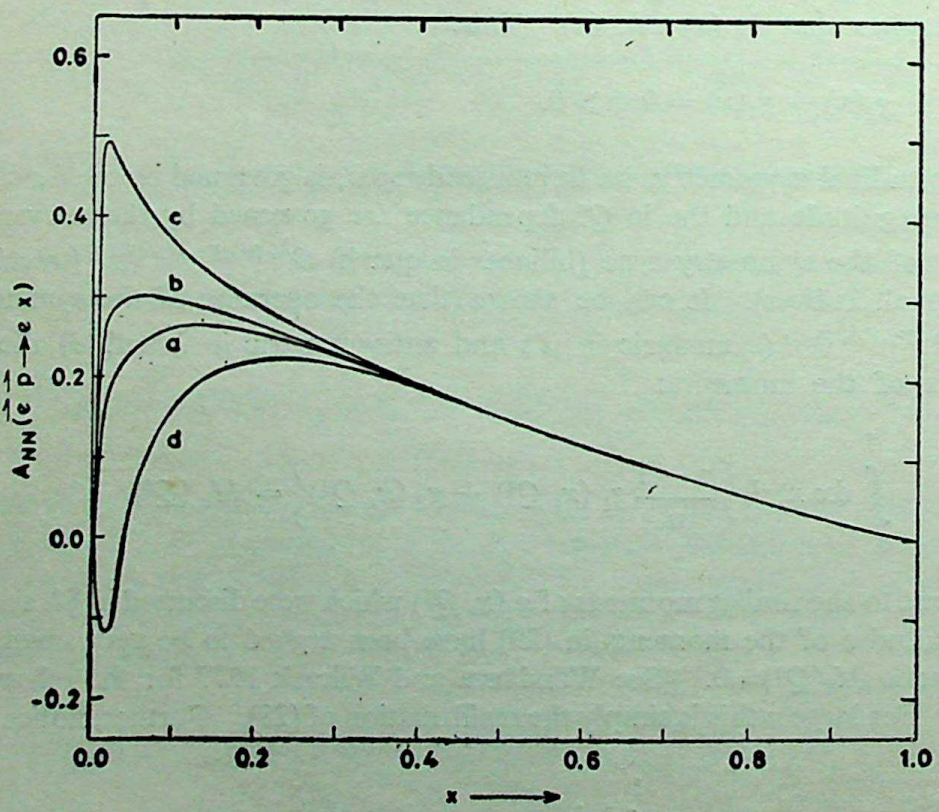

Figure 3. Transverse asymmetry in proton $A_{NN}(\vec{e} + \vec{p} \to e + X)$ vs x.

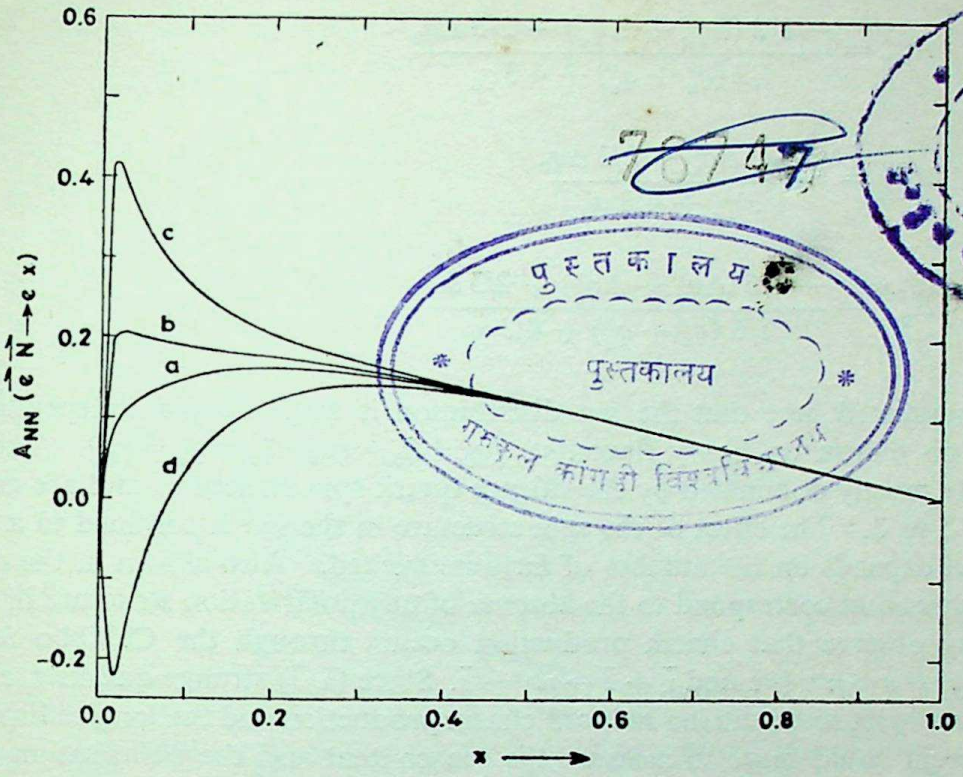

Figure 4. $A_{NN}(\vec{e} + \vec{N} \to e + X)$ vs x.

5. Neutrino induced asymmetries

In the charged current $\nu(\bar{\nu})N$ interactions, the unpolarised inelastic scattering is given by the functions $F_2(x, Q^2)$ and $F_3(x, Q^2)$. The longitudinal spin asymmetry (with target nucleon spin aligned parallel or antiparallel to the $\nu(\bar{\nu})$ spin) is once again given proportional to $g_1(x, Q^2)$. It is easily observed that the asymmetries A_{LL} are given by (with $y = (E' - E)/E$, where E and E' are the energies of $\nu(\bar{\nu})$ and charged lepton respectively):

$$A^{\nu}_{LL}(x, y) = \frac{-\Delta q_d \cos^2\theta - \Delta q_s \sin^2\theta + (1-y)^2 \Delta\bar{q}_u}{q_d \cos^2\theta + q_s \sin^2\theta + (1-y)^2 \bar{q}_u}. \tag{33}$$

and

$$A^{\bar{\nu}}_{LL}(x, y) = \frac{-\Delta q_u (1-y)^2 + \Delta\bar{q}_d \cos^2\theta + \Delta\bar{q}_s \sin^2\theta}{q_u (1-y)^2 + \bar{q}_d \cos^2\theta + \bar{q}_s \sin^2\theta}, \tag{34}$$

where $\cos\theta$ is the Cabibbo angle. $\nu(\bar{\nu})$ acts as a selective probe that measures separately d and $\bar{u}$ (u and $\bar{d}$) content of the hadrons, differentiated by the $(1-y)^2$ dependence of the antiquark (quark) portion. Integrating over the y (range y=0 to 1; the weak y dependance implicit in the ln Q^2 dependence of $q(x, Q^2)$ and $\Delta q(x, Q^2)$ may be ignored), we have for the proton and isoscalar nucleon targets.

$$A^{\nu p}_{LL} = \frac{-\Delta q^v_d \cos^2\theta - 2/3\,\Delta q_0}{q^v_d \cos^2\theta + 4/3\, q_0}, \tag{35a}$$

$$A_{LL}^{\nu N} = \frac{-1/2\,(\Delta q_d^v + \Delta q_u^v) - 2/3\,\Delta q_0}{1/2\,(q_u^v + q_d^v) + 4/3\,q_0} \tag{35b}$$

$$A_{LL}^{\bar{\nu}p} = \frac{-1/3\,\Delta q_u^v + 2/3\,\Delta q_0}{1/3\,q_u^v + 4/3\,q_0} \tag{36a}$$

$$A_{LL}^{\bar{\nu}N} = \frac{-1/6\,(\Delta q_u^v + \Delta q_d^v) + 2/3\,\Delta q_0}{1/6\,(q_u^v + q_d^v) + 4/3\,q_0} \tag{36b}$$

We have assumed here that the sea distribution is SU(3) flavour-independant and contains no charm or heavy flavours. ($q_{0u}=\bar{q}_{0u}=q_{0d}=\bar{q}_{0d}=q_{0s}=\bar{q}_{0s}$). The asymmetries are mostly dominated by the valence quark spin structures and are as shown in figures 5 to 8. The effect of the spin structure in the sea is confined to a small x region and depends on the number of flavours excited. Also shown in the diagram are the curves that correspond to the absence of any polarization structure in the sea.

We may observe that charm production occurs through the Cabibbo favoured processes $\nu + s \to \mu^- + c$ and $\bar{\nu} + \bar{s} \to \mu^+ + \bar{c}$. Since ($s$, $\bar{s}$) strange quarks are part of the flavour singlet sea, neutrino induced charm production and the longitudinal asymmetry therein could serve to measure the sea content and the polarisation thereof. They will have flat y distributions (because there is no admixture of $\nu\bar{q}$ or $\bar{\nu}q$

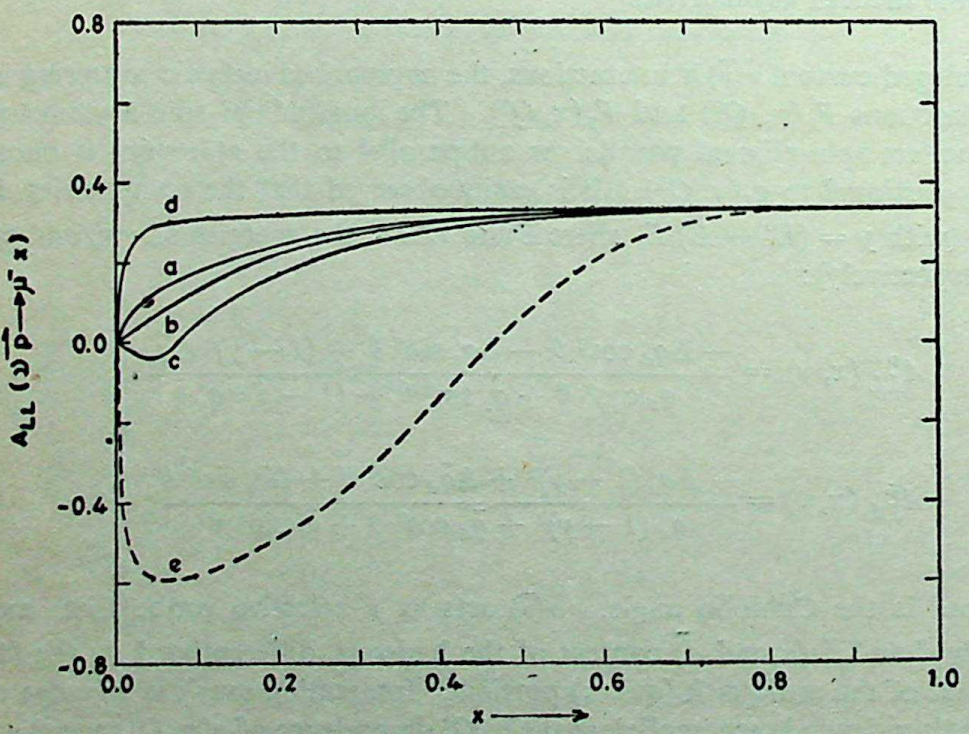

Figure 5. ν-induced longitudinal asymmetry. $A_{LL}\,(\nu + \vec{p} \to \mu^- + X)$ vs x. **a-d.** refer to the same parametrisation as in figure 1. **e.** (. .) is the prediction when charmed particle is produced in the final state ($A_{LL}\,(\nu + \vec{p} \to \mu^- + C + X)$ vs x where C is any charmed hadron.

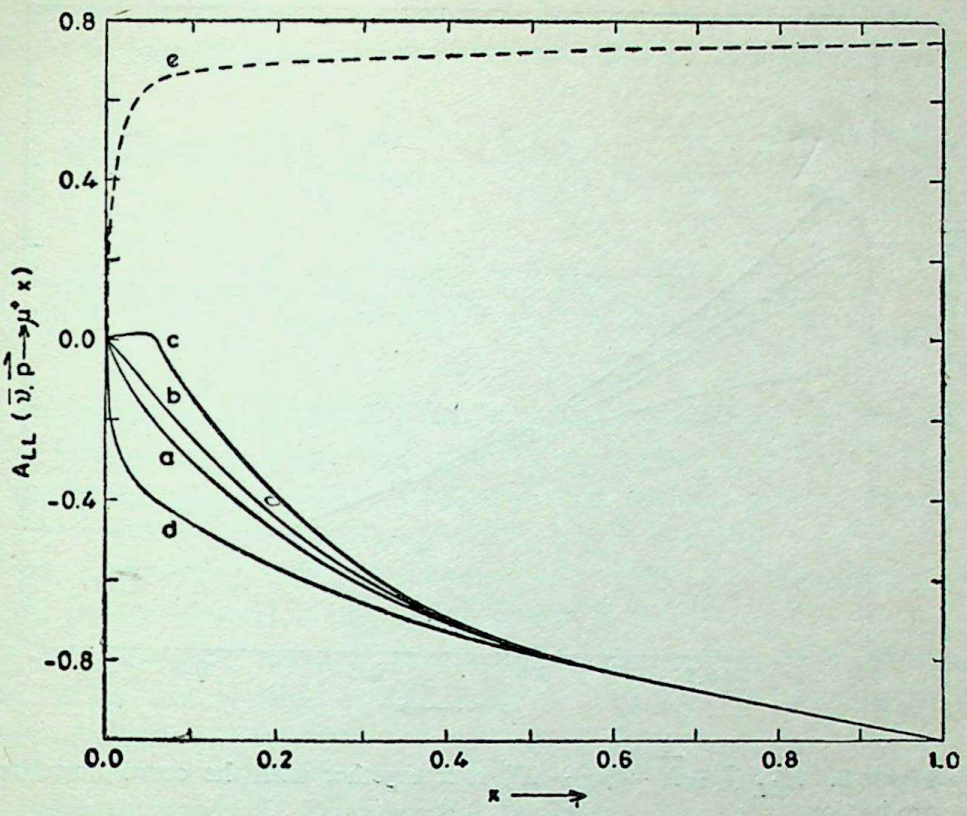

Figure 6. $A_{LL}(\vec{\nu} + \vec{p} \to \mu^- + X)$ vs x together with the curve for related charm production.

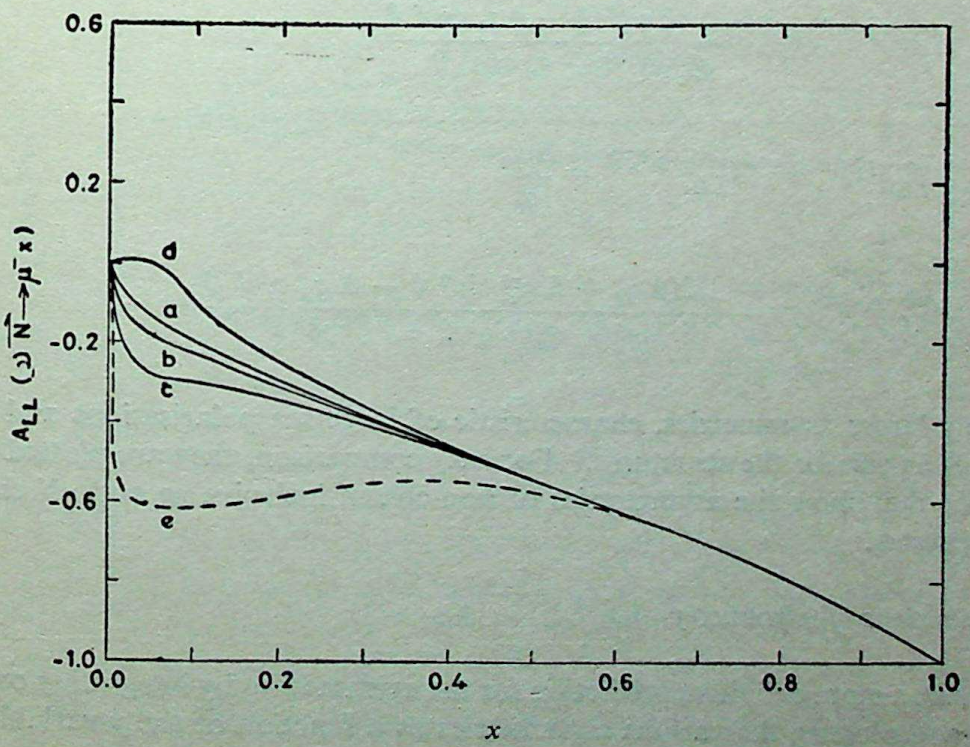

Figure 7. $A_{LL}(\nu + \vec{N} \to \mu^- + X)$ vs x together with the curve for related charm production.

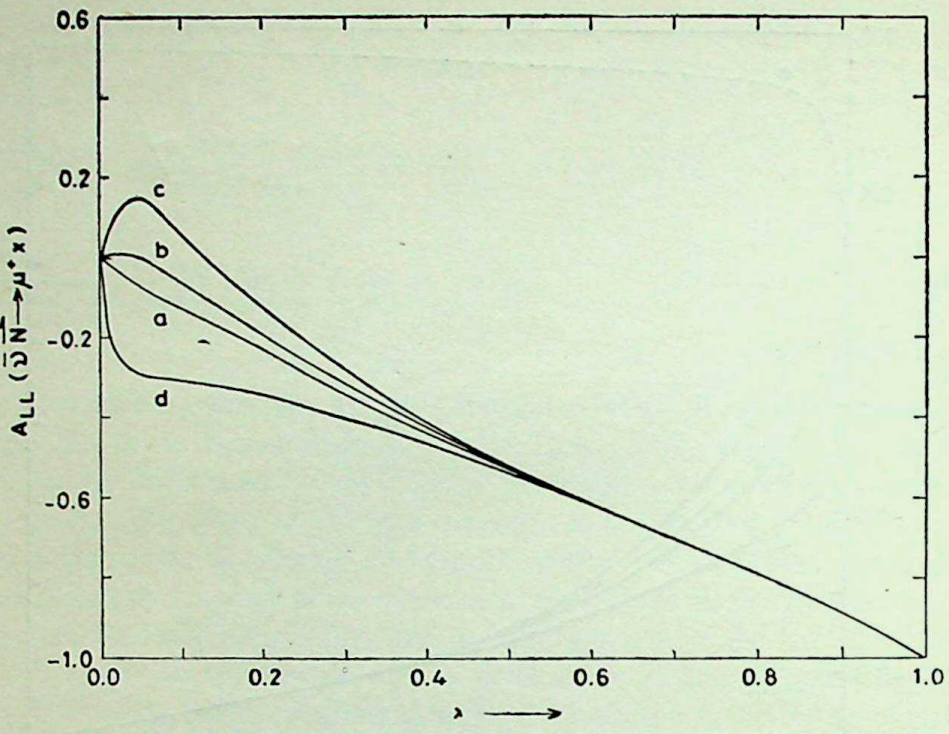

Figure 8. $A_{LL}(\bar{\nu} + \vec{N} \to \mu^+ + X)$ vs x together with the curve for related charm production.

interactions, when we have a charmed quark as a final state) and the predicted asymmetries are:

$$A_{LL}^{\nu p \to \mu^- c X} = \frac{-\Delta q_d^v \sin^2\theta - \Delta q_0 \cos^2\theta}{q_d^v \sin^2\theta + q_0 \cos^2\theta} \tag{37}$$

$$A_{LL}^{\bar{\nu} p \to \mu^+ \bar{c} X} = A_{LL}^{\nu N \to \mu^+ \bar{c} X} = \frac{\Delta q_0}{q_0} \tag{38}$$

$$A_{LL}^{\nu N \to \mu^- c X} = \frac{-1/2(\Delta q_d^v + \Delta q_u^v)\sin^2\theta - \Delta q_0 \cos^2\theta}{1/2(q_d^v + q_u^v)\sin^2\theta + q_0 \cos^2\theta} \tag{39}$$

These imply larger asymmetries, characteristic of large sea polarisations and could provide a clean test for the structures. For easy comparison, they are plotted in the same graphs that show the asymmetries of non-charm inclusive νp and νN charged current processes.

5.1 *y distributions of asymmetry*

We may make a more definitive prediction for the asymmetries by integrating over the x variable and plotting the various asymmetries as a function of the y-variable. In view of the fact that the first moment of the spin structures are given by the constraints on the flavour singlet piece and further are more or less model-independent for the

valence spin, our predictions for y-distributions (which involve the second moments only) should be free from any serious model-dependent ambiguity. We find

$$A_{LL}^{\nu p}(y) = \frac{-\Delta q_d^{v,2}\cos^2\theta + \Delta q_0^2[-1+(1-y)^2]}{q_d^{v,2}\cos^2\theta + q_0^2[1+(1-y)^2]} \tag{40}$$

$$A_{LL}^{\bar{\nu}p}(y) = \frac{-(1-y)^2\Delta q_2^{v,2} + \Delta q_0^2[1-(1-y)^2]}{(1-y)^2 q_u^{v,2} + q_0^2[1+(1-y)^2]}. \tag{41}$$

Similar expressions for $A_{LL}^{\nu N}$ and $A_{LL}^{\bar{\nu}N}$ can be written by substituting for $\Delta q_u^{v,2}$, $\Delta q_d^{v,2}$; $q_u^{v,2}$ and $q_d^{v,2}$ the average values $1/2(\Delta q_u^{v,2} + \Delta q_d^{v,2})$ and $1/2(q_u^{v,2} + q_d^{v,2})$ respectively. For the parametrisation we have presented, the various second moments are as follows: $q_u^{v,2} = 0{\cdot}233$, $q_d^{v,2} = 0{\cdot}095$, $q_0^2 = 0{\cdot}03$, $\Delta q_u^{v,2} = 0{\cdot}158$, $\Delta q_d^{v,2} = -0{\cdot}029$ and $\Delta q_0^2 = 0{\cdot}007$ (3 flavours), $0{\cdot}020$ (4 flavours) and $-0{\cdot}019$ (5 flavours). The graphs showing the y-dependances of A_{LL} form figures 9 and 10.

For the corresponding charmed particle production by ν and $\bar{\nu}$ beam, there will be flat y-distribution with a value $\mp 0{\cdot}67$ (being $\mp \Delta q_0^2/q_0^2$) if we may ignore the small Cabibbo suppressed contributions.

The neutrino asymmetries, requiring polarised targets are not easily determined with the presently available experimental facilities.

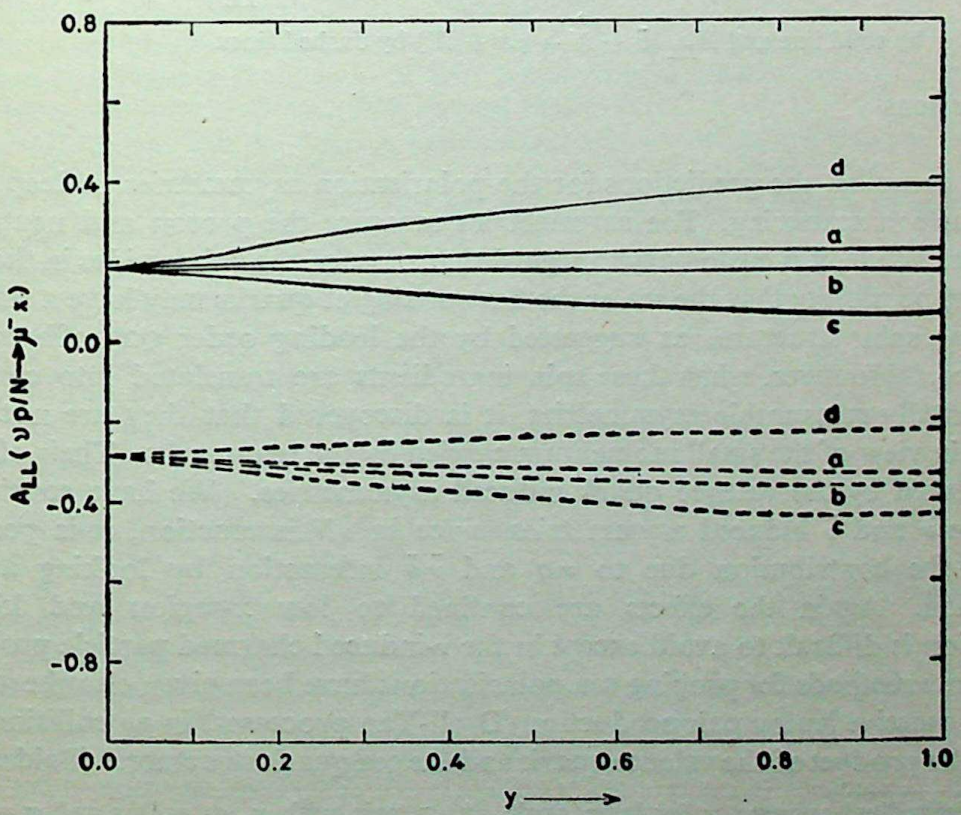

Figure 9. The y-distributions of longitudinal ν-asymmetries: $A_{LL}(\nu + \vec{p} \to \mu^- + X)$ are given by solid lines and $A_{LL}(\nu + \vec{N} \to \mu^- + X)$ by dashed lines. $y = E'/E$, where E and E' are energies of ν and μ respectively.

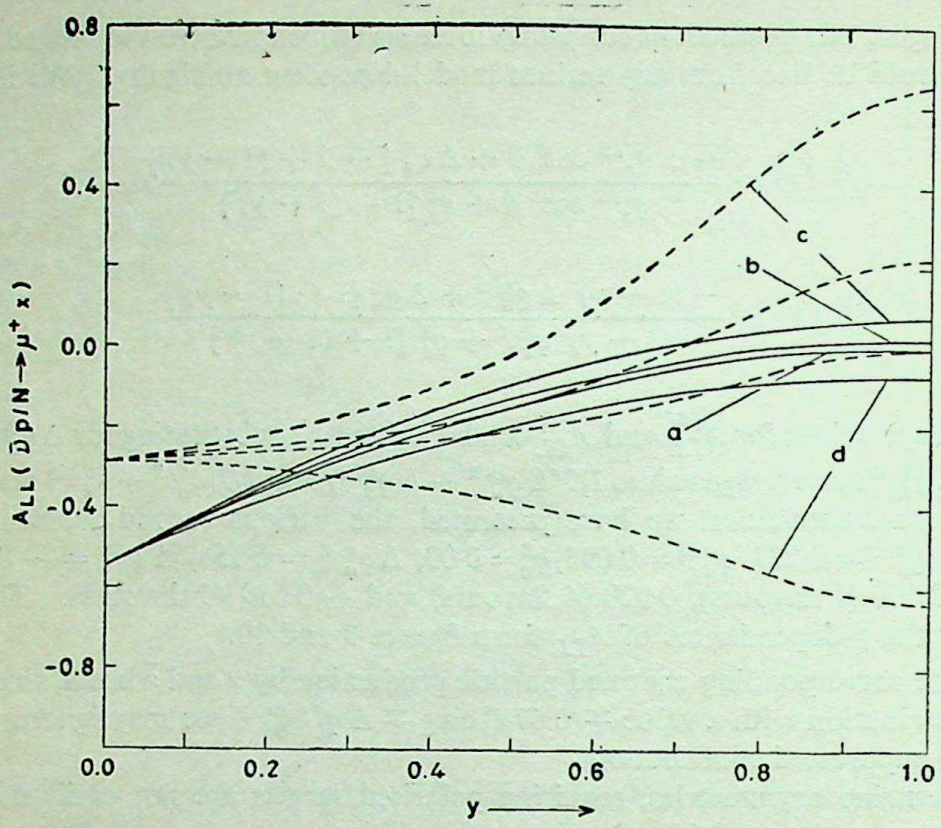

Figure 10. The y distributions for $\bar{\nu}$-asymmetries. $A_{LL}(\bar{\nu} + \vec{p} \to \mu^+ + X)$ is given by solid line and $A_{LL}(\bar{\nu} + \vec{N} \to \mu^+ + X)$ by dashed lines.

6. Conclusions

We have compiled the predictions for the polarisation asymmetries in deep inelastic lepton-nucleon scattering. The asymmetries measure the proton and neutron spin structures. While, it is customary to regard that most of the spin resides in the valence quark, the possibility that the sea or the flavour singlet quarks may have a substantial non-trivial spin structure, as suggested by the leading order QCD effects is also considered. However, when these spin ingredients are translated into consequent experimentally measurable asymmetries, it is discovered that they are not easy to confirm, in view of the small momentum carried by the sea quarks. Their effects are often masked by the valence quark induced asymmetries. We have considered in detail the ν and $\bar{\nu}$ induced asymmetries, since in νN interaction, it is possible to separate the contribution due to νq and $\bar{\nu}\bar{q}$ interaction by looking at the y-distribution. Again the effects are confined to low x-region and kinematic suppression is difficult to avoid except in the ν-induced charmed particle production.

Alternate methods for probing sea polarisations have been given elsewhere. Asymmetry in massive lepton pair production (Drell-Yan processes) in pp collision probes directly the product of the valence quark and the sea quark structure.* (Baldrachchini

*The longitudinal asymmetry for large angle $\mu^+ \mu^-$ pair with $x_F = p_{\|}/\sqrt{s}$ and $\tau = m_{\mu\mu}/\sqrt{s}$ (where $p_{\|}$ is the longitudinal momentum of $\mu^+ \mu^-$ pair and $m_{\mu\mu}$ is the invariant mass of $\mu^+ \mu^-$ pair) is given by

$$A_{LL}(\tau, x_F) = \frac{\Delta V(x_a, Q^2)\, \Delta q_0(x_b, Q^2) + (x_a \leftrightarrow x_b)}{V(x_a, Q^2)\, q_0(x_b, Q^2) + (x_a \leftrightarrow x_b)}$$

where $V(x_a, Q^2) = 4/9\, q_u^v + 1/9\, q_d^v$, $\tau^2 = x_a\, x_b$ and $x_F = x_a - x_b$

et al 1980). At large momentum transfers, the asymmetries in similar process measure, in addition, gluon spin structure (Bajpai *et al* 1981) and they appear to be quite sensitive to the large polarisation structures in the flavour singlet sector of the nucleon. It is also possible to study the initial state spin structure by looking for the transmitted asymmetries in processes such as $p + p \rightarrow \Lambda + X$. However, since the relevant hard processes involve u and d quarks (in addition to the s-quarks) and further since their fragmentation into Λ_s is not very much less when compared with the fragmentation of s-quark (Ramachandran and Bajpai 1982) the resultant asymmetries are found dominated by the valence spin structure and no reliable information regarding flavour singlet spin structure emerges.

Acknowledgement

The author acknowledges useful discussions with R P Bajpai, M Rafat and H S Mani. He also thanks K S Sateesh for computations.

References

Alguard M J *et al* 1976 *Phys. Rev. Lett.* **37** 1258, 1261
Alguard M J *et al* 1978 *Phys. Rev. Lett.* **41** 70
Altarelli G and Parisi G 1977 *Nucl. Phys.* **B126** 298
Bajpai R P and Ramachandran R 1980 *Phys. Lett.* **B97** 125
Bajpai R P, Noman M and Ramachandran R 1981 *Phys. Rev.* **D24** 1832
Baldrachchini F, Craigie N S, Roberto V and Socolowsky M 1980 *A survey of polarisation asymmetries predicted by QCD*. ICTP preprint IC/80/148
Baum G *et al* 1980 *Proc. 20th Int. Conf. on High Energy Physics at Madison, Wisconsin* July 1980
Björken J D 1970 *Phys. Rev.* **D1** 1376
Björken J D 1982 *Fermilab-conf*-82/65 Thy (to be published in the Proc. 5th Int. Symposium on High Energy Spin Physics at BNL September 1982)
Buras A 1980 *Rev. Mod. Phys.* **52** 199
Carlitz R and Kaur J 1977 *Phys. Rev. Lett.* **38** 673, 1102
Close F 1974 *Nucl. Phys.* **B80** 269
de Groot J G H *et al* 1979 *Phys. Lett* **B82** 456
Falciano S 1981 *Phys. Lett* **B104** 416
Hidaka K, Monsay E and Sivers D 1979 *Phys. Rev* **D19** 1503
Jaffe R 1975 *Phys. Rev.* **D11** 1953
Kaur J 1977 *Nucl. Phys.* **B128** 219
Kuti J and Weisskopf V F 1971 *Phys. Rev.* **D4** 3418
Look G and Fishbach E 1977 *Phys. Rev.* **D16** 211
Oppenheim R 1982 *Proc. 5th International Symposium on High Energy Spin Physics at BNL* September 1982
Politzer H D 1974 *Phys. Rep.* **C14** 1290
Preparata G 1981 *Proc. 4th International Symposium on High Energy Spin Physics at Lausanne* September 1982
Ramachandran R and Bajpai R P 1982 *Phys. Lett.* **B115** 313
Schwinger J 1977 *Nucl. Phys.* **B123** 223
Sehgal L M 1974 *Phys. Rev.* **D10** 1663
Wandzura S and Wilczek F 1977 *Phys. Lett.* **B72** 195

Pramāṇa, Vol. 21, No. 1, July 1983, pp. 29–34. © Printed in India.

Successive approximation to determine rotational temperature

M I SAVADATTI and N N MATH
Department of Physics, Karnatak University, Dharwad 580 003, India

MS received 9 July 1982; revised 2 March 1983

Abstract. A method using successive approximation is developed for determining the rotational temperatures, when the rotational lines are overlapped. The method is applied to CH ($B^2\,\Sigma^- — X^2\,\Pi$) band as a test.

Keywords. Line intensity; Maxwell-Boltzmann distribution; successive approximation; rotational temperature; rotational lines.

1. Introduction

A standard method to determine rotational temperatures from the spectrum of a diatomic molecule is to plot the logarithm of the intensity (I) of rotational lines against E_J, the energy values of the upper state (line intensity graph method) and if the graph is a straight line, the slope yields rotational temperature (Herzberg 1950).

Sometimes the method leads to a nonstraight line graph indicating the possibility of the existence of a non-Maxwellian distribution (Kini and Savadatti 1977; Brennen and Currington 1967; Suzuki and Kuchitsu 1977; Mohl mann *et al* 1976; Oldenberg 1934; Edels 1950; Gorbal and Savadatti 1980; Math 1980) and hence is useful in understanding the mechanisms operating under the prevailing experimental conditions. However, in many experiments involving weak sources it is not feasible to use high resolution to separate all the lines and still have adequate intensity to employ the method in a straightforward way. Quite often one has to deal with experimental situations where a number of lines are overlapped. In such cases the measurements do not normally lead to reliable determination of rotational temperatures. In order to overcome this difficulty a method using successive approximation is developed. This method along with its application to the determination of rotational temperature of CH($B^2\Sigma^- - X^2\,\Pi$) band is described in the following sections.

2. Successive approximation theory

The intensity of a rotational line is represented by (Herzberg 1950)

$$I_{K'K''} = C(\nu)\,\nu^4\,S_{K'K''}\,N_0 \exp\,(-E_{K'}/kT), \tag{1}$$

or

$$\log_{10} I_{K'K''}/S_{K'K''}\,\nu^4 = \text{const} - 0{\cdot}6247 \times E_{K'}/T, \tag{2}$$

where $C(\nu)$ is the instrument constant, ν is the frequency of the transition, $S_{K'K''}$ is the line strength, N_0 is the population in $K' = 0$, $E_{K'}$ is the rotational energy of level K', k is the Boltzmann constant, T is the rotational temperature and 0·6247 is the numerical value of $(hc/k) \log_{10} e$.

If two lines (p and q) overlap and appear as an unresolved or a poorly-resolved line, then the resultant intensity I_{p+q} can be represented as follows:

$$I_{p+q} = I_p + I_q$$

$$= C\, S^p\, \nu_p^4 \exp(-E^p_{K'}/kT) + C\, S^q\, \nu_q^4 \exp(-E^q_{K'}/kT), \tag{3}$$

$C = c(\nu)\, N_0$, S^p and S^q are intensity factors for p and q lines. Since $\nu_p = \nu_q\ (= \nu)$, expression (3) can be rewritten as

$$I_{p+q} = C\, \nu^4 \exp(-E^q_{K'}/kT) \{S^q + S^p \exp(E^q_{K'} - E^p_{K'})/kT\} \tag{4}$$

$$= C\, \nu^4\, X \exp(-E^q_{K'}/kT), \tag{5}$$

where $$X = S^q + S^p \exp(E^q_{K'} - E^p_{K'})/kT. \tag{6}$$

The intensities of unoverlapped lines are initially used and an approximate value of rotational temperature (T_0) is determined using the line intensity graph method (equation (2)). This value of T_0 as well as the relevant values of S^p, S^q (calculated by the formula of Mulliken 1927) and $E^p_{K'}$, $E^q_{K'}$ (approximated as $E_{K'} = B_{v'}\, K'(K'+1)$ where $B_{v'}$ is the rotational constant) are substituted in (6) to obtain X for the observed lines. Using the experimentally measured I_{p+q} and also the I values of unoverlapped lines $\log I/X\nu^4$ is plotted against $E_{K'}$. These points are fitted to a straight line (equation (5)) and from its slope the rotational temperature T_1 is determined. The value of T_1 is substituted back in (6) and the X values are redetermined (say X_1) which are used in (5) to determine the rotational temperature again. If this temperature is T_2, then T_2 is used to determine X_2 using (6) from which T_3 is determined by (5). This procedure is continued till the temperature so determined is not different from the preceding one. The resulting temperature is taken as the true temperature. The method can be extended if more than two lines overlap.

3. Determination of rotational temperature of CH ($B^2\,\Sigma^- - X^2\,\Pi$) band

3.1 *Experimental*

A π type discharge tube with fused tungsten electrodes and the associated vacuum system with provision for metering of gases were fabricated in pyrex glass. CH bands were excited in a condensed discharge through flowing C_2H_2 and C_2H_4. A 15 kV transformer was used to charge 0·005 μF capacitor which discharged *via* a spark gap through the gases in the discharge tube.

The bands were photographed on a Hilger Littrow Quartz Spectrograph using

Ilford R-40 plates and the integrated intensities of the lines were measured using microphotometric technique. A typical microphotometer record of the (0·0) band of CH is shown in figure 1.

3.2 *Results and determination of rotational temperatures*

Figure 1 shows that all the rotational lines are not resolved, and some are overlapped. Therefore, the system has been chosen to apply the procedure as outlined above.

For the (0,0) band the wavelength spread is about 50 Å at 3900 Å; the change in ν^4 is not appreciable and hence is treated as a constant. Table 1 gives the lines used for intensity measurement along with other molecular parameters. The measured intensities of the seven unoverlapped lines were plotted against $E_{K'}$, on a semi-logarithmic plot and T_0 was determined (equation (1)) (see figure 2a). Using T_0 and the calculated S^p and S^q values, X values were determined (equation(6)) which were then used along with measured intensity values for all the lines to determined T_1 (equation (5)) (see figure 2b). Now T_1 was used to redetermine X, (say X_1). This X_1 was used in (5) to determine T_2 which was in turn used to determine X_2. X_2 in turn yielded T_3 which was identical with T_2 in all cases examined and hence no further approxima-

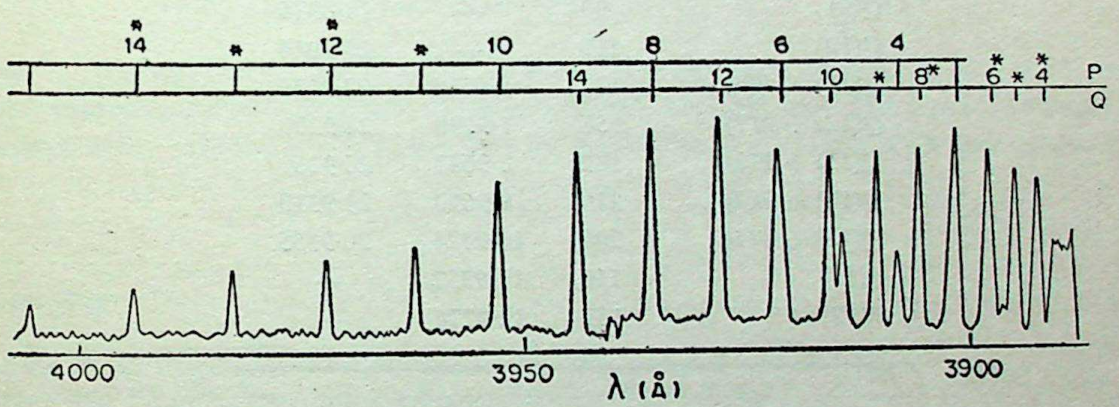

Figure 1. A typical microphotometer record of the 0-0 band of CH ($B^2\Sigma^- - X^2\Pi$). *unoverlapped lines.

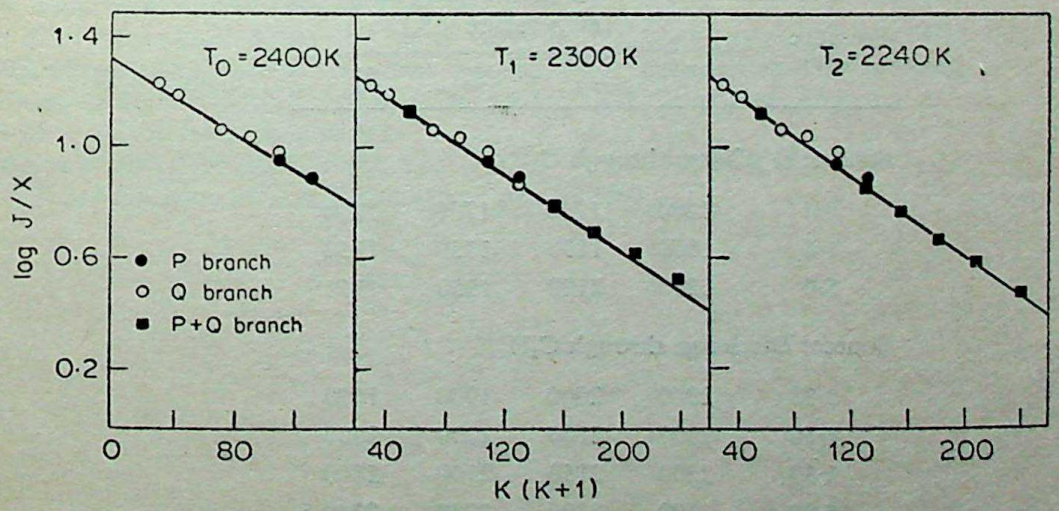

Figure 2. Rotational temperature determination of the 0-0 band of CH ($B^2\Sigma^- - X^2\Pi$) obtained from discharge through C_2H_2 (5·0 torr).

tions were necessary. A similar procedure was used for the CH rotational lines excited under different experimental conditions. In each of these cases there was no need to determine beyond T_3. The different rotational temperature under different experimental conditions reflect the changed experimental conditions and will be analysed in another paper. All these results are collected in table 2.

In order to check the reliability of the method the intensities of these lines are calculated using the determined rotational temperature and the intensity values are reproduced within experimental errors. A typical result of the calculation is gvien in

Table 1. Rotational lines used for measurements and their energy and line strength values.

Rotational lines	$E_{K'}$	Line strengths	
		P	Q
$Q(5)$	30	—	10·8091
$Q(6)$	42	—	12·8431
$Q(7) + P(3)$	56	7·9590	14·8633
$Q(8)$	72	—	16·8812
$Q(9)$	90	—	18·8944
$Q(10)$	110	—	20·9044
$Q(11) + P(6)$	132	6·9510	22·9130
$Q(12) + P(7)$	156	7·9590	24·9200
$Q(13) + P(8)$	182	8·9647	26·9260
$Q(14) + P(9)$	210	9·9690	28·9310
$Q(15) + P(10)$	240	10·9724	30·9355
$P(11)$	110	11·9752	—
$P(12)$	132	12·9774	—

Table 2. Measured rotational temperatures of CH ($B^2\Sigma^- - X^2\Pi$) 0-0 band.

Pressure (torr)	Temperature (°K)			
	T_0	T_1	T_2	T_3
Source: Discharge through C_2H_4				
0·4	1800	1750	1700	1700
1·6	1900	1850	1750	1750
5·0	2200	2100	1950	1950
Source: Discharge through C_2H_2				
0·38	2200	2000	1900	1900
1·50	2300	2100	2000	2000
2·30	2300	2150	2100	2100
5·00	2400	2300	2240	2240

Table 3. Comparison of the measured intensities with calculated ones for the 0-0 band of the $B^2\Sigma^- - X^2\Pi$ system of CH.

Rotational lines	Intensities	
	measured	calculated (at $T = 2240°K$)
$Q(5)$	16·98	17·77
$Q(6)$	19·25	18·93
$Q(7) + P(3)$	26·30	27·74
$Q(8)$	19·50	20·00
$Q(9)$	20·89	19·40
$Q(10)$	19·25	18·18
$Q(11) + P(6)$	25·12	28·05
$Q(12) + P(7)$	26·30	26·75
$Q(13) + P(8)$	23·44	24·37
$Q(14) + P(9)$	22·90	21·85
$Q(15) + P(10)$	20·40	20·40
$P(11)$	10·00	9·49
$P(12)$	9·12	8·70

Condition: C_2H_2 discharge at 5 torr

table 3. Successive approximation method has also been applied to this data using least squares technique, in place of the graphical methods, and this leads to same final temperatures. Hence the method can be used with confidence wherever lines overlap.

References

Brennen W and Carrington T 1967 *J. Chem. Phys.* **46** 7
Edels H 1950 *Br. Elec. Appl. Ind. Res. Assoc. Technol. Rep.* L/T 230
Gorbal M R and Savadatti M I 1980 *J. Quant. Spectrosc. Radiat. Transfer* **24** 471
Herzberg G 1950 *Molecular spectra and molecluar structure. Spectra of diatomic molecules* (New York: Van Nostrand) Vol. 1, Ch. III and IV
Kini K S and Savadatti M I 1977 *J. Phys.* **B10** 1139
Math N N 1980 *Spectroscopic studies of diatomic molecules: Investigation of CH, CD, NH and BH emission band systems in various sources* Ph. D. Thesis, Karnatak University
Mohlmann G R, Beenakker C I M and De Her F J 1976 *Chem. Phys.* **13** 375
Mulliken R S 1927 *Phys. Rev.* **30** 785
Oldenberg O 1934 *Phys. Rev.* **45** 291, 738
Suzuki K and Kuchitsu 1977 *Bull. Chem. Soc. Jpn.* **50** 1905

Pramāṇa, Vol. 21, No. 1, July 1983, pp. 35-39, © Printed in India.

Effect of collision-induced phase-shifts on the line widths and line shifts of CO_2-Ar system

M L KURTADIKAR* and S C MEHROTRA**
Department of Physics, Marathwada University, University Campus, Aurangabad 431 004, India
*Government Polytechnic, Station Road, Aurangabad 431 005, India
**Department of Chemical Physics, University of Kiel, Kiel, West Germany

MS received 19 April 1982; revised 16 May 1983

Abstract. The theoretical calculation of line widths and line shifts for CO_2-Ar system is computed by the Mehrotra-Boggs theory. It is shown for this system that the phase shift effect is very important at large values of $|m|$ where m is the value of rotational quantum number J in the lower vibrational state. It is also pointed out that the Salesky-Korff theory is the same as the Mehrotra-Boggs theory.

Keywords. Collision-induced line shape; phase shift effect; CO_2-Ar system; Mehrotra-Boggs theory.

1. Introduction

The spectral line width and shift parameters of a microwave transition from initial state n to final state m are related to the real and imaginary parts of interruption function S given by

$$S = 1 - T_{nn}\, T^*_{mm} \tag{1}$$

where T is the time development operator which is governed by the time-dependent interaction due to collision between two molecules. The time-development operator T must be solved to get information about the line shape. Since it is not easy to solve the time-dependent Schrödinger equation for two colliding molecules, many approximations have been used. The simplest and the most popular technique for the solution of T is to expand it as

$$T = T_0 + T_1 + T_2 + \ldots . \tag{2}$$

where T_0, T_1, T_2, ... are 0th, 1st, 2nd, ... order terms. It is practical to terminate the series at second order as was done by Anderson (1949). The third order term was also evaluated by Rabitz and Gordon (1970). The main disadvantages of this series are that it is not unitary and it is expected to be accurate only for small intervals of time and for those cases in which the perturbation $V(t)$ is much smaller than the unperturbed Hamiltonian H_0 of the system. So, for the treatment of intermediate interaction where the calculated transition probability is greater than one, the method

is not accurate. For the treatment of strong collisions, the value of the transition probability diverges. Anderson (1949) suggested three approximations for the strong collisions (Tsao and Curnutte 1962).

Another method of expanding the time development operator is in the form (Pechukas and Light 1967)

$$T(t) = \exp\left[A_0 + A_1 + A_2 + \ldots.\right] \tag{3}$$

where $A_0, A_1, A_2 \ldots$ are operators. The expansion is known as the Magnus method. The method has not become popular because it is difficult to evaluate numerically an exponential of the operator.

Murphy and Boggs (1967) have expanded the diagonal element of the time development operator T in exponential form neglecting some terms in the series. This formulation was suitable only for microwave spectral line broadening. Cattani (1972) has formulated a modified Murphy-Boggs theory by combining the treatments of Murphy and Boggs (1967) and Anderson (1949).

Mehrotra and Boggs (1976) treated the expansion of the time development operator in a more general way. They have shown that the Nth term of the time-dependent perturbation theory is

$$T_{nm}^{(N)}(t) = T_{nm}^{(N)}(-\infty) \exp\Big[\int_{-\infty}^{t} \mathrm{d}t_1\, G^{(N)}(t_1)\Big]$$

$$+ \int_{-\infty}^{t} \mathrm{d}t_1 \exp\Big[-\int_{t}^{t_1} \mathrm{d}t_2\, G^{(N)}(t_2)\Big] F^{(N)}(t_1). \tag{4}$$

The functions $G^{(N)}$ and $F^{(N)}$ can be obtained by the following recurrence formulae

$$G^{(N+1)}(t) = \sum_{\beta} G_\beta(t, t_\beta) \exp\Big[-\int_{t_\beta}^{t} \mathrm{d}t_1\, G^{(N)}(t_1)\Big] \tag{5}$$

$$F^{(N+1)}(t) = F(t) - \sum_{\beta} G_\beta(t, t_\beta) \int_{t_\beta}^{t} \mathrm{d}t_1\, F^{(N)}(t_1) \times$$

$$\exp\Big[-\int_{t_\beta}^{t_1} \mathrm{d}t_2\, G^{(N)}(t_2)\Big] \tag{6}$$

with $\quad G^{(1)}(t) = \sum_{\beta} G_\beta(t, t_\beta) \cdot 1$ and $F^{(1)}(t) = F(t)(1 - \delta_{nm})$.

The function $F(t)$ is given as

$$F(t) = \sum_{\alpha=0}^{\infty} (i\hbar)^{-1-\alpha} \sum_{m_1}' \ldots \sum_{m_\alpha}' \exp(i\omega_{nm_1} t)\, V_{nm_1}(t)$$

$$\times \int_{-\infty}^{t} \mathrm{d}t_1 \exp(i\omega_{m_1 m_2} t_1)\, V_{m_1 m_2}(t_1) \ldots \int_{-\infty}^{t_{\alpha-1}} \mathrm{d}t_\alpha$$

$$\times \exp(i\omega_{m_\alpha m} t_\alpha)\, V_{m_\alpha m}(t_\alpha) \tag{7}$$

and $G_\beta(t, t_\beta)$ is an integral operator which is defined as

$$G_\beta(t, t_\beta) f(t_\beta) = (i\hbar)^{-1-\beta} \sum_{m_1}' \ldots \sum_{m_\beta}' \exp(i\omega_{nm_1} t)\, V_{nm_1}(t)$$

$$\times \int_{-\infty}^{t} \mathrm{d}t_1 \exp(i\omega_{m_1 m_2} t_1)\, V_{m_1 m_2}(t_1) \int_{-\infty}^{t_1} \mathrm{d}t_2$$

$$\times \exp(i\omega_{m_2 m_3} t_2)\, V_{m_2 m_3}(t_2) \ldots \int_{-\infty}^{t_{\beta-1}} \mathrm{d}t_\beta$$

$$\times \exp(i\omega_{m_\beta m} t_\beta)\, V_{m_\beta m}(t_\beta) f(t_\beta) \tag{8}$$

where $f(t_\beta)$ is some function of time t_β.

The first order of the theory and neglecting the isotropic part of the potential gives the same expression as obtained by Murphy and Boggs (1967). The first order treatment has been applied to the collision induced line shape (Mehrotra and Boggs 1977) which turns out to be the same as that formulated by Cattani (1972), if the isotropic term in the potential is neglected.

2. Comparison with the Salesky-Korff theory

Salesky and Korff (1979) presented a graphical technique to expand the time development operator in the exponential form. The formulation (Salesky and Korff 1980) seems to be exactly the same as done by Mehrotra and Boggs (1977). Using the first approximation ($N = 1$, in (4)), one can approximate the interruption function $S(b)$ as

$$S(b) = 1 - T_{nn}^{(1)}(+\infty)\, T_{mm}^{(1)*}(+\infty)$$

$$= 1 - \exp[-\tfrac{1}{2}\Gamma_n - \tfrac{1}{2}\Gamma_m]$$

$$\times \exp\left[-\frac{1}{i\hbar}\int_{\infty}^{\infty} (V_{nn} - V_{mm})\,\mathrm{d}t + i(\phi_n - \phi_m)\right].$$

The line width parameter $\Delta\nu$ for the transition $n \to m$ can be written as

$$\Delta\nu = N \sum_{J_2} \rho_{J_2} \int_0^\infty db \int_0^\infty dv\, v f(v) \left[1 - \exp\left(-\tfrac{1}{2}\Gamma_n - \tfrac{1}{2}\Gamma_m\right)\right]$$

$$\times \cos\left(\frac{1}{\hbar}\int_{-\infty}^{\infty} (V_{nn} - V_{mm})\, dt + \phi_n - \phi_m\right) \tag{9}$$

and the line shift parameter $\Delta\nu_s$ is given by

$$\Delta\nu_s = N \sum_{J_2} \rho_{J_2} \int_0^\infty db \int_0^\infty dv\, v f(v) \left[\exp\left(-\tfrac{1}{2}\Gamma_n - \tfrac{1}{2}\Gamma_m\right)\right]$$

$$\times \sin\left(\frac{1}{\hbar}\int_{-\infty}^{\infty} (V_{nn} - V_{mm})\, dt + \phi_n - \phi_m\right). \tag{10}$$

The same expressions for the line width and line shift have been obtained by Salesky and Korff (1980).

3. Discussion of results for CO_2-Ar system

The theory of Mehrotra and Boggs (1977) is applied to CO_2-Ar system. The potential is taken as (Boulet *et al* 1974)

$$V = V_{LJ} + 4\epsilon(\sigma/R)^{12} a_2 p_2(\cos\theta) - 4\epsilon(\sigma/R)^6 b_2 p_2(\cos\theta)$$

where V_{LJ} is the Lennard-Jones potential. The coefficient of $p_1(\cos\theta)$ for the system will not be important because the center of mass of the molecule coincides with its center of charge.

The calculated results are shown in figure 1 along with the experimental results of Boulet *et al* (1974). As pointed out by Boulet *et al* (1974) that a short range anisotropic potential must be introduced in the calculation of the interruption function, the same conclusion is also obtained here. The significant aspect of the results is that the effect of collision induced phase shift (*i.e.* cosine term in (9)) is also very important to explain $|m|$ dependence. Curve (b) of figure 1 is obtained when the cosine term in (19) of Mehrotra and Boggs (1977) is approximated to one as done in the Murphy-Boggs theory. It can also be seen from the curve that the effect of the cosine term is more important for large values of $|m|$ for vibrational-rotational spectral lines. The collision induced line shift is also computed and shown in figure 1 (curve c). The experimental data for shift is not known, but it can be seen that shifts are not negligible and can be measured by the present experimental techniques.

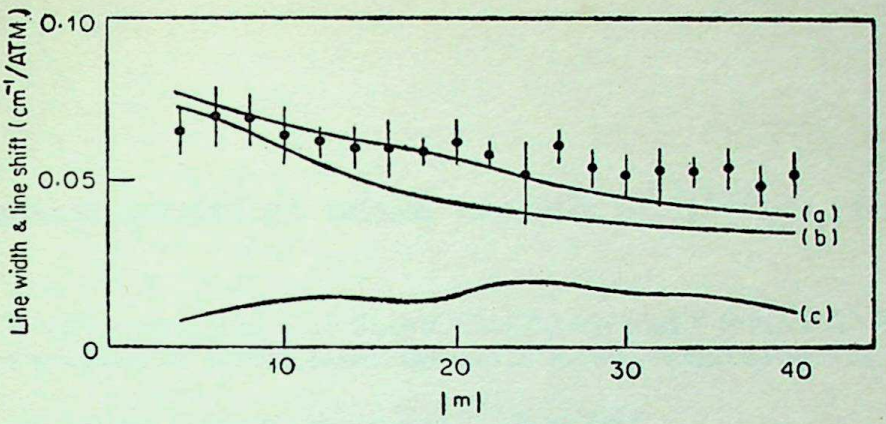

Figure 1. Collision induced line width and line shift in cm^{-1}/Atm for 001—(10°0, 02°0) of CO_2–Ar system *vs* | *m* |. Experimental results (Boulet *et al* 1974); **a.** theoretical results with phase shift; **b.** theoretical results without phase shift; **c.** the calculated values of collision induced line shift. The parameters chosen are $\epsilon = 150{\cdot}00$ °K, $\sigma = 3{\cdot}95$ Å, $a_2 = b_2 = 0{\cdot}27$, $B_0 = 11{\cdot}6139$ GHz, and $B_1 = 11{\cdot}7060$ GHz. B_0 is the rotational constant in the lower vibrational state and B_1 is that in the upper vibrational state.

4. Conclusions

The conclusions of the paper are as follows:

(i) The theoretical formulation of Salesky and Korff (1979, 1980) is not new as claimed by Salesky and Korff (1979) but is the same as obtained earlier by Mehrotra and Boggs (1977). (ii) The Mehrotra and Boggs theory (1977) as the Anderson theory (Boulet *et al* 1974) predicts that the microwave-infrared spectral line shapes are sensitive to the short range interaction. Unlike for microwave spectral lines, one must take the short range interaction to explain $|m|$ dependence. (iii) It is shown here for the first time that the $|m|$ dependence of the microwave-infrared spectral line shapes is also dependent on the phase shifts which appear as cosine term in the Mehrotra and Boggs theory (1977). In the previous calculations (Boulet *et al* 1974), the $|m|$ dependence was explained only by taking the repulsive part of the isotropic potential but one must consider the phase shift effect as well as the repulsive part of the potential to explain the $|m|$ dependence of microwave-infrared spectral line shape. This is not so in the case of microwave spectral line shape. (iv) The collision induced line shifts are found to be significant and can be measured experimentally.

References

Anderson P W 1949 *Phys. Rev.* **76** 647
Boulet C, Isnard P and Arie E 1974 *J. Quant. Spectrosc. Radiat. Transfer* **14** 637.
Cattani M 1972 *Phys. Lett.* **38** 147
Mehrotra S C and Boggs J E 1976 *J. Chem. Phys.* **64** 2796
Mehrotra S C and Boggs J E 1977 *J. Chem. Phys.* **66** 5306
Murphy J S and Boggs J E 1967 *J. Chem. Phys.* **47** 691
Pechukas P and Light J C 1967 *J. Chem. Phys.* **44** 691
Rabitz H and Gordon R G 1970 *J. Chem. Phys.* **53** 1815
Salesky E T and Korff D 1979 *Phys. Lett.* **A72** 431
Salesky E T and Korff D 1980 *J. Quant. Spectrosc. Radiat. Transfer* **23** 399
Tsao C J and Curnutte B 1962 *J. Quant. Spectrosc. Radiat. Transfer* **2** 41

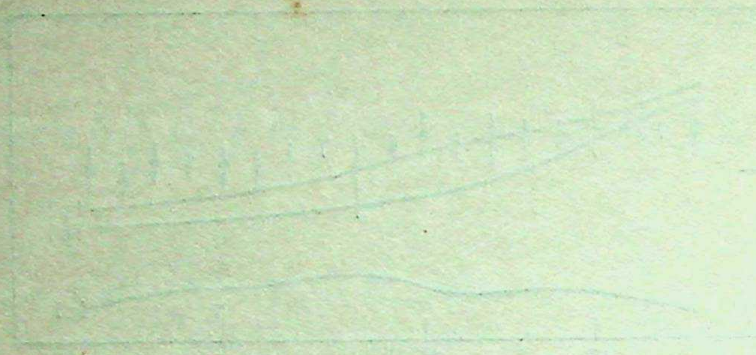

Pramāṇa, Vol. 21, No. 1, July 1983, pp. 41–50. © Printed in India.

Laser Raman spectra of mixed crystals of $[(NH_4)_{1-x}K_x]_2SO_4$

V SRINIVASAN, C K SUBRAMANIAN and P S NARAYANAN
Department of Physics, Indian Institute of Science, Bangalore 560 012, India

MS received 7 August 1982; revised 25 March 1983

Abstract. The Raman spectra of mixed crystals of $[(NH_4)_{1-x}K_x]_2SO_4$ in the region 50-3400 cm^{-1} at 293 K and below 223 K have been reported. At room temperature 293 K, as the concentration of K^+ ion increases in the crystal up to 50%, the frequencies of the totally symmetric vibrations of SO_4^{2-} and NH_4^+ ions increase and thereafter the frequency of SO_4^{2-} vibration decreases and attains the value in K_2SO_4. This change in frequency up to 50% of potassium concentration is due to the breaking of hydrogen bonds of the type N-H...O. The behaviour of Raman intensities of A_g (ν_1) mode of SO_4^{2-} for various concentrations ($x = 0, 0{\cdot}03, 0{\cdot}11, 0{\cdot}5, 0{\cdot}85$) suggest that the phase transition changes from first order type to one of second order. The phase transition in mixed crystals of $[(NH_4)_{1-x}K_x]_2SO_4$ can be a cooperative phenomenon arising from a coupling between $(NH_4)^+$ ions through hydrogen bonds with the distorted SO_4^{2-} ions in the low temperature phase.

Keywords. Laser Raman spectra; mixed crystals; hydrogen bond; infrared spectra; order-disorder.

1. Introduction

Ammonium sulphate undergoes a first-order ferroelectric phase transition at $T_c = 223$ K (Matthias and Remeika 1956; Hoshino *et al* 1958). The heat of transition and the change in entropy are $Q = 0{\cdot}93$ kcal/mole, $S = 4{\cdot}2$ cal/mole/deg (Hoshino *et al* 1958). The crystal exhibits an anomalous change in polarization; a very low value of Curie-Weiss constant (~ 15 K) (Unruh 1970) and a large spontaneous strain (Aniskatov and Martinov 1970).

Neutron diffraction, ESR, infrared (Jain *et al* 1973), NMR, Raman spectroscopy and dielectric methods have been applied to study the phase transition in ammonium sulphate. Based on the type of experimental technique used and the results obtained an order-disorder model (O'Reilly and Tsang 1967), an improper ferroelectric model (Ikeda *et al* 1973), a coupled oscillator model (Sawada *et al* 1973), a coupled-oscillator relaxator model (Petzelt *et al* 1974), a ferroelectric sublattice model (Sawada *et al* 1975; Kopsky 1976) and one involving changes in hydrogen bonding (Schlemper and Hamilton 1966) have been proposed to explain the mechanism of phase transition in this crystal. However, a fully satisfactory theoretical model explaining all the observed features is still lacking for reasons discussed below.

The order-disorder model as proposed by O'Reilly and Tsang by deutron resonance technique attributes the transition to a disordering of NH_4^+ ions with respect to the *ab* plane in the paraelectric phase. Schlemper and Hamilton have found by neutron diffraction methods, that the strength of hydrogen bonds were different in the two phases and hence the change in the H-bond scheme could be a triggering mecha-

nism. Sawada *et al* (1973) have proposed a phenomenological soft mode theory to explain the small Curie constant and other thermodynamical quantities of $(NH_4)_2SO_4$. The theory is based on the assumption that the phase transition is associated with two normal coordinates which are given by the superposition of a polar-translational symmetry coordinate and a nonpolar vibrational one. The softening of the normal mode with a large component of the vibrational mode induces the phase transition. However no such soft mode has been found as yet in the infrared absorption measurements (Torrie *et al* 1972). Sawada *et al* (1975), have studied the role of NH_4^+ ions by measuring the spontaneous polarization and the dielectric constant in $[(NH_4)_{1-x}K_x]_2SO_4$ for various values of x and proposed a two non-equivalent sublattice model to explain the phenomena. Neutron scattering measurements of mixed crystals of ammonium sulphate and potassium sulphate have been carried out (Goyal and Dasannacharya 1978). Spin lattice relaxation time of proton measurements have been carried out in $(NH_4)_2SO_4$-K_2SO_4 mixed crystals (Masaru Kasahara *et al* 1975). It has been found that potassium ions prefer to occupy the $(NH_4)_I^+$ sites rather than $(NH_4)_{II}^+$ sites and only one type of NH_4^+ ions, namely $(NH_4)_{II}^+$ remains at higher concentrations of K_2SO_4. X-ray crystal studies of the mixed system of $(NH_4)_2SO_4$-K_2SO_4 have been done (Yochi Shiozaki *et al* 1977). Abe *et al* (1978) have studied the ESR of pure and mixed crystals of ammonium and potassium sulphate. Substitution of $(NH_4)_I^+$ by potassium lowers the value of P_s and deuteration does not alter significantly the T_c. A recent ESR study of radiation damaged $(NH_4)_2SO_4$ crystal doped with CrO_4 in our laboratory suggests that a distortion of the (SO_4) groups in the low temperature phase could also be a transition parameter (Misra 1982).

As the laser Raman spectra of the $[(NH_4)_{1-x}K_x]_2SO_4$ can throw light on the extent of deformation of the SO_4^{2-} and NH_4^+ groups in different phases and the consequent changes in the N-H ... O bond strengths, the present study was made.

2. Experimental

$(NH_4)_2SO_4$ forms a continuous series of mixed crystals $[(NH_4)_{1-x}K_x]_2SO_4$ with K_2SO_4. Single crystals of various concentrations of K ($x = 0{\cdot}03$, $0{\cdot}06$, $0{\cdot}11$, $0{\cdot}28$, $0{\cdot}5$, $0{\cdot}6$ and $0{\cdot}85$) were grown by a slow evaporation of an aqueous solution at room temperature. The values of x in the crystals were determined by using the data of Bovalini and Fabris (Seidel 1965). Infrared spectra and powder x-ray diffraction pictures were used to identify the crystals.

Raman spectra were recorded with a Spex-Ramalog-6 spectrometer. The spectral slitwidth was set to 1–2 cm^{-1} band pass. Detection was by a photon-counting system using a RCA (C31034) photomultiplier with Ga-As photocathode and with thermoelectric cooling. The IR absorption spectra of the crystal were recorded using a Perkin Elmer 580 IR spectrophotometer and KBr pellet method.

The sample was illuminated with 4880 Å radiation of Ar^+ ion laser with power output in the range 100–200 mW. The temperature of the sample was varied using a simple continuous flow cryostat and the temperature stability was $\pm$ 1K.

The x-ray (Ogg and Hopwood 1916; Ogg 1928, 1930; Tutton 1930; Taylor and Boyer 1928), electron diffraction (Dalova and Pinsker 1964) and neutron diffraction

studies (Schlemper and Hamilton 1966) show that the structure has the space group D_{2h}^{16} in the paraelectric phase and C_{2v}^{9} in the ferroelectric phase and there are four molecules per unit cell. The sulphur atoms, two oxygen atoms, the nitrogen atoms and four hydrogen atoms lie in the mirror plane (001). Hence NH_4^+ and SO_4^{2-} ions occupy sites of symmetry C_s in the high temperature phase and C_1 symmetry in the low temperature phase.

The polarizability tensor components associated with the Raman active modes are α_{xx}, α_{yy} and α_{zz} for Ag, α_{xy} for B_{1g}, α_{xz} for B_{2g} and α_{yz} for B_{3g}. Raman spectra of mixed crystals of ammonium sulphate and potassium sulphate were taken for six orientations at room temperature 293 K.

3. Results and discussion

Raman spectra of $[(NH_4)_{1-x}K_x]_2SO_4$ were taken at room temperature 293 K for concentrations, $x = 0$, 0·03, 0·06, 0·11, 0·28, 0·5 and 0·6 for six orientations. The frequencies and the assignments of the various bands are given for $[(NH_4)_{0.97}K_{0.03}]_2SO_4$ in table 1 and the correlation diagram for this crystal in the para and ferroelectric phases are given in tables 2 and 3 respectively. In the paraelectric phase, all the gerade components are Raman active and the ungerade components excepting A_u

Table 1. Frequencies and assignment of single crystal Raman spectra of paraelectric $[(NH_4)_{0.97}K_{0.03}]_2SO_4$.

Frequency (cm^{-1})	Symmetry	Assignment	Frequency (cm^{-1})	Symmetry	Assignment
41	A_g		624	A_g	
60	B_{1g}	SO_4^{2-} translation	637	B_{1g}	
68	B_{3g}		976	A_g	SO_4^{2-} ν_1 vibration
71	B_{2g}		976	B_{1g}	
76	A_g	SO_4^{2-} libration	1065	A_g	SO_4^{2-} ν_3 vibration
82	B_{1g}		1074	B_{1g}	
90	B_{2g}		1087	B_{3g}	
152	B_{2g}		1090	B_{2g}	
184	A_g	NH_4^+ translation	1102	A_g	
193			1120	B_{1g}	
358	B_{3g}	NH_4^+ libration	1413	A_g	
375	A_g		1419	B_{1g}	NH_4^+ ν_4 vibration
451	A_g		1424	B_{3g}	
451	B_{1g}	SO_4^{2-} ν_2 vibration	1660	A_g	
454	B_{2g}		1665	B_{2g}	NH_4^+ ν_2 vibration
453	B_{3g}		1670	B_{1g}	
612	A_g		1690	B_{3g}	
615	B_{3g}	SO_4^{2-} ν_4 vibration	3030	B_{1g}	NH_4^+ ν_1 vibration
618	B_{1g}		3150	A_g	NH_4^+ ν_3 vibration
618	B_{2g}		3175		
			3290		

Table 2. Symmetry correlation for paraelectric $(NH_4)_2SO_4$ in the room temperature 293 K.

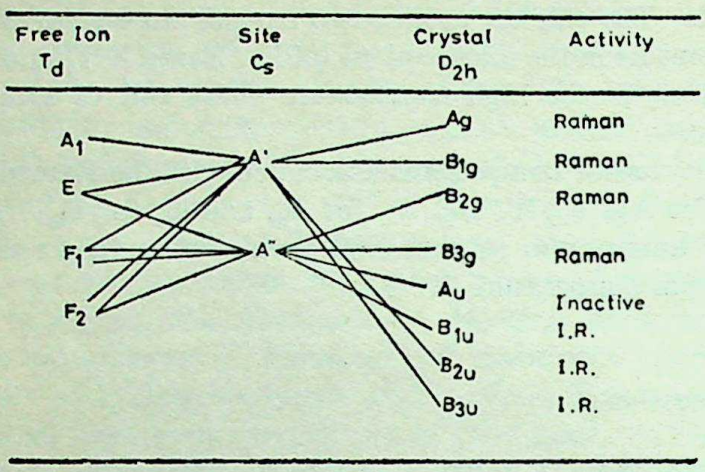

Table 3. Correlation diagram for $(NH_4)_2SO_4$ in the ferroelectric phase (below $T_c = 223°$ K).

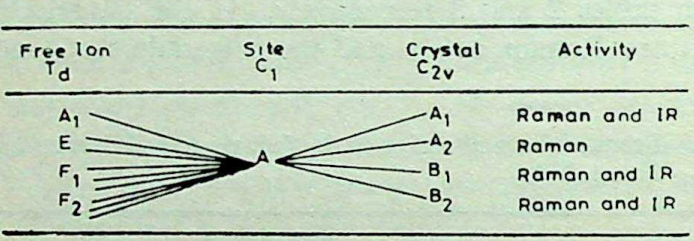

are active in IR. In the ferroelectric phase the atoms occupy only general positions. As the concentration x of K^+ ions increases in the mixed crystal up to 50%, the frequencies of totally symmetric vibration (ν_1) of SO_4^{2-} and NH_4^+ increase, while that of antisymmetric vibrations of NH_4^+ decrease which is shown in figure 1 (a, b). The infrared spectra of mixed crystals at different concentrations of K^+ ions are shown in figure 2. The crystal structure of ammonium sulphate at 293 K is shown in figure 3. The ammonium sulphate structure consists of one type of SO_4^{2-} group and two types of NH_4^+ groups, namely $(NH_4)_I^+$ and $(NH_4)_{II}^+$. One hydrogen from each type of ammonium is coupled to the sulphate group through the oxygens O(1) and O(2) which lie in the *ab* mirror plane. From NMR results, it is seen that the potassium prefers to occupy only $(NH_4)_I^+$ site. Therefore, if a K^+ ion replaces one of the $(NH_4)_I^+$ ion, the charge distribution of SO_4^{2-} ion is modified because of the disappearance of the hydrogen bond. The change in the charge distribution of SO_4^{2-} ion affects the state of the remaining hydrogen bonds. Therefore the strength of S-O bond increases and hence the frequency of the totally symmetric SO_4^{2-} vibrations increases. This continues until all the $(NH_4)_I^+$ ions are replaced by K^+. From figure 4, it can be seen that up to a concentration of 50% of potassium the frequency increases and thereafter it decreases up to 60%. Then the frequency increases and attains the value of 983 cm^{-1} which is that of K_2SO_4. The increase in (ν_1) frequency of SO_4^{2-} vibrations up to 50% of potassium is due to the disappearance of more and more hydrogen bonds. Once the concentration of K^+ ions is greater than 50%, all the hydrogen bonds are broken

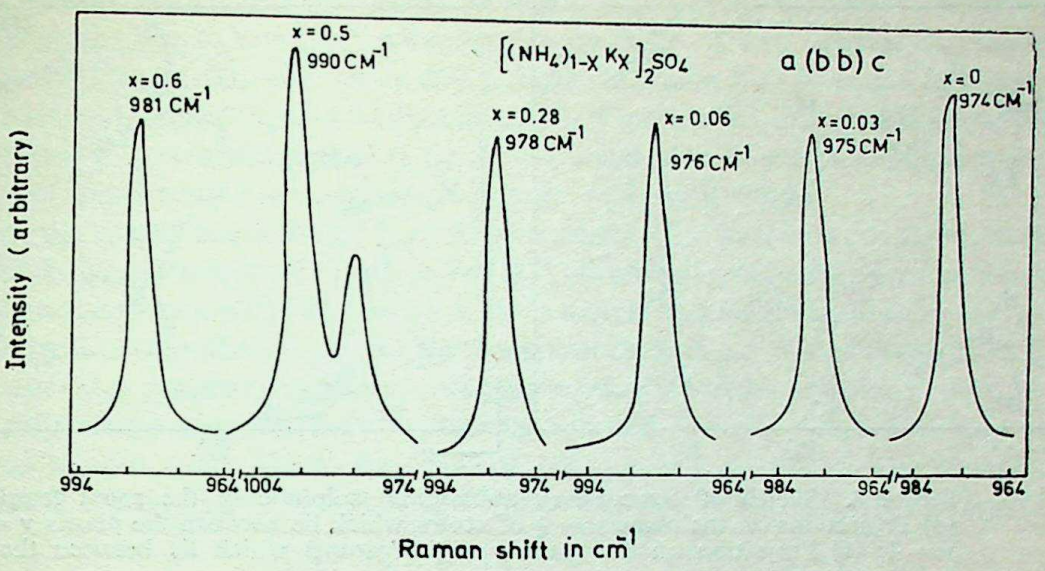

Figure 1a. Raman spectra of totally symmetric frequency (ν_1) of $(SO_4)^{2-}$ vibrations.

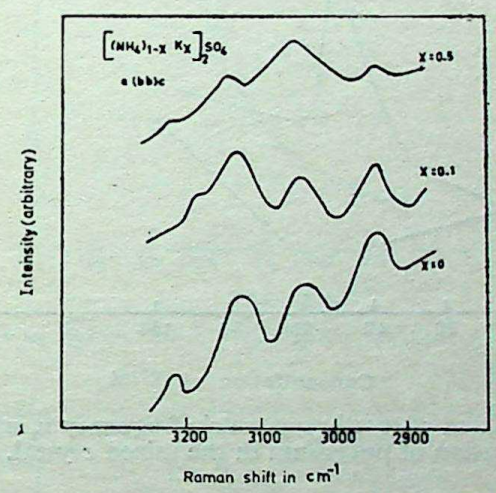

Figure 1b. The NH_4^+ stretch frequency with the different concentrations of potassium in $(NH_4)_2SO_4$-K_2SO_4 mixed crystals.

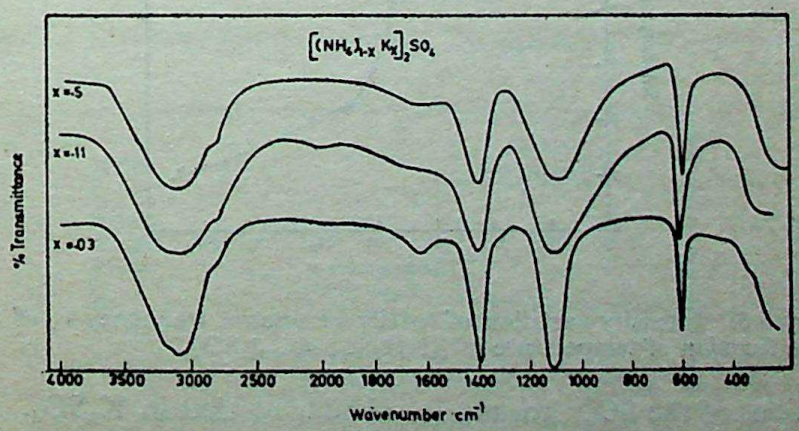

Figure 2. Infrared spectra of $[(NH_4)_{1-x}K_x]_2SO_4$ in various concentrations at 298 K.

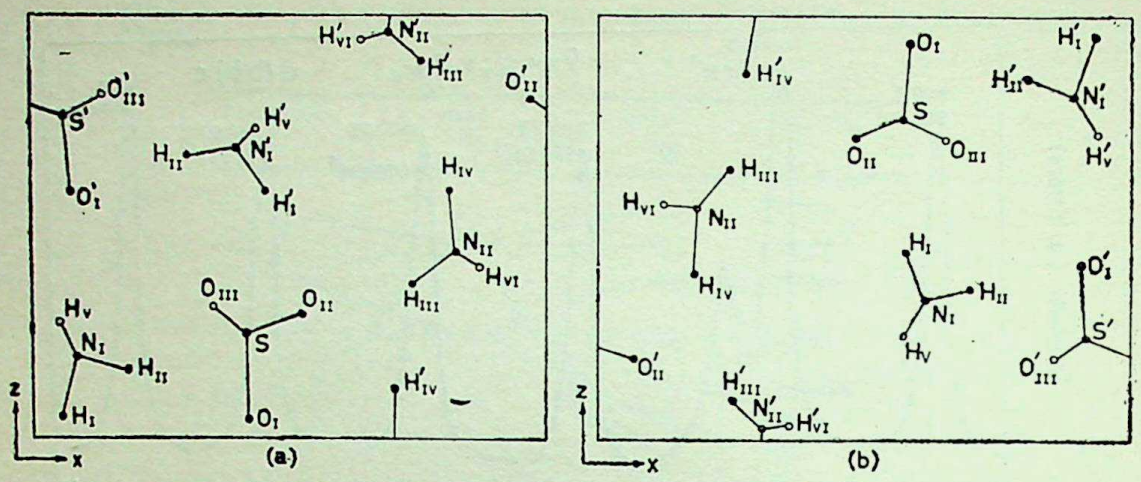

Figure 3. Sketch of structure of ammonium sulphate in the room temperature. (a) Projections on the plane $y = \frac{1}{4}$ of atoms which lie between the planes $y = 0$ and $y = \frac{1}{2}$; (b) Projection on the plane $y = \frac{3}{4}$ of atoms which lie between the planes $y = \frac{1}{2}$ and $y = 1$.

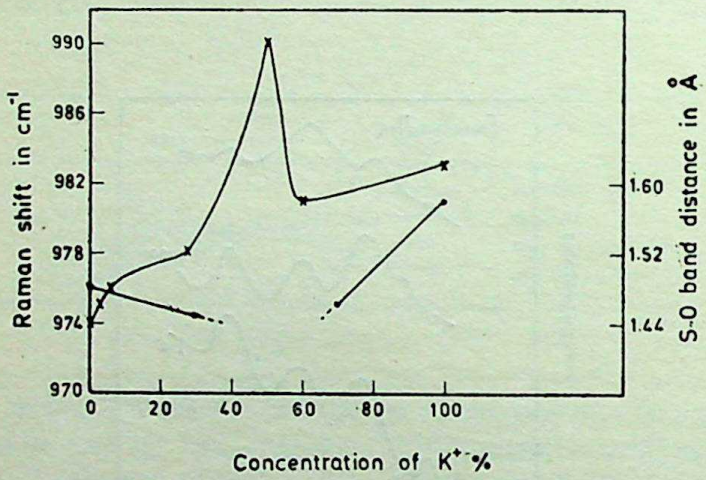

Figure 4. Variation of totally symmetric frequency ν_1 of $(SO_4)^{2-}$ vibration as a function of concentration of potassium in the mixed crystal.

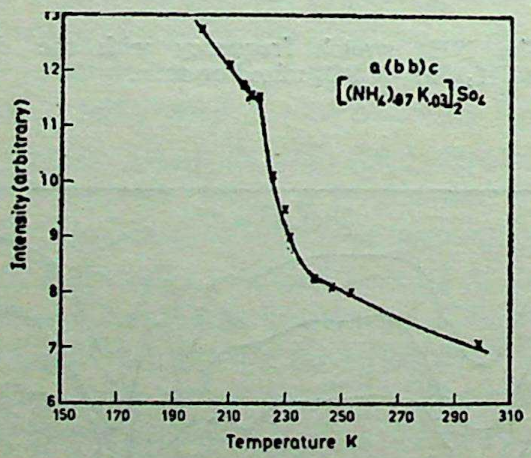

Figure 5. Intensity variation of totally symmetric frequency ν_1 of $(SO_4)^{2-}$ vibration as a function of temperature in $[(NH_4)_{0\cdot97}\ K_{0\cdot03}]_2SO_4$.

and the vibrations of the SO_4^{2-} groups are similar to that in K_2SO_4. The frequency of the totally symmetric vibration falls down up to 60% of K^+ and thereafter it in-

creases gradually and reaches 983 cm^{-1} which is the frequency of the totally symmetrical frequency (ν_1) of SO_4^{2-} vibration in K_2SO_4. X-ray studies on the mixed crystals of $(NH_4)KSO_4$ also show this behaviour where S-O distance decreases first up to 30% and from 70% of K^+ concentration, it increases. The region between 30% and 60% of K^+ concentration may be the critical region in which the hydrogen bond effect and ionic radii consideration compete with each other.

When the crystal containing 3% of K^+ is cooled to the ferroelectric phase, the intensity of totally symmetric vibration (ν_1) of SO_4^{2-} increases gradually and near the phase transition temperature 223 K, there is a steep increase in intensity and the slope of the line changes rather abruptly. As the concentration of K^+ is increased to 11% and 50%, there is a gradual increase in intensity of this vibration and the change of slope with temperature becomes smooth (figures 5, 6 and 7). The transition temperature is found to shift from 221 K for $[(NH_4)_{0.97}\ K_{0.03}]_2\ SO_4$ crystal to 216 K and 165 K for crystals containing 11% and 50% of potassium sulphate. When the concentration

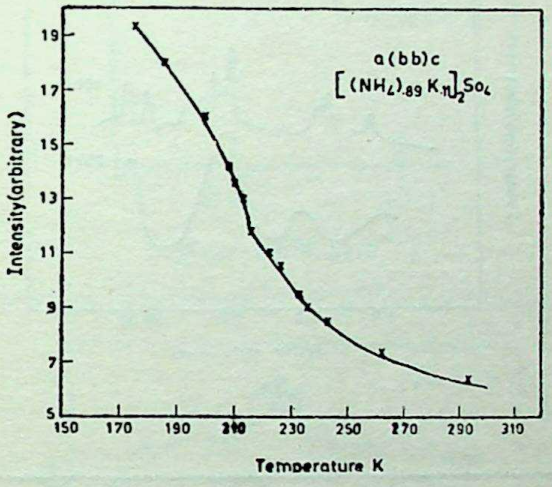

Figure 6. Same as figure 5 in $[(NH_4)_{0.89}\ K_{0.11}]_2SO_4$.

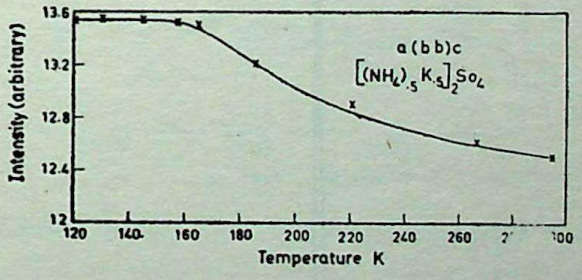

Figure 7. Same as figure 5 in $[(NH_4)_{0.5}\ K_{0.5}]_2SO_4$.

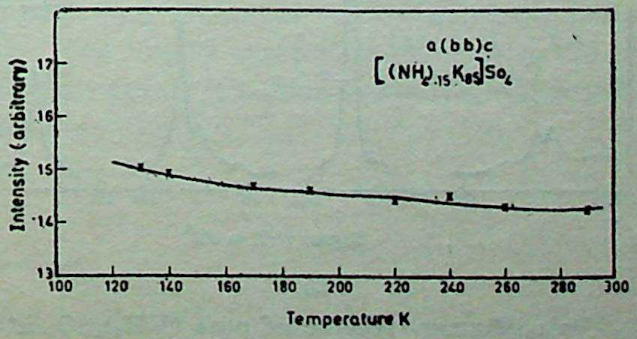

Figure 7a. Same as figure 5 in $[(NH_4)_{0.15}\ K_{0.85}]_2SO_4$.

of K^+ ions increases, in the mixed crystal, the transition is found to change from a first order type to one of second order, as is seen from the variation of the slope of the intensity of ν_1 line of SO_4^{2-} vibrations with temperature. For the crystal containing 85% of potassium, there is no phase transition, as the intensity almost linearly increases with temperature (figure 7a). This result is in conformity with the dielectric studies of mixed crystals (Sawada 1975).

In the lattice region of the spectra of $(NH_4)_2SO_4$ and other mixed crystals, the lines become sharp at low temperature but no sudden changes either in intensity or frequencies are observed. Typical Raman spectra of $(NH_4)_2SO_4$ at 293 K and low temperatures are shown in figure 8 (a, b). However, the ν_4 mode of sulphate at 614 cm^{-1} in $(NH_4)_2SO_4$ gives rise to 612, 618, 627 and 637 cm^{-1} respectively in the ferroelectric phase (figure 9). This result is similar to the one observed for ν_3 line of $(SO_4)^{2-}$ where

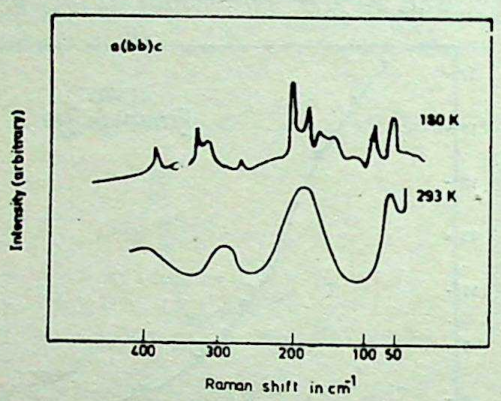

8a.

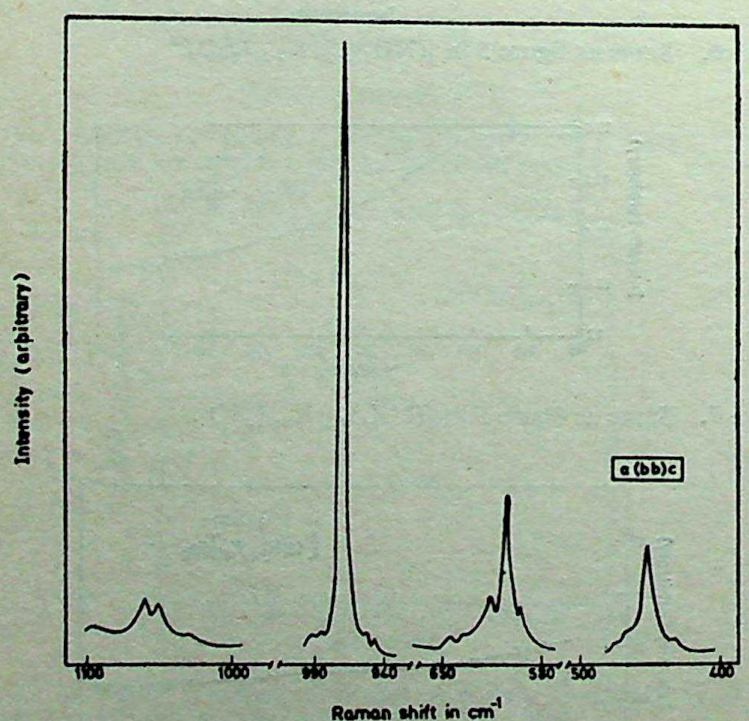

8b.

Figure 8a. Typical Raman spectra of pure $(NH_4)_2SO_4$ at 293 and 180 K in the spectral region 50–400 cm^{-1}. b. in the spectral region 400–1100 cm^{-1} at 293 K.

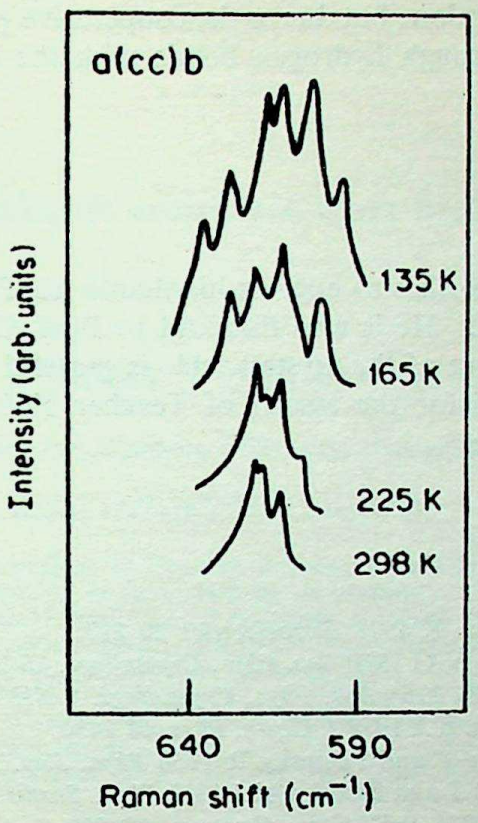

Figure 9. Variation of ν_4 mode of $(SO_4)^{2-}$ as a function of temperature.

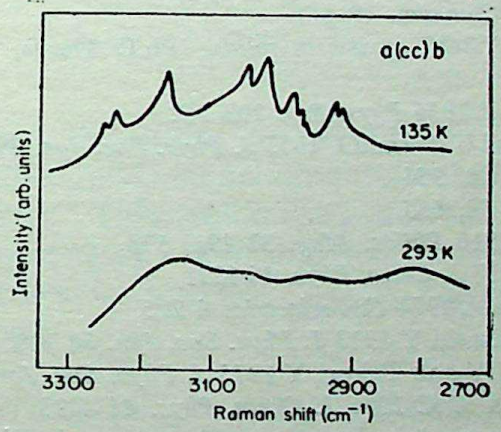

Figure 10. Raman spectra of $(NH)_4^+$ stretch frequency region at 293 and 135 K.

the SO_4^{2-} ion is said to be distorted in the ferroelectric phase (Iqbal and Christoe 1976). No sudden change in intensity or width or frequency is observed in the N-H bond region of this crystal excepting a general narrowing of the band as the temperature is lowered (figure 10). The totally symmetric line (ν_1) at 976 cm^{-1} decreases to 973 cm^{-1} in $(NH_4)_2SO_4$ as the crystal is cooled below T_c, which means that the strength of hydrogen bond increases.

4. Conclusion

From the above results, it can be inferred that the phase transition in mixed crystals of $[(NH_4)_{1-x}\ K_x]_2\ SO_4$ is not simply due to the order-disorder of (NH_4) radicals or

due to hydrogen bonding alone but due to the cooperative phenomena of the coupling between $(NH_4)^+$ ions through hydrogen bonds with the distorted SO_4^{2-} ions in the low temperature phase.

Acknowledgements

One of the authors (vs) wishes to express his thanks to Prof. R Srinivasan, for his keen interest in this work. He is also thankful to Prof. C N R Rao, for getting the infrared absorption spectra of the crystals. He is grateful to the University Grants Commission, New Delhi for the award of Teacher Fellowship under the faculty improvement programme.

References

Abe R, Shibata N and Dejima K 1978 *Ferroelectrics* **20** 217
Aniskatov A T and Martinov V G 1970 *Sov. Phys. Crystallogr.* **15** 256
Dalova V V and Pinsker Z G 1964 *Sov. Phys. Crystallogr.* **8** 433
Goyal P S and Dasannacharya B A 1978 *J. Chem. Phys.* **68** 2430
Hoshino S, Vedam K, Okaya Y and Pepinsky R 1958 *Phys. Rev.* **112** 405
Ikeda T, Fujbayashi K, Nagai T and Kobayashi J 1973 *Phys. Status Solidi* **A16** 279
Iqbal A and Christoe C W 1976 *Solid State Commun.* **18** 269
Jain J S, Bist H D and Upreti G C 1973 *Chem. Phys. Lett.* **22** 572
Kopsky V 1976 *Solid State Commun.* **19** 417
Misra N C 1982 *ESR and ENDOR studies in solids.* Ph.D Thesis, Indian Institute of Science, Bangalore
Mathias B T and Remeika J P 1956 *Phys. Rev.* **103** 262
Kasahara M, Sasakawa K and Tatsuzaki I 1975 *J. Phys. Soc. Jpn.* **39** 1022
Ogg A 1928 *Philos. Mag.* **5** 28, 354
Ogg A 1930 *Philos. Mag.* **9** 58, 665
Ogg A and Hopwood F L 1916 *Philos. Mag.* **32** 191, 578
O'Reilly D E and Tsang T 1967 *J. Chem. Phys.* **46** 1291
Petzelt J, Gragas I Mayerova A 1974 *Ferroelectrics* **6** 225
Sawada A, Takagi Y and Ishibashi Y 1973 *J. Phys. Soc. Jpn.* **34** 748
Sawada A, Ohya S, Ishibashi Y and Takagi Y 1975 *J. Phys. Soc. Jpn.* **38** 1408
Schlemper E O and Hamilton W C 1966 *J. Chem. Phys.* **44** 4498
Seidel A 1965 *Solubilities of inorganic and metal organic compounds* (Washington: Am. Chem. Soc.)
Tutton A E H 1929 *Philos. Mag.* **VIII** 195
Taylor W and Boyer T 1928 *Mem. Proc. Manchester Philos. Soc.* **72** 125
Torrie B H, Lin C G, Binbrek O S and Anderson A 1972 *J. Phys. Chem. Solids* **33** 697
Unruh H G 1970 *Solid State Commun.* **8** 1951
Shiozaki Y, Koh S I, and Sawaguchi E 1977 *J. Phys. Soc. Jpn.* **43** 721

Pramāṇa, Vol. 21, No. 1, July 1983, pp. 51–63. © Printed in India.

Evaluation of photoelastic constants from first-order Raman intensities of MgF_2

G SWARNA KUMARI, N SATYAVATHI and N RAJESWARA RAO*
Department of Physics, Osmania University, Hyderabad 500 007, India

MS received 14 August 1982; revised 17 May 1983

Abstract. A formalism to connect first-order Raman intensities of MgF_2 and its photoelastic constants is developed by developing a method of writing internal co-ordinates in terms of displacement gradients u_{ij} which are not symmetric. It is found that for crystals containing only one line in A_1 species, the ratios P_{13}/P_{33} and $(P_{11}+P_{12})/P_{31}$ can be directly evaluated from the intensities, without having to derive the intensity formulae; while $(P_{11}+P_{12})/P_{13}$ is independent of the intensities as well as the refractive index of the crystal. It is a function of only the dimensional parameters. In this crystal, since the species B_{1g} and B_{2g} also contain only one line each, the ratio $(P_{11}-P_{12})/P_{66}$ can also be directly obtained from the intensities.

Keywords. Photo-elastic constants; Raman intensities; displacement gradients

1. Introduction

When a crystal is stressed, the strains produced resolve themselves into phonons. Suitable groupings of Raman phonons manifest themselves as photoelastic constants according to their symmetry. This natural connection between Raman intensity and photoelasticity was recognised by Maradudin and Burstein (1967) who derived an expression for photo-elastic anisotropy $(P_{11}-P_{12}-P_{66})$ of diamond in terms of the intensity of its Raman line:

$$P = (a_0^2\,\epsilon_0^2/8\pi)\,(P_{11}-P_{12}-P_{66})/[1-8\,G/(a_0\,M\,\nu_R^2)]. \tag{1}$$

P is the polarizability change with respect to the frequency ν_R. ϵ_0 is equilibrium dielectric constant, a_0 radius of the carbon atom, M its mass and G an expression involving a product of force constant and length. P is the sign of the photoelastic anisotropy $(P_{11}-P_{12})-P_{66}$. But this formalism does not seem to have been followed up later.

Nelson and his colleagues (Nelson and Lax 1970; Nelson and Lazay 1971) have connected intensities of Brillouin components of a crystal to its photoelastic constants. They have pointed out that, in place of strain tensor e_{ab}, we have to use u_{ab}, given by

$$2u_{ab} = u_{ab} + u_{ba} + u_{ab} - u_{ba} = e_{ab} + w_c \tag{2}$$

where a, b, c indicate the axes x, y, z; w_c is the rotation in the plane of ab. Thus, one has 9 components u_{ab} instead of 6 e_{ab} and the corresponding photoelastic constant

tensor is of order 9×9 instead of 6×6. It will be 9×9 if the polarizability tensor is taken to be unsymmetrical as in resonance or near resonance Raman spectra. For Raman spectra far from resonance the matrix is of the order 6×9. It is also pointed out that the photoelastic constant tensor does not follow the symmetry of the crystal for piezoelectric-type crystals, as the Raman phonons which are also infrared active create electric fields that produce additional polarizability changes.

Meera *et al* (1978) applied stress on a crystal of silicon and connected the changed intensities of Raman spectra to photoelastic constants. Briggs and Ramdas (1976) again studied the Raman spectra of CdS under properly stressed conditions and related the altered frequency changes to deformation potentials.

In this paper we try to relate the Raman intensities of a crystal (under unstrained conditions) and photoelastic constants. For this purpose, the bond polarizability theory of Raman intensities (Eliashevich and Wolkenstein 1945; Long 1953) has been applied to the crystals. A serious problem in this field is the sign ambiguity of the polarizability change $\partial\alpha_{ij}/\partial Q_k$. In papers published earlier (Kumar *et al* 1974; Buddha and Rajeswara Rao 1976, 1977; Pratibha *et al* 1979; Swarna Kumari and Rajeswara Rao 1981), it has been shown as to how this problem can be avoided. Maradudin and Burstein (1967) also pointed out the difficulty in obtaining photoelastic constants from Raman intensities.

A parallel theory of Raman intensities was earlier developed by Loudon (1963). But as pointed by Maradudin and Burstein (1967), 'the model of electric polarizability we choose, must contain as many parameters as there are pieces of experimental information, no more, no less'. Tubino and Piseri (1975) have justified this theory for crystals. Thus the bond polarizability theory has come to stay. It has also the advantage of understanding the properties of the crystal from molecules and may pave the way to relate photoelastic constants of different crystals having the same or similar molecules.

2. Sign ambiguity in intensity analysis

The sign ambiguity problem connecting Raman intensities and electro-optical constants has earlier been solved for both molecules and crystals. The intensity formulae are of the type

$$I = L'\,A, \tag{3}$$

where $I = \partial P_i/\partial Q_k$ or $\partial\alpha_{ij}/\partial Q_k$ for IR or Raman intensities. I should not be confused with intensity which is proportional to I^2 and will be referred to later. L' is transpose of L matrix and A contains the electrooptical constants. I' can be plus or minus depending on the nature of the oscillation. It has been suggested that (3) may be written as

$$I'\,I = A'\,LL'\,A = A'\,GA. \tag{4}$$

We have one equation of this type for each species. If the parameters in A are larger in number than the equations, one may obtain the data from isotopic mole-

cules. A elements have thus been determined by us earlier in a number of molecules and crystals and these elements can be used to evaluate the photoelastic constants.

3. Internal co-ordinates and strains

For any crystal, polarizability change

$$\Delta\alpha_{ij} = \frac{\partial\alpha_{ij}}{\partial Q} \cdot \frac{\partial Q}{\partial S} \cdot \frac{\partial S}{\partial R} \cdot \Delta R, \tag{5}$$

S and R are symmetry and internal coordinates respectively. We seek to connect $\Delta\alpha_{ij}$ to photoelastic constants by deriving a relationship between ΔR and the strain parameters. For this purpose we start with

$$u_i^k = u_{ij}\, r_j^k \tag{6}$$

as explained by Born and Huang (1954). Repetition of the index j indicates summation. Here i and j stand for x, y, z, u_i^k is displacement of the kth atom in the ith direction. r^k is its position vector and $u_{ij} = \partial u_i/\partial r_j$ are related to strain parameters. In general $u_{ij} \neq u_{ji}$. However,

$$u_{ii} = e_{ii}, \tag{7a}$$

and

$$u_{ij} + u_{ji} = e_{ij}, \tag{7b}$$

where e_{ij} are the strain parameters. The internal oscillations in a molecule (or crystal) are generated by displacements of atoms according to a system given by

$$\Delta R = \sum_k u^k \cdot s^k, \tag{8}$$

u^k is the displacement and s^k is the unit vector along the displacement. s^k are Wilson's (1955) s vectors and (8) is explained in detail in books on molecular physics. As an example, if ΔR is stretching between two atoms 1 and 2 of a bond, displacements u^1 and u^2 should be along the bond in opposite directions and s^1 and s^2 are unit vectors (figure 1). In this case, $s^1 = -s^2$.

Taking 0, midway between 1 and 2 as origin, the position vectors $r^1 = -r^2$, r_j^k in (6) is equal to $r^1\, 1j$, $1j$ being the direction cosine of r^1. Since s^1 and r^1 are in the same direction, $1j$ are direction cosines of s^1 also. Similar direction cosines $2j$ apply to r^2 and s^2. Now, expanding (6) for atoms 1 and 2,

$$u_x^1 = (u_{xx}\, 1x + u_{xy}\, 1y + u_{xz}\, 1z)r^1, \tag{9a}$$

$$u_y^1 = (u_{yx}\, 1x + u_{yy}\, 1y + u_{yz}\, 1z)r^1, \tag{9b}$$

$$u_z^1 = (u_{zx}\, 1x + u_{zy}\, 1y + u_{zz}\, 1z)\, r^1. \tag{9c}$$

Writing similar equations for u_x^2, u_y^2 and u_z^2, we have

$$\Delta R = (u_x^1\, 1x + u_y^1\, 1y + u_z^1\, 1z) + (u_x^2\, 2x + u_y^2\, 2y + u_z^2\, 2z)$$

$$= R(e_{xx}\, 1x^2 + e_{yy}\, 1y^2 + e_{zz}\, 1z^2 + e_{xy}\, 1x\, 1y + e_{yz}\, 1y\, 1z + e_{zx}\, 1z\, 1x). \tag{10}$$

Here we have introduced a simplification $r^1 = r^2$ taking the origin at the centre of the bond. Also, since r^1 and r^2 are along the same line, but in opposite directions, $ij = -2j$. We have also put $R = 2r$.

Equation (10) is derived in standard books on elasticity (for example by Love 1952) though in a different manner. We may point out at this stage that this formula is derived for two points in a continuous medium but is applied for a bond between two atoms. We follow this approximation in all these calculations (as Dayal 1950, Saxena 1944 and others have done). We have considered this format as it can be adopted to any internal coordinate, bending, out-of-plane oscillation, rotation, etc. We shall demonstrate this for rotation.

Taking a simple linear molecule MgF_2 (figure 2) with Mg at the centre, we shall derive an expression for rotation about y-axis which takes place by F_1 and F_2 moving along z in the opposite directions. According to (8),

$$R_y = u^1 \cdot s^1 + u^2 \cdot s^2 = u_z^1 (-e_z/R) + u_z^2 (e_z/R). \tag{11}$$

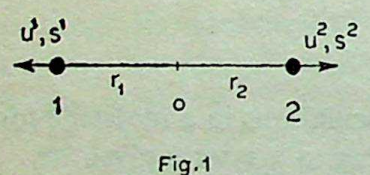

Fig.1

Figure 1. Symmetric stretching of atoms 1 and 2. u^1 and u^2 are displacements, s^1 and s^2 are unit vectors in those directions.

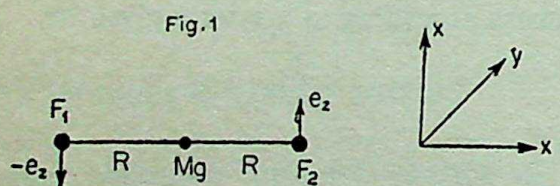

Fig. 2

Figure 2. Rotation about *Y*-axis

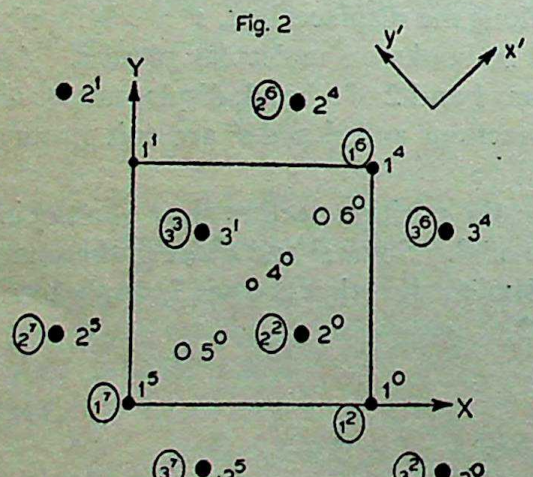

Fig. 3

Figure 3. Unit cell of MgF_2. The light shaded atoms are in the plane of the paper. The dark ones are above or below the plane of the paper at a distance $c/2$. Those in circles are above the plane of paper. The superscripts represent the cell numbers.

Here, we have used $s^1 = -e_z/R$ (e_z is the unit vector along z direction) as it indicates bending of the bond MF_1. Since $u_x = u_y = 0$

$$-\frac{1}{R}u_z^1 = u_{zx}\, 1x\, R \times \frac{1}{R}, \tag{12a}$$

and,
$$\frac{1}{R}u_z^2 = u_{zx}\, 2xR \times \frac{1}{R}. \tag{12b}$$

Therefore $R_y = 2u_{zx} = u_{zx} + u_{xz} + u_{zx} - u_{xz} = e_{zx} + w_y$, (13)

in the notation used by Love (1952). Thus ΔR in (5) can be replaced by the appropriate expressions involving strains. Equation (10) can be written in the form Rle. R is a diagonal matrix of bonds, l row matrix of products of direction cosines taken two at a time (writing l, m, n for $1x$, $1y$, $1z$) and e column matrix of strains. Substituting in (5)

$$\Delta\alpha_{ij} = I'\, L^{-1}\, URle, \tag{14}$$

I' is row matrix of $\partial\alpha_{ij}/\partial Q$. We have put $S = LQ$ and $S = UR$. Now, photoelastic constants are defined by (Born and Huang 1954)

$$\Delta\,(\epsilon^{-1})_{ij} = P_{ijkl}\, e_{kl} \tag{15}$$

From,
$$\epsilon\,\epsilon^{-1} = 1,\ \Delta\,\epsilon = -\,\epsilon_0\,\Delta\,\epsilon^{-1}\,\epsilon_0 \tag{16}$$

Here we have written ϵ_0 for ϵ as an approximation. ϵ_0 is the dielectric constant of the unstrained crystal and ϵ is that of the strained crystal. Substituting in (16)

$$\Delta\epsilon_{ab} = (\epsilon_0)_{ai}\, P_{ijkl}\, (\epsilon_0)_{bj}\, e_{kl} = P'_{ijkl}\, e_{kl}. \tag{17}$$

Since $\epsilon = 1 + 4\pi\alpha bN$, where α is the polarizability tensor and N, the number of molecules per unit volume; b is related to crystal structure

$$\Delta\epsilon = 4\pi bN\Delta\alpha, \tag{18}$$

and $\Delta\alpha_{ij}$ in (14) can be replaced by $\Delta\epsilon_{ij}$. As we propose to derive expressions for photoelastic constants in units of polarizability derivatives, $4\pi bN$ cancels off. In order to compare with experimental photoelastic constants, we have to multiply them with ϵ_0 elements according to the scheme given by (16). To make such multiplication simple, we take the coordinates along the symmetry axes of the crystal and make ϵ_0 a diagonal tensor having only the principal elements. For a crystal like MgF_2 for which we shall derive the photoelastic constants, P' and P are related as follows. Here $(\epsilon_0)_{xx} = n_x^2$ and $(\epsilon_0)_{zz} = n_z^2$, are refractive indices along a and c axes of the crystal:

$$P'_{11} = n_x^4\, P_{11}, \qquad P'_{22} = n_x^4\, P_{22},$$

$$P'_{33} = n_z^4\, P_{33}, \qquad P'_{44} = n_x^2\, n_z^2\, P_{44}. \tag{19}$$

P_{11}, P_{22} etc have the usual meaning (Born and Huang 1954) with respect to the co-ordinate axes x, y, z. Then, we have from (14)

$$P' = I'L^{-1}\,URIe. \tag{20}$$

4. Raman intensity analysis of MgF_2

As we propose to get $\partial\alpha_{ij}/\partial Q$ from Raman intensities, we shall first derive formulae connecting intensities and bond polarizabilities of this crystal as was done earlier for other cyrstals (Kumar *et al* 1974).

MgF_2 is a rutile-type crystal of symmetry D_{4h}^{17}, with two molecules in the unit cell. The molecules are oriented perpendicular to each other and their levels separated by $c/2$. But the a_1 and a_2 axes of the cell are oriented at 45^0 to the orientations of the molecules (figure 3). We shall refer to molecule 213 as 1 and 546 as 2. As it becomes necessary to take into account distances of the atoms in the neighbouring unit cells also, to construct symmetry coordinates, the central cell is marked 0, and the other cells with different numbers. The bonds like 12, 13, 45 and 46 are mostly of covalent nature while bonds like 42 or 51 are ionic but have also some covalent nature and oscillations are possible between them.

The dimensions of the crystal and of the bonds (Wyckoff 1962) are calculated to be $a_1 = a_2 = 4{\cdot}623$ Å, $c = 3{\cdot}052$ Å, $r_{12} = r_{13} = r_{45} = r_{46} = 2{\cdot}026$ Å, $r_{42} = 1{\cdot}967$ Å. The angle 42 makes with XY plane is θ which is equal to $50^051'$.

Since there are 6 atoms in the unit cell, there are 15 optical modes and they are distributed among the species as $1A_{1g}$, $1B_{1g}$, $1B_{2g}$, $1E_g$, $1A_{2g}$, $2A_{2u}$, $2B_{1u}$, $4E_u$. Among them, $1A_{2u}$, and $1E_u$ are translations. In addition to the ungerade modes, A_{2g} is inactive. Raman modes are of frequencies 410, 515, 92 and 295 cm^{-1} 410 being observed in α_{xx}, α_{yy} and α_{zz} spectra, 92 in α_{xx} and α_{yy}, 515 in α_{xy} and 295 in α_{zx} and α_{yz}. These spectra are taken by Porto (1967).

5. Intensity formulae

To derive intensity formulae, it is necessary to determine the symmetry coordinates in the way explained in our earlier papers. They are

$$S_1^{A_{1g}} = \frac{1}{\sqrt{2}}\Big[(1/2)\{(1^02^0 + 1^13^1) + (4^05^0 + 4^06^0)\}$$

$$- \frac{1}{2\sqrt{2}}\{(4^02^0 + 4^02^2) + (4^03^1 + 4^03^3) + (5^01^5 + 5^01^7)$$

$$+ (6^01^4 + 6^01^6)\}\Big], \tag{21a}$$

$$S_2^{B_{1g}} = \frac{1}{\sqrt{2}}\Big[(1/2)\{(4^05^0 + 4^06^0) - (1^02^0 + 1^13^1)\}$$

$$+ \frac{1}{2\sqrt{2}}\{(4^02^0 + 4^02^2) + (4^03^1 + 4^03^3) - (5^01^5 + 5^01^7)$$

$$- (6^01^4 + 6^01^6)\}\Big], \tag{21b}$$

$$S_3^{B_{2g}} = -\frac{1}{\sqrt{2}}[R_{z1} + R_{z2}] = R_z, \tag{21c}$$

$$S_{4a}^{E_g} = \frac{1}{\sqrt{2}}[R_{y'} + R_{x'}] = R_x, \tag{21d}$$

$$S_{4b}^{E_g} = \frac{1}{\sqrt{2}}[R_{y'} - R_{x'}] = R_y, \tag{21e}$$

x' and y' are directions along molecules 2 and 1. The first coordinate shows that both the molecules stretch in and out while in the second, one stretches, and the other contracts. The other coordinates describe R_z, R_x and R_y rotations of these coordinates about the axes.

The intensities are functions of the bond polarizabilities and their derivatives. The derivation is described in our papers. The intensities are

$$I_{xx}^{A_{1g}} = I_{yy}^{A_{1g}} = (14{\cdot}19)\ K = \left[\sqrt{2}\ \alpha_{12}'^{T} + \frac{1}{\sqrt{2}}\gamma_{12}' - a\ \gamma_{42}\right] L_{11} = A_1 L_{11}, \tag{22a}$$

$$I_{zz}^{A_{1g}} = (?) = [\sqrt{2}\ \alpha_{12}'^{T} + 2a\ \gamma_{42}]\ L_{11} = A_1' L_{11}, \tag{22b}$$

$$I_{xy}^{B_{1g}} = (3{\cdot}527)\ K = \left(\frac{1}{\sqrt{2}}\gamma_{12}' - a\ \gamma_{42}\right) L_{22} = A_2 L_{22}, \tag{22c}$$

$$I_{xx}^{B_{2g}} = I_{yy}^{B_{2g}} = (1{\cdot}017)\ K = [\sqrt{2}\ \gamma_{12} - b\ \gamma_{42}]\ L_{33} = A_3 L_{33}, \tag{22d}$$

$$I_{yz}^{E_g} = I_{zx}^{E_g} = (?) = [\gamma_{12} - c\ \gamma_{42}]\ L_{44} = A_4 L_{44}. \tag{22e}$$

These equations are expanded forms of (3). These A elements are transferred to table 1.

where $$\alpha_{12}'^{T} = \frac{\partial}{\partial r_{12}}(\alpha_{12}^{T} + \alpha_{13}^{T}),$$

$$\gamma_{12}' = \frac{\partial}{\partial r_{12}}(\gamma_{12} + \gamma_{13}),$$

$$a = \frac{4 \cos\theta \cdot \sin^2\theta}{r_{42}\,[(1/\sqrt{2}) + \cos\theta]} = 0{\cdot}5667,$$

$$b = (2\sqrt{2}\, r_{12} \cos\theta)/r_{42} = 1{\cdot}8386,$$

$$c = (2\, r_{12} \cos\theta \cdot \cos 2\theta)/r_{42} = -\,0{\cdot}2640.$$

L elements are the square roots of the G elements which are calculated in the usual way and are given below:

$$G_{11} = G_{22} = [(1/\sqrt{2}) + \cos\theta]^2\, \mu_F = (0{\cdot}0568) \times 10^{24},$$

$$G_{33} = G_{44} = (2/r_{12}^2)\, \mu_F = (0{\cdot}0154) \times 10^{24}$$

γ_{12} is the difference between the polarizability along the bond 12 and perpendicular to it. γ'_{12} is its derivative. α'^{T}_{12} is polarizability derivative perpendicular to the bond. γ'_{42} is taken to be negligible as it is mostly electrovalent.

The areas A under the lines 515, 410 and 92 cm^{-1} are taken and I^2, the intensity, is defined by the formula

$$I^2 = \frac{K^2 A \nu_i\, [1 - \exp(-hc\nu_i/kT)]\, n^2}{(\nu_0 - \nu_i)^4}. \tag{23}$$

K is a constant of proportionality, ν_i the frequency of the line, ν_0 the frequency of the exciting line. Exp $(hc\nu_i/kT)$ is the usual Boltzmann factor. These values are also shown in the intensity formulae (22).

K, which is a function of the experimental conditions, has the same value for these three lines, as they are recorded in the same spectrum. It is not possible to say if the experimental conditions for zz and xz spectra are the same as for those lines. Hence, we cannot use these intensities and are shown as (?) in (22). Equations (22) contain five parameters to be determined, γ_{12}, γ_{42}, γ'_{12}, α'^{T}_{12} and K while we have only three equations (22a, c and d).

6. Photoelastic constants

As explained earlier, formulae (22) are like $I = L'A$, where I is a column vector. Transposing and substituting in (20)

$$P' = A'URle. \tag{24}$$

We thus get rid of a very inconvenient factor L^{-1}. Though, in the case of MgF_2, the species contain only one line each and calculation of L^{-1} elements is not difficult, in other crystals each species may contain more than one line and calculation of L elements requires correct evaluation of force constants which is generally not possible, particularly for crystals. In simple molecules, the secular determinant is supple-

mented by data on Coriolis interaction constants and the force constants can be evaluated to some degree of reliability. For crystals, this facility is not always available.

Formulation of (24) avoids another important hurdle, that is, the sign ambiguity of I. The sign ambiguity arises because, the polarizability can increase or decrease during an oscillation, depending on the A elements and their interaction with L elements. But, we have the same set of A elements for all the lines of a species. Hence, this ambiguity is avoided. Elements of A can be determined in the manner explained in our previous papers.

7. Determination of URIe

There are only two types of coordinates, ΔR and rotation which are connected to strains by (10) and (13). While (10) is a general equation suitable for any coordinate system, (13) is derived for X axis along molecule 2, (figure 3). As the axes of the crystal are inclined to it by 45°, the equation can be modified as

$$R_{x'} = -\sqrt{2}\,(u_{zx} - u_{zy}), \qquad \text{for molecule 1,}$$

$$R_{y'} = \sqrt{2}\,(u_{zx} + u_{zy}), \qquad \text{for molecule 2,}$$

$$R_x = R_{x'} + R_{y'} = 2\sqrt{2}\,u_{zy} = \sqrt{2}\,(e_{yz} + w_x). \tag{25a}$$

Similarly,

$$R_y = \sqrt{2}\,(e_{zx} + w_z), \tag{25b}$$

and

$$R_x = -\,2\,(e_{xx} - e_{yy}). \tag{25c}$$

It is seen that w_x and w_y occur in these equations but not w_z. This is due to the crystal having symmetry about z axis.

URIe can be computed and writing A and this matrix separately, we have in table 1

Table 1. A' and *URIe* matrices.

A	$S_1^{A_{1g}}$	$S_2^{B_{1g}}$	$S_3^{B_{2g}}$	$S_{4a}^{E_g}$	$S_{4b}^{E_g}$	*URIe*
a_{xx}	A_1	—	A_3	—	—	$S_1^{A_{1g}}(e_{xx}+e_{yy})(P)-e_{zz}(Q)$
a_{yy}	A_1	—	$-A_3$	—	—	$S_2^{B_{1g}}\,e_{xy}\,(P)$
a_{zz}	A_1'	—	—	—	—	$S_3^{B_{2g}}\,2\,(e_{xx}-e_{yy})$
a_{yz}	—	—	—	A_4	—	$S_{4a}^{E_g}\,e_{yz}+w_x=2u_{zy}$
a_{zx}	—	—	—	—	A_4	$S_{4b}^{E_g}\,e_{zx}+w_y=2\,u_{zx}$
a_{xy}	—	A_2	—	—	—	

P' is obtained by multiplying these two matrices as in eq. (24).

Here

$$P = \left(\frac{\gamma_{12}}{\sqrt{2}} - r_{42}\cos^2\theta\right) = (0{\cdot}6491),$$

$$Q = 2\sin^2\theta \cdot r_{42} = (2{\cdot}367).$$

In the 9×9 photoelastic constant matrix, in place of P_{44}, P_{55} and P_{66}, Grimsditch and Ramdas (1980) have given

$$\begin{vmatrix} P_{yz\ yz} & P_{yz\ zy} \\ P_{zy\ yz} & P_{zy\ zy} \end{vmatrix} \quad \text{etc.}$$

Since the Raman spectra used here are of non-resonance type, we have $\alpha_{yz} = \alpha_{zy}$. Also, in our formalism, R_x is a function of only u_{zy}. Therefore, there is only one term $P_{yz\ zy}$ or $P_{zy\ zy}$. Therefore, one should write $P_{44} = 2A_4\, u_{zy}$ or $A_4\, e_{yz}$ assuming $w_x = 0$. Since the experimental value available is for P_{44} we have put $w_x = 0$ and used the equation $P_{44} = A_4\, e_{yz}$.

8. Calculation of photoelastic constants

Expressions for A elements are taken from (22) and we obtain the equations for the photoelastic constants in terms of the electro-optical constants and strains.

As already stated, there are 5 parameters while only 3 intensity equations are available. We are, therefore, adding to them equations for P_{44} and P_{66}. Afanas' ev *et al* (1975) published the photoelastic data for this crystal (tables 2 and 3). Values of the 5 parameters are obtained by solving the following equations:

$K = 0{\cdot}0174 \times 10^{12}$; $\gamma_{12} = 0{\cdot}2536$

$\gamma_{42} = 0{\cdot}1175$; $\alpha'^{T}_{12} = 0{\cdot}5516$ and

$\gamma'_{12} = 0{\cdot}4605$.

Table 2. Photoelastic constants.

	P'	P	MgF_2 (Afanas' ev *et al* 1975)	P for rutile (Grimsditch and Ramdas 1980)
$P_{11}=P_{22}$	0·8754	0·2345		0·017
$P_{12}=P_{21}$	0·4720	0·1264		0·143
$P_{13}=P_{23}$	−2·456	−0.6581		−0·139
$P_{31}=P_{32}$	0·5942	0·1648		−0·080
P_{33}	−2·167	−0·6010		−0·057
$P_{44}=P_{55}$	0·2847	0·0776	0·0776	−0·009
P_{66}	0·1674	0·0448	0·04485	−0·060

Table 3. Combinations of photoelastic constants.

	Calculated values MgF_2	Experimental values	
		Afanas'ev *et al* (1975) MgF_2	Rutile
$P_{11} - P_{12}$	0·1080	0·0892	− 0·126
$P_{11} - P_{31}$	0·0696	0·0695	0·097
$P_{33} - P_{13}$	0·0571	0·1128	0·082

For this purpose, we assume that all the I values are positive. Since there is only one line in each species, it is not necessary to use (4) to avoid the sign of I. Using these parameters, the other P' values are calculated and given in table 2. Afanas'ev *et al* (1975), however, have given only the combinations $P_{11} - P_{12}$, $P_{11} - P_{31}$ and $P_{33} - P_{13}$. To compare with these values we have prepared similar combinations and given in table 3. The agreement seems to be satisfactory.

There are some interesting relations among these photoelastic constants.

$$\frac{P_{11} - P_{12}}{P_{66}} = \frac{2A_3\,(1{\cdot}414)}{A_2\,(0{\cdot}6491)} = \frac{2(1{\cdot}414)}{(0{\cdot}6491)} \times \frac{I_{xx}^{B_{2g}}}{I_{xy}^{B_{1g}}} \times \frac{L_{22}}{L_{33}} = 2{\cdot}409 \tag{26a}$$

$$\frac{P'_{13}}{P'_{33}} = \frac{A_1}{A'_1} = \frac{I_{xx}^{A_{1g}} \cdot n_x}{I_{zz}^{A_{1g}} \cdot n_z} \tag{26b}$$

$$\frac{P'_{11} + P'_{12}}{P'_{31}} = \frac{2A_1}{A'_1} = \frac{2I_{xx}^{A_{1g}} \cdot n_x}{I_{zz}^{A_{1g}} \cdot n_z} \tag{26c}$$

$$(P_{11} + P_{12})/P_{13} = 2A_1\,(0{\cdot}6491)/A_1\,(-2{\cdot}36) = -0{\cdot}55 \tag{26d}$$

Equations (26a, b, c) show that the photoelastic constant ratios can be determined using the intensities directly and without having to derive the intensity formulae (22). For (26a) the experimental value 1·99 is very near the ratio calculated by the above method 2·41. Unfortunately, the intensities $I_{xy}^{B_{1g}}$ and $I_{xx}^{B_{2g}}$ are very low and their experimental determination is uncertain. Hence, the nearness of these values can be taken to be satisfactory. The ratio of the ratios given by (26a) and (26b) is really equal to 2. Equation (26d) indicates that this ratio is independent of even intensities or refractive index of the crystal. It is a function only of the dimensional parameters.

Equations (22) show that the photoelastic constants can be obtained from only 4 electro-optical constants. This does not violate the group theoretical result that there are 7 independent constants. Group theory simply says that any one of them cannot be transformed into the other or a combination of them by symmetry operation. It does not preclude a relation among them through some independent parameters smaller or larger in number. As an example, for calcite, n_x and n_y are two independent quantities in the second-order tensor. But they are calculated in terms of a single parameter (Bhagavantam 1940) polarizability of the oxygen atom.

9. Comparison with rutile

The photoelastic constants of rutile taken from the data given by Grimsditch and Ramdas (1980) are also given in table 2, for comparison, as this is of the same structure. It is interesting to note that:

(a) P_{11} and P_{12} are so different for MgF_2 and TiO_2. But $P_{11} + P_{12}$, which is a function of the intensity of A_{1g} line, is comparable and assumes similar importance in the two cases.

(b) Equation (26b) shows, that P_{13} being proportional to A_1 is larger than P_{33}. A_1 and A'_1 are proportional to the intensities of 410 in xx and zz spectra. Generally, the intensity in zz, being proportional to the polarizability of the bond perpendicular to it, is smaller. Therefore, P_{13} is generally larger than P_{33}. But experiment shows that $P_{33} - P_{13}$ is positive and small. This is possible only if both P_{33} and P_{13} are negative. This shows that the negative value of P_{33} is correct.

10. Discussion

This crystal is particularly suitable to determine photoelastic constants from Raman intensities as each species consists of only one line. Equations (26a, b, c, d) are possible only if the A_1 type oscillation consists of one line, for example, for calcite-like crystals also.

Table 2 shows that the photoelastic constants of rutile are much smaller than that of MgF_2. Partly it may be due to its large refractive index (n=2·584) compared to 1·39 of MgF_2. The P' values are divided by n^4, to get P. n^4=44·58 for rutile and 3·73 for MgF_2. Hence, smaller values for rutile are understandable. P' will be comparable and hence they stand a better chance to be called the photoelastic constants, similar to q's defined by Gavini and Cardona (1969) by

$$\Delta \epsilon_{ij} = q_{ijkl}\, \sigma_{kl}$$

It is obvious that with a similar procedure one can evaluate piezo-electric constants from infrared intensities.

Acknowledgement

The results reported in this paper were presented at the Twelfth National Conference on Crystallography. Hyderabad, February 1980. One of the authors (GSK) thanks the University Grants Commission, New Delhi, for a research fellowship.

References

Afanas'ev I I, Andrianova L K, Mamontov I Ya and Reiterov V M 1975 *Sov. Phys. Solid State* **17** 2006

Bhagavantam, S 1940 *Light scattering and Raman effect* (Andhra University Press), p. 111

Born M and Huang K 1954 *Dynamical theory of crystal lattices* (Oxford University press)

Briggs R J and Ramdas A K 1976 *Phys. Rev.* **B13** 5518

Buddha Addepalli V and Rajeswara Rao N 1976 *Indian J. Pure Appl. Phys.* **14** 117
Buddha Addepalli V and Rajeswara Rao N 1977 *Indian J. Pure Appl. Phys.* **15** 157
Dayal B 1950 Proc. Indian *Acad. Sci.* **A32** 304
Eliashevich M and Wolkenstein M W 1945 *J. Chem. Phys.* **9** 101 326
Gavini A and Cardona M 1969 *Phys. Rev.* **177** 1351
Grimsditch M H and Ramdas A K 1980 *Phys. Rev.* **B22** 4094
Kumar S P, Padma V A and Rajeswara Rao N 1974 *J. Chem. Phys.* **60** 4156
Long D A 1953 *Proc. R. Soc. London* **217** 203
Loudon R 1963 *Proc. R. Soc. London* **A275** 218
Love A E H 1952 *Treatiseon the mathematical theory of elasticity* 4th Edn
Maradudin A A and Burstein E 1967 *Phys. Rev.* **164** 1081
Meera Chandrasekhar, Grimsditch M H and Gardona M 1978 *J. Opt. Soc. Am.* **68** 523
Nelson D F and Lax M 1970 *Phys. Rev. Lett.* **24** 379
Nelson D F and Lazay P D 1971 *Phys. Rev. Lett.* **25** 1187
Nelson D F and Lax M 1971 *Phys. Rev.* **B3** 2778
Porto S P S 1967 *Phys. Rev.* **154** 522
Pratibha Naik, Padma V A and Rajeswara Rao N 1979 *Pramana* **13** 111
Saxena B D 1944 *Proc. Indian Acad. Sci.* **A19** 357
Swarna Kumari G and Rajeswara Rao N 1981 *Indian J. Pure Appl. Phys.* **19** 326
Tubino R and Piseri L 1975 *Phys. Rev.* **B11** 5145
Wilson Jr. E S, Decius J C and Cross P C 1955 *Molecular vibrations* (New York: McGraw Hill)
Wyckoff R W G 1962 *Crystal srructures* (New York: Interscience), Vol. 1, p. 15

Pramāṇa, Vol. 21, No. 1, July 1983, pp. 65–70. © Printed in India.

Hyperfine interaction parameters and ground-state wavefunctions of vanadyl ion complexes

V P SETH, S K YADAV and V K JAIN
Department of Physics, Maharshi Dayanand University, Rohtak, India

MS received 20 September 1982; revised 30 May 1983

Abstract. Using crystal field approach a theoretical estimate of the ground-state wavefunctions of vanadyl ion doped in various crystals have been made using ESR data and is found to be d_{xy} in our coordinate system with slight admixture of the excited states $d_{x^2-y^2}$, d_{xz} and d_{yz}. The hyperfine interaction parameter P and Fermi contact coupling parameter K have also been estimated for these vanadyl-doped crystals. Results agree with similar studies made earlier.

Keywords. Hyperfine interaction parameters; ground-state wavefunctions; vanadyl ion; crystal field approach; electron spin resonance.

I. Introduction

Electron spin resonance (ESR) is useful to study the properties of various materials containing paramagnetic impurities such as transition metal ions. The spin Hamiltonian parameters give information about the internal structure of its environment. One of these is the vanadyl ion VO^{2+}. Since tetravalent vanadium exists as a stable vanadyl a number of workers (Rao *et al* 1968; Manoharan and Rogers 1968; Flowers *et al* 1973; Jain and Srinivasan 1977; Jain 1979) have studied these ion-doped lattices. The chemistry of this ion has been reviewed by Selbin (1965, 1966). This ion is formulated as having V^{4+} ion with electronic structure $[Ar]^{18}\ 3d^1$ and a closed shell oxide, O^{2-}, ion and VO^{2+} contains a single unpaired d electron attached to the V^{4+} ion. Its configuration would be similar to the d^1 configuration Ti^{3+} or the conjugate configuration ions, such as Cu^{2+}.

The knowledge of ground-state wavefunction of such a paramagnetic ion doped in crystal is useful to study the ESR parameters g and A and to evaluate the dipolar hyperfine coupling constant P and the Fermi contact parameter K. K is related to the unpaired electron density at the vanadium nucleus and describes the isotropic hyperfine interaction. K is very sensitive to small deformations of the electron orbitals of the vanadium ion resulting in changes in spin polarization of inner s-shells caused by the unpaired electron.

It was, therefore, considered worthwhile to study the ground-state wavefunction of VO^{2+} and calculate the P and K values using crystal field approach. The K values obtained agree with the corresponding calculated values using molecular orbital theory. Further, the optical absorption spectra of these complexes support our calculations for the ground state of vanadyl-doped crystal.

2. Theory and calculations

In vanadyl ion (Kohin 1979) the V-O bond has considerable covalent character and a better description involves a $(V \equiv O)^{3+}$ closed shell molecular core having a substantial covalent triple bond character. To this is added the single unpaired d electron. This d orbital (one of the orbitally degenerate $Y_2^{\pm 2}$ or d_{xy}, $d_{x^2-y^2}$ orbitals) is centred on the vanadium ion and lies in the plane perpendicular to the V-O bond. With this picture of the molecular structure for the axially symmetric ion, three of the five atomic d orbitals participate in the formation of the triple bond. The lowest energy d_{z^2} orbital when suitably hybridized by inclusion of $4s$ orbital forms of σ-bond with the oxygen p_z orbital, while the doubly degenerate d_{xz} and d_{yz} orbitals form π bonds with the p_x and p_y oxygen orbitals. In general one very short V-O bond preserves the identity of the VO^{2+} ion. The bonding to the oxygen atom along the z-axis affects (McGarvey 1966) only the value of $g_\perp$ $g_\parallel$ being affected only by bonding with ligands in the xy plane with x and y-axes coinciding with V-ligand bonds. Further, the spin-orbit interaction on the ligand atoms in the xy plane can affect the spin-Hamiltonian but not any interaction on the oxygen atom.

When the VO^{2+} ion is embedded in a crystal lattice, it is subjected to the crystalline field due to surrounding ligands. In such vanadyl-doped crystals the crystal field is of octahedral symmetry with tetragonal distortion and a small perturbation lowering the symmetry. In the present calculations we have neglected small perturbation. Thus the crystalline field is assumed to be basically of octahedral symmetry with tetragonal distortion, where the tetragonal crystal field is assumed to be larger than the magnitude of the Zeeman splitting.

In a octahedral field with a tetragonal distortion, the equivalent Hamiltonian operator is (Abragam and Bleaney 1970)

$$H_{CF} = B_4 (O_4^0 + 5O_4^4) + B_2^0 O_2^0 + B_4^0 O_4^0. \tag{1}$$

where the B_4 is magnitude of the octahedral field and the last two terms represent the tetragonal distortion of second and fourth degree in the potential, respectively. For d^1 configuration in octahedral symmetry B_4 is a positive (Abragam and Bleaney 1970) quantity, and B_2^0 and B_4^0 are negative (Wertz and Bolton 1972; Poole and Farach 1972) for a compression along the z axis which is applicable in the present case. The splitting of the five levels due to these fields for the D state electron is shown in figure 1.

The lowest state d_{xy} mixes with $d_{x^2-y^2}$, d_{xz} and d_{yz} states due to spin-orbit coupling. The spin-orbit coupling matrix (Poole and Farach 1972) is of the form

$$\langle \psi_i | \lambda \, \mathbf{L.S.} | \psi_j \rangle.$$

Applying the first order perturbation theory it is found that the ground state is of the following form:

$$| \pm \rangle = \pm C_1 | \pm 2, \pm \tfrac{1}{2} \rangle \mp C_2 | \mp 2, \pm \tfrac{1}{2} \rangle \pm C_3 | \mp 1, \mp \tfrac{1}{2} \rangle, \tag{2}$$

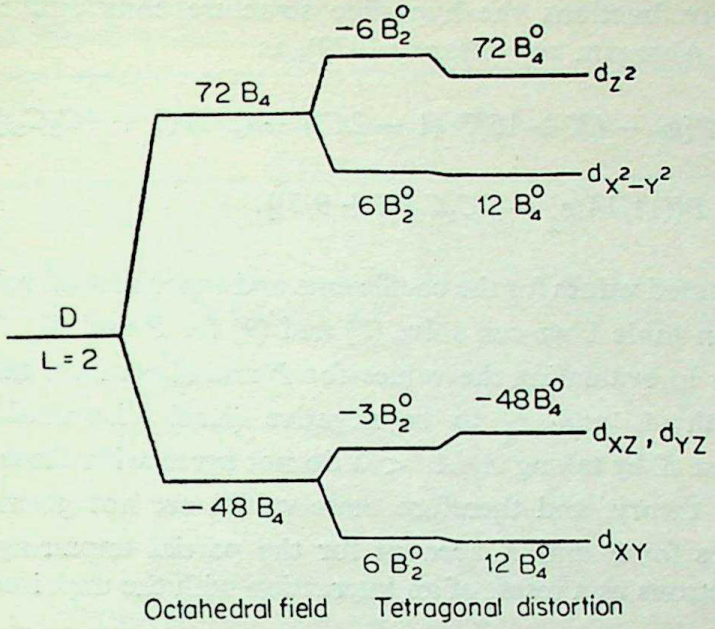

Figure 1. Schematic representation of energy levels of the configuration d^1 as split by octahedral field and by tetragonal distortion.

where the coefficients C_1, C_2 and C_3 give information about the admixture of these states. It is appropriate to relate C_1, C_2 and C_3 with the g factor. This is done by assuming the identity (Poole and Farach 1972)

$$\beta\ \mathbf{H}.\ (\mathbf{L} + 2\,\mathbf{S}) = \beta\ \mathbf{H}.\vec{g}.\ \tilde{\mathbf{S}}, \tag{3}$$

where $\tilde{\mathbf{S}}$ is the effective spin and $\mathbf{S}$ is the actual spin. This is equivalent to

$$i\,(L_x+2S_x) + j\,(L_y+2S_y) + k\,(L_z+2S_z) = g_\perp\,(\tilde{S}_x\,i + \tilde{S}_y\,j) + g_\parallel\,\tilde{S}_z\,k. \tag{4}$$

The matrices of the left and right side components are compared to determine the quantities $g_\perp$ and $g_\parallel$. The effective spin ground state eigenfunctions $|\pm\rangle$ given in (2) are used and we obtain

$$g_\parallel = 2(3C_1^2 - C_2^2 - 2C_3^2), \tag{5}$$

and

$$g_\perp = 4C_1(C_2 - C_3). \tag{6}$$

Further the normalization of the eignfunctions $|\pm\rangle$ give

$$C_1^2 + C_2^2 + C_3^2 = 1 \tag{7}$$

With experimental values of $g_\parallel$ and $g_\perp$ solution of (5), (6) and (7) for C_1, C_2 and C_3 will define the ground-state wavefunction of the system as given in (2).

Using these wavefunctions the hyperfine structure constants can be obtained (McGarvey 1966; Abragam and Bleaney 1970), as

$$A_{\parallel} = P[g_{\parallel} - (K + 15/7)(1 - 2C_3^2) - (3/7)(1 + 4C_2C_3)], \tag{8}$$

and

$$A_{\perp} = P[(11/14)g_{\perp} - 2C_1C_2(K + 9/7)]. \tag{9}$$

Substituting computed values for the coefficients and experimental values of $g_{\parallel}$, $g_{\perp}$, $A_{\parallel}$ and $A_{\perp}$ as given in table 1 we can solve (8) and (9) for P and K. These values are given in table 2. In evaluating the values for P and K we have taken $A_{\parallel}/A_{\perp}$ to be positive with both $A_{\parallel}$ and $A_{\perp}$ to be negative (Kasi Viswanath 1977). Values obtained for P and K by taking $A_{\parallel}/A_{\perp} < 0$ do not agree with those obtained by the molecular orbital theory, and therefore these values are not given for $A_{\parallel}/A_{\perp} < 0$. Appreciable values for P and K account for the partial unpairing or polarization of the inner s electrons as a result of an interaction with the unpaired d electrons.

3. Discussion

In the crystals discussed here vanadium ion has generally been located at the centre of an octahedron of ligands which hold the vanadyl in a fixed direction. Therefore, the crystal field considered here is octahedral with small tetragonal distortion. The ground-state wavefunctions calculated are given in table 2. In our coordinate system (Selbin *et al* 1967) these wavefunctions are of the d_{xy} type with a slight admixture of the excited states d_{xz}, d_{yz} and $d_{x^2-y^2}$. Since unpaired s-electron contributes considerably to the hyperfine structure splitting by virtue of core polarization parameter, K, a small amount of admixture may be necessary to explain the splitting. The contribution of the unpaired s-electron is taken phenomenologically as $PK\mathbf{S}\cdot\mathbf{I}$. For transition ions K is positive. P also varies from crystal to crystal. Van Wieringen (1955) had shown that there is a regular variation of P with covalency. The more ionic the crystal, the larger will be the splitting and hence larger P.

Table 1. Experimental values of g and A for vanadyl-doped crystals.

Crystal lattice	g value		A value in units of 10^{-4} cm^{-1}		Reference
	$g_{\parallel}$	$g_{\perp}[=\frac{1}{2}(g_x + g_y)]$	$A_{\parallel}$	$A_{\perp}[=\frac{1}{2}(A_x + A_y)]$	
$Cs_2Zn(SO_4)_2.6H_2O$	1·936	1·984	181	70·8	Jain and Srinivasan (1977)
$NH_4Al(SO_4)_2.12H_2O$	1·940	1·978	176	67·0	Rao *et al* (1968)
$(NH_4)_2SeO_4$	1·920	1·987	188	75·48	Jain (1979)
$(NH_4)_2SbCl_5$	1·948	1·979	168·8	62·8	Flowers *et al* (1973)
$(NH_4)_3AlF_6$	1·937	1·977	178	64·0	Manoharan and Rogers 1968

Table 2. Ground-state wavefunctions and the calculated values of P and K for vanadyl-doped crystals.

Crystal lattice	Ground-state wave function	$\lvert P \rvert$ in 10^{-4} cm^{-1}	K
$Cs_2Zn(SO_4)_2.6H_2O$	$\pm\frac{1}{\sqrt{2}}(\lvert \pm 2, \pm\frac{1}{2}\rangle - \lvert \mp 2, \pm\frac{1}{2}\rangle)$ $\mp 0{\cdot}0056(\lvert \pm 2, \pm\frac{1}{2}\rangle + \lvert \mp 2, \pm\frac{1}{2}\rangle)$ $\pm 0{\cdot}0054 \lvert \mp 1, \mp\frac{1}{2}\rangle$	120·54	0·86
$NH_4Al(SO_4)_2.12H_2O$	$\pm\frac{1}{\sqrt{2}}(\lvert \pm 2, \pm\frac{1}{2}\rangle - \lvert \mp 2, \pm\frac{1}{2}\rangle)$ $\mp 0{\cdot}0052(\lvert \pm 2, \pm\frac{1}{2}\rangle + \lvert \mp 2, \pm\frac{1}{2}\rangle)$ $\pm 0{\cdot}0076 \lvert \mp 1, \mp\frac{1}{2}\rangle$	119·84	0·83
$(NH_4)_2SeO_4$	$\pm\frac{1}{\sqrt{2}}(\lvert \pm 2, \pm\frac{1}{2}\rangle - \lvert \mp 2, \pm\frac{1}{2}\rangle)$ $\mp 0{\cdot}0070(\lvert \pm 2, \pm\frac{1}{2}\rangle + \lvert \mp 2, \pm\frac{1}{2}\rangle)$ $\pm 0{\cdot}0043 \lvert \mp 1, \mp\frac{1}{2}\rangle$	120·60	0·90
$(NH_4)_2SbCl_5$	$\pm\frac{1}{\sqrt{2}}(\lvert \pm 2, \pm\frac{1}{2}\rangle - \lvert \mp 2, \pm\frac{1}{2}\rangle)$ $\mp 0{\cdot}0045(\lvert \pm 2, \pm\frac{1}{2}\rangle + \lvert \mp 2, \pm\frac{1}{2}\rangle)$ $\pm 0{\cdot}0071 \lvert \mp 1, \mp\frac{1}{2}\rangle$	117·49	0·80
$(NH_4)_3AlF_6$	$\pm\frac{1}{\sqrt{2}}(\lvert \pm 2, \pm\frac{1}{2}\rangle - \lvert \mp 2, \pm\frac{1}{2}\rangle)$ $\mp 0{\cdot}0054(\lvert \pm 2, \pm\frac{1}{2}\rangle + \lvert \mp 2, \pm\frac{1}{2}\rangle)$ $\pm 0{\cdot}0079 \lvert \mp 1, \mp\frac{1}{2}\rangle$	124·94	0·78

Table 3. Optical data for vanadyl-doped crystals.

Host lattice	Wave numbers for transitions $d_{xy}\rightarrow d_{xz}$ and d_{yz} in cm^{-1}	Wave numbers for transitions $d_{xy}\rightarrow d_{x^2-y^2}$ in cm^{-1}	Calculated value of K using molecular orbital theory	Reference
$Cs_2Zn(SO_4)_2.6H_2O$	13·365	16·390	0·88	Lakshman Rao and Purandar (1980)
$NH_4Al(SO_4)_2.12H_2O$	13·000	15·700	–	Rao *et al* (1968)
$(NH_4)_2SeO_4$	13·333	16·129	0·90	Jain (1979)
$(NH_4)_2SbCl_5$	11·750	13·500	–	Flowers *et al* (1973)
$(NH_4)_3AlF_6$	14·100	18·200	0·85	Manoharan and Rogers (1968)

Various experiments on optical absorption spectra of VO^{2+}-doped crystals show broad bands (see table 3) at such values of wavenumbers which correspond to the *d-d* transition in vanadyl. The corresponding transition are $d_{xy}\rightarrow d_{x^2-y^2}$ and $d_{xy}\rightarrow d_{xz}$ and d_{yz}. These bands support our argument that d_{xy} is the ground state in our coordinate system.

Calculations based on the molecular orbital theory (Kohin 1979) for vanadyl-doped crystals give the values (table 3) of Fermi contact coupling parameter which closely agree with the corresponding values obtained by the present calculations.

Acknowledgements

This work was supported in part by the CSIR, New Delhi. The authors wish to thank Prof. T S Jaseja for his interest and encouragement.

References

Abragam A and Bleaney B 1970 *Electron Paramagnetic Resonance of Transition Ions* (Oxford: Clarendon Press) pp. 372–74, 787

Flowers J M, Hempel J C, Hatfield W E and Dearman H H 1973 *J. Chem. Phys.* **58** 1479

Jain V K and Srinivasan T M 1977 *Z. Naturforsch.* **32a** 1068

Jain V K 1979 *J. Phys. Soc. Jpn.* **46** 1250

Kasi Viswanath 1977 *J. Chem. Phys.* **67** 3744

Kohin R P 1979 *Magnetic resonance review* (ed.) C P Poole (New York: Gordon and Breach) Vol. 5 p. 75

Lakshmana Rao J and Purandar K 1980 *Solid State Commun.* **33** 363

Manoharan P T and Rogers M T 1968 *J. Chem. Phys.* **49** 3912

McGarvey B R 1966 in *Transition Metal Chemistry* Vol 3 (ed.) R L Carlin (New York: Marcel Dekker) pp. 115, 150.

Poole C P Jr. and Farach H A 1972 *The theory of magnetic resonance* (New York: Wiley Interscience) p. 357

Rao K V S, Sastry M D and Venkateswarlu P 1968 *J. Chem. Phys.* **49** 4984

Selbin J 1965 *Chem. Rev.* **65** 153

Selbin J 1966 *Coord. Chem. Rev.* **1** 293

Selbin J, Maus C and Johnson D L 1967 *J. Inorg. Nucl. Chem* **29** 1735

Van Wieringen J S 1955 *Discus. Faraday Soc.* **19** 118

Wertz J E and Bolton J R 1972 *Electron spin resonance elementary theory and practical applications* (New York: McGraw Hill) p. 274

Pramāṇa, Vol. 21, No. 1, July 1983, pp. 71–78 © Printed in India.

Electrical resistance and dielectric constant anomaly in the critical liquid mixture methanol + cyclohexane

C SHETTY, M K GUNASEKARAN, V VANI and E S R GOPAL
Department of Physics, Indian Institute of Science, Bangalore 560 012, India

MS received 7 March 1983; revised 10 May 1983

Abstract. The electrical resistance R and the dielectric constant ϵ of the critical binary liquid mixture methanol plus cyclohexane has been measured near the critical point at five different spot frequencies from 10—100 kHz. The data are analysed using a nonlinear least squares routine. The fit is equally good for an α (= 0·1) divergence or a $1-\nu$ (= 0·35) divergence of dR/dT and $d\epsilon/dT$. Additional reasons are advanced to indicate that the α divergence is a better description.

Keywords. Electrical resistance; dielectric constant; critical phenomena.

1. Introduction

Many thermodynamic quantities exhibit anomalous behaviour near their second-order phase transition point. The universality and other features of the critical point phenomena are well known (Stanley 1971; Ma 1976; Kumar *et al* 1982). The temperature derivatives of the resistance R and the dielectric constant ϵ are expected to show singular behaviour near the critical point

$$(R - R_c)/R_c = A\,(1)\,t + A\,(2)\,t^{\theta} + A\,(3)\,t^{\theta+\Delta} + \ldots,$$

and

$$(\epsilon - \epsilon_c)/\epsilon_c = B''\,(1)\,t + B''\,(2)\,t^{\theta} + B''\,(3)\,t^{\theta+\Delta} + \ldots, \qquad (1)$$

where $t = (T - T_c)/T_c$, T is the temperature, T_c is the critical temperature, R_c is the resistance at $T = T_c$, ϵ_c is the dielectric constant at $t = 0$, θ is an exponent, whose value lies betwen 0 and 1, and $\Delta = 0{\cdot}5$ is the first Wegner correction exponent (Wegner 1972). When $T \to T_c$, dR/dt and $d\epsilon/dt$ both diverge to infinity with the leading singular term being $t^{-(1-\theta)}$.

The theoretical and the experimental situation regarding the exponent $(1 - \theta)$ is inconclusive. As regards the resistance divergence, the theoretical calculations as well as the experimental observations yield both values of the exponent $(1 - \theta)$ as $1 - 2\beta$ or $1 - \nu = 0{\cdot}35$ and as $(1 - \theta) = \alpha = 0{\cdot}1$ (Jasnow *et al* 1974; Shaw and Goldburg 1976; Ramakrishnan *et al* 1978). In the dielectric anomaly, the theoretical predictions favour $1 - \theta = \alpha = 0{\cdot}1$ (Sengers *et al* 1980) while the experimental situation is not clear between the choice of 0·1 or 0·35 (Thoen *et al* 1980, 1981; Balakrishnan *et al* 1982; Gunasekaran and Gopal 1982) for the exponents. On very general theoretical considerations, one should get the same exponent for the

dR/dt and $d\epsilon/dt$ divergences (Kumar and Jayannavar 1981). Thus the situation warrants further investigation.

So far no studies have been undertaken to investigate the resistivity and dielectric constant on the same samples, in spite of the interrelation between the two. The present work seems to be the first such investigation. A preliminary account of this has been briefly reported earlier (Shetty *et al* 1981; 1982).

2. Experimental measurements

A novel double ratio transformer bridge has been developed to measure the dielectric constant of partially conducting liquids (Gunasekaran *et al* 1981). This method uses two ratio transformers for balancing the resistive and capacitive components of an a.c. bridge. Independent estimates of R and C with 10–100 ppm resolutions are possible without interference from ground capacitances and leakage inductances. A fixed standard resistance and capacitance are needed. The error signal from the bridge is detected for its in-phase and quadrature components using a vector lock-in-amplifier built here. The ratio-transformers, wound on supermumetal toroidal cores become ineffective at high frquencies and thus the absolute errors in the R and C values approach 1 % at 100 kHz. The low frequency limit of 10 Hz is set again by the large magnetizing currents of the transformer. At frequencies of 1 kHz the absolute accuracies are in the region of 0·1 to 0·03 %.

The experiment is carried out in a paraffin oil bath of 35 litres capacity, whose temperature is controlled to ± 1 mK using a PID controller. Initially the bath temperature is raised to 5 or 6 ° above the critical temperature and all measurements are made while cooling the bath temperature in steps of a few mK. The experiment is conducted with the liquids filled in a glass cell of height 1 cm into which a pair of platinum electrodes, 1mm apart, are dipped. The liquids used are of Analar grade and are used without further purification. The critical concentration of this liquid mixture is X_c=0·2903 mass fraction of methanol with a critical temperature T_c= 319·026 K (Huang and Webb 1969). Since the dielectric constant and the resistivity depend upon a fixed cell constant, measured resistance and capacitance are analysed to preserve the high resolution of the data.

3. Analysis

The data consist of resistance R and capacitance C readings as a function of temperature at different frequencies 10 and 100Hz, 1, 10 and 100 kHz for the resistance, and 5, 10, 50 and 100 kHz for the capacitance. The electrode polarization problem makes the capacitance measurements at lower frequencies difficult.

The data are analysed by fitting them to the equations of the form (1) using a non-linear least squares procedure like the CURFIT program (Bevington 1969). This type of analysis proves to be indecisive. The estimation of R_c and C_c proves to be uncertain and different choices lead to different values of the other parameters. The exponent $(1-\theta)$ has values ranging from 0·05 to 0·5. Also because of the large number of parameters to be estimated, correlations among their values are set up yielding χ^2 which cannot be separated out, for instance the residuals become less than the

errors in the measurements for a range of the parameter values. The possibility of leaving R_c or C_c as a free parameter, to be obtained from the least square analysis itself, adds one more parameter to be estimated and makes the correlations even worse.

As a result, a better procedure of data analysis seems to work with the differentiated forms of (1) eliminating the need to know R_c and C_c. The increase of scatter in data during the numerical differentiation is countered by other criteria of judging the goodness of fit, instead of using χ^2 as a test. For instance one has

$$\mathrm{d}R/\mathrm{d}t = L + Mt^{-(1-\theta)} + Nt^{-(1-\theta+\Delta)},$$

$$\mathrm{d}C/\mathrm{d}t = \bar{L} + \bar{M}t^{-(1-\theta)} + \bar{N}t^{-(1-\theta+\Delta)}. \tag{2}$$

The M or $\bar{M}$ term is the asymptotic singularity and the N or $\bar{N}$ term with Δ taken as 0·5 is the first Wegner correction to scaling. One may use the criterion that the correction to scaling must be smaller than the main singularity in order to choose the preferred values of the parameters.

Consider the resistance data first. To analyse the $\mathrm{d}R/\mathrm{d}T$ data, the $(1 - \theta)$ value was fixed at 0·1 and 0·35, the theoretically predicted exponents. The best fitted data are reproduced in figures 1 and 2. Table 1 gives the values of the best fit parameters.

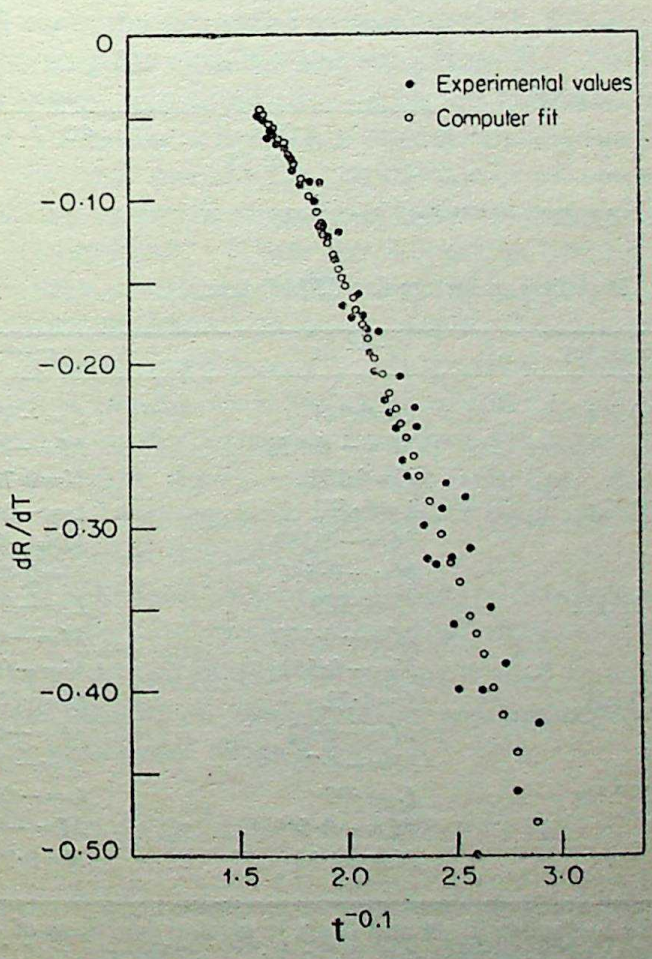

Figure 1. $\mathrm{d}R/\mathrm{d}T$ *vs* $t^{-0.1}$ data for 1 kHz.

From the parameters one can discuss whether the magnitude of the Wegner correction term is smaller than the main singular term in the critical region.

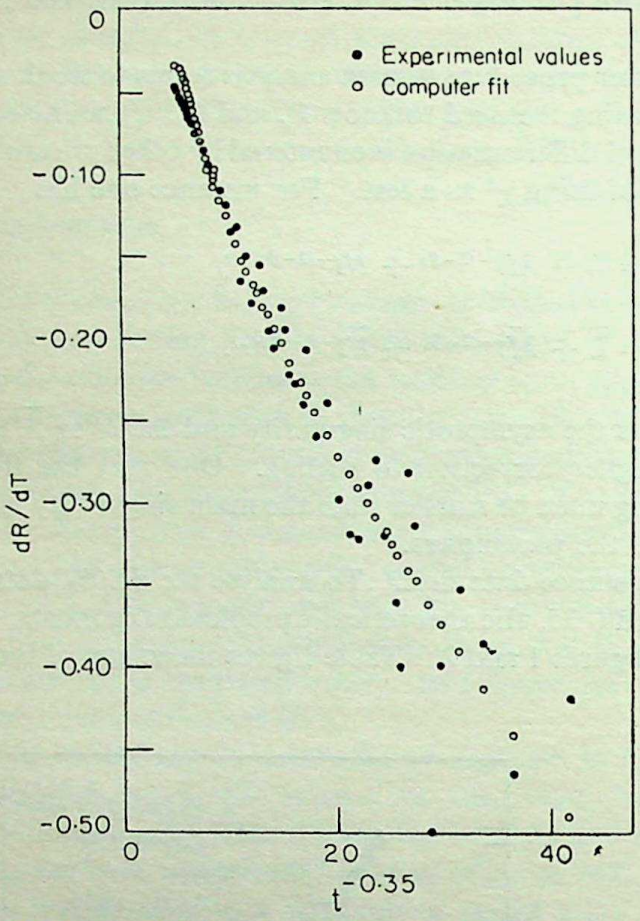

Figure 2. dR/dT *vs* $t^{-0.35}$ data for 1 kHz.

Table 1. Best fit parameters for dR/dT data.

Frequency	$t^{-0.1}$ fit	$t^{-0.35}$ fit
10 Hz	$L=0{\cdot}341$	$L=-0{\cdot}373$
	$M=-0{\cdot}253$	$M=-0{\cdot}004$
	$N=0{\cdot}191$	$N=0{\cdot}743$
100 Hz	$L=0{\cdot}672$	$L=-0{\cdot}189$
	$M=-0{\cdot}389$	$M=-0{\cdot}009$
	$N=-0{\cdot}641$	$N=0{\cdot}402$
1 kHz	$L=0{\cdot}669$	$L=-0{\cdot}250$
	$M=-0{\cdot}392$	$M=-0{\cdot}008$
	$N=-0{\cdot}562$	$N=-0{\cdot}535$
10 kHz	$L=1{\cdot}22$	$L=0{\cdot}075$
	$M=-0{\cdot}62$	$M=-0{\cdot}018$
	$N=-1{\cdot}74$	$N=-0{\cdot}618$
100 kHz	$L=1{\cdot}05$	$L=-0{\cdot}058$
	$M=-0{\cdot}549$	$M=-0{\cdot}013$
	$N=-1{\cdot}39$	$N=0{\cdot}776$

Note: The coefficients L, M and N are in general functions of ω and θ where ω is the frequency and θ is the exponent (0·1 or 0·35). The values of the coefficients are given to three significant figures.

Table 2. Coefficients and ratios of singular and correction terms for dR/dT data.

Frequency	0·1 fit			0·35 fit		
	$Mt^{-0.1}$	$Nt^{+0.4}$	X	$Mt^{-0.35}$	$Nt^{+0.15}$	Y
Datum point closest to T_c						
10 Hz	−0·683	0·003	22·7	−0·136	0·163	0·834
100 Hz	−1·05	−0·012	87·5	−0·306	0·088	3·47
1 kHz	−1·05	−0·010	105·0	−0·272	0·117	2·32
10 kHz	−1·68	−0·032	52·5	−0·612	−0·136	4·50
100 kHz	−1·48	−0·026	56·9	−0·442	0·170	2·60
Datum point farthest from T_c						
10 Hz	−0·404	0·029	13·9	−0·020	0·372	0·053
100 Hz	−0·622	−0·097	6·41	−0·045	0·201	0·223
1 kHz	−0·627	−0·085	7·37	−0·040	0·268	0·149
10 kHz	−1·00	−0·265	3·77	−0·090	−0·309	0·291
100 kHz	−0·878	−0·211	4·16	−0·065	0·389	0·167

X represents $|M(0{\cdot}1, \omega)t^{-0.5}/N(0{\cdot}1, \omega)|$ and Y represents $|M(0{\cdot}35, \omega)t^{-0.5}/N(0{\cdot}35, \omega)|$

Consider the fit of 1 kHz dR/dT data. In the $t^{-0.1}$ plot, the singular term $M\,t^{-0.1}$ is nearly 100 times larger than the correction to the singular term when $T \simeq T_c$ and nearly 7·34 times larger when T is farthest away from T_c. In the $t^{-0.35}$ fitting the singular term $Mt^{-0.35}$ is nearly 2·31 times the correction to singular term closest to T_c and only 0·149 times the correction to singular term farthest away from T_c. The contributions from the singular and correction terms and their ratios are tabulated for all the different frequencies in table 2. To test the suitability of parameters one can use the χ^2 or similar numerical criteria. But, this method has the difficulties of correlations among the parameters and of having to decide among residuals which are all less or comparable to the experimental uncertainties. If one uses a criterion that the contribution from correction-to-singular term should be smaller than the contribution from the singular term, when the $t^{-0.1}$ fit is found to be more acceptable. The correction term becomes important when one is going away from T_c. At the data points farthest away from T_c the correction term is smaller than the main singular term for the 0·1 fit at all frequencies. For the 0·35 fit the correction term becomes larger than the main term.

To analyse the dC/dT data, the $(1-\theta)$ value is once again fixed at 0·1 and 0·35. Figures 3 and 4 show the fits obtained and table 3 gives the values of the test fit parameters for all the different frequencies.

Consider the fit for 50 kHz data. One notices that the fit obtained with one Wegner correction to scaling term for $(1-\theta)=0{\cdot}1$ gives a maximum at small values of dC/dT. Since the estimation of $\overline{L}$, $\overline{M}$ and $\overline{N}$ with the exponent fixed amounts to a linear least square estimation, this implies an inadequacy of the functional form. Therefore, a fit was tried with the next order Wegner term

$$\overline{L} + \overline{M}t^{-(1-\theta)} + \overline{N(1)}t^{-(1-\theta+\Delta)} + \overline{N(2)}t^{-(1-\theta+2\Delta)}. \qquad (3)$$

The addition of a second correction term removes the pronounced maximum and gives a good fitting. The values of correction and singular terms, and their ratios for all the frequencies, *i.e.* 5, 10, 50 and 100 kHz are summarised in table 4. Once again,

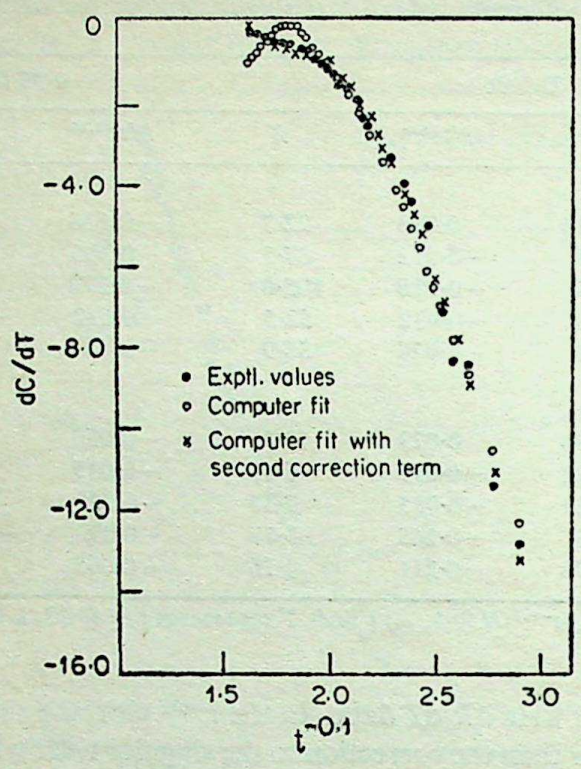

Figure 3. dC/dT *vs* $t^{-0.1}$ data for 50 kHz.

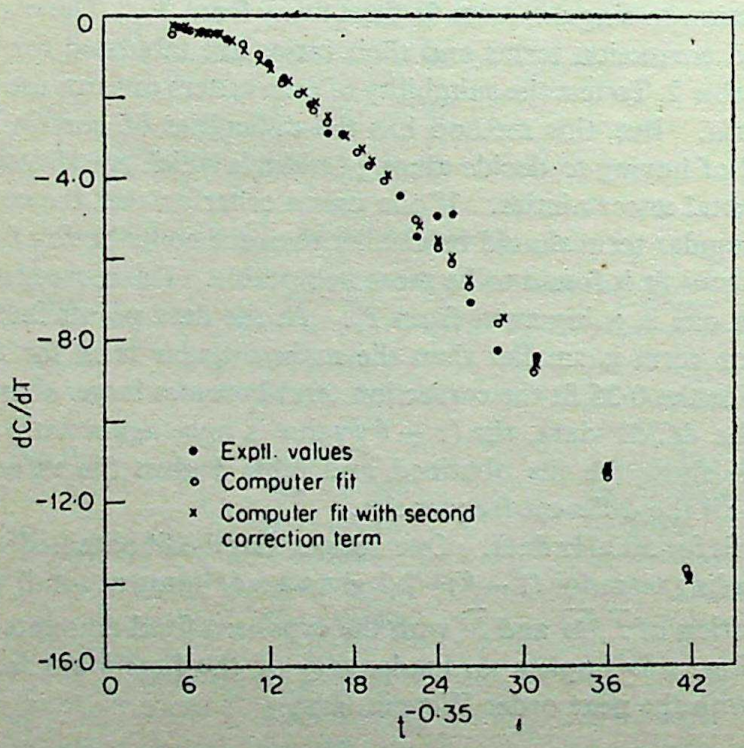

Figure 4. dC/dT *vs* $dt^{-0.35}$ data for 50 kHz.

if the criterion regarding the relative magnitudes of the singular and correction terms is used, the $t^{-0.1}$ fit would be preferred. At the datum point farthest away from T_c where the correction term begins to be important, the main singularity is still larger

for the 0·1 fit, while it becomes 1/4 to 1/5 of the correction contribution in the 0·35 fit. Therefore this criterion indicates an $\alpha(=0{\cdot}1)$ singularity for dC/dT. However two correction terms are needed for the alpha exponent fitting, while the $(1-\nu)=0{\cdot}35$ exponent fitting gives a reasonable shape of the curve with one correction term as in figure 4. This point makes it difficult to prefer the exponent categorically. Clearly this question needs to be investigated further.

Table 3. Best fit parameters for dC/dT data.

Frequency	$t^{-0.1}$ fit	$t^{-0.35}$ fit
5 kHz	$\bar{L} = 68{\cdot}68$	$\bar{L} = 23{\cdot}22$
	$\bar{M} = -27{\cdot}45$	$\bar{M} = -0{\cdot}6940$
	$\bar{N}(1) = -271{\cdot}5$	$\bar{N}(1) = -49{\cdot}88$
	$\bar{N}(2) = 1192$	$\bar{N}(2) = 105{\cdot}7$
10 kHz	$\bar{L} = 69{\cdot}77$	$\bar{L} = 22{\cdot}70$
	$\bar{M} = -27{\cdot}93$	$\bar{M} = -0{\cdot}6970$
	$\bar{N}(1) = -274{\cdot}4$	$\bar{N}(1) = -48{\cdot}20$
	$\bar{N}(2) = 1198$	$\bar{N}(2) = 97{\cdot}74$
50 kHz	$\bar{L} = 56{\cdot}77$	$\bar{L} = 14{\cdot}78$
	$\bar{M} = -23{\cdot}11$	$\bar{M} = -0{\cdot}5490$
	$\bar{N}(1) = -212{\cdot}2$	$\bar{N}(1) = -28{\cdot}81$
	$\bar{N}(2) = 888{\cdot}4$	$\bar{N}(2) = 43{\cdot}78$
100 kHz	$\bar{L} = 47{\cdot}04$	$\bar{L} = 13{\cdot}11$
	$\bar{M} = -19{\cdot}15$	$\bar{M} = -0{\cdot}4640$
	$\bar{N}(1) = -177{\cdot}6$	$\bar{N}(1) = -26{\cdot}68$
	$\bar{N}(2) = 757{\cdot}2$	$\bar{N}(2) = 49{\cdot}18$

Note. The coefficient $\bar{L}$, $\bar{M}$, $\bar{N(1)}$ and $\bar{N(2)}$ are in general functions of ω and θ where ω is the frequency and θ is the exponent (0·1 or 0·35). The values of the coefficients are given to four significant figures.

Table 4. Coefficients and ratios of singular and correction terms for dC/dT data.

Frequency	0·1 fit				0·35 fit			
	$\bar{M}t^{-0.1}$	$N(1)t^{+0.4}$	$N(2)t^{+0.9}$	$\bar{X}$	$\bar{M}t^{-0.35}$	$N(1)t^{+0.15}$	$N(2)t^{+0.65}$	$\bar{Y}$
Datum point closest to T_c								
5 kHz	−79·60	−3·801	0·0715	21·34	−28·45	−10·12	0·1057	2·840
10 kHz	−80·99	−3·841	0·0718	21·48	−28·57	− 9·784	0·0977	2·949
50 kHz	−67·01	−2·970	0·0533	22·97	−22·54	− 5·848	0·0437	3·883
100 kHz	−55·53	−2·486	0·0454	22·75	−19·02	− 5·416	0·0491	3·543
Datum point farthest from T_c								
5 kHz	−43·92	−41·26	16·69	1·787	−3·747	−24·19	4·652	0·1917
10 kHz	−44·68	−41·70	16·77	1·792	−3·763	−23·37	4·300	0·1973
50 kHz	−36·97	−32·25	12·43	1·865	−2·964	−13·97	1·926	0·2460
100 kHz	−30·64	−26·99	10·60	1·869	−2·505	−12·93	2·163	0·2326

$\bar{X}$ represents $|\bar{M}t^{-0.1}/N(1)t^{+0.4} + N(2)t^{+0.9}|$ and $\bar{Y}$ represents $|\bar{M}t^{-0.35}/N(1)t^{+0.15} + N(2)t^{+0.65}|$

Finally we note that the standard deviations* obtained for L, M and N of dR/dT data at 1 kHz are 0·0030, 0·0064 and 0·27 for the 0·1 fit and $0{\cdot}47\times10^{-4}$, 0·0130 and 0·11 for 0·35 fit. For dC/dT data at 50 kHz the standard deviations of $\overline{L}$, $\overline{M}$, $\overline{N(1)}$ and $\overline{N(2)}$ are as follows: 0·0044, 0·019, 3·1 and 78 for the 0·1 fit and $0{\cdot}75\times10^{-4}$, 0·0190, 0·140 and 5·1 for the 0·35 fit.

In conclusion, we may say that when the dR/dT and dC/dT data are analysed for their critical divergence, both 0·1 and 0·35 exponents give good fit. As mentioned in §1, the mere experimental data is probably unable to resolve this ambiguity. The 0·1 exponent seems to be preferred if we expect the contribution from the singular term to be the leading contribution in the critical region.

Acknowledgements

The authors acknowledge financial help from CSIR, UGC, DST and the Electronics Commission and also thank Dr (Mrs.) Jyothi Balakrishnan and Mr S Guha for their help.

References

Balakrishnan J, Gunasekaran M K and Gopal E S R 1982 *Chem. Phys. Lett.* **88** 305

Bevington P R 1969 *Data reduction and error analysis for the physical sciences* (New York: McGraw-Hill)

Gunasekaran M K, Gopal E S R, Shetty C and Jyothi S 1981 *J. Phys.* **E14** 381

Gunasekaran M K and Gopal E S R 1982 *Eighth symp. on thermophysical properties, Maryland.* (ed) J V Sengers. p. 474

Huang J and Webb W W 1969 *J. Chem. Phys.* **50** 3694

Jasnow D, Goldburg W I and Semura J S 1974 *Phys. Rev.* **A9** 355

Kumar A, Krishnamurthy H R and Gopal E S R 1982 *Equilibrium critical phenomena in binary liquid mixtures.* NTPP Report (unpublished)

Kumar N and Jayannavar A M 1981 *J. Phys.* C **14** 785

Ma S K 1976 *Modern theory of critical phenomena* (New York: Benjamin)

Ramakrishnan J, Nagarajan N, Kumar A, Gopal E S R, Chandrasekhar P and Ananthakrishnan G 1978 *J. Chem. Phys.* **68** 4098

Scott R L 1982 (private communication)

Sengers J V, Bedeaux D, Mazur P and Greer S C 1980 *Physica* **A 104** 573

Shaw C H and Goldburg W I 1976 *J. Chem. Phys.* **65** 4906

Shetty C, Gunasekaran M K, Vani V, Jyothi S and Gopal E S R 1981 *Nucl. Phys. Solid State Phys. Symp.* **C24** 347

Shetty C, Gunasekaran M K, Vani V, Jyothi Balakrishnan, Guha S and Gopal E S R 1982 *Second National Conference on Dielectrics and Ferroelectrics*, Raipur, India

Stanley H E 1971 *Introduction to phase transitions and critical phenomena.* (New York: Oxford University Press)

Thoen J, Kindt R and Wan Deal W 1980 *Phys. Lett.* **A 76** 445

Thoen J, Kindt R and Wan Deal W 1981 *Phys. Lett.* **A 87** 73

Wegner F J 1972 *Phys. Rev.* **135** 4529

*There exists a logical complication in the CURFIT program published in Bevington's book, which was pointed out to us by Dr Scott of the University of California (Scott 1982). The parameter FLAMDA becomes very large if the iterations are allowed to continue after the convergence and affects the standard deviation values. The program is to be changed slightly. The unmodified ARRAY matrix must be stored as ARSAV and finally the ARSAV matrix is inverted to get the standard deviations.

Pramāṇa, Vol. 21, No. 1, July 1983, pp. 79–88. © Printed in India.

Two-photon excitation spectrum of benzonitrile vapour

N PERIASAMY and S DORAISWAMY
Chemical Physics Group, Tata Institute of Fundamental Research, Bombay 400 005, India

MS received 4 March 1983

Abstract. The two-photon excitation spectrum of benzonitrile in the gas phase at about 1 torr has been recorded and analysed in the total energy region of 36300 to 40500 cm^{-1} using both linearly and circularly polarised light from a Nd-YAG pumped dye laser. The two-photon spectrum consists of strong Franck Condon (FC) transitions bearing a good resemblance to the one-photon spectrum and also vibronic coupling (VC) transitions essentially arising out of the analogue of the benzene ν_{14}. By a comparative study of the TP spectra of various other monosubstituted benzenes, it has been inferred that the strong TP spectrum of benzonitrile should be ascribed to a considerable π charge delocalization over the phenyl and nitrile groups.

Keywords. Two-photon spectroscopy; benzonitrile.

1. Introduction

The last decade has seen the emergence of two-photon spectroscopy as a powerful spectroscopic tool for investigating the excited electronic states of molecules, which are not possible by conventional one-photon excitation (Wunsch *et al* 1977, Mikami and Ito 1975; Robey and Schlag 1978; Vasudev and Brand 1979a, b; Goodman and Rava 1981; Chia and Goodman 1982; Rava and Goodman 1982). The two-photon excitation spectrum is generally obtained by monitoring the fluorescence intensity from the sample excited by the simultaneous absorption of two photons from a tunable dye laser beam focussed on to the sample cell. The two-photon absorption process is feasible with either two identical photons from a single laser beam or two distinguishable photons from two different laser beams. The advantages of two-photon (TP) spectroscopy are: (i) the selection rules for the two-photon absorption are complementary to those of one-photon (OP) absorption. Forbidden transitions in OP spectroscopy may be permitted in TP spectroscopy and vice versa. (ii) the symmetry assignments of excited states can be made on the basis of the absorption intensity for linearly and circularly polarized light even in randomly-oriented samples.

According to the predictions of simple molecular orbital theory, benzene has four low-lying $\pi\pi^*$ singlet states. They are generally labelled as $^1B_{2u}$, $^1B_{1u}$, $^1E_{1u}$ and $^1E_{2g}$ [^1L_b, ^1L_a, $^1B_{ab}$ and $^1C_{ab}$ in Platt's notation] having energies of nearly 4.9, 6, 6.5 and 8 eV respectively with respect to the ground state $^1A_{1g}$. The first three states arise from the excitation of an electron from the highest occupied molecular orbital (e_{1g}) to the lowest unoccupied orbital (e_{2u}), while the E_{2g} state arises from the promotion of the electron to the highest unoccupied π-electron molecular orbital b_{2g}.

The well-known, much studied symmetry- and parity-forbidden $^1B_{2u} \leftarrow {}^1A_{1g}$ tran-

sition of benzene occurring at 260 nm derives its intensity in both OP and TP spectra through vibronic interactions. While the OP spectrum is built on the vibronic origin from the ν_6 (e_{2g}) vibration (Sklar 1937), the TP spectrum is mainly induced by the ν_{14} (b_{2u}) vibration and to a lesser extent by ν_{17} (e_{2u}) and ν_{18} (e_{1u}) vibrations (Wunsch *et al* 1977; Lombardi *et al* 1976). Monosubstitution lowers the molecular symmetry from D_{6h} to C_{2v} symmetry. The lowest-lying $\pi^* \leftarrow \pi$ transition in monosubstituted benzene derivatives generally falls in the range of 260–320 nm and are essentially derived from the 260 nm band in benzene. The orbitals involved in forming the lowest excited benzene configuration (e_{1g}, e_{2u}) now in C_{2v} give rise to four states, two of symmetry A_1 and two of symmetry B_2. In spite of the fact that transitions to these states are group theoretically permitted, the lowest one is often weak due to the fact that the transition moment is small (Hartford and Lombardi 1971).

There are two ways in which a substituent may affect the electronic structure of benzene: (i) inductive effect, in which a substituent may change the potential acting on the π electrons. It has been shown (Murrell 1963) that because of the inductive effect, the intensity of the ^1L_b OP spectrum gets enhanced; (ii) mesomeric effect, in which the electrons are transferred between a substituent and the benzene ring resulting in an interaction between the states arising from such a transfer [often referred to as charge transfer (CT) or electron transfer states] and the locally excited states. The energy of a charge-transfer state, in which there is no overlap of donor and acceptor orbitals is given by (I-A-C) where I is the ionization potential of the donating group, A is the electron affinity of the acceptor group and C is the Coulombic interaction between the donated electron and the positive hole left behind by it. The amount of charge transfer contamination in the locally excited states depends linearly on the perturbation matrix element (given by the resonance integral β) and inversely on the energy separation between the CT state and locally excited state. Based on the energies of charge transfer configurations, which have a strong influence on the nature of the absorption spectra of the monosubstituted benzenes, the substituents are classified as weak or strong. It has been shown (Goodman and Rava 1981) that the inductive substituents cause a mixing of ^1B_b state with ^1L_b state and contributes to an enhancement of the intensity of the $^1B_2 \leftarrow {}^1A_1$ OP spectrum, whereas mesomeric substituents, by imparting charge transfer character to the locally-excited states, contribute to the intensity of the $^1B_2 \leftarrow {}^1A_1$ two-photon spectrum.

In this communication, we report the two-photon spectrum of benzonitrile, the first aromatic molecule with a moderately strong π electron acceptor substituent. From an extensive microwave work on a number of isotopic species of benzonitrile (Bak *et al* 1962), it has been inferred that in the electronic ground state the contribution of ionic structures is not significant to account for the geometrical modifications in the ring due the nitrile group. This is in good agreement with the small mesomeric dipole moment of 0·2 debye (Bak *et al* 1962). The 33 normal vibrations of benzonitrile — ($12a_1 + 11b_2$) in-plane and ($3a_2 + 7b_1$) out-of-plane have been characterised by infrared studies (Green and Harrison 1976). The near ultraviolet spectrum of benzonitrile (Hirt and Howe 1948) has confirmed that benzonitrile has a very strong O_0^0 band at 36516 cm^{-1} (compared with 36512 cm^{-1} recorded by Brand and Knight 1970) and most of the spectral intensity arises from the excitation of totally symmetric vibrations. From a rotational analysis of the O_0^0 band of the $^1B_2 \leftarrow {}^1A_1$ transition, it has been found (Brand and Knight 1970) that the increase in the long axis moment of inertia is greater than the increase about

the short axis. These results have been rationalized by assuming the B_2 state to have a charge transfer character together with local excitation character and it has been concluded that the phenyl group acts as an electron donor in the charge transfer process.

2. Theory

In the ground state, benzonitrile has been shown by microwave studies to be a planar molecule having C_{2v} symmetry (Bak *et al* 1962). If the molecule is chosen to be in the yz plane with the z axis along the C — C ≡ N axis and x axis perpendicular to the molecular plane, then the one-photon transition moment to the B_2 state is given by

$$M_y = \langle A_1 \mid \mu_y \mid B_2 \rangle.$$

The simultaneous absorption of two photons causing an excitation of a molecule from the ground state g to an excited state f through an intermediate state i can be described by a tensor S_{gf} (McClain and Harris 1977). For the absorption of two identical photons, as it happens in a single laser beam experiment, the tensor becomes symmetric and can be written as

$$S^{gf}_{\rho\sigma} = \sum_i \frac{1}{(\Delta E_{ig} - \hbar\omega)} [\langle g \mid \mu_\rho \mid i \rangle \langle i \mid \mu_\sigma \mid f \rangle + \langle g \mid \mu_\sigma \mid i \rangle \langle i \mid \mu_\rho \mid f \rangle],$$

where the intermediate states i are other eigenstates. ΔE_{ig} is the energy difference between the ground and intermediate states, $\hbar\omega$ is the laser photon energy, μ_ρ and μ_σ are the appropriate electric dipole component, and ρ, σ are any two axes of the molecule-fixed set, x, y, z. For a molecule of C_{2v} symmetry such as benzonitrile, $S_{\rho\sigma}$ mostly involves only the in-plane S_{yz} component for a transition to the L_b state having B_2 symmetry.

$$S_{yz} = \sum_i \frac{1}{(\Delta E_{ig} - \hbar\omega)} [\langle A_1 \mid \mu_y \mid i \rangle \langle i \mid \mu_z \mid B_2 \rangle + \langle A_1 \mid \mu_z \mid i \rangle \langle i \mid \mu_y \mid B_2 \rangle].$$

The low-lying, strongly-allowed $B_{a,\,b}$ (E_{1u}) state of benzene, which splits into A_1 and B_2 states in C_{2v} symmetry will be the dominant intermediate state and is expected to contribute significantly to the TP intensity. The prominent absorption in the OP spectrum of benzonitrile occurs near 53000 cm^{-1} (Kimura and Nagakura 1965) and correspond to the transition that correlate with the E_{1u} state of benzene.

In two-photon spectroscopy the orientationally averaged two-photon absorptivity δ_{av} may be expressed in terms of three invariants (McClain and Harris 1977):

$$\delta_{av} = \delta_F F + \delta_G G + \delta_H H,$$

where F, G and H are functions of the incident beam polarizations e_1 and e_2. If common proportionality constants are ignored

$$\delta_F = \sum_{\rho\sigma} S_{\rho\rho} S^*_{\sigma\sigma}, \delta_G = \sum_{\rho\sigma} S_{\rho\sigma} S^*_{\rho\sigma}, \delta_H = \sum_{\rho\sigma} S_{\rho\sigma} S^*_{\sigma\rho}.$$

For a measurement using single laser beam $S_{\rho\sigma} = S_{\sigma\rho}$, so that $\delta_G = \delta_H$ and hence only two unique absorptivities δ_F and δ_G can be determined. Since δ_F is a measure of the diagonal elements, it obviously indicates totally symmetric transitions. $\delta_F = 0$ when transition is to a non-totally symmetric state. δ_G being a measure of the sum of the squares of all elements in the transition tensor, can be considered to represent the overall strength of the transition. In a single laser experiment, the independent polarizations are linear and circular and the corresponding absorptivities can be written

$$\langle \delta_{\text{lin}} \rangle = 2 (\delta_F + 2 \delta_G),$$

and

$$\langle \delta_{\text{cir}} \rangle = 2 (- \delta_F + 3 \delta_G).$$

The value of (δ_F/δ_G) can never exceed 3. The polarization ratio is essentially defined as

$$\Omega = \delta_{\text{cir}}/\delta_{\text{lin}} = \frac{3 \delta_G - \delta_F}{2 \delta_G + \delta_F}.$$

The range of value for Ω is $0 \leqslant \Omega \leqslant 3/2$.

A spectrum is usually recorded for both kinds of polarisation and the excited state symmetry is assigned by comparing the ratio with Ω predicted by tensors of different possible excited state symmetries (McClain and Harris 1977).

The band system representing the $^1B_2 \leftarrow {}^1A_1$ electronic transition of monosubstituted benzenes can be classified into two parts: one part, often referred to as electronically allowed system and other an electronically forbidden but vibrationally induced part. The allowed system exhibits a B_2 tensor pattern, while the forbidden system exhibits an A_1 tensor pattern and the inducing vibrations are of b_2 species. 'Forbidden' transitions can be identified by near vanishing intensities under circular polarisation of the laser beam.

3. Experimental

The experimental set up for the study of two-photon excitation spectrum of benzonitrile is shown in figure 1. A sample of benzonitrile (E. Merck) was repeatedly chilled and thawed to expel any dissolved air before being filled into a cylindrical quartz cell (18 cm × 2 cm). The third harmonic 355 nm laser pulse from a Molectron Nd-YAG (MY 35) laser was used to pump a Molectron (DL 18) dye laser. The pulsed (10 sec^{-1}), linearly polarised dye laser beam was focussed in to the quartz

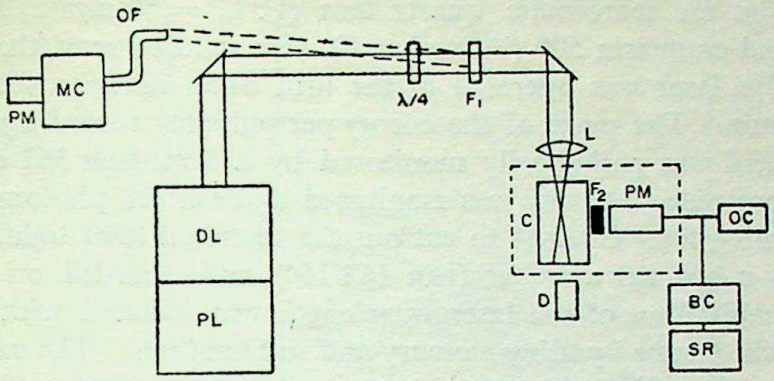

Figure 1. Experimental set-up for recording the two-photon fluorescence excitation spectrum. PL: Nd-YAG laser. DL: dye laser. λ/4: quarter wave plate. F_1: filter. L: achromatic lens. D: beam dump. C: quartz cell. F_2: corning filter CS 7-54. PM: photomultiplier tube. BC: box car averager. SR: strip chart recorder. OC: oscilloscope. OF: optical fiber MC: monochromator.

Table 1. Prominent bands in the two-photon excitation spectrum of benzonitrile.

λ (Å)	ν (cm^{-1})	Δν (cm^{-1})	Symmetry of the tensor	Intensity	Assignment
5476·8	36517	0	B_2	VS(100)	origin
5421·6	36889	372	B_2	MW	?
5416·0	36927	410	B_2	M	$6a_0^1$
5373·3	37221	704	B_2	W	12_0^1
5340·1	37452	935	B_2	S(70)	1_0^1
5336·7	37476	959	B_2		$18a_0^1$
5304·9	37701	1184	B_2	M	$7a_0^1$
5283·6	37853	1336	A_1		
5252·0	38081	1564	A_1	S(50)	14_0^1
5241·3	38158	1641	B_2		$1_0^1\ 12_0^1$
5238·0	38183	1666	B_2		$18a_0^1\ 12_0^1$
5210.4	38385	1868	B_2	MW	1_0^2
5208·2	38400	1884	B_2	MW	$12_0^1\ 7a_0^1$
5206·0	38417	1901	B_2	MW	$1_0^1\ 18a_0^1$
5203·0	38439	1922	B_2	W	$18a_0^2$
5198·0	38476	1959	A_1	W	$14_0^1\ 6a_0^1$ (?)
5181·2	38601	2084		W	
5177·2	38631	2114	A_1	W	
5175·6	38643	2126	B_2		$1_0^1\ 7a_0^1$
5163·3	38735	2218	A_1	W	seq. of $14_0^1\ 12_0^1$ (?)
5158·3	38772	2255	A_1	W	$14_0^1\ 12_0^1$ (?)
5151·6	38823	2306	A_1		
5145·5	38869	2352	B_2	W	$7a_0^2$
5126·9	39011	2494	A_1	MS	$14_0^1\ 1_0^1$
5123·6	39035	2518	A_1	MS	$14_0^1\ 18a_0^1$
5094·2	39260	2743	A_1	W	$14_0^1\ 7a_0^1$
5043·5	39655	3138	A_1	W	
5036·8	39708	3191	A_1	VW	$14_0^1\ 1_0^1\ 12_0^1$
5033·4	39735	3218	A_1	VW	$14_0^1\ 18a_0^1\ 12_0^1$
5004·2	39966	3449	A_1	VW	$14_0^1\ 1_0^2$
4998·2	40014	3497	A_1	VW	$14_0^1\ 18a_0^2$

The intensity of the lines is denoted by VW = very weak, W = weak, MW = medium weak, M = medium, MS = medium strong, S = strong, VS = very strong.

absorption cell by an achromatic quartz lens (F. L. = 50 mm). Dyes coumarin 7 (in DMF) and coumarin 500 (in methanol) were used to scan the range 4900-5500 Å. The dye laser was operated in the fifth order and the wavelength was scanned at 3 Å/min. The range of the energy per pulse for recording the spectrum was 100-600 μj and was periodically monitored by a Scientech 362 energy meter. Two-photon fluorescence intensity was monitored by an IP 28 photomultiplier with 6 mm thick Corning filter CS 7-54 to cut out the scattered laser light. The signal was averaged by a box car averager (PAR 162/164) and recorded on a strip chart recorder. The calibration of the laser wavelength was effected with a Carl-Zeiss 0·5 metre monochromator by using mercury and sodium lines. The calibration was cross-checked by recording the two-photon excitation spectrum of benzene for which measurements are available to an accuracy better than $\pm$ 2 cm^{-1} (Wunsch *et al* 1977). Circular polarization of the laser beam was achieved by using a $\lambda/4$ plate. The frequencies of benzonitrile quoted in table 1 correspond to the peak of the absorption lines and is believed to be accurate to $\pm$ 4 cm^{-1} in OP energy.

The one-photon absorption spectrum of benzonitrile ($\sim$ 1 torr) was recorded (using Cary 17 D spectrophotometer) with a cylindrical quartz cell of 12 cm path length.

4. Results

The one-photon absorption spectrum of benzonitrile is shown in the upper part of figure 2. It may be seen that the origin band around 2740 Å is the strongest. In the two-photon spectrum shown in the lower part of the same figure, it may be seen that the most intense band 0_0^0 occurring at $2\bar{\nu}$ (36518 cm^{-1}) is nearly identical to the value of the origin band reported for OP spectrum and hence it is obvious that it is the two-photon spectrum of benzonitrile.

The fundamentals observed in the two-photon spectrum which belong to symmetric a_1 modes are $6a_0^1$ (+ 410 cm^{-1}), 12_0^1 (+710 cm^{-1}), 1_0^1 (+935 cm^{-1}), $18a_0^1$ (+ 958 cm^{-1}) and $7a_0^1$ (+ 1184 cm^{-1}). All these fundamentals also appear in combinations. The indexing of the normal modes follows Wilson's convention (Wilson *et al* 1955). Excepting the FC mode $6a_0^1$, all the a_1 modes can be correlated with the OP spectrum. Sequence bands contribute a significant fraction of total intensity of many bands and are stacked towards the red side as in other benzenoid systems. For the 0_0^0 band (figure 3), the sequence bands were measured at -1×10, -1×23, -2×23, -1×77, -1×110, -1×127, -1×158 cm^{-1}, etc, a few of which should be expected to correspond to -1×40, -2×40, -3×40 cm^{-1} observed in OP spectrum (Hirt and Howe 1948). In table 1 are shown some of the important bands observed in the two-photon spectrum along with their behaviour under polarization.

The only active intense VC mode in the TP spectrum of benzonitrile is the analogue of benzene ν_{14}, occurring at 5252 Å (figure 4). It shows a polarization behaviour suitable for b_2 vibration—namely a sharp reduction in intensity under circular polarization. Further it occurs at about 1565 cm^{-1} above the band origin, similar to that found in other mono-substituted benzenes. Hence the assignment of 14_0^1 to this band seems to be correct. This band system is also heavily studded with sequences, prominent among which occur at -1×40, -2×40 and -3×40 cm^{-1}

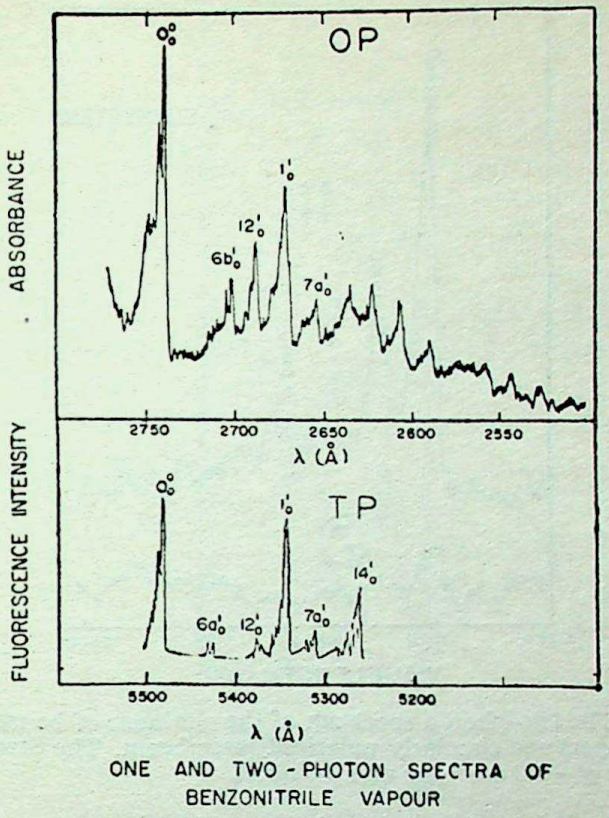

Figure 2. One- and two-photon spectra of benzonitrile vapour (~ 1 torr). The TP spectral bands were recorded at a constant energy of 100 μj.

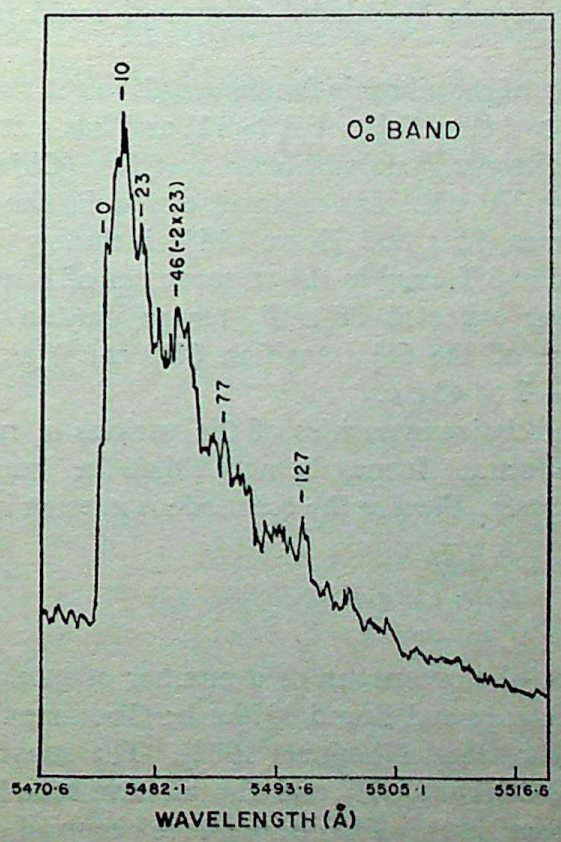

Figure 3. O_0^0 band of benzonitrile with a few sequence bands.

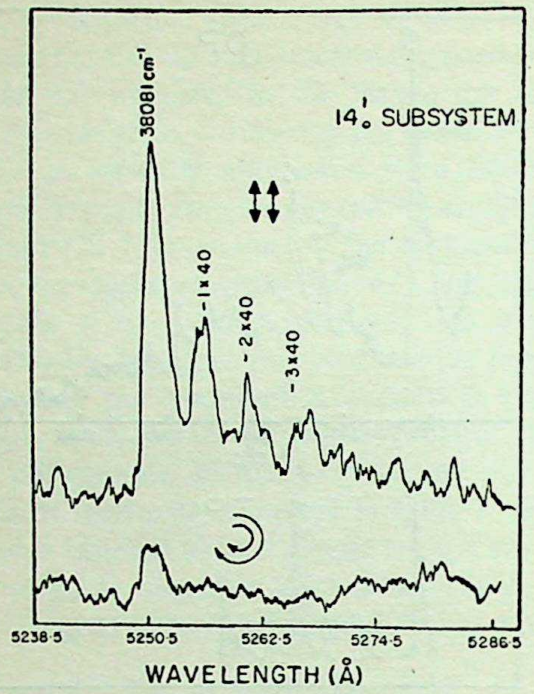

Figure 4. The two-photon spectrum of the analogue of benzene 14_0^1 subsystem using linearly (upper) and circularly polarized laser beam. The Strong sequence structures at multiples of -40 cm^{-1} are also included.

and can be reasonably ascribed (Hirt and Howe 1948) to the out-of-plane bending (170 cm^{-1}) of the nitrile tail. The a_1 fundamentals discussed above also appear in combination with 14_0^1 and exhibit a similar polarization behaviour appropriate of a b_2 vibration. No other vibronically-induced subsystem could be observed in the TP spectrum of benzonitrile.

The intensity ordering of the vibronic fundamentals in the TP spectrum of benzonitrile is $0_0^0 > 1_0^1$ (18 a_0^1) $> 14_0^1 > 7a_0^1 > 6a_0^1 > 12_0^1$ and has a strong similarity to the TP spectrum of its isoelectronic analogue phenyl acetylene (Chia and Goodman 1982).

A band around $O_0^0 + 370$ cm^{-1} has been observed in the OP spectra of some monosubstituted benzenes (Hirt and Howe 1948) including benzonitrile. A clear transition was observed at 370 cm^{-1} in the TP spectrum of benzonitrile, which shows a polarization behaviour expected of a B_2 tensor pattern (figure 5). It is not the -40 cm^{-1} sequence of the $6a_0^1$ transition (410 cm^{-1}) as there are no accompanying structures at -2×40 etc.

Table 2 indicates the relative intensities of the various a_1 modes observed in the one- and two-photon spectra. It may be noted that the intensities of $7a_0^1$ and 12_0^1 are reversed in the two cases. Further the $6a_0^1$ mode is missing in the OP spectrum.

5. Discussion

In recent years, the two-photon spectra of a number of mono-substituted benzenes have been reported (Vasudev and Brand 1979a, b; Goodman and Rava 1981; Chia and Goodman 1982; Rava and Goodman 1982). The substituents so far studied are halogens, CH_3, OH, CCH and NH_2, and they all have been known to be π electron donors (Pross and Radom 1981). The donors have occupied orbitals of π symmetry with relatively high energy, and donor strength decreases as their ionization potential

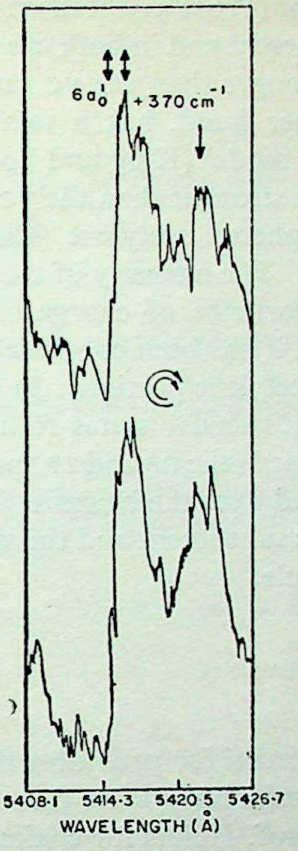

Figure 5. Two-photon spectrum of the $6a_0^1$ and an unassigned $O_0^0$370 cm^{-1} band using linear and circular polarization of laser beam.

Table 2. The a_1 modes: relative intensity of 1—0 transitions.

	One-photon	Two-photon	
	0—0	0—0	14_0^1
Origin	100	100	100
6*a* (410)	NO	16	10
12 (704)	30	10	25
1 (935)	50	70	30
18*a* (959)			20
7*a* (1184)	13	20	10

NO: not observed

increases (Murrell 1963). For example, fluorine (I. P: 15·8 eV) is the weakest donor among the halogens since the ionization potential varies as F > Cl > Br > I. Hence the two-photon spectrum of flurobenzene is very much similar to benzene with weak FC modes and a strong VC mode. Since the 14_0^1 band in various monosubstituted benzenes is believed to be of approximately equal intensity (Rava and Goodman 1982) its strength *vis-a-vis* the intensities of FC mode ν_1 and 0_0^0 band in the two-photon spectra is a measure of the mesomeric strength of the substituent. It may be seen that in the two-photon spectrum of aniline (Rava and Goodman 1982) the FC modes are predominant compared to the VC mode and the TP spectrum bears a strong resemblance to the OP spectrum.

The electron acceptors have low-lying vacant π orbitals and the acceptor strength increases with the electron affinity of these orbitals (Murrell 1963). It is known that

nitrile group is a strong acceptor (Pross and Radom 1981). Benzonitrile has a strong one-photon and two-photon spectra and in both cases the intensities of origin and the ring breathing ν_1 band are stronger than the VC modes. Its isoelectronic analogue phenyl acetylene, on the other hand, has a weak OP spectrum (meaning the FC modes are weaker than the VC mode) (King and So 1971) and a strong TP spectrum (meaning that the FC modes are stronger than the VC mode 14_0^1) (Chia and Goodman 1982). The TP spectrum of phenyl acetylene (Chia and Goodman 1982) is very similar to that of benzonitrile. The intensity of the TP spectrum of phenyl acetylene has been ascribed to the importance of charge transfer states resulting from the acetylene-ring* promotion and it has been concluded that the π electrons are strongly delocalised over the ring and acetylene portions. In benzonitrile, the results of the OP spctrum indicate that the charge transfer states result from ring-nitrile* promotion. Since the FC part is almost similar in the OP and TP spectra of benzonitrile, we conclude that the electrons are delocalised over the benzene ring and nitrile moiety. In other words CN is a strong mesomeric substituent and the strong coupling treatment is likely to be applicable for this molecule.

Acknowledgement

The authors thank Dr B B Kulkarni for providing the $\lambda/4$ plate and Dr A Deshpande for the coumarin 7 dye. Grateful thanks are due to Prof. B Venkataraman for his constructive suggestions and Prof. Hollas for critical comments.

References

Bak B, Christensen D, Dizon W B, Nygaard L H and Anderson J R 1962 *J. Chem. Phys.* **37** 2027
Brand J C D and Knight P D 1970 *J. Mol. Spectrosc.* **36** 328
Chia L and Goodman L 1982 *J. Chem. Phys.* **76** 4745
Goodman L and Rava R P 1981 *J. Chem. Phys.* **74** 4826
Green J H S and Harrison D J 1976 *Spectrochim. Acta* **32A** 1279
Hartford A and Lombardi J R 1971 *J. Mol. Spectrosc.* **40** 262
Hirt R C and Howe J P 1948 *J. Chem. Phys.* **16** 480
Kimura K and Nagakura S 1965 *Theor. Chim. Acta* **3** 164
King G W and So S P 1971 *J. Mol. Spectrosc.* **37** 543
Lombardi J R, Wallenstein R, Hansch T W and Friedrich D M 1976 *J. Chem. Phys.* **65** 2357
McClain W M and Harris R A 1977 in *Excited states* (ed.) E C Lim (New York: Academic Press) Vol. 3
Mikami N and Ito M 1975 *Chem. Phys. Lett.* **31** 472
Murrell J N 1963 *The theory and electronic spectra of organic molecules* (New York: John Wiley)
Pross A and Radom L 1981 *Progress in physical organic chemistry* (ed.) R W Taft (New York: John Wiley) Vol. 13, pp. 1-63
Rava R P and Goodman L 1982 *J. Am. Chem. Soc.* **104** 3815
Robey M J and Schlag E W 1978 *Chem. Phys.* **30** 9
Sklar A L 1937 *J. Chem. Phys.* **5** 669
Vasudev R and Brand J C D 1979a *J. Mol. Spectrosc.* **75** 288
Vasudev R and Brand J C D 1979b *Chem. Phys.* **37** 211
Wilson E B, Decious J C and Cross P C 1955 *Molecular vibrations* (New York: McGraw-Hill)
Wunsch L, Metz F, Neusser H J and Schlag E W 1977 *J. Chem. Phys.* **66** 386 and the references contained therein

Pramāṇa, Vol. 21, No. 2, August 1983, pp. 89–102. © Printed in India.

A new approach to charged-particle scattering in the presence of laser plus Coulomb-field

MAN MOHAN
Physics Department, KM College, Delhi University, Delhi 110 007, India

MS received 18 November 1982; revised 25 May 1983

Abstract. A new approach to charge-particle scattering in the presence of laser plus coulomb-field by using Fourier analysis technique is described. Explicit expressions for positive energy states and their asymptotic limits for the zero, one and two photon processes are evaluated exactly.

Keywords. Scattering; laser; Coulomb field; Fourier analysis; photon

1. Introduction

Recently extensive studies have been carried out in the field of atomic and molecular collision processes in the presence of EM field (Levine and Bernstein 1974; Walther 1976; Hertal *et al* 1980; Mohan and Chand 1979; Mohan 1981) due to its importance in laser-induced chemistry, working of different type of lasers, laser-induced gas-breakdown, plasma-heating by laser etc. The understanding of the laser-plasma interaction related to the laser-fusion reactions requires a knowledge of the collision process in the presence of EM field occurring under various conditions among atoms, molecules, neutrals and charged particles.

This paper investigates the positive energy states in the presence of laser and strong Coulomb field which are very important in the study of various physical processes like (a) free-free transition process in laser plus strong Coulomb field (Kroll and Watson 1973; Burkin and Fedorov 1965, 1966; Mohan 1974; Henneberger 1968; Rosenberg 1979), (b) electron impact ionization of an atom or a molecule in the presence of laser beam etc (Gavrila 1978; Gavrila and van der Wiel 1978). In our analysis we use the Fourier analysis technique as introduced by Karplus and Kolker (1963), Dalgarno (1966) and others for treating the time-dependent problem. We have tried to explain the salient features involved in the above mentioned physical processes. In §§ 2 and 3, the theory from the first-principle is developed and the one-photon process discussed. In § 4 we deal with the two-photon process and the corresponding positive energy state with the asymptotic states is evaluated. In § 5, the elastic scattering in the presence of EM field plus strong coulomb-field is discussed using partial wave analysis technique. The results thus obtained are discussed.

2. Theory

The Schrödinger equation for the system consisting of a charged particle (*e.g.* elec-

tron) moving in the presence of an EM field plus a Coulomb field (*e.g.* a proton) can be written as

$$i\hbar \frac{\partial \psi_k(\mathbf{r}, t)}{\partial t} = \{H(\mathbf{r}) + v(\mathbf{r}, t)\} \psi_k(\mathbf{r}, t) \tag{1}$$

where $H(\mathbf{r}) = H_0(\mathbf{r}) + v(\mathbf{r})$; $H_0(\mathbf{r})$ is the free electron Hamiltonian and $v(\mathbf{r})$ is the Coulomb potential, $v(\mathbf{r}, t) = -e\,\mathbf{E}\cdot\mathbf{r}\cos\omega t$ is the interaction Hamiltonian representing the interaction between the electron and EM field (E) with frequency ω.

From (1), the time dependent solution of the (time dependent) unperturbed Schrödinger equation (where $v(\mathbf{r}, t)$ is the perturbation) i.e.

$$i\hbar \frac{\partial \psi_k^0(\mathbf{r}, t)}{\partial t} = H(\mathbf{r})\, \psi_k^0(\mathbf{r}, t), \tag{2}$$

can be written as:

$$\psi_k^0(\mathbf{r}, t) = \chi_k^0(\mathbf{r}, 0)\, [\exp(-iE_k t)]/\hbar \tag{3}$$

where $\chi_k^0(\mathbf{r}, 0)$ represents the first term for the zero photon process, which will be clear in the next sections.

Expanding the solution of (1) *i.e.* $\psi_k(\mathbf{r}, t)$ as (Mohan 1981)

$$\psi_k(\mathbf{r}, t) = \psi_k^0(\mathbf{r}, t) + \sum_{s=1}^{\infty} \psi_k^{(s)}(\mathbf{r}, t), \tag{4}$$

and putting in (1) we obtain

$$\left(H - i\hbar \frac{\partial}{\partial t}\right) \psi_k^0(\mathbf{r}, t) = 0, \tag{5}$$

$$\left(H - i\hbar \frac{\partial}{\partial t}\right) \psi_k^1(\mathbf{r}, t) + v(\mathbf{r}, t)\, \psi_k^0(\mathbf{r}, t) = 0, \tag{6}$$

$$\left(H - i\hbar \frac{\partial}{\partial t}\right) \psi_k^2(\mathbf{r}, t) + v(\mathbf{r}, t)\, \psi_k^1(\mathbf{r}, t) = 0, \tag{7}$$

$$\left(H - i\hbar \frac{\partial}{\partial t}\right) \psi_k^s(\mathbf{r}, t) + v(\mathbf{r}, t)\, \psi_k^{s-1}(\mathbf{r}, t) = 0. \tag{8}$$

For finding the solutions of (5) to (8) the time-dependent equations are made into time-independent ones by using the Fourier analysis technique (Mohan 1981).

As the perturbation in (1) is harmonic *i.e.* $v(\mathbf{r}, t) = -e\,\mathbf{E}\cdot\mathbf{r}\cos\omega t$, solution to (6) is written as

$$\psi_k^1(\mathbf{r}, t) = \chi_k^1(\mathbf{r}, \omega) \exp[i(\omega - \omega_k) t] + \chi_k^1(\mathbf{r}, -\omega) \exp[-i(\omega + \omega_k) t] \tag{9}$$

where the first term represents one photon emission and the second term represents one photon absorption process.
The second term of (6) can be written by using (3) as

$$v(\mathbf{r}, t)\, \psi_k^0(\mathbf{r}, t) = -\frac{e\,\mathbf{E}\cdot\mathbf{r}}{2} \times \{\exp[+ i(\omega - \omega_k)\, t]$$

$$+ \exp[- i(\omega + \omega_k)\, t]\}\, \chi_k^0(\mathbf{r}) \tag{10}$$

Here $\omega_k = E_k/\hbar$ and ω is the frequency of the radiation.

Substituting (3) into (5), (9) and (10) into (6) and equating the coefficients of $\exp[- i(\omega - \omega_k)\, t]$ and $\exp[- i(\omega + \omega_k)\, t]$ the following set of equations is obtained.

$$(H - E_k)\, \chi_k^0(\mathbf{r}, 0) = 0 \tag{11}$$

$$(H - E_k - \hbar\omega)\, \chi_k^1(\mathbf{r}, -\omega) = (e, \mathbf{E}\cdot\mathbf{r}/2)\, \chi_k^0(\mathbf{r}, 0) \tag{12}$$

$$(H - E_k + \hbar\,\omega)\, \chi_k^1(\mathbf{r}, \omega) = (e\,\mathbf{E}\cdot\mathbf{r}/2)\, \chi_k^0(\mathbf{r}, 0) \tag{13}$$

Clearly $\chi_k^0(\mathbf{r}, 0)$, $\chi_k^1(\mathbf{r}, -\omega)$, $\chi_k^1(\mathbf{r}, +\omega)$ represents zero photon, one photon absorption and one photon emission processes respectively.

Similar to (9) the second order solution can be written as

$$\chi_k^2(\mathbf{r}, t) = \chi_k^2(\mathbf{r}, 2\omega) \exp[i(2\omega - \omega_k)]\, t + \chi_k^2(\mathbf{r}, 0)$$

$$\exp(- i\omega_k\, t) + \chi_k^2(\mathbf{r}, -2\omega) \exp[- i(2\omega + \omega_k)]\, t \tag{14}$$

Substituting (14) and (9) into (7) and equating the coefficients of $\exp[i(2\omega - \omega k)\, t]$. $\exp(- i\omega_k\, t)$ and $\exp[- i(2\omega + \omega_k)]\, t$ the following set of equations is obtained,

$$(H - E_k + 2\,\hbar\,\omega)\, \chi_k^2(\mathbf{r}, +2\omega) = (e\,\mathbf{E}\cdot\mathbf{r}/2)\, \chi_k^1(\mathbf{r}, +\omega) \tag{15}$$

$$(H - E_k)\, \chi_k^2(\mathbf{r}, 0) = (e\,\mathbf{E}\cdot\mathbf{r}/2)\, (\chi_k^1(\mathbf{r}, \omega) + \chi_k^1(\mathbf{r}, -\omega)) \tag{16}$$

$$(H - E_k - 2\,\hbar\,\omega)\, \chi_k^2(\mathbf{r}, -2\omega) = (e\,\mathbf{E}\cdot\mathbf{r}/2)\, \chi_k^1(\mathbf{r}, -\omega) \tag{17}$$

The solutions of equations (15) to (17), (i.e. $\chi_k^2(\mathbf{r}, -2\omega)$, $\chi_k^2(\mathbf{r}, 0)$ $\chi_k^2(\mathbf{r}, +2\omega)$) represent two-photon absorption, zero photon and two photons emission processes respectively.

Similarly, the time-independent equations corresponding to higher order processes can be obtained.

3. First order processes

For a linearly polarized light and polarization along the polar axis we have

$$\mathbf{E}\cdot\mathbf{r} = (4\pi/3)^{1/2}\, |\mathbf{E}|\, r\, y_1^0(\theta, \phi) \tag{18}$$

Substituting (18) into (12) we obtain

$$(H - E_k - \hbar\,\omega)\,\chi_k^1\,(\mathbf{r}, -\omega) = (4\pi/3)^{1/2}\,e\,|\,\mathbf{E}\,|\,r\,y_1^0\,(\theta, \phi)\,\chi_k^0\,(\mathbf{r}, \omega) \qquad (19)$$

Expanding $\chi_k^1\,(\mathbf{r}, \omega)$ and $\chi_k^0\,(\mathbf{r}, \omega)$ in terms of radial and angular part we have

$$\chi_k^1\,(\mathbf{r}, -\omega) = \sum_{l=0}^{\infty} \sum_{m=-l}^{+l} \phi_{k,\,l}^1\,(\mathbf{r}, \omega)\,y_l^m\,(\theta, \phi)$$

and

$$\chi_k^0\,(\mathbf{r}, 0) = \sum_{l=0}^{\infty} \sum_{m=-l}^{+l} \phi_{k\,l}^0\,(\mathbf{r}, 0)\,y_l^m\,(\theta, \phi) \qquad (20)$$

Substituting (20) and (21) in (19) and using the property of spherical harmonics

$$y_1^0\,(\theta, \phi)\,y_l^m\,(\theta, \phi) = \left[\left\{\frac{(l+1-m)}{(2l+1)} \times \frac{(l+1-m)}{(2l-1)}\right\}^{1/2} y_{l+1}^m\,(\theta, \phi)\right.$$

$$\left. + \left\{\frac{(l+m)}{(2l+1)}\,\frac{(l-m)}{(2l-1)}\right\}^{1/2} y_{l-1}^m\,(\theta, \phi)\right] \qquad (21)$$

we obtain

$$(H - E_k - \hbar\,\omega)\,\phi_{k,\,l}^1\,(\mathbf{r}, -\omega)\,y_l^m\,(\theta, \phi) = (4\pi/3)^{1/2}\,e\,|\,\mathbf{E}\,|\,\mathbf{r}\,\phi_{k,\,i}^0\,(\mathbf{r}, 0)$$

$$\times\left[\left\{\frac{(l+1+m)}{(2l+1)}\,\frac{(l+1-m)}{(2l-3)}\right\}^{1/2} y_{l+1}^m\,(\theta, \phi)\right.$$

$$\left. + \left\{\frac{(l+m)}{(2l+1)}\,\frac{(l-m)}{(2l-1)}\right\}^{1/2} y_{l-1}^m\,(\theta, \phi)\right] \qquad (22)$$

Multiplying (23) by $y_{l'}^{m'}\,(\phi, \theta)$ and integrating over $d\Omega$ the following radial equation is obtained

$$(h\,(r) - E_k - \hbar\,\omega)\,\phi_{k,\,l,}^1\,(\mathbf{r}, -\omega) = (4\pi/3)^{1/2}\,e\,|\,E\,|\,r$$

$$\times\left[\left\{\frac{(l+1-m)}{(2l+1)}\,\frac{(l+1-m)}{(2l+3)}\right\}^{1/2} \delta_{l',\,l+1}\,\phi_{k,\,l}\,(\mathbf{r}, 0)\right.$$

$$\left. + \left\{\frac{(l+m)}{(2l+1)}\,\frac{(l-m)}{(2l-1)}\right\}^{1/2} \delta_{l',\,l-1}\,\phi_{k,\,l}^0\,(\mathbf{r}, 0)\right] \qquad (23)$$

where $h(r)$ is the radial part of H and is given by

$$h(r) = -\frac{\hbar^2}{2m}\left(\frac{1}{r^2}\,\frac{\partial}{\partial r}\left(r^2\,\frac{\partial}{\partial r}\right)\right) + \frac{\hbar^2}{2m}\,\frac{l'\,(l'+1)}{r^2} + v(\mathbf{r}) \qquad (24)$$

Using the property of Kronecker δ, (24) reduces to (changing the notation l' to l later on)

$$(h(r) - E_k - \hbar\omega)\, \phi^1_{k,l}(\mathbf{r}, -\omega) = A_l(k, \mathbf{r}) \tag{25}$$

where
$$A_l(k, \mathbf{r}) = (4\pi/3)^{1/2}\, e\, |E|\, r \times \left[\left\{ \frac{(l+m)}{(2l-2)} \frac{(l-m)}{(2l+1)} \right\}^{1/2} \phi^0_{k,l-1}(\mathbf{r}, 0) \right.$$
$$\left. + \left\{ \frac{(l+m+1)}{(2l+1)} \frac{(l-m+1)}{(2l-3)} \right\}^{1/2} \phi^0_{k,l+1}(\mathbf{r}, 0) \right]$$

The above equation is an inhomogeneous second order differential equation and the solution of this can be found out by finding the solution of the homogeneous part i.e.

$$(h(r) - E_k - \hbar\omega)\, \phi^1_{k,l}(\mathbf{r}, -\omega) = 0 \tag{26}$$

where $E_k = \hbar^2 k^2/2m$ is the energy of the free particle which is defined after one photon absorption as

$$E_{k_1} = \hbar^2 k_1^2/2m = E_k + \hbar\omega = \hbar^2 k^2/2m + \hbar\omega \tag{27}$$

Equation (26) is a second order radial equation with Coulomb potential $v(r)$ and can be solved easily (Mott and Massey 1965; Bethe and Salpeter 1957). It has two solutions one regular and another irregular defined by $L_l(kr)$ and $K_l(kr)$ respectively. The functional form and their behaviours near the origin and in the asymptotic limit is given in the appendix A. The solution of the inhomogeneous equation (Mott and Massey 1965) can thus be written as

$$\phi^1_{k,l}(\mathbf{r}, -\omega) = -L_l(k_1, r) \int_r^\infty K_l(k_1, r')\, A_l(k_1, r')\, r'^2\, dr'$$
$$- K_l(k_1, r) \int_0^r L_l(k_1, r')\, A_l(k_1, r')\, r'^2\, dr' \tag{28}$$

From (28) the corresponding asymptotic solution is given by

$$\phi^1_{k,l}(\mathbf{r}, -\omega) \underset{r\to\infty}{\simeq} -K_l(k_1, r\to\infty) \int_0^\infty L_l(k_1, r')\, A_l(k_1, r')\, r'^2\, dr' \tag{29}$$

For the determination of the scattering amplitude we are only interested in the outgoing solution. Therefore substituting $K_l(k_1, r\to\infty)$ from (24) $A_l(k, r')$ from (25) and taking the coefficient of the term

$$\exp\left[i(k_1 r - \alpha \log 2k_1 rr)\right]/r$$

the amplitude for one photon absorption is obtained as $f_l'(k_1, r)\, y_l^m(\theta, \phi)$ where

$$f_l'(k_1, r) = -\frac{1}{2ik}\left(\frac{4\pi}{3}\right)^{1/2} e\,|E|$$

$$\times \left\{\left[\frac{(l+m)}{(2l-1)}\frac{(l-m)}{(2l+1)}\right]^{1/2} \int_0^\infty dr'\, r'^3\, L_l(k_1, r')\, \phi^0_{k,l-1}(r')\right.$$

$$\left. + \left[\frac{(l+m+1)}{(2l+1)}\frac{(l-m+1)}{(2l+3)}\right]^{1/2} \int_0^\infty dr'\, r'^3\, L_l(k_1, r')\, \phi^0_{k,l+1}(r')\right\} \quad (30)$$

Taking the regular solution (Bethe and Salpeter 1957) for $\phi^0_{k,l+1}(r)$, substituting (A1) into (30) and performing the integral (Landau and Lifshitz 1959) we obtain

$$f_l'(k_1, r, -\omega) = -\left(\frac{\pi}{3}\right)^{1/2} \frac{e\,|E|}{(ik)} \exp\left[-\pi/2(\alpha+\alpha_1)\right] \left|\Gamma(l+1+i\alpha_1)\right| (4kk_1)^l$$

$$\times \left\{\left[\frac{(l+m)}{(2l-1)}\frac{(l-m)}{(2l+1)}\right]^{1/2} \left|\Gamma(2l+1+i\alpha)\right| (2k_1)\, J_\nu^{3,-2}(\beta, \beta_1)\right.$$

$$\left. + \left[\frac{(l+m+1)}{(2l+1)}\frac{(l-m+1)}{(2l+3)}\right]^{1/2} \left|\Gamma(l+i\alpha)\right| (2k_1)^{-1}\, J_\nu^{1,-2}(\beta, \beta_2)\right\} \quad (31)$$

where $\nu = (2l+2)$, $\beta = i\alpha_1 + l + 1$, $\beta_1 = i\alpha + 2l + 1$ and $\beta_2 = i\alpha + l$.

The term $J_\nu^{s,p}$ occurring in the above equation can be determined through the recurrence relation

$$J_\nu^{s,p}(\beta, \beta') = \frac{\nu - 1}{(-2ik_1)} \times \left\{J_\nu^{2,p-1}(\beta, \beta') - J_{\nu-1}^{s,p-1}(\beta - 1, \beta')\right\} \quad (32)$$

where $J_\nu^{s+1,0}(\beta, \beta') = 1/(k^2 - k_1^2) \times \left\{[\nu(k - k_1) + 2i(k_1\beta - k\beta' + ks)]\, J_\nu^s(\beta, \beta')\right.$

$$\left. + s(\nu - 1 + s - 2\beta')\, J_\nu^{s-1,0}(\beta, \beta') + 2\beta' s\, J_\nu^{s-1,0}(\beta', \beta' + 1)\right\} \quad (33)$$

$$J_\nu^{0,0}(\beta, \beta_1) = (2l+2)\,\Gamma(2l+2)\,(k + k_1)^{\beta+\beta_1-\nu}$$

$$\times (k - k_1)^{-\beta} (k_1 - k)^{-\beta_1} F(\beta, \beta_1\, \nu, -4kk_1/(k - k_1)^2 \quad (34)$$

and $J_\nu^{0,0}(\beta, \beta_2) = (2l+2)\,\Gamma(2l+2)\,(k + k_1)^{\beta+\beta_2-\nu}$

$$\times (k - k_1)^{-\beta} (k_1 - k)^{-\beta_2} F(\beta, \beta_2\, \nu, -4kk_1/(k - k_1)^2) \quad (35)$$

Similarly the amplitude for one photon emission can be obtained from (31) by replacing k_1 by k_1' where k_1' is determined as

$$k_1' = (k^2 - 2m_1\omega/\hbar)^{1/2} \tag{36}$$

where m_1 is the electron mass.

Further replacement of k_1 by k_1' in (28) gives the first order solution for one photon emission. Thus substitution of $\chi_k'(r, \omega)$ and $\chi_k'(r, -\omega)$ as described in the above paragraph in (9), gives the first-order term occurring in (4) which describes the one photon absorption and emission processes. In § 4 the second order term and emission processes are discussed.

4. Second-order processes

Proceeding as in §2 and substituting (18) in (17) we get

$$(H - E_k - 2\hbar\omega)\, \chi_k^2(\mathbf{r}, -2\omega) = (4\pi/3)^{1/2}\, e\, |E|\, r\, y_1^0(\theta, \phi)\, \chi_k^1(\mathbf{r}, -\omega) \tag{37}$$

for the plane-polarized light with polarization along the polar axis.

Expanding $\chi_k^2(\mathbf{r}, 2\omega)$ in terms of radial and angular part we have

$$\chi_k^2(\mathbf{r}, -2\omega) = \sum_{l=0}^{\infty} \sum_{m=-l}^{+l} \phi_{k,l}^2(\mathbf{r}, -2\omega)\, y_l^m(\theta, \phi) \tag{38}$$

Substituting (38) and (20) into (37), using (A1), and providing as in §3 the following radial equation for the two photon absorption process is obtained

$$(h(r) - E_k - 2\hbar\omega)\, \phi_{k,l}^2(\mathbf{r}, -2\omega) = C_l(k_1, \mathbf{r}) \tag{39}$$

where

$$C_l(k_1, \mathbf{r}) = (4\pi/3)^{1/2}\, e\, |E|\, r \left\{ \left[\frac{(l+m)}{(2l-1)} \frac{(l-m)}{(2l+1)} \right]^{1/2} \phi_{k,l-1}^1(\mathbf{r}, -\omega) \right.$$

$$\left. + \left[\frac{(l+m+1)}{(2l+1)} \frac{(l-m+1)}{(2l+3)} \right]^{1/2} \phi_{k,l-1}^1(\mathbf{r}, -\omega) \right\} \tag{39a}$$

The above equation is again a second-order inhomogeneous differential equation and the solution is given by

$$\phi_{k,l}^2(\mathbf{r}, -2\omega) = -L_l(k_2, r) \int_r^{\infty} K_l(k_2, r')\, C_l(k_1, r')\, r'^2\, dr'$$

$$- K_l(k_2, r) \int_0^r L_l(k_2, r')\, C_l(k_1, r')\, r'^2\, dr' \tag{40}$$

where $L_l\,(k_2, r')$, $K_l\,(k_2, r')$ are the regular and irregular solutions defined in (A1), (A3) respectively with k_1 replaced by k_2 defined by

$$k_2 = (k^2 + 4\,m_1\,\omega/\hbar)^{1/2}$$

Clearly from (40) the asymptotic solution can be easily evaluated and is given by

$$\phi^2_{k,l}\,(\mathbf{r}, -2\omega) \underset{r\to\infty}{\simeq} K_l\,(k_2, r\to\infty) \int_0^\infty L_l\,(k_2, r')\,C_l\,(k_1, r')\,r'^2\,\mathrm{d}r' \qquad (41)$$

Putting (39a) for $C_l\,(k_1, r)$, (A1) for $L_l\,(k_2, r)$ in the above equation, and performing the resulting integral as in § 2, the amplitude $f_l\,(k_2, r, 2\omega)$ for two photon absorption is obtained by taking the coefficient of the term $\exp\,[i\,(kr - \alpha \ln 2\,kr)]/r$ in the expansion of $K_l\,(k_2, r\to\infty)$.

Also we can obtain $\phi^2_{k,l}\,(r\to\infty, 2\omega)$ and corresponding amplitude for two photon emission from (41) by replacing k_2 by k_2' where k_2' is defined as

$$k_2' = (k^2 - 4\,m_1\,\omega/\hbar)^{1/2}$$

Similarly the second order term for zero-photon process can be obtained i.e. $\phi^2_{k,l}\,(r, 0)$. The corresponding asymptotic solution i.e. $\phi^2_{k,l}\,(r\to\infty, 0)$ obtained is given by

$$\phi^2_{k,l}\,(r\to\infty, 0) = -\,K_l\,(k, r\to\infty) \int_0^\infty L_l\,(k, r')\,B_l\,(k, r')\,r'^2\,\mathrm{d}r' \qquad (42)$$

where
$$B_l(k_1, r) = (4\pi/3)^{1/2}\,e\,|E|\,r\left[\frac{(l+m)}{(2l-1)}\,\frac{(l-m)}{(2l+1)}\right]^{1/2}\{\phi^1_{k,l-1}(\mathbf{r}, \omega) + \phi^1_{k,l-1}(\mathbf{r}, -\omega)\}$$

$$+\left[\frac{(l+m+1)}{(2l+1)}\,\frac{(l-m+2)}{(2l+3)}\right]^{1/2}\{\phi^1_{k,\,l+1}\,(\mathbf{r}, \omega) + \phi^1_{k,\,l+1}\,(\mathbf{r}, -\omega)\}$$

Substituting $\phi^1_{k,\,l+2}\,(\mathbf{r}, \omega)$ from (28); $L_l\,(k, r')$, $K_l\,(k, r\to\infty)$ from Appendix A, and performing the integral in (42) as in § 2, we can easily obtain the second order elastic scattering amplitude.

Also substitution of the solutions thus obtained, i.e. $\phi^2_{k,\,l}\,(\mathbf{r}, \pm 2\,\omega)$ and $\phi^2_{k,\,l}\,(\mathbf{r}, 0)$ second order term $\psi^2_k\,(\mathbf{r}, t)$ can be obtained from (14).

In the next § the elastic scattering in the presence of laser plus coulomb field is discussed.

5. Elastic scattering

The wave-function (time independent) of elastic scattering can now be easily written from (4) by collecting the terms representing zero photon processes (*e.g.* $\chi^{2n}_k\,(\mathbf{r}, 0)$

where $n = 0, 1, 2, \ldots$etc.) from it. Expanding these terms in terms of radial and angular parts as in (21), the elastic scattering wavefunction is finally obtained as

$$\psi_{k,\,\text{elastic}}(\mathbf{r}) = \sum_{l=0}^{\infty} \xi_{k,\,l}(r)\, P_l(\cos\theta) \tag{43}$$

where $\xi_{k,\,l}(r) = (4\pi/2l+1)^{\frac{1}{2}} \times \{\phi^0_{k,\,l}(r,0) + \phi^2_{k,\,l}(r,0) + \phi^4_{k,\,l}(r,0) + \ldots\}$ for $m = 0$ (or ϕ-independent). Also as the radial parts etc. are solutions of the second-order differential equation these can be written as the sum of the regular $L_l(k, r)$ and irregular solution $K_l(k, r)$, i.e.

$$\phi^0_{k,\,l}(r,0) = A_1 L_l(k,r) + B_1 K_l(k,r) \tag{44}$$

$$\phi^2_{k,\,l}(r,0) = A_2 L_l(k,r) + B_2 K_l(kr) \tag{45}$$

and so on. Substituting (44) and (45), etc. in (43) we obtain

$$\psi_{k,\,\text{elastic}}(r) = \sum_{l=0}^{\infty} G_l(kr)\, P_l(\cos\theta) \tag{46}$$

where
$$G_l(k,r) = (4\pi/2l+1)^{1/2} \times \{(A_1 + A_2 + \ldots) L_l(kr) + (B_1 + B_2 + \ldots) K_l(Kr)\} \tag{46a}$$

In the asymptotic limit $G_l(kr)$ from (46a) caa be written as

$$G_l(kr) \simeq C_l \sin(kr - l\pi/2 - a\log 2kr + \eta_l + \sigma_l) \tag{47}$$

where σ_l is the partial wave-phase shift due to EM interaction and is given by

$$\tan\sigma_l = (B_1 + B_2 + \ldots)/(A_1 + A_2 + \ldots)$$

while normalization constant C_l must be chosen so that we still have the Coulomb modified incoming plane wave plus an outgoing spherical wave namely

$$\sum_l G_l(kr)\, P_l(\cos\theta) \simeq \exp[-ikz + ia\log(r-z) + [f_c(\theta) + f_m(\theta)]\frac{1}{r}\exp(ikr - ia\log 2kr) \tag{48}$$

where f_c is the Coulomb scattering amplitude.

Using the asymptotic relation for Coulomb function, (48) can be written as

$$\sum_l G_l(kr)\, P_l(\cos\theta) \simeq \sum (2l+1)\, i^l \exp(i\eta_l)\, L_l(k, r\to\infty)\, P_l(\cos\theta) + f_m(\theta)\exp[i(kr - \alpha_1\log 2kr)]/r \tag{49}$$

Also the amplitude due to non-Coulomb potential for interaction potential can be expanded as

$$f_m(\theta) = \sum_l a_l P_l(\cos\theta) \tag{50}$$

Substituting (47) and (50) on the left and right sides respectively of (49), we obtain

$$C_l \sin(kr - l\pi/2 - (\alpha \log 2kr + \eta_l + \sigma_l))$$

$$= (2l+1)\, i^l \exp(i\eta_l) \sin(kr - l\pi/2 - \alpha \log 2kr + \eta_l)$$

$$+ ka_l \exp i(kr - \alpha \log 2kr) \tag{51}$$

where $L_l(k, r \to \infty)$ is given by (B2).

Equating the coefficient of exp $i(kr - \alpha \log 2kr)$ and exp $-i(kr - \alpha \log 2kr)$ on the left and right sides of (51) we get

$$C_l = (2l+1)\, i^l \exp i(\eta_l + \sigma_l) \tag{52}$$

and
$$a_l = (1/2ik)(2l+1) \exp(2i\eta_l) \exp(2i\sigma_l) - 1 \tag{53}$$

Substituting (53) into (52) the scattering amplitude in the presence of EM field and Coulomb field is obtained as

$$f_m(\theta) = 1/2ik \times \sum_{l=0}^{\infty} (2l+1) \exp(2i\eta_l) [\exp(2i\sigma_l) - 1] P_l(\cos\theta) \tag{54}$$

Substituting (54) into (48) the differential cross-section for elastic scattering in the presence of laser plus Coulomb field (Mott and Massey 1965) is obtained as

$$\frac{d\sigma}{d\Omega} = |f_c(\theta) + f_m(\theta)|^2 = R \frac{d\sigma}{d\Omega_c} \tag{55}$$

where
$$R = \left|1 + \frac{f_m(\theta)}{f_c(\theta)}\right|^2;$$

$$f_c(\theta) = \alpha/2k \sin^2\theta/2 \exp[-i\alpha \ln(\sin^2\theta/2) + i\pi + 2i\eta_0]$$

$$f_m(\theta)/f_c(\theta) = -2\alpha \sin^2\theta/2 \exp(i\alpha) \ln(\sin^2\theta/2)$$

$$\times \sum_{l=0}^{\infty} (2l+1) \sin\sigma_l \exp(2i(\eta_l - \eta_0)) \times P_l(\cos\theta)$$

and
$$\eta_0 = \arg\Gamma(1 + i\alpha)$$

Equation (55) thus provides a formal solution of the elastic scattering problem in the presence of a laser beam. In the next section the results thus obtained are discussed.

6. Discussions

As described in earlier sections the positive energy state of a charge particle *i.e.* $\psi_k(\mathbf{r}, t)$ can be obtained using the Fourier analysis technique, in the presence of laser plus strong Coulomb field.

Substituting (3), (9) and (14) into (4) $\psi_k(\mathbf{r}, t)$ can be expanded in terms of χ's as

$$\begin{aligned}\psi_k(\mathbf{r}, t) = {} & [\chi_k^0(\mathbf{r}, 0) + \chi_k^2(\mathbf{r}, 0) + \ldots.] \exp(-i\omega_k t) \\ & + [\chi_k^1(\mathbf{r}, -\omega) + \chi_k^3(\mathbf{r}, -\omega) + \ldots.] \exp[-i(\omega + \omega_k) t] \\ & + [\chi_k^1(\mathbf{r}, \omega) + \chi_k^3(\mathbf{r}, \omega) + \ldots.] \exp[i(\omega - \omega_k) t] \\ & + [\chi_k^2(\mathbf{r}, -2\omega) + \chi_k^4(\mathbf{r}, -2\omega) + \ldots.] \exp[-i(2\omega + \omega_k) t] \\ & + [\chi_k^2(\mathbf{r}, +2\omega) + \chi_k^4(\mathbf{r}, 2\omega) + \ldots.] \exp[-i(2\omega - \omega_k) t] \end{aligned} \tag{58}$$

where the first term represents zero photon process, the second and third terms represent one photon absorption and emission respectively, while the fourth and fifth terms represent two photon absorption or emission respectively, etc.

Equation (58) can be represented in terms of simple diagrams as shown below showing clearly the zero, one, two and higher order processes, *i.e.*

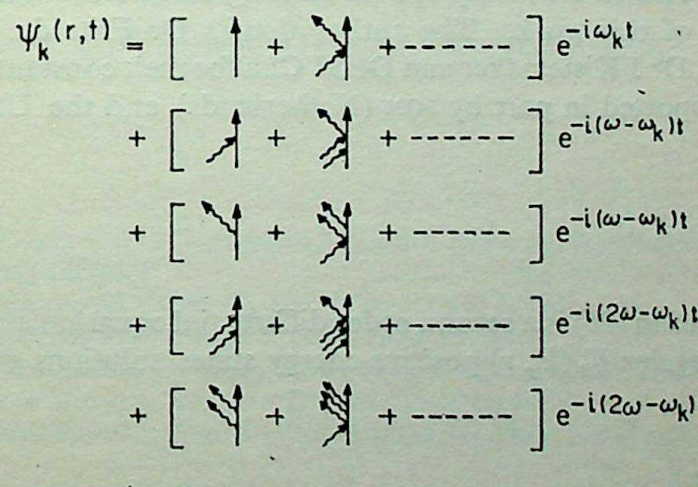

(59)

wherein (59) the symbol (↑) represents the potential line (either ionic or atomic depending upon the scattering system); wavy line towards potential line represents photon absorption; while wavy line away from potential line represents photon emission. Also (59) shows that $\psi_k(r, t)$ is a dressed state.

It is quite evident from (1) that for low values of electric field strength E(a.u.) $= 5 \times 10^{-6}$ (or $I \lesssim 10^6$ W/cm^2) the Coulomb field is quite dominant over the EM inter-

action term (*i.e.* $e\,|E|\,r/\sqrt{2}$) from small to larger values of radial distances (*e.g.* for r near the origin to r (a.u.) = 100). Thus for intensities $I \lesssim 10^6$ W/cm^2, the higher order terms in (58) will be smaller than the preceding lower order terms, resulting the series in (58) to be convergent. Therefore the positive energy state $\psi_k(r, t)$ obtained here for intensities $I \lesssim 10^6$ W/cm^2 will give fairly accurate results.

However, for higher value of intensities *e.g.* $E=6\times10^{-2}$ (a.u.) (or $I=10^{14}$ W/cm^2) the EM interaction term becomes equal to the Coulomb term at r(a.u.) = 5 beyond which the EM interaction dominates over Coulomb term, so that in the asymptotic limit, *i.e.* for higher values of radial distances and for $I \gtrsim 10^{14}$ W/cm^2, (1) reduces to the free-particle equation in the presence of the laser beam with the solution given by

$$\psi_k(\mathbf{r}, t) = \exp\left\{i\mathbf{k}\cdot\mathbf{r} - (i/\hbar)\sum_{-\infty}^{t} \tfrac{1}{2}m\,(\hbar k - (e\mathbf{E}/\omega)\sin\omega t')^2\,dt'\right. \tag{60}$$

as also derived by Kroll and Watson (1973).

Lastly, the analysis as described from §§ 2 to 4 is extended for both elastic and inelastic processes during charge-particle scattering in the presence of laser plus real potentials (*e.g.* Coulombic type in case of ions, etc.). As described in §4, the total elastic cross-section is found out by evaluating σ, the phase shift arising due to EM interaction.

It is hoped that the formulation of free-free transition with resonances in the presence of laser plus strong Coulomb field can be done exactly. Further work in this direction is in progress.

Acknowledgements

The author is indebted to Dr A Tip for stimulating discussions and encouragement during the course of this work. The author thanks Dr Frits de Heer, Prof. M J van der Wiel, Prof. Dr J Kistemaker and Dr S I Chu for their constant encouragement. This work was supported in part by FOM (Netherlands) and the US Department of Energy.

Appendix

(A) The radial equation (26) is a second order differential equation and has the regular ($L_l(k_1, r)$) and irregular $K_l(k_1, r)$ positive energy states solutions which are defined as follows:

(a) *Regular solution*

$$L_l(k_1, r) = \exp(-\pi a/2)\,|\Gamma(l+1+ia_1)|\,(2k_1 r)^l \exp(-ik_1 r)\,[W_1+W_2]$$

where
$$W_1 + W_2 = F(ia_1 + l + 1, 2l + 2, -2ik_1 r) \tag{A1}$$

with
$$L_l(k_1 r) \underset{r\to\infty}{\simeq} 1/kr \sin(kr - l\pi/2 + \eta_l - a_1 \log 2k_1 r) \tag{A2}$$

(b) *Irregular solution*

$$K_l(k_1 r) = i \exp(-\pi a/2) \,|\, \Gamma(l+1+ia_1)/(2l+1)! \,|\, (2k_1 r)^l \exp(-ik, r)$$
$$\times [W_1(ia_1 + l + 1, 2l + 2, -2ik_1 r)$$
$$+ W_2(ia_1 + l + 1, 2l + 2, -2ik_2 r)] \quad \text{(A3)}$$

with $$K_l(k_1 r) \underset{r\to\infty}{\simeq} 1/kr \cos(k_1, r - l\pi/2 + \eta_l - a_1 \log 2k_1 r) \quad \text{(A4)}$$

where $$W_1(a, b, z) = (\Gamma(b)/\Gamma(b-a))(-z)^{-a} g(a, a-b+1; -z) \quad \text{(A5)}$$

$$W_2(a, b, z) = (\Gamma(b)/\Gamma(a)) e^z z^{a-b} g(1-a, b-a, z); \quad \text{(A6)}$$

$$g(a, \beta, z) \underset{z\to\infty}{\simeq} 1 + a\beta/z + a(a+1)/z^2 \; \beta(\beta+1)/2! + \ldots; \quad \text{(A7)}$$

$$\eta_l = \arg \Gamma(l+1+ia_1) \quad \text{(A8)}$$

and $$a_1 = -ze^2/hv = -(ze^2/h^2) m_1/k_1 \quad \text{(A9)}$$

Solutions near the origin $r \to 0$ takes the following form

$$L_l(k_1, r) \underset{r\to 0}{\simeq} C_l r^{l+1} \{1 + [(-2ik)/(l+1)] r + \ldots.\} \quad \text{(A10)}$$

and $$K_l(k_1, r) \underset{r\to 0}{\simeq} 1/(2l+1) C_l r^{-l} [1 + \begin{cases} 0 \; (-2ikr \ln r) \text{ if } l = 0 \\ 0 \; (-2ikr/l) \text{ if } l \neq 0 \end{cases}] \quad \text{(A11)}$$

where $$C_l = 2^l \exp(-i\pi kr) \,|\, \Gamma(l+1-2ikr)/(2l+1)! \,| \quad \text{(A12)}$$

References

Bethe H A and Salpeter E E 1957 *Quantum Mechanics of one and two-electron atoms*;(Springer Verlag) Chapt. I

Bunkin F V and Fedorov M V 1965 *Zh. Eksp. Teor. Fiz.* **49** 1215

Bunkin F V and Fedorov M V 1966 *Sov. Phys. JETP* **22** 844

Dalgarno A 1966 In *Perturbation theory and its application in Quantum Mechanics* (ed.) C H Wilcox (John Wiley and Sons) pp. 145–184 and references therein

Gavrila M 1978 in *Electronic and Atomic Collisions* (ed.) G Matel (Amsterdam: North-Holland Publ. Co.)

Gavrila M and van der Wiel M 1978 *Comments on atomic and molecular physics* **8** 1

Hertal I V, de Vries P L, Lam K S, George T F, Andrick R, Weiner J, Ph Cahuzac, Brechignac C, Toschek P E, Orel A E and Miller W H 1980 in *Electronic and Atomic Collisions;* (ed.) M Oda and K Takayanagi (Amsterdam: North-Holland Publ. Co) pp. 675-719 and references therein

Henneberger W C 1968 *Phys. Rev. Lett.* **21** 838

Karplus M and Kolker M J 1963 *J. Chem. Phys.* **39** 1493

Kroll N M and Watson K M 1973 *Phys. Rev.* **A8** 804

Landau L D and Lifshitz E M 1959 *Quantum mechanics* (Pergamon Press) p. 503
Levine R D and Bernstein R B 1974 *Molecular reaction dynamics*; (Oxford: Clarendon Press) p. 125
Mohan M 1974 *Phys. Lett.* **A50** 283
Mohan M 1980 *Electron impact ionization of an atom in the presence of e.m. field*; *2nd Int. Conf. on Multiphoton Processes, in Budapest, Hungary*, 14–18
Mohan M 1981 *J. Chem. Phys.* **75** 1772
Mott N F and Massey H S W 1965 *The theory of atomic collisions* (Oxford: Clarendon Press) 3 edn. Chap. III-IV
Rosenberg L 1979 *Phys. Rev.* **A20** 457
Walther H 1976 *Laser Spectroscopy of Atoms and Molecules* (Berlin: Springer Verlag; New York: Heidelberg) 1

Pramāṇa, Vol. 21, No. 2, August 1983, pp. 103–110. © Printed in India.

Core electron binding energies in heavy atoms

M P DAS
Department of Physics, Sambalpur University, Jyoti Vihar, Sambalpur 768 017, India

MS received 8 October 1982; revised 26 April 1983

Abstract. Inner shell binding of electrons in heavy atoms is studied through the relativistic density functional theory in which many electron interactions are treated in a local density approximation. By using this theory and the Δ SCF procedure binding energies of several core electrons of mercury atom are calculated in the frozen and relaxed configurations. The results are compared with those carried out by the non-local Dirac-Fock Scheme. *K*-shell binding energies of several closed shell atoms are calculated by using the Kohn-Sham and the relativistic exchange potentials. The results are discussed and the discrepancies in our local density results, when compared with experimental values, may be attributed to the non-locality and to the many-body effects.

Keywords. Atomic structure; binding energy; relaxed orbitals; density functional; Breit interaction.

1. Introduction

Calculations on the electronic structure of heavy atoms based on the relativistic theory, such as multi-configurational Dirac-Fock (MCDF) method (Desclaux 1980) are in reasonably good agreement with experimental findings. This theory employs one-electron Dirac Hamiltonian that contains the kinematics of the electrons and their interactions with the classical nuclear field. The electron-electron interaction is then added in two parts. The first part is treated in the Hartree-Fock sense by applying variational principle to a many-electron wavefunction as an antisymmetric product of one-electron orbitals. The second part is a quantum electrodynamical correction known as Breit interaction treated in the lowest order of the fine structure constant and is due to exchange of a transverse photon in two-electron interactions. The Breit term is treated as a first-order perturbation to the unperturbed Dirac Hamiltonian that includes the aforesaid first part of electron interaction. We shall refer to this as the MCDFB approach.

In nonrelativistic theory the orbital angular momentum (L) and the spin (S) are separately good quantum numbers. But in the relativistic theory parity and the total angular momentum (J) are constants of motion. We have to consider several (JJ) configurations for a system where LS coupling scheme is appropriate which is true even at the Hartree-Fock level. This aspect has given rise to a multi-configurational Dirac-Fock scheme that rests on a very involved analysis. The use of MCDFB approach particularly for a large and complex system like a molecule or a solid is a formidable task. Therefore there is a need for a theory based on a local approximation like Slater's X-α method (Slater 1974; Connolly 1977) or more correctly a

relativistic density functional theory (MacDonald and Vosko 1979; Rajagopal 1980; Das *et al* 1980) based on the Hohenberg-Kohn theorem. The basic aim of this approach is to obtain an effective one-body density-dependent potential which should be a reasonable representation for a many-particle interacting system, particularly in the ground state. One distinct advantage of this local density approach over the MCDFB scheme is that the exchange-correlation interaction can be treated in a self-consistent manner instead of a perturbative approach as in the MCDFB case.

In a relativistic situation a quantum electrodynamical correction due to transverse photon-electron interaction (TPE) is important. When two Dirac electrons interact through a transverse photon, the exchange force between the electrons becomes repulsive unlike ordinary Coulomb exchange. The physics of the TPE interaction has been extensively discussed in the literature in the context of high density matter (Salpeter 1961; Jancovici 1962). Recently the present author (Das 1980) calculated the TPE energy in the local density approximation (LDA) for several closed shell atoms. It is worthwhile to point out that when one makes a further approximation to the TPE interaction by neglecting the energy of the exchanged photon in the denominator of the expression of the TPE term (Brown and Ravenhall 1951, Jancovici 1962) one obtains the Breit interaction. In relativistic atomic physics the Breit interaction has been amply used (Mann and Johnson 1971). It contains two parts, one is known as the Gaunt interaction derived from two Dirac currents and the second part is known as retardation derived from the Hamiltonian of Darwin. More recently Grant and Mackenzie (1980) incorporated full transverse interaction in their non-local atomic structure calculations.

In the local density approximation we have calculated both the transverse and the Breit potentials (figure 1). It is found that the Breit potential is deeper than the TPE presumably because we have ignored the exchanged-transverse photon energy in the energy denominator which has made the Breit energy larger than that of the TPE (Das 1982). Since the potential is obtained as the density derivative of energy the Breit potential is deeper than the TPE one. In the non-local analysis the difference between the Breit and the TPE energies is quite small (Grant and Mackenzie 1980)

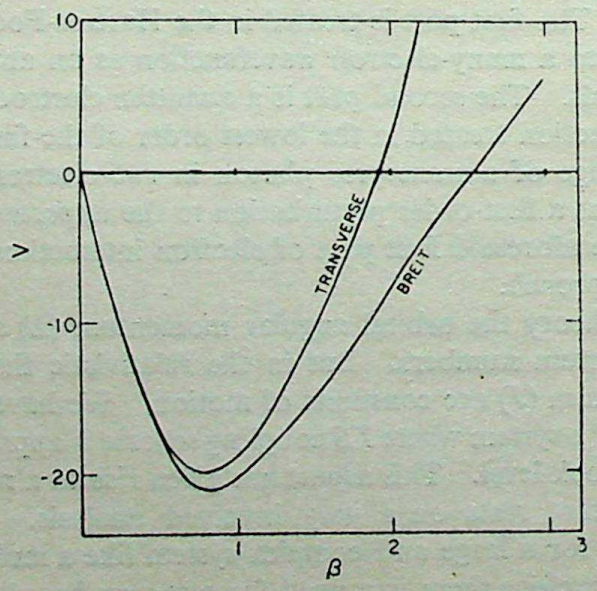

Figure 1. Breit potential and transverse potential shown as a function of β, the ratio of momenta of electron and photon.

contrary to our LDA results. This may be due to certain non-local effects which need further investigation.

As regards correlation contribution, this is considered to be the left-out part of the interactions beyond the mean Hartree-Dirac field. Several theoretical methods are available to calculate correlation energies involving heavy computational efforts. Such methods are non-local and are known as the configuration interaction scheme. Considerable simplification is attained if one adopts an LDA of the electron gas model as in the case of exchange. Considerable literature is available on the calculation of correlation energies in the non-relativistic cases (see for example, Kohn and Vashishta 1982, Singwi and Tosi 1982). It is well known that in the LDA the correlation contribution is over-estimated. Cowan (1981) has an improved interpolation scheme over his earlier one for high densities in the non-relativistic framework. Using his formula the correlation energy for Yb atom is $-3{\cdot}04$ Hartree atomic units and the correlation contribution to the K-shell binding is $-0{\cdot}09$ a.u. (Mann and Waber 1973). From table 2 of Mann and Waber it seems clear that the correlation contribution is negligible for inner shells whereas it is not so for outer shells. We have considered a relativistic electron gas model and have estimated the correlation energy by incorporating transverse photon contribution (Das 1981b). For Hg atom we obtain the correlation energy to be $-3{\cdot}5$ a.u., a contribution of 10^{-4} to the total energy. In view of the above any significant effect of correlation on the inner shells may be ruled out. We shall come back later to this point in the context of Δ SCF.

2. Outline of the theory

In the present paper we adopt the self-consistent local density functional formalism (SCRDF) (Das *et al* 1980). In the past, Huang *et al* (1976) carried out relaxed orbital binding energy calculations. Their method is hybrid in which they calculate wavefunctions in the relativistic local density approximation but by using Kohn-Sham exchange potential. They then calculated energies exactly using these wavefunctions and included the Breit term and Lamb shift as perturbative corrections. In our SCRDF method the TPE included exchange potential is very different from the nonrelativistic Kohn-Sham or X-α type exchange potentials (Das 1981a). In the deep interior of an atom where the electron density is very high, the TPE contribution makes the exchange potential positive. In figure 2 we display the relativistic and Kohn-Sham non-relativistic exchange potentials for Hg atom where the above distinction can be seen.

In order to obtain the ground-state energy or binding energies in an atom one has to solve the following equations in a self-consistent manner.

$$H\psi_i \equiv [c\alpha \cdot p + \beta c^2 + V_{\text{eff}}[n(\bar{r}), \bar{r}]]\,\psi_i = \epsilon_i \psi_i, \tag{1}$$

$$V_{\text{eff}}[n(\bar{r})] = -\frac{Z}{r} + \int \frac{n(\bar{r}')\,\mathrm{d}\bar{r}'}{|\bar{r} - \bar{r}'|} + \frac{\delta E_{xc}[n(\bar{r})]}{\delta n(\bar{r})}, \tag{2}$$

and

$$n(\bar{r}) = \sum_{i}^{\text{occ}} |\psi_i(\bar{r})|^2. \tag{3}$$

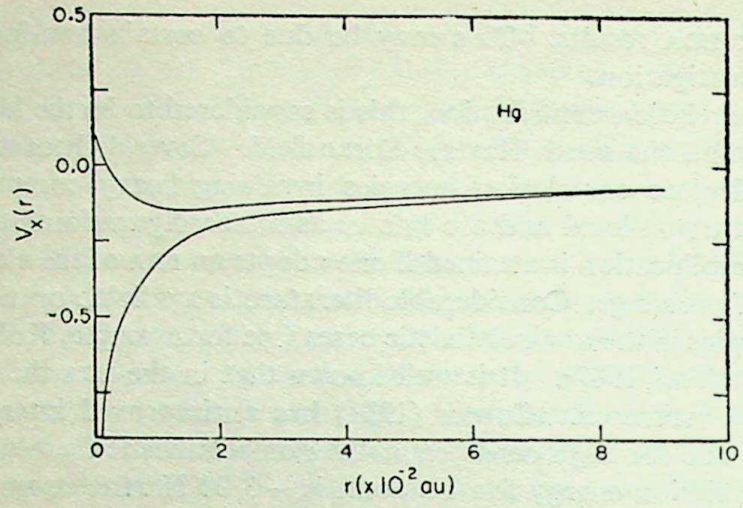

Figure 2. The self-consistent exchange potential for mercury. The lower curve is for the non-relativistic $X-\alpha$ potential while the upper is for the relativistic one (Hartree atomic units used).

Quantities in (1) to (3) have their usual meanings (Das *et al* 1980). E_x in (2) is the exchange-correlation (in the present case exchange only) energy given by

$$E_x\,[n(\bar{r})] = E_x^{\mathrm{NR}}\,[n(\bar{r})]\left\{1-\frac{3}{2}\left(\frac{\beta(\beta^2+1)^{1/2}-\sin h^{-1}\beta}{\beta^2}\right)^2\right\} \tag{4}$$

where $\beta = (3\pi^2 n)^{1/3}/c$, c being the velocity of light and E_x^{NR} is the nonrelativistic exchange energy. Note that we use Hartree a.u.

This formalism has been employed to calculate the total energies of several closed shell atoms (Das 1980) and the results are compared with non-local Dirac-Fock calculations giving reasonable agreements. The eigenvalues obtained from the above self-consistent equation (1) are somewhat fictitious and do not represent physical energies (Kohn and Vashishta 1982) as one obtains through Hartree-Fock or Dirac-Fock method in conjunction with Koopmans' theorem. Therefore binding energies are often calculated by the Δ SCF method (Rosen and Lindgren 1968). In this method the total energy of a neutral atom is calculated by incorporating the effective potential of the groundstate density. The total energy of an ion with a hole in a particular orbital is then calculated following the same prescription (Rosen and Lindgren 1968). In the latter situation the ion with a hole is considered to be in a quasi-stationary state, therefore the density functional theory is approximately used. The difference of these two energies gives the binding energy of the electron in the orbital in which there was a hole. It is important to note that while calculating the energy of the ion, the hole is not frozen but it relaxes so that the electron density adjusts to the presence of the hole. This procedure is also known as the relaxed orbital method (Huang *et al* 1976).

3. Results and discussion

3.1 *Core-electron binding in mercury atom*

We have calculated binding energies of several core electrons in Hg atom. Hg is a closed shell atom for which LDA is suitable. There exist nonlocal Dirac-Fock

calculations (McGilp and Weightman 1980) for binding energies. Besides, the gas phase data for Hg are also avilable from the high resolution ESCA measurements (Siegbahn *et al* 1967).

In table 1 we present the core electron binding energies for Hg. The values of relaxed orbital binding energies with Kohn-Sham potential only are tabulated together with the TPE contributions in both the frozen and the relaxed configurations. We also give the calculated relaxed orbital binding energies due to McGilp and Weightman (1980) which include only the Breit corrections. These values are given in order to compare similar physical quantities (electric and Breit or transverse). McGilp and Weightman (1980) showed that their DFB results are in excellent agreement with the Dirac-Slater-Breit results of Huang *et al* (1976). Both these approaches are self-consistent at the non-relativistic level so far as exchange is concerned and the Breit term is treated as a perturbation. In our approach the TPE term which is more general than the Breit term is included in the self-consistent potential. The Lamb shift corrections available for some inner shell orbitals are also given in table 1. After adding the Lamb shift corrections to the corresponding quantities the contribution to the binding energies could be compared with the experimental values (table 1). It is found that in most cases our binding energies in the frozen configurations are closer to the DFB results when compared with the relaxed ones. The difference between the energies in these two configurations is known as the rearrangement energy. For $1s$ and $2s$ orbitals the rearrangement energies are 101 and 60 eV respctively. The next correction considered is the Lamb shift (Desiderio and Johnson 1971). It constitutes two parts: (i) vacuum polarization correction, essentially due to nuclear Coulomb field and is calculated as an expansion in (αZ), (ii) self-energy correction, arising out of emission and reabsorption of photons by a moving electron. Cheng and Johnson (1976) obtained this correction numerically for the K shell binding energies for several heavy atoms. On adding these McGilp and Weightman (1980) obtained excellent agreement with the experimental values.

Table 1. Relaxed orbital energies for mercury (in eV).

Levels	Kohn-Sham (relaxed) (−)	Present (frozen) (−)	Present (relaxed) (−)	DF + Breit (McGilp and Weightman 1980) (−)	Lamb-Shift (+)	Expt. (−)
$1s$	83598	83235	83134	83254	155	83108
$2s$	14804	14790	14730	14883	24	14844
$2p$	14248	14245	14180	14215	2	14214
$2\bar{p}$	12277	12294	12233	12292		12289
$3s$	3517	3535	3501	3583		3567
$3p$	3252	3274	3239	3292		3284
$3\bar{p}$	2817	2842	2809	2860		2852
$3d$	2380	2413	2376	2398		2390
$3\bar{d}$	2287	2319	2283	2303		2300

The Lamb-shift contribution for $1s$, $2s$ and $2p$ are obtained from Huang *et al* (1976) which are to be added to the corresponding binding energies in the present calculations and also to that of McGilp and Weightman (1980).

3.2 *K-shell binding*

Two sets of Δ SCF calculations were performed for the K shell binding of almost all the closed shell atoms. The first is the SCRDF calculations with Kohn-Sham exchange potential and the second is another SCRDF calculation with relativistic exchange potential (equation (4)). In figure 3 we have presented the results. The quantities along the y-axis $\%\ E_K$ show the percentage of departure of calculated values of K shell binding energy from that of experiments. The latter are used from the tables of Bearden and Burr (1967) and Porter and Freedman (1978). These are very high precision data available from x-ray and internal conversion spectroscopies. The straight line connecting small dots is for the non-relativistic Hartree-Fock calculations of Froese-Fischer (1977) and the line connecting the crosses is the Dirac-Fock results of Desclaux (1973). In general one believes that the conventional Hartree (Dirac)-Fock eigenvalues in conjunction with Koopmans' theorem represent the orbital binding energies. Therefore we have used these calculated data from the tables of Froese-Fischer (1977) and Desclaux (1973). But from the work of Fricke *et al* (1972) it is well known that the Δ SCF binding energy takes into account the rearrangement or relaxation arising due to creation of a hole in a particular orbital. In the Δ SCF procedure only static or monopole type of relaxation is included. There are further many-body effects like dynamical relaxation arising out of virtual Auger processes (Wendin 1979). To our knowledge there are Δ SCF Dirac-Fock calculations for some atoms (Fricke *et al* 1972, McGilp and Weightman 1980; Grant and Mackenzie 1980), though the method

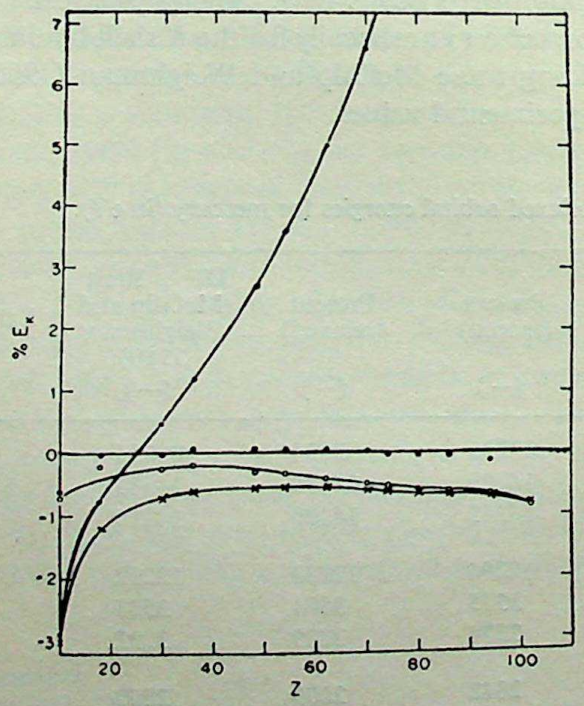

Figure 3. $\%\ E_K$ is the percentage of departure of calculated K shell binding energy from experiments, i.e. $(E^K_{\text{exp}} - E^K_{\text{th}}) / E^K_{\text{exp}} \times 100$.
The departure of various calculations are shown as a function of atomic number Z. .—.—. non relativistic, x—x—x DFB, o–o–o SCRDF Kohn-Sham, ● ● ● SCRDF relativistic. Experimental data for *Rn* and after, are used from Porter and Freedmann (1978) while all others are used from Bearden and Burr (1967).

and the program are readily available. If the rearrangement energy is added to the Dirac-Fock binding energies the departure as shown in figure 3 will be substantially reduced. The non-relativistic results of Froese-Fischer (1977) show reasonable departure from experiment for atoms having $Z<20$. In this range the departure is essentially due to correlation whose importance is well understood in non-relativistic atomic physics (Cowan 1981; Froese-Fischer 1977). Of course one should not use non-relativistic theory for high Z atoms.

Our first set of calculations of SCRDF with Kohn-Sham potential is shown by open circles in figure 3. These results are closer to the experiment than the Dirac-Fock results (see also Fricke and Soff 1977). The second set of calculations of SCRDF with the relativistic exchange potential is shown by heavy dots. As mentioned before this potential includes the TPE contributions unlike Kohn-Sham potential. In DF results of Desclaux (1973) shown by crosses the magnetic part of the Breit term is included. Figure 3 shows that the SCRDF and DFB results differ nearly by a constant. If the relaxation and Lamb shift corrections are added to the DFB results it should yield a better agreement compared to ours as can be seen from Zn, Cd, Hg and Fm atoms (Das 1981a, 1982).

There are discrepancies in our calculated values when compared with experimental values. One knows that DFB method is a more accurate method but it involves an order of magnitude more computer time. This difficulty is substantially reduced by resorting to the LDA. Therefore in our view the discrepancies may be attributed to the non-locality and further many-body effects (like dynamical relaxation etc.).

References

Bearden J A and Burr A F 1967 *Rev. Mod. Phys.* **39** 125

Brown G E and Ravenhall D G 1951 *Proc. R. Soc.* (*London*) **A208** 552

Cheng K T and Johnson W R 1976 *Phys. Rev.* **A14** 1943

Connolly J W D 1977 in *Semiempirical methods of electronic structure calculations* Part-A (ed.) G A Segal (New York: Plenum) 105

Cowan R D 1981 *Theory of atomic structure and spectra* (Berkeley: Univ. of California Press)

Das M P 1980 *Int. J. Quantum Chem.* **S14** 66

Das M P 1981a *Phys. Rev.* **A23** 391

Das M P 1981b Sanibel Quantum Chem. Symposium (unpublished)

Das M P 1982 *Int. J. Quantum Chem.* **21** 845

Das M P, Ramana M V and Rajagopal A K 1980 *Phys. Rev.* **A22** 9

Desclaux J P 1973 *Atomic Data and Nuclear Data* **12** 311

Desclaux J P 1980 *Phys. Scr.* **21** 436

Desiderio A M and Johnson W R 1971 *Phys. Rev.* **A3** 1267

Fricke B, Desclaux J P and Waber J T 1972 *Phys. Rev. Lett.* **28** 714

Fricke B and Soff G 1977 *Atomic Data and Nuclear Data* **19** 83

Froese-Fischer C 1977 *The Hartree-Fock method for atoms* (New York: Wiley)

Grant I P and Mackenzie B J 1980 *J. Phys.* **B13** 2671

Huang K N, Aoyagi M, Chen M H and Craseman B 1976 *Atomic Data and Nuclear Data* **18** 243

Jancovici B 1962 *Nuovo Cimento* **25** 429

Kohn W and Vashishta P 1982 in *Theory of inhomogeneous electron gas* (eds) S Lundqvist and N H March (New York: Plenum)

MacDonald A K and Vosko S H 1979 *J. Phys.* **C12** 2977

Mann J B and Johnson W R 1971 *Phys. Rev.* **A4** 41

Mann J B and Waber J T 1973 *Atomic Data* **5** 201

McGilp J F and Weightman P 1980 *J. Phys.* **B13** 1953

Porter F T and Freedman M S 1978 *Phys. Chem. Ref. Data* **7** 1267
Rajagopal A K 1980 *Adv. Chem. Phys.* **41** 59
Rosen A and Lindgren I 1968 *Phys. Rev.* **176** 114
Salpeter E E 1961 *Ap. J.* **134** 669
Siegbahn K *et al* 1967 ESCA Almqvist and Wiksells, Uppsala, Sweden
Singwi K S and Tosi M P 1982 in *Solid State Physics* (eds.) H Ehrenreich, F Seitz and D Turnbull (New York: Academic Press)
Slater J C 1974 *The Self-consistent field for molecules and solids* (New York: McGraw Hill) Vol. 4
Wendin G 1979 *Int. J. Quantum Chem.* **S13** 659

Pramāṇa, Vol. 21, No. 2, August 1983, pp. 111–122. © Printed in India.

First passage time distributions for finite one-dimensional random walks

M KHANTHA and V BALAKRISHNAN
Department of Physics, Indian Institute of Technology, Madras 600 036, India

MS received 5 April 1983

Abstract. We present closed expressions for the characteristic function of the first passage time distribution for biased and unbiased random walks on finite chains and continuous segments with reflecting boundary conditions. Earlier results on mean first passage times for one-dimensional random walks emerge as special cases. The divergences that result as the boundary is moved out to infinity are exhibited explicitly. For a symmetric random walk on a line, the distribution is an elliptic theta function that goes over into the known Lévy distribution with exponent 1/2 as the boundary tends to ∞.

Keywords. Biased random walks; Markov processes; first passage time; finite chains.

1. Introduction

There is considerable current interest (Weiss 1966, 1981; Montroll and West 1979; Seshadri *et al* 1980; Gillespie 1981; Seshadri and West 1982) in the classic problem of the first passage time in one-dimensional random walks owing to its diverse applications in physical problems: for example, the calculation of reaction rates in chemical processes, chemical dissociation induced by surface catalysis, optical bistability, decay of metastable states, etc. In general, such applications require the estimation of the mean first passage time for diffusion in the presence of specific potentials. In this paper, our aim is to present *exact* results for a simpler situation that takes account, however, of certain physical circumstances common to most applications. Thus, we study a random walk on a bounded set with perfectly reflecting boundaries, so that there is no 'leakage of probability'. We consider both discrete and continuous sets (finite chains or line segments). Further, we allow for an arbitrary uniform bias in the random walk — thus simulating the effect of a constant external field, or a finite temperature in the case of spectral diffusion, etc. Finally, we present closed-form expressions for the *characteristic function* of the first passage time distribution. The corresponding mean and variance can be deduced from this. The known results for the mean first passage time on the (semi-) infinite chain or line emerge, of course, as special cases of the expressions obtained here. Our primary result for the characteristic function follows from a lengthy calculation the outlines of which are sketched in the Appendix; the structure of the final result will be seen to comply with that required by a formal theorem on the first passage time problem for Markov processes (Darling and Siegert 1953). Our result facilitates an analytic examination of the

effects of the finite 'probability-conserving' boundary and of the superposed drift on the distribution of the first passage time.

The standard procedure (Pontryagin *et al* 1933; Stratonovich 1963) used in solving first passage time problems for a continuous Markov process whose conditional density satisfies a Fokker-Planck equation is *via* the solution of the adjoint equation. Our procedure, however, will be to present first the results for random walk on a discrete chain (a somewhat more difficult case), and then to pass to the continuum limit. We shall exploit for this purpose our recent exact solution (Khantha and Balakrishnan 1983) of the biased random walk problem on finite chains, obtained in the context of the frequency-dependent hopping conductivity in a bond-percolation model as well as the study of a spectral diffusion problem.

2. Biased random walk on a finite chain

We consider first a biased random walk on a finite chain with site label $m = 0, 1, \ldots, N$ (the lattice constant a being set equal to unity for convenience), *via* nearest-neighbour jumps at an average rate $2W$ and respective *a priori* probabilities $(1+g)/2$ and $(1-g)/2$ for jumps to the right and left, with $-1 < g < 1$. The end points of the chain are reflecting boundaries. Let $Q(m, t \mid m_0)\, \mathrm{d}t$ be the probability of reaching m for the first time in the time interval $(t, t+\mathrm{d}t)$ starting from m_0 at $t = 0$, where $0 \leqslant m_0 < m \leqslant N$. (The solution for $m_0 > m$ can be deduced from this with the help of a symmetry present in the problem.) Let $P(m, t \mid m_0)$ denote the conditional probability of finding the walker at the point m at time t, given that she starts from m_0 at $t = 0$. Then, *because* the simple random walk under consideration is a *Markov chain**, Q is related to P *via* the Siegert equation (Siegert 1951; Montroll and West 1979)

$$P(m_1, t \mid m_0) = \int_0^t P(m_1, t-t' \mid m)\, Q(m, t' \mid m_0)\, \mathrm{d}t', \quad m_0 < m \leqslant m_1. \tag{1}$$

Hence, in terms of the corresponding Laplace transforms,

$$\tilde{Q}(m, u \mid m_0) = \tilde{P}(m_1, u \mid m_0) / \tilde{P}(m_1, u \mid m), \quad m_0 < m \leqslant m_1, \tag{2}$$

where u is the transform variable. Analytic continuation to $u = i\omega$ will now yield the characteristic function of the distribution $Q(m, t \mid m_0)$ since the latter is defined only for positive values of t. The first passage to the point m from a point $m_0 < m$ (with $0 \leqslant m_0 < m < N$) involves the consideration of a random walk in the restricted range $[0, m]$ with an absorbing barrier at m. (We have already specified that 0 is a reflecting barrier.) Though $\tilde{P}(m_1, u \mid m_0)$ depends explicitly on m_1 and N (the loca-

*The non-Markov case, in particular the one in which the sequence of steps exhibits a memory in time as governed by a renewal process with a non-exponential pausing time distribution, is of interest in its own right. Some results for mean first passage times in such 'continuous time random walks' on an infinite chain have been given in Weiss (1981) using a generalised master equation. We have recently obtained an exact solution for $\tilde{Q}$ in the case of a general CTRW by other methods. These results will be reported separately (Balakrishnan and Khantha 1983).

tion of the boundary on the right), one would expect the dependence on m_1 and N to cancel out in the ratio on the right side of (2): $\tilde{Q}(m, u \mid m_0)$ must depend only on m_0, m and the reflecting barrier at the origin; as $0 \leqslant m_0 < m$, the effects of any boundary at a site to the right of m will not appear in $Q(m, t \mid m_0)$.

The mean first passage time from m_0 to m is given by

$$E[(t(m_0 \to m)] = -\lim_{u \to 0} \partial \tilde{Q}(m, u \mid m_0) / \partial u, \tag{3}$$

while the second moment is

$$E[t^2(m_0 \to m)] = \lim_{u \to 0} \partial^2 \tilde{Q} / \partial u^2, \tag{4}$$

provided these limits exist. As $E[t]$, $E[t^2]$, etc. diverge in certain simple situations corresponding to random walks on an infinite chain (see below), it is advantageous and instructive to derive first the exact results for a finite chain and then pass to the appropriate limit carefully so as to bring out the origin of these divergences.

As already mentioned in § 1, we now employ in (2) the solution we have obtained for $\tilde{P}(m, u \mid m_0)$ (Khantha and Balakrishnan 1983). The derivation of this solution is outlined in the Appendix. It turns out that the result can be written very compactly if we identify certain convenient variables. Accordingly, let us characterise the bias by the parameter $\alpha = \text{arc tanh } g$, so that the ratio of the probability of a jump to the right to that of a jump to the left is $(1+g)/(1-g) = \exp(2\alpha) = f$. We further define the quantity $\xi_0 = \text{arc cosh } (1 + u/2W)$, and finally introduce the variable ξ defined by $\cosh \xi = \cosh \xi_0 \cosh \alpha = (1 + u/2W)/(1-g^2)^{1/2}$. (As the Laplace transform is initially defined (is analytic) in a right half plane in u, it is appropriate to use hyperbolic functions. Note also that $\xi \to \xi_0$ when there is no bias). Then, for $0 \leqslant m, m_0 \leqslant N$, our answer for $\tilde{P}$ reads

$$\tilde{P}(m, u \mid m_0) = f^{(m-m_0)/2} [\sinh (N - m_> + 1)\, \xi - \sqrt{f} \sinh (N - m_>)\xi]$$

$$\times [\sqrt{f} \sinh (m_< + 1)\, \xi - \sinh m_< \, \xi] / [u \sinh \xi \sinh (N+1)\, \xi], \tag{5}$$

where $m_> = \max(m, m_0)$ and $m_< = \min(m, m_0)$. This representation of $\tilde{P}$ is in conformity with a general theorem on the structure of the Laplace transform of the conditional probability density for a temporally homogeneous Markov process (Darling and Siegert 1953; Siegert 1951). According to this thorem, $\tilde{P}(m, u \mid m_0)$ for such a process can always be written as a product of a function of m and a function of m_0. The proof of the theorem is based on the Siegert equation given earlier, and is valid for solutions on finite or infinite intervals. Our solution for $\tilde{P}(m, u \mid m_0)$ in (5) is explicitly a product of two such factors: one of them is a function of $m_>$ (and the right boundary at N), while the other is a function of $m_<$ (and the left boundary at 0).

Substitution of (5) in (2) yields, for $0 \leqslant m_0 < m \ (\leqslant N)$,

$$\tilde{Q}\,(m, u \,|\, m_0) = f^{(m-m_0)/2}\left[\frac{\sqrt{f}\sinh\,(m_0+1)\ \xi - \sinh m_0\ \xi}{\sqrt{f}\sinh\,(m+1)\ \xi - \sinh m\ \xi}\right]. \tag{6}$$

This is (after a straightforward analytic continuation to $u = i\omega$) the desired result for the characteristic function of the first passage time distribution in the presence of a reflecting barrier at the point 0. For a first passage from m_0 to m with $0 \leqslant m_0 < m < N$, the barrier at N is irrelevant, as already stated. The effect of the bias is measured by the deviation of the quantity f from unity, or, more accurately, of α from zero (recall that $f = \exp(2\alpha)$). For instance, in the application of the random walk model to the problem of spectral diffusion (Alexander *et al* 1978, 1981) at a finite temperature T, involving the non-radiative transfer of energy among a set of energy levels in a system with level spacing Δ, the parameter α is equal to Δ/KT. The unbiased case then corresponds to the $T \to \infty$ limit in which all the levels have equal occupation probabilities.

The mean first passage time corresponding to the characteristic function (6) is, using (3),

$$E\,[t\,(m_0 \to m)] = \frac{1}{2W}\,\frac{(f+1)}{(f-1)}\left[(m-m_0) - \frac{(f^{-m}-f^{-m_0})}{(f-1)}\right],\ (0 \leqslant m_0 < m). \tag{7}$$

A result equivalent to (7) is already known (see, *e.g.*, Parzen 1962)* for a discrete-time random walk on the set $\{0, 1, .., N\}$.

3. The continuum limit

The solution to the first passage time problem for diffusion on a finite segment $(0 \leqslant x \leqslant L)$ with reflecting boundary conditions can be obtained by proceeding to the continuum limit of the foregoing. Let the lattice spacing $a \to 0$, the bias factor $g \to 0$, the jump rate $W \to \infty$ and the number of sites $N \to \infty$ such that the following quantities are finite. the segment length $L = \lim Na$, the diffusion constant $D = \lim Wa^2$, and the drift velocity $c = \lim 2Wag$. ($c > 0$ signifies a drift to the right, $c < 0$ a drift to the left. We use the term bias for a random walk on a discrete chain, and drift when referring to diffusion on a continuous line. Further, in the discrete case, $D = Wa^2$ is the static diffusion constant on an infinite chain) Alternatively, one may employ the continuum version of (2) after solving for the Laplace transform $\tilde{P}\,(x, u \,|\, x_0)$ of the conditional probability density from the Smoluchowski equation

$$(D\,d^2/dx^2 - c\,d/dx - u)\,\tilde{P} = -\,\delta\,(x - x_0), \tag{8}$$

*In Parzen 1962 (see equation (7.29) therein), this result has been derived by solving the recursion relation obeyed by $E[t(m_0 \to m)]$ in the variable m_0. (The numerator of the first factor on the right in that equation should read p instead of q.)

with the reflecting boundary conditions

$$(D\, d/dx - c)\, \tilde{P} = 0, \tag{9}$$

at $x = 0$ and L for all u. Let $Q(x, t \mid x_0)\, dt$ be the probability of reaching the point x for the first time in the interval $(t, t + dt)$ starting from the point $x_0 < x$ at $t = 0$. We find the following solution for $\tilde{Q}$:

$$\tilde{Q}(x, u \mid x_0) = \left[\frac{R \cosh(Rx_0) + (c/2D)\sinh(Rx_0)}{R\cosh(Rx) + (c/2D)\sinh(Rx)}\right] \times$$

$$\exp\left[c(x - x_0)/2D\right] \quad (0 \leqslant x_0 < x), \tag{10}$$

where $R = R(u) = (c^2 + 4uD)^{1/2}/2D$. This last quantity can be recast in the form $R = (1 + 2u\tau)^{1/2}/\lambda$, where $\tau = 2D/c^2$ $(= \lim 1/(2Wg^2))$ and $\lambda = 2D/c$ $(= \lim a/g)$ respectively define natural time and length scales for diffusion with drift. $\tilde{Q}(x, i\omega \mid x_0)$ is the characteristic function of the first passage time distribution from x_0 to x $(0 \leqslant x_0 < x)$ in the presence of a reflecting barrier at the origin. As in the discrete case, the barrier on the right at L is irrelevant in this context, and (10) is valid even for a first passage from x_0 to x on a semi-infinite line $[0, \infty]$ with a reflecting barrier at the origin.

Using (3) and (4), the mean and variance of the distribution $Q(x, t \mid x_0)$ are found to be respectively

$$E[t(x_0 \to x)] = \frac{(x - x_0)}{c} + \tfrac{1}{2}\tau\left[\exp(-2x/\lambda) - \exp(-2x_0/\lambda)\right] \tag{11}$$

and

$$\mathrm{Var}\,[t(x_0 \to x)] = \tau\left[\left\{\frac{x}{c} + \left(\tau + \frac{2x}{c}\right)\exp(-2x/\lambda) + \tfrac{1}{4}\tau\exp(-4x/\lambda)\right\} - \{x \to x_0\}\right]. \tag{12}$$

4. Infinite random walks

According to Polya's classic result (Polya 1921), the mean first passage time from m_0 to m $(m_0 < m)$, or from x_0 to x $(x_0 < x)$, for a random walk on a (semi-)infinite chain or line is *infinite* if the bias (or drift) is zero; it is finite if the bias or drift is to the right. (We shall comment shortly on what happens when the bias is to the left.) For the discrete chain the emergence of these results is conveniently exhibited with the help of the general formula in (7) if we first translate the origin to the point $-M$ and eventually let $M \to +\infty$. When the bias is to the right $(0 < g < 1$, or $1 < f < \infty$, or $0 < a < \infty)$, we find

$$E[t(m_0 \to m)] = (m - m_0)/(2Wg) + O\left[\exp(-2Ma)\right]$$

$$\underset{M\to\infty}{\to} (m - m_0)/(2Wg) \qquad (-\infty < m_0 < m). \tag{13}$$

The corresponding variance in the limit $M \to \infty$ is

$$\text{Var}\,[t\,(m_0 \to m)] = (m - m_0)/(4W^2 g^3) \quad (-\infty < m_0 < m). \tag{14}$$

The continuum analogues of (13) and (14) for diffusion with a drift to the right ($c > 0$) on an infinite line are obtained similarly, using (11) and (12). We find

$$E\,[t\,(x_0 \to x)] = (x - x_0)/c \qquad (-\infty < x_0 < x), \tag{15}$$

and

$$\text{Var}\,[t\,(x_0 \to x)] = 2D\,(x - x_0)/c^3 \qquad (-\infty < x_0 < x). \tag{16}$$

When the bias is zero ($g = 0, f = 1, \alpha = 0$), we find

$$E\,[t\,(m_0 \to m)] \to M\,(m - m_0)/W \qquad (-M \ll m_0 < m), \tag{17}$$

which diverges *linearly* as $M \to \infty$. On the other hand, for a bias to the left ($-1 < g < 0$, or $0 < f < 1$, or $-\infty < \alpha < 0$),

$$E\,[t\,(m_0 \to m)] \to \text{O}\,[\exp\,(2M\,|\,\alpha\,|)] \qquad (-M \ll m_0 < m), \tag{18}$$

which diverges *exponentially* as the boundary is moved out to infinity on the left. What is happening is best understood as follows. The characteristic function for first passage on the (semi-) infinite chain is found from (6) by replacing m and m_0 by $m + M$ and $m_0 + M$ respectively, and then taking the limit $M \to +\infty$. We obtain

$$\tilde{Q}(m, u \mid m_0) = f^{(m-m_0)/2}\left[\frac{u + 2W - (u^2 + 4uW + 4W^2 g^2)^{1/2}}{2W(1 - g^2)^{1/2}}\right]^{m-m_0}, \tag{19}$$

which is *apparently* valid for all f in $0 < f < \infty$, or $-1 < g < +1$, *i.e.* for left, right, or zero bias. Now, an examination of the general formula of (2) in the limit $u \to 0$ immediately reveals that

$$\tilde{Q}\,(m, 0 \mid m_0) = \lim_{u \to 0}\left\{\frac{u^{-1} P^{\text{st}}\,(m_1)}{u^{-1} P^{\text{st}}\,(m_1)}\right\} = 1, \tag{20}$$

so that the Siegert equation ensures that the first passage time distribution is *inherently* normalised according to

$$\int_0^\infty Q(m, t \mid m_0)\,\mathrm{d}t = 1. \tag{21}$$

On the other hand, taking the limit $u \to 0$ carefully in (19) yields

$$\tilde{Q}(m, 0 \mid m_0) = \begin{cases} 1, \text{ for } f > 1 \text{ (or } g > 0) \\ f^{m-m_0}\ (< 1), \text{ for } f < 1 \text{ (or } g < 0). \end{cases} \tag{22}$$

The distribution is therefore not normalised to unity when the bias is to the left. The resolution of the paradox lies in the fact that, when the bias is to the left, a passage to the right (equivalently, absorption at a site $m > m_0$) is not a *certain* event if the chain extends infinitely far to the left: *i.e.*.

$$\int_0^\infty Q(m, t \mid m_0)\, \mathrm{d}t < 1 \tag{23}$$

in that case. Therefore the first passage time from m_0 to $m > m_0$ is not a proper random variable in the sense of Darling and Siegert (1953), and its moments do not exist. This circumstance appears to have been overlooked by Montroll and West (1979), and hence the distribution function $Q(m, t \mid m_0)$ and the mean first passage time obtained from it (see equations (6.14) and (6.16) in Montroll and West 1979) are not valid when the bias is to the left.* For the sake of completeness, let us record the (known) expression for the first passage time distribution on the (semi-) infinite chain when the bias is to the right or is absent. This is the inverse transform of (19):

$$Q(m, t \mid m_0) = [(m - m_0)/t]\, f^{(m-m_0)/2}$$

$$\exp(-2\,W\,t)\, I_{m-m_0}\,[2\,Wt\,(1 - g^2)^{1/2}] \quad (-\infty < m_0 < m). \tag{24}$$

Here I_r is the modified Bessel function of order r, and $1 \leqslant f < \infty$ or $0 \leqslant g < 1$, as already explained. One may verify that the first moment of this distribution is $(m - m_0)/(2Wg)$ when $0 < g < 1$ and infinite when $g = 0$, in accord with the preceding remarks.

4. Symmetric random walks

Going back to the finite chain considered earlier, taking the limit $g \to 0$ ($f \to 1$) gives very simple answers for unbiased or symmetric random walks. We find (for $0 \leqslant m_0 < m$ as usual)

$$E[t(m_0 \to m)] = [(m + \tfrac{1}{2})^2 - (m_0 + \tfrac{1}{2})^2]/(2\,W),$$

$$\text{Var}\,[t(m \to m)] = [(m + \tfrac{1}{2})^4 - (m_0 + \tfrac{1}{2})^4]/(6\,W^2), \tag{25}$$

and so on. The continuum analogues are, again with $0 \leqslant x_0 < x$,

$$E[t(x_0 \to x)] = (x^2 - x_0^2)/(2\,D),$$

$$\text{Var}\,[t(x_0 \to x)] = (x^4 - x_0^4)/(6\,D), \text{ etc.} \tag{26}$$

*There are also typographical errors in (6.10) and (6.13)-(6.16) of that reference: *e.g.*, $\eta/(1 - \eta)$ should be replaced by its reciprocal in several places.

The characteristic function $\tilde{Q}$ in (6) itself reduces in this case to

$$\tilde{Q}(m, u \mid m_0) = \cosh(m_0 + \tfrac{1}{2})\xi_0 / \cosh(m + \tfrac{1}{2})\xi_0 \quad (0 \leqslant m_0 < m), \tag{27}$$

where $\cosh \xi_0 = (1 + u/2W)$ as already defined. The first passage time distribution can then be written as

$$Q(m, t \mid m_0) = (1/t)\ \exp(-2Wt) \sum_{r=0}^{\infty} (-1)^r [a_r \{I_{a_r}(2Wt) + I_{b_r}(2Wt)\} + (2m_0 + 1)\, I_{b_r}(2Wt)], \tag{28}$$

where
$$a_r = (m - m_0) + (2m + 1)\, r,\ b_r = a_r + 2m_0 + 1. \tag{29}$$

The continuum version of (27) is

$$\tilde{Q}(x, u \mid x_0) = \cosh(ux_0^2/D)^{1/2} / \cosh(ux^2/D)^{1/2} \quad (0 \leqslant x_0 < x). \tag{30}$$

Inversion of the transform yields (Oberhettinger and Badii 1973)

$$Q(x, t \mid x_0) = \frac{D}{x} \frac{\partial}{\partial x_0} \theta_1\left(\frac{x_0}{2x} \middle| \frac{Dt}{x^2}\right), \qquad (0 \leqslant x_0 < x), \tag{31}$$

where θ_1 is the elliptic theta function of the first kind. As before. if we shift the origin to the point $-L$ and let L become very large, we can find the form of the 'correction' to the known result for an infinite line (see, *e.g.*, Feller 1966; Itô and McKean 1974) owing to the introduction of a (distant) boundary. We get

$$Q(x, t \mid x_0) = (x - x_0)(4\pi Dt^3)^{-1/2} \exp[-(x - x_0)^2/(4Dt)] + O[\exp(-L^2/Dt)], \qquad (-L \ll x_0 < x). \tag{32}$$

The term that survives when $L \to +\infty$ is the familiar one-sided Lévy distribution (in the *time* t) with exponent 1/2, all of whose moments diverge. To get an idea of the effect of introducing a reflecting barrier, we have plotted in figure 1 the first passage time distribution function for drift-free diffusion on a line. Curve (a) is the Lévy distribution that applies when the line extends infinitely far to the left of the starting point x_0. Curve (b) represents the other extreme in which the confining barrier is at x_0 itself. All other intermediate cases, in which the barrier is at a finite distance to the left of x_0, fall in between these two extremes.* The *exponential* fall off as $t \to \infty$ in the case of a finite barrier changes to a power law ($\sim t^{-3/2}$) when the barrier is moved out to infinity—causing, incidentally, the divergence of the moments of the distribution.

*For numerical accuracy, in the case of a finite boundary (as in figure 1b) one must use different representations for the θ_1 function in different time regimes: for small t, an expansion in terms of the form $t^{-3/2} \exp(-\mu_n / t)$; for large t, of the form $\exp(-\lambda_n t)$.

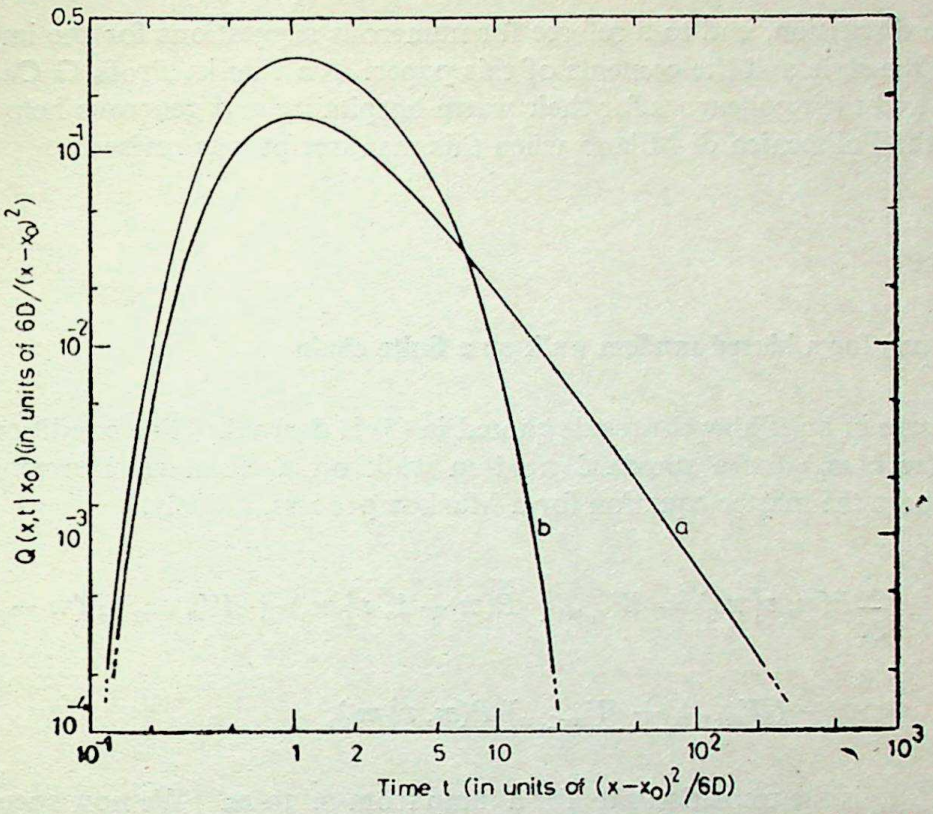

Figure 1. The normalized first passage time distribution function $Q(x, t \mid x_0)$ for unbiased diffusion on a line. Curve (a) (a Lévy distribution) corresponds to diffusion on an infinite line. Curve (b), related to an elliptic theta function, corresponds to a reflecting barrier at the starting point x_0 itself. Both distributions are unimodal, with the peak at $t = (x - x_0)^2/(6\,D)$. The total area under each curve is unity. Curve (b) falls off exponentially as $t \to \infty$, while (a) decays according to a power law. Both the abscissa and the ordinate in this figure are on logarithmic scales, to highlight this fact.

Finally, it is noteworthy that the Lévy distribution given in (32) [or its discrete counterpart in (24), with $f = 1$ and $g = 0$)] is just $(x - x_0)/t$ [or $(m - m_0)/t$] times the corresponding conditional probability density $P(x, t \mid x_0)$ [probability $P(m, t \mid m_0)$] for drift-free diffusion [symmetric random walk] on the infinite line [chain]. One may ask whether this property is shared by any other type of random walk on the infinite line or chain. We have been able to show* that, of the entire class of 'continuous time random walks', this property holds good only in the Markov case, *i.e.* only if the distribution of the pausing time between the steps of the random walk is an exponential one, the situation considered in this paper. Remarkably enough, however, there exist even more general types of temporally-correlated random walks for which the property does hold good. And there are, too, 'temporally fractal' continuous time random walks for which a simple generalisation of the property obtains. These results will be presented elsewhere.

Acknowledgements

MK acknowledges the financial support of the Department of Atomic Energy, India, in the form of a fellowship. The authors are grateful to Prof. R Vasudevan for a

*See footnote on p. 112

valuable discussion, and to a referee for numerous suggestions for the improvement of both the style and the contents of this paper. VB thanks Profs G Caglioti, C E Bottani and their colleagues for their warm hospitality and generous help during his stay at the Politecnico di Milano when this manuscript was revised.

Appendix

$P(m, t \mid m_0)$ for a biased random walk on a finite chain

We indicate in brief how the result quoted in (5) is derived. The conditional probability $P(m, t \mid m_0)$ for a standard random walk on a chain *via* nearest-neighbour jumps obeys the master equation for a Markov process, namely,

$$\frac{\partial}{\partial t}P(m, t \mid m_0) = W_{m,m+1}\ P(m+1, t \mid m_0) + W_{m,m-1}\ P(m-1, t \mid m_0) - (W_{m+1,m} + W_{m-1,m})\ P(m, t \mid m_0), \tag{A1}$$

where $W_{m,m'}$ is the transition rate for a jump from m' to m. We now specialise to a biased random walk on the bounded set $\{0, 1, \ldots, N\}$, with reflecting boundaries at 0 and N, and the initial condition $P(m, 0 \mid m_0) = \delta_{m,m_0}$. The Laplace transform of the master equation can then be written in the matrix form

$$\mathbf{A}\ \tilde{P}(u; m_0) = \delta(m_0). \tag{A2}$$

Here the mth element of the column vector $\tilde{\boldsymbol{P}}(u; m_0)$ [or $\delta(m_0)$] is $\tilde{P}(m, u \mid m_0)$ [or δ_{m,m_0}]. The elements of the asymmetric, tridiagonal matrix **A** are given by

$$\left.\begin{aligned} A_{mm'} &= (u + 2W)\ \delta_{mm'} - W(1-g)\ \delta_{m+1,m'} - W(1+g)\ \delta_{m-1,m'} \\ A_{0m'} &= [u + W(1+g)]\ \delta_{0m'} - W(1-g)\ \delta_{1m'} \\ A_{Nm'} &= -W(1+g)\ \delta_{N-1,m'} + [u + W(1-g)]\ \delta_{Nm'}, \end{aligned}\right\} \tag{A3}$$

where $1 \leqslant m \leqslant N$, $0 \leqslant m' \leqslant N$, and the bias is parametrised by g, with $-1 < g < 1$. The $(N+1)$ eigenvalues of **A** are

$$\lambda_0 = u,\ \lambda_r = u + 2W[1 - (1-g^2)^{\frac{1}{2}} \cos\{r\pi/(N+1)\}],\ r = 1, \ldots, N, \tag{A4}$$

with λ_0 corresponding to the steady-state solution. Using the right and left eigenvectors of the asymmetric matrix **A**, we can construct a matrix that diagonalises **A**, and thence the inverse $\mathbf{A}^{-1}$. This procedure yields, after all the algebra is done, the result

$$\tilde{P}(m, u \mid m_0) = \frac{1}{u}\frac{(1-f)\,f^m}{(1-f^{N+1})} + \frac{2}{(N+1)}\,f^{(m-m_0)/2}\cdot$$

$$\cdot \sum_{r=1}^{N} \frac{\left\{\sqrt{f}\sin\left(\frac{(m+1)\,r\pi}{N+1}\right) - \sin\left(\frac{m\,r\,\pi}{N+1}\right)\right\}\{m\to m_0\}}{\left(1-2\sqrt{f}\cos\frac{r\pi}{N+1}+f\right)\left[u+2W(1-g^2)^{1/2}\cos\left(\frac{r\pi}{N+1}\right)\right]},$$

$$(0 \leqslant m, m_0 \leqslant N), \tag{A5}$$

where $f = (1+g)/(1-g)$. The first term on the right represents, as may be guessed, the transform of the steady-state solution. It is expedient to split this term into partial fractions and to combine it with the second term, to obtain

$$\tilde{P}(m, u \mid m_0) = \frac{1}{u}\delta_{N,m}\,\delta_{N,m_0} + \frac{2}{(N+1)}f^{(m-m_0)/2}$$

$$\sum_{r=1}^{N}\left[u+2W(1-g^2)^{1/2}\cos\left(\frac{r\pi}{N+1}\right)\right]^{-1}\cdot$$

$$\cdot\left[\sin\left(\frac{(m+1)\,r\pi}{N+1}\right)\sin\left(\frac{(m_0+1)r\pi}{N+1}\right) + \frac{2W}{u(1+f)}\sin\left(\frac{r\pi}{N+1}\right)\cdot\right.$$

$$\left.\left\{\sin\left(\frac{(m+m_0+1)\,r\pi}{N+1}\right) - \sqrt{f}\sin\left(\frac{(m+m_0+2)\,r\pi}{N+1}\right)\right\}\right]. \tag{A6}$$

To find a closed form for $\tilde{P}(m, u \mid m_0)$, we must carry out the finite summations in (A6). We have done this, with the help of several auxiliary trigonometric summation formulas we have derived in a straightforward manner, and also the following formulas (Hansen 1975):

$$\sum_{k=1}^{[(N-1)/2]} \frac{\cos(2\pi\,k\,m/N)}{\cosh x - \cos(2\pi\,k/N)} = \frac{N}{2}\,\mathrm{cosech}\,x\,\mathrm{cosech}\,(Nx/2)$$

$$\cosh\left\{\left(\frac{N}{2} - m + N\left[\frac{m}{N}\right]\right)x\right\} - \frac{1}{4}\mathrm{cosech}^2(x/2) - \frac{1}{8}(-1)^m$$

$$(1+(-1)^N)\,\mathrm{sech}^2(x/2), \tag{A7}$$

$$\sum_{k=1}^{[(N-2)/2]} \frac{\cos((2k+1)\,m\pi/N)}{\cosh x - \cos((2k+1)\pi/N)} = (-1)^{[m/N]}\frac{N}{2}\,\mathrm{cosech}\,x\,\mathrm{sech}\,(Nx/2).$$

$$\cdot\sinh\left\{\left(\frac{N}{2} - m + N\left[\frac{m}{N}\right]\right)x\right\} + \frac{1}{8}(-1)^m((-1)^N - 1)\,\mathrm{sech}^2(x/2). \tag{A8}$$

Here $[a/b]$ stands for the largest integer less than (a/b). A great deal of algebra is involved, but the end result is simply

$$\tilde{P}(m, u\,|\,m_0) = \frac{f^{(m-m_0)/2}}{\sinh\,(N+1)\,\xi}\left[\frac{(1+f)}{2W\sqrt{f}}\frac{\sinh\,(N-m_>)\xi\,\sinh\,(m_<+1)\xi}{\sin\,h\,\xi}\right.$$

$$\left. + \frac{1}{u}\left\{\frac{1}{\sqrt{f}}\sinh\,(N-m_>-m_<)\xi - \sinh\,(N-m_>-m_<-1)\xi\right\}\right], \tag{A9}$$

where $m_> = \max\,(m, m_0)$, $m_< = \min\,(m, m_0)$, and $\xi = \cosh^{-1}\,[(1 + u/2W\ 1 - g^2)^{-1/2}]$, as defined in the text. Further simplification leads to the surprisingly compact answer quoted in (5), namely,

$$\tilde{P}(m, u\,|\,m_0) = (\sqrt{f})^{m-m_0}\,[\sinh\,(N-m_>+1)\xi - \sqrt{f}\sinh\,(N-m_>)\xi\,]$$

$$\times\,[\sqrt{f}\sinh\,(m_<+1)\xi - \sinh\,m_<\xi]/[(u\,\sinh\,\xi\,\sinh\,(N+1)\xi]. \tag{A10}$$

When there is no bias ($g = 0$, or $f = 1$), this becomes even simpler:

$$\tilde{P}(m, u\,|\,m_0) = \frac{\cosh\,(N-m_>+\tfrac{1}{2})\xi_0\,\cosh\,(m_<+\tfrac{1}{2})\xi_0}{W\sinh\,\xi_0\,\sinh\,(N+1)\xi_0}, \tag{A11}$$

where $\xi_0 = \cosh^{-1}\,(1 + u/2W)$. This is, incidentally, the closed-form result for the sum obtained as a solution for $\tilde{P}$ in the bias-free case by Odagaki and Lax (1980) in the study of a bond-percolation model.

References

Alexander S, Bernasconi J and Orbach R 1978 *Phys. Rev.* **B17** 4311

Alexander S, Bernasconi J, Schneider W R and Orbach R 1981 *Rev. Mod. Phys.* **53** 175

Balakrishnan V and Khantha M 1983 *Pramana* (to be published)

Darling D A and Siegert A J F 1953 *Ann. Math. Stat.* **24** 624

Feller W 1966 *An Introduction to probability theory and its applications* (New York: Wiley) Vol. 2

Gillespie D T 1981 *J. Chem. Phys.* **74** 5295

Hansen E R 1975 *A table of series and products* (Englewood Cliffs, N. J.: Prentice-Hall)

Itô K and McKean J P 1974 *Diffusion processes and their sample paths* (Berlin: Springer-Verlag)

Khantha M and Balakrishnan V 1983 (submitted for publication)

Montroll E W and West B J 1979 in *Fluctuation phenomena* (eds.) E W Montroll and J L Lebowitz (Amsterdam: North-Holland)

Oberhettinger F and Badii L 1973 *Tables of Laplace transforms* (New York: Springer-Verlag)

Odagaki T and Lax M 1980 *Phys. Rev. Lett.* **45** 847

Parzen E 1962 *Stochastic processes* (San Francisco: Holden-Day)

Polya G 1921 *Math. Ann.* **84** 149

Pontryagin L, Andronov A and Witt A 1933 *Zh. Eksp. Teor. Fiz.* **3** 172

Seshadri V, West B J and Lindenberg K 1980 *J. Chem. Phys.* **72** 1145

Seshadri V and West B J 1982 *Proc. Natl. Acad. Sci. (USA)* **79** 4501

Siegert A J F 1951 *Phys. Rev.* **81** 617

Stratonovich R L 1963 *Topics in the theory of random noise* (New York: Gordon-Breach) Vol. 1

Weiss G H 1966 *Adv. Chem. Phys.* **13** 1

Weiss G H 1981 *J. Stat. Phys.* **24** 587

Pramāṇa, Vol. 21, No. 2, August 1983, pp. 123–129. © Printed in India.

Significance of Hall measurements in Ga_{1-x} Al_xAs alloys at 300 K

ASHOK K SAXENA and B B SINGH
Department of Electronics and Communication Engineering, University of Roorkee, Roorkee 247 667, India

MS received 20 October 1982; revised 1 July 1983

Abstract. The Hall mobility, electron concentration and resistivity have been measured as a function of alloy composition for Ga_{1-x} Al_x As alloys at 300 K. The data have been explained on the multiconduction band structure of the alloys. The alloy composition for the direct-indirect conduction band minima cross-over, the electron mobility in the X minima and the activation energy of the deep level below these minima have been determined.

Keywords. Ga_{1-x} Al_x As; Hall measurement; cross-over composition; mobility; deep levels.

1. Introduction

It is well known that Ga_{1-x} Al_x As is a very potential semi-conductor material among the series of 3-5 group ternary compounds because of the minimal lattice mismatch (Neuberger 1968) between the end compounds GaAs and AlAs and the consequent minimal defect density for heterostructure devices (Lang and Logan 1977). From the point of view of practical applications these ternary compounds have great advantages in various optical (Craford and Groves 1973), microwave (Sitch *et al* 1975), current limiting (Immorlica and Pearson 1974, Sugeta *et al* 1977), switching (Immorlica and Pearson 1975) and pressure sensing (Saxena 1982a) devices. Hence there is considerable interest in the electrical transport properties of these alloys. Deep energy levels have been found to dominate the transport properties of Ga_{1-x} Al_x As alloys intentionally doped with various impurities. The presence of such levels has either been determined indirectly from the temperature dependence ($T < 300$K) of the Hall carrier concentration (Springthorpe *et al* 1975; Kaneko *et al* 1977; Nelson 1977; Dzhafarov *et al* 1977; Saxena 1981) or in order to explain the photoluminescence spectra in the alloys (Gonda *et al* 1976; Dingle *et al* 1977). Capacitance techniques on the Schottky barrier diodes have also been used to detect and characterize such levels in Ga_{1-x} Al_x As (Bhattacharya *et al* 1979).

For optical devices of Ga_{1-x} Al_x As material, it is important to know the critical alloy composition at which the direct and indirect conduction band minima are equal in energy. For alloy compositions at which the material has an indirect energy band gap, the efficiency of optical recombinations will be reduced due to the involvement of phonons. Various techniques have been used to obtain the value of this critical composition and the quoted values in the literature vary from 0·36 to 0·46 (Monemar *et al* 1976). Recently Saxena (1980) has shown that the value of this composition is

0·43 as obtained from the pressure dependence of the Hall electron concentration for the alloys. For high field devices of $Ga_{1-x}Al_xAs$, the electron mobility in the X conduction band minima is an important parameter. There have been some doubts, as the measured value of the electron mobility in the X minima of the alloys with indirect energy band gap has been found to be very different from the electron mobility in the X minima of GaAs (Pitt and Lees 1970, Saxena and Gurumurthy 1982).

In this paper, we report the direct evidence of deep energy levels in the alloys with high Al content and also estimate their activation energy. The alloy composition for the direct-indirect cross-over is also determined and the electron mobility in the X minima estimated from a simple interpretation of the Hall data for $Ga_{1-x}Al_xAs$ alloys at 300 K.

2. Experimental

Single crystal layers of $Ga_{1-x}Al_xAs$ were grown on semi-insulating GaAs substrates by liquid phase epitaxial technique (Saxena 1982 b). The layer thickness measured by angle lapping and staining was between 10 and 15 μm for various crystals. The alloy compositions were determined by measuring the cathodoluminescence band-gap energy and converted to compositions using the data given by Panish (1973). The compositions were also cross-checked by electron beam microprobe analysis and were consistent with the previous measurements to within $\pm$ 0·5%.

The Van-der Pauw (1958/59) pattern was delineated on the epitaxial layers using photolithographic techniques. Sn metal was used to make the ohmic contacts to the samples which were subsequently annealed in H_2 atmosphere at about 600°C for 2 min. The Hall measurements were made in a magnetic field of 5 gauss and with a reasonable current through the epitaxial layers to avoid the ohmic heating. The current varied from 10 μa to 1 ma to give a measurable signal from the sample. It is because the resistivity rises with composition by almost two orders of magnitude at $x \simeq 0{\cdot}45$ (figure 1). Also the direction of the current was reversed for each measurement and an average of the measured values used to eliminate the contact effects. A small correction factor ($\sim 5\%$) was applied to calculate the actual sample resistivity and the Hall mobility to account for the finite size of the ohmic contacts relative to the samples. Van-der Pauw has given the formulae for such corrections.

3. Results and interpretation of data

The measured values of the sample resistivity ρ and the Hall electron mobility μ_h for various alloys compositions are shown in figure 1. The average variation of ρ and μ_h is also shown in figure 1. These curves have been designated as average variations since they represent the best fit to the experimental data scattered around these lines. Using these variations, the Hall electron concentration n_h is calculated from the simple relation: $n_h = 1/e\,\mu_h \cdot \rho$, where e is the electronic charge and the Hall scattering factor has been assumed to be unity for all the alloy compositions. The variation of n_h with the alloy composition x, thus obtained is shown in figure 2.

For simplicity, these variations can be qualitatively explained on a two- conduction band model involving the Γ minimum at the Brillouin zone centre and a subsidiary

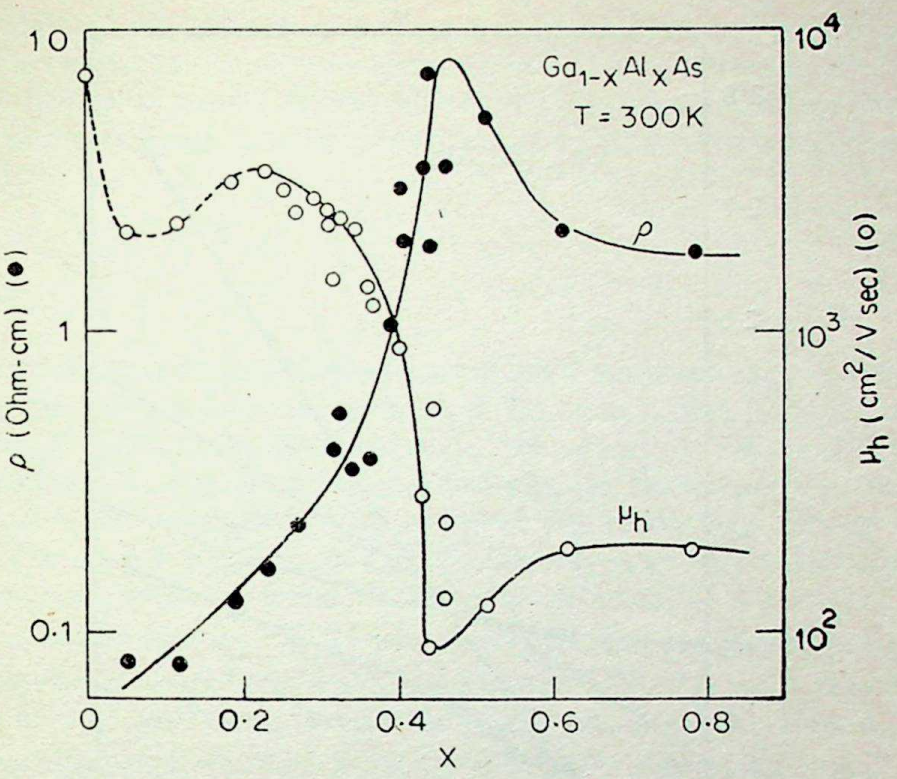

Figure 1. Composition dependence of the resistivity and Hall mobility for Ga_{1-x} Al_xAs alloys at 300 K.

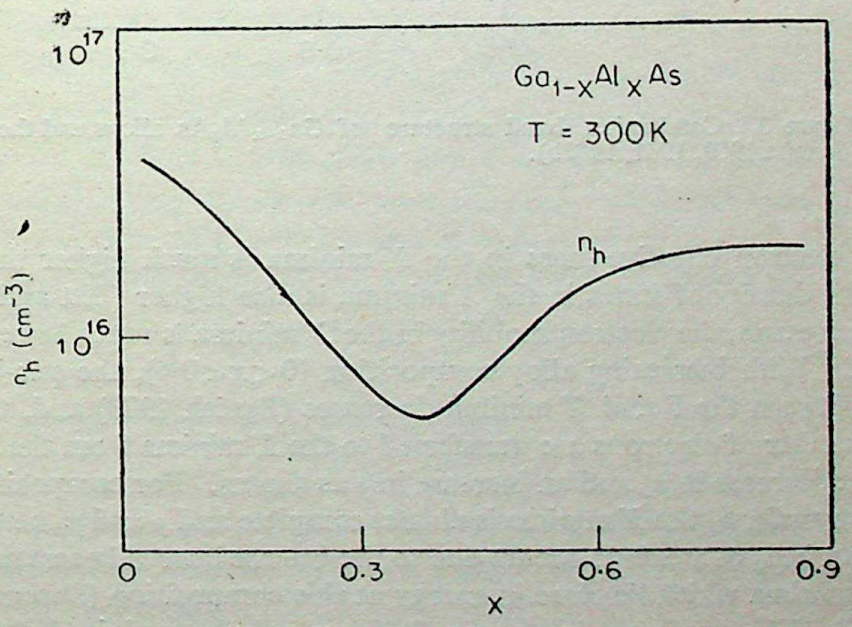

Figure 2. Composition dependence of the average Hall electron concentration for Ga_{1-x} Al_x As alloys at 300 K.

minima (X) at a higher energy. For a full understanding, the complete schematic diagram of the conduction band structure of Ga_{1-x} Al_x As alloys is given in figure 3 (Saxena 1980, 1981, 1982b).

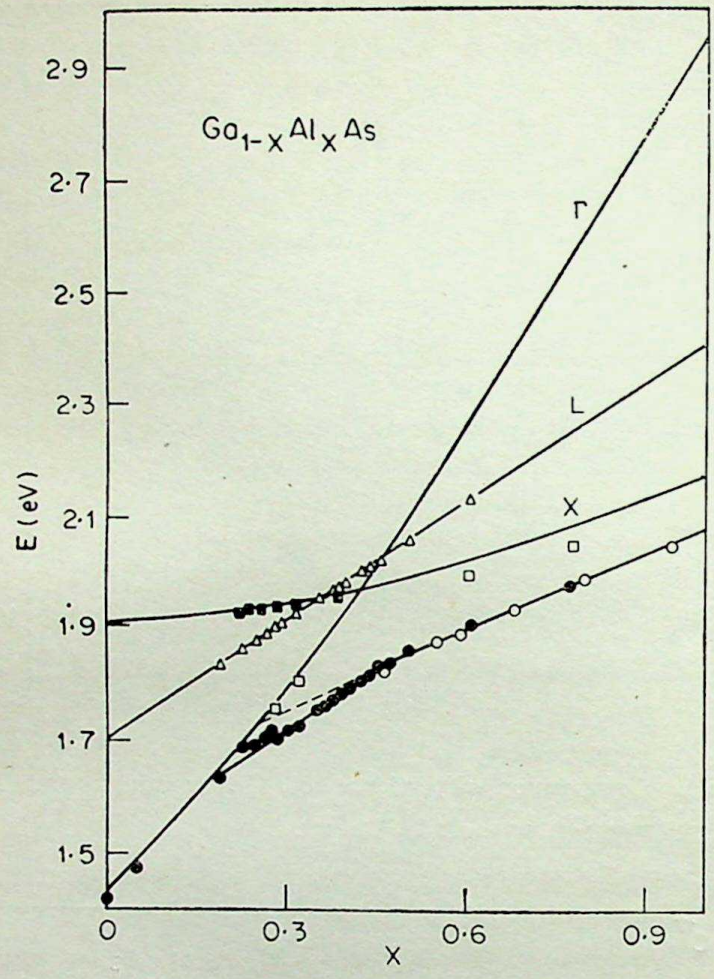

Figure 3. Conduction band structure of $Ga_{1-x}Al_xAs$ alloys and the energy levels (Saxena 1980, 1981, 1982b).

Since the electron effective mass in the X minima is much higher than in the Γ minimum, the density of states in the X minima is also higher (Pitt and Lees 1970). For the same reason, the electron mobility in the X minima is much lower than in the Γ minimum. With increasing alloy composition ($0<x<0{\cdot}4$), the sub-band energy separation between the Γ and X minima decreases (Panish 1973) and, therefore, an increasing number of electrons are transferred to the X minima from the Γ minimum. This causes a decrease in μ_h and an increase in ρ as shown. For compositions $x>0{\cdot}6$, the electron transfer to the X minima is almost complete and ρ and μ_h saturate with x. The minimum in μ_h at $x \simeq 0{\cdot}45$ occurs due to the intense intervally scatterings among the various minima which lie close in energy at this composition (Saxena and Gurumurthy 1982). The maximum in ρ at $x \simeq 0{\cdot}45$ can only be explained if the electrons are lost to the deep energy states at this composition. For $x>0{\cdot}45$, the energy of these states decreases, thus decreasing the resistivity.

At $x \simeq 0{\cdot}4$, the resistivity and mobility curves cross each other, hence the Hall electron concentration n_h shows a minimum at this composition as shown in figure 2. For compositions on either side of this value, n_h rises. Again the decrease in n_h for $0<x<0{\cdot}4$ is due to electron transfer from the Γ to the X minima. For $x>0{\cdot}6$, this

transfer is almost complete and n_h saturates with x. For $x<0{\cdot}6$, the sub-band energy separation between the two minima again decreases, thus decreasing n_h. The reason for the anomalous behaviour of electron mobility for low alloy compositions (shown by broken curve in figure 1) is not yet understood and is, therefore, left without any explanation.

4. Analysis

In GaAs ($x=0$), mot of the electrons stay in the Γ minimum and, therefore, $n_h \simeq n_\Gamma \simeq n_t$ since there are no deep energy levels in GaAs as found from the temperature dependence ($T<300$K) of n_h (Saxena 1981). Here n_Γ and n_t are the electron densities in the Γ minimum and the total density of conduction electrons, respectively. As the composition is increased (figure 2), the electrons redistribute among the various minima. For $x>0{\cdot}8$, the X states are considerably lower in energy than the Γ and, therefore, $n_h \simeq n_X$ where n_X is the number of electrons in the X minima. The experimental observation that $n_X<n_\Gamma$ clearly shows that there is a 'freeze out' of electrons to the deep energy levels lying below the X states. From figure 2, it is obvious that $n_\Gamma=N_D \simeq 4\times10^{16}$ cm^{-3} since there is no 'freeze out' at $x=0$. Here N_D is the net donor concentration. Further $n_X \simeq 2\times10^{16}$ cm^{-3} because an equal number of electrons are lost to the deep levels below the X minima ($x>0{\cdot}8$), assuming N_D to be constant. Thus, we obtain $n_\Gamma \simeq 2n_X$.

For low alloy compositions $x=0{\cdot}05$, the conduction band structure of the alloy is almost the same as for GaAs and the sample resistivity is thus: $\rho_\Gamma = 1/n_\Gamma e\mu_\Gamma$. Similarly for the alloy compositions $x>0{\cdot}7$ $\rho_X = 1/n_X e\mu_X$. From figure 2, we find that $\rho_\Gamma \simeq 0{\cdot}08$ ohm-cm and $\rho_X \simeq 2$ ohm-cm. Therefore, we get $\mu_X \simeq 0{\cdot}08\ \mu_\Gamma$. The measured value of μ_Γ for $x=0{\cdot}05$ is only 2200 cm^2/V-sec (figure 1), giving $\mu_X \simeq 176$ cm^2/V-sec. This value is very close to the measured value of 190 cm^2/V-sec for the electron mobility in the X minima ($x>0{\cdot}6$) as shown in figure 1.

The number of electrons n_d on the deep donor sites N_D below the X state is given by the expression

$$n_d/N_D = \frac{1}{1+\frac{1}{2}\exp\left[(E_D-E_F)/KT\right]} \tag{1}$$

where E_D and E_F are the energies of the deep level and Fermi energy below the X minima, respectively. Since $n_d=N_D-n_X \simeq 2\times10^{16}$ cm^{-3}, equation (1) at $T=300$ K gives $(E_D-E_F) \simeq 20$ meV.

The Fermi energy is calculated from the relation

$$n_X = N_C^X \exp(-E_F/KT), \tag{2}$$

where N_C^X is the density of states in the X minima. Using an effective density of states mass m_X^{*d} of $0{\cdot}73\ m_0$ in all the equivalent X minima (Saxena and Gurumurthy 1982),

we find that $E_F \simeq 170$ meV at 300 K, thus giving $E_D \simeq 150$ meV for $x > 0{\cdot}8$. The actual value will of course depend on the impurity compensation in the crystal, which has been neglected in the present calculations.

Since the minimum in n_h at $x \simeq 0{\cdot}4$ occurs due to the cross-over of the Γ and X minima only (Saxena 1980), the expression for n_h can be written as:

$$n_h = \frac{n_\Gamma \left(1 + \frac{n_X}{n_\Gamma} \cdot \frac{\mu_X}{\mu_\Gamma}\right)^2}{\left(1 + \frac{n_X}{n_\Gamma} \cdot \frac{\mu_X^2}{\mu_\Gamma^2}\right)}, \tag{3}$$

where μ_Γ and μ_X are the electron mobilities in the Γ and X minima, respectively. Also

$$n_X/n_\Gamma = (m_X^{*d}/m_\Gamma^*)^{3/2} \exp(-\Delta E_{\Gamma X}/KT), \tag{4}$$

where m_Γ^* is the electron effective mass in the Γ minimum. Therefore, at the minimum in n_h, $en_X\mu_X \simeq en_\Gamma\mu_\Gamma$ from (3). This condition together with (4), therefore, leads to

$$\exp(-\Delta E_{\Gamma X}/KT) = \frac{\mu_\Gamma}{\mu_X}(m_\Gamma^*/m_X^{*d})^{3/2} \tag{5}$$

provided $\mu_X \ll \mu_\Gamma$, which holds true for $Ga_{1-x}Al_xAs$ alloys. Using $m_\Gamma^* = 0{\cdot}088\, m_0$, $\mu_\Gamma = 1200$ cm^2/V-sec and $\mu_X = 120$ cm^2/V-sec for $x \simeq 0{\cdot}4$ (Saxena and Gurumurthy 1982), we get $\Delta E_{\Gamma X} = 28{\cdot}5$ meV. Since $\Delta E_{\Gamma X} = 0{\cdot}485$ eV in GaAs ($x=0$) (Saxena 1980), this energy separation, therefore, decreases at the rate of 11·4 meV/%Al. This directly gives $x_c = 0{\cdot}425$ as the alloy composition at which the Γ and X minima should be equal in energy. This value found from a simple interpretation of the present data is very close to the value of $x_c = 0{\cdot}43$ obtained from a rigorous analysis of the pressure dependence of n_h for various alloy compositions (Saxena 1980).

5. Conclusions

The activation energy of the deep level has been determined below the X minima along with the critical composition for the Γ-X minima cross-over and the electron mobility in the X minima from a simple interpretation of data on composition dependence of the resistivity, Hall electron concentration and moblity in $Ga_{1-x}Al_xAs$ alloys at 300 K.

Acknowledgements

The authors thank Dr I G A Davies, STL, for contributing $Ga_{1-x}Al_xAs$ samples for this work. Financial assistance to the authors from the Ministry of Education and Social Welfare, Department of Science and Technology, Indian National Science Academy, Kothari Scientific and Research Institute and University of Roorkee are highly appreciated. One of us (BBS) is thankful to the University Grants Commission for a fellowship.

References

Bhattacharya P K, Majerfeld A and Saxena A K 1979 *Proc. 7th Int. Symp. on GaAs and related compounds* (ed.) L F Eastman (London: Inst. of Phys.) p. 199

Craford M G and Groves W O 1973 *Proc. Inst. of Electron and Electrical Engg.* **61** 862

Dingle R, Logan R A and Arthur J R 1977 *Proc. 6th Int. Symp. on GaAs and related compounds* (ed.) by C Hilsum (London: Inst. of Phys.) p. 210

Dzhafarov T D, Demakov Y P, Skoryatina E A and Khudyakov S V 1977 *Sov. Phys. Semicond.* **11** 821

Gonda S, Makita Y, Mukai S, Tsurushina T and Tanoue H 1976 *Appl. Phys. Lett.* **29** 196

Immorlica A A and Pearson G L 1974 *Appl. Phys. Lett.* **25** 570

Immorlica A A and Pearson G L 1975 *Inst. of Electron. and Electrical Engg. Trans. on Electron Devices* **22** 829

Kaneko K, Ayabe M and Watanabe N 1977 *Proc. 6th Int. Symp. on GaAs and related compounds* (ed.) C Hilsum (London: Inst. of Phys.) p. 216

Lang D V and Logan R A 1977 *Appl. Phys. Lett.* **31** 683

Monemar B, Shih K K and Petit G D 1976 *J. Appl. Phys.* **47** 2604

Nelson R J 1977 *Appl. Phys. Lett.* **31** 351

Neuberger M 1968 *Handbook of electronic materials* **3-5** *Group semiconducting compounds* (New York: IFI/Plenum Data Corpn.) **7** 8

Panish M B 1973 *J. Appl. Phys.* **44** 2687

Pitt G D and Lees J 1970 *Phys. Rev.* **B2** 4144

Saxena A K 1980 *J. Phys.* **C13** 4323

Saxena A K 1981 *Phys. Status Solidi* **B105** 777

Saxena A K 1982a *Electron. Lett.* **18** 644

Saxena A K 1982b *Proc. 1st National Convention of Young Scientists* Gaya (ed) B N Pandey p. 184

Saxena A K and Gurumurthy K S 1982 *J. Phys. Chem. Solids* **44** 801

Sitch J E, Majerfeld A, Robson P N and Hasegawa F 1975 *Electron. Lett.* **11** 957

Springthorpe A J, King F D and Becke A 1975 *J. Electronic Mater.* **4** 101

Sugeta T, Majerfeld A, Saxena A K, Robson P N and Hill G 1977 *Proc. Biennial Conf. on active microwave semiconductor devices and circuits* (New York: IEEE) p. 45

Van-der Pauw L J 1958/59 *Philips Tech. Rev.* **20** 220

Pramāṇa, Vol. 21, No. 2, August 1983, pp. 131–148. © Printed in India.

Analytical studies of gain optimization in CO_2-N_2 gasdynamic lasers employing two-dimensional wedge nozzles

V SHANMUGASUNDARAM* and N M REDDY
Department of Aerospace Engineering,
Indian Institute of Science, Bangalore 560 012, India
*Now at University of Edinburgh, England

MS received 12 January 1983; revised 4 June 1983

Abstract. An analytical method has been proposed to optimise the small-signal-optical gain of CO_2–N_2 gasdynamic lasers (GDL) employing two-dimensional (2D) wedge nozzles. Following our earlier work the equations governing the steady, inviscid, quasi-one-dimensional flow in the wedge nozzle of the GDL are reduced to a universal form so that their solutions depend on a single unifying parameter. These equations are solved numerically to obtain similar solutions for the various flow quantities, which variables are subsequently used to optimize the small-signal-gain. The corresponding optimum values like reservoir pressure and temperature and 2D nozzle area ratio also have been predicted and graphed for a wide range of laser gas compositions, with either H_2O or He as the catalyst. A large number of graphs are presented which may be used to obtain the optimum values of small signal gain for a wide range of laser compositions without further computations.

Keywords. Gasdynamic laser; population inversion; small signal gain; area ratio; wedge nozzle.

1. Introduction

In recent times a great deal of effort has gone into the study of small-signal optical-gain performance of CO_2-N_2 gasdynamic laser (GDL) system (see Christiansen *et al* 1975 and Anderson 1976 for extensive surveys on the literature). The emphasis has been to study (to a limited extent) the influence of either one of the parameters like reservoir conditions, gas mixture composition etc., on the performance characteristics of these devices. Even the recent analytical optimization study for the small-signal gain in 2D wedge nozzles by Losev and Makarov (1975) and the closed form engineering correlation for the peak small-signal gain by McManus and Anderson (1976) were only limited in their approach in the sense that they were restricted to either a prescribed nozzle configuration, reservoir condition or gas composition; they did not propose any generalized approach which would yield some universal correlating parameter (combining all of the GDL parameters). In an attempt to overcome this deficiency, the present authors have developed a completely generalized characterization of the GDL performance in a formal way and have identified the general correlating parameters controlling the GDL performance; these correlating parameters were then used to optimize the small-signal gain on a pre-selected vibrational-rotational transition and subsequently obtained the combination of operating parameters that would yield such optimum gain values (Reddy and Shanmugasundaram 1979a).

Detailed results from such an optimization study of the small-signal gain in CO_2-N_2 GDL on the P(20) 001 → 100 vibrational-rotational transition have been presented for families of conical and hyperbolic nozzles (Reddy and Shanmugasundaram 1979b), with H_2O and He as catalysts. Some preliminary results for two-dimensional (2D) wedge nozzle-flows, with He as catalyst were also presented at the second International Symposium on Gas flow and Chemical Lasers (Reddy and Shanmugasundaram 1978). The present paper presents the complete optimization results in detail for 2D wedge nozzles, with either He (to be called system 1) or H_2O (to be called system 2) as catalyst. Further, unlike as in Reddy and Shanmugasundaram (1979a, b), where the nozzle-flow solutions have been presented only for the region downstream of the nozzle throat, here the solutions are obtained starting right from the nozzle reservoir. This way, any possible non-equilibrium condition in the flow upstream of the nozzle throat (Anderson 1969, 1970) is treated in the calculations.

The analysis in the present paper is based on the method given by Reddy and Shanmugasundaram (1979a), according to which the system of equations governing the steady, inviscid, quasi-one-dimensional, non-reacting flow of a mixture of gases in vibrational non-equilibrium in a GDL nozzle reduced to a universal form so that the solutions depend on a single correlating parameter χ_I, which combines all the other operating parameters of the problem. In this paper we shall present the numerical results from the parametric study of these equations for a particular family of nozzle shapes, *viz* 2D wedge, and discuss how these solutions can be used to optimize the small-signal-optical-gain coefficient G_0 for the P(20) 001→100 vibrational-rotational transition. We shall also discuss a method of obtaining the combination of optimum operating conditions like reservoir quantities and nozzle shape, which would yield the optimum value of small signal gain.

2. Governing equations

For the two-temperature vibrational model (see Anderson 1976 for details and figure 1 for the schematic) employed here, the governing equations to be considered are the three global conservation equations, the equation of state and the two rate equations governing the relaxation of the two vibrational modes, of temperatures T'_I and T'_{II}

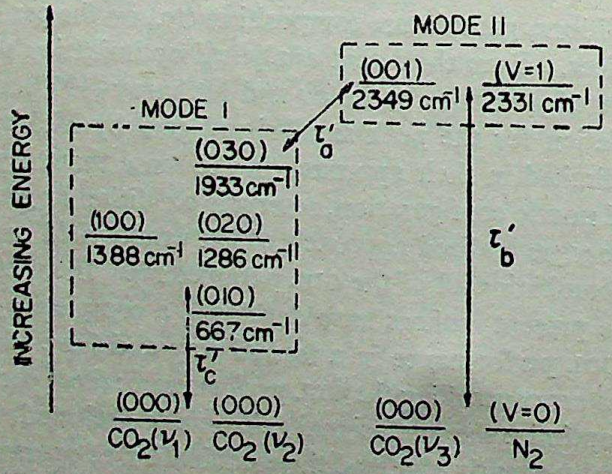

Figure 1. Schematic of the vibrational model (Anderson 1976).

respectively. Two more algebraic equations give the population inversion (PI) and the small-signal-optical-gain as functions of the flow quantities obtained from the afore-mentioned governing equations. The publications of Anderson (1976) and Losev and Makarov (1975) give complete details of these equations in their dimensional forms. The details of how these equations are normalized and then reduced to a universal form so that their solutions depend on a single parameter, which combines all the other parameters of the problem are given by Reddy and Shanmugasundaram (1979a). Here, we only reproduce the necessary equations in their final normalized forms, retaining the same nomenclature as in the above reference.

The generalized momentum equation, obtained by combining the momentum and energy equations, and the equation of state, is

$$\psi - \alpha \frac{\mathrm{d}\psi}{\mathrm{d}\xi} - X_C \sum_{m = I,\, II} \bar{G}_m \frac{\mathrm{d}\phi_m}{\mathrm{d}\xi} = 0. \tag{1}$$

The rate equation (of the Landu-Teller type), governing the relaxation of the vibrational energy of mode m (m=I, II), is

$$\frac{d\phi_m}{d\xi} = \frac{K_m \psi}{N_s} \exp\left[\chi_m + \xi\,(1 - 1/ij) - \gamma_{11}\,\psi^{-1/3}\right] \cdot \left[\frac{\bar{E}_e - \bar{E}}{\bar{G}}\right]_m. \tag{2}$$

In (2) the subscript e refers to local equilibrium value and l=C for m=I and l=N for m=II, where C and N denote respectively CO_2 and N_2.

In this analysis the P(20) transitions at a wavelength of 10·6 μm and occurring between J=19 rotational level of 001 and J=20 rotational level of 100 vibrational levels of CO_2 are considered. Further, only the optical line broadening mechanism in its Lorentz (homogeneous) limit is considered. Accordingly, the equations for the population inversion and small-signal gain are:

$$\mathrm{PI} = \frac{\exp\left(-\bar{\theta}_{\nu_3}/\phi_{\mathrm{II}}\right) - \exp\left(-\bar{\theta}_{\nu_1}/\phi_{\mathrm{I}}\right)}{\bar{Q}_{\mathrm{vib}}}, \tag{3}$$

and

$$G_0/m = 9{\cdot}77 \frac{(\mathrm{PI})}{P(X_l)\,\psi^{3/2}} \exp\left(-0{\cdot}0703/\psi\right), \tag{4}$$

where,

$$\bar{Q}_{\mathrm{vib}} = \left[1 - \exp\left(-\bar{\theta}_{\nu_1}/\phi_{\mathrm{I}}\right)\right]^{-1} \left[1 - \exp\left(-\bar{\theta}_{\nu_2}/\phi_{\mathrm{I}}\right)\right]^{-2} \times \left[1 - \exp\left(-\bar{\theta}_{\nu_3}/\phi_{\mathrm{II}}\right)\right]^{-1} \tag{5}$$

and

$$P(X_l) = 1 + 0{\cdot}7589\,(X_N/X_C) + b\,(X_H/X_C), \tag{6}$$

with b = 0·3836 for H_2O and b = 0·6972 for He catalyst.

In the above equations, X_C, X_N and X_H are respectively the mole fractions of CO_2, N_2 and the catalyst H_2O or He. In equation (1), $\alpha = [2{\cdot}5\,(X_C + X_N) + 0{\cdot}5n\,X_H]$, where n is the number of degrees of freedom of the catalyst. The parameters i and j

govern the shape of the nozzle; for example $i = 1$ and $j = 1$ for wedge nozzles. The normalized temperature $\psi = T'/\theta'_{\nu_N}$ and the vibrational temperatures for modes I and II, $\phi_m = T'_m/\theta'_{\nu_N}$, $m = \text{I, II}$, are normalized with respect to θ'_{ν_N} (= 3357°K), the characteristic temperature for the normal vibrational mode of N_2, where the primes denote dimensional quantities. The normalized characteristic temperatures for the three vibrational modes of CO_2 are defined as $\bar{\theta}_{\nu_n} = \theta'_{\nu_n}/\theta'_{\nu_N}$, $n = 1, 2, 3$ ($\theta'_{\nu_1} = 1999°K$; $\theta'_{\nu_2} = 960°K$; $\theta'_{\nu_3} = 3373°K$).

The independent variable ξ is defined as,

$$\xi = S_0 + \ln \rho = S_0 - \ln [(u/u_*)(A/\rho_*)], \tag{7}$$

where $\rho = \rho'/\rho'_0$ is the normalized density in which the suffix 0 refers to reservoir conditions, and S_0 is the specific entropy given by

$$S_0 = -\ln \rho_e + \alpha \ln \psi_e + \frac{X_C}{\psi_e}[\bar{E}_{\text{I}} + \bar{E}_{\text{II}}]_e - X_C \ln \{[1 - \exp(-\bar{\theta}_{\nu_1}/\psi)] \times [1 - \exp(-\bar{\theta}_{\nu_2}/\psi)]^2 [1 - \exp(-\bar{\theta}_{\nu_3}/\psi)] \times \cdot [1 - \exp(-1/\psi)]^{X_N/X_C}\}_e + S_r, \tag{8}$$

where S_r is a reference value of S_0 and for the wedge nozzles $S_r = 26{\cdot}29$ for He catalyst and $S_r = 29{\cdot}57$ for H_2O catalyst.

The various functions occurring in the above equations are defined as

$$\bar{E}_{\text{I}} = \frac{\bar{\theta}_{\nu_1}}{\exp(-\bar{\theta}_{\nu_1}/\phi_{\text{I}}) - 1} + \frac{2\bar{\theta}_{\nu_2}}{\exp(-\bar{\theta}_{\nu_2}/\phi_{\text{I}}) - 1}, \tag{9}$$

$$\bar{E}_{\text{II}} = \frac{\bar{\theta}_{\nu_3}}{\exp(\bar{\theta}_{\nu_3}/\phi_{\text{II}}) - 1} + \frac{X_N/X_C}{\exp(1/\phi_{\text{II}}) - 1}, \tag{10}$$

$$\bar{G}_{\text{I}} = \left(\frac{\bar{\theta}_{\nu_1}}{\phi_{\text{I}}}\right)^2 \frac{\exp(\bar{\theta}_{\nu_1}/\phi_{\text{I}})}{[\exp(\bar{\theta}_{\nu_1}/\phi_{\text{I}}) - 1]^2} + 2\left(\frac{\bar{\theta}_{\nu_2}}{\phi_{\text{I}}}\right)^2 \frac{\exp(\bar{\theta}_{\nu_2}/\phi_{\text{I}})}{[\exp(\bar{\theta}_{\nu_2}/\phi_{\text{I}}) - 1]^2}, \tag{11}$$

$$\bar{G}_{\text{II}} = \left(\frac{\bar{\theta}_{\nu_3}}{\phi_{\text{II}}}\right)^2 \frac{\exp(\bar{\theta}_{\nu_3}/\phi_{\text{II}})}{[\exp(\bar{\theta}_{\nu_3}/\phi_{\text{II}}) - 1]^2} + \frac{X_N}{X_C}\left(\frac{1}{\phi_{\text{II}}^2}\right) \frac{\exp(1/\phi_{\text{II}})}{[\exp(1/\phi_{\text{II}}) - 1]^2}, \tag{12}$$

$$K_{\text{I}} = X_C + X_N [(\tau'_c)_{CC}/(\tau'_c)_{CN}] + X_H [(\tau'_c)_{CC}/(\tau'_c)_{CH}], \tag{13}$$

$$K_{\text{II}} = [X_C K_a (\tau'_b)_{NN}/(\tau'_a)_{CC} + X_N K_b]/(X_C + X_N), \tag{14}$$

where $$K_a = X_C + X_N\,[(\tau'_a)_{CC}/(\tau'_a)_{CN}] + X_H\,[(\tau'_a)_{CC}/(\tau'_a)_{CH}], \tag{15}$$

and $$K_b = X_C\,[(\tau'_b)_{NN}/(\tau'_b)_{NC}] + X_N + X_H\,[(\tau'_b)_{NN}/(\tau'_b)_{NH}]. \tag{16}$$

In (13) to (16), τ's are the vibrational relaxation times for various collisional partners.

The parameters χ_m used in (2) are defined, in general, as

$$\chi_m = \ln\left(\frac{P'_0\,L'\,\theta'_{\nu_N}\,(\rho_*\,u_*)^{a+1/ij}}{ij\,R'^{1/2}_m\,T'^{3/2}_0\,J_{ll}}\right) - (1 - 1/ij)\,S_0, \quad m = \text{I, II} \tag{17}$$

where p'_0 is the reservoir pressure, T'_0 is the resevoir temperature, R'_m is the mixture gas constant, ρ_* and u_* are the normalized density and velocity at the throat and L' is the nozzle shape parameter. The values of the constants γ's and J's occurring in (2) and (17) are

$$\gamma_{CC} = 2{\cdot}7389; \qquad J_{CC} = 1{\cdot}555 \times 10^{-8} \text{ atm-sec.}$$

$$\gamma_{NN} = 14{\cdot}3098; \quad J_{NN} = 2{\cdot}450 \times 10^{-11} \text{ atm-sec.} \tag{18}$$

The parameters χ for the case of wedge nozzles is obtained by substituting $ij = 1$ and $a = 7{\cdot}2$ for He catalyst and $a = 8{\cdot}82$ for H_2O catalyst in (17).

The details of the derivation of these governing equations are given in Reddy and Shanmugasundaram (1979a).

The quantity N_s occurring in (2), for any given ij, is a function of local velocity, Mach number and area ratio and hence is indirectly dependent on the reservoir conditions. The computer program of Lordi *et al* (1966) is used to compute the function N_s. Since it was found that the variation of N_s with reservoir pressure very small we have assumed a constant reservoir pressure $p'_0 = 10$ atm. The N_s is computed for the reservoir temperatures, $T'_0 = 1000$, 1500, 2000 and 3000°K, for a wide range of mixture compositions. These values of N_s are plotted as a function of (ξ_*/ξ), where ξ_* is the value of independent variable ξ at the nozzle throat, for each composition at different reservoir temperatures. Then the different values of N_s for each (ξ_*/ξ) are tabulated with the help of above graphs. The final average correlation for N_s is computed from these tabulated values and plotted as a function of (ξ_*/ξ). Figure 2 shows these average N_s correlations for systems 1 and 2.

In the case of wedge nozzles, the N_s correlations for both the systems are represented (obtained by curve fitting) by the following simple analytical expressions:

$$N_s = 0 \text{ for } \xi_*/\xi \leqslant 0{\cdot}985$$

$$= 0{\cdot}088 - 0{\cdot}682\,(0{\cdot}995 - \xi_*/\xi)^{0{\cdot}45}, \text{ for } 0{\cdot}985 < \xi_*/\xi \leqslant 0{\cdot}995$$

$$= 0{\cdot}436 - 8{\cdot}6 \times 10^{-3}\,(\xi_*/\xi - 0{\cdot}85)^{-1{\cdot}9} \text{ for } \xi_*/\xi > 0{\cdot}995, \tag{19}$$

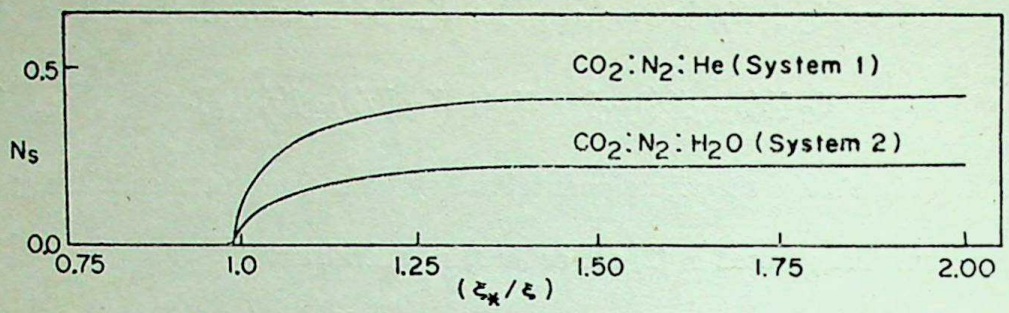

Figure 2. Correlation of function N_s with the parameter (ξ_*/ξ) for systems 1 and 2.

for system 1 and

$$N_s = 0 \text{ for } \xi_*/\xi \leqslant 0{\cdot}985$$

$$= 0{\cdot}039 - 0{\cdot}118\,(0{\cdot}995 - \xi_*/\xi)^{0{\cdot}241}, \text{ for } 0{\cdot}985 < \xi_*/\xi \leqslant 0{\cdot}995$$

$$= 0{\cdot}233 - 4{\cdot}410 \times 10^{-3}\,(\xi_*/\xi - 0{\cdot}816)^{-02{\cdot}186} \text{ for } \xi_*/\xi > 0{\cdot}995, \qquad (20)$$

for system 2.

Similarly the mass flow factor, $\rho_* u_*$ and the nozzle throat density ρ_* have also been correlated as functions of only the reservoir temperature in the case of wedge nozzles and are given by the following expressions.

For He catalyst:

$$\rho_* u_* = k_1 = 0{\cdot}686 - 8{\cdot}0 \times 10^{-8}\, T_0' \,(^\circ\text{K});$$

$$\rho_* = k_2 = \text{constant} = 0{\cdot}63. \qquad (21)$$

For H_2O catalyst:

$$\rho_* u_* = k_1 = \text{constant} = 0{\cdot}66;$$

$$\rho_* = k_2 = \text{constant} = 0{\cdot}63. \qquad (22)$$

Variations in the normalized velocity ratio (u/u_*) along the nozzle are also influenced significantly by the reservoir conditions (see Reddy and Shanmugasundaram 1978 for detailed results). Again, using the computer program of Lordi *et al* (1966) u/u_* has been correlated as a function of only the normalized area, $A = A'/A'_* = [1 + (x'/L')^j]^i$ (where $i = j = 1$ for wedge nozzles and x' is the distance in the flow direction), and is given by

For He catalyst:

$$k_1^{3{\cdot}37}\,(u/u_*) = [-0{\cdot}022 + 0{\cdot}049\,(0{\cdot}3 + \log_{10} A)^{-1{\cdot}5}] \text{ for } M < 1,$$

$$= [1{\cdot}165 - 0{\cdot}560\,(0{\cdot}1 + \log_{10} A)^{-0{\cdot}2}] \text{ for } M \geqslant 1; \qquad (23)$$

For H_2Ocatalyst:

$$k_1^{3.98}(u/u_*) = [-0.0217 + 0.0399\,(0.234 + \log_{10} A)^{-1.197}] \text{ for } M < 1,$$

$$= [0.669 - 0.216\,(0.194 + \log_{10} A)^{-0.467}] \text{ for } M \geqslant 1. \quad (24)$$

Here M is the Mach number. These correlations have been presented in figure 3.

The analytical expressions given in equations (19) to (24) for the correlations are obtained by curve fitting.

Since PI and G_0, as given by the algebraic equations (3) and (4), are only functions of the gas composition, and ϕ_I, ϕ_{II} and ψ, the emphasis here would be on obtaining the solutions for the last three variables. The differential equations (1) and (2) governing these three variables reveal that for a given gas mixture and value of ij, the solutions of these equations as a function of ξ depend on only one parameter χ_I, which combines, as can be seen from (17), all the other parameters of the problem, like p_0', T_0', L' etc. In this sense, the solutions obtained thus will be 'universal'.

3. Results and discussion

For any given laser mixture, (1) and (2) are solved simultaneously for the three unknowns ϕ_I, ϕ_{II} and ψ, with χ_I as the parameter. The numerical integration is carried out using the modified, fourth order *R-K-G* method. Since the flow in a GDL starts from a reservoir, wherein the hot gas mixture is in vibrational equilibrium, the initial values for the three temperatures correspond to this equilibrium state. To obtain the numerical solutions starting from the reservoir, the procedure is as follows: since (21) or (22) (corresponding to system 1 or 2) gives the value of ρ_*, ξ_* is estimated from (7)

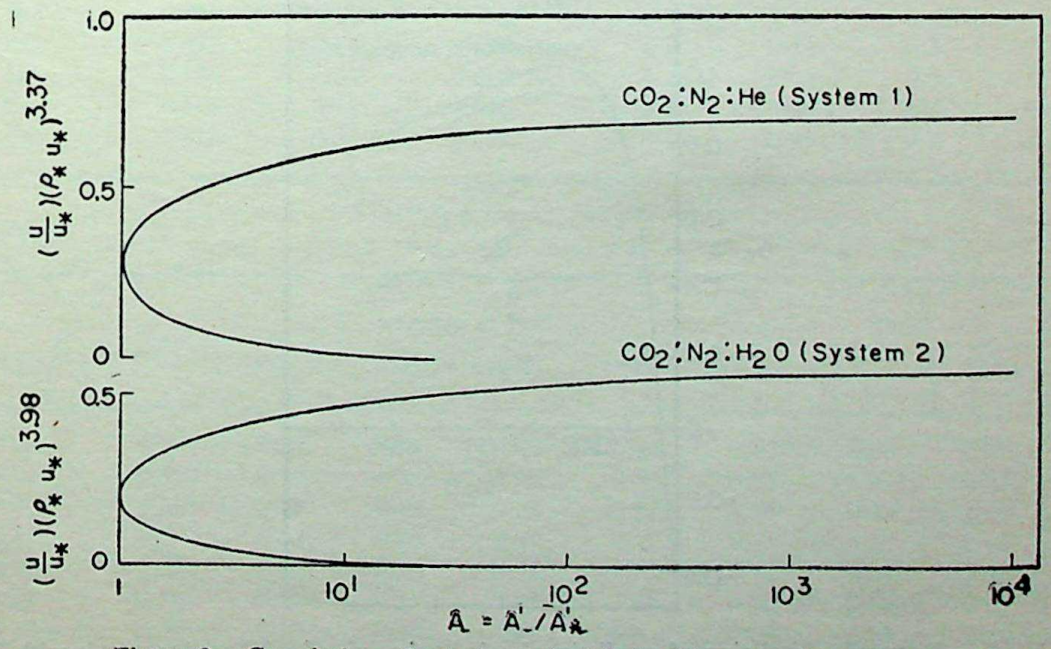

Figure 3. Correlation of velocity ratio (u/u_*) with area ratio for systems 1 and 2.

with known S_0 from the reservoir conditions. At every point along the nozzle, *i.e.* for every value of ξ (with ξ decreasing in the flow direction), ξ/ξ_* and the corresponding value of N_s from either (19) or (20) are calculated depending on whether it is system 1 or 2. If $N_s=0$, which means the flow is in local vibrational equilibrium (see (2)), the corresponding equilibrium solution is obtained using the method given by Reddy and Shanmugasundaram (1979a). For any other value of $N_s > 0$, implying the prevalence of non-equilibrium conditions within the nozzle, we solve the differential equations (1) and (2) for the three unknowns ϕ_I, ϕ_{II} and ψ; the appropriate initital values would correspond to the ψ_e value obtained at the last st:p of the local equilibrium calculations. Knowing the temperature distributions along the nozzle, PI and G_0 as functions of ξ are calculated from (3) and (4).

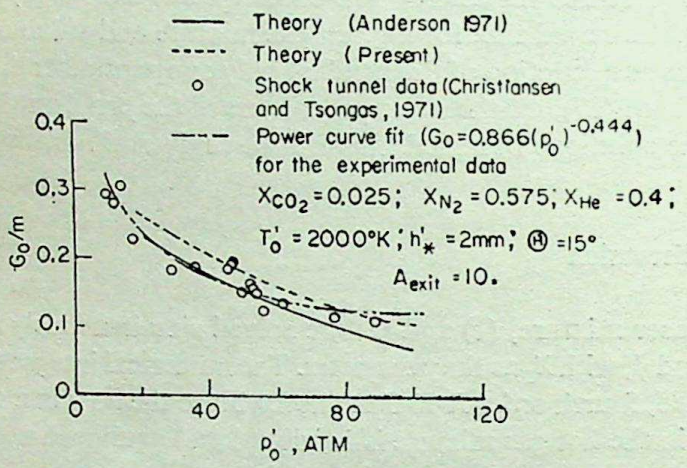

Figure 4. Variation of small-signal gain at the exit of a 2D wedge nozzle with reservoir pressure; comparison with existing results (Christiansen and Tsonges 1971; Anderson 1971).

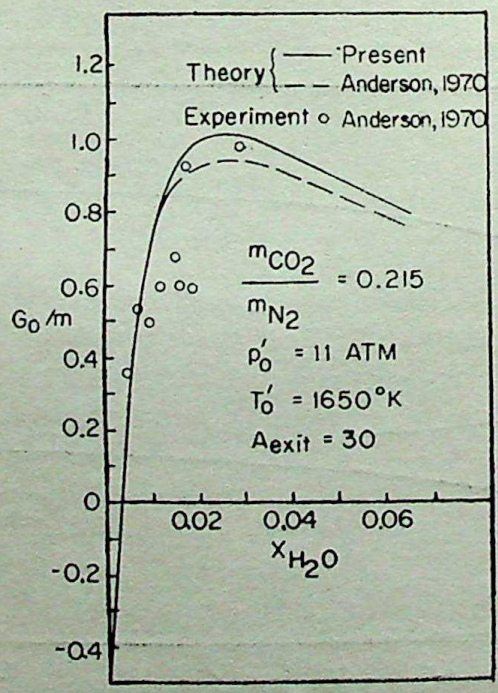

Figure 5. Variation of small-signal gain at the exit of a 2D wedge nozzle with H_2O content; comparison with existing results (Anderson 1970).

Figures 4 and 5 show values of G_0 at the exit of a wedge nozzle, obtained by the present method, for systems 1 and 2 respectively; for the exit area ratios of 10 and 30 considered here, values of L' are respectively 0·3732 cm and 0·1486 cm. The relevant operating conditions, also contained in the figures, have been taken from Anderson (1969, 1970) and Anderson *et al* (1971). For these conditions, first we estimate ξ_0 and χ_I from (7) and (17) and obtain the numerical solutions as described earlier. Figures 4 and 5 also contain results from experiments (Anderson 1970 and Christiansen and Tsonges 1971) as well as from Anderson's time-dependent analysis (Anderson 1970, Anderson *et al* 1971). The difference between the experiments and Anderson's theory is believed to be due to many uncertain factors like: (i) the errors involved in the estimation of vibration relaxation rates, (ii) use of simplified two-mode vibrational model and (iii) measurement errors which have not been discussed by Christiansen and Tsonges (1971). The difference between the theoretical values obtained by Anderson and the present computations is believed to be due to use of correlated values for N_s, $\rho_* u_*$ and ρ_* in the present analysis.

Computations are first carried out for a wide range of mixture compositions for both systems 1 and 2; Table 1 contains the details of the mixture compositions considered. Figures 6 and 7 show typical solutions for two sample cases, one each for the two systems. An interesting aspect of these solutions is the tendency of G_0 to attain a maximum while PI tends to remain constant far downstream of the nozzle throat and the reasons for such behaviour have been discussed in detail by Reddy and Shanmugasundaram (1979a).

Table 1. Values of N_2 mole-fraction

System 1

X_{He}	X_{CO_2}						
	0·025	0·05	0·075	0.1	0·15	0·2	0·25
0·2	0·775	0·75	0·725	0·7	0·65	0·6	0·55
0·3	0·675	0·65	0·625	0·6	0·55	0·5	0·45
0·4	0·575	0·55	0·525	0·5	0·45	0·4	0·35
0·5	0·475	0·45	0·425	0·4	0·35	0·3	0·25
0·6	0·375	0·35	0·325	0·3	0·25	0·2	0·15

System 2

X_{CO_2}	X_{H_2O}							
	0·01	0·02	0·04	0·06	0·08	0·1	0·15	0·2
0·050	0·94	0·93	0·91	0·89	0·87	0·85	0·80	0·75
0·075	0·915	0·905	0·885	0·865	0·845	0·825	0·775	0·725
0·10	0·89	0·88	0·86	0·84	0·82	0·80	0·75	0·70
0·15	0·84	0·83	0·81	0.79	0·77	0.75	0·70	0·65
0·20	0·79	0·78	0·76	0·74	0·72	0·70	0·65	60·0
0·25	0·74	0·73	0·71	0.69	0·67	0·65	0·60	0·55
0·30	0·69	0·68	0·66	0·64	0·62	0·60	0·55	0·50

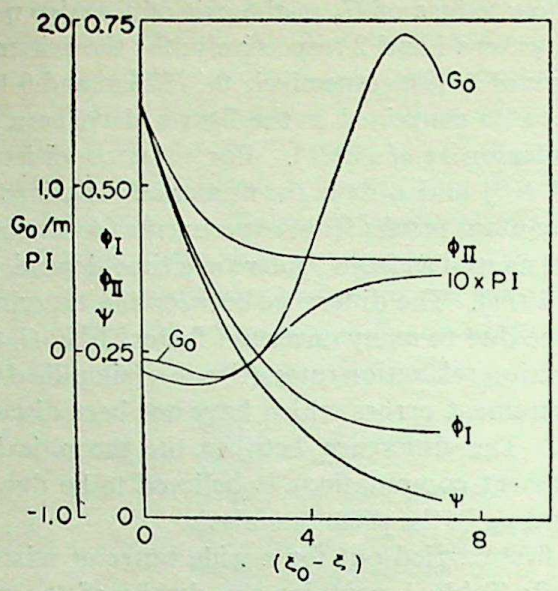

Figure 6. Variation of flow quantities along the GDL nozzle for $X_{CO_2} = 0{\cdot}15$; $X_{N_2} = 0{\cdot}35$; $X_{He} = 0{\cdot}5$; $ij = 1$; $\chi_I = 4{\cdot}5$; $\psi_0 = 0{\cdot}625$; $\xi_0 = 26{\cdot}36$.

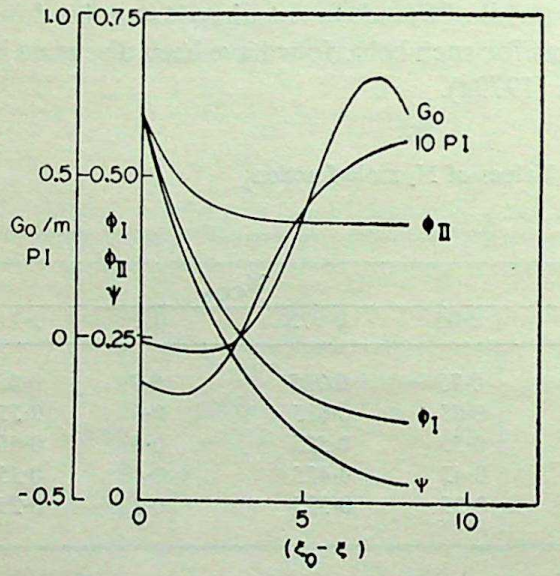

Figure 7. Variation of flow quantities along the GDL nozzle for $X_{CO_2} = 0{\cdot}05$; $X_{N_2} = 0{\cdot}94$; $X_{H_2O} = 0{\cdot}01$; $ij = 1$; $\chi_I = 4{\cdot}48$; $\psi_0 = 0{\cdot}601$; $\xi_0 = 29{\cdot}115$.

For each gas composition, such peak values of G_0 are obtained for a wide range of values of χ_I (with ψ_0 chosen appropriately in each case), and are plotted in figures 8 and 9 for systems 1 and 2 respectively. From these figures it is apparent that G_0 attains a maximum value at a particular value of χ_I for every gas composition and these two quantities are designated respectively as $(G_0)_{optimum}$ and $(\chi_I)_{optimum}$. Thus, for a given laser mixture, $(G_0)_{opt}$ represents the highest possible value of small-signal optical gain coefficient on the $P(20)$ transition at 10·6 μm. Larger gain coefficients could exist on other 001→100 vibrational-rotational transitions. The present analysis could be easily extended to calculate the maximum gain over the entire set of

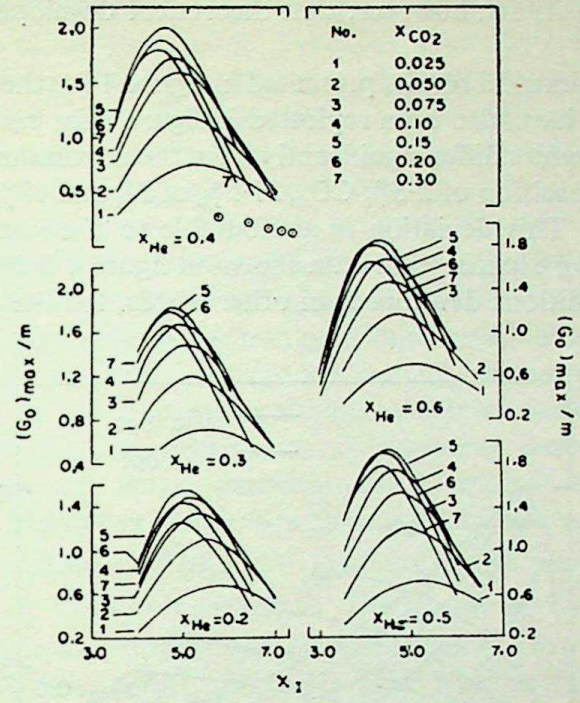

Figure 8. Variation of maximum values of small-signal gain on the P(20) 001→100 transition with x_I for various mixture compositions in system 1.

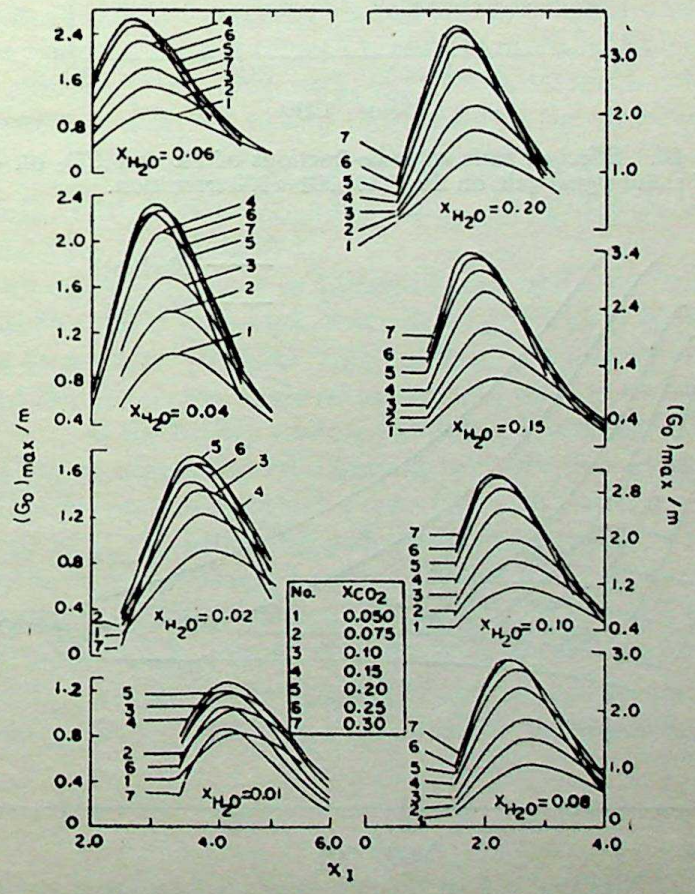

Figure 9. Variation of maximum values of small-signal-gain on the P(20) 001→100 transition with x_I for various mixture compositions in system 2.

allowed *P*-branch transitions; however, that theoretical development is not presented here.

For system 1, experimental results presented in figure 4 for the G_0 values at the exit of a 2D wedge nozzle have also been replotted in figure 8 for comparison. It can be easily seen that these values differ significantly from the maximum gain values possible for the same gas composition of 2·5% CO_2, 57·5% of N_2 and 40% He, as obtained by the present method. This deviation is attributable to the nozzle area ratio of 10 employed for obtaining experimental data shown in figure 4 being less than optimum for the operating conditions developed; in other words, for the experimental nozzle,

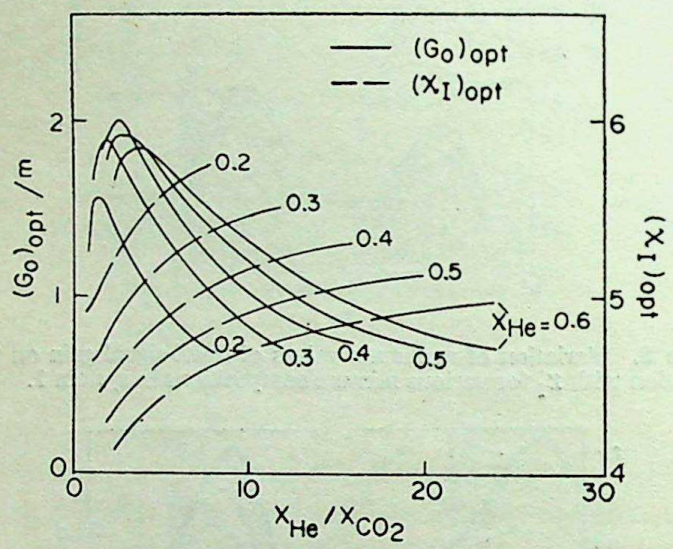

Figure 10. Effect of ratio of mole-fractions of He and CO_2 on optimum values of χ_I and small-signal-gain on the P(20) 001→100 transition.

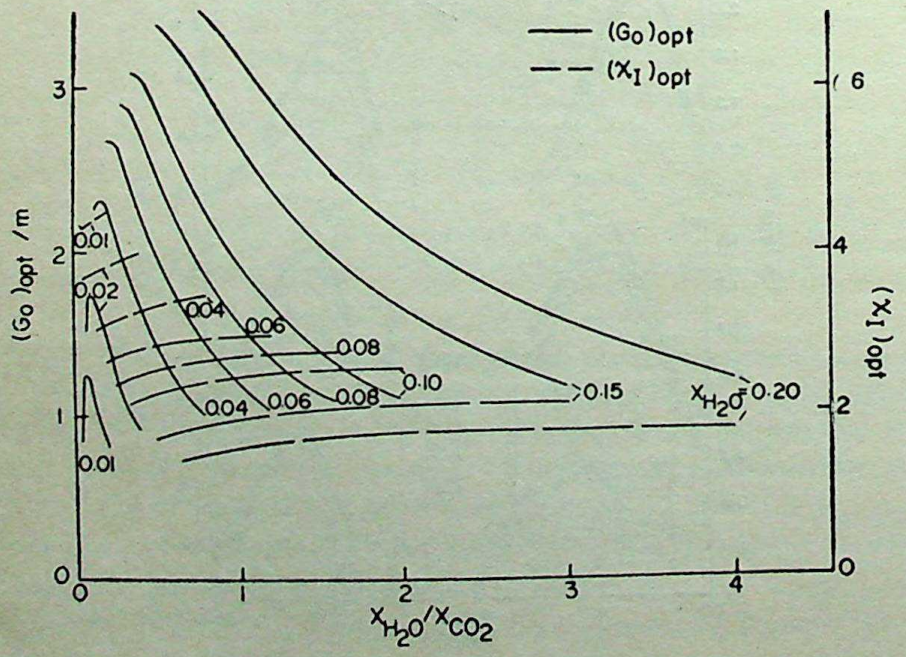

Figure 11. Effect of ratio of mole-fractions of H_2O and CO_2 on optimum values of χ_I and small-signal-gain on the P(20) 001→100 transition.

the GDL gas is only partially expanded as it approaches the exit, which results in much smaller values for the small-signal gain. Therefore, it can be inferred that by employing much larger expansion ratios than that given in figure 4, one would have obtained much higher values for G_0 for the same operating conditions. These observations are also true for the experimental results presented in figure 5 for H_2O catalyst.

To study the influence of CO_2 and catalyst concentration on the optimum value of G_0, these quantities have been cross-plotted in figures 10 and 11 as a function of the ratio of mole-fractions of the catalyst and CO_2. An inspection of these figures reveal that, for a given catalyst mole-fraction, $(G_0)_{opt}$ attains a maximum at some value of the CO_2 mole-fraction, which may be due to a combination of factors like (i) the decrease in the N_2 content because of the increase in the mole-fraction of CO_2, with a consequent adverse effect on the 'pumping reaction' which is essential for populating the upper laser level and (ii) the effectiveness of increasing concentration of the CO_2 molecules itself in the collisional de-activation of the upper laser level. This value of CO_2 at which $(G_0)_{opt}$ peaks out increases with increasing catalyst content. Figures 10 and 11 also show the tendency of $(G_0)_{opt}$ to peak around 40 mole-% of He in system 1 and around 20 mole-% of H_2O in system 2. The reason for such a trend in $(G_0)_{opt}$ is that as the catalyst number density increases, besides the lower laser level which is rapidly de-excited by the catalyst, the upper laser level population also is affected adversely with a consequence that the PI and hence G_0 are reduced. From the foregoing observations it may be concluded that small-signal optical-gains as high as $2/m$ in system 1 and $3{\cdot}5/m$ in system 2 are possible and that such high values can be obtained by employing laser mixtures containing CO_2 and He mole-fractions of 15% and 40% respectively in system 1 or CO_2 and H_2O mole-fractions of 30% and 20% respectively in system 2. Figures 10 and 11 also depict the variations of $(\chi_I)_{opt}$ with respect to X_{He}/X_{CO_2} and X_{H_2O}/X_{CO_2}. It is observed that, in general, variations in both CO_2 and H_2O contents strongly affect $(\chi_I)_{opt}$ in system 2, while variation in CO_2 content alone does so in system 1.

With the known optimum values of G_0 and χ_I the optimum operating conditions like p_0' and T_0' can be readily estimated, since χ_I, as given by (17), is a function of p_0', T_0' and the shape factor L'. However, since L' itself is a function of both the nozzle throat height and the expansion angle of the nozzle, $p_0' L'$ is directly computed as a function of T_0'. $p_0' L'$ is the binary scaling parameter (Anderson 1976) which would have more flexibility in estimating the reservoir pressure for any desired value of L'.

To estimate the appropriate optimum area ratio to be used corresponding to the optimum value of $p_0' L'$ the following procedure is adopted. First, for the given laser mixture and for the graphically known optimum value of χ_I, equations (1) to (4) are solved to obtain the optimum value of G_0 and also the value of ξ (to be designated ξ_{opt}) at which it occurs. $(G_0)_{opt}$ values can also be read-off from the graphs presented in figures 10 and 11. It can be shown (Reddy and Shanmugasundaram 1979a) that the optimum area ratio A_{opt} and ξ_{opt} are related by the following expression:

For He catalyst

$$[1{\cdot}165 - 0{\cdot}560\,(0{\cdot}1 + \log_{10} A_{opt})^{-0{\cdot}2}]\, A_{opt} = (k_1^{3{\cdot}37}\, k_2) \exp\,(S_0 - \xi_{opt}), \tag{25}$$

and for H_2O catalyst

$$[0{\cdot}669 - 0{\cdot}216\,(0{\cdot}194 + \log_{10} A_{opt})^{-0{\cdot}467}]\, A_{opt}$$

$$= (k_1^{3{\cdot}98}\, k_2) \exp\,(S_0 - \xi_{opt}), \qquad (26)$$

where k_1, k_2 and s_0 are functions of only T_0'. Hence, for the known value of ξ_{opt}, either (25) or (26) can be solved for A_{opt} as a function of T_0'.

Optimum values thus obtained for $p_0'L'$ and A have been plotted against T_0' in figures 12 to 24 for various mixture compositions for both systems 1 and 2. These figures show that, for any given gas composition, both $p_0'L'$ (therefore p_0' for a particular value of L') and A increases monotonically with T_0'. They also reveal a striking difference between systems 1 (He catalyst) and 2 (H_2O catalyst) namely, for the same order of optimum G_0 values, the optimum value of A is, in general, an order of magnitude larger in system 2 than that in system 1 and $p_0'L'$ values are of the same order in both the systems. This implies that system 2 is operationally superior to system 1. The data presented in figures 12 through 24 may appear numerous but these data are not repetitive in nature and useful in obtaining the optimum values of G_0 for a given laser composition; hence avoiding numerical computations.

Finally, it is to be pointed out that for the very large values ($\sim 10^3$) of A_{opt} obtained in some of the cases, the pressure levels in the nozzle are likely to be very low (approximately a few torr) with the result that Doppler line broadening might dominate or become comparable to collisional (Lorentz) line broadening. This aspect is being taken up by the authors as a next step. At very low gas densities, rapid intra-mode coupling of vibrational states, fundamental to the two-mode model of Anderson, might be lost. Under such circumstances a much more detailed analysis of the molecular kinetics would need to be invoked. If very low translational temperatures are

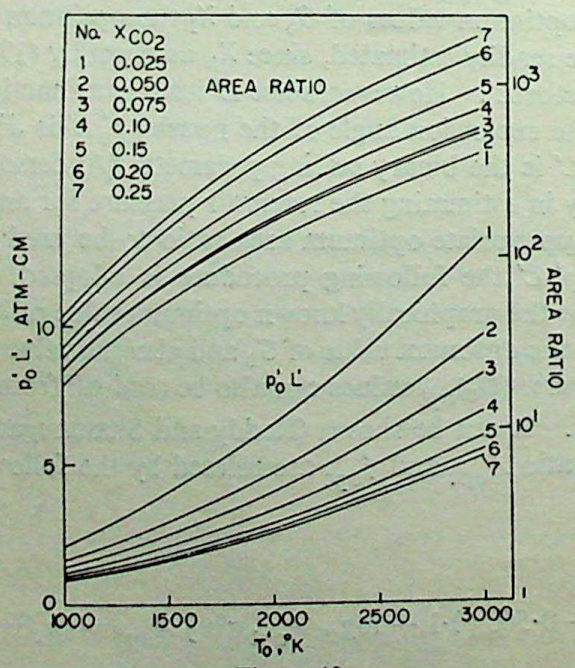

Figure 12

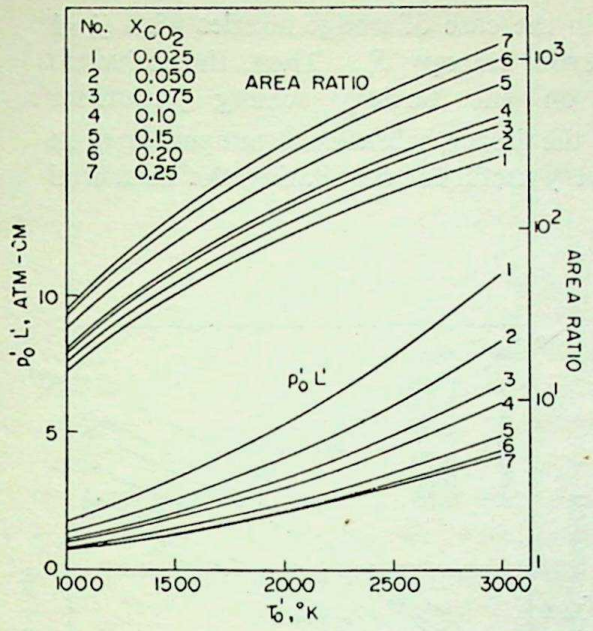

Figure 13

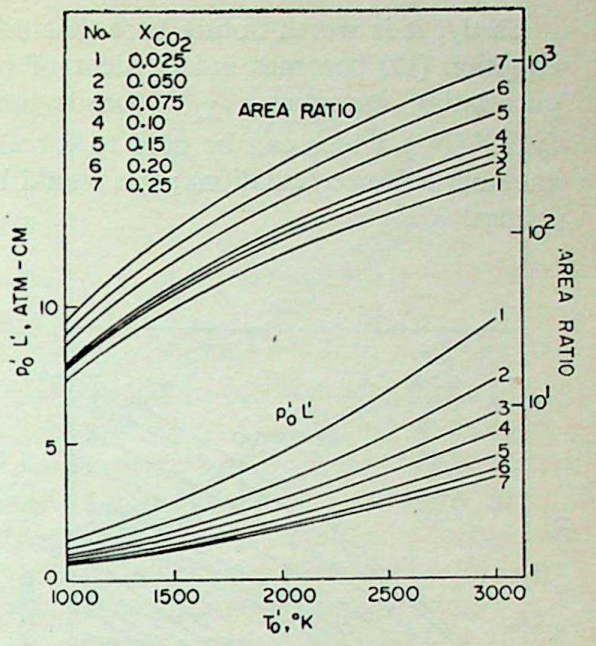

Figure 14

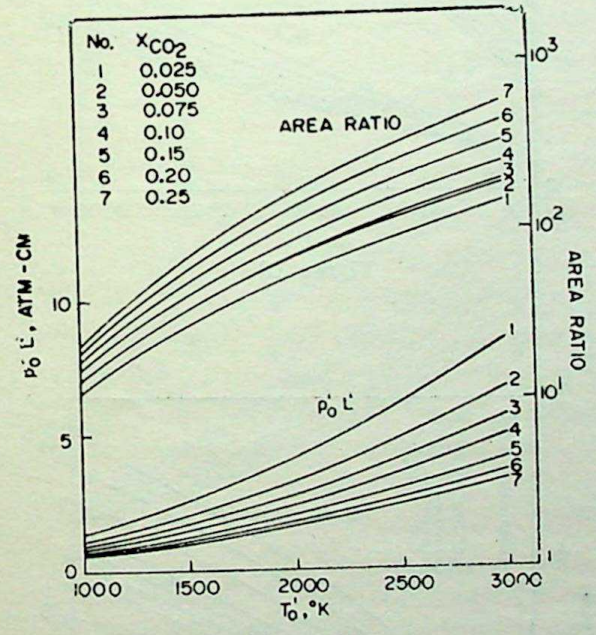

Figure 15

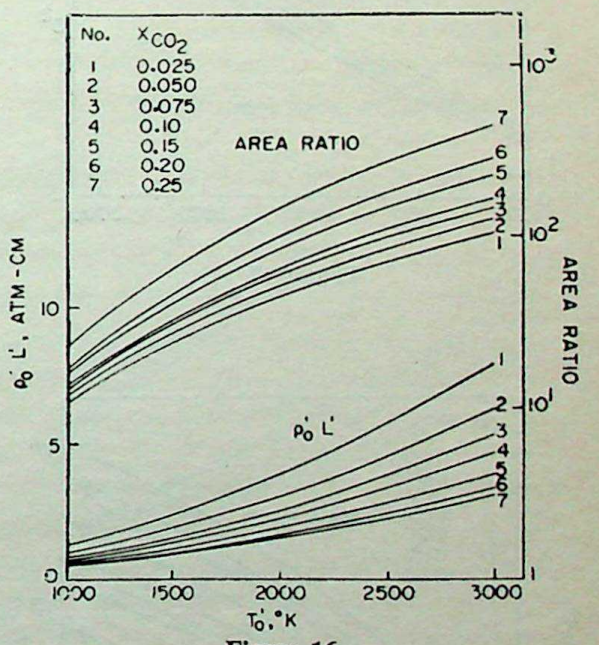

Figure 16

Figures 12–16. Variation of optimum area ratio and $p_0'L'$ with reservoir temperature and $ij = 1$ in system 1. **12.** $X_{He} = 0{\cdot}2$. **13.** $X_{He} = 0{\cdot}3$. **14.** $X_{He} = 0{\cdot}4$. **15.** $X_{He} = 0{\cdot}5$. **16.** $X_{He} = 0{\cdot}6$.

obtained at large expansion area ratios (A), as would be a reasonable expectation, additional concerns arise: (i) inadequate vibrational-relaxation kinetic data exist to support the extrapolation of the simplified τp correlations (see Appendix A of Reddy and Shanmugasundaram 1979a) to very low gas temperatures and (ii) maximum small-signal gain would be expected to shift far away from $P(20)$ to much lower-p-branch transitions, as dictated by the Botlzmann distribution of the rotational-state populations.

Lastly, it is worth noting here that only in the case of wedge nozzles with $ij=1$ equation (17) becomes independent of reservoir entropy S_0. Then, the universal correlating parameter χ_1 depends only on the tertiary scaling parameter $(p_0' L'/T_0'^{3/2})$, which can be used to correlate the frozen vibrational temperatures in the nozzle flow calculations; this would be very useful for correlating the measured values.

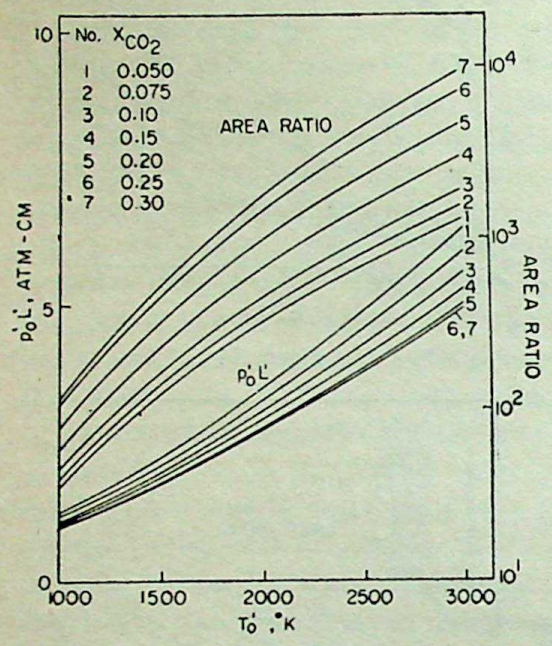

Figure 17

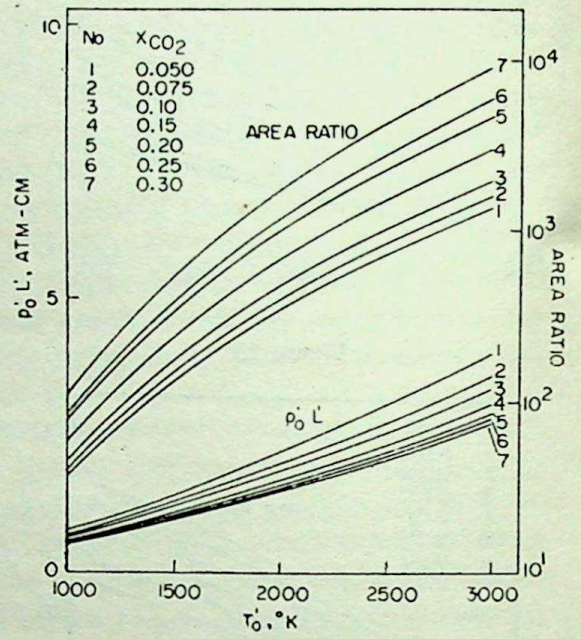

Figure 18

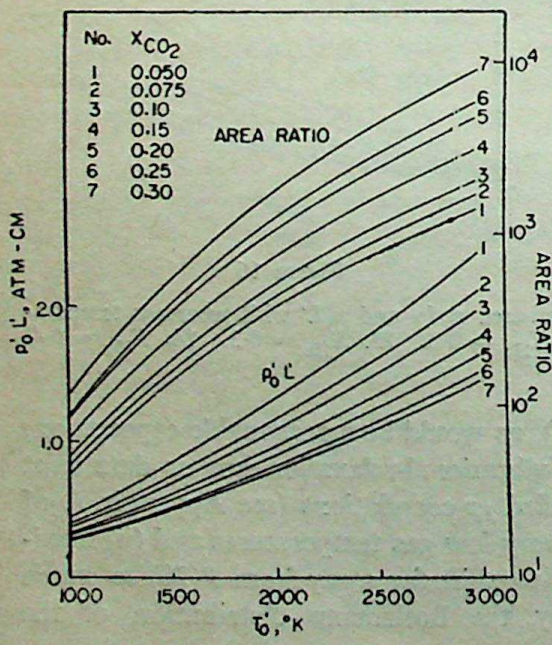

Figure 19

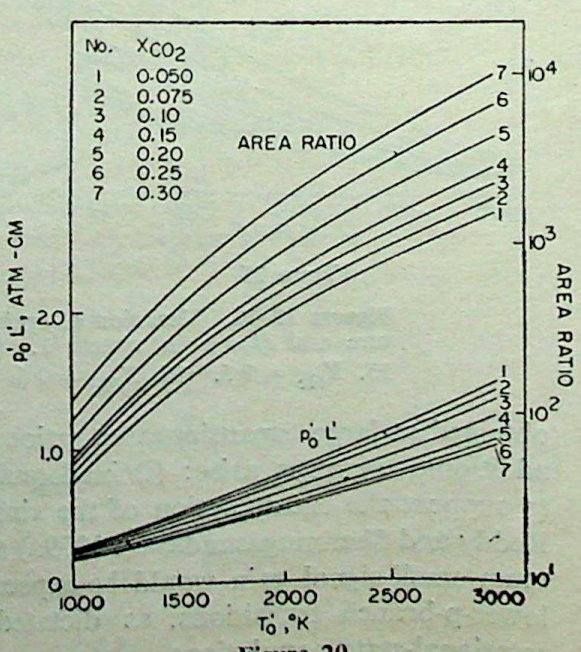

Figure 20

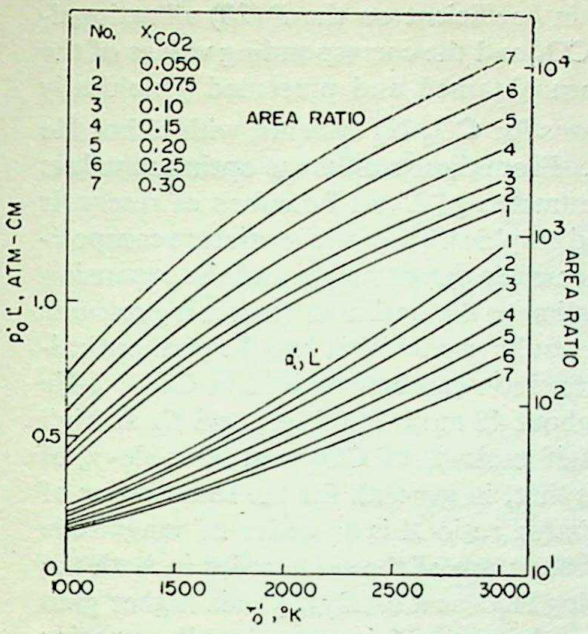

Figure 21

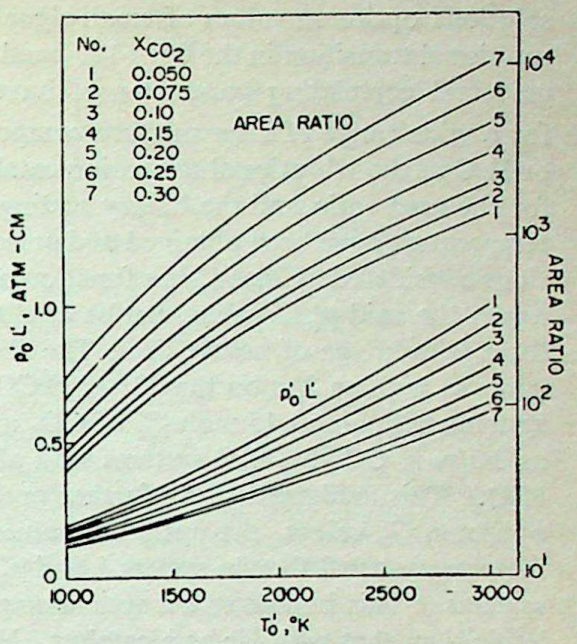

Figure 22

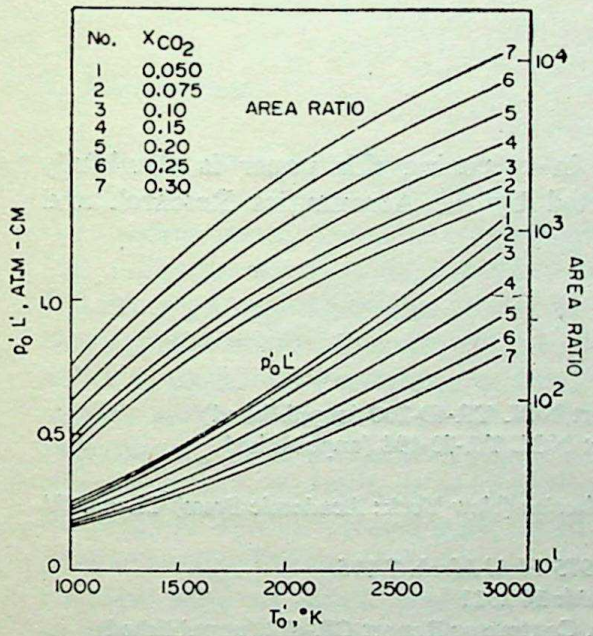

Figure 23

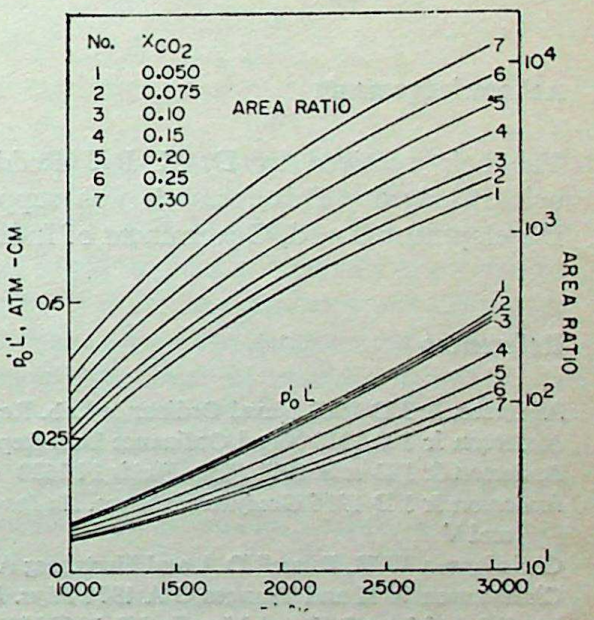

Figure 24

Figures 17–24. Variation of optimum area ratio and $p_0'L'$ with reservoir temperature and $ij = 1$ in system 2. **17.** $X_{H_2O} = 0{\cdot}01$. **18.** $X_{H_2O} = 0{\cdot}02$. **19.** $X_{H_2O} = 0{\cdot}04$. **20.** $X_{H_2O} = 0{\cdot}06$. **21.** $X_{H_2O} = 0{\cdot}08$. **22.** $X_{H_2O} = 0{\cdot}1$. **23.** $X_{H_2O} = 0{\cdot}15$. **24.** $X_{H_2O} = 0{\cdot}2$.

4. Conclusions

Based on the method given by Reddy and Shanmugasundaram (1979a), similar solutions have been obtained for the vibrational non-equilibrium flow along a family of GDL nozzles with $ij=1$, which represents a family of 2D wedge nozzles. From these

solutions optimum values of small-signal gain coefficient on the $P(20)$ vibrational-rotational transition in the 001→100 band of CO_2 and the corresponding values of the universal correlating parameter χ_I have been obtained and presented graphically for a wide range of laser mixture compositions for CO_2-N_2 systems, with either He or H_2O as the vibrational relaxation catalyst. From these results the optimum values for the area ratio and the binary scaling parameter, $p_0' L'$, as functions of reservoir temperature have been obtained and presented graphically for all the mixture compositions considered. Since L' is a function of the nozzle throat height and the expansion angle, the said $p_0' L'$ values can be used to estimate the optimum reservoir pressures for a wide range of nozzle sizes. The above results predict that small-signal optical-gains as high as $2/m$ on the 001→100 CO_2 transition can be obtained in CO_2-N_2-He systems with about 15 mole-% of CO_2 and about 40 mole-% of He; and G_0 as high as $3{\cdot}5/m$ in CO_2-N_2-H_2O systems with about 30 mole-% of CO_2 and 20 mole-% of H_2O. This analytical study further predicts that, in general, for the same order of optimum G_0 values, the optimum values of area ratio A is an order of magnitude larger in system 2 than in system 1 and $p_0' L'$ values are of the same order in both the systems. This implies that a system employing H_2O as a catalyst yields higher gain levels than that with He as a catalyst. Hence, the system 2 is operationally superior to system 1.

Acknowledgements

The help received by Dr K P J Reddy in preparing this paper is thankfully acknowledged. This research was supported by the Aeronautics Research and Development Board, Government of India.

References

Anderson Jr J D 1969 Naval Ordinance Lab. Report NOL TR-69-200 (unpublished)
Anderson Jr J D 1970 Naval Ordinance Lab. Report NOL TR-70-198 (unpublished)
Anderson Jr J D *et al* 1971 *Phys. Fluids* **14** 2620
Anderson Jr J D 1976 *Gasdynamic lasers. An Introduction* (New York: Academic Press) Chaps. IV and V
Christiansen W H, Russell D A and Hertzberg A 1975 *Fluid Mech.* **7** 115
Christiansen W H and Tsonges G A 1971 *Phys. Fluids* **14** 2011
Lordi J A, Mates R E and Moselle J R 1966 NASA Contractor Report CR-472 (unpublished)
Losev S A and Makarov V N 1975 *Sov. J. Quantum Electron.* **4** 905
McManus J I and Anderson Jr J D 1976 *AIAA J.* **14** 1770
Reddy N M and Shanmugasundaram V 1978 *Proc. Second Int. Symp. on Gasflow and Chemical Lasers, Brussels* (Washington: Hemisphere Publ., Corp.)
Reddy N M and Shanmugasundaram V 1979a *J. Appl. Phys.* **50** 2565
Reddy N M and Shanmugasundaram V 1979b *J. Appl. Phys.* **50** 2576

Pramāṇa, Vol. 21, No. 2, August 1983, pp. 149–158 © Printed in India.

Attenuation of shock parameters in air and water

J HARVEY, J NANDAKUMAR and L V KRISHNAN
Safety Research Laboratory, Reactor Research Centre, Kalpakkam 603 102, India

MS received 16 March 1983; revised 5 July 1983

Abstract. This paper describes the results of shock pressure measurements in the range of 1–25 MPa in water and in the range of 60–500 kPa in air. Pressure pulses were generated by exploding wire technique and measured with a quartz piezo-electric transducer. The attenuation with distance of shock overpressure, impulse and energy in shock front has been studied. Experimental data on shock attenuation in air is scarce and the results presented here confirm the attenuation behaviour derived from theoretical considerations.

Keywords. Exploding wire; shock overpressure; impulse; energy; piezo-electric transducer; attenuation; air; water.

1. Introduction

In nuclear safety analysis, it is required to evaluate the consequences of dynamic loading of structures resulting from a variety of phenomena such as (i) nuclear excursion (ii) thermal interactions due to accidental mixing of molten reactor fuel and coolant (iii) sodium water reactions in reactors using liquid sodium heated steam generators (iv) hydrogen explosions etc. Experiments carried out in the laboratory simulating these situations provide an insight into these phenomena and generate useful data for safety analysis. Determination of the degree of conversion of available energy in the shock front for doing mechanical work on structures, is an important objective of these experiments. The pressures in these experiments are invariably measured at some distance away from the zone of interaction. An understanding of the propagation of the pressure front in the medium is essential for extrapolation of the measured pressure profiles back to the zone of interaction. This paper presents the measured attenuation characteristics of shock pressure, impulse and energy, in air and water, using exploding wire technique to generate shock fronts.

A comparative review of available data on shock propagation in air, in the range 10 to 20 kPa has been made by Vortman (1970). It is seen that while considerable theoretical work has been carried out to determine shock attenuation characteristics in air in different pressure ranges, experimental data are rather scarce. Also the agreement between theory and experiment is not satisfactory.

Cole (1965) compared the empirical relationship between shock overpressure, distance and charge weight derived from theory and underwater experiments. The correlation for shock attenuation assumes a single expression to be valid over a range of pressures extending over almost three orders of magnitude from 3 to 3000 MPa.

Generation of experimental data on shock attenuation, in the low pressure range,

with chemical explosives calls for use of small quantities of charge material with attendant problems of reproducibility. Alternatively, measurements can be made at relatively large distances from reasonably-sized charges, but in this case shock propagation is likely to be affected by environmental factors such as temperature, its gradient, windspeed and so on. In this context, the application of exploding wire sources for experimental determination of shock attenuation in air and water has the advantages of easy repeatability and good reproducibility.

2. Experimental set-up

The schematic of the experimental set-up is shown in figure 1. A 10 kV 190 μF condenser bank is used for the generation of shock waves by exploding a copper wire of 0·18 mm diameter and 5 mm length. The capacitor bank is resistively damped to avoid ringing and enable generation of a single shock pressure pulse. The wire explosion is initiated by a two-electrode spark gap, with switching time less than 500 nsec. A special wire holding assembly has been made with pinvices for holding the copper wires. The base of the wire holder assembly is so shaped as to prevent reflected shock fronts from reaching the gauge face. For underwater studies, the entire assembly was immersed in a water tank (400 × 400 × 700 mm). For experiments in air as well as underwater, the geometry and dimensions of the experimental set-up are so chosen that the reflected shock fronts reach the transducer only after the direct overpressure pulse seen by the transducer has decayed.

3. Instrumentation

Quartz piezoelectric transducers (Kistler model 603H) were used to measure the shock pressures. The transducers have a rise time of 1 μsec and sensitivity of 25 pC/kPa. The transducer resonant frequency is 500 kHz. Charge amplifier (model 504 of Sundstrand Data Inc, USA) with a flat frequency response up to 150 kHz was used for

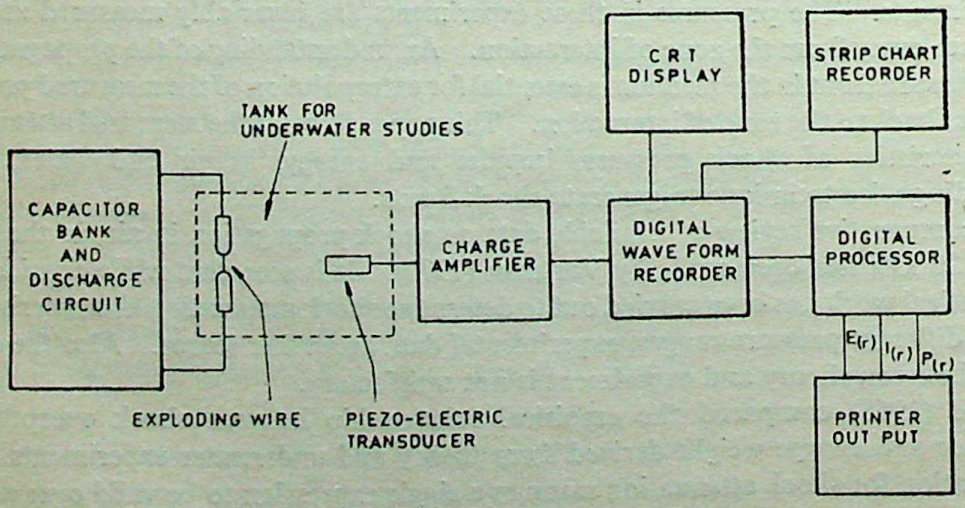

Figure 1. Experimental set-up for shock wave generation and measurement of shock parameters.

processing the pressure signals from the transducer. During the wire explosion, very high surge current of the order of 15 kA flows through the discharge circuit. The heavy electromagnetic field produced as a result was observed to induce an overriding noise in the signal lines. To provide the necessary shielding, charge amplifier and recording instruments were housed in a fully closed aluminium cabin. Double-shielded signal cables were used with the outer shield terminated at the cabin wall. The inner shield which is the common line for the signal was connected to the laboratory ground. The amplifier and the recording systems were separately connected to the laboratory ground. This type of grounding was found to be quite effective and reduced the noise due to the electromagnetic pick-up. During underwater measurements, the current flow path through water between the high voltage terminal and the transducer body was effectively blocked by electrically isolating the latter with a coat of insulating paint. To avoid leakage of water into the cable connectors and to isolate the connectors from water, the entire connector portion was wax moulded.

4. Recording devices

Pressure signals were recorded by a digital waveform recorder (Biomation 805) and read with 1% accuracy. A microprocessor-controlled digital interface connected to the waveform recorder was used to determine the peak pressure, impulse and energy flow.

5. Measurements

Keeping the wire material, length and diameter fixed, the distance of the transducer from the wire was varied for each of different capacitor voltages. Pressure measurements were repeated thrice for each setting and a reproducibility within 5% was observed. Figure 2 shows a typical waveform of the current through the exploding wire obtained in the present experimental set-up.

A typical pressure pulse produced in underwater wire explosion is given in figure 3. A rise time of 2 μsec and a pulse duration of 6 μsec was observed. However in the case of exploding wire in air, while the pressure signals had a similar rise time of 2 μsec, the pulse duration was observed to be longer, namely 40–50 μsec.

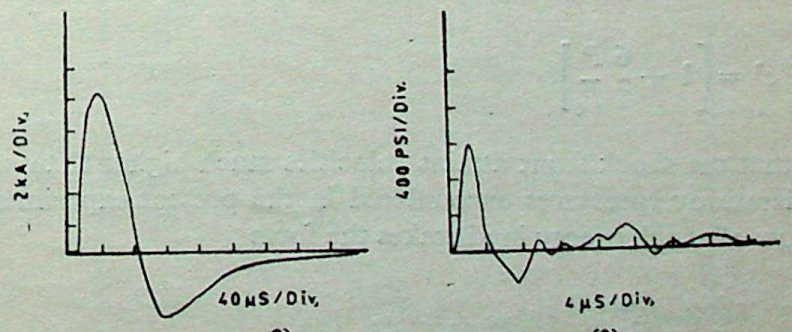

(2) (3)

Figure 2. Typical current pulse through the exploding wire.
Figure 3. Pressure signal in underwater wire explosion.

The impulse at distance r from the source is defined by the relation

$$I(r) = \int_0^{t_0} P(r, t)\, \mathrm{d}t, \tag{1}$$

where t_0 is the duration of the positive phase of the pressure pulse and $P(r,t)$ represents the variation of pressure with time behind the shock front. Impulse was evaluated by numerical integration of the pressure signal in the waveform recorder using the digital processor.

Assuming a spherical shock front the work done on a surface of radius r is given by

$$w(r) = \int_0^{t_0} 4\pi r^2 P(r, t)\, u_p(r)\, \mathrm{d}t, \tag{2}$$

where $u_p(r)$ is the particle velocity behind the shock front. From the conservation equations for mass and momentum we have

$$u_p = P/\rho_0 u_s, \tag{3}$$

whence
$$w(r) = \int_0^{t_0} 4\pi r^2 \frac{P^2(r, t.)}{\rho_0 u_s(r)}. \tag{4}$$

For the measured range of shock overpressures in water, the shock velocity u_s differs from the sonic velocity by just about 2% (table 2·2 of Cole 1965). This permits the replacement of the product $\rho_0 u_s$ by the acoustic impedance $\rho_0 c$. The energy flow per unit area associated with the propagation of the shock front in water is therefore given by

$$E(r) = \frac{1}{\rho_0 c} \int_0^{t_0} P^2(r, t)\, \mathrm{d}t. \tag{5}$$

$E(r)$ was computed by the digital processor from the pressure time history. Recalling that the governing equation for shock propagation in air is (Zeldovich and Raizer 1966),

$$u_s^2/c^2 = \left[1 + \frac{6}{7}\frac{P}{P_0}\right], \tag{6}$$

it is obvious that the shock front attains velocities much higher than sonic velocity even for moderate overpressures encountered in the present experiments. Consequently the flow of shock energy in air takes the form

$$E(r) = \frac{1}{\rho_0 c} \int_0^{t_0} \frac{P^2(r, t)\, \mathrm{d}t}{[1 + (6/7)\,[P(r, t)/P_0]]^{1/2}}. \tag{7}$$

To evaluate the integral in (7) it is necessary to know the functional form of the variation of pressure with time behind the shock front. As sugested by Leonard (1962) a relationship of the form

$$P(t)=P_m\left[\exp(-bt)\,\frac{\cos(\Omega t+\phi)}{\cos\phi}\right], \tag{8}$$

where $b=1/2t_0$, $\Omega=(\frac{1}{2}\pi-\phi)/t_0$, $\phi=23{\cdot}22°$,

has been used in the present studies. The pressure profile computed using (8) is given in figure 4. The profile matched fairly well with the typical pressure trace obtained with experiments. Shock impulse and energy flow per unit area in air were computed using (8) in (1) and (7). The impulse (equation (1)) is obtained by direct integration and leads to the result, $I=0{\cdot}3943\,P_m\,t_0$. To determine the energy integral, the integration was carried out using eighth order Gaussian quadrature.

6. Results and discussion

The impulse values for air computed by direct integration were in good agreement with the values obtained from the digital processor. The variation of the shock parameters with distance studied for water as well as air is presented in figures 5 to 10. It is observed that for a given capacitor bank voltage the attenuation with distance of shock overpressure, impulse and energy flow with respect to distance r obeys the well-known power law

$$P(r)=K_1\,r^{-\alpha_1},$$

$$I(r)=K_2\,r^{-\alpha_2},$$

$$E(r)=K_3\,r^{-\alpha_3}.$$

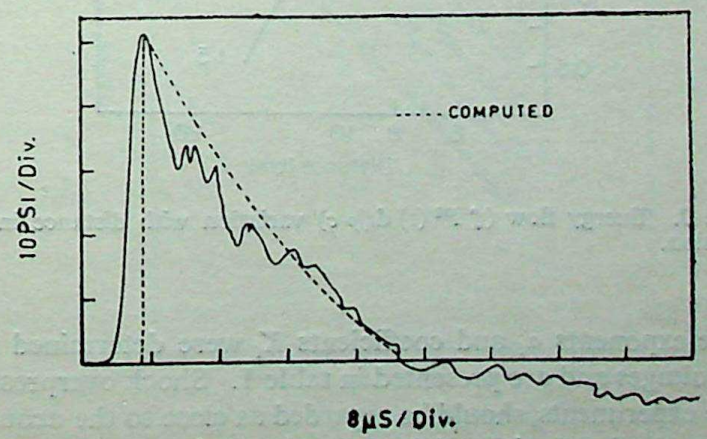

Figure 4. Actual and computed pressure profiles in air.

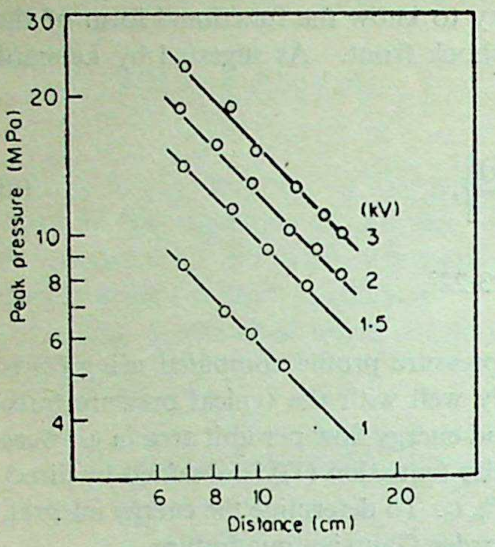

(5)

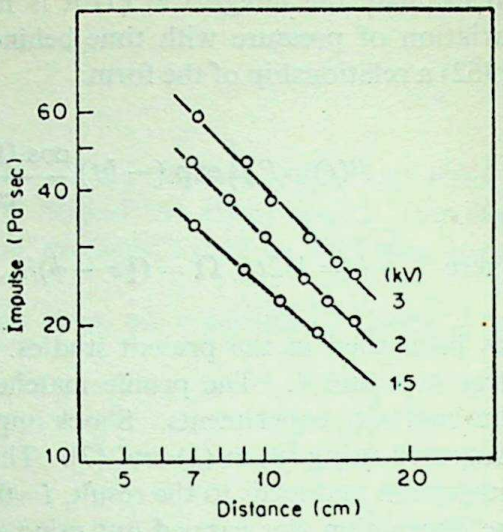

(6)

Figure 5. Pressure variation with distance in underwater wire explosion.

Figure 6. Impulse ($\int P(t)\,dt$) variation with distance in underwater wire explosion

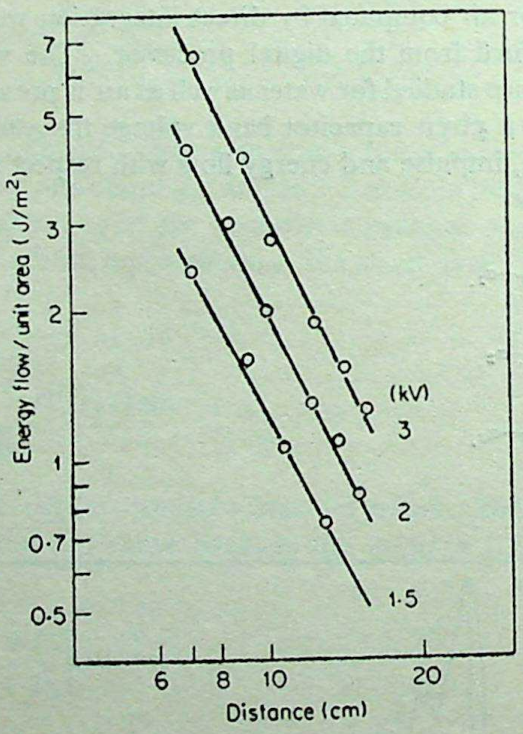

Figure 7. Energy flow ($\int P^2(t)\,dt/\rho c$) variation with distance in underwater wire explosion.

The values of the exponents a_i and coefficients K_i were determined for each of the capacitor bank voltages and are presented in table 1. Shock overpressures generated in water, in these experiments, should be regarded as close to the acoustic range since the corresponding shock velocities differ from the sonic velocity by about 2% only.

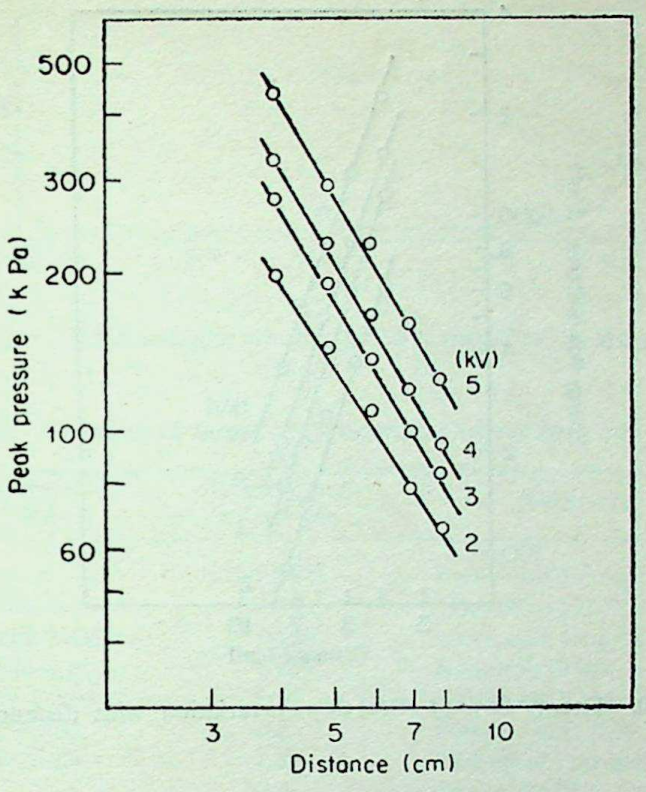

Figure 8. Pressure variation with distance in wire explosion in air.

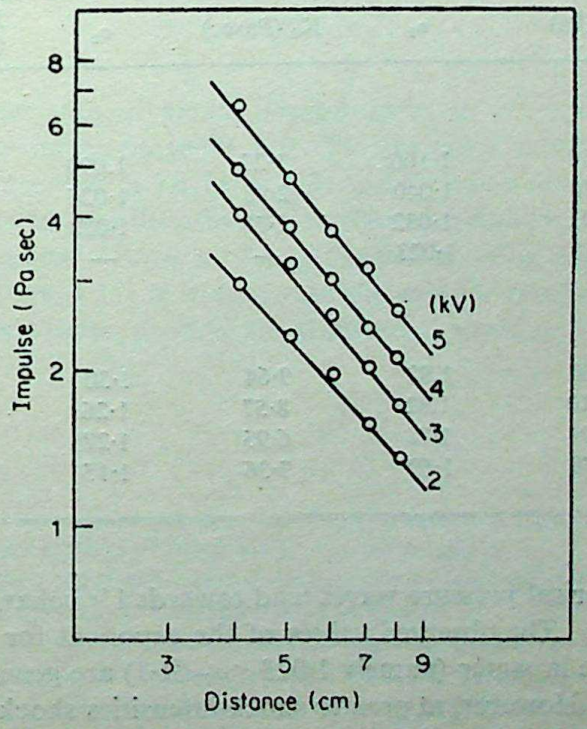

Figure 9. Impulse ($\int P(t)\,dt$) variation with distance in wire explosion in air.

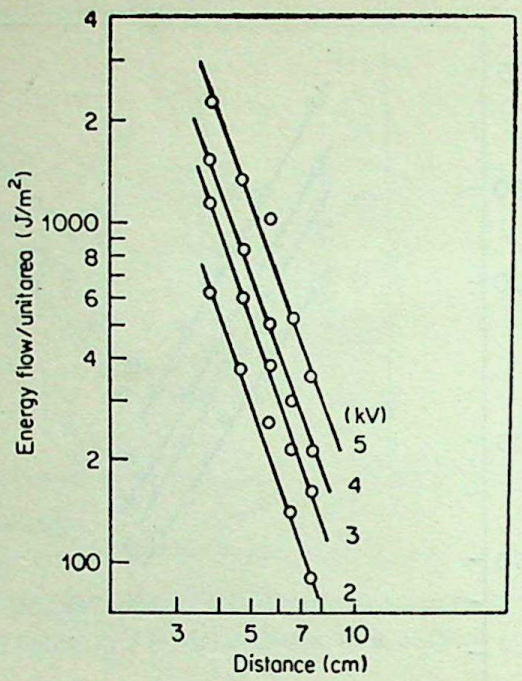

Figure 10. Energy flow ($\int P^2(t)\,dt/\rho c$) variation with distance in wire explosion in air.

Table 1. Values of constants K_i and α_i in the expressions for pressure, impulse and energy.

Capacitor voltage (kV)	Pressure		Impulse		Energy	
	K_1 (MPa)	α_1	K_2 (Pasec)	α_2	K_3 (j/m²) ($\times 10^{-3}$)	α_3
Water						
3	1·250	1·100	3·27	1.090	19·9	2·195
2	1·170	1·040	2·98	1·026	18·0	2·048
1·5	0·942	1·032	2·78	1·023	12·2	2·012
1	0·637	1·023	—	—	—	—
Air						
5	1·264	1.82	9·64	1·30	0·504	2.630
4	0·910	1.82	8·57	1·26	0·148	2·880
3	0·894	1·78	6·95	1·27	0·117	2·850
2	0·878	1·69	7·36	1·15	0·092	2·760

It is known that spherical pressure waves tend towards $1/r$ behaviour as the acoustic range is approached. The observed values of the exponent for the spatial profiles of shock overpressure in water (namely $1{\cdot}023 < \alpha_i < 1{\cdot}1$) are generally in accordance with this behaviour. However, at greater shock intensities shock overpressures tend to fall off with distance more rapidly.

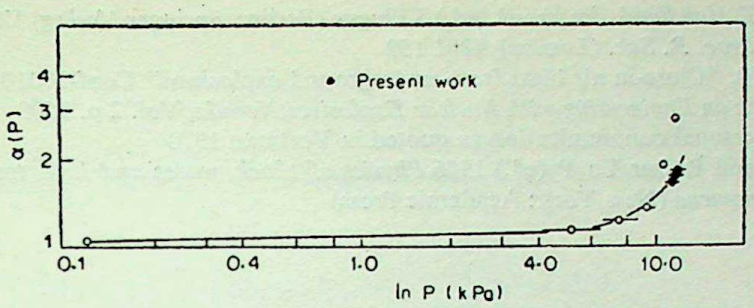

Figure 11. Variation with pressure of the exponent of the law $P \propto r^{-\alpha}$.

Table 2. Variation of shock overpressure with distance in air.

Overpressure (kPa)	Exponent of decay law	Reference
0·00113	1·0575	Lehto and Larson (1969)
0·06894–0·138	1·12	Whitaker (1970)
0·06894–0·6894	1·126	Lehto and Larson (1969)
0·06894–0·6894	1·35*	Kingery (1966)
0·6894–6·894	1·22	Lehto and Larson (1969)
2·757–6·894	1·2	Bethe *et al* (1955)
6·894–20·68	1·35	Kirkwood and Brinkley (1945)
49	1·9	Taylor (1950)
147	2·8	Taylor (1950)
60–195	1·69*	Present work
80–274	1·77*	Present work
92–324	1·82*	Present work

*Experimental.

The decay characteristics of shock overpressures in air observed in the present experiments (in the pressure range 60–320 kPa) are given in table 2 for comparison together with those reported in Taylor (1950) and Vortman (1970) for other pressure ranges. It may be noted that the attenuation characteristics are largely derived from theoretical considerations. From a plot of the variation of the exponent α against shock overpressure (figure 11) it is seen that the present results although restricted to a small range of pressures, confirm the theoretical estimate.

References

Bethe H *et al* 1955 *Blast wave* (New Mexico: Los Alamos Scientific Laboratory)

Cole R H 1965 *Underwater explosions* (New York: Dover) p. 142

Kingery C H 1966 Air blast parameters versus distance for hemispherical TNT surface burst, BRL report 1344, Ballistics Research Laboratories, Maryland

Kirkwood J C and Brinkley S R Jr 1945 Theoretical blast wave curve for cast TNT, OSRD 5481, NRDL A-341, Office of Scientific Research Development, Washington D C

Lehto D L and Larson R A 1969 Long range propagation of spherical shock waves from explosions in air, NOLTR-69-88 US Naval Ordinance Laboratory, Explosion Research Department. White Oak, Maryland

Leonard R W 1962 *Handbuck der physik* (ed.) S Flugge (Berlin: Springer Verlag) Vol. 11/2 p. 33
Taylor G I 1950 *Proc. R. Soc.* (*London*) **A201** 159
Vortman L J 1970, "Close-in air blast from underground explosions" Conf-700101, *Proceedings of the symposium on Engineering with Nuclear Explosives Nevada*, Vol. 2 p. 1509
Whitaker W A Personal communication as quoted in Vortman 1970
Zeldovich Ya B and Raizer Yu P (ed.) 1966 *Physics of shock waves and high temperature hydrodynamic phenomena* (New York: Academic Press)

Pramāṇa, Vol. 21, No. 3, September 1983, pp. 159–169. © Printed in India.

Mechanoluminescence of coloured KCl crystals

M ELYAS, S K SHUKLA and B P CHANDRA
Department of Physics, Government Science College, Raipur 492 002, India

MS received 16 November 1982; revised 4 May 1983

Abstract. The gamma-irradiated KCl crystals exhibit mechanoluminescence during elastic, plastic and fracture deformation. The mechanoluminiscence (ML) intensity varies linearly with the number of newly-created dislocations and decreases with successive application and release of uniaxial pressure. The total ML intensity increases with applied pressure as well as with the temperature of the crystals. On the basis of the movement of the dislocations, the pressure and temperature dependence of ML is discussed.

Keywords. Mechanoluminescence; alkali halides; mechanical deformation.

1. Introduction

Mechanoluminescence (ML) is a type of luminescence produced during mechanical deformation of solids. The mechanoluminescent substances may be divided into those whose ML spectra resemble (i) other type of luminescence spectra, (ii) molecular spectra of the surrounding gases and (iii) both these spectra. The possible uses of mechanoluminescent substances as mechano-optico transducers and in fuse system are attracting increasing interest. The crystal structure correlation of ML and the memory-effects related to plastic deformation may also be interesting (Chandra 1981; Chandra and Elyas 1979; Hardy *et al* 1981; Grabec 1974). The ML studies provide a suitable probe for studying the fracture dynamics of the crystals (Chandra and Zink 1980a). On the basis of mode of excitation, ML may be classified as piezo-induced, dislocation-induced, cleavage-induced, tribo-induced, chemi-induced and adsorption-induced. The coloured alkali halide crystals exhibit ML (Walton 1977); which is not satisfactorily understood. The present paper reports the ML of coloured KCl crystals and shows that the ML in alkali halide crystals may primarily be attributed to annihilation of the dislocations of opposite sign during the mechanical deformation.

2. Experimental

The KCl single crystals ($4 \times 3{\cdot}8 \times 2{\cdot}5$ mm) used in the present investigation were supplied by the National Physical Laboratory, New Delhi. The small size crystals were annealed at 450°C for 2hr and cooled very slowly. The γ-irradiated specimen wrapped in aluminium foil was kept in dark for an hour to allow the after-glow to decay to a value, well below that expected in the ML measurements. Exposure of the irradiated crystals to stray light was avoided. A uniaxial pressure was applied to the crystal by placing

heavy loads statically (Chandra and Elyas 1977). The crystal was kept pressed for 30 sec. The ML intensities both during pressing and release were measured in terms of the deflection of a ballistic galvanometer connected to the amplifier coupled to an IP 28 photomultiplier tube. The process of pressing and release was repeated periodically till the ML intensity became small. All measurements were made by applying pressure along (100) direction of the crystals. A heater coil was wound round a cylinder for heating the crystal. The cylinder was mounted on a crystal platform and by changing the voltage, the crystals could be heated to any desired temperature. The ML was measured when the device attained a steady temperature. The crystal temperature was measured by a copper-constanton thermocouple. Temperature effect on the ML of the crystals was studied for a fixed load of 12·5 kg. To avoid heating of photomultiplier tube, a thick rubber sheet with a hole at its centre was placed between the glass plate and the photomultiplier housing. Four crystals were studied at each temperature and the standard error was $\pm$ 6%.

The ML spectra, the stress-strain and the ML-strain curves were determined following the method described earlier (Hardy and Zink 1976; Chandra and Zink 1980). The ML intensity was monitored by a X–Y recorder. The dislocation density was measured by the etch pit technique in which a concentrated solution of NH_4Cl in a mixture of methyl alcohol and n-butyl alcohol in the ratio of 3:4 by volume was used as etchant (Naidu 1970).

3. Results

Figure 1 shows the ML *vs* compression and the force *vs* compression curves of 5 × 4 × 6·3 mm γ-irradiated KCl crystals. It is seen that the ML appears in the elastic, plastic as well as fracture regions of the crystals. The stress and the ML intensity of the crystals are seen to vary with strain. The plot of log of ML intensity *vs* log of the number of newly created dislocations (figure 2) suggests a linear rela-

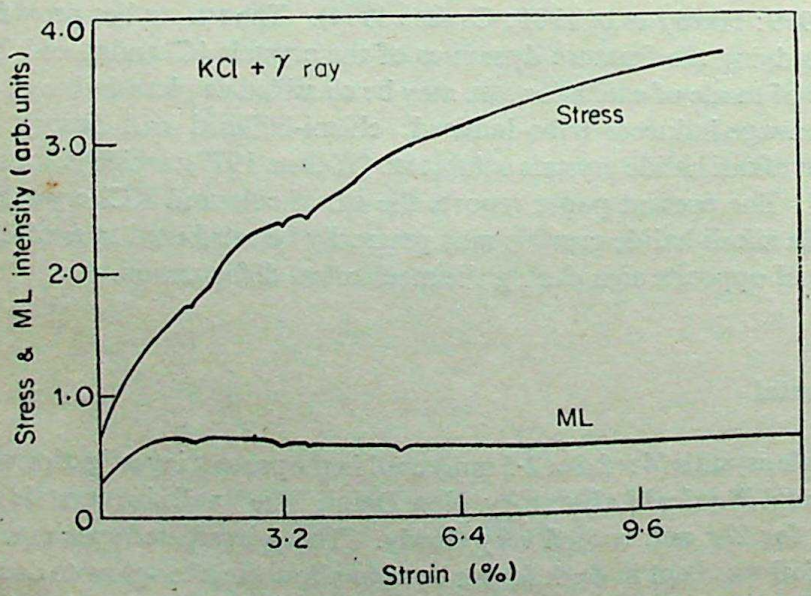

Figure 1. Mechanoluminescence *vs* compression and the force *vs* compression curves for γ irradiated KCl crystal.

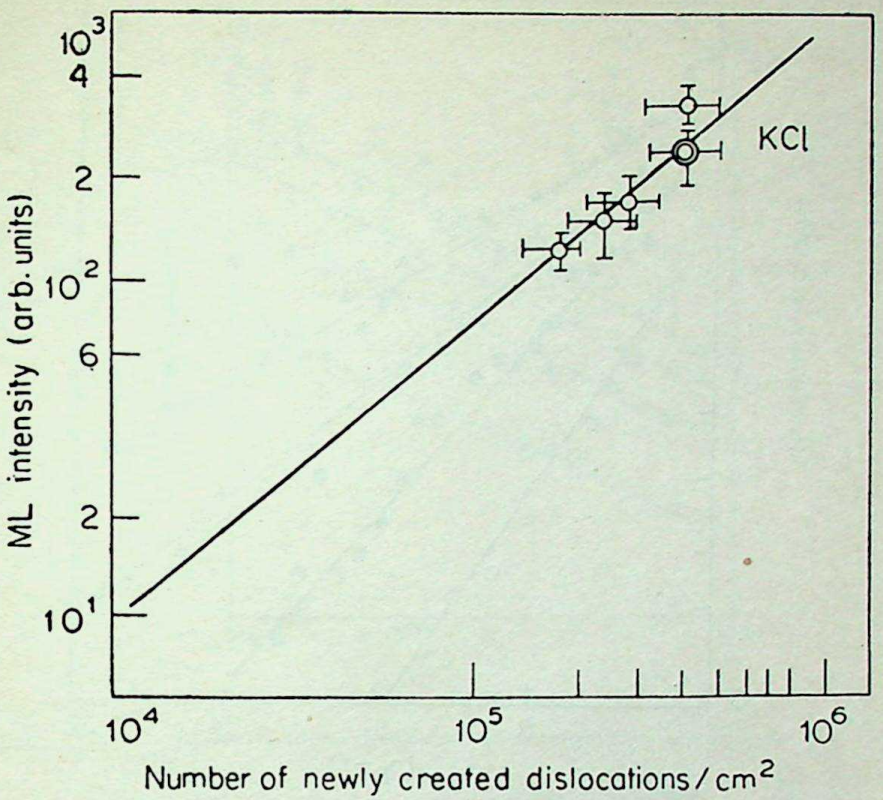

Figure 2. Plot of log ML intensity *vs* log number of newly created dislocations.

tion between the two. After certain number of applications of the uniaxial pressure, the dislocation density increases so much that it is difficult to determine the dislocation each pit counts for the highly deformed crystals.

The intensities of ML produced during application and release of the pressure, i.e. I_n^p and I_n^r of γ-irradiated KCl crystals decreases with the successive number n_p and n_r of application and release of pressure and follow the relations (figures 3a, b)

$$I_n^p = I_1^p \exp\,[-\beta(n_p - 1)], \tag{1}$$

$$I_n^r = I_1^r \exp\,[-\beta_1(n_r - 1)], \tag{2}$$

where β and β_1 are constants, and I_1^p and I_1^r are the ML intensity during the initial application and release of pressure respectively. The I_1^p and I_1^r values increase with pressure, however, the β and β_1 values decrease with pressure. For a given value of pressure β is always greater than β_1.

Figure 4 shows that the dependence of the ML intensity on successive application and release of pressure at different temperatures also follow (1) and (2). The β and β_1 values increase slightly with temperature. However, for a given temperature, the β_1 value is always $< \beta$.

Figure 5 reveals that the total ML intensity, i.e., the sum of the areas below I_n^p *vs* n_p and I_n^r *vs* n_r curves of γ-irradiated KCl crystals increases with temperature. The annealing time at this temperature, does not significantly alter the ML intensity of γ-irradiated KCl crystals.

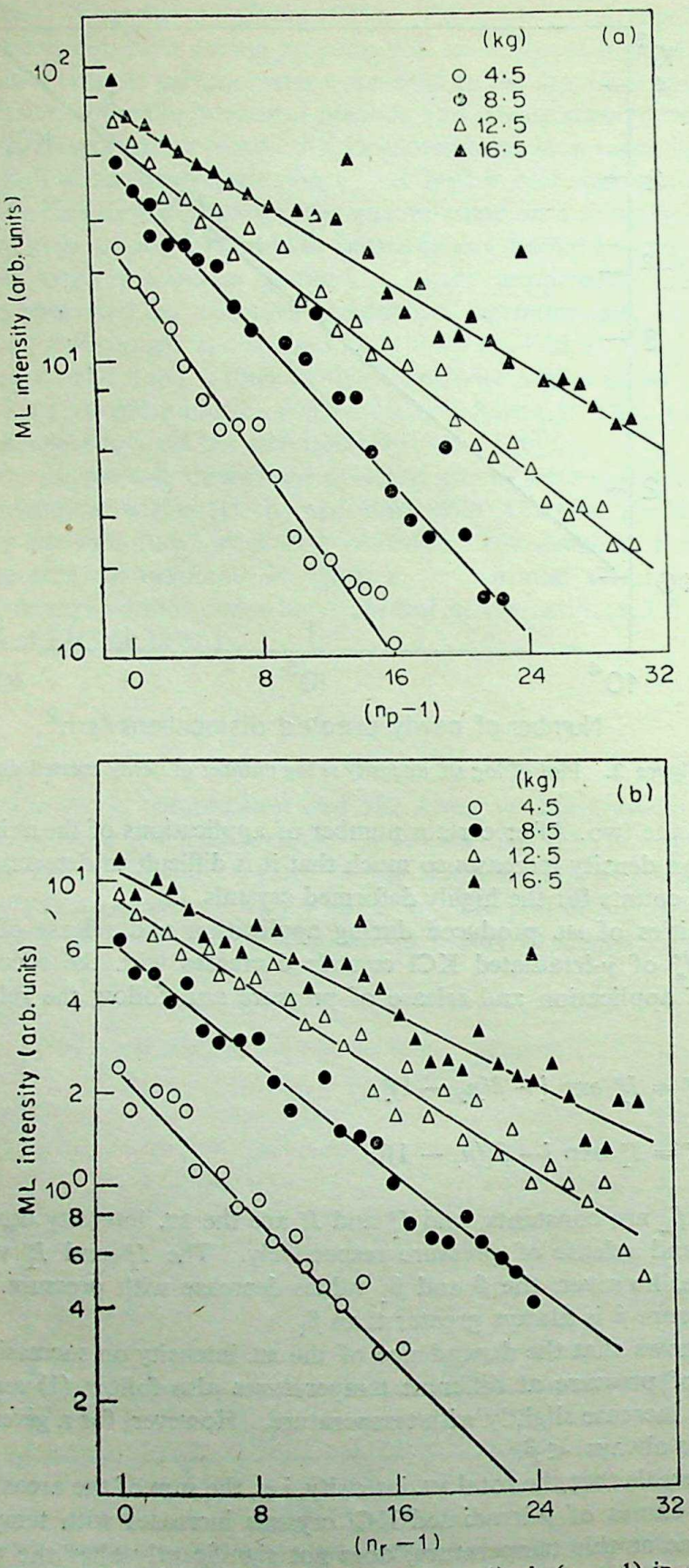

Figure 3. Plot of log ML intensity *vs* **a.** $(n_p - 1)$ **b.** $(n_r - 1)$ in γ irradiated KCl crystals for different values of uniaxial pressure.

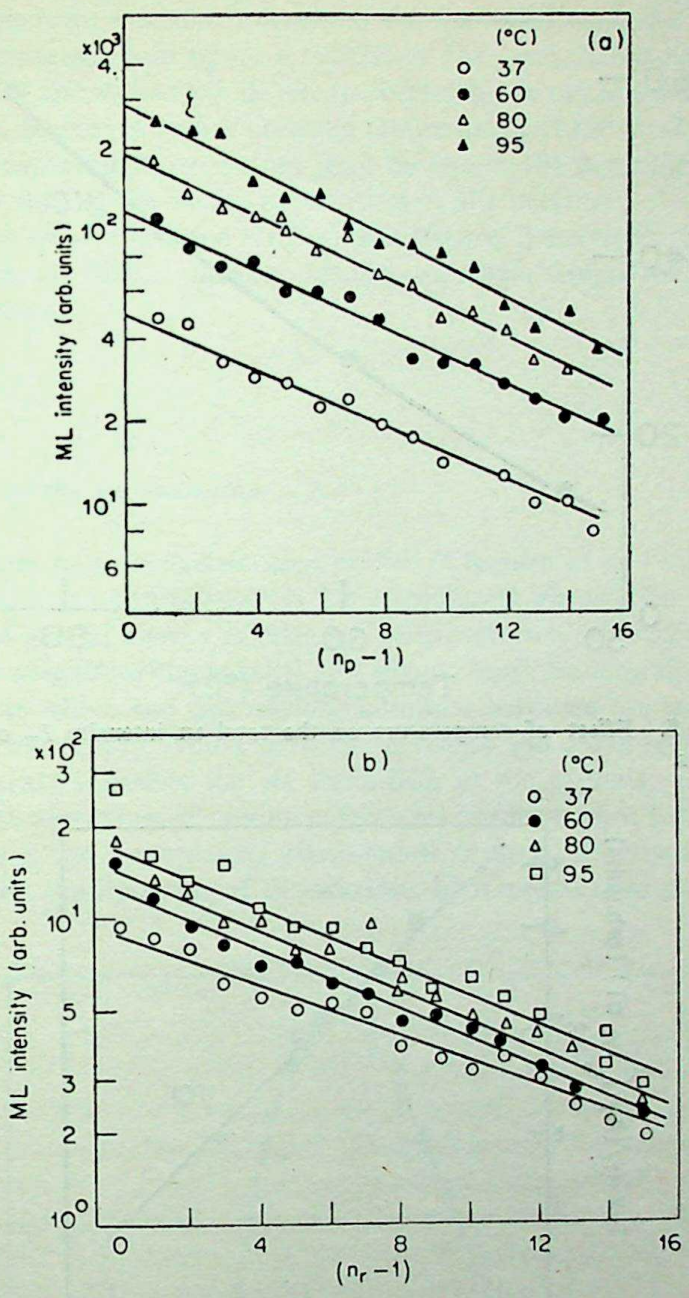

Figure 4. Plot of log ML intensity *vs* **a.** (n_p-1) **b.** (n_r-1) in γ irradiated KCl crystals for different values of temperature.

The ML intensity is directly related to the density of the colour centres (Butler 1966; Metz *et al* 1957), which is directly related to the area below the thermoluminescence (TL) glow curves of the crystals (Ausin and Alvarez 1972; Jain and Mahendru 1965). Hence, the ML intensity was normalized for the decrease in the density of the colour centres with temperature of the crystals using TL glow curves. The TL glow curves of these crystals have been reported earlier (Elyas *et al* 1982). The plot of $\log I_T \times A_T/(A_T - \int_{T_0}^{T} I_{TL}\,dT)$ *vs* $1/T$ (where I_{TL} is TL intensity, A_T is the

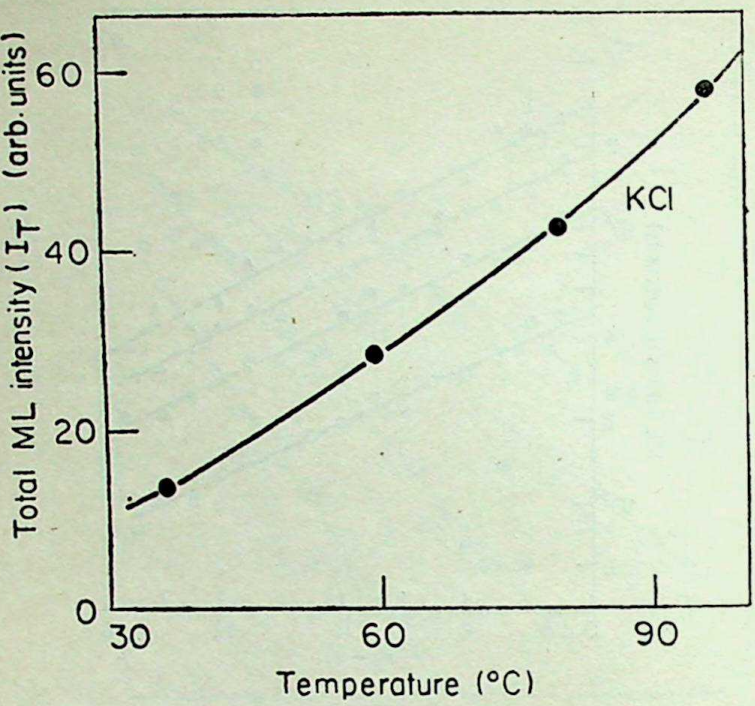

Figure 5. Effect of temperature on the total ML intensity I_T of γ irradiated KCl crystals.

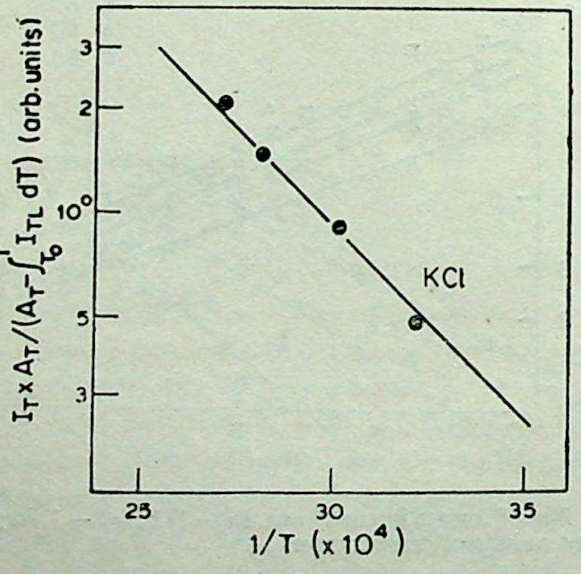

Figure 6. Plot of $I_T \times A_T / \left(A_T - \int_{T_0}^{T} I_{TL}\, dT\right)$ *vs* $1/T$.

total area below the glow curves and T_0 is the room temperature) is a straight line with a negative slope (figure 6), for γ-irradiated KCl crystals. This result suggests the relation

$$I_T \times A_T/A_T - \int_{T_0}^{T} I_{TL}\, dT = A_0 \exp(-E_0/kT), \tag{3}$$

where A_0 is a constant, k is the Boltzmann constant and E_0 is the activation energy. The E_0 value estimated from figure 6 is 0·25 eV for γ-irradiated KCl crystals.

Figures 3 and 4 show that the difference between the extrapolated and the experimental I_1^p values decreases with increasing temperature of the crystals. This suggests that the higher experimental I_1^p values may be due to the presence of shallow traps, which disappear during the initial application of the pressure.

The ML spectra of γ-irradiated KCl crystals (figure 7) are similar to their TL spectra (Ausin and Alvarez 1972). Similar results were also found for the ML of x-irradiated KCl crystals.

4. Discussion

4.1 *Mechansim of the* ML *excitation*

Many possibilities have been discussed earlier (Chandra *et al* 1982) and it has been found that dislocation annihilation is the dominating process for ML excitation. A large amount of stored energy is released whenever two dislocations moving in the same or closely neighbouring parallel slip planes unite by annihilation (Seitz 1952). Thus, the line at which the dislocations combine becomes the seat of a very large source of thermal energy which in turn increases the local temperature. The increase in temperature causes the ML excitation in the crystals. TL studies indicate that the thermal bleaching of colour centres takes place from room temperature to 300 or 400°C in x and γ-irradiated alkali halide crystals. The rise in the local temperature during the annihilation of dislocations of opposite sign may be sufficient to

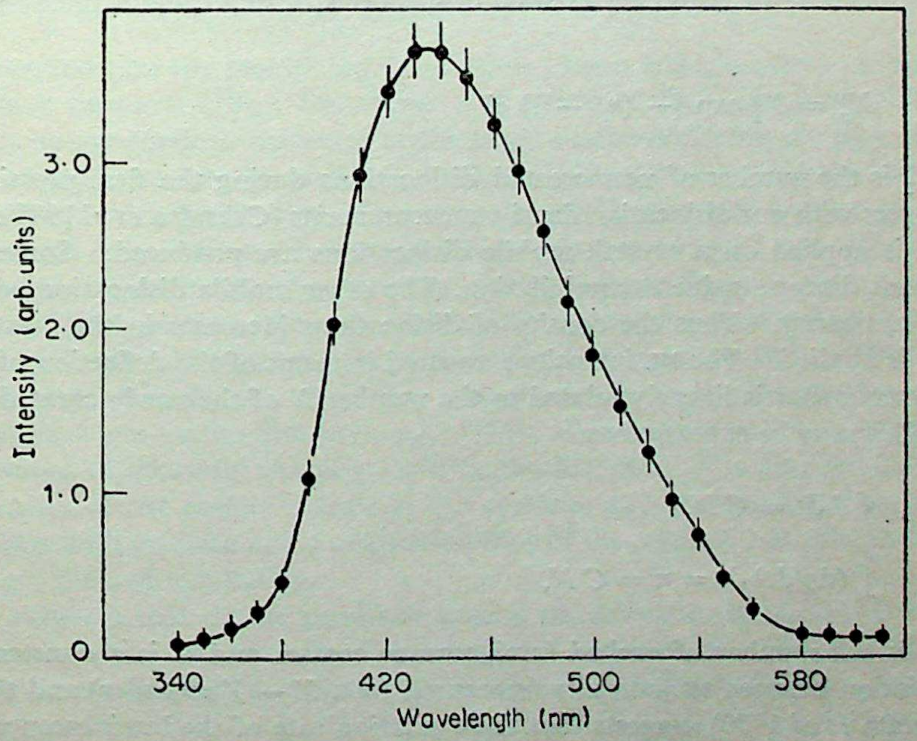

Figure 7. ML spectra of irradiated KCl crystals.

give rise to TL excitation. Although the crystal temperature may not rise considerably, the local temperature may be much higher during annihilation of the dislocations of opposite sign. In such cases the ML appears not only along the line of annihilation, but also in the surrounding regions. The similarity between ML and TL spectra of γ-irradiated KCl crystals supports the thermal origin of ML (Ausin and Alvarez 1972).

4.2 *Effects of pressure and temperature on* ML *excitation*

Let N_1, N_2, N_3, N_n be the number of dislocations created during the first, second, third and nth application of the pressure. The total number, N_{T_n} of newly created dislocations up to the nth pressing may be given by

$$N_{T_n} = N_1 + N_2 + N_3 + \ldots N_n \tag{4}$$

Assuming that the number of new created dislocations decreases exponentially with increasing number of application of pressure, the above equation may be written as

$$\begin{aligned} N_{T_n} &= N_1 + N_1 e^{-\alpha} + N_1 e^{-2\alpha} + \ldots N_1 \exp\,[-(n-1)\,\alpha], \\ &= N_1\,(1 - e^{-n\alpha}) \,/\, (1 - e^{-\alpha}) \\ &= N_0\,(1 - e^{-n\alpha}) \end{aligned} \tag{5}$$

where $N_0 = N_1 \,/\, (1 - e^{-\alpha})$ and α is a constant.

The number N_n^p of the newly created dislocations during the nth pressing may be given by

$$N_n^p = N_1^p \exp\,[-(n_p - 1)\,\alpha] \tag{6}$$

where N_1^p is the number of new created dislocations during the first pressing. This result agrees with our dislocation density measurements (Chandra *et al* 1982). When pressure is applied on a crystal, mobile dislocations are produced. Some of these dislocations disappear due to annihilation. The other mobile dislocations relax and become stationary. Thus the density of dislocations increases in the crystal when pressure is applied. The ML intensity measured in terms of the deflection of the ballistic galvanometer is linearly related to the number N of the newly created dislocations. This may be expressed as

$$\int I\,\mathrm{d}t = C\,N,$$

or
$$\int (\mathrm{d}n/\mathrm{d}t)\,\mathrm{d}t = n = C\,N, \tag{7}$$

where n is the number of excited luminescence centres and C is a constant. The linear relation between ML intensity (measured by a $X - Y$ recorder) and the strain rate (Alzetta *et al* 1970) suggests that the excitation rate of the luminescence centres is directly related to dislocation. This is in accord with (7).

If the dislocation annihilation model is the dominant process for the ML excitation in x and γ-irradiated alkali halide crystals, then (7) indicates that the annihilation rate (which is responsible for dn/dt) should be directly proportional to the mobile dislocations. This is because the number of dislocations responsible for the annihilations may be a fraction of the number of mobile dislocations. Thus, the intensity I_n^p of ML (monitored by the deflection of ballistic galvanometer) produced during the nth pressing may be expressed as

$$I_n^p = \eta N_1 \exp [-(n_p - 1)]\rho \tag{8}$$

where η is a factor related to the ML efficiency of the crystal, and ρ is the density of the colour centres which decreases with mechanical deformation of crystals (Butler 1966; Senchukov and Shmurak 1970). To simplify the problem, let us assume that the density of the colour centres decreases exponentially with the number of pressings, *i.e.*, it holds a relation

$$\rho_n^p = \rho_0 \exp (-\alpha_1 n_p), \tag{9}$$

where ρ_0 and ρ_n^p are the density of the colour centres without pressings and after nth pressings of the crystal respectively, and α_1 is a constant.

From (8) and (9), I_n^p may be written as

$$I_n^p = \eta N_1 \exp [-\alpha(n_p - 1)] \rho_0 \exp [-\alpha_1 (n_p - 1)],$$

or $$I_n^p = \eta \rho_0 N_1 \exp [-(\alpha + \alpha_1)(n_p - 1)],$$

or $$I_n^p = I_1^p \exp [-\beta(n_p - 1)], \tag{10}$$

where $I_1^p = \eta N_1 \rho_0$ is the ML intensity in the first pressing.

It is observed that the plot of log I_n^p *vs* $(n_p - 1)$ is a straight line with a negative slope, which supports (10). The value of β estimated from the plot of log I_n^p *vs* $(n_p - 1)$ is nearly equal to the value of the slope α estimated from the plot of log N_n^p *vs* $(n_p - 1)$ (for the same stress) (Chandra *et al* 1982). It seems that the decrease in the ML intensity with the number of pressings, is primarily due to the decreased creation of limited new dislocations with successive number of pressings. The decrease in the density of colour centres with the number of pressings, is only slightly responsible for the decrease in the ML intensity with the number of pressings.

The ML intensity increases with increasing values of pressure and irradiation time can be understood from (10). I_1^p is also related directly to N_1^p, the number of newly created dislocations in the first pressing. Thus, the intensity will be greater for increased values of pressure (Akulov 1964, Schoeck 1956). I_1^p is also related directly to the density of the colour centres in the crystals, and therefore, the ML intensity may increase with increase in the irradiation time of the crystals. It will get saturated for a longer time of irradiation.

If it is assumed that the ML produced during the pressure release is related to the ML produced during the corresponding number of applications of the pressure, then, from (10), the ML intensity during the nth release of the pressure may be given by

$$I_n^r = I_1^r \exp [-\beta_1 (n_r - 1)], \tag{11}$$

where β_1 is a constant. For a given pressure, β is always greater than β_1. The ML emission during the pressure release is related to the number of new traps produced during the deformation of crystal. The number of shallow traps may increase with crystal deformation, which in turn may increase the probability of the ML emission during pressure release. Thus β may be higher as compared to β_1.

It was found that β value decreases with increasing pressure value. This may be due to the plastic deformation in different stress-strain regions of the crystals, where the plastic behaviour may be different.

Since the probability of exciting an electron from the colour centres to the conduction band depends on the thermal spike rather than on the average temperature of the crystals, the smaller variation of the ML intensity with the temperature is expected. It has been described earlier that the ML intensity of γ-irradiated KCl crystals increases with their temperature, and follows the relation

$$I_T \times A_{TL} / A_{TL} - \int_{T_0}^{T} I_{TL}\, dT = A_0 \exp(-E_0 / kT) \qquad (12)$$

The E_0 value estimated from ML measurements is 0·25 eV for γ-irradiated KCl crystals. It is known that the number of newly created dislocations for a given value of the applied stress increases with the temperature of the crystals (Akulov 1964; Schoeck 1956). It appears that the increase of ML intensity with temperature (after normalization for the decrease in density of the colour centres with temperature) is due to increase in the number of newly created dislocations. Thus, the factor E_0, should be related to the activation energy for the increase in the number of dislocations with the temperature of the crystals.

The ratio of I_n^r/I_n^p decreases with increasing temperature of the crystals. The number of retrapped electrons may decrease with increasing temperature of the crystals. Since I_n^r is mainly related to the number of re-trapped electrons, its decrease with temperature is expected.

The factor β is related to the rate constant of the decrease in the number of newly created dislocations with the number of application of the pressure. The increase in β and β_1 values with increasing temperature may be due to the change in the stress-strain behaviour with the temperature of the crystals.

Because the ML in coloured alkali halide crystals occur during their plastic deforformation, the ML may have great potential for dynamic studies of dislocation interaction. The ML may provide a self-excited luminescence probe for the propagation of dislocation and may complement the techniques of defect luminescence where ultraviolet or cathode ray excitation can cause luminescence from defects formed at the onset of plastic deformation (Chandra *et al* 1975; Velendnilakaya *et al* 1975; Melton *et al* 1980).

Acknowledgements

The authors wish to thank Dr P R Khandekar for constant encouragement and Prof. J I Zink of the University of California for providing the facilities for some measurements.

References

Alzetta G, Chudacek I and Scarmozzino 1970 *Phys. Status Solidi* **A1** 775
Akulov N S 1964 *Dislocations and plasticity* (Delhi: Rajkamal Prakashan) p. 39
Ausin V and Alvarez J L 1972 *Phys. Rev.* **B6** 4828
Ausin V and Alvarez J L 1972 *J. Phys.* **5** 82
Butler C T 1966 *Phys. Rev.* **141** 750
Chandra B P 1981 *Phys. Status Solidi* **A64** 395
Chandra B P and Elyas M 1977 *Indian J. Pure Appl. Phys.* **15** 744
Chandra B P and Elyas M 1979 *J. Phys.* **C 12** 1695
Chandra B P and Zink J I 1980a *Phys. Rev.* **B21** 816
Chandra B P and Zink J I 1980b *J. Chem. Phys.* **73** 5933
Chandra B P, Elyas M and Majumdar B 1982 *Solid State Commun.* **42** 753
Chen Y, Abraham M M, Turner T J and Nelson C M 1975 *Philos. Mag.* **32** 99
Elyas M, Chandra B P and Kathuria S P 1983 *Radiation Effects* **70** 147
Grabec I 1974 *Polym. Phys. Lett.* **12** 573
Hardy G E, Kaska W C, Chandra B P and Zink J I 1981 *J. Am. Chem. Soc.* **103** 1074
Hardy G E and Zink J I 1976 *Inorg. Chem* **15** 3061
Jain S C and Mahendru P C 1965 *Phys. Rev.* **A140** 957
Metz F I, Schweinger R N, Leider H R and Girifalco 1957 *J. Phys. Chem.* **61** 86
Melton R, Danieley N and Turner T J 1980 *Phys. Status Solidi* (*A*) **57** 755
Naidu S M P 1970 *Study of crystal growth technique from melt under different conditions* Ph. D. thesis, Jabalpur University
Senchukov F D and Shmurak S Z 1970 *Fig. Tuerradogo. Tella* (*USSR*) **12** 9
Schoeck G 1956 *Adv. Appl. Mech.* **4** 229
Setz F 1952 *Adv. Phys.* **1** 43
Velendnilakaya M A, Razhansku V N, Comdova, Saparin G V, Schreiber J and Brummer O 1975 *Phys. Status Solidi* **A32** 123
Walton A J 1977 *Adv. Phys.* **26** 887

Pramāṇa, Vol. 21, No. 3, September 1983, pp. 171–182. © Printed in India.

A mean-field, effective medium theory of random binary alloys III. The Ising model with competing interactions

A MOOKERJEE and S B ROY
Department of Physics, Indian Institute of Technology, Kanpur 208 016, India

MS received 27 January 1983; revised 16 August 1983

Abstract. The Ising model with competing interactions is studied in a mean field effective medium approach. The phase diagram of such model alloys is studied. We conclude that for all ratios of the competing interaction moments, a spin glass phase always exists at low temperatures for certain concentration regimes.

Keywords. Random magnetic alloys; spin glasses; Ising model, competing interactions.

1. Introduction

The phases of the quenched random alloy systems one of whose components is magnetic (the so-called spin glass alloys) have been studied in great detail (Edwards and Anderson 1975; Plefka 1976; Kaneyoshi 1976; Morita and Horiguchi 1976; Mookerjee 1978, 1979). At the origin of the spin glass phase, which all of these alloys show at low temperatures and low concentrations of the magnetic constituent, is the fluctuating RKKY interaction. Focus on binary and ternary alloys all of whose constituents are magnetic began about the same time (Matsubara 1974; Katsura and Matsubara 1974; Aharony 1975, 1978; Luttinger 1976; Eggarter and Eggarter 1977; Oguchi and Ueno 1979; Katsura *et al* 1979; Medvedev and Zaborov 1982a, b). Here the dominant interaction is the short-ranged direct exchange. The sign of this interaction is governed by the type of atoms occupying the two neighbouring sites. These interactions could thus compete with one another, having random signs, and a spin glass phase may occur in a concentration range where there is a transition from a ferromagnetic low temperature phase to an antiferromagnetic one. There are ample experimental evidences of the spin glass phase in these alloys. Menshikov *et al* (1981) have shown, in the experimental phase diagram spin glass and mixed phases in γ-FeNiCr alloys. γ-FeNiMn alloys with a high iron concentration have a state very similar to that of amorphous magnets, characterised by a developed short-ranged ferro- and antiferromagnetic ordering which changes to a long-ranged antiferromagnetic at a higher and a long ranged ferromagnetic at a lower iron concentrations (Menshikov and Teplykh 1977). In a FeNi binary alloy with 70·3% Fe, a drop in the magnetisation and asymmetrically placed hysteresis loop about the origin was observed by Rode *et al* (1975) at low temperatures. This behaviour is peculiar to spin glass phases. In CrFe (Shull and Beck 1974) between 15 to 20 at % Fe 'micto-

magnetic' behaviour has been observed. Aitken *et al* (1982) have found spin glass behaviour with a susceptibility cusp at 8°K in a NiMn alloy with 26% Mn. They also report displaced hysteresis loops at 4°K in NiMn (22% Mn) in field cooling experiments. Low temperature critical neutron scattering in NiMn suggests that there may be spin glass type behaviour in certain concentration regions (Kuzmin and Menshikov 1979). But the spin glass type behaviour revealed in the alloy systems mentioned above may not be exactly identical to the canonical spin glasses (AuFe). In fact, Menshikov *et al* (1981) in explaining their experimental phase diagrams of γ-FeNiMn mentioned about the existence of non-collinear ferromagnets or more generally a mixed phase. In an earlier work (Mookerjee 1979) on canonical spin glasses, the probable existence of such non-collinear or randomly-canted phases was also indicated.

In this paper we report the phases of such binary systems with mixed interactions. We shall adopt the mean-field, effective medium approach of Mookerjee (1978, 1979). We do not consider a homogeneous, but a species-dependent local magnetisation and local field distribution. Some of the complicated interpenetrating sublattice ideas introduced by Katsura *et al* (1979) and Medvedev and Zaborov (1982a) are seen not to be essential to the physical understanding of the phases. The phase diagram obtained is qualitative similar to the studied mentioned above, but there are minor but not unimportant differences which we shall point out subsequently. It is also argued that our results are more in keeping with physical interpretation of the known experimental data.

2. The local internal field

We first consider a random Ising model where

$$H = -\tfrac{1}{2} \sum_{k \neq j} \sum J(|\mathbf{r}_k - \mathbf{r}_j|)\, S_k\, S_j;$$

here J is the direct exchange interaction, decaying fast with $|\mathbf{r}_k - \mathbf{r}_j|$. It is unnecessary to assume that J is nearest neighbour alone, that can be incorporated as a special case. However, J is random and depends upon the atoms at the sites $\mathbf{r}_k$ and $\mathbf{r}_j$. In the binary alloy AB, it can take three values J_{AA}, J_{AB} and J_{BB}.

The free energy is

$$F = \tfrac{1}{2}\Big[\sum_{ij \in AA} \sum J^{AA}\, \sigma_i^A\, \sigma_j^A + \sum_{ij \in AB} \sum J_{ij}^{AB}\, (\sigma_i^A\, \sigma_j^B + \sigma_i^B\, \sigma_j^A)$$

$$+ \sum_{ij \in BB} \sum J_{ij}^{BB}\, \sigma_i^B\, \sigma_j^B\Big] - k_B T \Big(\sum_{i \in A} \ln \cosh\,(\beta h_i^A)$$

$$+ \sum_{i \in B} \ln \cosh\,(\beta h_i^B)\Big)\Big]; \qquad (1)$$

here σ_i are the random local magnetisations $\langle S_i \rangle$ taking the values σ_i^A or σ_i^B depending whether the site r_i has an A or B atom. While the stable phases are found by minimising the free energy with respect to the local magnetisations. This yields a set of equations

$$\left.\begin{aligned} \sum J_{ik}^{AA} [\sigma_i^A - \tanh\ (\beta h_i^A)] + \sum J_{ik}^{AB} [\sigma_i^B - \tanh\ (\beta h_i^B)] = 0, \\ \sum J_{ik}^{AB} [\sigma_i^A - \tanh\ (\beta h_i^A)] + \sum J_{ik}^{BB} [\sigma_i^B - \tanh\ (\beta h_i^B)] = 0, \end{aligned}\right\} \tag{2}$$

since the J's are independent, this leads to

$$\sigma_i^A = \tanh\ (\beta h_i^A) \text{ and } \sigma_i^B = \tanh\ (\beta h_i^B). \tag{3}$$

While

$$h_i^A = \sum_j J_{ij}^{AA}\, \sigma_j^A + \sum_j J_{ij}^{AB}\, \sigma_j^B \text{ and } h_i^B = \sum_j J_{ij}^{BA}\, \sigma_j^A + \sum_j J_{ij}^{BB}\, \sigma_j^B, \tag{4}$$

are the random 'local' internal mean fields.

Unlike the canonical spin glass alloys (Mookerjee 1978, 1979), the probability density of the local internal field depends upon whether the site is occupied by a A or a B atom. The correspondence is $h_i^B = \sigma_i^B = 0$, if the atom B is nonmagnetic.

We shall now proceed to evaluate the conditional probability density $P_A(h_i^A)$ of the local internal field at $\mathbf{r}_i$, provided the site is occupied by an A atom. $P_B(h_i^B)$ follows in an exactly similar manner

$$P_A\,(h_i^A) = \sum_{\mathbf{r}_1 \ldots} \sum_{\mathbf{r}_{N-1}} \Pr\,(\mathbf{r}_1 \ldots \mathbf{r}_{N-1})\, \delta\,[h_i^A - \sum_j J\,(|\,\mathbf{r}_i - \mathbf{r}_j\,|)\, \sigma_j].$$

We assume first that there is no clustering or chemical correlations so that any atom can occupy any site with equal probability. The site $\mathbf{r}_i$ is occupied by an A atom, while the remaining $N-1$ atoms of which $N_1 - 1$ are A and $N_2 = N - N_1$ are B are distributed among the remaining $N-1$ sites. In the thermodynamic limit $N_1 - 1/N \to c_A$ and $N_2/N \to c_B$ the respective concentrations of the A and B constituents.

$$P_A\,(h_i^A) = (\tfrac{1}{2}\pi) \int \mathrm{d}k \exp\,[ikh_i^A] \sum_{\mathbf{r}_1 \ldots \mathbf{r}_{N-1}} \sum (1/N-1)^{N_1+N_2-1}$$

$$\int \ldots \int \prod_{j \in A} \mathrm{d}h_j^A\, \delta\Big[h_j^A - \sum J_{ij}^{AA}\, \sigma_j^A - \sum J_{ij}^{AB}\, \sigma_j^B\Big] \prod_{j \in B} \mathrm{d}h_j^B$$

$$\delta\left[h_j^B - \sum J_{ij}^{AB}\, \sigma_j^B - \sum J_{ij}^{BB}\, \sigma_j^B\right] \times$$

$$\exp\left[-\,i\,k\left(\sum J_{ij}^{AA} f(h_j^A) + \sum J_{ij}^{AB} f(h_j^B)\right)\right], \tag{5}$$

where $f(x)=\tanh(\beta x)$. We now replace the δ functions by their configuration averages (Klein 1968; Mookerjee 1978) so that the product term in (5) reduces to

$$\prod_{j \in \alpha,\ \alpha = A, B} P_\alpha (h_i^\alpha).$$

A little algebra then yields

$$P_A (h_i^A)=(\tfrac{1}{2}\pi) \int \mathrm{d}k \exp (ikh_i^A) [1-F_1 (k)/(N-1)]^{N_1-1} [1-F_2(k)/(N-1)]^{N_2}$$

where
$$F_1 (k) = \sum \int_{\mathbf{r}} \mathrm{d}h_j^A P_A (h_j^A)[1 - \exp \{- ikJ_{ij}^{AA} f(h_j^A)\}],$$

$$F_2 (k) = \sum \int_{\mathbf{r}} \mathrm{d}h_j^B P_B (h_j^B)[1 - \exp \{- ikJ_{ij}^{AB} f(h_j^B)\}]. \tag{6}$$

In the thermodynamic limit,

$$P_A (h_i^A) = (1/2\pi) \int \mathrm{d}k \exp [ikh_i^A - (c_A F_1 + c_B F_2)].$$

This is a complicated nonlinear integral equation. However, in case the spatial moments $I_{\alpha\alpha'}^{(n)}=\sum_R [J^{\alpha\alpha'}(R)]^n$ decrease rapidly with n, we may expand the exponentials in the F's and neglect all I_n $n \geqslant 3$. The integral then can be exactly carried through. Mookerjee (1978) showed the validity of this procedure for the RKKY interaction, and a very similar argument can also be carried out for any interaction falling as R^{-m}, $m > 3$. In any situation, if I_3, I_4 etc are not negligible then we may estimate all the moments of the distribution. Instead of having the simple Gaussian form, as shown subsequently, we shall have a distribution with skewness and kurtosis.

This yields

$$P_A (h_i^A) = (2\pi J_1^{A^2})^{-1/2} \exp [- (h_i^A - J_0^A)^2/(2J_1^{A^2}) \tag{7}$$

where
$$J_0^A = c_A m_A \sum_R J^{AA} (R) + c_B m_B \sum_R J^{AB} (R),$$

$$J_1^{A^2} = c_A q_A \sum_R J^{AA^2} (R) + c_B q_B \sum_R J^{AB^2} (R),$$

where $m_\alpha=[\sigma_i^\alpha]$ and $q_\alpha=[\sigma_i^{\alpha 2}]$ $\alpha=A$ or B, are the configuration-averaged Edwards-Anderson type order parameters for the A and B type of atoms. Similarly we may obtain:

$$P_B (h_i^B) = (2\pi J_1^{B^2})^{-1/2} \exp [- (h_i^B - J_0^B)^2/(2J_i^{B^2}). \tag{8}$$

The J_0^B and $J_i^{B^2}$ are defined as before replacing A by B at $\mathbf{r}_i$. From (4), (7) and (8) we obtain the equations for the order parameters

$$m_A = (2\pi)^{-1/2} \int dz \exp(-1/2\, z^2) \tanh \beta\, [(T_{11} m_A + T_{12} m_B) + (T_{g1}^2 q_A + T_{g2}^2 q_B)^{1/2} z],$$

$$m_B = (2\pi)^{-1/2} \int dz \exp(-1/2 z^2) \tanh \beta\, [(T_{21} m_A) + (T_{22} m_B) + (T_{g3}^2 q_A + T_{g4}^2 q_B)^{1/2} z],$$

$$q_A = (2\pi)^{-1/2} \int dz \exp(-1/2 z^2) \tanh^2 \beta\, [(T_{11} m_A + T_{12} m_B) + (T_{g1}^2 q_A + T_{g2}^2 q_B)^{1/2} z],$$

$$q_B = (2\pi)^{-1/2} \int dz \exp(-1/2 z^2) \tanh^2 \beta\, [(T_{21} m_A + T_{22} m_B) + (T_{g3}^2 q_A + T_{g4}^2 q_B)^{1/2} z], \tag{9}$$

where $k_B T_{\alpha\alpha'} = c_{\alpha'} \sum_R J^{\alpha\alpha'}(R)$ with $\alpha\alpha' = 1$ for A, and 2 for B

and $k_B^2 T_{gn}^2 = c_\alpha \sum_R J^{\alpha'\alpha''}(R)^2$ with $n = 1 = \alpha \in A$, $\alpha'\alpha'' \in AA$,

$n = 2 = \alpha \in B$, $\alpha'\alpha'' \in AB$,

$n = 3 = \alpha \in A$, $\alpha'\alpha'' \in BA$,

$n = 4 = \alpha \in B$, $\alpha'\alpha'' \in BB$.

3. The phase diagram

Equations (9) form the basis of our analysis of the phases. To start with we study the paramagnetic phase boundary. Near the vicinity of this all the four quantities m_A, m_B, q_A and q_B are small, so that we may expand the $\tanh(x)$ and $\tanh^2(x)$ functions in the integrand carry out the Gaussian integrals. This converts the complicated integral equations to tractable algebraic ones.

$$m_A = \frac{1}{T}(T_{11} m_A + T_{12} m_B) - (1/3T^3)(T_{11} m_A + T_{12} M_B)^3 - \frac{1}{T^3}(T_{11} M_A + T_{12} m_B)(T_{g1}^2 q_A + T_{g2}^2 q_B),$$

$$m_B = \frac{1}{T}(T_{21}\, m_A + T_{22}\, m_B) - (1/3T^3)\,(T_{21}\, m_A + T_{22}\, m_B)^3$$

$$- \frac{1}{T^3}(T_{21}\, m_A + T_{22}\, m_B)\,(T_{g3}^2 q_A + T_{g4}^2 q_B),$$

$$q_A = \frac{1}{T^2}(T_{g1}^2 q_A + T_{g2}^2 q_B) + \frac{1}{T^2}(T_{11}\, m_A + T_{12}\, m_B)^2,$$

$$q_B = \frac{1}{T^2}(T_{g3}^2 q_A + T_{g4}^2 q_B) + \frac{1}{T^2}(T_{21}\, m_A + T_{22}\, m_B)^2. \qquad (10)$$

The above equations contain, as their possible solutions, an inhomogeneous situation where the A and B sublattices order at different temperatures. Such situations were also inherent in the earlier work of Katsura *et al* (1979). In such cases complex situations where the A and B sublattices order differently: *e.g.* the A atoms order ferromagnetically while the B atoms antiferromagnetically. In ordered crystalline alloys this is a possibility. However, in the random alloys under study all experimental evidence points to unique Curie, Neel or spin glass temperatures, where the entire system orders in a particular way. The experimentally measured magnetisation is a bulk average $m = c_A m_A + c_B m_B$ and it is this which is the relevant order parameter. Moreover as this magnetisation vanishes at a unique Curie temperature T_c, we should seek solutions of the type

$$m_B = \eta\,(T, c)\, m_A \text{ and } q_B = \mu\,(T, c)\, q_A.$$

With this substitution, the set of equations (10) provide four equations for the four unknowns m_A, q_A, η and μ. A possible solution is $m_A = q_A = 0$ $(= m_B = q_B = 0)$. This corresponds to the paramagnetic phase. The non-zero solution for m_A is given by

$$m_A^2 = [3T^3(T^2 - T_{g1}^2 - \mu T_{g2}^2)/(3T^2 - 2T_{g1}^2 - 2\mu T_{g2}^2)]\; [(T - T_{11} - \eta T_{12})\,/$$

$$T(T_{11} + \eta T_{12})^3]$$

$$= [3T^3(\mu T^2 - \mu T_{g4}^2 - T_{g3}^2)/(3\mu T^2 - 2T_{g3}^2 - 2\mu T_{g4}^2]$$

$$[(\eta T - T_{21} - \eta T_{22})/T(T_{21} + \eta T_{22})^3]$$

Suppose that at T_c, $\eta = \eta_c$ and $\mu = \mu_c$, then T_c is that temperature at which this other solution vanishes. The above expressions may vanish if either of the two terms in the square brackets vanish. We shall later show that the vanishing of the first term occurs in those concentration ranges where we have a paramagnetic to a spin glass transition. In those regimes where $T_c > T_g$, these terms remain positive. Thus the equation for T_c is obtained from

$$T_c - T_{11} - \eta_c T_{12} = \eta_c T_c - T_{21} - \eta_c T_{22} = 0$$

Since $q_A = \beta^2(T_{11} + \eta T_{12})^2 m_A^2/(1 - \beta^2(T_{g1}^2 + \mu T_{g2}^2)]$ q_B also vanishes at the paramagnetic boundary. The above equation yields

$$T_c = \tfrac{1}{2}(T_{11} + T_{22}) \pm \tfrac{1}{2}\,[(T_{11} - T_{22})^2 + 4T_{12}T_{21}]^{1/2}.$$

If $T_{12}T_{21} - T_{11}T_{22} > 0$, then one of the above roots is positive and the other negative. The positive root gives the physical Curie temperature. For the nearest neighbour interaction we can show that the negative root is the negative of the Neel temperature. This can be easily seen if we rewrite the Hamiltonian in terms of the staggered spins $H = \tfrac{1}{2}\Sigma - J(R_{ij})\hat{S}_i\,\hat{S}_j$. For nearest neighbour interaction each $J_0 = ZJ$ is replaced by $-J_0 = -ZJ$ and the expression for T_N is $T_N = -\tfrac{1}{2}(T_{22} + T_{11}) \mp \tfrac{1}{2}\,[(T_{22} - T_{11})^2 + 4T_{21}\,T_{12}]^{1/2}$. The positive root of this has exactly the same magnitude as the negative root of T_c. For longer ranged forces, the T_N obtained from the negative root of T_c is not the Neel temperature and T_N has to be calculated from the Hamiltonian expressed in terms of the staggered magnetisation in a similar way.

In case $T_{12}T_{21} - T_{11}T_{22} < 0$, there is no negative root. The lower positive root has no physical significance and there is no antiferromagnetic regime.

For the spin glass boundary we must have $m_A = 0$, but $q_A \neq 0$. Such solutions are possible provided

$$T_g^2 - (T_{g1}^2 + \mu_g T_{g2}^2) = T_g^2\mu_g - T_{g3}^2 - \mu_g T_{g4}^2 = 0,$$

so that $$T_g^2 = \tfrac{1}{2}(T_{g1}^2 + T_{g4}^2) \pm \tfrac{1}{2}\,[(T_{g1}^2 - T_{g4}^2)^2 + 4T_{g2}^2T_{g3}^2]^{1/2}.$$

For the spin glass transition only the greater positive root has any significance. A spin glass transition from the paramagnetic phase will be observed only in those regions where the T_g lies above T_c or T_N. In the regions where this is not so the spin glass temperature T_g has no physical significance, as the small q expansion itself becomes invalid.

In another regime, *i.e.* $T=0$, equations (9) also reduce to soluble algebraic equation. $\tanh(x) \to 2H(x) - 1$ where $H(x)$ is the Heaviside step function, so that

$$m_A = \phi\,[(T_{11} + \eta T_{12})\,m_A/(\sqrt{2}(T_{g1}^2 + T_{g2}^2)^{1/2}],\ q_A = 1, \tag{13}$$

$$\eta m_A = \phi\,[(T_{21} + \eta T_{22})\,m_A/\sqrt{2}(T_{g3}^2 + T_{g4}^2)^{1/2}],\ \mu = 1,$$

where $\phi(x)$ is the error integral function. Equation (13) assume even simpler form in the neighbourhood of the spin-glass-ferromagnetic transition where m_A is small and $\phi(x) = (\sqrt{2/\pi})\,x \exp(-x^2)$. Using this expansion for small m_A we obtain one root $m_A = 0$, this is relevant to the spin glass phase. Another non-zero solution

$$m_A^2 = [(a_1 + \eta a_2) - \sqrt{\tfrac{1}{2}\pi}]/[\sqrt{\tfrac{1}{2}\pi}\,(a_1 + \eta a_2)^2] = [(a_3 + \eta a_4)$$

$$- \eta\sqrt{\pi/2}\ /\ \sqrt{\pi/2}\,(a_3 + \eta a_4)^2].$$

At the spin-glass, ferromagnetic boundary this second solution vanishes. This leads to an equation for the critical concentration after elimination of η:

$$F(c_0) = (\sqrt{\tfrac{1}{2}\pi} - a_1)(\sqrt{\tfrac{1}{2}\pi} - a_4) - a_2 a_3 = 0, \tag{14}$$

$$a_1 = T_{11}/[2(T_{g1}^2 + T_{g2}^2)^{1/2}],\ a_2 = T_{12}/[2(T_{g1}^2 + T_{g2}^2)^{1/2}],\ a_3 = T_{21}/[2(T_{g3}^2 + T_{g4}^2)]^{1/2},$$

and $$a_4 = T_{22}/[2(T_{g3}^2 + T_{g4}^2)]^{1/2}$$

At $c_A = 1$, $F(c) > 0$ and $m_A \neq 0$, this is expected since we do expect a ferromagnetic low temperature phase for the pure ferromagnetic A constituent ($J_{AA} > 0$. However, for different values of the three couplings J_{AA}, J_{AB} and J_{BB} (14) provides a simple equation for the determination of c_0.

In the nearest neighbour interaction case the determination of the spin-glass antiferromagnetic boundary is exactly similar to the above and we have to replace the $J_{aa'}$, by $-J_{aa'}$.

In the remainder of the c-T plane we cannot obtain such simple solutions, but knowing the solutions at the paramagnetic boundary and the $T=0$ line, we may iteratively solve the integral equations (9) and fill out the phase diagram.

4. Results and discussion

We display two model cases: a symmetric one with $J_{AA}=1$, $J_{AB}=0{\cdot}8$ and $J_{BB}=-1$ (in arbitrary units, $k_B=1$) and a asymmetric case with $J_{AA}=1$, $J_{AB}=2$, $J_{BB}=-6$. In each of the cases we take three possible ratios $K_{aa'}/J_{aa'}=0{\cdot}65$, $0{\cdot}75$ and $0{\cdot}8$ [$J_{aa'} = \sum_R J(R)^{aa'}$ and $K_{aa'}^2 = \sum_R J^2(R)^{aa'}$]. The phase diagrams are displayed in figures 1 to 3.

Let us first discuss the symmetric case, and compare the phase diagram of a similar case discussed by Katsura *et al* (1979). Qualitatively the two are very much a like. However, there are several differences. In our case the paramagnetic-spin glass phase boundary *i.e.* $T_g(c)$ is dependent on the ratio K/J. This is to be expected, since the K's determine the spread in the distribution of the internal field, which is finally responsible for the spin glass phase. For the ratios $0{\cdot}8$ and $0{\cdot}75$ in a concentration range around $c=0{\cdot}5$ this curve lies above either the para-ferro boundary $T_c(c)$ or the para-antiferro boundary $T_N(c)$. In both these cases, therefore, there is a possibility of transition from the paramagnetic to the spin glass phase at these concentrations. For the ratio $0{\cdot}65$ (and all smaller ratios) the $T_g(c)$ lies totally below the $T_c(c)$ and $T_N(c)$ curves, and therefore we do not expect a direct transition from the para to the spin glass phase. This is to be compared with figure 1 (b) of Katsura, where the ratio is apparently $0{\cdot}5$. Here too, the spin glass boundary lies below T_c and T_N, but it appears to be independent of c. Moreover, Katsura's T_c, T_N curves when extrapolated do not pass through 0 and 1, an exact feature of our solutions (11) and (12).

In such a case the question arises: is there a spin glass transition? Katsura's answer seems to be that the spin-glass phase is not realised. However, if one examines the

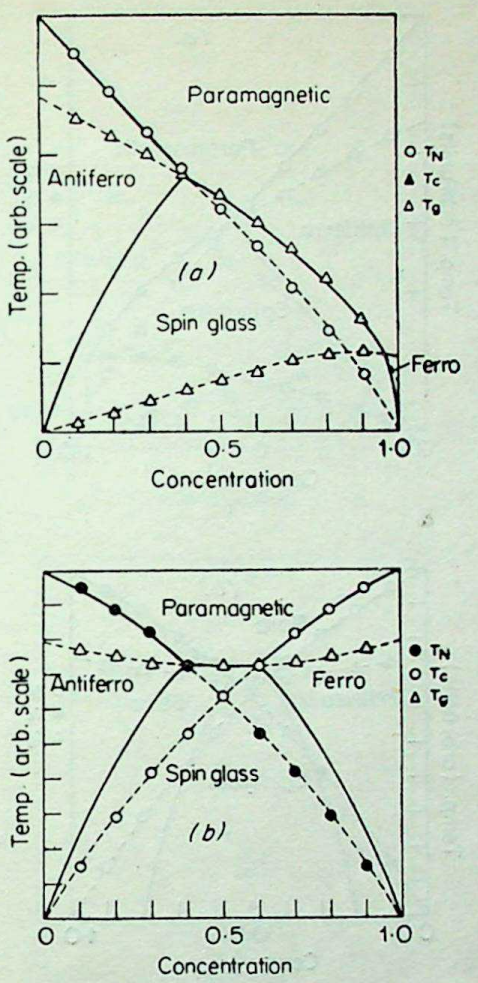

Figure 1. Phase diagram for k/J ratio 0·8 (a) $J_{AA}=1$, $J_{AB}=2$, $J_{BB}=-6$ (b) $J_{AA}=1$, $J_{AB}=0{\cdot}8$, $J_{BB}=-1$.

$T=0$ solutions, we see that in the concentration region between $c=0{\cdot}44$ and $0{\cdot}56$ the only possible solution is a spin glass with $q=1$, $m=0$. We can therefore surmise that at low temperatures in these concentration regime there is a spin glass region. Its upper boundary is not the curve $T_g(c)$, as at the actual boundary q will not be small and the approximations involved in deducing T_g will be invalid. However, this boundary may be found from the numerical solutions of (9). We may thus have a transition from a ferromagnetic to a glassy phase as we lower the temperature at these concentrations. There are several experimental evidences of such transitions (Mookerjee and Roy 1983).

For the ratio 0·8, no long-ranged ordered solution is possible at $T=0$, except at $c=0$ and 1. Thus the spin glass phase occupies the entire concentration regime at low temperatures.

Note that if instead of the approximations taken at $T=0$, we had done a numerical solution at $T=0$, the spin glass phase would still occupy a very large portion of the concentration range. A preliminary work done subsequently indicates that at $T=0$ spin glass phase spreads over $c_1<c<c_2$, where $c_2\sim0{\cdot}9$ and $c_1\sim0{\cdot}1$ for $k/J=0{\cdot}8$. A similar situation was reported by Medvedev.

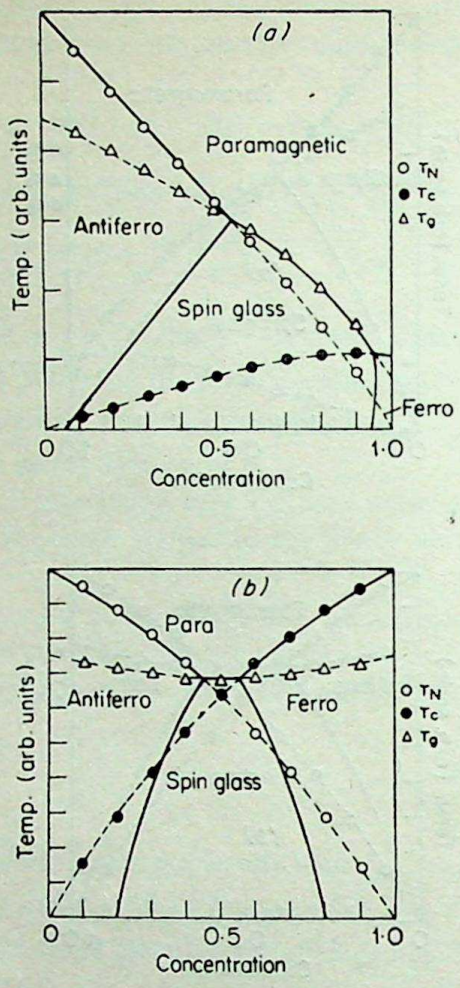

Figure 2. Phase diagram for the k/J ratio 0·75 (a) $J_{AA} = 1$, $J_{AB} = 2$, $J_{BB} = -6$ (b) $J_{AA} = 1$, $J_{AB} = 0{\cdot}8$, $J_{BB} = -1$.

The physical reason behind this may be the following: what really drives the break down of the ferro (or antiferro) magnetic phases and transition to a spin glass phase, even for very small concentrations of the B (or A) atom is the large spread of the distribution of the local molecular field. The spread or standard deviation of the local molecular field is measured by K and the mean by J, so for ratios $K/J \sim 1$, the spread is large compared with the mean, and large deviations away from the mean are probable. This may be responsible for the large spread of the spin glass phase. However, in any realistic systems such large ratios may not be realisable (e.g. RKKY simple cubic case quoted in paper I, $K/J \simeq 0{\cdot}08$ and nearest neighbour simple cubic $K/J = 0{\cdot}4$ so that the question may remain academic or mathematical one.

The asymmetric case does not provide any new features other than the ones already described, although the shapes of the boundaries are quite different.

From the qualitative similarity of the phase diagrams with that of Katsura's it is obvious that corrections to the simple mean field (e.g. Bethe approximation) will not yield any essentially new feature.

We have thus examined the phases of a random Ising model with competing interactions. We assert that a spin glass phase always exists, definitely at low temperatures

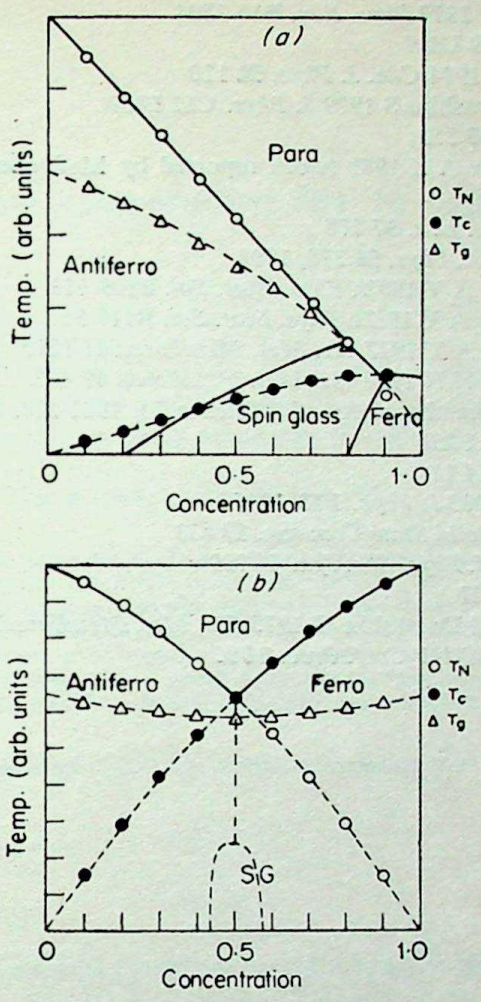

Figure 3. Phase diagram for the k/J ratio 0·65 (*a*) $J_{AA} = 1$, $J_{AB} = 2$, $J_{BB} = -6$ (b) $J_{AA} = 1$, $J_{AB} = 0{\cdot}8$, $J_{BB} = -1$.

for some concentration range; although a direct transition from a paramagnetic to the glass phase may not always be possible. This is at variance with some earlier studies (Katsura *et al* 1979), who maintain that a glassy phase is only possible for particular ratios of J_{AA}, J_{AB} and J_{BB}. Generalisation to the Heisenberg model will not only involve replacing $\tanh(x)$ by the Brillouin functions $B_S(x)$, but will also introduce instead of one glass order parameter q, two parameters $q_{\|}$ and $q_{\perp}$. We shall study the Heisenberg model in a further communication and elaborate more on the mixed phase reported by many experimentalists (Eggarter and Eggarter 1977; Mookerjee and Roy 1982).

References

Aharony A 1975 *Phys. Rev. Lett.* **34** 590
Aharony A 1978 *J. Magn. Mater.* **7** 198
Aitken R G, Cheung T D and Kouvel J S 1982 *J. Appl. Phys.* **53** 2239
Edwards S F and Anderson P W 1975 *J. Phys.* **F5** 965

Eggarter E and Eggarter T P 1977 *Phys. Rev.* **B15** 3804
Kaneyoshi T 1976 *J. Phys.* **C9** L289
Katsura S and Matsubara F 1974 *Can. J. Phys.* **52** 120
Katsura S, Fujiki S and Inawashiro S 1979 *J. Phys.* **C12** 2839
Klein M 1968 *Phys. Rev.* **B173** 552
Kuzmin N N and Menshikov A Z 1979 (work reported by Medvedev M V 1979 *Fiz Teverd Tela* (*Leningrad*) **21** 3356)
Luttinger J M 1976 *Phys. Rev. Lett.* **37** 778
Matsubara F 1974 *Prog. Theor. Phys.* **51** 378, 1694
Medvedev M V and Zaborov A V 1982a *Phys. Stat. Sol.* **B109** 773
Medvedov M V and Zaborov A V 1982b *Phys. Stat. Sol.* **B110** 387
Menshikov A Z and Teplykh A Y 1977 *Fiz. Met. Metalloved* **44** 1215
Menshikov A Z and Kuzmin N N 1980 *Fiz. Met. Metalloved* **49** 433
Menshikov A Z, Burtlet P, Chamberod A and Tholence J L 1981 *Sol. State Commun.* **V39** 1093
Mookerjee A 1978 *Pramana* **11** 223
Mookerjee A 1979 *Pramana* **14** 11
Mookerjee A and Roy S B 1983 *J. Phys.* **F13** 1945
Morita and Horiguchi 1976 *Solid State Commun.* **19** 833
Oguchi T and Ueno Y 1979 *J. Phys. Soc. Jpn.* **46** 729
Plefka T 1976 *J. Phys.* **F6** L327
Rode V Y, Deryabin A V and Damashke G 1975 *Fiz. Met. Metalloved* **40** 429
Shull R D and Beck P A 1974 *AIP Conf. Proc.* **24** 95

Pramāṇa, Vol. 21, No. 3, September 1983, pp. 183–186. © Printed in India.

Specific heat at low temperature due to negative U centres in disordered solids

S K GHATAK
Department of Physics and Meteorology,
Indian Institute of Technology, Kharagpur 721 302, India

MS received 5 March 1983; revised 11 July 1983

Abstract. The negative U-Anderson model is considered and energy spectrum is obtained using the Gorkov's decoupling scheme for one-electron Green's function. The correlation of localized electron pair (bipolaron) is explicitly taken into account in this scheme. The electronic specific heat of disordered solids with negative U-centres and having a distribution of negative U is then calculated. At low temperature the specific heat shows linear temperature dependence, and this linear T-term is a combined effect of distributed U and of the existence of localized electron pairs.

Keywords. Negative U centres; bipolaron; specific heat; disordered solids.

1. Introduction

Many amorphous solids exhibit linear temperature dependence of specific heat at low temperature. The origin of such behaviour of specific heat is related to the existence of distribution of level separation of two-level energy states which are assumed to be associated with the relaxation of amorphous structure (Anderson *et al* 1971, Philips 1972). In this paper it is shown that a similar behaviour of specific heat ($C_v \sim T$) can arise in distributed negative U-Anderson model (Anderson 1975) due to strong correlation between localized electron pair (bipolaron). The concept of negative intrasite electronic correlation and its relevance have been discussed by Anderson (1975, 1976). The attractive nature of interaction appears due to strong coupling of localized electronic density with the phonon. It has been argued that the negative U-Anderson model could explain some of the experimental results in amorphous chalcogenides (Chakraverty *et al* 1976)—in particular the pinning of Fermi level (Anderson 1975, Natoli *et al* 1978). We have earlier demonstrated that the pinning of the Fermi level in this model is due to strong correlation between spin-up and spin-down localized electron pair (Natoli *et al* 1978). For negative U, the pairs are the natural choice of ground state of the system and the theory of negative U-Anderson model must consider this correlation. As pointed out earlier (Anderson 1976-1979), negative U instead of taking single value, has a distribution in the disordered system. In this paper, the electronic specific heat has been calculated for the system described by negative U-Anderson model. (Anderson 1976, 1979). The electronic specific heat has been calculated in this paper for the system described by the negative U-Anderson model.

2. Model and calculation

The electronic Hamiltonian for centres with attractive intrasite interaction can be written as (Anderson, 1975)

$$H = \sum_{i,\sigma} (t_i - \mu)\,\hat{n}_{i\sigma} - \sum_i U_i\,\hat{n}_{i\uparrow}\,\hat{n}_{i\downarrow}, \tag{1}$$

where t_i and U_i are respectively the single-particle energy and the effective interaction at the ith site. The electron number operator $\hat{n}_{i\sigma} = c^+_{i\sigma}\,c_{i\sigma}$ and μ is the chemical potential. The hopping between different centres is neglected. The one-electron Green's functions are (Natoli *et al* 1978)

$$\langle\langle c_{i\sigma};\, c^+_{i\sigma}\rangle\rangle = \frac{1}{2\pi}\left[\frac{A_+}{\omega - \omega_+} + \frac{A_-}{\omega - \omega_-}\right] \text{ and } \langle\langle c^+_{i\sigma};\, c^+_{i-\sigma}\rangle\rangle$$

$$= A'\left[\frac{1}{\omega - \omega_+} - \frac{1}{\omega - \omega_-}\right], \tag{2}$$

where $$\omega_\pm = U_i\,(n_{i\sigma} - n_{i-\sigma}) \pm \omega_0;\ \omega_0 = \tfrac{1}{2}\,[(2t_i - \mu - U_i\,n)^2 + 4\,\alpha^2 U_i^2]^{1/2} \tag{3}$$

n_i is the average number of electron per centre. The respective spectral weight at energy level $\omega_\pm$ are

$$A_\pm = \frac{\pm\,(t_i - U_i\,n_{i\sigma} - \mu)}{\omega_+ - \omega_-} \text{ whereas } A' = \frac{U_i\,\alpha^*}{\omega_+ - \omega_-} \tag{4}$$

The quantity $\alpha = \langle c_{i\sigma}\,c_{i-\sigma}\rangle$ and is a measure of correlation of localized electron pair. In deriving the Green's functions, we have used the Gorkov's decoupling procedure in order to retain the pair correlation α which is non-zero here. The electron number n for paramagnetic case is given by

$$n = \left[1 - \frac{t - \mu - un/2}{\omega_0}\tanh\,(\beta\omega_0/2)\right], \tag{5}$$

and α satisfies the equation

$$1 = \frac{U}{2\,\omega_0}\tanh\,(\beta\omega_0/2). \tag{6}$$

The subscript i has been dropped from the above equation as the centres are independent in the absence of the hopping term. For non-zero α, (5) and (6) predict

$$\mu = t - \frac{U}{2} \quad \text{for all } n\ (0 < n \leqslant 2) \text{ (Natoli } et\ al \text{ 1978).}$$

As α is finite for negative U, the pinning of Fermi level is the consequence of the presence of localized pair. Using these results the entropy per centre with definite U is

$$S(U) = -2k\,[f(\omega_0)\ln f(\omega_0) + (1-f(\omega_0)]\ln[(1-f(\omega_0)], \tag{7}$$

where $f(\omega_0) = [1+\exp(\beta\omega_0)]^{-1}$

and $\omega_0 = \gamma U;\quad \gamma = [(1-n)^2 + 4\alpha^2]^{1/2}/2.$

Assuming that in amorphous solids U has a distribution over a certain range (say U_0) the total entropy becomes

$$S = \int_0^{U_0} S(U)\,P(U)\,\mathrm{d}U, \tag{8}$$

and the specific heat per negative U centre is

$$C_v = k^2T\int_0^{x_0}\left[\gamma^2x^2 - \frac{\gamma^2x^3}{4}\,\frac{\operatorname{sech}^2(x\gamma/2)}{1-(x/4)\operatorname{sech}^2(x\gamma/2)}\right]$$

$$\frac{\exp(x\gamma)}{(1+\exp[x\gamma])^2}\,P(xkT)\,\mathrm{d}x, \tag{9}$$

with $x=\beta U$, and $P(U)$ is the distribution function for U. In deriving (9), (6) is used to find $\mathrm{d}\omega_0/\mathrm{d}T$. As $T\to0$, γ tends to 1/2 for $0<n\leqslant2$ and X_0 can be replaced by ∞ as the integrand decreases fast for large X. For constant density of distribution $P(U)$ $=P_0$ for $U\leqslant U_0$ and 0 otherwise, the specific heat

$$C_v = k^2T\,P_0I_0$$

where I_0 is the value of the integral in (9) with $X_0=\infty$. Thus the specific heat at low temperature varies linearly with T. It is also possible to make a reasonable estimate for any other distribution. Physically, it is expected $P(U)$ would decrease rapidly as the magnitude of U increases. As the main contribution to integral in (9) comes from small X-region where variation of $P(U)$ may not be significant, C_v can be approximated as

$$C_v \simeq k^2T\,P(0)\,I_0$$

where $P(0)$ is the probability distribution at $U=0$.

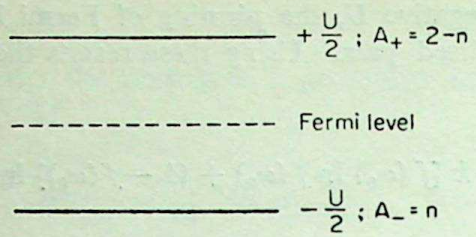

Figure 1. Energy level diagram for negative U centre at $T = 0°K$. The energy is measured from Fermi level taken as reference. n and $2-n$ are respectively spectral weight where n is the average number of electron/centre.

3. Conclusion

The linear temperature of specific heat can be understood physically from the energy evel considerations. In the presence of correlated localized pair ($\alpha \neq 0$) the one-electron energy levels measured with respect to Fermi level are at $+U/2$ with spectral weight $(2 - n)$ and $- U/2$ with weight n (Natoli *et al* 1978) (figure 1). In the case of distributed U ranging from zero upto some finite value (U_0-say) the energy levels spread from Fermi level in continuous fashion leaving no energy gap between occupied and empty states. Such an energy level structure of Fermion is known to produce linear T dependence of specific heat. It is to be noted that this contribution to specific heat is electronic in origin. In conclusion, the distribution of U in negative region and existence of correlated pair can be another source of linear T-term in specific heat in disordered solids.

References

Anderson P W 1975 *Phys. Rev. Lett.* **34** 953

Anderson P W 1976 *J. de Phys.* **C4** 339 and Les Hauches, Session XXXI (ed. Balian *et al*) North-Holland 1979 p. 162

Anderson P W, Halperin B I and Verma C M 1971 *Philos. Mag.* **25** 1

Chakraverty B K and Schllnker C 1976 *J. de Phys.* **C4** 353

Chakraverty B K, Mini A and Deneuvilli A 1976 *Phys. Rev. Lett.* **37** 296

Natoli C R, Chakraverty B K and Ghatak S K 1978 *Nuclear Physics Solid State Physics (India)* **21** 522

Philips W A 1972 *J. Low Temp. Phys.* **7** 351

Pramāṇa, Vol. 21, No. 3, September 1983, pp. 187–200. © Printed in India.

First passage time and escape time distributions for continuous time random walks

V BALAKRISHNAN and M KHANTHA
Department of Physics, Indian Institute of Technology, Madras 600 036, India

MS received 4 May 1983

Abstract. We consider an arbitrary continuous time random walk (CTRW) *via* unbiased nearest-neighbour jumps on a linear lattice. Solutions are presented for the distributions of the first passage time and the time of escape from a bounded region. A simple relation between the conditional probability function and the first passage time distribution is analysed. So is the structure of the relation between the characteristic functions of the first passage time and escape time distributions. The mean first passage time is shown to diverge for all (unbiased) CTRW's. The divergence of the mean escape time is related to that of the mean time between jumps. A class of CTRW's displaying a self-similar clustering behaviour in time is considered. The exponent characterising the divergence of the mean escape time is shown to be $(1 - H)$, where H $(0 < H < 1)$ is the fractal dimensionality of the CTRW.

Keywords. Continuous time random walk; first passage time; escape time; fractal random walks.

1. Introduction

The study of first passage times and times of escape from a given region (exit times) in random walks and diffusion processes finds application in a variety of physical problems (Montroll and Weiss 1965; Montroll and West 1979; Hänggi and Talkner 1981). Recently, the subject has evoked interest (Seshadri and West 1982) as a means of characterising fractal random walks (Hughes *et al* 1981, 1982). A vast literature exists on the classic first passage time problem for a variety of Markov processes (Pontryagin *et al* 1933; Darling and Siegert 1953; Stratonovich 1963; Weiss 1966; Montroll and Weiss 1965; Montroll 1969; Goel and Richter-Dyn 1974). The extension of such results to non-Markov processes in general, and to continuous-time random walks (CTRW's) in particular, would enable one to apply them to more complicated physical situations that incorporate, for instance, strong memory effects. This is the task carried out in this paper. All the known results for the Markov case are of course recovered as special cases of our general solutions. Some of the results obtained below for general CTRW's (specifically, results for the *mean* first passage and escape times) have also been found by Weiss (1981) in a different form (*viz.* formal expressions involving infinite sums) using the generalised master equation for a CTRW, assuming that the first waiting-time distribution is identically equal to the waiting-time distribution specifying the renewal process (that is, CTRW). We do not need this restriction in our approach.

We first obtain an exact solution for the characteristic function $\tilde{Q}$ of the first

passage time distribution $Q(m, t \mid m_0)$ for a general continuous-time random walk on an infinite one-dimensional chain by two different methods. (For simplicity, we consider a symmetric walk *via* nearest-neighbour jumps; m, m_0 denote integers). In the first method, we construct an explicit solution for the conditional probability $P(m, t \mid m_0)$ for an arbitrary CTRW on an infinite chain and then use the reflection principle for symmetric random walks to obtain the first passage time distribution. The second is a direct 'first principles' calculation of $\tilde{Q}$. Next, the mean first passage time is shown to diverge for all CTRW's, as one would generally expect for a symmetric random walk on an infinite chain. Considering the entire class of CTRW's, we then show that there exists a certain simple relationship between Q and P, namely, $Q(m, t \mid m_0) = \mid m - m_0 \mid P(m, t \mid m_0)/t$, only when the pausing time is exponentially distributed, in which case the random walk is a Markov chain. Surprisingly, however, there are even more general types of temporally correlated random walks for which this relationship is valid, and we present an explicit example of this.

We then consider the distribution of the time of escape from a given region (the 'exit time') and derive a compact expression for its characteristic function using the method of images. We show that the mean escape time from a bounded domain for a general CTRW is finite only when the first moment of the pausing time distribution exists. In this sense, even though the positional probability density spreads out in time from an initial sharp distribution, no long range diffusion can be said to occur for a random walk involving a pausing time distribution with a divergent first moment (*i.e.*, mean residence time at a site).

Finally, we turn to 'fractal' random walks, *i.e.*, walks which exhibit self-similar clustering. One such class is obtained in the case of a pausing-time distribution that is an infinite superposition of suitably-scaled exponentials (Shlesinger and Hughes 1981). For such 'temporally fractal' random walks, we show that the mean escape time diverges with an exponent that is related to the fractal (Hausdorff-Besicovitch) dimension of the walk. The scaling of the mean escape time thus provides a convenient index of the fractal dimensionality associated with the walk.

2. Formulas for the first passage time distribution

2.1 *The Siegert equation*

Let $P(m, t \mid m_0)$ denote the probability of finding the random walker at site m at time t given that she started from m_0 at time $t = 0$. Let $Q(m, t \mid m_0)\, \mathrm{d}t$ be the probability of reaching m for the first time, in the time interval $(t, t + \mathrm{d}t)$. For a temporally homogeneous *Markov* process, P and Q are related *via* the Siegert equation (Siegert 1951; Darling and Siegert 1953)

$$P(m_1, t \mid m_0) = \int_0^t P(m_1, t - t' \mid m) Q(m, t' \mid m_0)\, \mathrm{d}t', \quad (m_0 < m \leqslant m_1). \tag{1}$$

Hence, in terms of the corresponding Laplace transforms (denoted by a tilde),

$$\tilde{Q}(m, u \mid m_0) = \tilde{P}(m_1, u \mid m_0)/\tilde{P}(m_1, u \mid m), \quad (m_0 < m \leqslant m_1), \tag{2}$$

where u is the transform variable. Using this simple relation, the first passage problem on finite or infinite Markov chains with specific reflecting or absorbing boundary conditions has been studied in detail (Darling and Siegert 1953; Goel and Richter-Dyn 1974; Montroll and West 1979; Khantha and Balakrishnan 1983). Equation (1) is based on a renewal principle that is *not valid* for non-Markov processes. In such cases, the first passage time problem must be solved by other methods.

2.2 *The method of images*

The problem of a first passage to the point m from a point $m_0 < m$ on an infinite chain is equivalent to that of a random walk in the restricted region $(-\infty, m)$ with an absorbing barrier at m. $Q(m, t \mid m_0)$ is given by (Montroll and West 1979)

$$Q(m, t \mid m_0) = -\frac{\mathrm{d}}{\mathrm{d}t} \sum_{m' = -\infty}^{m-1} \mathscr{P}_m(m', t \mid m_0), \tag{3}$$

where $\mathscr{P}_m(m', t \mid m_0)$ is the conditional probability of finding the random walker at m' at time t starting from m_0 at $t = 0$, in the presence of an absorbing barrier at m. By invoking the method of images (Chandrasekhar 1943; Feller 1966; Montroll and West 1979), $\mathscr{P}_m(m', t \mid m_0)$ can be easily determined from $P(m', t \mid m_0)$ (the solution for random walk on an infinite chain) according to

$$\mathscr{P}_m(m', t \mid m_0) = P(m', t \mid m_0) - P(2m - m', t \mid m_0). \tag{4}$$

If we assume (without loss of generality) that the random walker starts from the origin, we have the formula (for $m \geqslant 1$)

$$Q(m, t \mid 0) = -\frac{\mathrm{d}}{\mathrm{d}t} \sum_{m' = -\infty}^{m-1} [P(m', t \mid 0) - P(2m - m', t \mid 0)]. \tag{5}$$

Making use of the initial condition on P, the characteristic function $\tilde{Q}$ is then

$$\tilde{Q}(m, u \mid 0) = 1 + u \sum_{m' = -\infty}^{m-1} [\tilde{P}(2m - m', u \mid 0) - \tilde{P}(m', u \mid 0)] \quad (m \geqslant 1). \tag{6}$$

We shall use this in the next section.

2.3 *A direct method*

There is an alternative way of obtaining Q (or $\tilde{Q}$) directly. This is closely related to the route we follow to calculate P (or $\tilde{P}$) itself. The jumps of the random walker may be regarded as being caused by a random sequence of pulses with a specified distribution. The actual location of the walker at time t depends only on the number of transition-causing pulses or 'steps' executed in the time interval t. Let $W(n, t)$ be

the (normalized) probability that n pulses have occurred in $(0, t)$. Let $p_n(m)$ be the probability of reaching the point m from the point 0 in n steps. Then

$$P(m, t|0) = \sum_{n=0}^{\infty} W(n, t)\, p_n(m). \tag{7}$$

For the case at hand,

$$p_n(m) = \begin{cases} \left(\dfrac{n}{\frac{n-m}{2}}\right) 2^{-n} \text{ if } n = m \bmod 2 \text{ and } n \geqslant |m|, \\ 0 \qquad \text{otherwise.} \end{cases} \tag{8}$$

The problem then reduces to specifying (or computing) $W(n, t)$ in a given physical situation and then performing the summation in (7) (Balakrishnan and Venkataraman 1981).

With the help of a simple geometric argument (again related to the reflection principle), it can be shown (Chandrasekhar 1943) that the probability of reaching m from the origin for the *first* time in precisely n steps is $(|m|/n)p_n(m)$. Let $\pi(n, t)\,\mathrm{d}t$ be the probability that, starting at $t = 0$, the nth pulse occurs in the time interval $(t, t + \mathrm{d}t)$. Then it is evident that

$$Q(m, t|0) = \sum_{n=0}^{\infty} \pi(n, t)\, \frac{|m|}{n}\, p_n(m)\,. \tag{9}$$

As before, then, the problem amounts to specifying (or computing) $\pi(n, t)$ and then carrying out the summation. For the characteristic function $\tilde{Q}(m, u|0)$, the transform $\tilde{\pi}(n, u)$ occurs on the right in (9). We shall compute $\tilde{\pi}(n, u)$ and evaluate the sum for a general CTRW in the next section.

3. Continuous time random walks

3.1 *Calculation of W and* $\tilde{P}$

A CTRW on the infinite chain occurs when $W(n, t)$ is generated by a renewal process. The latter is specified by a normalized pausing time density $\psi(t)$: if a step (event) has occurred at time t_0, the probability of the next one occurring in the interval $(t_0 + t, t_0 + t + \mathrm{d}t)$ is $\psi(t)\,\mathrm{d}t$. Starting from an arbitrary origin $t = 0$, the *first* pausing time distribution $\psi_0(t)$ could, in general, be distinct from $\psi(t)$, and may be specified independently. For an ongoing *equilibrium* renewal process, ψ_0 is related to ψ according to $\tau\,\tilde{\psi}_0(u) = 1 - \tilde{\psi}(u)$, where τ is the mean time between successive events (*i.e.*, the first moment of $\psi(t)$) (Feller 1966; Cox 1967; Kehr and Haus 1978;

Balakrishnan 1980). It is seen easily that, among such *equilibrium* renewal processes, $\psi_0 = \psi$ if and only if $\psi(t)$ is the exponential density $\lambda \exp(-\lambda t)$. ($W(n, t)$ is then a Poisson distribution and the random walk is a Markov chain). In general, however, physical applications *may* correspond to ordinary renewal processes rather than equilibrium ones, and the choice of ψ_0 may be dictated by physical considerations. For example, in the application of CTRW theory to hopping conduction in amorphous media (Lax and Scher 1977), the correct prescription happens to be $\psi_0(t) = \psi(t)$, even though $\psi(t)$ is not an exponential density in that problem. We shall work with an arbitrary normalized density $\psi_0(t)$ in what follows.

Corresponding to the pausing time densities $\psi_0(t)$ and $\psi(t)$, we have the 'survivor functions' (or holding-time distributions)

$$p_0(t) = 1 - \int_0^t \mathrm{d}t' \, \psi_0(t'), \quad p(t) = 1 - \int_0^t \mathrm{d}t' \, \psi(t') \tag{10}$$

Then, clearly,

$$\left.\begin{aligned} &W(0, t) = p_0(t), \\ &W(n, t) = \int_0^t \mathrm{d}t_n \ldots \int_0^{t_2} \mathrm{d}t_1 \, p(t - t_n) \, \psi(t_n - t_{n-1}) \ldots \psi(t_2 - t_1) \, \psi_0(t_1) \\ &\qquad\qquad\qquad\qquad\qquad\qquad\qquad\qquad (n \geqslant 1). \end{aligned}\right\} \tag{11}$$

Hence

$$\left.\begin{aligned} &\tilde{W}(0, u) = u^{-1} \, [1 - \tilde{\psi}_0(u)] \\ &\tilde{W}(n, u) = u^{-1} \, \tilde{\psi}_0(u) \, [1 - \tilde{\psi}_0(u)] \, [\tilde{\psi}(u)]^{n-1}, \quad n \geqslant 1. \end{aligned}\right\} \tag{12}$$

The Laplace transform of the conditional probability, $\tilde{P}(m, u \mid 0)$, is then found by inserting (12) and (8) in (the Laplace transform of) (7). A summation of the type $\sum x^n p_n(m)$ arises. Using the result given in the Appendix, we obtain finally

$$\tilde{P}(m, u \mid 0) = \frac{1}{u}\left(1 - \frac{\tilde{\psi}_0}{\tilde{\psi}}\right) \delta_{m,0}$$

$$+ \frac{\tilde{\psi}_0 (1 - \tilde{\psi})}{u \tilde{\psi} (1 - \tilde{\psi}^2)^{1/2}} \left[\frac{1 - (1 - \tilde{\psi}^2)^{1/2}}{\tilde{\psi}}\right]^{|m|} (m = 0, \pm 1, \pm 2, \ldots). \tag{13}$$

This is a special case of the more general result found elsewhere (Balakrishnan and Venkataraman 1981). It is convenient to introduce the variable

$$\xi(u) = \operatorname{arc\,sech} \tilde{\psi}(u). \tag{14}$$

Then $\tilde{P}$ has the compact form

$$\tilde{P}(m, u \mid 0) = (1/u)\left[\left(1 - \frac{\tilde{\psi}_0}{\tilde{\psi}}\right)\delta_{m,0} + (\tilde{\psi}_0/\tilde{\psi}) \tanh(\xi/2) \exp(- \mid m \mid \xi)\right] \quad (m = 0, \pm 1, \ldots) \tag{15}$$

3.2 *Calculation of* $\tilde{Q}$

Substituting the result (13) in formula (6) obtained by the method of images, we get after simplification,

$$\tilde{Q}(m, u \mid 0) = \left(\frac{\tilde{\psi}_0}{\tilde{\psi}}\right)\left[\frac{1 - (1 - \tilde{\psi}^2)^{1/2}}{\tilde{\psi}}\right]^m = (\tilde{\psi}_0/\tilde{\psi}) \exp(- m\xi), (m \geqslant 1). \tag{16}$$

This is the characteristic function of the first passage time distribution for an arbitrary continuous time random walk *via* unbiased nearest-neighbour jumps on an infinite chain. As both $\psi_0(t)$ and $\psi(t)$ are normalized, $\tilde{\psi}_0(0) = \tilde{\psi}(0) = 1$; hence $Q(m, t \mid 0)$ is properly normalized; its integral form $t = 0$ to ∞ is equal to unity. As the random walk is unbiased, it is evident that $Q(m, t \mid 0) = Q(-m, t \mid 0)$, so that the exponent in (16) may be replaced by $|m|$, making the result valid for all non-zero m.

3.3 *Direct calculation of* $\tilde{\pi}$ *and* $\tilde{Q}$

Considering the definitions of $W(n, t)$ and $\pi(n, t)$ given in § 2.3, it is evident that, *for a renewal process*,

$$W(n, t) = \int_0^t \mathrm{d}t' \, \pi(n, t') \, p(t - t'), (n \geqslant 1), \tag{17}$$

where $p(t)$ is the holding time distribution defined in (10). Hence,

$$\tilde{\pi}(n, u) = \tilde{\psi}_0(u) (\tilde{\psi}(u))^{n-1} (n \geqslant 1). \tag{18}$$

If this is substituted in (the Laplace transform of) the ' direct ' formula of (9) for Q, we are left with a sum of the type $\Sigma \tilde{\psi}^n p_n(m)/n$. It is easily seen that $|\tilde{\psi}(u)| < 1$ for all Re $u > 0$, so that the result given in the Appendix may be used to obtain

$$\tilde{Q}(m, u \mid 0) = \left(\frac{\tilde{\psi}_0}{\tilde{\psi}}\right)\left[\frac{1 - (1 - \tilde{\psi}^2)^{1/2}}{\tilde{\psi}}\right]^{\mid m \mid} = (\tilde{\psi}_0 \mid \tilde{\psi}) \exp(- \mid m \mid \xi) \tag{19}$$

for $m = \pm 1, \pm 2, \ldots$.

3.4 *Mean first passage time*

The mean first passage time from the origin to the site m is equal to

$$\langle t(m)\rangle = \int_0^\infty t\, Q\,(m, t\,|\,0)\, \mathrm{d}t$$

$$= -\,[\partial\, \tilde{Q}\,(m, u\,|\,0)/\partial u]_{u=0}, \tag{20}$$

as $Q\,(m, t\,|\,0)$ is already normalized to unity. Using (19) we find

$$\langle t(m)\rangle \sim \lim_{u\to 0}\ (1 - \tilde{\psi}^2(u))^{-1/2} = \infty, \tag{21}$$

for all symmetric continuous time random walks on an infinite chain.(The special case $\tilde{\psi} = \lambda/(u+\lambda)$ corresponds to Polya's classic result (Polya 1921)).

3.5 *A simple relation between P and Q*

As stated earlier, $W(n, t)$ is a Poisson distribution and the random walk is a Markov chain when $\psi_0 = \psi = \lambda\, \exp\,(-\lambda t)$. The transforms $\tilde{P}$ and $\tilde{Q}$ can be inverted in this case, to yield the well-known results (Feller 1966)

$$\left.\begin{aligned} P\,(m, t\,|\,0) &= \exp\,(-\lambda t)\ I_m\,(\lambda t),\\ Q\,(m, t\,|\,0) &= |m|\, t^{-1} \exp\,(-\lambda t)\ I_m\,(\lambda t),\end{aligned}\right\} \tag{22}$$

where I_m is the modified Bessel function of order m. For this simplest of random walks, therefore, we have the interesting connection

$$Q\,(m, t\,|\,0) = (|m|/t)\ P\,(m, t\,|\,0). \tag{23}$$

Are there other random walks for which this relationship is satisfied?

Equation (23) is equivalent to

$$\frac{\partial}{\partial u}\,\tilde{Q}\,(m, u\,|\,0) + |m|\ \tilde{P}\,(m, u\,|\,0) = 0 \tag{24}$$

for $m = \pm 1, \pm 2, \ldots$. Using (13) and (19) for an arbitrary CTRW, we find that (24) requires that

$$\frac{\mathrm{d}}{\mathrm{d}u} \ln\,(\tilde{\psi}_0/\tilde{\psi}) + |m|\left(\frac{1}{u}\tanh\frac{\xi}{2} - \frac{\mathrm{d}\xi}{\mathrm{d}u}\right) = 0, \tag{25}$$

for every non-zero integral value of m. Hence, we *must* have $\psi_0 = \psi$, and further, $\tanh\,(\xi/2) = u\,(\mathrm{d}\,\xi/\mathrm{d}u)$. It is shown easily that this last condition is satisfied

only by the functional form $\tilde{\psi}(u) = \lambda/(u + \lambda)$, *i.e.* only in the Markovian case specified by (22).

Remarkably enough, there do exist random walks that are even more strongly correlated (temporally) than a CTRW, and which display property (23). An explicit example is provided by the geometric distribution (Balakrishnan 1981)

$$W(n, t) = (\lambda t)^n/(1 + \lambda t)^{n+1}. \tag{26}$$

This is not a CTRW (or renewal process), and we cannot write (17) connecting $W(n, t)$ and $\pi(n, t)$ in this case. (Roughly speaking, the pausing time density ψ may itself be n-dependent in such cases.) The explicit solution for $P(m, t \mid 0)$ now reads

$$P(m, t \mid 0) = (1 + 2\lambda t)^{-1/2} (\lambda t)^{|m|} [1 + \lambda t + (1 + 2\lambda t)^{1/2}]^{-|m|}. \tag{27}$$

The method of images then yields the result

$$Q(m, t \mid 0) = |m| t^{-1} P(m, t \mid 0) \tag{28}$$

where P is given by (27). Indeed, one can show that if $W(n, t) \propto x^n(t)$, with no further dependence on n, then property (23) is valid *only* for the functional form $x(t) = \lambda t/(1 + \lambda t)$, which is equivalent to (26) on taking into account the normalization of $W(n, t)$. The classification of *all* random walks satisfying relation (23) between P and Q will be dealt with elsewhere.

4. The escape time distribution

4.1 *General formula for* $Q(\pm m, t \mid 0)$

We now turn to the problem of the escape of the random walker out of the region $(-m, m)$, starting from the origin at $t = 0$. This is equivalent to considering first passage through *either* $-m$ *or* $+m$, and involves the solution to a random walk on the set $\{-m, \ldots, +m\}$ with absorbing barriers at both ends (eg. see Montroll and Scher 1973). Let $Q(\pm m, t \mid 0)$ denote the desired first passage time distribution, and $\mathscr{P}_{\pm m}(m', t \mid 0)$ the conditional probability for the random walk referred to. Then (Montroll and West 1979)

$$Q(\pm m, t \mid 0) = -\frac{\mathrm{d}}{\mathrm{d}t} \sum_{m'=-(m-1)}^{(m-1)} \mathscr{P}_{\pm m}(m', t \mid 0), (m \geqslant 1), \tag{29}$$

for the sum is just the probability that the random walker has survived without absorption at either of the barriers till time t. $\mathscr{P}_{\pm m}$ may be found once again by the

method of images. As there are two barriers, the number of images of the interval is infinite, and we have

$$\mathscr{P}_{\pm m}(m', t \mid 0) = \sum_{n=-\infty}^{\infty} [P(m' + 4nm, t \mid 0) - P(-m' - 4nm - 2m, t \mid 0)]. \tag{30}$$

Using the symmetry properties of P, this may be simplified to yield

$$Q(\pm m, t \mid 0) = -\frac{\mathrm{d}}{\mathrm{d}t} \sum_{m'=-(m-1)}^{(m-1)} \sum_{n=-\infty}^{\infty} (-1)^n P(m'+2nm, t \mid 0). \tag{31}$$

This is the formula desired. Its form may be compared with that of (5) for first passage from the point 0 to the point m on an infinite chain (a problem with a single absorbing barrier).

4.2 *Calculation of* $Q(\pm m, t \mid 0)$ *for a* CTRW

For an arbitrary CTRW, $\tilde{P}$ is given by (15). Inserting this in the Laplace transform of (31) and carrying out the summations involved, we get (after a considerable amount of algebra) the very simple answer

$$\tilde{Q}(\pm m, u \mid 0) = (\tilde{\psi}_0/\tilde{\psi}) \operatorname{sech}(m\xi). \tag{32}$$

Here $\sec h\, \xi = \tilde{\psi}$, as already defined (equation (14)). This is the result required. As the right side of (32) tends to unity as $u \to 0$, the distribution $Q(\pm m, t \mid 0)$ is also normalised to unity.

A comparison of (32) with (16) for the characteristic function $\tilde{Q}(m, u \mid 0)$ of the first passage time distribution shows that (setting $\psi_0 = \psi$)

$$\tilde{Q}(\pm m, u \mid 0) = 2\tilde{Q}(m, u \mid 0) \,/\, [1 + \tilde{Q}^2(m, u \mid 0)]. \tag{33}$$

The structure of this result suggests the following interesting connection between the escape time distribution and the distribution of the time of first passage to *either* end of the region of interest, *i.e.*, $\pm m$, in the *absence* of the other barrier. Owing to the symmetry of the problem, we have already seen that $Q(m, t \mid 0) = Q(-m, t \mid 0)$. For brevity, let us write $Q_{\pm}(t)$ for $Q(\pm m, t \mid 0)$, $Q_+(t) = Q(m, t \mid 0)$, $Q_-(t) = Q(-m, t \mid 0)$. Then (33) can be recast as

$$\left.\begin{aligned} \tilde{Q}_{\pm}(u) &= \tilde{Q}_+/(1 + \tilde{Q}_-\tilde{Q}_+) + \tilde{Q}_-/(1 + \tilde{Q}_+\tilde{Q}_-) \\ &\equiv \tilde{Q}_{\text{right}}(u) + \tilde{Q}_{\text{left}}(u), \end{aligned}\right\} \tag{34}$$

where $Q_{\text{right}}(t)$ is the probability per unit time of absorption at $+m$ *in the presence* of the other absorbing barrier at $-m$, with a similar interpretation for $Q_{\text{left}}(t)$. We have solved the problem under consideration for *biased* random walks as well (Khantha and Balakrishnan 1983a), and equation (34) continues to hold good in that case. These matters will be elaborated upon in the paper referred to above.

4.3 *Mean escape time*

As in the case of the mean first passage time (equation (20)), the mean time of escape from the region $(-m, m)$, starting from the origin, is

$$\left.\begin{aligned}\langle t(\pm m)\rangle &= \int_0^\infty \mathrm{d}t\, Q(\pm m, t|0)\,\mathrm{d}t \\ &= -\left[\partial\, \tilde{Q}(\pm m, u|0)/\partial u\right]_{u=0}.\end{aligned}\right\} \tag{35}$$

For a CTRW, $\tilde{Q}(\pm m, u|0)$ is given by (32). It turns out that the derivative required in (35) is finite (see below) when the mean residence time τ at a site is finite —that is, when the Laplace transform of $\psi(t)$ has the small u expansion

$$\tilde{\psi}(u) \simeq 1 - u\tau + (\text{higher orders in } u). \tag{36}$$

In all such cases, we have (taking $\psi_0 = \psi$ for simplicity)

$$\langle t(\pm m)\rangle = m^2\,\tau. \tag{37}$$

The Markov case $\psi(t) = \lambda \exp(-\lambda t)$ thus yields $\langle t(\pm m)\rangle = m^2/\lambda$, as is known (Seshadri and West 1982).

It is interesting to examine $\langle t(\pm m)\rangle$ when the pausing time distribution has a long tail (does not fall off like an exponential, or a finite sum of exponentials) (see e.g. Shlesinger 1973). Such distributions are necessary to explain anomalies in charge transport phenomena in amorphous solids (Scher and Lax 1973; Tunaley 1976; Montroll and West 1979). In these cases, $\tilde{\psi}(u)$ has in general a small u expansion of the form

$$\tilde{\psi}(u) \simeq 1 - ru^\alpha + su^\beta + \text{higher orders}, \tag{38}$$

where $0 < \alpha < 1$ and $\beta > \alpha$. The mean residence time is evidently infinite in all these instances. Using the asymptotic expansion (38), we find (recalling that $\xi = \operatorname{sech}^{-1}\tilde{\psi}$) the expansion

$$\exp(-\xi) = 1 - (2r)^{1/2}\, u^{\alpha/2} + O(u^\gamma), \tag{39}$$

where $\gamma = \text{Min}\,(\alpha, \beta - \alpha/2)$. This leads to

$$\tilde{Q}(\pm m, u|0) \simeq 1 - m^2\, ru^\alpha + \text{higher orders in } u, \tag{40}$$

and hence (remembering that $\alpha < 1$)

$$\langle t\ (\pm m)\rangle \to \infty. \tag{41}$$

This is the reason (*i.e.* a divergent mean time for escape out of a *bounded* region) why we stated in § 1 that such pausing time distributions do not lead to a true long range diffusion of the random walker. This is reinforced by the fact (Khantha and Balakrishnan 1983a) that the foregoing conclusions are not altered by the inclusion of a bias in the random walk.

4.4 *Temporally fractal random walks*

When the pausing time distribution $\psi(t)$ has no finite first moment, the mean time between the jumps of the random walker is infinite, and there is no finite time scale in the problem. This is a necessary condition (but of course not a sufficient one) for a self-similar clustering or fractal behaviour (Mandelbrot 1977) of the epochs at which jumps occur, as described by the distribution $W(n, t)$. A class of such processes that is within the purview of CTRW's is provided by the (normalized) pausing time distribution (Shlesinger and Hughes 1981)

$$\psi(t) = \frac{\lambda(1-a)}{a} \sum_{k=1}^{\infty} (a\ b)^k \exp(-\lambda\ b^k\ t), \tag{42}$$

where $0 < a, b < 1$, and λ^{-1} is a positive constant with the dimensions of time. This expression is an infinite superposition of exponentials in which the jump rate $\lambda\ b^k$ occurs with a probability proportional to a^k. The mean residence time is

$$\tau = \int_0^{\infty} t\ \psi(t)\ \mathrm{d}t = \frac{(1-a)}{\lambda\ a} \sum_{k=1}^{\infty} (a/b)^k, \tag{43}$$

so that τ is infinite if $a \geqslant b$. If this is so, there is no finite time scale in the problem. The long-time decay of such a 'frozen' process is governed by a power law when $a > b$, *i.e.*

$$\psi(t) \simeq O\ (t^{-1-H}) \tag{44}$$

where H is a positive number to be identified shortly. Equivalently, the Laplace transform of $\psi(t)$ is not analytic at $u = 0$, and can be shown (Shlesinger and Hughes 1981) to have the small u behaviour

$$\tilde{\psi}(u) \simeq 1 + u^H\ K(u) + O(u), \tag{45}$$

where $K(u)$ is a periodic function of $\ln(u/\lambda)$ that does not seriously affect the behaviour of $\tilde{\psi}$ as $u \to 0$. The leading power H is given by

$$H = \ln a / \ln b \tag{46}$$

so that $0 < H < 1$ (since $0 < b < a < 1$). The exponent H can be viewed (in an average sense) as the fractal or Hausdorff-Besicovitch dimension characterising the CTRW. How does one probe this quantity?

The mean escape time from a bounded region, say $(-m, m)$ provides a direct answer. It is immediately evident from what has been deduced earlier that for the CTRW specified by (42) with $b < a$,

$$\tilde{Q}(\pm m, u \mid 0) \simeq 1 + m^2 u^H K(u) + O(u), \tag{47}$$

with H given by (46). Hence $\langle t(\pm m)\rangle \to \infty$ in this case. As

$$\langle t(\pm m)\rangle = \lim_{T\to\infty} \int_0^T t\, Q(\pm m, t \mid 0)\, \mathrm{d}t, \tag{48}$$

the divergence of $\langle t(\pm m)\rangle$ with the time of observation T goes like T^{1-H} for very large times T. This therefore yields a convenient index for the estimation of the fractal dimensionality H of the CTRW. The introduction of a uniform bias in the random walk does not affect this result, as stated earlier.

Acknowledgement

MK acknowledges the financial support of the Department of Atomic Energy, India, in the form of a fellowship.

Appendix

The function $\tilde{P}(m, u \mid 0)$ (eqns. (7), (12)) involves the sum

$$S_1(x) = \sum_{n=0}^{\infty} x^n p_n(m), \quad (|x| < 1),$$

where x is a function of u, and (see (8))

$$p_n(m) = \begin{cases} \binom{n}{\frac{n-m}{2}} 2^{-n} \text{ if } n = m \bmod 2,\ n \geqslant |m|; \\ 0 \quad \text{otherwise.} \end{cases}$$

After a change of variables,

$$S_1(x) = \sum_{k=0}^{\infty} \binom{2k + |m|}{k} \left(\frac{x}{2}\right)^{2k+|m|},$$

which reduces after some manipulation to

$$S_1(x) = (x/2)^{|m|}\, {}_2F_1\left(\frac{|m|+1}{2},\ \frac{|m|}{2}+1;\ |m|+1;\ x^2\right)$$

$$= (x/2)^{|m|}\,(1-x^2)^{-1/2}\ F\left(\frac{|m|}{2},\ \frac{|m|+1}{2};\ |m|+1;\ x^2\right).$$

Call $x^2 = 4z\,(1-z)$, and use a transformation property of the hypergeometric function that relates the above to a function with argument z. It is then possible to identify S_1 to be

$$S_1(x) = (1-x^2)^{-1/2}\left(\frac{1-(1-x^2)^{1/2}}{x}\right)^{|m|}.$$

Similarly, the characteristic function of the first passage time distribution, $\tilde{Q}\,(m, u|0)$, involves the sum (see (9), (18))

$$S_2(x) = \sum_{n=0}^{\infty} (1/n)\, x^n\, p_n(m), \quad (|x| < 1).$$

Proceeding as before, we find

$$S_2(x) = (x/2)^{|m|}\, {}_2F_1\left(\frac{|m|+1}{2},\ \frac{|m|}{2};\ |m|+1;\ x^2\right),$$

which, by an inspection of the earlier result, is just

$$S_2(x) = \left(\frac{1-(1-x^2)^{1/2}}{x}\right)^{|m|}.$$

References

Balakrishnan V 1980 in Proc. Meeting on Spin-Glass Alloys, University of Roorkee, Roorkee, India (unpublished)

Balakrishnan V 1981 *Pramana* **17** 55

Balakrishnan V and Venkataraman G 1981 *Pramana* **16** 109

Chandrasekhar S 1943 *Rev. Mod. Phys.* **15** 1

Cox D R 1967 *Renewal theory* (London: Methuen)

Darling D A and Siegert A J F 1953 *Ann. Math. Stat.* **24** 624

Feller W 1966 *An introduction to probability theory and its applications* (New York: Wiley) Vols. 1 and 2

Goel N S and Richter-Dyn N 1974 *Stochastic models in biology* (New York: Academic)

Hänggi P and Talkner P 1981 *Z. Phys.* **B45** 79

Hughes B D, Shlesinger M F and Montroll E W 1981 *Proc. Natl. Acad. Sci. (USA)* **78** 3287

Hughes B D, Montroll E W and Shlesinger M F 1982 *J. Stat. Phys.* **28** 111

Kehr K W and Haus J W 1978 *Physica* **A93** 412

Khantha M and Balakrishnan V 1983 *Pramana* (Accepted)
Khantha M and Balakrishnan V 1983a manuscript in preparation
Lax M and Scher H 1977 *Phys. Rev. Lett.* **39** 781
Mandelbrot B B 1977 *Fractals: form, chance and dimension* (San. Francisco: Freeman)
Montroll E W 1969 *J. Math. Phys.* **10** 753
Montroll E W and Weiss G H 1965 *J. Math. Phys.* **6** 167
Montroll E W and Scher H 1973 *J. Stat. Phys.* **9** 101
Montroll E W and West B J 1979 in *Fluctuation phenomena* (eds.) E W Montroll and J L Lebowitz (Amsterdam: North-Holland)
Polya G 1921 *Math. Ann.* **84** 149
Pontryagin L, Andronov A and Witt A 1933 *Zh. Eskp. Theor. Fiz.* **3** 172
Scher H and Lax M 1973 *Phys. Rev.* **B7** 4491
Seshadri V and West B J 1982 *Proc. Natl. Acad. Sci. (USA)* **79** 4501
Shlesinger M F 1973 *J. Stat. Phys.* **10** 421
Shlesinger M F and Hughes B D 1981 *Physica* **A109** 597
Siegert A J F 1951 *Phys. Rev.* **81** 617
Stratonovich R L 1963 *Topics in the theory of random noise* (New York: Gorden-Breach) Vol. 1
Tunaley J K E 1976 *J. Stat. Phys.* **15** 149
Weiss G H 1966 *Adv. Chem. Phys.* **13** 1
Weiss G H 1981 *J. Stat. Phys.* **24** 587

Pramāṇa, Vol. 21, No. 3, September 1983, pp. 201–206. © Printed in India.

CP invariance: A point of view

GYAN MOHAN
Department of Physics, Indian Institute of Technology, Kanpur 208 016, India

MS received 13 December 1982

Abstract. That the longlived component L of K_0 has both CP $= +1$ and CP $= -1$ modes of decay is often cited as evidence of violation of CP invariance. The careful ones find the compelling evidence to be the non-dilution of the regeneration interference pattern when the incident K_0 beam is mixed even substantially with $\overline{K}_0$. However the two phenomena comprehensively imply that L has a CP $= +1$ component L_+ and a CP $= -1$ component L_- and that the longlived component of both K_0 and $\overline{K}_0$ are one and the same L. This does not demand abandoning CP invariance. It does imply that $\overline{K}_0$ is not the CP conjugate of K_0.

Keywords. CP conjugate; charge asymmetry; 2π interference; quark sea polarization.

1. Introduction

There is no theorem that demands that a resonance or a particle must be eigenstate of CP. Thus, for example, K_0 is a superposition of CP eigenstates K_+ and K_- with CP equal to $+1$ and -1 respectively. Hence if the longlived component L of K_0 has the structure

$$|L\rangle = N_+ |L+\rangle + N_- |L-\rangle$$

it does not imply CP violation. However, all the CP preserving models that have been advanced earlier have been proven fallacious (Kabir 1969) invoking the fact that the regeneration interference patterns of K_0 and $\overline{K}_0$ are found to be in phase. A common feature of all these models and also of the currently accepted view point of CP violation is the unsubstantiated assumption that $\overline{K}_0$ is CP conjugate of K_0. There does not exist any experimental verification of this assumption. Consequently one must take a second look at these experiments with an open mind. We reverse the traditional bias (Mohapatra 1979). We accept CP invariance and abandon CP conjugate relationship between K_0 and $\overline{K}_0$ and follow through the consequences (Mohan 1976). The regeneration interference experiment now has the simple interpretation that the same L is the longlived component of both K and $\overline{K}_0$. To follow other detailed consequences we need to be more precise about the neutral kaon states.

2. The signatures

Let us assume the structure

$$|K_0\rangle = \frac{(1+|\epsilon|^2)^{1/2}}{\sqrt{2}\,(1+\epsilon)}[|L\rangle + |S\rangle],$$

$$|\bar{K}_0\rangle = \frac{(1+|\epsilon|^2)^{1/2}}{\sqrt{2}\,(1-\epsilon)}[-|L\rangle + |S\rangle],$$

where $|S\rangle = M_+|S_+\rangle + M_-|S_-\rangle$.

We will find that N_- and M_+ are nearly unity while N_+ and M_- are about a thousandth.

On account of CP invariance we are forced to conclude the existenee of two-charge conjugate states

$$|K_0^c\rangle = \frac{(1+|\epsilon|^2)^{1/2}}{\sqrt{2}\,(1+\epsilon)}[|L^c\rangle + |S^c\rangle],$$

$$|\bar{K}_0^c\rangle = \frac{(1+|\epsilon|^2)^{1/2}}{\sqrt{2}\,(1-\epsilon)}[-|L^c\rangle + |S^c\rangle],$$

where $|L^c\rangle = N_+|L_+\rangle - N_-|L_-\rangle,$

$$|S^c\rangle = M_+|S_+\rangle - M_-|S_-\rangle.$$

All the states abvoe are normalized to unity. We also demand the orthogonality

$$\langle K_0|\bar{K}_0\rangle = \langle K_0|K_0^c\rangle = \langle \bar{K}_0|\bar{K}_0^c\rangle = 0.$$

These requirements imply

$$|N_+|^2 + |N_-|^2 = |M_+|^2 + |M_-|^2 = 1,$$

$$|N_+|^2 - |M_-|^2 = |N_-|^2 - |M_+|^2,$$

$$N_+^* M_+ \langle L_+|S_+\rangle = N_- M_-^* \langle S_-|L_-\rangle,$$

$$\langle L|S\rangle = 2\,\mathrm{Re}\,\{N_+ M_+^* \langle S_+|L_+\rangle\} = \frac{2\,\mathrm{Re}\,\epsilon}{1+|\epsilon|^2},$$

and rather large overlaps

$$\langle K_0|\bar{K}_0^c\rangle = \langle \bar{K}_0|K_0^c\rangle^* = \frac{1+|\epsilon|^2}{2\,(1-|\epsilon|^2+\epsilon^*-\epsilon)}[|N_-|^2 + |M_+|^2$$

$$-|N_+|^2 - |M_-|^2 + 4i\,\mathrm{Im}\,\{N_+^* M_+ \langle L_+|S_+\rangle\}].$$

The questions arise: where are K_0^c and $\bar{K}_0^c$, why haven't they been seen, what are their signatures, how do they fit in the recognized families of particles?

Irrespective of details of any model it is clear that if nucleon-nucleon collision produces K_0 and $\bar{K}_0$ then the corresponding antiparticle collisions must produce K_0^c and $\bar{K}_0^c$ with certainty. Before advancing our conjecture on the production mechanism we will investigate the signatures of the four neutral kaons in their decay amplitudes.

To keep inferences clean we consider decays in vacuum only leaving out the regeneration experiments. The most successful vacuum decay experiments study the two pi interference parameter η and the lepton charge asymmetry parameter δ. For the K_0 decay these parameter become

$$\eta_{ab} \equiv \frac{\langle \pi^a \pi^b \,|\, T \,|\, L\rangle}{\langle \pi^a \pi^b \,|\, T \,|\, S\rangle} = \frac{N_+ \langle \pi^a \pi^b \,|\, T \,|\, L_+\rangle}{M_+ \langle \pi^a \pi^b \,|\, T \,|\, S_+\rangle},$$

and

$$\delta_L \equiv \frac{N_L^+ - N_L^-}{N_L^+ + N_L^-} = \frac{2 \operatorname{Re} [N_+ N_-^* c_1 c_2^*]}{|N_+ c_1|^2 + |N_- c_2|^2},$$

$$c_1 = \langle l^+ \nu \pi^- \,|\, T \,|\, L_+\rangle,$$

$$c_2 = \langle l^+ \nu \pi^- \,|\, T \,|\, L_-\rangle.$$

Both these parameters look at the neutral K beam at a stage where the shortlived part $|S\rangle$ has largely decayed. For a total investigation a short time charge asymmetry parameter δ_s is necessary. This studies $(N_s^+ - N_s^-)/(N_s^+ + N_s^-)$ in the short life-time just as δ_L studies in the long life-time. The asymmetry is now caused by the interference of the dominant parts $|S_+\rangle$ and $|L_-\rangle$ of the shortlived and longlived entities. The expression is

$$\delta_s = \frac{N_s^+ - N_s^-}{N_s^+ + N_s^-} = \frac{2 \operatorname{Re} [M_+ N_-^* d_1 c_2^*]}{|M_+ d_1|^2 + |N_- c_2|^2},$$

$$d_1 = \langle l^+ \nu \pi^- \,|\, T \,|\, S_+\rangle.$$

Corresponding parameters for beams of each of the particles $\bar{K}_0$, K_0^c, $\bar{K}_0^c$ can be directly read off by looking at the coefficients of $|L_\pm\rangle$, $|S_\pm\rangle$ in the expressions for each of these particle states. These are tabulated below.

	K_0	$\bar{K}_0$	K_0^c	$\bar{K}_0^c$
$\pi\pi$ interference	η	$-\eta$	η	$-\eta$
long time charge asymmetry	δ_L	δ_L	$-\delta_L$	$-\delta_L$
short time charge asymmetry	δ_S	$-\delta_S$	$-\delta_S$	δ_S

In a mixed beam of K_0, $\overline{K}_0$, K_0^c, and $\overline{K}_0^c$ with concentrations $N(K_0)$, $N(K_0)$, $N(K_0^c)$, and $N(\overline{K}_0^c)$ respectively the dilution factors R_η, $R_{\delta L}$, and $R_{\delta S}$ for the above experiments are as follows.

$$R_\eta = N(K_0) - N(\overline{K}_0) + N(K_0^c) - N(\overline{K}_0^c),$$

$$R_{\delta L} = N(K_0) + N(\overline{K}_0) - N(K_0^c) - N(\overline{K}_0^c),$$

$$R_{\delta S} = N(K_0) - N(\overline{K}_0) - N(K_0^c) + N(\overline{K}_0^c)$$

The dilution factors are directly measurable. The inverse relations

$$N(K_0) = \tfrac{1}{4}\,[R_\eta + R_{\delta L} + R_{\delta S} + 1],$$

$$N(\overline{K}_0) = \tfrac{1}{4}\,[R_{\delta L} - R_\eta - R_{\delta S} + 1],$$

$$N(K_0^c) = \tfrac{1}{4}\,[R_\eta - R_{\delta L} - R_{\delta S} + 1],$$

$$N(\overline{K}_0^c) = \tfrac{1}{4}\,[R_{\delta S} - R_\eta - R_{\delta L} + 1],$$

then give the desired individual concentrations. The neutral K beam emerging from e^+e^- collision or from proton antiproton collision is likely to be, largely, an equal mixture of K_0 and K_0^c. Such a beam is sharply distinguished from a pure K_0 beam by the fact that the mixture will show no charge asymmetry but it will display undiluted $\pi\pi$ interference pattern. Such an investigation is doable today and is extremely interesting. It will restore CP invariance in scientific literature.

3. Conjecture

We now attempt to understand why K_0^c and $\overline{K}_0^c$ are not observed. It has to be related with the mode of production. In the laboratory we always produce kaons from nucleon-nucleon collisions. It seems that when the kaon is produced in a quark-dominated environment the result is K_0 and $\overline{K}_0$ and when it is produced in an antiquark-dominated environment the result is K_0^c and $\overline{K}_0^c$. Looking at the strong interaction phenomenology which does not permit enlargement of spectrum of strangeness values we conclude that the basic quark composition of K_0 and $\overline{K}_0^c$ cannot be different; similarly the basic quark composition of $\overline{K}_0$ and K_0^c cannot be different. The difference within each of the pairs must lie in the polarization of the quark sea.

$$K_0 \sim d\bar{s} + d\bar{s}\,(\bar{q}q)_1 + \ldots., \qquad \overline{K}_0 \sim \bar{d}s + \bar{d}s\,(\bar{q}q)_1 + \ldots.$$

$$\overline{K}_0^c \sim d\bar{s} + d\bar{s}\,(\bar{q}q)_{-1} + \ldots., \qquad K_0^c \sim \bar{d}s + \bar{d}s\,(\bar{q}q)_{-1} + \ldots.$$

We make the fundamental assumption that the lowest state of a system of zero charge, zero baryon number, and strangeness ± 1 is degenerate in quark-sea polarization. However, each production environment sharply distinguishes the different polarizations, selecting one and rejecting the other.

The particular sea-quark configuration favoured in a production mechanism dominated by quark may be assigned a quantum number $SQ=1$ and the configuration favoured under antiquark dominated production mechanism may be assigned $SQ=-1$. In the language of S-matrix, the resonant poles at $m_L - i/2\,\Gamma_L$ and $m_S - i/2\,\Gamma_S$ are both doubly degenerate due to the two valued spectrum of SQ. However under quark-dominated production the poles associated with $SQ=+1$ stay put at $m_L - i/2\,\Gamma_L$ and $m_S - i/2\,\Gamma_S$ but those associated with $SQ=-1$ move away so far that they can no longer be recognized as resonances. Similarly under antiquark-dominated production the poles associated with $SQ=-1$ stay put at $m_L - i/2\,\Gamma_L$ and $m_S - i/2\,\Gamma_S$ while those associated with $SQ=+1$ move away washing out the corresponding resonances.

It is natural to expect an extension of these ideas to other mesons. It may be that, like baryons, family of mesons are distinct from family of antimesons. Former being characterized by $SQ=1$ and latter by $SQ=-1$. However, unlike baryons, these are not orthogonal families. Just as there is large overlap between K_0 and $\bar{K}_0^c$ there may be even larger overlap between π^- and π^{+c}.

The study of a $SQ=-1$ particle scattering off a nucleon would show an interesting feature of a flip to $SQ=+1$ particle. Due to this the passage of a $SQ=-1$ beam through thin film of matter deserves to be studied in detail. One can see the two strong-interaction processes of SQ flip and of regeneration proceeding together.

4. Estimates

Some oversimplified estimates of the decay parameters can be made (Review of Particle Properties 1982). The polarization of the quark sea is only slight. From this we extrapolate that the Hilbert space of the (not completely orthogonal) four neutral kaons K_0, $\bar{K}_0$, K_0^c, $\bar{K}_0^c$ is not very different from that of just the two K_0, $\bar{K}_0$, which mean that $|L_+\rangle$ is almost the same as $|S_+\rangle$ and $|S_-\rangle$ is almost the same as $|L_-\rangle$. One then has the following approximate results:

$$\langle L \mid S\rangle \sim 2\ \mathrm{Re}\,(N_+ M_+^*) \sim 2\ \mathrm{Re}\ N_+,$$

$$\eta_{ab} = \frac{N_+ \langle \pi^a \pi^b \mid T \mid L_+\rangle}{M_+ \langle \pi^a \pi^b \mid T \mid S_+\rangle} \sim \frac{N_+}{M_+} \sim N_+,$$

$$c_1 = \langle l^+ \nu \pi^- \mid T \mid L_+\rangle \sim \langle l^+ \nu \pi^- \mid T \mid S_+\rangle$$

$$\sim (1+x)\,\langle l^+ \nu \pi^- \mid T \mid K_0\rangle,$$

$$c_2 = (1-x)\,\langle l^+ \nu \pi^- \mid T \mid K_0\rangle,$$

$$\delta_L = \frac{2\ \mathrm{Re}\,[N_+ N_-^* (1+x)(1-x^*)]}{|N_+(1+x)|^2 + |N_-(1-x)|^2} \sim 2\ \mathrm{Re}\left[N_+ \frac{1+x}{1-x}\right].$$

The unitary relation

$$(-i\Delta m + \bar{\bar{\Gamma}})\langle L|S\rangle = \sum_F \langle F|T|L\rangle^* \langle F|T|S\rangle$$

with the assumption of saturation by $\pi\pi$ intermediate states becomes

$$(-i\Delta m + \bar{\bar{\Gamma}})\langle L|S\rangle \sim \eta^* \Gamma_s,$$

or $$\eta = \frac{\bar{\bar{\Gamma}} + i\Delta_m}{\Gamma_S}\langle L|S\rangle,$$

or $$N_+ = \frac{\bar{\bar{\Gamma}} + i\Delta m}{\frac{1}{2}\bar{\Gamma}_S} \text{Re } N_+,$$

(for consistency we must have $\dfrac{2\bar{\bar{\Gamma}}}{\Gamma_S} \sim 1$),

or $$\eta = (\sec \phi_{\Delta m})(\text{Re } N_+) \exp(i\phi_{\Delta m})$$

where $$\tan \phi_{\Delta m} = \frac{\Delta m}{\bar{\bar{\Gamma}}}.$$

Hence the approximate relation (with $x \sim 0$),

$$\eta = (\sec \phi_{\Delta m}) \frac{\delta_L}{2} \exp(i\phi_{\Delta m}).$$

5. Conclusion

The experiments that are supposed to establish violation of CP invariance have an alternate interpretation. There are clear-cut doable experiments that can decide between the two stands.

References

Gyan Mohan 1976 International report No. IC/76/73 International Centre for Theoretical Physics Publication Office, Trieste, Italy

Kabir P K 1969 *Phys. Rev. Lett.* **22** 1018

Mohapatra R N 1979 *Proc. XIX Int. Conf. on High Energy Physics, Tokyo, Japan*, (eds.) S Homma, M Kawaguchi and H Miyazawa (Tokyo: Physical Society of Japan)

Review of Particle Properties 1982 *Phys. Lett.* **111B** 85

Pramāṇa, Vol. 21, No. 3, September 1983, pp. 207–225. © Printed in India.

Quantum chromodynamics predictions in renormalization scheme invariant perturbation theory

A DHAR and V GUPTA
Tata Institute of Fundamental Research, Homi Bhabha Road, Bombay 400 005, India

MS received 13 June 1983

Abstract. It has recently been shown that any physical quantity $\mathcal{R}$, in perturbation theory, can be obtained as a function of only the renormalization scheme (RS) invariants, ρ_0, ρ_1, ρ_2, ... Physical predictions, to any given order, are renormalization scheme independent in this approach. Quantum chromodynamics (QCD) predictions to second order, within this RS-invariant perturbation theory, are given here for several processes. These lead to some novel relations between experimentally measurable quantities, which do not involve the unknown QCD scale parameter Λ. They can therefore be directly confronted with experiments and this has been done wherever possible. It is suggested that these relations can be used to probe the neglected higher order corrections.

Keywords. Renormalization scheme independence; perturbation theory; quantum chromodynamics.

1. Introduction

In the conventional perturbative approach to any quantum field theory, finite order predictions for physical quantities depend on the renormalization scheme (RS) used to define the renormalized parameters of the theory. This RS-dependence of the perturbative predictions is especially severe in quantum chromodynamics (QCD) where the running coupling is not so small at the currently available energies. The various schemes used (Buras 1981) give substantially different higher order corrections. The difficulty in meaningfully comparing such predictions with experiments is obvious and has been widely discussed in the literature (Buras 1981). At a deeper level, one cannot even begin to ask questions about the convergence of the perturbation series before resolving this RS-ambiguity.

The usual approach to the problem of the RS-dependence in QCD has been to look for an expansion parameter in terms of which the higher order corrections to several processes are small. This approach has been questioned by Stevenson (1981) according to whom the best scheme to use for a given physical quantity is the one in which a perturbative approximant to it is the least sensitive to small changes in the RS. The point being that in this 'optimal' scheme the perturbative approximant has to some extent the property which the actual physical quantity is known to have, namely, RS-independence. However, Stevenson's criterion for determining the 'optimal' scheme does not make *full* use of the RS-independence of the physical quantities.

The RS-dependence problem has recently been solved (Dhar 1982, hereafter referred to as I) by making use of the full renormalization group invariance of the physical

quantities. It has been shown that, for a massless field theory with a single coupling constant, any physical quantity R in perturbation theory is determined as a function of only the RS-invariants, $\rho_0, \rho_1, \rho_2, \ldots$ (see § 2 for definition), through the transcendental equation

$$\rho_0 = \frac{1}{R} - \rho_1 \ln\left(1 + \frac{1}{\rho_1 R}\right) + \int_0^R \mathrm{d}x \left(\frac{1}{x^2(1+\rho_1 x)} + \frac{1}{\rho(x)}\right), \tag{1}$$

$$\rho(x) = -x^2(1 + \rho_1 x + \rho_2 x^2 + \ldots). \tag{2}$$

The purpose of this paper is to cast QCD predictions for a number of processes in this RS-invariant form and to confront them with experiments wherever possible. In § 2 we first give a brief summary of I and establish the notation. This section also includes a general discussion of (1). In § 3 general tests, based on the second order approximation to (1) are given. These tests remarkably involve only experimental quantities and can be directly confronted with the data. Theoretical estimates of the third order corrections are discussed in § 4. In § 5 second order RS-invariant QCD predictions for several physical processes are given and confronted with the data wherever possible. Finally, § 6 contains a discussion and summary of the results.

2. Renormalization scheme invariant perturbation theory (RESIPE)

Consider a physical quantity $\mathscr{R}$, which has the perturbation expansion

$$\mathscr{R} = a^p \sum_{n=0}^{\infty} R_n a^n, \; R_0 = 1. \tag{3}$$

Here $a = a(\mu) \equiv \alpha(\mu)/\pi$ is the couplant ($\alpha(\mu)$ being the renormalized coupling constant) and μ is the renormalization point. The power p can be non-integral or even negative. The couplant a satisfies the β-function equation

$$\mu \frac{\partial a}{\partial \mu} = \beta(a) = -ba^2 \sum_{n=0}^{\infty} c_n a^n, \quad c_0 = 1. \tag{4}$$

The first two coefficients b and c_1 are RS-invariant. Their values in QCD are $b = (33 - 2f)/6$, $c_1 = (153 - 19f)/2(33 - 2f)$, where f is the number of fermion flavours. The other coefficients $c_n (n \geqslant 2)$ are RS-dependent and only c_2 has been calculated (Tarasov *et al* 1980). Its value in the $\overline{\text{MS}}$ scheme is $(c_2)_{\overline{\text{MS}}} = 3(2857/2 - 5033f/18 + 325f^2/54)/16(33 - 2f)$. The RS in which a and the coefficients R_n are evaluated in (3) can be labelled by the set of parameters $\{\tau \equiv b \ln \mu/\Lambda, c_2, c_3, \ldots\}$ where Λ is the scale parameter which determines the boundary condition for the solution to (4).

The derivation of (1) proceeds as follows. Corresponding to $\mathcal{R}$ we first construct the physical quantity $(\mathcal{R})^{1/p}$ since it is this which satisfies (1). We write

$$(\mathcal{R})^{1/p} \equiv R = a \sum_{n=0}^{\infty} r_n a^n, \tag{5}$$

where $$r_0 = 1;\ r_n = \sum_{m=0}^{n-1} \frac{1}{(n-m)!} \frac{1}{p}\left(\frac{1}{p}-1\right)\left(\frac{1}{p}-2\right).\ldots.$$

$$\left(\frac{1}{p} - n + m + 1\right)\tilde{F}_m^{(n-m)}, \quad n \geqslant 1; \tag{6}$$

and $\tilde{F}$'s satisfy the recursion relation

$$\tilde{F}_l^{(n+1)} = \sum_{m=0}^{l} R_{m+1}\ \tilde{F}_{l-m}^{(n)},\ n \geqslant 1; \tag{7}$$

$$\tilde{F}_l^{(1)} = R_{l+1}. \tag{8}$$

we give below explicit expressions for the first few r_n 's:

$$r_1 = R_1/p, \tag{9}$$

$$r_2 = R_2/p + (1-p)\ R_1^2/2p^2, \tag{10}$$

$$r_3 = R_3/p + (1-p)\ R_1\ R_2/p^2 + (1-p)\ (1-2p)\ R_1^3/6\,p^3, \tag{11}$$

etc. The RS-invariants, $\rho_0, \rho_1, \rho_2, \ldots$, are simple polynomial functions of the c_n 's and r_n ' s. The first few are

$$\rho_0 = \tau - r_1, \tag{12}$$

$$\rho_1 = c_1, \tag{13}$$

$$\rho_2 = c_2 + r_2 - \rho_1\, r_1 - r_1^2, \tag{14}$$

$$\rho_3 = c_3 + 2r_3 - 4r_1\, r_2 - 2r_1\, \rho_2 - r_1^2\, \rho_1 + 2r_1^3, \tag{15}$$

etc. For a proof of the RS-invariance of the ρ_n's we refer the reader to I. The derivation of (1), given in I, is then based on the following observation: In the RS in which all r_n 's vanish* ρ_0 equals τ and ρ_n 's ($n \geqslant 1$) are equal to the β-function co-

*It is always possible to choose this RS because r_n's are in one-to-one correspondence with c_n's and furthermore r_n depends linearly on c_n (see equations (12) to (15)).

efficients, the c_n's. Moreover, in this RS the value of the couplant a is numerically equal to the value of the physical quantity R. Using this information* in the solution to (4) we get (1) which determines R implicitly as a function of only the RS-invariants, $\rho_0, \rho_1, \rho_2, \ldots$. The nth order approximation to R in RESIPE corresponds to setting $\rho_i = 0$ for $i \geqslant n$.

The ρ_n's contain all the information coming from the Feynman diagram calculations. They are different for different physical quantities and, in general, depend on the external kinematic variables on which the physical quantity itself depends. However, for an R that depends on only one external energy scale Q, the ρ_n's ($n \geqslant 1$) are constants independent of Q. To see this, note that, in this case, the r_n's are functions of the dimensionless variable μ/Q only. Thus, in the scheme in which $\mu = Q$, they are given by

$$\bar{r}_n = r_n(\mu/Q)\big|_{\mu = Q}, \tag{16}$$

which are constants independent of Q. Therefore the ρ_n's will not depend on Q, except for ρ_0 which is given by**

$$\rho_0 = \frac{b}{2} \ln \frac{Q^2}{\Lambda^2} - \bar{r}_1 \equiv t - \bar{r}_1. \tag{17}$$

For more than one energy scale, $Q, Q', Q'', \ldots$, the $\bar{r}_n$'s will be functions of $\eta' = Q'/Q$, $\eta'' = Q''/Q$, etc. and so will be the ρ_n's.

A striking property of (1) is that it is not a perturbation expansion for R in the conventional sense since there is *no* expansion parameter in it. One can, however, recover the usual perturbative results from it, under certain approximations. For example, the second order approximation to (1) is

$$\rho_0 = \frac{1}{R} - \rho_1 \ln (1 + 1/\rho_1 R). \tag{18}$$

Then, for fixed η', η'', etc., in the limit $t \to \infty$, one gets from (17) and (18).

$$R \underset{t \to \infty}{\sim} a(t)\,[1 + \bar{r}_1\, a(t) + \ldots], \tag{19}$$

$$a(t) = \frac{1}{t} - \rho_1 \frac{\ln t}{t^2}, \tag{20}$$

which is the usual renormalization group improved, but RS-dependent, second order perturbation approximation for R.

One can meaningfully ask questions about the convergence of a perturbation series in RESIPE. It is clear from (1) that for good convergence R should be small, which

*Note that this scheme is being used only as a mathematical device to arrive at the final result. Equation (1) is independent of any RS because of its manifest RS invariant form.

**In this case one can differentiate (1) w.r.t. t to obtain $dR/dt = \rho(R)$, which is analogous to (4).

implies that ρ_0 should be large. In addition, we must also require the ρ_n's ($n \geqslant 1$) to be small. More precisely, the following convergence criterion can be set:

$$\rho_0 R \sim 1, \tag{21}$$

$$|\rho_n R^n| \ll 1, \text{ i.e. } |\rho_n| \ll \rho_0^n, \; n \geqslant 1. \tag{22}$$

Clearly for large ρ_0 (22) is quite a weak condition on the ρ_n's ($n \geqslant 1$). If these criteria are satisfied then one can confidently hope to use low order approximations to (1) to make predictions for R.

The above discussion and what follows demonstrate the central role that ρ_0 plays in RESIPE. In a sense, one can compare ρ_0^{-1} with the running coupling of the conventional perturbation theory. There is, however, a crucial difference between the two, namely, that ρ_0 is RS-invariant but process-dependent while just the opposite is true for the running coupling. An important consequence of this property of ρ_0 is that, in RESIPE, it automatically picks up a scheme independent scale, Λ_{eff}, for each process.

$$\Lambda_{\text{eff}} = \Lambda \exp(\bar{r}_1/b). \tag{23}$$

In general, Λ_{eff} will depend on η', η'', etc. through $\bar{r}_1$. For example, Λ_{eff} will be a function of the other variable x for the deep inelastic structure functions and the photon structure function. For a given process perturbation theory will make sense only if $Q \gg \Lambda_{\text{eff}}$ for it. Perturbation theory will not apply for those values of the kinematic variables η', η'', etc. for which Λ_{eff} becomes large. This happens for example in the case of the deep inelastic structure functions where, in the limit $x \to 1$,

$$\Lambda_{\text{eff}}^2(x) \sim \frac{\Lambda^2}{(1-x)}.$$

Comparison of RESIPE predictions with experiments proceeds as usual. Massless field theories with a single coupling constant have only one free parameter, the scale Λ. In principle this can be determined by a single experimental input. Everything else can then be predicted. In practice it may be better to determine Λ separately from experimental data for each process and then compare the values of Λ thus obtained. Of course, Λ is scheme-dependent and so its value must be accompanied by a scheme label. It is, however, entirely meaningful to compare the values of Λ *in a given scheme* for different processes to see how well perturbation theory works. The important point to keep in mind is that in RESIPE physical predictions are *order-by-order* RS-invariant.

3. The second-order formula

Since a third order calculation does not exist for any QCD process we shall restrict our discussion to the second order formula given in (18). From this equation

physical predictions are made most conveniently in a graphical form. To that end we define

$$\hat{\rho}_0 \equiv \rho_0/\rho_1, \quad \hat{R} \equiv \rho_1 R, \tag{24}$$

and rewrite (18) as follows:

$$\hat{\rho}_0 = \hat{R}^{-1} - \ln(1 + \hat{R}^{-1}). \tag{25}$$

Figure 1 shows the graph of $\hat{R}$ vs. $\hat{\rho}_0$. From this figure one can immediately read off $\hat{R}$ for any given value of $\hat{\rho}_0$ and vice versa. Note the strong dependence of $\hat{R}$ on $\hat{\rho}_0$ for small values of $\hat{\rho}_0$ ($\lesssim 1$). Thus predictions for $\hat{R}$ are not expected to be reliable for such values of $\hat{\rho}_0$. For large values of $\hat{\rho}_0$ ($\gtrsim 5$), $\hat{R}$ is sufficiently small for one to be able to use (25) with some measure of confidence.

The conventional method of testing QCD predictions is to fit the theoretical expressions to the data and compare the values of Λ so obtained from different processes. However, one cannot assess the reliability of the values of Λ so extracted without actually doing higher order calculations. It is therefore highly desirable to devise tests through which one can directly check with the data the reliability of a perturbative approximant for a process without having to know the value of Λ. RESIPE provides us precisely such tests. We discuss these below.

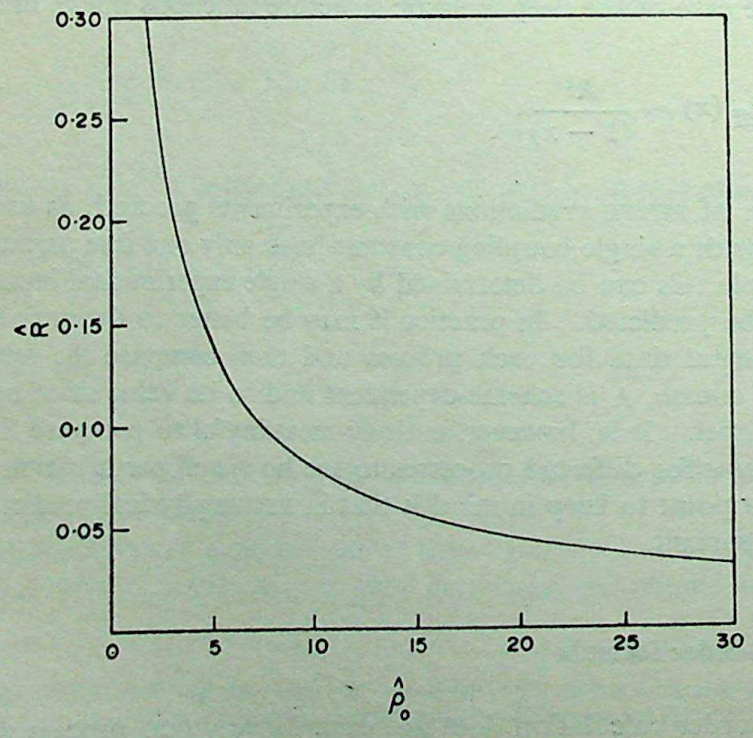

Figure 1. $\hat{R}$ as a function of $\hat{\rho}_0$ as given by equation (25).

3.1 *The geometric test*

Consider a process with only one external scale Q. For such a process we have from (17)

$$\hat{\rho}_0 (Q^2) = \frac{b}{2\rho_1} \ln \frac{Q^2}{\Lambda^2} - \bar{r}_1/\rho_1. \tag{26}$$

The geometric test follows from the identity

$$\hat{\rho}_0(Q_1^2) + \hat{\rho}_0(Q_2^2) = 2\hat{\rho}_0 [(Q_1^2 Q_2^2)^{1/2}] \tag{27}$$

which together with (25) gives

$$\hat{R}^{-1} (Q_1^2) + \hat{R}^{-1} (Q_2^2) - \ln [(1 + \hat{R}^{-1} (Q_1^2)) (1 + \hat{R}^{-1} (Q_2^2))]$$

$$= 2\hat{R}^{-1} [(Q_1^2 Q_2^2)^{1/2}] - 2 \ln \{[1 + \hat{R}^{-1} [(Q_1^2 Q_2^2)]^{1/2}]\} \tag{28}$$

Equation (28) relates the values of the physical quantity $\hat{R}(Q^2)$ at two different values of Q^2 to its value at their geometric mean. A simple way of testing (28) would be to vary Q_1^2 and Q_2^2 holding $Q_1^2 Q_2^2 = Q_0^4$ fixed. This equation then simplifies to

$$\hat{R}^{-1} (Q^2) + \hat{R}^{-1} (Q_0^4/Q^2) = \ln [(1+\hat{R}^{-1} (Q^2)) (1+\hat{R}^{-1} (Q_0^4/Q^2))] + c, \tag{29}$$

where $\frac{1}{2} c = \hat{R}^{-1} (Q_0^2) - \ln (1 + \hat{R}^{-1} (Q_0^2))$ is independent of Q^2. Any deviations of the data from (29) would indicate the magnitude of the higher order corrections.

3.2 *The scaling test*

This test follows from the identity

$$\hat{\rho}_0 (Q_2^2) - \hat{\rho}_0 (Q_1^2) = \frac{b}{2\rho_1} \ln (Q_2^2/Q_1^2). \tag{30}$$

If we keep $Q_2^2/Q_1^2 = \eta$ fixed then (30) implies the following relation between the values of $\hat{R}$ at Q^2 and the scaled-up point ηQ^2:

$$\hat{R}^{-1} (\eta Q^2) - \ln (1+\hat{R}^{-1} (\eta Q^2)) = \hat{R}^{-1} (Q^2) - \ln (1+\hat{R}^{-1} (Q^2)) + c', \tag{31}$$

where $c' = b/2\rho_1 \ln \eta$ is independent of Q^2. Equation (31) can be tested by varying Q^2 for different fixed values of η. Any deviations of the data from it would again indicate the magnitude of the higher order corrections.

3.3 *The average value test*

Often it is convenient to consider the average of a physical quantity over a range of Q^2. Since the natural variable here is $\ln Q^2$, we calculate the quantity

$$\langle \mathscr{R} \rangle \equiv \frac{1}{\ln (Q_2^2/Q_1^2)} \int_{\ln Q_1^2}^{\ln Q_2^2} \mathrm{d} \ln Q^2 \, \mathscr{R}(Q^2), \tag{32}$$

where, in general, $\mathscr{R} = (\hat{R}/\rho_1)^p$ (see equation (5) and (24)).

To evaluate the integral in (32) we note that (25) can be written in the following equivalent form

$$\hat{R} = 1/[\hat{\rho}_0 + F(\hat{\rho}_0)], \tag{33}$$

where $F(\hat{\rho}_0)$ satisfies the transcendental equation

$$e^F - F - 1 = \hat{\rho}_0 \tag{34}$$

Since,

$$\mathrm{d} \ln Q^2 = \frac{2\rho_1}{b} \frac{d\hat{\rho}_0}{\mathrm{d}F} \mathrm{d}F = \frac{2\rho_1}{b} (e^F - 1) \, \mathrm{d}F,$$

we get, with $\mathscr{R}_i^{-p} = \mathscr{R}(Q_i^2)$,

$$\langle \mathscr{R} \rangle = \frac{2}{b \ln (Q_2^2/Q_1^2)} \int_{\mathscr{R}_1}^{\mathscr{R}_2} \mathrm{d}z \, \frac{z^{1-p}}{(\rho_1 + z)} \tag{35}$$

Of special interest are the cases with $p = -1$ (the photon structure function) and $p = +1$ (the $e^+ e^-$ ratio R). We shall discuss these in detail in § 5.2 and § 5.3 respectively.

Some remarkable features of the above tests need to be emphasized. The geometric and the scaling tests exploit the $\ln Q^2$ dependence of $\hat{\rho}_0$ directly. It is this which also helps us to calculate the average $\langle \mathscr{R} \rangle$. All the tests give simple relations between experimentally measurable quantities. Further, they do not require any knowledge of Λ or even of the second order coefficient $\bar{r}_1$ and as such can be directly confronted with the data. This makes them ideal for probing the neglected higher order corrections. Once the region(s) of the external kinematic variables where higher order corrections are small is (are) determined one can fit (25) to the data and determine Λ. An example of this procedure is given in § 5.1 where we discuss the moments of the non-singlet structure functions.

4. Third order corrections

To make theoretical estimates of the higher order corrections to the second-order approximant $\hat{R}$, we consider the third order approximation to (1):

$$\hat{\rho}_0 = \hat{R}_3^{-1} - \ln(1 + \hat{R}_3^{-1}) + \int_0^{\hat{R}_3} dx \left[\frac{1}{x^2(1+x)} - \frac{1}{x^2(1+x+\hat{\rho}_2 x^2)}\right], \tag{36}$$

where $\hat{\rho}_2 = \rho_2/\rho_1^2$ and we have attached the subscript '3' to $\hat{R}_3$ to distinguish it from the second order approximant $\hat{R}$. The integral in (36) can be done analytically and is equal to

$$\frac{1}{2}\ln\frac{(1+\hat{R}_3)^2}{(1+\hat{R}_3+\hat{\rho}_2\hat{R}_3^2)} + \frac{(2\hat{\rho}_2 - 1)}{\sqrt{(4\hat{\rho}_2 - 1)}}$$

$$\times\left[\tan^{-1}\frac{(1+2\hat{\rho}_2\hat{R}_3)}{\sqrt{(4\hat{\rho}_2-1)}} - \tan^{-1}\frac{1}{\sqrt{(4\hat{\rho}_2-1)}}\right]$$

for $\hat{\rho}_2 > 1/4$ and

$$\frac{1}{2}\ln\frac{(1+\hat{R}_3)^2}{(1+\hat{R}_3+\hat{\rho}_2\hat{R}_3^2)} + \frac{1}{2}\frac{(2\hat{\rho}_2-1)}{\sqrt{(1-4\hat{\rho}_2)}}\ln\left[\frac{2+\hat{R}_3(1+\sqrt{(1-4\hat{\rho}_2)})}{2+\hat{R}_3(1-\sqrt{(1-4\hat{\rho}_2)})}\right]$$

for $\hat{\rho}_2 < 1/4$.

In figure 2 $\hat{R}_3$ *vs* $\hat{\rho}_0$ is plotted for $\hat{\rho}_2 = \pm 5, \pm 10$ and ± 15, where for comparison the curve for $\hat{\rho}_2 = 0$ has also been included. We see that $\hat{R}_3$ depends sensitively on $\hat{\rho}_2$ for small values of $\hat{\rho}_0$. On the other hand $\hat{R}_3$ varies little with $\hat{\rho}_2$ for large values of $\hat{\rho}_0$. The second order formula, equation (25), will therefore break down for sufficiently small $\hat{\rho}_0$. The precise value of $\hat{\rho}_0$ for which this happens will depend on the magnitude of $\hat{\rho}_2$. It has been suggested (Duke and Kimel 1982; Abbot 1980; Blumenfeld and Moshe 1982) that the general trend of the existing higher order calculations is consistent with taking $r_2 \sim r_1$ and $r_2 \sim r_1^2$. With these guesses for r_2 and a typical value of $r_1 = 4$ we find that a safe estimate for $\hat{\rho}_2$ is $\hat{\rho}_2 \sim \pm 5$. Using these values in figure 2 we see that the error in the predicted value of $\hat{R}$ (*i.e.* of $\hat{R}_3$ for $\hat{\rho}_2 = 0$) is reasonably small ($\lesssim 20\%$) for $\hat{\rho}_0 \gtrsim 4$. Of course, in particular cases the actual value of $\hat{\rho}_2$ could be much smaller than the above estimate and so (25) could be valid down to much smaller values of $\hat{\rho}_0$. It is here that the tests mentioned in § 3.1 to 3.3 play a crucial role. Thus, while in general one should restrict the use of (25) only to value of $\hat{\rho}_0 \gtrsim 4$, one may use it confidently even for lower values of $\hat{\rho}_0$ if the data so indicate.

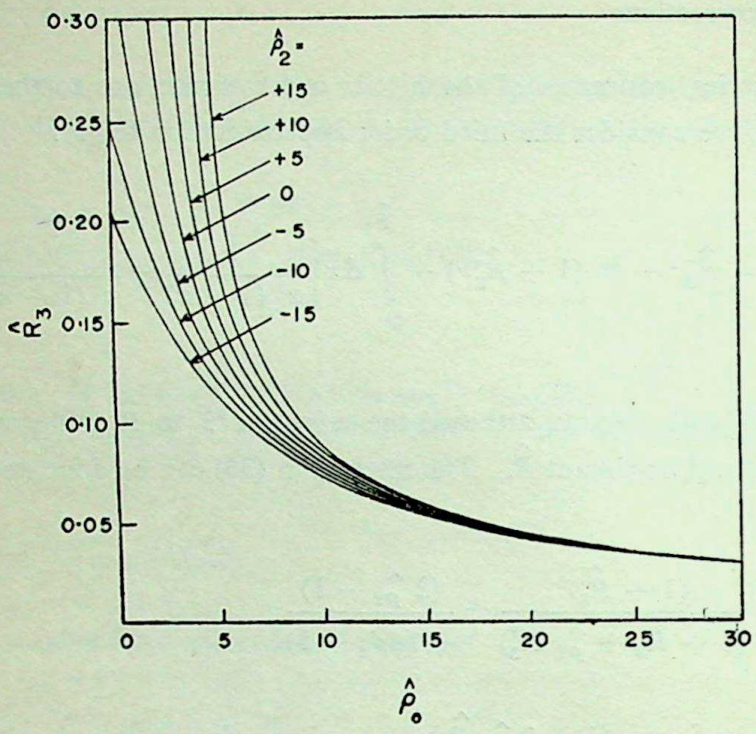

Figure 2. $\hat{R}_3$ as a function of $\hat{\rho}_0$ (equation 36) for various values of $\hat{\rho}_2$. For comparison, the curve for $\hat{\rho}_2 = 0$ is also shown.

5. Applications to QCD

We now consider the predictions of the second order RESIPE for some QCD processes in detail. Throughout the following we shall use the $\overline{\text{MS}}$ scheme as the base scheme. However, for ease of notation we shall not use this label explicitly, it being understood that all the scheme-dependent quantities are given in the $\overline{\text{MS}}$ scheme.

5.1 *Deep inelastic scattering: moments of nonsinglet (structure functions)*

The physical quantities which are perturbatively calculable here are not the moments but their Q^2 variation (Duke and Kimel 1982)

$$\hat{R}_i^{(n)}(Q^2) = -\frac{2\rho_1}{b\mathrm{d}_i^{(n)}} \frac{\mathrm{d} \ln M_i^{(n)}(Q^2)}{\mathrm{d} \ln Q^2}, \; i = 2, 3, L, \tag{37}$$

$$\mathrm{d}_{2,3}^{(n)} = \mathrm{d}_n, \; \mathrm{d}_L^{(n)} = (\mathrm{d}_n + 1), \tag{38}$$

where
$$M_i^{(n)}(Q^2) \equiv \int_0^1 \mathrm{d}x \, x^{n-2} F_i^{NS}(x, Q^2), \quad n \geqslant 2, \tag{39}$$

and $i = 2$, 3 and L refer to moments of the structure functions F_2^{NS}, xF_3 and F_L respectively. Also, we have (Duke and Kimel 1982)

$$\hat{\rho}_{0,i}^{(n)}(Q^2) = \frac{b}{2\rho_1} \ln \frac{Q^2}{\Lambda^2} - \frac{\alpha_i^{(n)}}{\rho_1}. \tag{40}$$

The quantities d_n and $\alpha_i^{(n)}$* have been calculated (Bardeen *et al* 1978; Buras 1980; Duke *et al* 1981) and are listed for 4 flavours for $i = 2$ and 3 for the first few moments in table 1. The effective scale in this case is

$$\Lambda_{\text{eff},i}^{(n)} = \Lambda \exp(\alpha_i^{(n)}/b), \tag{41}$$

which increases with n for all the structure functions. Thus the uncertainty in the second-order predictions will increase with n for all the structure functions.

To second order $\hat{R}_i^{(n)}$ and $\hat{\rho}_{0,i}^{(n)}$ satisfy (25). This equation can be easily integrated (see § 3.3) to get the following prediction for the moments:

$$M_i^{(n)}(Q^2) = M_i^{(n)}(Q_0^2) \exp[-\mathrm{d}_i^{(n)} \{F_i^{(n)}(Q^2) - F_i^{(n)}(Q_0^2)\}], \tag{42}$$

where $F_i^{(n)}$ satisfies the transcendental equation

$$\exp(F_i^{(n)}) - F_i^{(n)} - 1 = \hat{\rho}_{0,i}^{(n)}. \tag{43}$$

From (42) and (43) we find that the moments satisfy the equation

$$\frac{\ln [M_i^{(n)}(Q_0^2)/M_i^{(n)}(Q^2)]^{1/d_i^{(n)}} + \dfrac{b}{2\rho_1} \ln (Q^2/Q_0^2)}{[M_i^{(n)}(Q_0^2)/M_i^{(n)}(Q^2)]^{1/d_i^{(n)}} - 1} = K_i^{(n)} \tag{44}$$

where $K_i^{(n)}$ is constant independent of Q.

Table 1. Numerical values of the quantities d_n and $\alpha_i^{(n)}$ $(i = 2, 3)$ for the first few moments.

n	d_n	$\alpha_2^{(n)}$	$\alpha_3^{(n)}$
2	0·427	2·768	1·467
3	0·667	3·476	2·892
4	0·837	3·964	3·606
5	0·970	4·334	4·082
6	1·080	4·628	4·438
7	1·173	4·875	4·722
8	1·255	5·082	4·956
9	1·327	5·265	5·159
10	1·392	5·425	5·333
11	1·451	5·570	5·490
12	1·505	5·700	5·629

*$\alpha_{2,3}^{(n)}$ can be obtained from $\bar{R}_{i,n}^{NS}$'s given in table 1 of Buras (1980) by using $\alpha_2^{(n)} = (R_{2,n}^{NS}/4d_n) + c_1$ and $\alpha_3^{(n)} = (\bar{R}_{3,n}^{NS}/4d_n) + c_1$.

Equation (44) involves only experimentally measurable quantities and can be tested directly using the data on the moments. Knowledge of Λ or the second-order coefficients, $a_i^{(n)}$, is not required to carry out this test. Deviation of $K_i^{(n)}$ from a constant value, as Q^2 is varied, is a measure of the higher order corrections. Provided (44) is satisfied one can obtain the value of Λ from a measurement of $K_i^{(n)}$ by using the following relation

$$\Lambda^2 = Q_0^2 \exp\left(-\frac{2\rho_1}{b}(K_i^{(n)} - \ln K_i^{(n)} - 1 + a_i^{(n)}/\rho_1)\right). \tag{45}$$

We have carried out this novel test on the moments of xF_3 and F_2^{ep-en} using the moments computed by Duke *et al* (1982) from the CDHS and SLAC data*. Tables 2 and 3 give the values of $K_i^{(n)}$ for different Q^2, using $n = 4$, 5 and $Q_0^2 = 90$ (GeV)^2 for xF_3 and $n = 5$, 6 and $Q_0^2 = 22{\cdot}5$ (GeV)^2 for F_2^{ep-en}. We see that the data satisfies (44) fairly well down to low Q^2 values. There seems to be no indication of large higher order corrections or any other effects like higher twist. This fair constancy of $K_i^{(n)}$ with respect to Q^2 encourages us to evaluate Λ using (45). In table 4 we have listed tthe best values of $K_i^{(n)}$ and the corresponding values of Λ for the four cases studied here. All the data are consistent with a value of Λ of 450–500 MeV. A more detailed and complete analysis of the data using (44) is in progress and will be reported elsewhere.

Table 2. Values of $K_i^{(n)}$ for the fourth and fifth moments of the structure function xF_3 for $Q^2 \leqslant 28{\cdot}4$ (GeV)^2, with $Q_0^2 = 90$ (GeV)^2, obtained from the moments of the CDHS data computed by Duke *et al* (1982). Data at higher Q^2 were not used because the errors on $K_i^{(n)}$ becomes too large as Q^2 approaches Q_0^2.

Q^2 (GeV)^2	$K_3^{(4)}$	$K_3^{(5)}$
5·7	$9{\cdot}037 \begin{smallmatrix}+0{\cdot}882\\-0{\cdot}573\end{smallmatrix}$	$8{\cdot}620 \begin{smallmatrix}+0{\cdot}833\\-0{\cdot}566\end{smallmatrix}$
7·0	$9{\cdot}579 \begin{smallmatrix}+1{\cdot}981\\-1{\cdot}121\end{smallmatrix}$	$8{\cdot}873 \begin{smallmatrix}+0{\cdot}994\\-0{\cdot}684\end{smallmatrix}$
9·0	$9{\cdot}709 \begin{smallmatrix}+2{\cdot}161\\-1{\cdot}243\end{smallmatrix}$	$8{\cdot}741 \begin{smallmatrix}+1{\cdot}058\\-0{\cdot}733\end{smallmatrix}$
11·3	$8{\cdot}996 \begin{smallmatrix}+1{\cdot}894\\-1{\cdot}115\end{smallmatrix}$	$8{\cdot}392 \begin{smallmatrix}+1{\cdot}168\\-0{\cdot}780\end{smallmatrix}$
14·2	$9{\cdot}540 \begin{smallmatrix}+2{\cdot}470\\-1{\cdot}402\end{smallmatrix}$	$8{\cdot}492 \begin{smallmatrix}+1{\cdot}290\\-0{\cdot}869\end{smallmatrix}$
18·0	$8{\cdot}646 \begin{smallmatrix}+2{\cdot}144\\-1{\cdot}236\end{smallmatrix}$	$7{\cdot}713 \begin{smallmatrix}+1{\cdot}153\\-0{\cdot}779\end{smallmatrix}$
22·5	$7{\cdot}362 \begin{smallmatrix}+1{\cdot}510\\-0{\cdot}923\end{smallmatrix}$	$6{\cdot}745 \begin{smallmatrix}+0{\cdot}898\\-0{\cdot}621\end{smallmatrix}$
28·4	$8{\cdot}490 \begin{smallmatrix}+3{\cdot}570\\-1{\cdot}675\end{smallmatrix}$	$7{\cdot}319 \begin{smallmatrix}+1{\cdot}801\\-1{\cdot}048\end{smallmatrix}$

*We are grateful to D P Roy for getting the moments computed by Duke *et al* (1982) for us.

Table 3. Values of $K_i^{(n)}$ for the fifth and sixth moments of the structure function $F_2^{ep\text{-}en}$ for $Q^2 \leqslant 9{\cdot}0$ (GeV)^2, with $Q_0^2 = 22{\cdot}5$ (GeV)^2 obtained from the moments of the SLAC data computed by Duke *et al* (1982). Data at $Q^2 = 12{\cdot}5$ (GeV)^2 were not used for the same reason as in table 2.

Q^2 (GeV)^2	$K_2^{(5)}$	$K_2^{(6)}$
2·5	$6{\cdot}430 \begin{smallmatrix}+0{\cdot}479\\-0{\cdot}327\end{smallmatrix}$	$6{\cdot}313 \begin{smallmatrix}+0{\cdot}298\\-0{\cdot}220\end{smallmatrix}$
3·5	$6{\cdot}301 \begin{smallmatrix}+0{\cdot}743\\-0{\cdot}491\end{smallmatrix}$	$6{\cdot}169 \begin{smallmatrix}+0{\cdot}449\\-0{\cdot}333\end{smallmatrix}$
4·5	$5{\cdot}924 \begin{smallmatrix}+0{\cdot}870\\-0{\cdot}539\end{smallmatrix}$	$5{\cdot}778 \begin{smallmatrix}+0{\cdot}504\\-0{\cdot}360\end{smallmatrix}$
5·5	$6{\cdot}250 \begin{smallmatrix}+3{\cdot}167\\-1{\cdot}091\end{smallmatrix}$	$6{\cdot}178 \begin{smallmatrix}+2{\cdot}221\\-0{\cdot}909\end{smallmatrix}$
6·5	$5{\cdot}644 \begin{smallmatrix}+1{\cdot}522\\-0{\cdot}772\end{smallmatrix}$	$5{\cdot}595 \begin{smallmatrix}+0{\cdot}902\\-0{\cdot}566\end{smallmatrix}$
7·5	$5{\cdot}668 \begin{smallmatrix}+2{\cdot}401\\-0{\cdot}988\end{smallmatrix}$	$5{\cdot}466 \begin{smallmatrix}+1{\cdot}164\\-0{\cdot}663\end{smallmatrix}$
9·0	$5{\cdot}548 \begin{smallmatrix}+3{\cdot}215\\-1{\cdot}141\end{smallmatrix}$	$5{\cdot}378 \begin{smallmatrix}+1{\cdot}437\\-0{\cdot}774\end{smallmatrix}$

Table 4. The best values of $K_i^{(n)}$ obtained from tables 2 and 3, and the corresponding values of Λ obtained using (45).

$K_i^{(n)}$	Best value of $K_i^{(n)}$	Λ (MeV)
$K_3^{(4)}$	$8{\cdot}866 \pm 0{\cdot}470$	$489 \begin{smallmatrix}+81\\-70\end{smallmatrix}$
$K_3^{(5)}$	$8{\cdot}146 \pm 0{\cdot}318$	$551 \begin{smallmatrix}+60\\-54\end{smallmatrix}$
$K_2^{(5)}$	$6{\cdot}232 \pm 0{\cdot}285$	$477 \begin{smallmatrix}+44\\-41\end{smallmatrix}$
$K_2^{(6)}$	$6{\cdot}090 \pm 0{\cdot}177$	$464 \begin{smallmatrix}+26\\-25\end{smallmatrix}$

5.2 *The photon structure function*

The point-like contribution to the photon structure function, $F_2^\gamma(x, Q^2)$, is calculable in perturbative QCD. The second order calculations give (Bardeen and Buras 1979):

$$\frac{1}{\alpha^2} F_2^\gamma(x, Q^2) = \frac{2h(x)}{b} \frac{1}{a(Q)} \left(1 - \frac{bg(x)}{2} a(Q)\right). \tag{46}$$

Here α is the fine structure constant and the functions $h(x)$ and $g(x)$ are listed for 4 flavours in table 5 for $0{\cdot}4 \leqslant x \leqslant 0{\cdot}9$.

Table 5. Numerical values of $h(x)$ and $g(x)$ for $0{\cdot}4 \leqslant x \leqslant 0{\cdot}9$. The approximate analytic forms given by Bardeen and Buras (1979) have been used.

x	$h(x)$	$g(x)$
0·40	1·249	1·186
0·45	1·342	1·087
0·50	1·422	1·047
0·55	1·490	1·061
0·60	1·545	1·127
0·65	1·588	1·240
0·70	1·618	1·401
0·75	1·636	1·607
0·80	1·641	1·861
0·85	1·634	2·163
0·90	1·613	2·523

This is an example of the case with $p = -1$. So, to second order, the physical quantity

$$\hat{R}(x, Q^2) = \left[\frac{b}{2\rho_1 h(x)} \frac{1}{a^2} F_2^\gamma(x, Q^2)\right]^{-1}, \tag{47}$$

with $$\hat{\rho}_0(x, Q^2) = \frac{b}{2\rho_1}\left(\ln \frac{Q^2}{\Lambda^2} - g(x)\right). \tag{48}$$

satisfies (25).

Tests mentioned in § 3.1 to 3.3 can be carried out in this case. Particularly interesting from a practical point of view is the average value test. In this case, (35) gives

$$\left\langle \frac{1}{a^2} F_2^\gamma(x, Q^2) \right\rangle = [2h(x) \ln (Q_2^2/Q_1^2)]^{-1} \left(\left\{ \frac{1}{a^2} F_2^\gamma(x, Q_2^2) \right\}^2 - \left\{ \frac{1}{a^2} F_2^\gamma(x, Q_1^2) \right\}^2 \right) - \frac{2\rho_1 h(x)}{b}. \tag{49}$$

A simple way of testing the above prediction would be to study its x dependence. If the data satisfy (49) then a value of Λ can be obtained by using the experimental data in (25), (47) and (48). Alternatively, in the absence of precise data, given Λ one can theoretically calculate the right side of (49) using (25). As an illustration the prediction for $\left\langle \frac{1}{a^2} F_2^\gamma \right\rangle$ as a function of x is given in figure 3 or $\Lambda = 0{\cdot}2$ and $0{\cdot}4$ GeV with $Q_1^2 = 5$ (GeV)^2 and $Q_2^2 = 20$ (GeV)^2. Clearly the curve for $\Lambda = 0{\cdot}2$ GeV lies much above the curve for $\Lambda = 0{\cdot}4$ GeV for all x. Thus a precise measurement of $\left\langle \frac{1}{a^2} F_2^\gamma \right\rangle$ may provide a good indication of the magnitude of Λ.

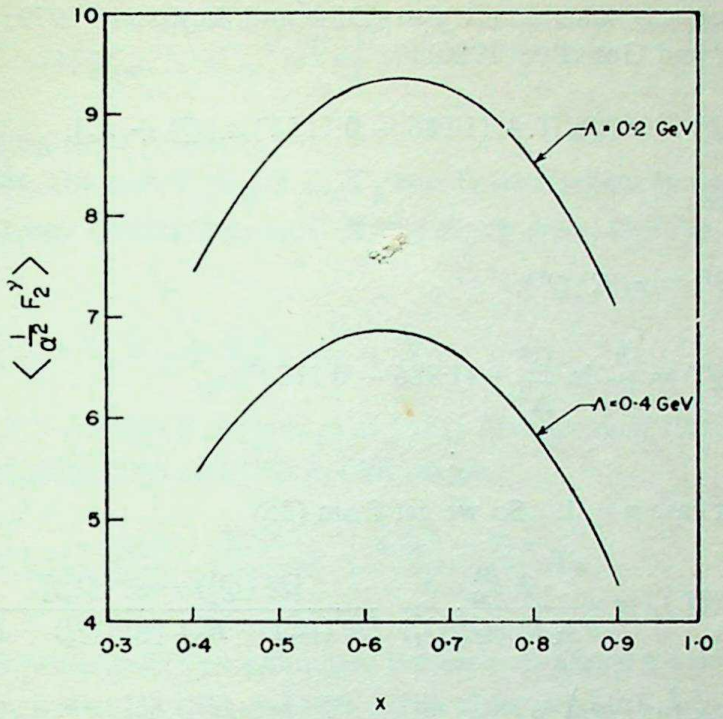

Figure 3. The x dependence of $\left\langle \frac{1}{a^2} F_2^\gamma (x, Q^2) \right\rangle$ (equation (49)) for $\Lambda = 0{\cdot}2$ and 0·4 GeV. The average is taken for $Q_1^2 = 5$ (GeV)^2 and $Q_2^2 = 20$ (GeV)^2.

In the present case the effective scale picked up by $\hat{\rho}_0$ is a function of x and is given by

$$\Lambda_{\text{eff}}(x) = \Lambda \exp [g(x)/2]. \tag{50}$$

This decreases from 1·81 Λ to 1·69 Λ as x goes from 0·4 to 0·5 and then increases to 3·53 Λ at $x = 0{\cdot}9$.

5.3 $e^+ e^-$ *Annihilation*

We write the experimentally-measured cross-section ratio as

$$\frac{\sigma(e^+ e^- \to \text{hadrons})}{\sigma(e^+ e^- \to \mu^+ \mu^-)} \equiv \mathcal{R}(Q^2) = R_0 [1 + R(Q^2)], \tag{51}$$

where Q is the total c.m. energy and

$$R_0 = 3 \sum_{i=1}^{f} e_i^2$$

is the parton model value, independent of Q. So what will enter (1) is the quantity $[\mathcal{R}(Q^2)/R_0 - 1] = R(Q^2)$ which has a perturbative expansion in the form of (5).

The second-order QCD calculations give (Dine and Sapirstein 1979; Chetyrkin *et al* 1979; Celmaster and Gonsalves 1980)

$$R(Q^2) = a(Q)\,[1 + (1{\cdot}986 - 0{\cdot}115f)\,a(Q) + \ldots]. \tag{52}$$

To this order then

$$\hat{R}(Q^2) = \rho_1\, R(Q^2), \tag{53}$$

and

$$\hat{\rho}_0(Q^2) = \frac{b}{2\rho_1} \ln \frac{Q^2}{\Lambda^2} - (1{\cdot}986 - 0{\cdot}115f)/\rho_1, \tag{54}$$

satisfy (25).

In the present case $p = 1$. So we get from (35)

$$\langle \mathscr{R}(Q^2) \rangle = \frac{2\,R_0^2}{b\,\rho_1 \ln (Q_2^2/Q_1^2)} \frac{[\mathscr{R}(Q_1^2) - \mathscr{R}(Q_2^2)]}{[\mathscr{R}(Q_1^2) - R_0]\,[\mathscr{R}(Q_2^2) - R_0]}$$

$$+ \left(1 - \frac{1}{\rho_1}\right) R_0. \tag{55}$$

Experimentally, $\mathscr{R}$ is found to be constant within errors for c.m. energies between 14 and 37 GeV with an average value of $\mathscr{R} = 4{\cdot}01 \pm 0{\cdot}03 \pm 0{\cdot}20$ (Lüke 1982). The difference $[\mathscr{R}(Q_1^2) - \mathscr{R}(Q_2^2)]$ in this range of Q is less than the systematic uncertainty of about 5%. Consequently it is not possible to test (55) meaningfully at present.

5.4 *Heavy quark-antiquark systems*

Calculations upto second order now exist for a number of processes in the J/ψ and Υ systems. We shall consider here only two examples, namely, Υ-decay and the hyperfine splitting in the J/ψ system.

5.4a Υ-*decay:* The widths Γ_g, Γ_γ and Γ_μ for Υ decaying into gluons, a direct photon plus gluons and $\mu^+\mu^-$ pair respectively have been calculated upto the second order (Mackenzie and Lepage 1981). The quantities predictable in perturbative QCD are the ratios

$$\Gamma_g/\Gamma_\mu = \frac{10(\pi^2 - 9)\pi^2}{9\alpha^2}\, a^3(M_\Upsilon)\,[1 + 9{\cdot}1a(M_\Upsilon) + \ldots], \tag{56}$$

and

$$\Gamma_\gamma/\Gamma_\mu = \frac{8(\pi^2 - 9)\pi}{9\alpha}\, a^2(M_\Upsilon)\,[1 + 3{\cdot}7a(M_\Upsilon) + \ldots]. \tag{57}$$

Here α is the fine structure constant. We have here examples of physical quantities with $p=3$ and $p=2$ respectively. Thus the quantities which should satisfy (25) are

$$\hat{R}_g = \rho_1 \left(\frac{9\alpha^2}{10(\pi^2 - 9)\pi^2}\,\Gamma_g/\Gamma_\mu\right)^{1/3},\quad \hat{\rho}_{0,g} = \frac{b}{\rho_1} \ln \frac{M_\Upsilon}{\Lambda} - \frac{3{\cdot}03}{\rho_1}; \tag{58}$$

and $$\hat{R}_\gamma = \rho_1 \left[\frac{9\alpha}{8(\pi^2-9)\pi}\Gamma_\gamma/\Gamma_\mu\right]^{1/2}, \hat{\rho}_{0,\gamma} = \frac{b}{\rho_1}\ln\frac{M_\Upsilon}{\Lambda} - \frac{1{\cdot}85}{\rho_1}. \tag{59}$$

The $\hat{\rho}_0$'s are given for 4 flavours.

Experimentally, the sum $\Gamma_g/\Gamma_\mu + \Gamma_\gamma/\Gamma_\mu$ can be determined by using the measured values for the leptonic branching ratio B_μ for the Υ-decay and the $e^+ e^-$ ratio $\mathscr{R}$ in the relation

$$\Gamma_g/\Gamma_\mu + \Gamma_\gamma/\Gamma_\mu = B_\mu^{-1} - (3 + \mathscr{R}). \tag{60}$$

Taking $B_\mu = (3{\cdot}3 \pm 0{\cdot}05)$ % (Alam *et al* 1981; Mueller *et al* 1981), $\mathscr{R} = 3{\cdot}5$ for 4 light quarks and using (58) and (59) in (60) we get

$$23{\cdot}8^{+5{\cdot}4}_{-4{\cdot}0} = \frac{10(\pi^2-9)\pi^2}{9\alpha^2\rho_1^3}\hat{R}_g^3 + \frac{8(\pi^2-9)\pi}{9\alpha\rho_1^2}R_\gamma^2. \tag{61}$$

Equation (61) involves only one unknown, the scale Λ. Given a value of Λ, one can obtain $\hat{R}_g$ and $\hat{R}_\gamma$ from (25), (58) and (59). The right side of (61) can be then evaluated. In this way one can fit a value of Λ to (61). We find for $M_\Upsilon = 9{\cdot}46$ GeV and 4 flavours that

$$\Lambda = 105^{+35}_{-26}\,\text{MeV}. \tag{62}$$

For this value of Λ, $\hat{\rho}_{0,g} = 10{\cdot}2 \pm 0{\cdot}8$ $(\Gamma_g/\Gamma_\mu = 23{\cdot}2)$ and $\hat{\rho}_{0,\Upsilon} = 11{\cdot}0 \pm 0{\cdot}8$ $(\Gamma_\gamma/\Gamma_\mu = 0.6)$ are both large. Higher order corrections are therefore not expected to change it appreciably.

5.4b. *Hyperfine splitting in the J/ψ system:* The physical observable calculable in perturbative QCD in this case is the ratio of the hyperfine splitting to the leptonic width (Buchmuller *et al* 1981)

$$\frac{\Delta E(\psi)}{\Gamma(\psi \to \mu^+\mu^-)} = \frac{2\pi}{\alpha^2}a(m_c)\,[1 + 6{\cdot}1\,a(m_c) + \ldots]. \tag{63}$$

This calculation has been done for 3 flavours. The quantities that should satisfy (25) in this case are

$$\hat{R} = \frac{\alpha^2}{2\pi}\rho_1\left(\frac{\Delta E(\psi)}{\Gamma(\psi\to\mu^+\mu^-)}\right), \quad \hat{\rho}_0 = \frac{b}{\rho_1}\ln\frac{m_c}{\Lambda} - \frac{6{\cdot}1}{\rho_1}. \tag{64}$$

The experimental value for the ratio $\Delta E/\Gamma$ is $0{\cdot}21 \pm 0{\cdot}03$ (Berkelman 1981). Therefore, $\hat{R} = 0{\cdot}37 \pm 0{\cdot}05$ and the corresponding value of $\hat{\rho}_0$ from figure 1 is

$$\hat{\rho}_0 = 1{\cdot}39^{+0{\cdot}32}_{-0{\cdot}23}. \tag{65}$$

For $m_c = M_\psi/2 = 1{\cdot}55$ GeV and 3 flavours this implies

$$\Lambda = 232^{+22}_{-28}\ \text{MeV}. \tag{66}$$

Because of the very small value of $\hat{\rho}_0$ in this case, higher order corrections could appreciably change the value of Λ obtained above. This number is therefore not expected to be very reliable.

6. Discussion and summary

In this paper we have given second-order RESIPE predictions for (i) moments of the nonsinglet structure functions, (ii) photon structure function, (iii) cross-section ratio in e^+e^- annihilation, (iv) gluonic width of Υ and (v) hyperfine splitting in the J/ψ system. Some of these predictions remarkably do not involve the unknown scheme-dependent QCD scale parameter Λ. Consequently they can be directly confronted with experiments. Any deviations from them would indicate the magnitude of the neglected higher order corrections which can thus be probed by these tests. We have carried out such a test, equation (44), for the moments of the nonsinglet structure functions xF_3 and $F_2^{\text{ep}-\text{en}}$. The data satisfy (44) fairly well within errors, indicating that higher order corrections are small. One can therefore consider the value of $\Lambda = 450$–500 MeV obtained in this case as quite reliable. Such tests can be carried out for the cases (ii) and (iii) also when more accurate data, then at present, become available. In the case of (iv) and (v) the data consist of only one number each. As such, one can only extract Λ in these cases. The values we obtain are $\Lambda = 105^{+35}_{-26}$ MeV from the gluonic width of the Υ and $\Lambda = 232^{+22}_{-28}$ MeV from the hyperfine splitting in the J/ψ system. In the former case ρ_0 is large and so higher order corrections are not expected to appreciably change the value of Λ obtained. However, in the latter case the extracted value of Λ is not expected to be reliable because of the smallness of ρ_0. The values of Λ quoted above are in the $\overline{\text{MS}}$-scheme which was used as the base scheme throughout this work. It is clear that Λ is much smaller for the heavy quark systems than for the moments of the structure functions. At the level of the present analysis it does not seem possible to reconcile the two values and give a definite value of Λ. This is a serious problem, in our view, which deserves further careful and detailed study.

Finally, a word about RESIPE and the central role of ρ_0 in it. The basic equation of RESIPE, equation (1), can be approximated to any given order to get a scheme-independent approximation for the physical quantity R which satisfies it. The magnitude of ρ_0 for the process then provides a guide to the convergence of such a perturbation series for R. Through the $\ln Q^2$ term, ρ_0 gives the basic energy dependence for R. Actually, for processes with only one external energy scale, Q, ρ_0 alone depends on Q, all the other invariants being constants. The new second order tests (§ 3) are a consequence of the $\ln Q^2$ dependence of ρ_0 and essentially test this. Moreover, ρ_0 is instrumental in automatically defining a scheme-independent scale Λ_{eff} (equation (23)) for each process. This Λ_{eff} depends on the other dimensionless kinematic variables (e.g. x for the structure functions) in precisely the way phenomenology and other theoretical considerations seem to require.

Clearly further work is required to extend the RESIPE ideas to massive theories and also theories with more than one coupling constant. This is necessary for treating quark mass effects in QCD. It would also open up applications to electroweak gauge theories and grand unified theories.

Acknowledgements

Our warmest thanks are due to M V N Murthy, A Hema and Sourendu Gupta for their help with numerical computations.

References

Abbott L F 1980 *Phys. Rev. Lett.* **44** 1569
Alam M S *et al*, 1981 (CLEO Collaboration), contributed paper to the 1981 *International Symposium on Lepton and Photon Interactions at High Energies, Bonn.*
Bardeen W A and Buras A J 1979 *Phys. Rev.* **D20** 166
Bardeen W A *et al* 1978 *Phys. Rev.* **D18** 3998
Berkelman K 1981 *Proceedings of the XXth International conference on high energy physics, Madison, Wisconsin* (eds.) L Durand and L G Poudrom (New York: AIP)
Blumenfeld A and Moshe M 1982 *Phys. Rev.* **D26** 648
Buchmuller W *et al* 1981 *Phys. Rev.* **D24** 3003
Buras A J 1980 *Rev. Mod. Phys.* **52** 199
Buras A J 1981 *Proceedings of the* 1981 *International symposium on lepton and photon interactions at high energies, Bonn.*
Celmaster W and Gonsalves R J 1980 *Phys. Rev.* **D21** 3112
Chetyrkin K G *et al* 1979 *Phys. Lett.* **B85** 277
Dhar A 1982 1983 *Phys. Lett.* **B128** 407 (referred to as I in the present paper)
Dine M and Sapirstein J 1979 *Phys. Rev. Lett.* **43** 668
Duke D W and Kimel J D 1982 *Phys. Rev.* **D25** 2960
Duke D W *et al* 1981 *Phys. Rev.* **D25** 71
Duke D W, Owens J F and Roberts R G 1982 *Nucl. Phys.* **B195** 285
Luke D 1982 *Proceedings of the XXI International Conference on High Energy Physics, Paris* (eds) P Pctiau and M Porncuf
Mackenzie P B and Lepage G P 1981 *Phys. Rev. Lett.* **47** 1244
Mueller J J *et al* 1981 *Phys. Rev. Lett.* **46** 1181
Stevenson P M 1981 *Phys. Rev.* **D23** 2916
Tarasov O V *et al* 1980 *Phys. Lett.* **B93** 429

Pramāṇa, Vol. 21, No. 3, September 1983, pp. 227–231. © Printed in India.

He II spectra of La, Ce and Yb: Novel features in the valence band region*

D D SARMA
Solid State and Structural Chemistry Unit, Indian Institute of Science, Bangalore 560 012, India

MS received 24 August 1983

Abstract. He II photoelectron spectra of La, Ce and Yb show features which cannot be explained in terms of single electron excitations. It is proposed that these are due to formation of electron-hole pairs.

Keywords. UPS; valence fluctuation; valence band; rare earth metals.

We have been interested in the investigation of electron states in rare earth materials for some time (Rao and Sarma 1980). During the course of these investigations, we have observed unusual features in the valence bands of La, Ce and Yb which cannot be accounted for by the known electronic configurations of these metals. These features appear as sharp peaks in the valence band region and seem to represent an electronic process occurring in the bulk of the metal and not due to a surface effect. Such structures have been noticed at times (Steiner *et al* 1977; Baer *et al* 1981; Gudat *et al* 1981; Alvarado *et al* 1980), though with poor resolution (Steiner *et al* 1977; Baer *et al* 1981; Gudat *et al* 1981), and attributed to surface states (Gudat *et al* 1981; Alvarado *et al* 1980). We have investigated these features in the valence band region to understand their nature and origin and their possible relevance to the problem of spontaneous valence fluctuation.

In figure 1, we have shown the He II spectra of La, Ce and Yb. Lanthanum with the $4f^0\,(6s,\,5d)^3$ configuration is expected to show a single peak (marked 1 in figure 1) near the E_F originating mainly from $5d$-states, but we see two additional peaks at 2·1 and 3·5 eV (marked 2 and 3 respectively) in the spectrum. These features of La have not been described hitherto in the literature. Cerium is expected to exhibit a single structure due to $4f$ emission, besides an emission at E_F due to the conduction band (peak 1 in figure 1); we however see two peaks (2 and 3) besides peak 1. Peak 2 which appears distinctly in the spectrum shown in figure 1 has been noticed as a shoulder or an asymmetry on the higher binding energy side of the conduction band in earlier studies (Steiner *et al* 1977; Baer *et al* 1981). Ytterbium shows a weak feature due to the conduction band near E_F in He II spectra; in addition it shows four peaks (marked 1, 2, 3 and 4 in figure 1) due to $4f$-emission instead of the expected doublet due to the spin-orbit split structure.

*Communication No. 227.

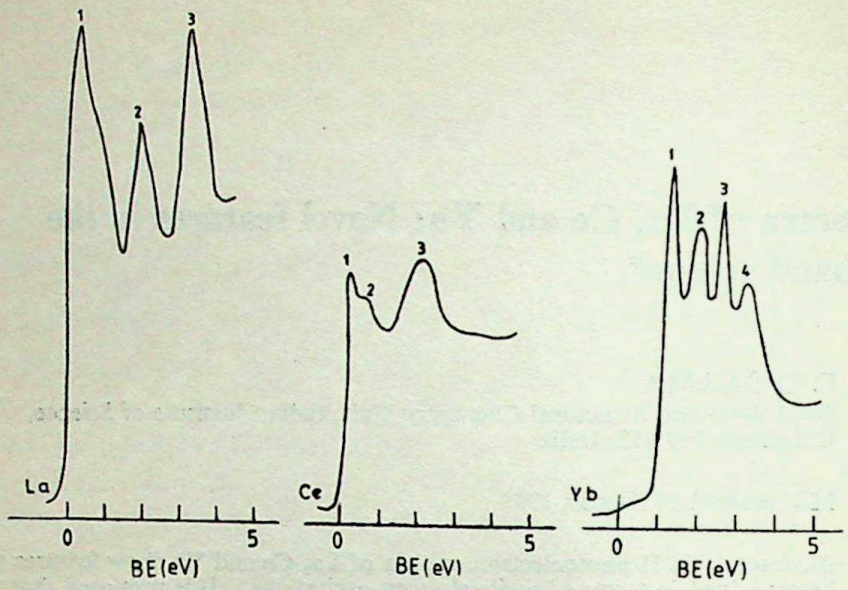

Figure 1. UV photoelectron spectra of La, Ce and Yb using He II radiation; various peaks in the spectra are marked by numbers.

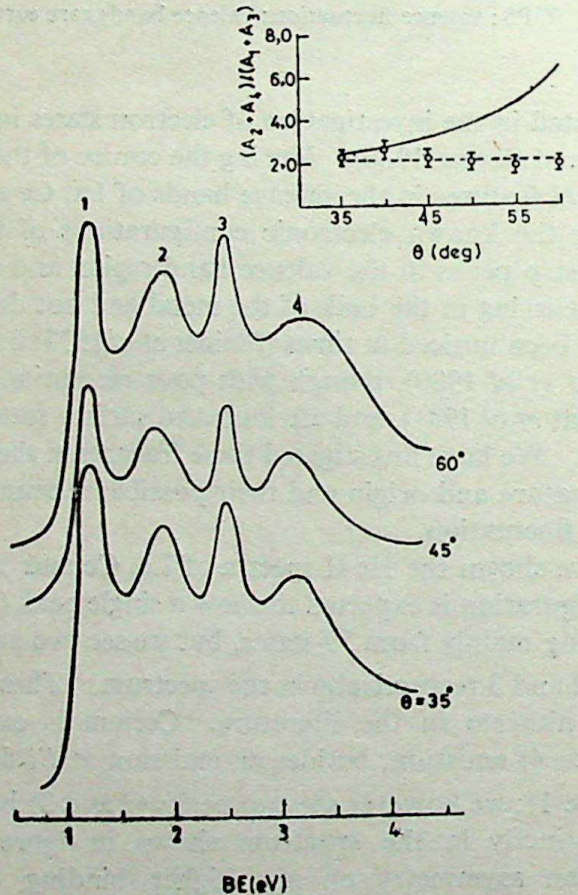

Figure 2. UV photoelectron spectra of Yb using He II radiation at various angles of acceptance into the analyzer. In the inset, the intensity ratio of peaks 2 and 4 to that of peaks 1 and 3 is plotted against the acceptance angle, θ, measured from the normal to the sample surface; the solid curve indicates the expected trend of the ratio if peaks 2 and 4 were due to surface states.

To investigate whether the additional features found in the valence band region could arise from surface states, we recorded the spectra of Yb inclined at various

angles of acceptance, θ (figure 2). We see that the relative intensities of the various peaks remain constant over the entire range of θ. The ratio of the combined areas of peaks 2 and 4 to that of peaks 1 and 3 have been measured by fitting the background subtracted spectra with four gaussians and the result is plotted against θ (figure 2, inset).

Alvarado *et al* (1980) have observed marked changes in the relative intensities of the peaks of Yb with the energy of the radiation and have therefore attributed peaks 2 and 4 to surface states. Our measurements with He I and He II radiations, however, gave unity as the value of K, where K is defined as $K = \ln(1+R^{II})/\ln(1+R^{I})$, with R^{I} (using He I) and R^{II} (using He II) representing the relative intensities of peaks 2 and 4 compared to that of peaks 1 and 3, indicating that all the peaks arise due to the bulk state. The angle dependence of relative intensities of the peak is probably more diagnostic of a surface state than variation of the relative intensities with the energies of radiations. This is because the photoejected electrons with low kinetic energies feel the effect of reorganisation of the residual electrons and decay of the final states considerably (Fuggle 1981).

In Ce, while peak 1 (figure 1) is due to conduction band emission, there is some doubt (Allen *et al* 1981; Croft *et al* 1981; Steiner *et al* 1977; Baer *et al* 1981) whether peaks 2 or 3 (in figure 1) is due to $4f$ emission. When the surface of Ce is oxidized to form Ce_2O_3 with the $(6s, 5d)^0\ 4f^1$ configuration of Ce, both peaks 1 and 2 vanish, but peak 3 is unaffected, showing unambiguously that peak 3 is due to $4f^1$ state. This observation suggests that peak 2 is in some way connected with the conduction band. Furthermore, peak 2 exhibits resonance photoemission (Gudat *et al* 1981) characteristic of the f-state and we therefore suggest that this feature represents the formation of an electron-hole pair where the hole in the $4f$ level following the photoemission is screened by localizing a conduction electron. This kind of screening is indeed known for deep core levels (Fuggle *et al* 1980). According to our assignment, the energy difference between peaks 2 and 3 ($\sim$1·5 eV) represents the binding energy of the electron-hole pair. Interestingly, peak 2 has a low FWHM compared to peak 3 which is due to unscreened $4f$ emission (table 1). In Yb, peaks 1 and 3 are sharp while 2 and 4 are relatively broad (table 1). The energy separation (1·3 eV) between 1 and 3 is the same as that between 2 and 4, which is equal to the spin-orbit splitting of the $4f^{13}$ final state. By analogy with Ce, we can assign peaks 2 and 4 to the unscreened

Table 1. Positions and FWHM (in eV) of valence band structures in La, Ce and Yb.

Metal	Peak No.	Binding energy	FWHM
La	1	0·4	—
	2	2·1	0·5
	3	3·5	0·7
Ce	1	0·3	—
	2	0·7	0·5
	3	2·2	0·9
Yb	1	1·2	0·3
	2	1·8	0·8
	3	2·4	0·3
	4	3·1	0·8

$4f_{7/2}$ and $4f_{5/2}$ states respectively while peak 1 (or peak 3) corresponds to electron-hole pair formation with the hole in the $4f_{7/2}$ (or $4f_{5/2}$) state. The binding energy of the electron-hole pair in Yb is the energy difference (0·7 eV) between peaks 1 and 2 (or between 3 and 4). As in Ce, we find that the state representing electron-hole pair formation has a smaller FWHM.

The assignment of peak 2 of Ce and of peaks 1 and 3 of Yb as due to electron-hole pair seems quite reasonable as we can rule out the possibility of shake-up processes or surface states. One of the difficulties of attributing peak 3 in the spectrum of Ce (figure 1) to the $4f^1$ emission has been that it would be impossible for Ce to manifest valence fluctuation with such a large energy ($\sim$2·1 eV) of the $4f$ level within the promotional mode. A similar difficulty will arise with Yb as well if peaks 2 and 4 are assigned to the $4f$ level. However, since the electron-hole pair formation is an integral part of $4f$ hole creation, the binding energy of this pair to a large extent compensates for the large excitation energy required for promoting a $4f$ electron.

The case of La is somewhat different from Ce and Yb in that there is no $4f$ population in the ground state, the empty $4f$ level lying $\sim$4 eV above E_F. As mentioned earlier, peak 1 in the spectrum of La (figure 1) is due to the conduction band. Peak 3 is 3·5 eV below E_F; this prompts us to speculate that peak 3 may arise from the promotion of a conduction band electron to the $4f$ level akin to a shake-up satellite accompanying the photoemission from the conduction band. Peak 2 which is narrower than peak 3 (see table 1) can be assigned to electron-hole pair formation with the electron in the $4f$ level; the binding energy of such a pair will then be $\sim$1·4 eV.

It is noteworthy that an extra feature has been noticed in the valence band of Eu in $EuPd_2Si_2$ which the authors have attributed to a surface state (Martensson *et al* 1982). It is possible that the valence band features of Eu may as well be due to electron-hole pair accompanying the unscreened $4f$ emission indicating the presence of a broad $4f$ level. Uranium, with its broad $5f$ level, also seems to exhibit an extra peak in the valence band region (Iwan *et al* 1981). On the basis of theoretical considerations, Liu and Ho (1982) have pointed out that such an electron hole pair formation is indeed possible in Ce. However, the model proposed by these authors is somewhat different. We believe that unscreened $4f$ emission is more probable if the $4f$ level is not highly localized.

Acknowledgement

The author is thankful to Prof. C N R Rao for suggesting the problem and helpful discussion. The author is also thankful to Prof. T V Ramakrishnan for helpful discussion. Financial support from DST is gratefully acknowledged.

References

Allen J W, Oh S J, Lindau I, Lawrence J M, Johansson L I and Hagstrom S B 1981 *Phys. Rev. Lett.* **46** 1100

Alvarado S F, Campagna M and Gudat W 1980 *J. Electron Spectrosc. Relat. Phenom.* **18** 43

Baer Y, Ott H R, Fuggle J C and DeLong L E 1981 *Phys. Rev.* **B24** 5384

Croft M, Weaver J M, Peterman D J and Franciosi A 1981 *Phys. Rev. Lett.* **46** 1104

Fuggle J C, Campagna M, Zolnierek Z, Lässer R and Platau A 1980 *Phys. Rev. Lett.* **45** 1597
Fuggle J C 1981 *Electron spectroscopy: Theory, techniques and applications* (eds) C R Brundle and A D Baker (New York: Academic Press) Vol. 4 p. 85
Gudat W, Campagna M, Rosei R, Weaver J H, Eberhardt W, Hulliger F and Kaldis E 1981 *J. Appl. Phys.* **52** 213
Iwan M, Koch E E and Himpsel F J 1981 *Phys. Rev.* **B26** 613
Liu S H and Ho K M 1982 *Phys. Rev.* **B26** 7052
Martensson N, Reihl B, Schneider W D, Murgai V, Gupta L C and Parks R D 1982 *Phys. Rev.* **B25** 1446
Rao C N R and Sarma D D 1980 *Science and Technology of rare earth materials* (eds) E C Subbarao and W E Wallace (New York: Academic Press) p. 291
Steiner P, Hochst H and Hüfner S 1977 *J. Phys.* **F7** L145

Pramāṇa, Vol. 21, No. 4, October 1983, pp. 233–240. © Printed in India.

Emission of large-p_T particles in p-nucleus and nucleus-nucleus collisions

D S NARAYAN
Tata Institute of Fundamental Research, Homi Bhabha Road, Bombay 400 005, India

MS received 8 June 1983

Abstract. The observed dependence of the yield of high p_T particles on the atomic number A of the target and the incident energy, in p-α, α-α and p-nucleus collisions, is explained in a coherent tube model.

Keywords. High p_T particles; proton-nucleus; nucleus-nucleus collision.

1. Introduction

Large p_T reactions have been studied extensively (Jacob and Landschoff 1978; Antreasyn *et al* 1979; Cronin *et al* 1975; Bromberg *et al* 1979) using both nucleons and heavy nuclei as targets. The latter, however, have been used until quite recently more for convenience rather than for any particular merit in their use to yield new physics of intrinsic value. Now there has come a shift in our understanding of the importance of p-nucleus and nucleus-nucleus collisions due to two factors. Firstly, the few existing results in such collisions have shown rather anomalous features (Bromberg *et al* 1979). Secondly there have been several speculations (Domokos and Goldman 1981; Anishetty *et al* 1980) about the production of exotic forms of nuclear matter or dense quark-gluon plasmas in heavy ion collisions at highly relativistic energies and a possible similarity of these states with conditions that existed during the first few seconds after the 'big bang' which created the universe.

The purpose of this paper is to present a model for large p_T reactions involving heavy nuclei and to explain the data on p-nucleus collisions at Fermilab (Antreasyn *et al* 1979; Cronin *et al* 1975) and the recent ISR data (Karabarbounis *et al* 1981; Bell *et al* 1982; Angelis *et al* 1982) on p-α and α-α collisions. A gratifying feature of the model is that experimental results which look anomalous or mutually conflicting are seen to be, in fact, consistent with the model and that the differences are due to different kinematical situations.

2. Description of the model

The model discussed here is an elaboration of the model, proposed by Fredriksson (1976) to explain the data of Chicago-Princeton collaboration (CP) (Antreasyn *et al*

1979) on p-nucleus collisions. The essential idea of the model is that in a p-nucleus collision, a large fraction of the target nucleons, lying in a tube along the straight line path of the projectile through the target nucleus, acts collectively and coherently in the interaction. An immediate conseqence of this assumption is that the N-N C. M. energy $\sqrt{s}$ gets enhanced to an effective value $(s_{\text{eff}})^{\frac{1}{2}} = (\nu(A)\, s)^{\frac{1}{2}}$, where $\nu(A)$ is the average number of nucleons in the tube which interact collectively. The model is often referred to as a coherent tube model (CTM) (Bergstrom *et al* 1983). Narayan and Sarma (1964) had invoked the model several years ago to explain the features of deuteron production in 25 GeV P-A collisions.

All the struck nucleons in the tube presumably form a localized hot-dense quark-gluon composite which interacts with the projectile. It is assumed that the composite remains in the environment of the residual nucleus (nucleons outside the tube) during hadronization. A consequence of this assumption is that the particles, emitted at large angles and hence with large p_T, can undergo secondary collisions in traversing nuclear matter and suffer an attenuation in the yield of particles at higher p_T values. This consideration is particularly important in the CP experiments where the targets are relatively heavy nuclei and the particles are detected at 90° in the C. M. system. In ISR experiments, the internuclear cascade would be negligible as the nuclei are light α-particles.

3. p-nucleus collisions

To implement the CTM for p-nucleus collisions, we need to make two changes in relation to p-p collisions. One expects that p-nucleus cross-section would be larger than the p-p cross-section by a factor like A^{δ}, with a 'geometrical' value of $\delta \sim 2/3$. So we first multiply the p-p cross-section by a factor A^{δ}. Secondly the N-N C. M. energy $\sqrt{s}$ is replaced, as mentioned earlier, by $(s_{\text{eff}})^{\frac{1}{2}}$. These changes can be made in the conventional formulation of any model for large p_T reactions. In the present work, we merely use a parametrized form of the inclusive large p_T cross-sections and make the necessary changes, as was done by Fredriksson (1976).

The large p_T inclusive cross-sections for $p + N \to \pi^- + X$ have been parametrized (Busser *et al* 1973) as

$$\Sigma(pp) \equiv E\,(d\sigma\,(pp)/d^3p) = (K/p_T^n)\exp(-Bp_T/\sqrt{s});\ B = 26. \tag{1}$$

In the light of our remarks, one can parametrize the inclusive p-nucleus collisions as

$$\Sigma(PA) = E\,(d\sigma\,(PA)/d^3p) = (K/p_T^n)\,A^{\delta}\exp[-Bp_T/(s_{\text{eff}})^{\frac{1}{2}}] \tag{2}$$

From (1) and (2), we have

$$R(PA) \equiv \Sigma(PA)/\Sigma(pp) = \exp\{\log A\,[\delta + B\,(p_T/\sqrt{s})\,f_1(A)]\}, \tag{3}$$

$$\Sigma(PA)/\Sigma(PA_0) = \exp\{a_{\pi^-}(s, p_T)\log A\}, \tag{4}$$

where

$$\alpha_{\pi^-}(s, p_T) = \delta + (Bp_T/\sqrt{s})\, f_1(A_0) + (Bp_T/\sqrt{s})\, [f_1(A_0) - f_1(A)]$$

$$[\log A]\, [\log A_0/A]^{-1}, \tag{5}$$

$$f_m = [\log A]^{-1} \left\{1 - [\nu(A)]^{-m/2}\right\}, \tag{6}$$

one can write $\nu(A) = \lambda A^{1/3}$ where λ is a constant which is treated as a free parameter. In CTM, $\lambda = (r_{\text{int}}/r_N)^2$, where r_{int} is the 'interaction radius' and r_N is the 'radius' of the nucleon. The last term on the right side of (5) is an A-dependent correction to α_{π^-}, which is, as we shall see, quite small for most nuclei. From (5), one finds that $\alpha_{\pi^-}(s, p_T)$ increases linearly with p_T and decreases inversely as $\sqrt{s}$.

4. Nucleus-nucleus Collisions

To calculate the yield of large p_T particles in α-α collisions, we need to make an appropriate extension of our model to deal with collisions between heavy nuclei. One trivial change is that A^δ gets replaced by $A_1^\delta A_2^\delta$, where A_1 and A_2 are the nucleon numbers of the colliding nuclei. A new ingredient is the occurrence of tube-tube (t-t) collisions, *i.e.* the interactions between massive composites formed out of tubes, aligned opposite to each other in the target and the projectile. In a t-t collision, the available C. M. energy is further augmented to $(s_{\text{eff}})^{\frac{1}{2}} = [\nu(A_1)\nu(A_2)s]^{\frac{1}{2}}$. The other new ingredient is the occurrence of more than one t-t collision. To make an estimate of this number, we draw an analogy between the collision of two heavy nuclei and the collision between two bunches in a linear collider, by regarding a nucleus as a bunch. Due to differences in the dimensions and the densities involved, the former results in t-t interactions and the latter in particle-particle (P_a-P_a) interactions. The number of P_a-P_a interactions in a single head-on collision between two bunches would be $\Delta_B = n_1 n_2 \sigma/F$ where n_1 and n_2 are the numbers of particles in the two bunches, F is the cross section of a bunch and σ is the p_a-p_a cross-section. We formally take the same expression to give the number of t-t interactions. For a head-on collision between two identical nuclei, we take $n_1 = n_2 = A$ and $F = 4\pi r_N^2 A^{2/3}$, and $\sigma = \pi r_{\text{int}}^2$. For a collision which is not head-on, we have to find n_1, n_2 and F for a given impact parameter, find the number of t-t interactions and finally average its value over all impact parameters. One can show that for identical nuclei, the average number Δ_A of the t-t interactions is

$$\Delta_A = C\lambda A^{4/3}\, [1 - (8A)^{-1/3}]^{-2}, \tag{7}$$

where C is a slowly varying function of A, $C \to 0{\cdot}165$ as $A \to \infty$. In individual events, the number of t-t interactions would have a Poisson distribution. The quantity of interest is not Δ_A but the average number N_A for events in which there has been at least one t-t interaction, which is needed to trigger the event. This number N_A is simply $N_A = \Delta_A/(1 - \exp(-\Delta_A))$. The number N_A enters as a multiplying factor in

the inclusive cross-section for nucleus-nucleus collisions. Incorporating the new ingredients in the parametrization of the inclusive cross-section for nucleus-nucleus collisions, the ratio $R(AA)$ can be written as:

$$R(AA) = \Sigma(AA)/\Sigma(pp) = N_A \exp\{\log A[2\delta + B(p_T/\sqrt{s})]f_2(A)\}. \quad (8)$$

The Chicago-Princeton (CP) data (Antreasyn *et al* 1979) on $p + \text{nucleus} \to \pi^-(p) + X$ has been parametrized as in (4), where A_0 is the nucleon number of some reference target. A significant result of this parametrization is that the exponent $\alpha_h(p_T)$ is independent of A. Secondly, the values of $\alpha_h(p_T)$ are larger than unity for values of $p_T > 2$ GeV/c. The values of α_h versus p_T for π^- and $\bar{p}$ are shown in figure 1. For π^-, the value of α_{π^-} increases linearly with p_T upto $p_T \sim 3$ GeV/c. For values of $p_T > 3$ GeV/c, the rate of increase slows down until it actually decreases with p_T. On the other hand, the value of $\alpha_{\bar{p}}$ shows a continuous increase upto the highest measured value of $p_T = 6{\cdot}15$ GeV/c. The ISR results (Karabarbounis *et al* 1981) on the reactions $p + \alpha \to \pi^0 + X$ and $\alpha + \alpha \to \pi^0 + X$ have been presented as the ratios $R(p\alpha)$ and $R(\alpha\alpha)$. The values of $R(p\alpha)$ and $R(\alpha\alpha)$ are shown in figure 2. One would expect that the values of $R(p\alpha)$ to be greater than 4 and those of $R(\alpha\alpha)$ to be greater than 16, in the light of CP data on the values of α. Surprisingly, the measured values of $R(p\alpha)$ are consistently less than 4 except at one point, while the values of $R(\alpha\alpha)$ are considerably greater than 16. If the observed values of $R_{\alpha\alpha}$ are parametrized as

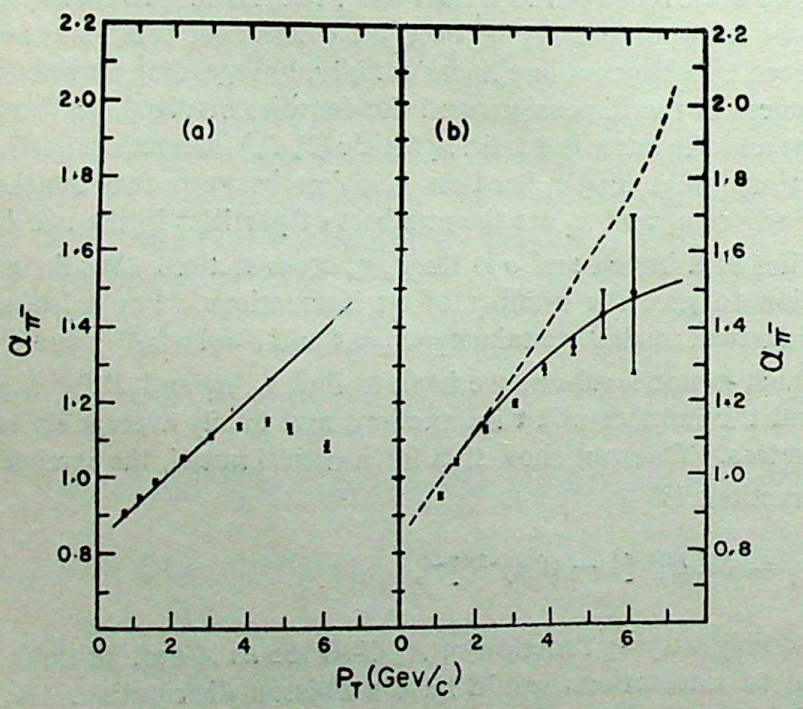

Figure 1. (a) α_{π^-} versus p_T for π^- at $E_L = 400$ GeV. (b) Same as in (a) for $\bar{p}$. Data from Anishetty *et al* (1980). Dashed and continuous curves: calculated values before and after correction.

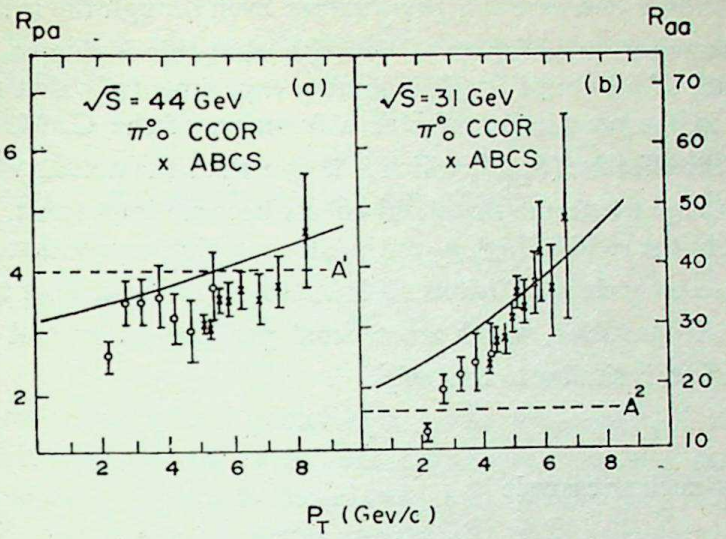

Figure 2. (a) $R(pa)$ versus p_T. (b) $R(aa)$ versus p_T. Data from Karabarbounis *et al* (1981) and rapporteur talk by H G Fisher at the Int. Nat. Conf. on High Energy Physics, Lisloon 9-15 July 1981. Curves give predictions.

$(A_{He})^{2\alpha_{\pi^0}}$, the value of α_{π^0} shows a linear increase with p_T, in apparent contradiction with CP data on π^-, but in agreement with the data on $\bar{p}$.

5. Comparison with experiment

The values of δ and λ in the present model, chosen to reproduce the initial linear rise of α_{π^-}, are $\delta=0{\cdot}83$ and $\lambda=0{\cdot}73$. With these parameters, the values of α_{π^-} have been calculated for some typical nuclei at $p_T = 3$ GeV/c and lab-energy $E_L = 400$ ($s \simeq 2ME_L$), taking tungsten (as per CP data) as the reference nucleus. The calculated values of α_{π^-} for tungsten, titanium, aluminium and beryllium are 1·11, 1·08, 1·11 and 1·12 respectively. These values of α_{π^-} can be regarded as almost independent of A. The solid line in figure 1a shows the calculated values of α_{π^-} at lab-energy $E_L =$ 400 GeV. The calculated values are in agreement with data for $p_T < 3$ GeV/c but in disagreement for $p_T > 3$ GeV/c, as the experimental values start deviating from the predicted linear rise. One may be inclined to regard this discrepancy as a failure of the model but the recent ISR data brings in a see-saw change in the results which necessitates a closer examination of them *vis-a-vis* the model.

The decrease of α_{π^-} (p_T) at higher p_T values in the Fermilab experiment shows that the pions at higher p_T values are attenuated relative to the pions at lower p_T values. But the same thing does not happen for π^0 in the ISR experiment. A meaningful way (there does not seem to be any other) by which one can understand the attenuation of π^- and lack of attenuation for π^0, is to postulate that particles created in primary collisions inside a heavy nucleus, as in the Fermilab experiment, undergo secondary interactions and suffer an attenuation at higher p_T values. The absence of attenuation in the ISR experiment is explained as due to the lack of any significant internuclear cascade in p-α and α-α collisions. But we have a problem in regard to $\bar{p}$ for which

$a_{\bar{p}}(p_T)$ does not show a decrease at high p_T values, even though the measurements were made with the same set-up as for π^-. We argue that this is due to an extra feature present in the case of $\bar{p}$ but not π^-. It is known experimentally that there is a strong threshold effect in the production of $\bar{p}$ as a function of the C. M. energy. In the context of CTM, the effective $(S_{\text{eff}})^{\frac{1}{2}}$, which is larger than the actual $\sqrt{S}$ lifts the C. M. energy into the range where the threshold effects become important. This results in an enhancement in the yield of high p_T antiprotons, which compensates more than the attenuation due to secondary collisions. It is interesting to note that the general trend of $a_{K^-}(p_T)$ for K^- particles, which are created particles as π^- and which exhibit a mild threshold effect, is similar to that of $\bar{p}$.

6. Effect of Inter-nuclear cascade

In the absence of a realistic treatment of the inter-nuclear cascade, we intend to proceed heuristically and try to show a consistency in the behaviour of $a_{\pi^-}(p_T)$ and $a_{\bar{p}}(p_T)$ by invoking both attenuation due to secondary collisions and an enhancement due to threshold effects. Since there is no threshold in the production of pions (at these energies), we may take the degree of attenuation for π^- as simply the amount of deviation from the predicted linear rise. In the case of $\bar{p}$, both attenuation and enhancement are present. We can calculate the amount of enhancement in our model but one does not know the attenuation. We assume that the degree of attenuation for particles of a given type is proportional to its inelastic cross-section on nucleons. We would then be able to obtain $a_{\bar{p}}(p_T)$ using the data on $a_{\pi^-}(p_T)$.

According to the CP data (Antreasyn *et al* 1979), the ratio of $\bar{p}$ to π^- in p-p collisions and hence the ratio of their inclusive cross-sections, can be parametrized as

$$1/p_T^n\left(1-\frac{2p_T}{\sqrt{s}}\right)^b$$

with $n = 0{\cdot}27 \pm 1{\cdot}7$ and $b = 4{\cdot}29 \pm 1{\cdot}9$. Using this information the $\bar{p}$ inclusive cross-section in p-A collisions can be parametrized as (normalization to a proton target, this differs only slightly from the original normalization)

$$\Sigma(P + A \to \bar{p} + X)/\Sigma(P + P \to \bar{p} + X) = \exp\,[a_{\bar{p}}(s, p_T)\ \log A], \qquad (9)$$

where

$$a_{\bar{p}}(s, p_T) = a_{\pi^-}(s, p_T) + \frac{b}{\log A}\log\frac{\zeta - v}{\zeta\,(1-v)}, \qquad (10)$$

$$v = 2p_T/\sqrt{s} \text{ and } \zeta = \sqrt{(\lambda A^{1/3})}.$$

Taking $b=6$, which is consistent with experiment, we calculate $a_{\bar{p}}$ according to (10). The calculated values are shown in figure 1b as a dotted curve. This curve has to be

corrected for attenuation. To this end, we define an 'attenuation factor' at each p_T value, which is the ratio of the calculated inclusive cross-sections before and after correction for attenuation. For π^-, the corrected value of α_{π^-} are identified with the experimental values. We assume, as stated earlier, that the ratio of the attenuation factors for π^- and p^- would be equal to the ratio of their inelastic cross-sections on nucleons. With this assumption, we have the relation

$$\alpha_{\bar{p}}^{\text{cal}} \to \alpha_{\bar{p}}^{\text{corr}} = \frac{\sigma_{\text{inel}}^{\bar{p}N}}{\sigma_{\text{inel}}^{\pi N}} \left(\alpha_{\pi^-}^{\text{cal}} - \alpha_{\pi^-}^{\text{expt}}\right),$$

where α^{cal} refer to values before attenuation. The values of $\alpha_{\bar{p}}^{\text{cal}}$, calculated in this manner, are shown in figure 1b. The corrected values are now in satisfactory agreement with experiment. The slight disagreement at two or three points can perhaps be improved by a better choice of the parameters. The present set of parameters have been chosen to get an over all agreement with results of p-nucleus as well as p-α and α-α collisions. As the results of p-α and α-α collisions have large errors and cannot be regarded as final, it would not be worthwhile to look for close agreement on one set of data.

7. Results on p — ∝ and ∝ — ∝ collisions

Coming to ISR results, the calculated values of $R(p\alpha)$ are shown by the curve in figure 2a. The calculated and experimental values agree within errors which are rather large. The unexpectedly small values of $R(p\alpha)$ are due to A_{He} ($A_{\text{He}} = 4$) being small and the equivalent lab-energy E_L ($S \sim 2ME_L$) being large, $E_L \sim 1000$ GeV. The curve in figure (2b) shows the calculated values of $R(\alpha\alpha)$ versus p_T according to (8). The calculated curve, besides being in agreement with data, reproduces the observed increase with p_T. The factors which cause $R(\alpha\alpha)$ to have a larger magnitude and a faster increase with p_T, in contrast to $R(p\alpha)$, are a lower value of E_L ($E_L \sim 512$ GeV) and the occurrence of t-t interactions. The model presented here is fairly well defined and it can be applied to any p-nucleus and nucleus-nucleus collision of equal or unequal masses. For instance, the model predicts that the ratio $R(AA)$ for the collision of two nitrogen ions at $p_T = 6$ GeV/c and a C. M. energy of 16 GeV per nucleon would be around 4000, a factor 20 larger than the naively expected value (14) while for aluminium the value of $R(AA)$ would be $\sim 2{\cdot}9 \times 10^4$ a factor 400 larger than (28).[2]

References

Angelis A L S *et al* 1982 CERN Preprint, CERN-EP/82-106
Anishetty R, Koehler P and Mc Lerran L 1980 *Phys. Rev.* **D22** 2793
Antreasyn D, Cronin J W, Frish H J, Schochet M J, Kluberg L, Pirone P A and Sumner R L 1979 *Phys. Rev.* **D19** 764
Bell B *et al* 1982 *Phys. Lett.* **B112** 271

Bergstrom L, Fredriksson S, Berlad G and Eilam G 1983 *Phys. Rep.* (to be published)
Bromberg C *et al* 1979 *Phys. Rev. Lett.* **42** 1202
Busser F W *et al* 1973 *Phys. Lett.* **B46** 471
Cronin J W, Frish H J, Schochet M J, Boymond J P, Pirone P A and Sumner R L 1975 *Phys. Rev.* **D11** 3105
Domokos G and Goldman J I 1981 *Phys. Rev.* **D23** 203
Fredriksson S 1976 *Nucl. Phys.* **B111** 167
Jacob M and Landshoff P V 1978 *Phys. Rev.* **C48** 285
Karabarbounis A *et al* 1981 *Phys. Lett.* **B104** 75
Narayan D S and Sarma K V L 1964 *Prog. Theor. Phys.* **31** 93

Pramāṇa, Vol. 21, No. 4, October 1983, pp. 241–246. © Printed in India.

Baryon magnetic moments in quark-diquark model

M P KHANNA and R C VERMA*
Department of Physics, Panjab University, Chandigarh 160 014, India
*Department of Physics, Kumaun University, Nainital 263 002, India

MS received 3 June 1983

Abstract. The baryon magnetic moments in quark-diquark model are studied and it is found that the diquark (spin 1 and 0) mixing which may arise as a result of quark-gluon interaction inside a hadron, leads to a good agreement of theory with experiment.

Keywords. Baryon magnetic moments; quark.

1. Introduction

Spurred by recent improved measurements of hyperon magnetic moments, a number of new calculations (Kamal 1978, Bohm and Teese 1979; Tomozawa 1978; Franklin 1979, 1980; Geffen and Wilson 1980; Isgur and Karl 1980; Verma 1980; Lichtenberg 1981; Bohm *et al* 1982) of these moments have been made within the framework of the quark model. With the quark mass ratio determined from baryon masses, the simple quark model (De Rujula *et al* 1975) gave $\mu(\Lambda) = -0{\cdot}61$ in excellent agreement with experiment. But the measurements of other hyperon magnetic moments (Cox *et al* 1981) have clearly demonstrated that these cannot be fitted within the simple quark model. As a matter of fact the simple SU(6) approach is unable to explain some other properties like the neutron charge radius, g_A/g_V ratio as well. All these observations indicate SU(6) violation. Due to the lack of complete knowledge of hadron dynamics, such effects at low energy can at best be treated phenomenologically guided by quantum chromodynamics.

In the present investigation we study the effects of baryon wavefunction modification on the magnetic moments. We work in the framework of quark-diquark model for baryons. This model has been used to study some properties of the baryons. For example Zralek *et al* (1979) observed that SU(6) broken diquark model explains well the SU(6) violation in several static and dynamic properties like the total and differential cross-sections for a large body of quasi two-body reactions, neutron charge radius, neutron-proton structure functions etc. In the diquark model, a baryon is assumed to be made up of a diquark and a quark. The diquark can be in spin one or spin zero states. The SU(6) symmetry of the wavefunction can be broken by assigning different probabilities to these two types of diquarks which can be controlled through a mixing angle. We find that such a SU(6) breaking in the wavefunction leads to a good agreement between theory and experiment for the baryon magnetic moments.

2. Baryon wavefunction due to quark-quark interaction

The diquark model assumes that a baryon is made up of a diquark belonging to the symmetric 21 representation of SU(6) and a quark. A diquark can be in spin one or spin zero states. A diquark with two identical constituents exists only in spin one state while that made up of two different quarks can appear in both spin 1 and spin 0 multiplets. In the limit of exact SU(6) symmetry the probability amplitude for a diquark in a baryon to be in spin zero or spin one state will be governed by the CG coefficients involved. But due to SU(6) breaking caused by quark-gluon interaction, we may expect mixing between spin 1 and spin 0 states of a diquark in a baryon to become different from that given by the CG coefficient of SU(6). As we cannot calculate the coefficients in the wavefunction, we parametrize through a mixing angle in the following manner,

$$|ab\rangle_1 = |ab\rangle_1 \cos\phi_{ab} + |ab\rangle_0 \sin\phi_{ab},$$

$$|ab\rangle_0 = |ab\rangle_0 \cos\phi_{ab} - |ab\rangle_1 \sin\phi_{ab},$$

where the subscript denotes the spin of the diquark made up of two different quarks a and b and the parameter ϕ_{ab} contains the whole of dynamics. For the octet baryons, we have three types of diquarks containing ud, us and ds pairs and they would require three angles ϕ_{ud}, ϕ_{us} and ϕ_{ds} in the baryon wavefunction. Invoking isospin invariance we get

$$\phi_{us} = \phi_{ds} \,(= \phi)$$

and we fix $\phi_{ud}=0$ to preserve the successful results of SU(6) namely the ratio $\mu_p/\mu_n = -3/2$ in the nonstrange sector. This may be due to the fact that u and d have same mass and hence are identical with respect to strong interaction, so we demand the complete symmetry of the wavefunction while u and s being quarks with different masses, the symmetry may not be required.

In SU(6) symmetry, the wavefunction for the Σ^+ hyperon, for example, is given by

$$|\Sigma^+\uparrow\rangle = \frac{1}{\sqrt{6}}\sqrt{2}\left(\sqrt{\tfrac{2}{3}}\, s_1^+ s\downarrow - \frac{1}{\sqrt{3}} s_1^0 s\uparrow\right) - \left(\sqrt{\tfrac{2}{3}}\, s_4^+ u\downarrow - \frac{1}{\sqrt{3}} s_4^0 u\uparrow\right)$$

$$+ \frac{1}{\sqrt{2}} t_2 u\uparrow,$$

where

$$s_1^+ = u\uparrow u\uparrow,$$

$$s_1^0 = \frac{1}{\sqrt{2}}(u\uparrow u\downarrow + u\downarrow u\uparrow),$$

$$s_4^+ = \frac{1}{\sqrt{2}}(u\uparrow s\uparrow + s\uparrow u\uparrow),$$

$$s_4^0 = \tfrac{1}{2}\,(u\uparrow\, s\downarrow + u\downarrow\, s\uparrow + s\uparrow\, u\downarrow + s\downarrow\, u\uparrow),$$

$$t_2 = \tfrac{1}{2}\,(u\uparrow\, s\downarrow - u\uparrow\, s\downarrow - s\uparrow\, u\downarrow + s\downarrow\, u\uparrow).$$

As a result of spin 1 and spin 0 mixing due to hadron dynamics, the wavefunctions for Σ^+ now becomes

$$|\Sigma^+\uparrow\rangle = \frac{1}{\sqrt{6}}\Big[\sqrt{2}\left\{\sqrt{\frac{2}{3}}s_1^+ s\downarrow - \frac{1}{\sqrt{3}}s_1^0 s\uparrow\right\}$$

$$- (\cos\phi + \sqrt{3}\sin\phi)\times\left\{\sqrt{\frac{2}{3}}s_4^+ u\downarrow - \frac{1}{\sqrt{3}}s_4^0 u\uparrow\right\}\Big]$$

$$+ \frac{1}{\sqrt{2}}\,t_2\,u\uparrow\left(\cos\phi - \frac{\sin\phi}{\sqrt{3}}\right).$$

The wavefunctions for all the baryons are given in the appendix.

3. Magnetic moments

Taking the expectation value of the magnetic moment operator

$$\frac{e_i}{2m_i}\,\bar{q}_i\,\vec{\sigma}q_i,$$

Table 1.

Moment	Present model* expression $xe/2m_u$	$\phi = 0°$, $y = 0{\cdot}63$	$\phi = 20°$, $y = 0{\cdot}79$	$\phi = 25°$, $y = 0{\cdot}88$	$\phi = 30°$, $y = 1$	exp ($n\,m$)
p	1	2·79*	2·79*	2·79*	2·79*	2·793
n	$-2/3$	− 1·86	− 1·86	− 1·86	1·86	− 1·913
Λ	$-y/3 + (y + 1/2)\mathrm{B}$	− 0·61*	− 0·61*	− 0·61*	− 0·61*	− 0·6138 ± 0·0047
Σ^+	$\frac{8+y}{9} - (y+2)\mathrm{B}$	2·69	2·46	2·33	2·16	2·33 ± 0·13
Σ^0	$\frac{2+y}{9} - (y+1/2)\mathrm{B}$	0·82	0·74	0·69	0·61	—
Σ^-	$\frac{y-4}{9} + (1-y)\mathrm{B}$	− 1·04	− 0·98	− 0·95	− 0·93	− 0·89 ± 0·14
Ξ^0	$\frac{-2-4y}{9} + (y+2)\mathrm{B}$	− 1·44	− 1·33	− 1·28	− 1·22	− 1·236 ± 0·014
Ξ^-	$\frac{1-4y}{9} + (y-1)\mathrm{B}$	− 0·50	− 0·70	− 0·79	− 0·93	− 0·75 ± 0·07
$\Sigma\Lambda$	$\frac{1}{\sqrt{3}}\left(1 - \frac{9}{2}\mathrm{B}\right)$	1·61	1·36	1·23	1·08	1·82 $^{+0·25}_{-0·18}$
Ω	$-y$	− 1·84	− 2·21	− 2·45	− 2·79	—

*$\mathrm{B} = 8\sin^2\phi/27$

in the baryon state expressed by the wavefunction given in the appendix, we obtain the corresponding value of the magnetic moment.

All the baryon magnetic moments are then expressed in terms of y *i.e.* m_u/m_s mass ratio and the diquark mixing angle as displayed in table 1. We compute the values of magnetic moment for different values of angle ϕ starting from the conventional SU(6) value of $\phi = 0$ to $\phi_{max} = 30°$ required by $\mu(\Lambda)$ in the limit of SU(3) symmetry ($y = 1$). The magnetic moments specially of Σ^+, Ξ^0 and Ξ^- are in good agreement for the value of ϕ lying between 20° and 30°. $\mu(\Sigma^-)$ is not affected much and stays around -1 in better agreement with a recent value $-0{\cdot}89 \pm 0{\cdot}14$ obtained by Ramieka (1981). The $\Sigma^0 - \Lambda^0$ transition moment is lowered as in any other model incorporating SU(3) breaking only. Ω^- is also calculated for different cases. It appears that the wavefunction modification due to presence of gluons inside the baryons, helps to bring the magnetic moment values closer to the experimental values.

Appendix

Diquark states SU(3) × SU(2) ⊂ SU(6)

(i) $(6, 3) \subset 21$.

$$s_1^+ = u\uparrow u\uparrow, \qquad s_1^0 = \frac{1}{\sqrt{2}}(u\uparrow u\downarrow + u\downarrow u\uparrow)$$

$$s_2^+ = \frac{1}{\sqrt{2}}(u\uparrow d\uparrow + d\uparrow u\uparrow), \qquad s_2^0 = \tfrac{1}{2}(u\uparrow d\downarrow + u\downarrow d\uparrow + d\uparrow u\downarrow + d\downarrow u\uparrow),$$

$$s_3^+ = d\uparrow d\uparrow, \qquad s_3^0 = \frac{1}{\sqrt{2}}(d\uparrow d\downarrow + d\downarrow d\uparrow),$$

$$s_4^+ = \frac{1}{\sqrt{2}}(u\uparrow s\uparrow + s\uparrow u\uparrow), \qquad s_4^0 = \tfrac{1}{2}(u\uparrow s\downarrow + u\downarrow s\uparrow + s\uparrow u\downarrow + s\downarrow u\uparrow),$$

$$s_5^+ = \frac{1}{\sqrt{2}}(d\uparrow s\uparrow + s\uparrow d\uparrow), \qquad s_5^0 = \tfrac{1}{2}(d\uparrow s\downarrow + d\downarrow s\uparrow + s\uparrow d\downarrow + s\downarrow d\uparrow),$$

$$s_6^+ = s\uparrow s\uparrow, \qquad s_6^0 = \frac{1}{\sqrt{2}}(s\uparrow s\downarrow + s\downarrow s\uparrow).$$

(ii) $(3^*, 1) \subset 21$

$$t_1 = \tfrac{1}{2}(u\uparrow d\downarrow - u\downarrow d\uparrow - d\uparrow u\downarrow + d\downarrow u\uparrow),$$

$$t_2 = \tfrac{1}{2}(u\uparrow s\downarrow - u\downarrow s\uparrow - s\uparrow u\downarrow + s\downarrow u\uparrow),$$

$$t_3 = \tfrac{1}{2}(d\uparrow s\downarrow - d\downarrow s\uparrow - s\uparrow d\downarrow + s\downarrow d\uparrow).$$

Baryon wave functions

$$|p\uparrow\rangle = \frac{1}{\sqrt{18}}\{2\,s_1^+ d\downarrow - \sqrt{2}\,s_1^0 d\uparrow - \sqrt{2}\,s_2^+ u\downarrow + s_2^0 u\uparrow + 3\,t_1 u\uparrow\},$$

$$|n\uparrow\rangle = \frac{1}{\sqrt{18}}[\sqrt{2}s_2^+ d\downarrow - s_2^0 d\uparrow - 2\,s_3^+ u\downarrow + \sqrt{2}\,s_3^0 u\uparrow + 3\,t_1 d\uparrow],$$

$$|\Lambda\uparrow\rangle = \frac{1}{\sqrt{12}}\left[\left(\cos\phi - \frac{\sin\phi}{\sqrt{3}}\right)(\sqrt{2}\,s_4^+ d\downarrow - s_4^0 d\uparrow - \sqrt{2}\,s_5^+ u\downarrow + s_5^0 u\uparrow)\right.$$

$$\left. + (\cos\phi + \sqrt{3}\,\sin\phi)\,(t_2 d\uparrow - t_3 u\uparrow) + 2t_1 s\uparrow\right],$$

$$|\Sigma^+\uparrow\rangle = \frac{1}{\sqrt{18}}\left[(2\,s_1^+ s\downarrow - \sqrt{2}\,s_1^0\,s\uparrow) - (\cos\phi + \sqrt{3}\,\sin\phi)\,(\sqrt{2}\,s_4^+\,u\downarrow\right.$$

$$\left. - s_4^0\,u\uparrow) + 3\left(\cos\phi - \frac{\sin\phi}{\sqrt{3}}\right) t_2\,u\uparrow\right],$$

$$|\Sigma^-\uparrow\rangle = \frac{1}{\sqrt{18}}\left[(2\,s_3^+ s\downarrow - \sqrt{2}\,s_3^0 s\uparrow) + (-\sqrt{2}\,s_5^+ d\downarrow + s_5^0 d\uparrow)\,(\cos\phi\right.$$

$$\left. + \sqrt{3}\,\sin\phi) + 3\,t_3 d\uparrow\left(\cos\phi - \frac{\sin\phi}{\sqrt{3}}\right)\right],$$

$$|\Sigma^0\uparrow\rangle = \tfrac{1}{3}\,(-\sqrt{2}\,s_2^+ s\downarrow + s_2^0 s\uparrow) + \tfrac{1}{6}\,(\cos\phi + \sqrt{3}\sin\phi)\,(\sqrt{2}\,s_5^+ u\downarrow - s_5^0 u\uparrow$$

$$+ \sqrt{2}\,s_4^+ d\downarrow - s_4^0 d\uparrow) - \tfrac{1}{2}\left(\cos\phi - \frac{\sin\phi}{\sqrt{3}}\right)(t_3 u\uparrow + t_2 d\uparrow),$$

$$|\Xi^0\uparrow\rangle = \frac{1}{\sqrt{18}}\left[(\sqrt{2}\,s_4^+ s\downarrow - s_4^0 s\uparrow)\,(\cos\phi - \sqrt{3}\,\sin\phi)\right.$$

$$\left. - 2\,s_6^+ u\downarrow + \sqrt{2}\,s_6^0 u\uparrow + 3\left(\cos\phi + \frac{\sin\phi}{\sqrt{3}}\right) t_2 s\uparrow\right],$$

$$|\Xi^-\uparrow\rangle = \frac{1}{\sqrt{18}}\left[(\sqrt{2}\,s_5^+\,s\downarrow - s_5^0 s\uparrow)\,(\cos\phi - \sqrt{3}\,\sin\phi)\right.$$

$$\left. - 2\,s_6^+ d\downarrow + \sqrt{2}\,s_6^0 d\uparrow + 3\left(\cos\phi + \frac{\sin\phi}{\sqrt{3}}\right) t_3 s\uparrow\right].$$

References

Bohm A and Teese R B 1979 *Phys. Lett.* **B87** 111
Bohm M, Huerta R and Zepeda A 1982 *Phys. Rev.* **D25** 223
Cox P T *et al* 1981 *Phys. Rev. Lett.* **46** 877
De Rujula A, Georgi H and Glashow S L 1975 *Phys. Rev.* **D12** 147
Franklin 1979 *Phys. Rev.* **D20** 1742
Franklin 1980 *Phys. Rev. Lett.* **45** 1607
Geffen A and Wilson W 1980 *Phys. Rev. Lett.* **44** 370
Isgur N and Karl G 1980 *Phys. Rev.* **D21** 3175
Kamal A N 1978 *Phys. Rev.* **D18** 3512
Lichtenberg D B 1981 *Z. Phys.* **C7** 143
Ramieka R 1981 Ph.D. Thesis, Rutgers University
Tomozawa Y 1979 *Phys. Rev.* **D19** 1626
Zralek M *et al* 1979 *Phys. Rev.* **D20** 341
Verma R C 1980 *Phys. Rev.* **D22** 1156

Pramāṇa, Vol. 21, No. 4, October 1983, pp. 247–255. © Printed in India.

Mass spectra of light and heavy mesons in the Dirac equation with power-law potential

S N JENA
Department of Physics, Aska Science College, Aska 761 110, India

MS received 25 February 1983; revised 27 July 1983.

Abstract. The mass spectra of both light and heavy mesons are studied in the Dirac equation with an equally mixed 4-vector and scalar power-law potential model. This potential provides an excellent fit not only to the mass spectra of ρ^0, ϕ, Ψ and Υ families but also to those of D, F and B mesons. The light quark masses in ρ^0 and ϕ as well as in atom-like mesons are very close to the current quark masses.

Keywords. Dirac bound state mass; mass spectra; meson; quark; atom-like meson; current quark mass; power-law potential.

1. Introduction

A number of theoretical and phenomenological interquark potential models (Appelquist *et al* 1978; Eichten *et al* 1980; Krammer and Krasemann 1979; Gottfried 1981) have been suggested and investigated in the spectroscopy of Ψ and Υ families. Most of these potentials are quantum chromodynamics (QCD) motivated in the sense that they exhibit asymptotic freedom at small radii and linear confinement at large radii. Recently a simple non-QCD based potential of the form

$$V(r) = V_0 + Ar^\nu \tag{1}$$

with $\nu \approx 0{\cdot}1$ and $A>0$ has been found (Martin 1980; Barik and Jena 1980; Khare 1981) to be quite proficient in reproducing the most up-to-date data on the Ψ and Υ spectroscopies. Although this phenomenological potential gives quark confinement (A, $\nu>0$) at long distances, its short distance non-singular behaviour is in apparent contradiction with what one expects from QCD. However, such non-Coulombic short-distance behaviour of this potential does not pose any problem in understanding the fine-hyperfine splittings (Barik and Jena 1980) of the charmonium and upsilon spectra, where it is expected to play an important role. It has been found that this potential can successfully explain the fine-hyperfine levels of light and heavy mesons in a unified manner (Barik and Jena 1982a), if the spin dependence of the confining potential is assumed to be generated in the form of an approximately equal admixture of scalar and vector interactions. In spite of such quantitative success in understanding the experimental data on meson spectra through non-relativistic Schrödinger-type approach, it is also observed that this potential can realize (Magyari 1980 a,b) relativistic quark confinement to yield quark-antiquark bound states in the Dirac equation. Magyari (1980a) showed that the power-law potential considered as the fourth component $V(r)$ of a Lorentz vector, can realize a relativistically consistent

confinement of quarks, if it is assumed that the surrounding gluon field generates simultaneously an accompanying scalar interaction $V_s(r)$, which in the rest frame of the hadron is formally identical to $V(r)$. Following such an idea, it has been shown recently (Barik and Jena 1982b; Barik and Barik 1981) that an equally mixed 4-vector and scalar power-law potential (1), when used appropriately in the Dirac equation is able to generate relativistic $Q\bar{Q}$ bound states of $c\bar{c}$ and $b\bar{b}$ systems in exact agreement with the corresponding experimental data. Now, considering flavour independence as a guiding factor, one may be tempted to extend these considerations (Barik and Jena 1982b) of $Q\bar{Q}$ systems to the lighter $q\bar{q}$ and $Q\bar{q}$ systems in order to generate their relativistic bound states. The $q\bar{q}$ system is composed of a light quark q and its anti-quark $\bar{q}$ whereas the $Q\bar{q}$ system consists of a heavy quark Q and a light anti-quark $\bar{q}$ similar to a hydrogen atom.

In the present paper we aim to obtain the Dirac bound state masses for the light mesons of $q\bar{q}$ and Qq systems along with those for the heavy mesons of $Q\bar{Q}$ systems with an equally mixed four vector and scalar power-law potential (1). Our main interest in this piece of work is to understand how this potential is able to describe the Dirac mass spectra of both light and heavy mesons in a unified manner. Here we are interested only in the gross-level structure but not in the detailed fitting to data including fine-hyperfine splittings.

Following our previous work (Barik and Jena 1982b) we decide to use the Dirac equation in an independent particle approach for finding the bound states of $Q\bar{Q}$ and $q\bar{q}$ systems. On the other hand we use the same equation for finding the relativistic energy levels of the $Q\bar{q}$ systems in the same spirit as is done in the hydrogen atom problem. In fact the use of Dirac equation for the atom-like $Q\bar{q}$ systems to find out their bound states is quite appropriate and meaningful. In the present work we obtain the Dirac bound state masses of the heavy mesons of $Q\bar{Q}$ systems such as Ψ $(c\bar{c})$ and Υ $(b\bar{b})$ and also those of the light mesons of $q\bar{q}$ systems such as ρ^0 $\left(\frac{1}{\sqrt{2}}(u\bar{u} - d\bar{d})\right)$ and ϕ $(s\bar{s})$. We also obtain the relativistic mass spectra of atom-like mesons $Q\bar{q}$ such as $D(c\bar{u})$ or $D(c\bar{d})$, $F(c\bar{s})$, $B(b\bar{u})$ or $B(b\bar{d})$, $G(b\bar{s})$ and $H(b\bar{c})$. Out of these atom-like mesons, the D and F mesons have been observed experimentally only in ground states with their hyperfine mass splittings whereas the b-flavoured masons are expected to be found in the near future.

This work is organized as follows. In § 2 we briefly sketch how to solve the Dirac equation with an equally mixed 4-vector and scalar power-law potential to obtain the expressions for bound state masses of $Q\bar{Q}$, $q\bar{q}$ and $Q\bar{q}$ systems. These results are shown to be true for any power $\nu > 0$ of confining potentials. The potential parameters and quark masses are uniquely determined in § 3. In this section we compute the Dirac mass levels of Ψ, Υ, ϕ and ρ^0 mesons along with those of charmed and b-flavoured mesons in a unified way with the flavour-independent power-law potential. In § 4 concluding remarks are given.

2. Dirac bound states

In this section we would like to generate the bound states of $q\bar{q}$, $Q\bar{Q}$ and $Q\bar{q}$ systems in the Dirac equation with an equally mixed 4-vector and scalar power-law potential

of the form given in (1). First of all, let us obtain an expression for quark binding energy by solving the Dirac equation.

With the scalar and vector interactions $V_s(r)$ and $V_v(r)$ simultaneously present, the Dirac equation for a quark of mass m_q can be written as ($\hbar=c=1$) as

$$(\boldsymbol{\alpha}\cdot\mathbf{p}+m_q\beta)\,\Psi(\mathbf{r})=[E-V_v(r)-V_s(r)\beta]\,\Psi(\mathbf{r}), \tag{2}$$

where E refers to the Dirac quark-binding energy. Now with an equally mixed scalar and 4-vector power-law potential ($V_s(r)=V_v(r)=V(r)$) we can obtain from (2) an equation satisfied by the reduced radial part of the 'large' component of the Dirac spinor $\Psi(\mathbf{r})$ in the form (Magyari 1980a)

$$\frac{\mathrm{d}^2U(r)}{\mathrm{d}r^2}+\left[(E+m_q)\,(E-m_q-2V(r))-\frac{1\,(1+1)}{r^2}\right]U(r)=0 \tag{3}$$

Taking $V(r)$ as given in (1) and introducing a dimensionless variable $\rho=(r/r_0)$ with the scale factor

$$r_0=[2(E+m_q)A]^{-1/(\nu+2)} \tag{4}$$

equation (3) would reduce to the Schrödinger form

$$\frac{\mathrm{d}^2U(\rho)}{\mathrm{d}\rho^2}+\left[\epsilon-\rho^\nu-\frac{1(1+1)}{\rho^2}\right]U(\rho)=0 \tag{5}$$

where

$$\epsilon=(E-m_q-2V_0)\,[(E+m_q)\,(2A)^{-2/\nu}]^{\nu/(\nu+2)} \tag{6}$$

The solution of (5) for $\nu>0$ would yield a positive definite value of $\epsilon=\epsilon_{nl}$ corresponding to the confined bound states of quarks. If we take $A=a^{\nu+1}$,

$$(E_{nl}-m_q-2V_0)=ax_{nl}, \tag{7}$$

and

$$2(m_q+V_0)=ab, \tag{8}$$

(6) would be converted to the form

$$x_{nl}^{(\nu+2)/\nu}\cdot(x_{nl}+b)=2^{2/\nu}\,\epsilon_{nl}^{(\nu+2)/\nu}. \tag{9}$$

Then using ϵ_{nl} from exact numerical solutions of (5) and b from (8) with the known potential parameters V_0, a and m_q, we can solve (9) for a unique positive root x_{nl} which would yield independent quark binding energy E_{nl} as

$$E_{nl}=m_q+2V_0+ax_{nl}. \tag{10}$$

Now in the framework of our relativistic independent particle model the mass levels of $q\bar{q}$ system can be expressed as

$$M_{nl}(q\bar{q}) = 2E_{nl} = 2m_q + 4V_0 + 2ax_{nl}. \tag{11}$$

A similar line of approach for $Q\bar{Q}$ system would also lead to the formula for relativistic bound state masses as

$$M_{nl}(Q\bar{Q}) = 2m_Q + 4V_0 + 2ax_{nl}, \tag{12}$$

where m_Q is the mass of heavy quark Q.

Now for an atom-like $Q\bar{q}$ meson where a light quark $\bar{q}$ is moving with a high speed around an almost fixed heavy quark Q similar to a hydrogen atom, the Dirac bound state mass can be easily obtained from the expression of quark binding energy (10) as

$$M_{nl}(Q\bar{q}) = m_Q + E_{nl} = m_Q + m_q + 2V_0 + ax_{nl}. \tag{13}$$

Here, of course, we do not consider the recoil effects of the heavy quark Q.

In this way we obtain the expressions for Dirac bound state masses of $Q\bar{Q}$, $q\bar{q}$ and $Q\bar{q}$ systems. These results are independent of any particular $\nu>0$. Hence for any confining potential, logarithmic, linear or harmonic with an equally mixed vector-scalar Lorentz structure, these expressions are true.

3. Fixation of parameters, results and discussion

First of all, we fix the parameter $\nu=0{\cdot}1$ in close agreement with the findings of Martin (1980) and Barik and Jena (1980) and solve numerically (5) to obtain ϵ_{nl} values for different quark-antiquark bound states. Now using the observed masses of the $1S$ state of $c\bar{c}$, $J/\Psi(3097)$ and of the $2S$ state, Ψ' (3686) as inputs we solve (9) by one of the standard iterative methods to obtain unique positive root x_{nl}. For this purpose we take the help of (8) and (12). This process fixes the potential parameters a, V_0 and the quark mass m_c as

$$(a, V_0, m_c) = (1{\cdot}6923, -1{\cdot}99, 1{\cdot}5974; \text{GeV}). \tag{14}$$

With these values of potential parameters a and V_0 we repeat the above procedure by taking the experimental masses of the $1S$ state of $b\bar{b}$, Υ (9434) and of the $1S$ state of $s\bar{s}$, ϕ (1020) as inputs respectively in (12) and (11) and we obtain the b-and s-quark masses as

$$(m_b, m_s) = (4{\cdot}9707, 0{\cdot}295; \text{GeV}). \tag{15}$$

Moreover, for the light meson ρ^0 (770) considered to be a $q\bar{q}$ configuration such as $(u\bar{u} - d\bar{d})/\sqrt{2}$, we similarly fit its experimental mass to obtain the effective quark mass $m_q = 0{\cdot}041$ GeV.

Now with the help of the potential parameters and the quark masses thus obtained, we can find out the unique positive root x_{nl} of (9) for each quark-antiquark bound state. Then using the corresponding extracted roots x_{nl} in (12) for Ψ and Υ systems and in (11) for ρ^0 and ϕ systems, we can obtain the Dirac mass spectra of Ψ, Υ, ρ^0 and ϕ systems. These results in comparison with the corresponding experimental masses are presented in tables 1 and 2. We find that particularly for Ψ and Υ systems, for which numerous and convincing experimental data are available, the agreement with our computed values is excellent. For the light meson ϕ, some new experimental material has come out. The first radial excitation of ϕ called ϕ' has been discovered by the Orsay group at DCI with a mass around 1·65 GeV (Bizot 1980). The second radial excitation ϕ'' is experimentally obscure, with a possible candidate at $\sim$ 1·9 GeV (Aston *et al* 1980). A new evidence for the old E meson (Baillon *et al* 1967) has been obtained both in hadron collisions (Dionisi *et al* 1980; Bromberg *et al* 1980) and in radiative decay of the J/Ψ (Feldman 1980; Ashman 1980), with a mass 1·44 GeV. From our calculation

Table 1. Dirac mass spectrum for Ψ and Υ systems.

n	l	ϵ_{nl}	M_{nl} (Ψ) GeV Theory	M_{nl} (Ψ) GeV Experiment	M_{nl} (Υ) GeV Theory	M_{nl} (Υ) GeV Experiment
1	S	1·2364	3·097	3·097 ± 0·002	9·4336	9·4336 ± 0·0002
2	S	1·3347	3·686	3·686 ± 0·003	10·0147	9·9944 ± 0·00004
3	S	1·3923	4·0303	4·030 ± 0·005	10·3547	10·3231 ± 0·00004
4	S	1·4335	4·2761	—	10·5976	10·5476 ± 0·00011
5	S	1·4657	4·4680	4·417 ± 0·01	10·7872	—
1	P	1·3071	3·5208	3·521	9·8517	—
2	P	1·3731	3·9156	—	10·2414	—
1	D	1·3544	3·8038	3·772	10·1310	—

Table 2. Dirac mass spectrum for ρ^0 and ϕ systems.

n	l	ϵ_{nl}	M_{nl} (ρ^0) (GeV) Theory	M_{nl} (ρ^0) (GeV) Experiment	M_{nl} (ϕ) (GeV) Theory	M_{nl} (ϕ) (GeV) Experiment
1	S	1·2364	0·770	0·770 ± 0·005	1·0196	1·0196 ± 0·0001
2	S	1·3347	1·2584	1·25 (ρ'?)	1·5622	1·65
3	S	1·3923	1·5608	1·60 (ρ''?)	1·8857	$\sim$ 1·90
4	S	1·4335	1·7819	—	2·1189	—
5	S	1·4657	1·9568	—	2·3019	—
1	P	1·3071	1·1170	1·31 (A_2 ?)	1·4084	1·44 ± 0·005
2	P	1·3731	1·4590	—	1·7775	—
1	D	1·3544	1·3608	—	1·6725	—

we find the $2S$, $3S$, and $1P$ levels for ϕ at mass values 1·56, 1·89 and 1·41 GeV respectively. For the radially excited states of the light meson ρ^0, the experimental situation is also not clear yet. There have been several experiments (Becker *et al* 1979; Delcourt *et al* 1979; Atiya *et al* 1979; Kaufman and Jacob 1974; Sidrov 1979) in favour of a ρ' (1600), whereas some other experiments (Ballam *et al* 1974; Bartlucci *et al* 1978; Barter *et al* 1980; Renard 1971; Aston *et al* 1980) at the same time claim good evidence for a ρ' (1250) as the $2S$ excited states of ρ^0. But from our calculation we find the $2S$ and $3S$ levels for ρ^0 at mass values 1258 and 1561 MeV respectively. However, we would not like to attach too much quantitative significance to these results, since for the excited states of these light mesons, convincing experimental data are not yet available.

Finally we find out the Dirac bound state masses of atom like mesons $Q\bar{q}$ using the same set of potential parameters and quark masses as obtained in (14) and (15). We can determine the light quark masses $m_u(m_d)$ by making a fit to the energy level of of $D(c\bar{u}$ or $c\bar{d})$ meson. It is noted that the D meson level we want to fit corresponds to the spin-average of D and D^* *i.e.* $\langle D\rangle = (3D^* + D)/4$, because the hyperfine splitting is not taken into account in our calculation. From such a fit to the observed mass of $\langle D\rangle$, we see that the u or d quark mass is extremely light in D meson, having a value comparable to the so-called current quark mass (Fritzsch 1979). It is very interesting to note that the light quark masses m_u or m_d, m_s and as well as the effective quark mass in ρ^0 which we obtain in our calculation, are very light and that their values are close to the current quark masses (Fritzsch 1979) rather than the phenomenological constituent quark masses (Rujula *et al* 1975). We are not going to discuss the relation between current and constituent quark masses from theoretical point of view. However, this point has been discussed in the frame-work of QCD by Kaburagi *et al* (1981).

Now it is interesting to take current quark mass values for u or d quarks to describe the Dirac mass spetra of atom-like meson $Q\bar{q}$. Taking the values (Fritzsch 1979).

$$m_u \sim m_d = 0{\cdot}01 \text{ GeV} \tag{16}$$

for u and d quark masses along with the same set of potential parameters and quark masses as in (14) and (15), we obtain from (9) and (13), the spin-averaged ground state mass values of $D(c\bar{u})$ or $D(c\bar{d})$, $F(c\bar{s})$ and $B(b\bar{u})$ or $B(b\bar{d})$ mesons as follows:

$$\begin{aligned} M_{1S}(c\bar{u})_{\text{cal}} &= 1{\cdot}972 \text{ GeV}; \; M_{1S}(c\bar{u})_{\text{exp}} = 1{\cdot}970 \text{ GeV}, \\ M_{1S}(c\bar{s})_{\text{cal}} &= 2{\cdot}107 \text{ GeV}; \; M_{1S}(c\bar{s})_{\text{exp}} = 2{\cdot}113 \text{ GeV}, \\ M_{1S}(b\bar{u})_{\text{cal}} &= 5{\cdot}346 \text{ GeV}; \; M_{1S}(b\bar{u})_{\text{exp}} = 5{\cdot}16 \sim 5{\cdot}27 \text{ GeV} \end{aligned} \tag{17}$$

Our calculated results are in excellent agreement with the corresponding experimental spin-averaged mass values (Rapidis *et al* 1977; Brandelik *et al* 1977, 1979; Bebek *et al* 1981; Chadwick *et al* 1981; Monti 1980) written to the right of each result in (17).

Lastly with the same parameters fixed as in (14), (15) and (16), we generate some higher spin-averaged mass levels of $c\bar{u}$ or $c\bar{d}$, $c\bar{s}$ systems along with all such levels of

Table 3. Spin-averaged Dirac mass spectrum for the atom-like mesons of $D(c\bar{u})$, $F(c\bar{s})$, $B(b\bar{u})$, $G(b\bar{s})$ and $H(b\bar{c})$ families.

n	l	M_{nl} $(c\bar{u})$ (GeV)	M_{nl} $(c\bar{s})$ (GeV)	M_{nl} $(b\bar{u})$ (GeV)	M_{nl} $(b\bar{s})$ (GeV)	M_{nl} $(b\bar{c})$ (GeV)
1	S	1·9722	2.1071	5·3455	5·4805	6·5192
2	S	2·2110	2·3784	5·5843	5·7518	6·8187
3	S	2·3602	2·5402	5·7335	5·9135	6·9858
4	S	2·4696	2·6568	5·8429	6·0301	7·1087
5	S	2·5563	2·7483	5·9297	6·1216	7·2047
1	P	2·1415	2·3016	5·5148	5·6749	6·7311
2	P	2·3099	2·4861	5·6832	5·8594	6·9284
1	D	2·2614	2·4336	5·6348	5·8069	6·8726

$b\bar{u}$ or $b\bar{d}$, $b\bar{s}$ and $b\bar{c}$ systems. The calculated values of the spin-averaged Dirac bound state masses of $D(c\bar{u})$, $F(c\bar{s})$, $B(b\bar{u})$, $G(b\bar{s})$ and $H(b\bar{c})$ mesons are displayed in table 3. All these predictions will shortly be tested in future experiments at CERN and FNAL.

We find that our potential unlike the QCD based ones is non-singular at the origin having a finite bottom of the order of $\approx$ 1·99 GeV. It does not possess the short distance Coulombic part of the potential as given by QCD (*i.e.* r^{-1} or $r^{-1}\,|\log(r/r_0)|^{-1}$). Therefore even if the non-singular behaviour of this potential does not conform to the expectations of QCD, it can successfully describe the Dirac mass spectra of both light and heavy mesons in a unified manner. We further find in this work that the power-law potential can realize relativisitc confinement of quarks to yield the bound states of light and heavy mesons in the Dirac equation, if the Lorentz structure of the confining potential is assumed to be generated in the form of an equal admixture of vector and scalar interactions. Here it must be pointed out that since our results obtained in § 2 are independent of any particular $\nu>0$, any confining potential (logarithmic, linear or harmonic) with the aforementioned Lorentz structure will also be consistent in giving relativistic quark confinement. In fact, Magyari (1980) has already shown that with the above prescription for the Lorentz structure the logarithmic potential, the linear potential and the oscillator-like potential are able to realize relativistic confinement of independent quarks. But it has been observed (Critchfield 1975) that the logarithmic potential as well as other conventional forms of the confining potentials of heavy quarks, if considered in the rest frame of the quarks as the time component of a four vector, cannot generate relativistic bound states of quarks in the Dirac equation. Again it has been shown that although a linear scalar potential realizes a relativistic confinement (Critchfield 1975; Gunion and Li 1975), the oscillator-like scalar potential does not generate real eigenvalues of the Dirac equation (Ram and Halasa 1979). Thus an independent approach to realize the relativistic confinement of quarks with a confining potential assumed either as the fourth component of a four-vector or as a pure scalar does not always meet with success. Therefore we find that, for a power-law potential, a unified approach in realizing the Dirac bound

states of light and heavy mesons is possible with an equally mixed vector-scalar Lorentz structure of the confining potential. Such a Lorentz structure was also a phenomenological requirement in the non-relativistic Schrödinger type perturbative approach to explain the fine-hyperfine splittings of the light and heavy meson spectra (Barik and Jena 1982a). This observation about the Lorentz structure of the static confining potential is also in line with earlier phenomenological findings (Beavis *et al* 1979; Appelquist *et al* 1978) in the context of different potential models, which derives further support from a gauge-invariant formalism of Eichten and Feinberg (1979). However, recently Kaburagi *et al* (1981) used a purely scalar Lorentz structure for the power-law potential to generate bound states of atom-like $Q\bar{q}$ mesons in the Dirac equation. But it is found that if such a power-law potential generating spin dependence in the usual manner with its Lorentz structure as a scalar, is used in a non-relativistic perturbative approach for the system, it would be impossible in this case to explain the observed fine-hyperfine splittings (Barik and Jena 1980). Therefore we believe that, for a power-law potential model, a more consistent and unified approach in realizing fine-hyperfine spectra of light and heavy mesons in a non-relativistic formalism (Barik and Jena 1982), which at the same time guarantees relativistic quark confinement to generate successfully the Dirac bound states of $Q\overline{Q}$, $q\bar{q}$ and $Q\bar{q}$ systems, is mainly based on the formal assumption of an equally mixed scalar-vector Lorentz structure of the static potential.

4. Concluding remarks

In this work we have made a unified study of the mass spectra of bound light and heavy-quark systems with an equally mixed 4-vector and scalar power-law potential. This potential has been found to provide an excellent fit not only to the mass spectra of ρ^0, ϕ, ψ and Υ families but also to those of D, F and B mesons. Flavour-independence has been strictly maintained by taking the same set of potential parameters and quark masses to generate the Dirac bound states of all systems. We have found the remarkable result that the light quark masses in ρ^0, ϕ and atom-like mesons are very close to the current quark masses rather than the phenomenological constiutent quark masses.

In conclusion, we point out that with an equally mixed 4-vector and scalar power-law potential it is possible to describe the Dirac mass spectra of both light and heavy mesons in a unified manner.

Acknowledgements

The author is thankful to Dr N Barik at the Department of Physics of Utkal University for his constant inspiration and valuable suggestions, and acknowledges the financial assistance given by UGC, New Delhi.

References

Appelquist T, Barnett R M and Lane K D 1978 *Annu. Rev. Nucl. Part. Sci.* **28** 387
Ashman D 1980 XV Recontres de Moriond, Lec Acrcs

Aston D *et al* 1980 *Phys. Lett.* **B92** 211
Aston D *et al* 1980 CERN Report No. CERN-EP/80-06 (unpublished)
Atiya M S *et al* 1979 *Phys. Rev. Lett.* **43** 1691
Baillon P *et al* 1967 *Nuovo Cimento* **A50** 393
Ballam J *et al* 1974 *Nucl. Phys.* **B76** 375
Barik N and Barik B K 1981 *Pramana* **17** 489
Barik N and Jena S N 1980 *Phys. Lett.* **B97** 261, 265
Barik N and Jena S N 1981 *Phys. Lett.* **B101** 282
Barik N and Jena S N 1982a *Phys. Rev.* **D26** 618
Barik N and Jena S N 1982b *Phys. Rev.* **D26** 2420
Barter D P *et al* 1980 *Z. Phys.* **C4** 169
Bartlucci S *et al* 1978 *Nuovo Cimento* **A49** 207
Beavis D, Desai B R and Kaus P 1979 *Phys. Rev.* **D20** 2345
Bebek C *et al* 1981 *Phys. Rev. Lett.* **46** 84
Becker H *et al* 1979 *Nucl. Phys.* **B151** 46
Bizot J C 1980 *Proc. Twentieth Int. Conf. in high energy physics*, Madison, Wisconsin, (eds) B Durand and L G Pondrom (New York: A I P)
Brandelik R *et al* 1977 *Phys. Lett.* **B70** 132
Brandelik R *et al* 1979 *Phys. Lett.* **B80** 412
Bromberg C *et al* 1980 Cal Tech. Report No. CALT-68-747 (unpublished)
Chadwick K *et al* 1981 *Phys. Rev. Lett.* **46** 88
Critchfield C L 1975 *Phys. Rev.* **D12** 923
Delcourt B *et al* 1979 *Proc. Int. Symp. on Lepton and Photon Interactions at High Energies Fermi Lab.* (Ref. 1) p. 499
Dionisi C *et al* 1980 *Nucl. Phys.* **B169** 1
Eichten E and Feinberg E L 1979 *Phys. Rev. Lett.* **43** 1205
Eichten E, Gottfried K, Kinoshita T, Lane K D and Yan T M 1980 *Phys. Rev.* **D21** 203
Feldman G 1980 XV Reconteres de Moriond, Lec Arcs
Fritzsch H 1979 Lecture at the 10th GIFT Seminar on Theor. Phys. Jacca, Spain (CERN) Preprint TH 2699
Gottfried K 1981 *Commun. Nucl. Part. Phys.* **9** 141
Gunion J F and Li L F 1975 *Phys. Rev.* **D12** 3583
Kaburagi M *et al* 1981 *Z. Phys.* **C9** 213
Kaufman W B and Jacob R J 1974 *Phys. Rev.* **D10** 1051
Khare A 1981 *Phys. Lett.* **B98** 385
Krammer M and Krasemann H 1979 *Acta Phys. Austr. Suppl.* **21** 259
Magyari E 1980a Preprint University of Berne
Magyari E 1980b *Phys. Lett.* **B95** 295
Martin A 1980 *Phys. Lett.* **B93** 338
Monti G 1980 SLAC Preprint HEPSY MEMO 15-80
Ram B and Halasa R 1979 *Lett. Nuovo Cimento* **26** 551
Rapidis P A *et al* 1977 *Phys. Rev. Lett.* **39** 526
Renard F M 1971 *Nuovo Cimento* **A66** 134
Rujula A De, Georgi H and Glashow S L 1975 *Phys. Rev.* **D12** 147
Sidrov V 1979 *Proc. Int. Symp. on Lepton and Photon Interactions at High Energies, Fermi Lab.* p. 490

Pramāṇa, Vol. 21, No. 4, October 1983, pp. 257–260. © Printed in India.

The δ-function expansion of the modified two-particle Ursell function of a hard-sphere fluid

N ANSARI* and B KUMAR
Physics Department, Ranchi University, Ranchi 834 008, India
*Permanent Address: Department of Physics, Jamshedpur Co-operative College, Jamshedpur 831 001, India

MS received 1 March 1983

Abstract. The expansion of the modified two-particle Ursell function $U(r)$ of a hard-sphere quantal fluid is obtained in terms of a series of derivatives of δ-function. This expansion has been used to expand the second virial co-efficient B_2 of the fluid. The expansion is correct up to the fourth power in thermal wavelength and the terms of the order of λ^3 and λ^4 in the first expansion are new.

Keywords. Ursell function; thermal wavelength; second virial co-efficient.

1. Introduction

The expansion of any function in terms of Dirac δ-function and its derivatives is some times convenient if the function is to be used in an integral. In this paper we shall expand $U(r)$ in terms of δ-function and its derivatives correct up to the fourth power in thermal wavelength λ. The coefficients of λ^3 and λ^4 in the expansion are new but those of λ and λ^2 were first suggested by others (Hemmer 1968; Gibson 1975).

To test that the expansion is right we use it to obtain the expansion of B_2 up to the order λ^4. This expansion has also been derived by others (Handelsmann and Keller 1966; Hemmer and Mork 1967) after making lengthy calculations.

In §2, we outline the calculation for the expansion of $U(r)$. An alternative method for obtaining the expansion of B_2 is presented in §3.

2. Expansion of U (r)

The expansion of $U(r)$ is:

$$U(r) = \sum_{i=0}^{3} f_i(q) + \text{higher terms}, \tag{1}$$

where $f_i(q)$'s are given by (Gibson and Byrnes 1975)

$$f_0(q) = -\exp(-q^2), \tag{2}$$

$$f_1(q) = \frac{1}{\sqrt{2}}(\lambda/a)\, q^2 \operatorname{erfc} q, \tag{3}$$

$$f_2(q) = \frac{1}{(3\pi)}(\lambda/a)^2\, q^2\, [(1+q^2)\exp(-q^2) - (3+q^2)\sqrt{\pi}\, q \operatorname{erfc} q] \tag{4}$$

and

$$f_3(q) = \frac{1}{(24\sqrt{2})}\pi^{-3/2}(\lambda/a)^3 q^3\, [-(16+26q^2+4q^4)\exp(-q^2)$$

$$+ (39+28q^2+4q^4)\sqrt{\pi}\, q \operatorname{erfc} q] \tag{5}$$

Here $$q \equiv \frac{(2\pi)^{1/2}}{\lambda}(r-a), \tag{6}$$

$$\operatorname{erfc} q = \frac{2}{\sqrt{\pi}} \int_q^\infty \exp(-t^2)\, \mathrm{d}t \tag{7}$$

and a is the hard-sphere diameter.

The expansion of any one of the integrable functions $f_i(q)$ in terms of a series of derivatives of δ-function is given by (Messel and Green 1952; Kim 1969)

$$f_i(q) = \sum_{k=0}^{\infty} \frac{(-1)^k f_i(k)\, \delta^{(k)}(q)}{k!} \tag{8}$$

where the moment $$f_i(k) = \int_0^\infty q^{(k)} f_i(q)\, \mathrm{d}q \tag{9}$$

and the superscript in (8) and in any other equations after (8) represents the number of differentiations with respect to the argument of the function.

We can calculate the moments of any $f_i(q)$ from (9) and its expansion given in one of the equations (2) to (5). The calculations are lengthy but straightforward. We quote here the relevant results:

$$f_0(0) = -\frac{\sqrt{\pi}}{2};\ f_0(1) = f_0(3) = -1/2;\ f_0(2) = -\sqrt{\pi}/4, \tag{10}$$

$$f_1(0) = \lambda/3\sqrt{2\pi}\, a;\ f_1(1) = 3\lambda/16\sqrt{2}\, a;\ f_1(2) = 2\lambda/5\sqrt{2\pi}\, a, \tag{11}$$

$$f_2(0) = -\lambda^2/12\sqrt{\pi}\, a^2;\ f_2(1) = -13\lambda^2/70\pi\, a^2, \tag{12}$$

$$f_3(0) = 8\lambda^3/45\sqrt{2}\,\pi^{3/2}\, a^3. \tag{13}$$

We can also see from (6) that

$$\delta^{(k)}(q) = \left(\frac{\lambda}{\sqrt{2\pi}}\right)^{k+1} \delta^{(k)}(r-a). \tag{14}$$

The explicit expansion of $f_i(q)$'s can be easily written using (8) and (10) to (14). If we substitute these expansions in (1) we find

$$U(r) = -2^{-3/2}\lambda\,\delta(r-a) + \frac{r^2}{12\pi a}[2\,\delta(r-a) + 3a\,\delta^{(1)}(r-a)]$$

$$- \frac{\lambda^3}{96\sqrt{2}\pi a^2}[8\delta(r-a) + 9a\delta^{(1)}(r-a) + 6a^2\delta^{(2)}(r-a)]$$

$$+ \frac{\lambda^4}{5040\pi^2 a^3}[448\delta(r-a) + 468a\delta^{(1)}(r-a) + 252a^2\delta^{(2)}(r-a)$$

$$+ 105a^3\delta^{(3)}(r-a)] + 6(\lambda^5) \tag{15}$$

3. Expansion of B_2

At constant density number ρ and absolute temperature T the quantal pressure P^q of the quantal hard-sphere fluid in terms of its classical pressure P, its classical radial distribution function $g(r)$ and $U(r)$ is given by (Hemmer 1968; Jancovici 1969; Gibson 1975; Sinha and Singh 1977; Kumar and Giri 1980)

$$\beta P^q = \beta P - 2\pi\rho^2 \int g(r)\,U(r)\,r^2\,dr + 6(\rho^3), \tag{16}$$

where $\beta = (KT)^{-1}$, K being the Boltzmann constant.

We also know (Hill 1956) that

$$g(r) = 1 + 6(\rho), \text{ if } r \geqslant a, \tag{17}$$

$$= 0 \quad , \text{ if } r < a, \tag{18}$$

$$\beta P^q = \rho + \rho^2 B_2 + 6(\rho^3), \tag{19}$$

$$\beta P = \rho + \rho^2 B_2^{(cl)} + 6(\rho^3), \tag{20}$$

and $B_2^{(cl)}$ $(= 2\pi a^3/3)$ is the classical second virial co-efficient of the fluid.

Substitution of (17)–(20) in (16) we find an expression for B_2:

$$B_2 = \frac{2\pi a^3}{3}\left[1 - \frac{3}{a^3}\int_a^\infty U(r)\,r^2\,dr\right]. \tag{21}$$

We have evaluated the quadrature in (21) with the aid of (15) and a formula given below:

$$\int_{-\infty}^{+\infty} F(r)\,\delta^{(k)}(r-a)\,\mathrm{d}r = (-1)^k F^{(k)}(a). \tag{22}$$

Finally we obtain the well known expansion of B_2 correct up to λ^4:

$$B_2 = \frac{2\pi a^3}{3}\left[1 + \frac{3}{2\sqrt{2}}\left(\frac{\lambda}{a}\right) + \frac{1}{\pi}\left(\frac{\lambda}{a}\right)^2 + \frac{1}{16\sqrt{2}\pi}\left(\frac{\lambda}{a}\right)^3 - \frac{1}{105\pi^2}\left(\frac{\lambda}{a}\right)^4 + 6\left(\frac{\lambda}{a}\right)^5\right]. \tag{23}$$

This verifies that (15) is correct.

4. Conclusion

The expansion of $U(r)$ in (15) might be conveniently used for calculating the quantal corrections to the equilibrium thermodynamic quantities of the fluid.

References

Gibson W G 1975 *Mol. Phys.* **30** 1, 13
Gibson W G and Byrnes S C 1975 *Phys. Rev.* **A11** 270
Hemmer P C 1968 *Phys. Lett.* **A27** 377
Hemmer P C and Mork K J 1967 *Phys. Rev.* **158** 144
Handelsmann R A and Keller J B 1966 *Phys. Rev.* **148** 94
Hill T L 1956 *Statistical mechanics* (New York: McGraw Hill) Ch. 6
Jancovici B 1969 *Phys. Rev.* **178** 295
Jancovici B 1969 *Phys. Rev.* **184** 119
Kim S 1969 *Phys. Fluids* **12** 2046
Kumar B and Giri V S 1980 *Physica* **A104** 339
Messel H and Green H S 1952 *Phys. Rev.* **87** 738
Sinha S K and Singh Y 1977 *J. Math. Phys.* **18** 367

Pramāṇa, Vol. 21, No. 4, October 1983, pp. 261–272. © Printed in India.

Ultrasonic studies in binary liquid mixtures of benzene and coconut oil near the critical region

A C BHATTACHARYA and B B DEO
Department of Physics, Utkal University, Vani Vihar, Bhubaneswar 751 004, India

MS received 6 June 1983; revised 25 August 1983

Abstract. Velocity and attenuation of ultrasonic waves have been measured in complex binary mixtures of benzene and multicomponent coconut oil near the critical temperature in the low MHz region. The experimental results are analysed in terms of theories developed by Kawasaki and Mistura. The characteristic frequency and amplitude parameter determined by fitting the data in the relations proposed by Kawasaki-Mistura are scaled at reduced temperature and these agree with scaling exponents. A small velocity dispersion is also observed.

Keywords. Ultrasonic attenuation; amplitude parameter; reduced temperature; scaling exponent.

1. Introduction

The anomalous increase of ultrasonic attenuation near the critical point has been a subject of intensive research. The present paper reports the absorption and velocity measurements in mixtures of benzene and coconut oil near the plait point. This mixture behaves like a complex binary system. Coconut oil is a multicomponent organic compound composed of esters of saturated and unsaturated fatty acids. The physical and chemical properties of coconut oil have been extensively studied. Bhattacharya and Deo (1981) reported the ultrasonic behaviour of coconut oil near the liquid-solid phase transition. Benzene has also been studied ultrasonically. The coexistence curve for phase separation in mixtures of benzene and coconut oil can be obtained by a very simple method. To our knowledge, ultrasonic behaviour of such a complex binary system which throws light on the nature of acoustic response in the megacycle range near the critical point has not been studied so far (Bhattacharya 1981).

The mode-mode coupling theory proposed by Kawasaki (1970) and Mistura (1971) has been applied in pure fluids and binary liquid mixtures (Garland and Lai 1978) to explain the behaviour of ultrasonic propagation in the critical region.

In critical binary liquid mixtures, as the critical temperature is approached the fluctuations of the order parameter greatly increase due to the divergence of the generalised susceptibility of the system. This brings about an anomalous increase of ultrasonic absorption in the low MHz region. The concentration fluctuations are supposed to cause mode-mode couplings between the various modes of liquid mixtures. As the consolute temperature is approached, ultrasound attenuation gets increasingly coupled to the mass diffusion mode. This is reflected in the mode-mode coupling

theory of Kawasaki and Mistura predicting the behaviour of ultrasonic propagation in the critical systems near the critical temperature. The critical divergence of ultrasonic attenuation in complex binary mixtures of benzene and coconut oil near the critical region can be explained in terms of the mode-mode coupling theory which is yet to be rigorously tested in complex binary mixtures. In the present paper, we have analysed the experimental results in the light of the mode coupling theory.

2. Theory

The total ultrasonic absorption of critical binary mixtures can be represented by three terms (Harada 1979)

$$\phi(\epsilon, w) = \phi_{\text{crit}}(\epsilon, w) + \phi_{\text{Bg}}(\epsilon, w) + \phi_{\text{NS}}(\epsilon, w), \tag{1}$$

where ϵ is the reduced temperature given by

$$\epsilon = (T - T_c)/T_c,$$

T_c being the critical temperature. The first term $\phi_{\text{crit}}(\epsilon, w)$ denotes the critical absorption of sound. The second term $\phi_{\text{Bg}}(\epsilon, w)$ is the background relaxation and the third term $\phi_{\text{NS}}(\epsilon, w)$ is the classical Navier-Stokes absorption given by

$$\phi_{\text{NS}}(\epsilon, w) = \frac{\alpha_\lambda}{u^2}(\text{NS}) = \frac{\pi w}{\rho u^4}\left\{\left(\frac{4}{3}\phi_0 + \epsilon_0\right) + \Lambda\,(C_v^{-1} - C_p^{-1})\right\} \tag{2}$$

where $\alpha_\lambda = \alpha\lambda$ is the absorption per wavelength, u is the acoustic velocity, ϕ_0 is the shear viscosity, ϵ_0 is the relaxing bulk viscosity, Λ is the thermal conductivity, C_v is the specific heat at constant volume and C_p is the specific heat at constant pressure. $\phi_{\text{Bg}}(\epsilon, w)$ refers to a variety of non-classical and non-critical relaxation processes.

The Kawasaki-Mistura mode-mode coupling theory connects absorption and velocity with frequency. The relevant expressions are

$$\frac{\alpha_\lambda}{u^2}(\epsilon, w) = \pi\, c(\epsilon)\, I(w^*) + \pi \sum_i \frac{S_i\, w\, \tau_i}{1 + w^2\, \tau_i^2} + \phi_{\text{NS}}(\epsilon, w), \tag{3}$$

$$u^{-2}(0) - u^{-2}(w) = c(\epsilon)\, J(w^*) + \sum_i \frac{S_i\, w^2\, \tau_i^2}{1 + w^2\, \tau_i^2}. \tag{4}$$

The first term in (3) and (4) represents contributions from critical behaviour. The term containing the sum refers to set of instantaneous simple relaxations with relaxation times τ_i and strengths S_i. $I(w^*)$ and $J(w^*)$ are

$$I(w^*) = \int_0^\infty \frac{x^2\, dx}{(1 + x^2)^2}\, \frac{w^*\, K(x)}{K^2(x) + w^{*2}}, \tag{5}$$

and

$$J(w^*) = \int_0^\infty \frac{x^2\,dx}{(1+x^2)^2}\,\frac{w^{*2}}{K^2(x)+w^{*2}}, \tag{6}$$

where $K(x) = \frac{3}{4}\{(1+x^2) + (x^3 - x^{-1})\arctan x\}$,

and $x = k_0\,\xi$.

k_0 is the wavenumber and ξ is the correlation length of the order parameter fluctuation. w^* is the reduced frequency given by

$$w^* = w/w_D = f/f_D,$$

f is the frequency of ultrasonic waves and f_D is the characteristic frequency of ultrasonic propagation. In binary fluids, f_D is defined as

$$f_D(\epsilon) = \frac{D}{\pi}\,\xi^{-2}$$

where D is the diffusion coefficient.

Equation (4) is the velocity dispersion formula, $u(0)$ being the static limiting velocity and equals $1/(\rho k_s)^{\frac{1}{2}}$ where ρ is the density and k_s is the adiabatic compressibility.

The critical relaxation strength or the amplitude parameter $c(\epsilon)$ is given by the Kawasaki version of the mode-mode coupling theory for a binary fluid as

$$c(\epsilon) = \left(\frac{c_p}{c_v} - 1\right)^2 \rho\,\frac{kT}{\pi^2}\,\frac{C_v^2}{C_p^2}(\partial P/\partial T)_v^{-2}\left(1 - \frac{\phi}{2}\right)^2 k'\,(\partial k'/\partial T)^2, \tag{7}$$

where k is the Boltzmann constant and $k' \equiv \xi^{-1}$. ϕ is the critical exponent arising from the Fisher correction to the Ornstein-Zernike correlation function. The Mistura version of the theory gives $c(\epsilon)$ as

$$\frac{kT}{\pi^2}\,\rho\,\frac{c_v^2}{c_p^2}(\partial P/\partial T)_v^{-2}\left(1 - \frac{\phi}{2}\right)^2 k'\,(\partial k'/\partial T)^2. \tag{8}$$

3. Experiment

The phase diagram (concentration versus miscibility temperature curve) for the binary mixture of benzene coconut oil is shown in figure 1. The estimated critical or consolute temperature (T_c) for the system is approximately equal to 25·4°C ± 0·1°C and the critical composition (n_c) is 60·37% by weight of benzene. The critical point investigated here is actually a plait point in a multicomponent system (Mistura 1972). The experiment requires one boiling tube fitted with a thermometer and stirrer placed inside the test liquids and an arrangement for heating or cooling. Phase separation

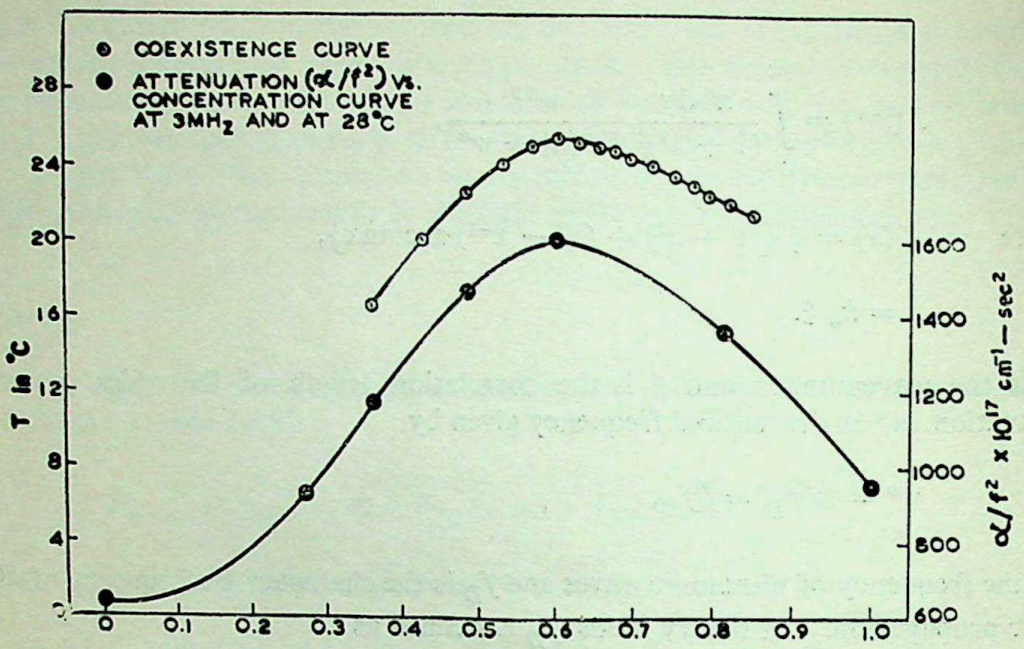

Figure 1. Coexistence curve *i.e.* concentration (n) versus miscibility temperature (T) curve for benzene-coconut oil mixture giving critical concentration and consolute temperature.

or transition temperature is detected by visual method when the mixtures become opalescent (milky-white) under the equilibrium conditions. Benzene used is of Analar Grade. Coconut oil used is of 'Expressed' type and IA Grade according to standard specifications (ISI 1973). The ultrasonic interferometer has a measuring cell provided with inlet and outlet attached with a constant temperature bath and a motor-pump system.

The temperature can be controlled and kept constant to an accuracy of $\pm$ 0·1°C. The velocity measurements are accurate to within 0·5%. The error in attenuation measurement is within $\pm$ 5%. The velocity and attenuation were measured at temperatures ranging from 25·7 to 30°C and at frequencies of 1, 2, 3 and 5 MHz by the continuous wave interferrometric technique (Bhattacharya 1981). The lower curve of figure 1 represents the composition dependence of ultrasonic attenuation (α/f^2) at 3 MHz and 28°C. The peak of attenuation curve corresponds to the peak of coexistence curve giving critical temperature at critical concentration.

4. Results and analysis

4.1 *Absorption*

Figure 2 shows the temperature dependence of ultrasonic attenuation (α/f^2) in the phase $T > T_c$ for the binary mixture of benzene-coconut oil at various frequencies. Only at 2 MHz the temperature dependence of α/f^2 has been taken at $T < T_c$. At low frequencies α/f^2 falls rapidly with temperature while at the higher frequencies it is almost temperature-independent for $T \gg T_c$. The anomalous behaviour of ultrasonic absorption near T_c is within low MHz region.

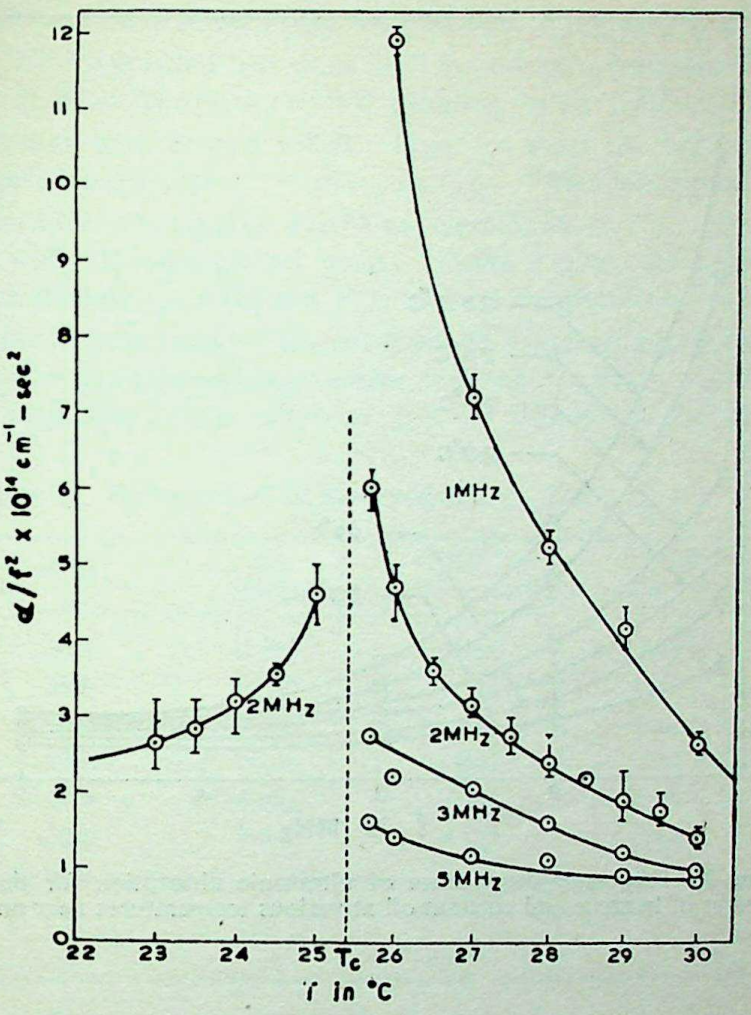

Figure 2. Temperature dependence of ultrasonic absorption for the critical binary mixtures of benzene-coconut oil.

Figure 3 gives the frequency dependence of attenuation at various temperature near and above T_c. It is observed that α/f^2 falls rapidly with frequency and is quite significant near T_c.

We have analysed our data in terms of mode-coupling theory of Kawasaki-Mistura. We have fitted our data using (3) in which the set of "simple relaxation" terms has been excluded for the system benzene-coconut oil. Benzene is a non-polar or unassociated liquid and coconut oil is composed of esters of saturated fatty acids (91%) and unsaturated fatty acids (9%) with the characteristic feature that whatever be its origin its compositions are approximately the same (Anon 1950). The composition of coconut oil earlier has been determined by Anon (1950).

The set of relaxations as observed in a critical system like triethylamine-water involving acid-base hydrolysis (Garland and Lai 1978) is supposed to be absent in benzene-coconut oil. Therefore, (3) reduces to

$$\frac{\alpha_\lambda}{u^2}(\epsilon, w) = \pi c(\epsilon)\, I(w^*) + \phi_{NS}(\epsilon, w). \tag{9}$$

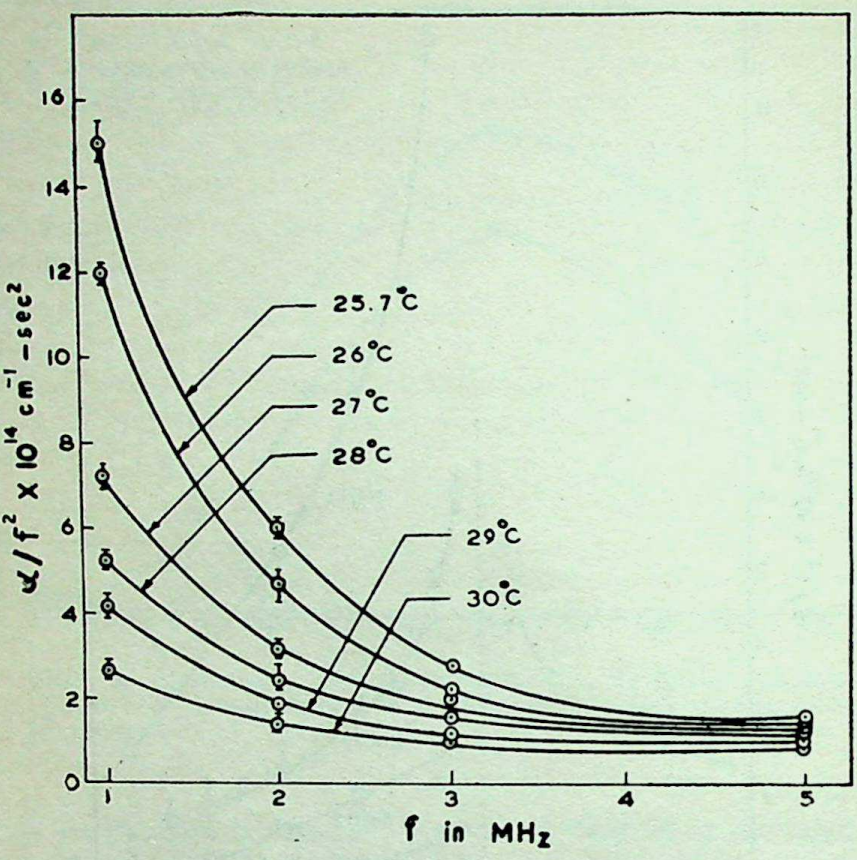

Figure 3. Frequency dependence of ultrasonic absorption for the critical binary mixtures of benzene and coconut oil at various temperatures near and above T_c.

While considering the Navier-Stokes term $\phi_{NS}(\epsilon, w)$, we shall neglect the contribution due to the thermal conductivity appearing in (2) since the viscosity term is very large compared to the thermal conductivity. Equation (2) becomes

$$\phi_{NS}(\epsilon, w) = \frac{\pi w}{\rho u^4}\left(\frac{4}{3}\phi_0 + \epsilon_0\right) = B_f/u, \tag{10}$$

where $$B_f = Bf = \frac{2\pi^2 f}{\rho u^3} b, \tag{11}$$

and $$b = \frac{4}{3}\phi_0 + \epsilon_0.$$

We can assume b as constant since it is roughly independent of T. But B is dependent on temperature because of ρ and u appearing at the denominator of (11). Equation (9) can be written in the form of

$$(\alpha_\lambda/u^2)^* = \frac{(\alpha_\lambda/u^2) - (B_f/u)}{\pi c(\epsilon)} = I(w^*). \tag{12}$$

In (12) $(\alpha_\lambda/u^2)^*$ may be defined as the reduced absorption and α_λ/u^2 as the observed absorption. We have fitted our data in (12) and have determined the parameters f_D, $c(\epsilon)$ and B by a computer search program using least square minimisation technique (Flecher and Powell 1963). Figure 4 gives the reduced absorption at various reduced frequencies $w^* = w/w_D = f/f_D$. The solid curve has been drawn from the theoretical expression $I(w^*)$ as mentioned in (5). The data points fit satisfactorily with the theoretical curve. Table 1 gives the computed values of the parameters namely f_D, $c(\epsilon)$ and B at various temperatures.

According to the prediction of the mode-mode coupling theory, the mass diffusion near critical point in binary mixture scales as $D \approx \xi^{-1}$. From Ising lattice gas calculation, the correlation length scales as $\xi \sim \epsilon^{-\nu}$ where ν is the critical exponent.

Table 1. Parameters of the Kawasaki-Mistura Theories.

T(°c)	f_D (MHz)	$c(\epsilon)10^{-13}$ (cm^{-2} — sec^2)	B (cm^{-1} — sec^2)
25·7	0·061	1·964	$0{\cdot}93 \times 10^{-3}$
26·0	0·063	1·595	$0{\cdot}10 \times 10^{-2}$
27·0	0·860	1·149	$0{\cdot}26 \times 10^{-7}$
28·0	2·434	1·048	$0{\cdot}69 \times 10^{-5}$
29·0	4·051	0·961	$0{\cdot}17 \times 10^{-5}$
30·0	8·942	1·125	$0{\cdot}11 \times 10^{-3}$

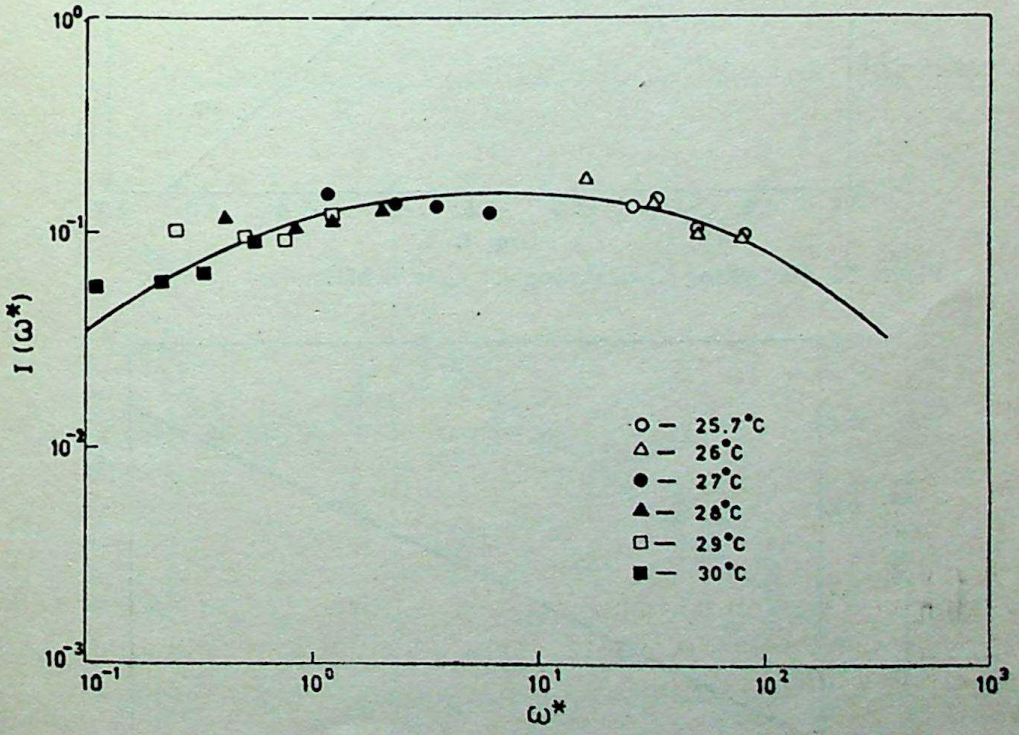

Figure 4. Relation between reduced absorption and reduced frequency. The solid curve has been drawn from the theoretical expression $I(w^*)$ and as given in equation (5).

Hence the scaling relation of the characteristic or reduced frequency f_D is obtained as

$$f_D = (D/\pi)\ \xi^{-2}$$

or

$$f_D = f_0\ \epsilon^{3\nu} \tag{13}$$

where f_0 is a constant.

Figure 5 which represents the relation between $\log f_D$ and $\log \epsilon$ is a straight line and the intercept giving the value of 3ν is determined as 1·9. So $\nu = 0{\cdot}63$. This value of ν is quite consistent with the theoretically predicted value (Swift 1968).

We have also determined the scaling exponent for the critical relaxation strength $c(\epsilon)$. Figure 6 shows the relation between $\log c(\epsilon)$ and $\log \epsilon$ following a power law as

$$c(\epsilon) = c_0\ \epsilon^{-\alpha}. \tag{14}$$

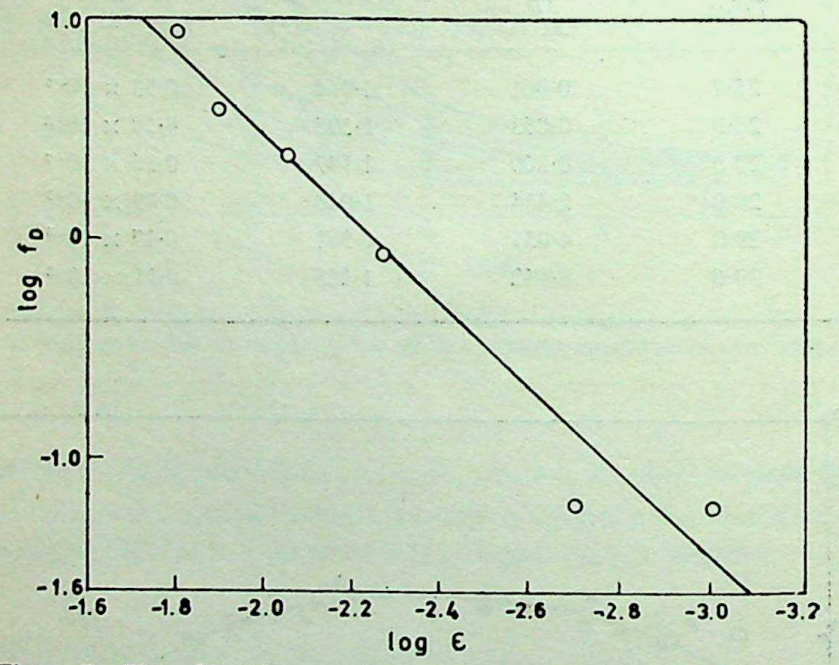

Figure 5. Plot of $\log f_D$ versus $\log \epsilon$. f_D is in MHz.

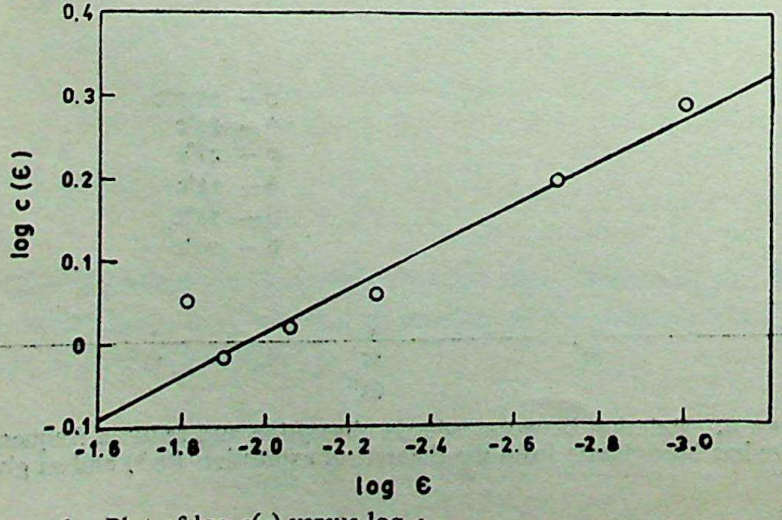

Figure 6. Plot of $\log c(\epsilon)$ versus $\log \epsilon$.

The exponent α as determined from the slope of the line in figure 6 is 0·25. This value of the exponent is sufficiently large to satisfy the well-known hyper-scaling relation $\alpha=2-3\nu$. From the Josephson (Stanley 1971) scaling inequality $3\nu-2\geqslant-\alpha$, and the Ising lattice gas value for $\alpha=0{\cdot}11$, it is shown that $c(\epsilon)$ should scale as $c(\epsilon)\approx\epsilon^{-\alpha}$ for $\alpha\geqslant 0{\cdot}11$ (Fenner and Bowen 1980). The exponent value of 0·25 agrees with this inequality but not with equality. $c(\epsilon)$ cannot be evaluated from (7) or (8) as some of the quantities are not known for our system.

Table 1 indicates that B is a small quantity and it varies irregularly with temperature. For all temperatures studied the Navier-Stokes term ϕ_{NS} (ϵ, w) is quite small compared with our observed $\alpha\lambda/u^2$ values. The reason for the irregular variation of B with respect to temperature is not clear, probably it is linked with the complicacy of our system which is not a true binary fluid but a complex mixture of benzene and a multicomponent coconut oil.

4.2 *Velocity*

Figure 7 shows the variation of ultrasonic velocity with temperature for the critical mixtures of benzene-coconut oil at 3 MHz. The velocity behaves as a linearly decreasing function of temperature above the consolute temperature satisfying a relation $u=mT+c$. The m and c values are $-7{\cdot}5$ mt/sec^2c and 1523 mt/sec respectively. A similar behaviour relating to velocity and temperature was reported by Fenner and Bowen (1980) in sulphur dioxide and carbon tetrachloride liquid mixtures and also by Arrigo and Sette (1968) in nitro-benzene-n-hexane. The critical mixtures of benzene-coconut oil exhibits a very small dispersion as shown in figure 8. This dispersion appears to be unreal and may be due to the large scatter in the velocity data. We have attempted to analyse our data in terms of velocity dispersion formula

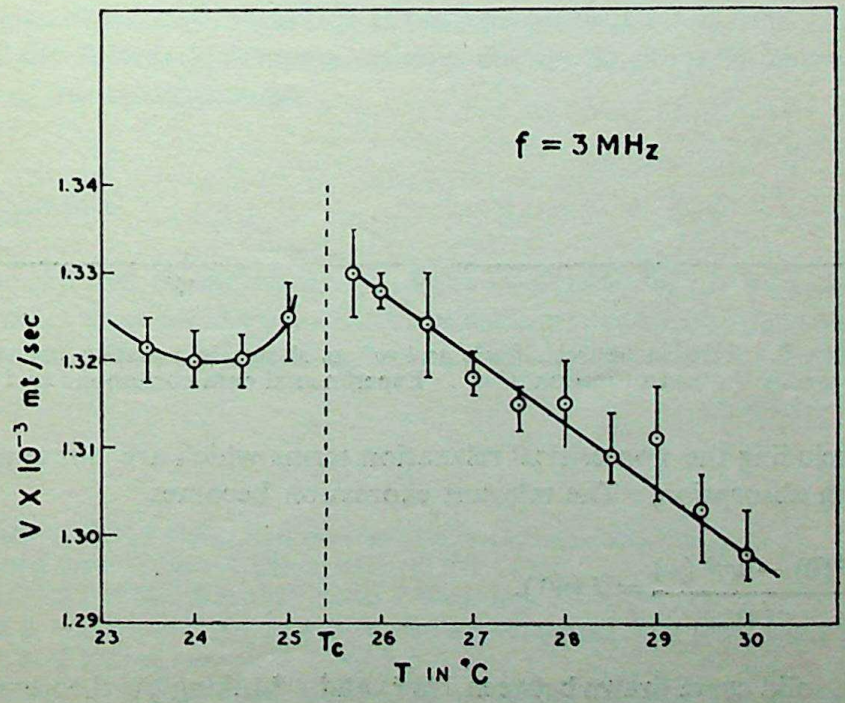

Figure 7. Temperature dependence of ultrasonic velocity at 3 MHz.

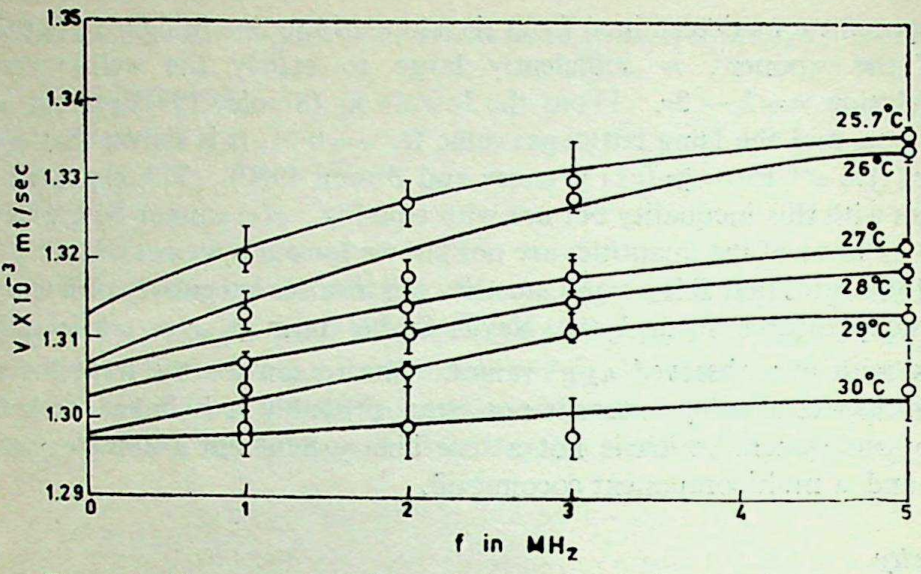

Figure 8. Frequency dependence of ultrasonic velocity at various temperatures.

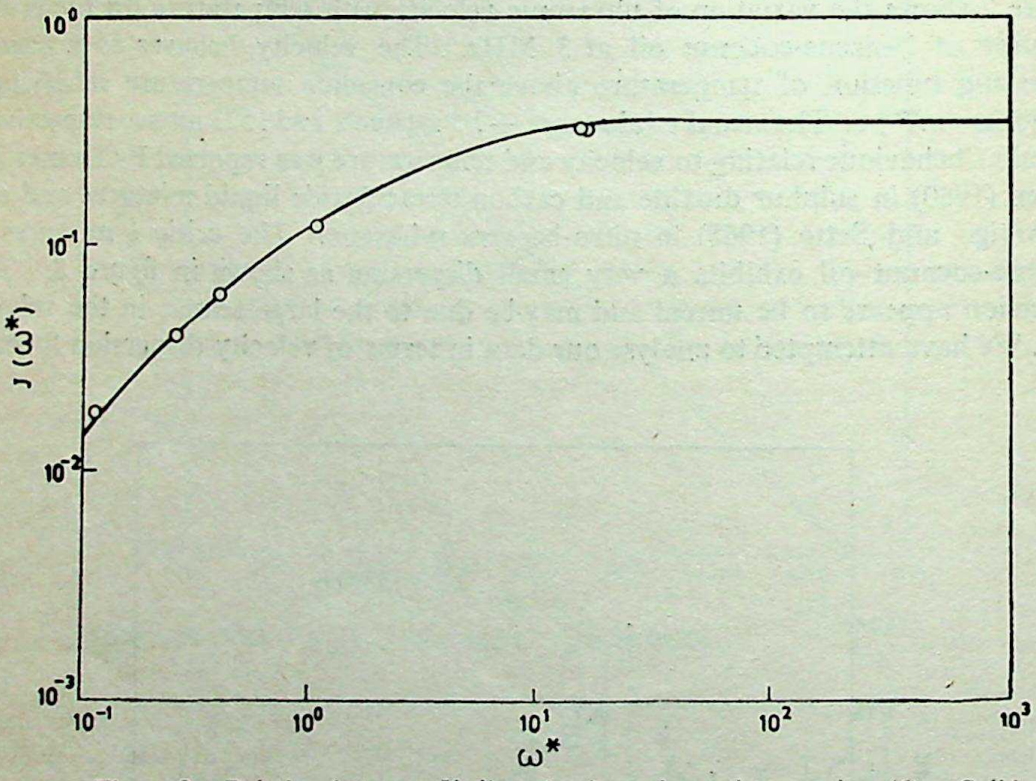

Figure 9. Relation between $J(w^*)$ and w^* as shown in equation (6). Solid curve represents $J(w^*)$ as a function of w^*. Experimental data correspond to 1 MHz only.

given by (4) excluding the non-critical relaxation terms which are not considered in connection with absorption. The relevant expression becomes

$$\frac{u^{-2}(0) - u^{-2}(w)}{c(\epsilon)} = J(w^*). \tag{15}$$

Figure 9 is a solid curve drawn between $J(w^*)$ and w^* taking the theoretical expression $J(w^*)$ given by (6); $u(0)$ values have been extrapolated from figure 8 at different

Table 2. Experimental velocity at 1 MHz and the extrapolated $u(0)$ values at different temperatures.

T (°c)	u (1 MHz) ($\times 10^3$ mt/sec)	$u(0)$ ($\times 10^3$ mt/sec)
25·7	1·320	1·313
26·0	1·313	1·307
27·0	1·307	1·306
28·0	1·304	1·303
29·0	1·299	1·298
30·0	1·298	1·297

temperatures as shown in table 2. The values of $c(\epsilon)$ have been taken from table 1. It is observed that the experimental data corresponding to 1 MHz only can fit the theoretical curve in figure 9. At other higher frequencies our data do not fit to the curve obeying (15). This discrepancy may be due to negligible dispersion presumably due to the large scatter in the velocity data.

5. Conclusion

The ultrasonic attenuation of the complex binary mixtures of benzene and coconut oil exhibits strong temperature and frequency dependences near T_c. The experimental results have been analysed in terms of the mode-mode coupling theories developed by Kawasaki and Mistura. Both the characteristic frequency and the amplitude parameters determined from (3) are consistent with scaling relations. There exists only a very small velocity dispersion in benzene-coconut oil system. The dispersion relation of the Kawasaki-Mistura theories cannot be properly analysed within the accuracies of our measurements.

Acknowledgements

Our thanks are due to the members of the Computer Centre of Utkal University, Bhubaneswar, Orissa for the use of IBM 1130 computer for computation. This work has been supported in part by UGC, New Delhi.

References

Anon 1950 *The wealth of India, Raw materials* (New Delhi: CSIR) Vol. 2
Arrigo G D and Sette D 1968 *J. Chem. Phys.* **48** 691
Bhattacharya A C and Deo B B 1981 *Indian J. Pure Appl. Phys.* **19** 1172
Bhattacharya A C 1980 *Int. Conf. and Exhibition on Ultrasonics, New Delhi*, Conf. Papers, p. 284
Bhattacharya A C 1981 *J. Pure Appl. Ultra.* **3** 7
Bhattacharya A C 1981 *Solid State physics*, Silver Jubilee Physics Symposium (Bombay: BARC). Vol. **C24** 345

Fenner D B and Bowen D E 1980 *Phys. Rev.* **A21** 998
Flecher and Powell 1963 *Comp. J.* **6** 163
Garland C W and Lai C N 1978 *J. Chem. Phys.* **69** 1342
Harada Y 1979 *J. Phys. Soc. Jpn.* **46** 221
Indian Standard Specification for coconut oil 1978 (New Delhi: ISI) IS:542-1968
Kawasaki K 1970 *Phys. Rev.* **A1** 1750
Mistura L 1972 *J. Chem. Phys.* **57** 2311
Mistura L 1971 *Critical phenomena* (ed.) M S Green (New York: Academic Press) p. 563
Stanley H E 1971 *Phase transition and critical phenomena* (New York: Oxford University Press)
Swift J 1968 *Phys. Rev.* **173** 257

Pramāṇa, Vol. 21, No. 4, October 1983, pp. 273–282. © Printed in India.

Ultrasonic propagation in multicomponent system in the critical region

A C BHATTACHARYA and B B DEO
Department of Physics, Utkal University, Bhubaneswar 751 004, India

MS received 6 June 1983; revised 25 August 1983

Abstract. Ultrasonic propagation in a system consisting of coconut oil and carbon tetrachloride has been considered as a function of temperature near T_c in the low MHz region. A small velocity dispersion is seen in the system. The experimental results have been analysed with recent theories developed by Ferrell and Bhattacharjee. The data on attenuation per wavelength near T_c agree with the scaling relation developed by Kroll and Ruhland.

Keywords. Multicomponent critical system; critical temperature; scaling relation; attenuation.

1. Introduction

In recent years ultrasonic propagation, particularly anomalous behaviour of ultrasonic absorption in binary liquid mixtures near the critical temperature, has been widely studied. The theory of Fixman (1962) promoted the study of the critical phenomena of binary liquid mixtures using ultrasonic waves. There were also theories developed by Kawasaki (1970) and Mistura (1971). These were applied in many critical binary liquid mixtures but showed some inconsistencies. We have considered the theories developed by Ferrell and Bhattacharjee (1981) and Kroll and Ruhland (1981) to study the ultrasonic behaviour in critical systems.

In the present paper, we report the measurements of absorption and velocity in a complex binary system composed of coconut oil and carbon tetrachloride. Coconut oil itself is a multicomponent mixture of esters of saturated and unsaturated fatty acids with the characteristic feature that irrespective of its origin the composition remains the same. The physical and chemical properties of coconut oil are well known. Bhattacharya and Deo (1981) earlier reported the ultrasonic behaviour of coconut oil near the liquid-solid phase transition. Recently the ultrasonic study of benzene and coconut oil near the critical region was reported in the light of some important theories (Bhattacharya 1981; Bhattacharya and Deo 1982). The ultrasonic behaviour of carbon tetrachloride is already known. The coexistence curve for phase separation in mixtures of coconut oil and carbon tetrachloride can be drawn by a simple method. Ultrasonic studies on multicomponent critical systems are rather few, probably because of the complexity of the system. It reveals the nature of acoustic response in the megacycle range during phase transition. We have analysed the experimental results in the light of the theory of Ferrell and Bhat-

tacharjee (hereafter abbreviated as FB) which relates the attenuation per wavelength at the critical point $a_c\ \lambda_c$ through the equation

$$a_c\,\lambda_c = -2\pi\,(u_2/u_c) = (\pi g^2 u_c^2 A)/T_c B^2 \sin(\pi a_0/4)\,(\gamma_0/2\pi)^{a_0/2} f^{-a_0/2}, \qquad (1)$$

where $a_c\lambda_c$ is the negative imaginary part of the complex critical velocity $u_1 + iu_2$. u_c is the velocity at the critical temperature. g is the coupling constant. A and B are constants associated with the critical specific heat given by

$$C_{p,c} = A\epsilon^{-a_0} + B,$$

B is the constant-background specific heat. a_0 is the specific heat exponent. ϵ is the reduced temperature given by

$$\epsilon = (T - T_c)/T_c.$$

T_c is the critical temperature and f the frequency. γ_0 is a constant involved in the characteristic temperature-dependent relaxation rate equation expressed as

$$\gamma = \gamma_0\,\epsilon^2,$$

where γ is the characteristic relaxation rate of the system. Multiplying (1) by $(u_c f)^{-1}$ we obtain

$$\frac{a_c}{f^2} = \frac{\pi g^2 u_c A}{T_c B^2} \sin(\pi a_0/4)\,(\gamma_0/2\pi)^{a_0/2}\, f^{[-1-(a_0/2)]} \qquad (2)$$

Our data on attenuation are also consistent with an expression derived by FB and is of the form

$$\frac{a}{a_c} = \frac{2}{\pi}(1+p)\,\Omega \int_0^\infty \frac{u\,du}{(1+u)^2} \frac{u(1+u)^p}{\Omega^2 + u^2(1+u)^{2p}} \qquad (3)$$

where a/a_c is the attenuation relative to the critical point, $\sqrt{u}$ corresponds to the wavenumber of a relaxing order-parameter fluctuation. p is a parameter in the relaxational factor of the integrand. $p = \frac{1}{2}$ is taken for the three-dimensional fluid. Ω is the reduced frequency given by

$$\Omega = \omega/\gamma = 2\pi f/\gamma_0\epsilon^2$$

The real part of the complex critical velocity as obtained by FB is given by

$$\frac{u_1}{u_c} = \frac{g^2 u_c^2}{2T_c B} - \frac{A\,g^2 u_c^2}{2T_c B^2}\epsilon^{-a_0}, \qquad (4)$$

or

$$\frac{u_1}{u_c} \approx \text{constant} + \frac{A\,g^2 u_c^2\,a_0}{2T_c\,B^2} \ln\epsilon. \qquad (5)$$

Further, our experimental data on attenuation per wavelength (α_λ) agree with the new scaling relations obtained from the theory developed by Kroll and Ruhland (1981) for ultrasonic propagation in critical binary mixtures. Our data close to T_c follow the power-law relation of the form

$$\alpha_\lambda(f) = A_0 f^{-\alpha_0/\nu z_c} + B_0, \tag{6}$$

A_0 and B_0 are constants. ν is the critical exponent of correlation length $\xi = \xi_0 \epsilon^{-\nu}$ of the order-parameter fluctuation. z_c is the factor associated with the characteristic frequency of the order-parameter fluctuation given by

$$f_c = f_0 \xi^{-z_c},$$

or

$$f_c = f_{c0} \epsilon^{\nu z_c},$$

where f_0 and f_{c0} are constants.

2. Experiment

The experiment relating to the coexistence curve for the binary mixtures of coconut oil and carbon tetrachloride was performed taking one boiling tube fitted with a thermometer and stirrer placed inside the test liquids and an arrangement for cooling or heating. Phase separation or transition temperature for a particular concentration was determined by visual method as the mean of two temperatures at which opalescence appears and disappears under the equilibrium conditions. Figure 1

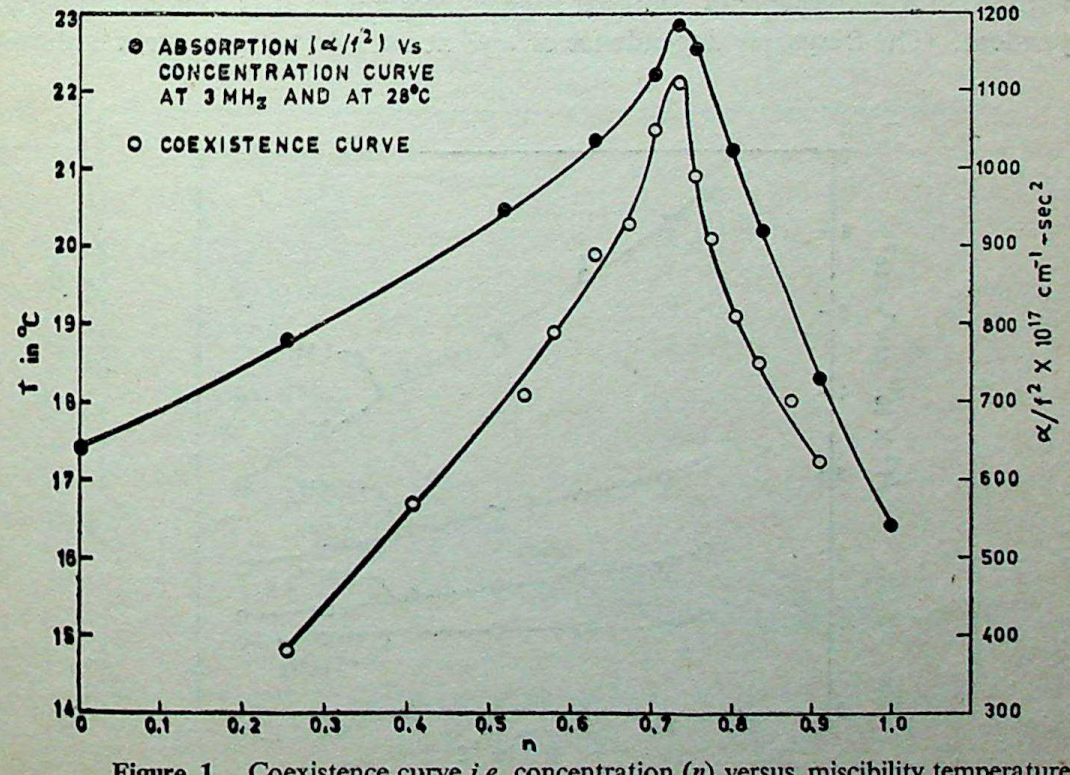

Figure 1. Coexistence curve *i.e.* concentration (n) versus miscibility temperature (T) curve for coconut oil-carbon tetrachloride mixtures giving critical concentration and critical temperature.

gives the phase diagram drawn with miscibility temperature as a function of concentration for coconut oil and carbon tetrachloride mixtures. The T_c value for the system is approximately 22·2 ± 0·1°C corresponding to the critical composition (n_c) of 0·732 by weight of carbon tetrachloride. Coconut oil used is of 'Expressed' type and IA grade according to the specifications (ISI 1973). Carbon tetrachloride is of Analar grade. Ultrasonic attenuation and velocity were measured at 1, 2, 3 and 5 MHz using an ultrasonic interferometer and following the continuous wave interferometric technique (Bhattacharya 1981). The temperature range of the measurements was 22·5 to 28°C. The measuring cell of the interferometer is provided with inlet and outlet attached with thermostatic device consisting of a constant temperature bath and a motor-pump system. The temperature can be regulated and kept constant with an accuracy of ± 0·1°C. The absorption measurement is accurate to within ± 5% and that of velocity to within 0·5%. Figure 1 also indicates the variation of ultrasonic absorption (α/f^2) with concentration taken at 28°C and at 3 MHz. The absorption peak corresponds to the peak of the coexistence curve giving consolute temperature at the critical concentration. The strange shape of the coexistence curve may be due to coconut oil itself being a multicomponent system. The critical point observed in the carbon tetrachloride coconut oil system is actually a plait point in a multicomponent system (Mistura 1972).

3. Results and analysis

Figure 2 represents the variation of ultrasonic absorption (α/f^2) with temperature for the critical system coconut oil and carbon tetrachloride. α/f^2 decreases rapidly with temperature at low frequencies, while at higher frequencies it is almost temperature independent. The frequency dependence of α/f^2 at various temperatures is shown in

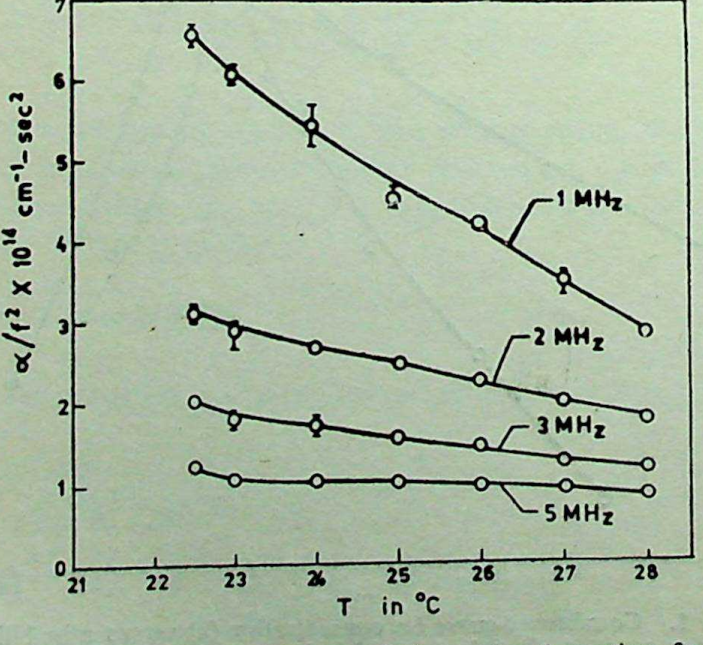

Figure 2. Temperature dependence of ultrasonic absorption for the critical binary mixtures of carbon tetrachloride-coconut oil.

figure 3 which indicates that α/f^2 falls rapidly with frequency. The frequency dependence of α/f^2 is remarkable when the critical temperature is approached. We have analysed our experimental results in terms of recent theories developed by FB on ultrasonic attenuation and velocity in critical binary mixtures of liquids. Our data on critical absorption (α_c/f^2) obey the relation expressed in (2) which can be written as

$$\alpha_c/f^2 = (\pi C/T_c) \sin(\pi\alpha_0/4)(\gamma_0/2\pi)^{\alpha_0/2} f^{[-1-(\alpha_0/2)]}, \tag{7}$$

where

$$C = g^2 u_c A/B^2.$$

The unknown parameters C, α_0 and γ_0 have been determined by fitting our data in(7) by computer search program using the least square minimisation technique. (Flecher and Powell 1963). The optimized values are

$$C = 0{\cdot}42 \times 10^{-4}\ \text{K/cm sec}^{-1}; \quad \alpha_0 = 0{\cdot}121; \quad \gamma_0/2\pi = 1{\cdot}1\ \text{GHz}.$$

The value of specific heat exponent (α_0=0·121) agrees with the theoretical value (0·12) of FB. C is associated with the unknown parameters A, B, g and u_c which can be determined experimentally. A and B can be obtained from specific heat measurements, g from thermodynamic measurement, u_c from Brillouin scattering experiment and γ_0 from Rayleigh linewidth measurement (Burstyn *et al* 1980). Unfortunately, the experimental data on A, B, g, u_c and γ_0 for our system are lacking. Figure 4 shows the straight line fit between α_c/f^2 and $f^{-1-\alpha_0/2}$ according to (7). The background absorption as determined from the intercept of

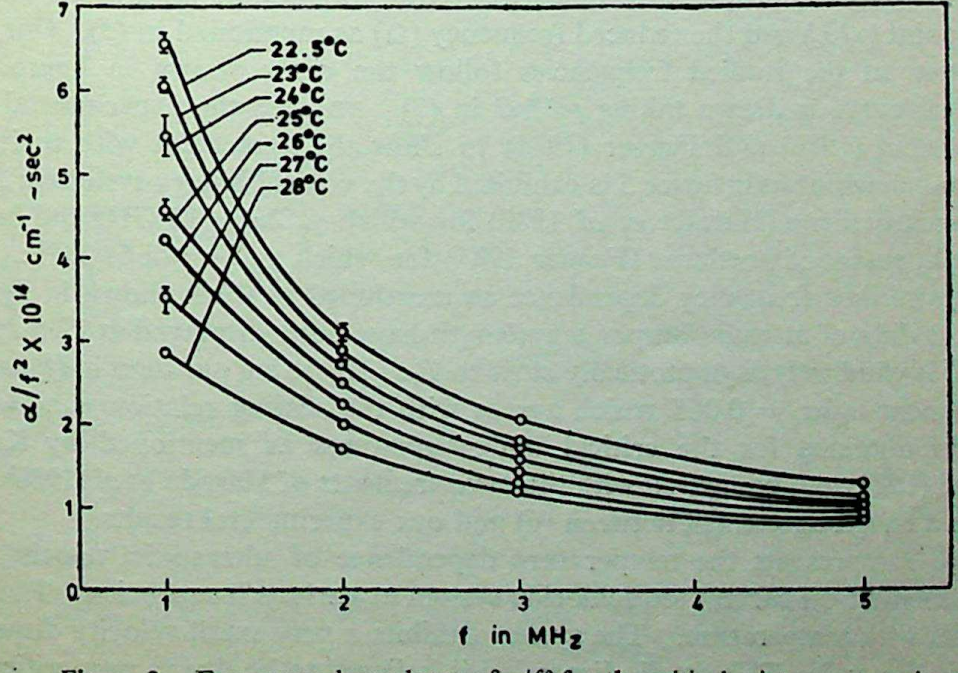

Figure 3. Frequency dependence of α/f^2 for the critical mixtures at various temperatures above T_c.

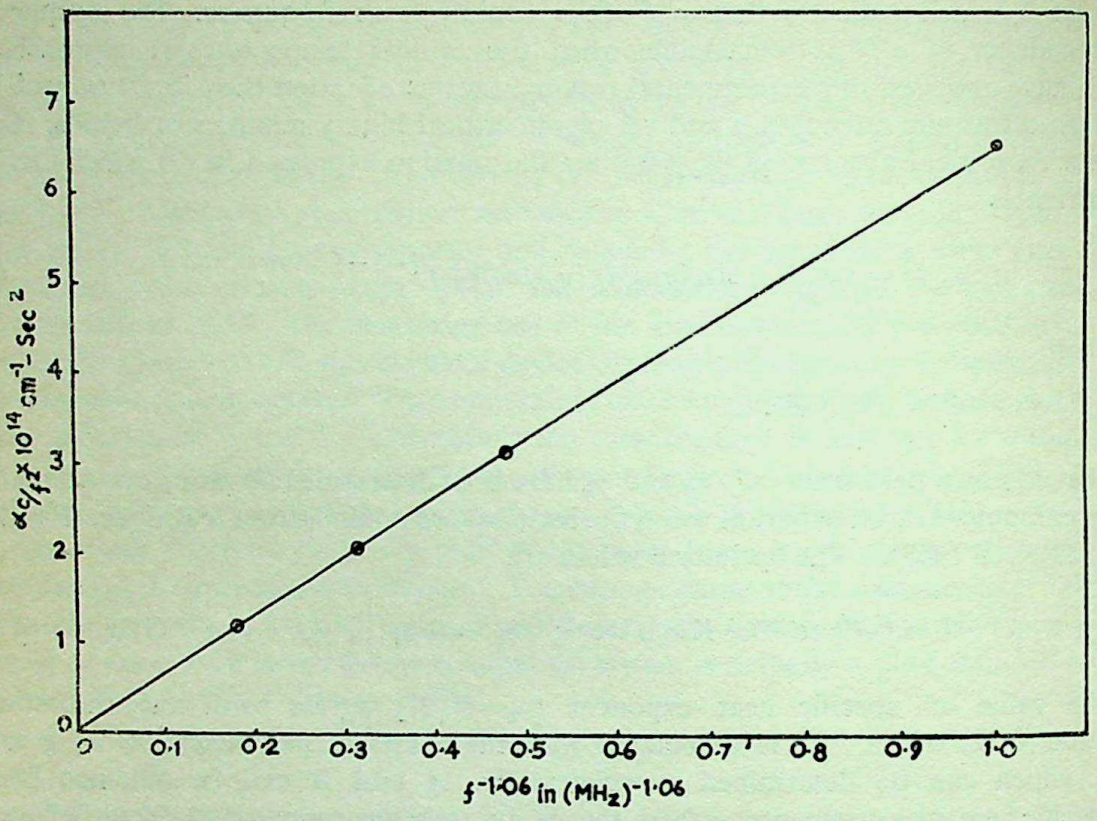

Figure 4. Linear relation between α_c/f^2 and $f^{-1.06}$. Solid line is the theoretical curve. The intercept gives the background absorption.

figure 4 is 25×10^{-17} cm^{-1} sec^2 and is due to the non-critical contributions. u_c is obtained by fitting our data in (1) since the optimized values of C, γ_0 and α_0 are known. The estimated value of $u_c = D/C = 1095$ mt/sec where $D = g^2 u_c^2 A/B^2 = 4{\cdot}6$ K.

Figure 5 represents the relation between the attenuation relative to that at the critical point (α/α_c) and the reduced frequency (Ω) as mentioned in (3). Our data on attenuation at the studied frequencies follow the curve shown in figure 5. The theoretical curve is drawn taking $p = 1/2$ in (3). FB used the experimental data of Harada *et al* (1980) and Fenner (1981) to show the agreement with their theory. Identical behaviour as in figure 5 is exhibited by the critical binary system of 3-methyl pentane-nitroethane (Harada *et al* 1980) for which $\gamma_0/2\pi = 15$ GHz and in 2, 2, 4-trimethyl-pentane-nitroethane (Fenner 1981) for which $\gamma_0/2\pi = 2{\cdot}67$ GHz.

The power-law frequency dependence as mentioned in (6) is shown in figure 6 in which the data of attenuation per wavelength have been displayed at 22·5 and 23°C, since (6) is valid only asymptotically close to T_c. By fitting our data in (6) we obtain the exponent $\alpha_0/\nu z_c = 0{\cdot}065$ which agrees with the scaling relation $\alpha_0/\nu = 0{\cdot}2$ and $z_c = 3{\cdot}07$ obtained for the critical binary mixtures as mentioned by Kroll and Ruhland (1981) and compared with the measurements of Harada *et al* (1980). Figure 6 shows a rough agreement between (6) and our experimental results.

Figure 7 represents the temperature dependence of ultrasonic velocity for the critical coconut oil-carbon tetrachloride system at various frequencies. The velocity decreases with temperature. The system exhibits a very small velocity dispersion as shown in figure 7. This small dispersion is believed to be due to non-critical effects and is almost independent of ΔT or reduced temperature ϵ.

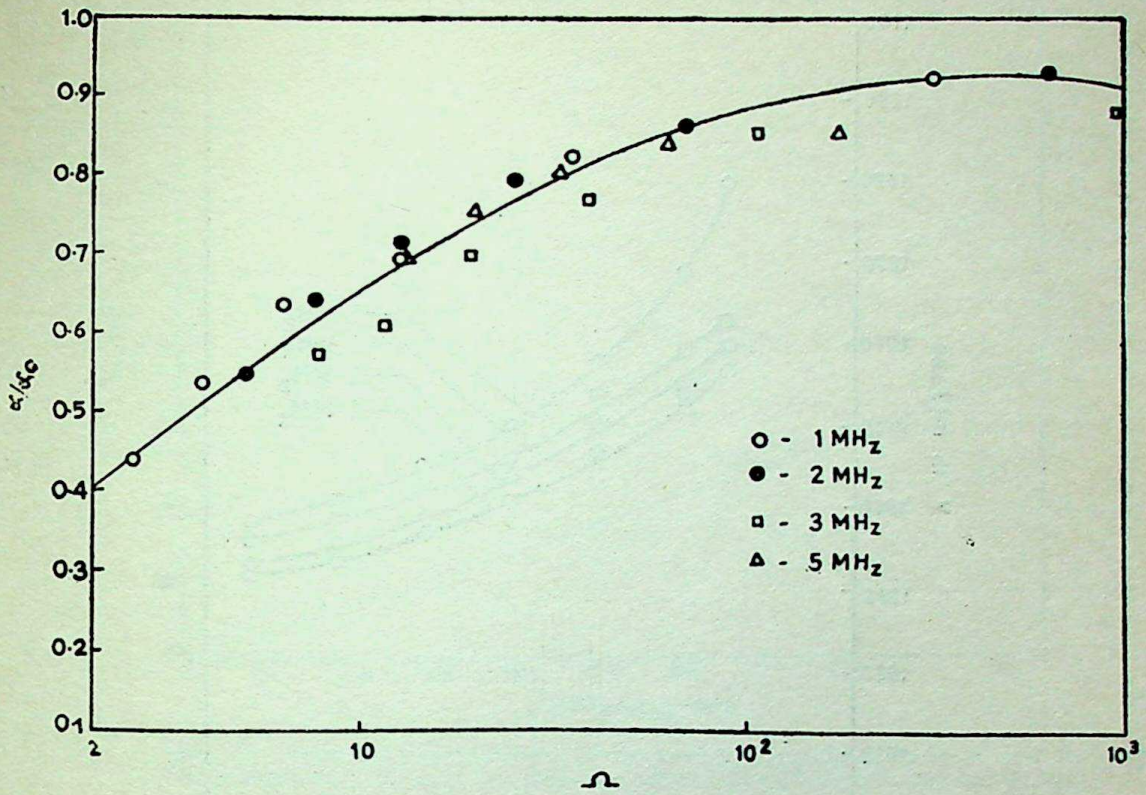

Figure 5. Variation of attenuation relative to the critical temperature with reduced frequency. Solid line is the theoretical curve corresponding to equation (1).

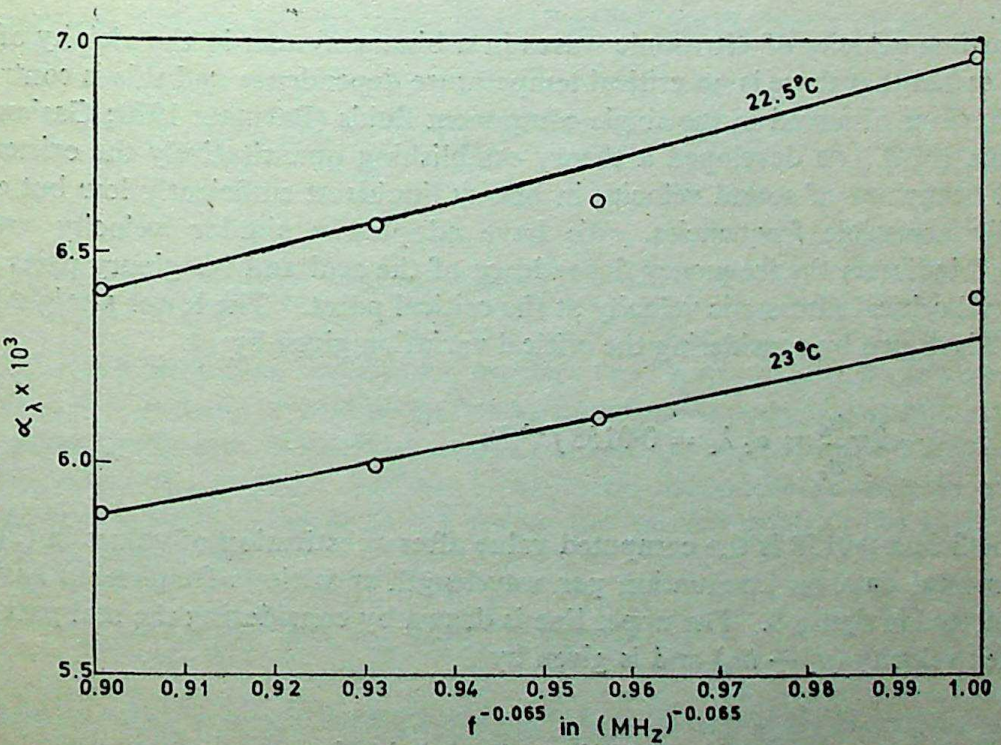

Figure 6. Relation between attenuation per wavelength and $f^{-0.065}$ at 22·5 and 23°C.

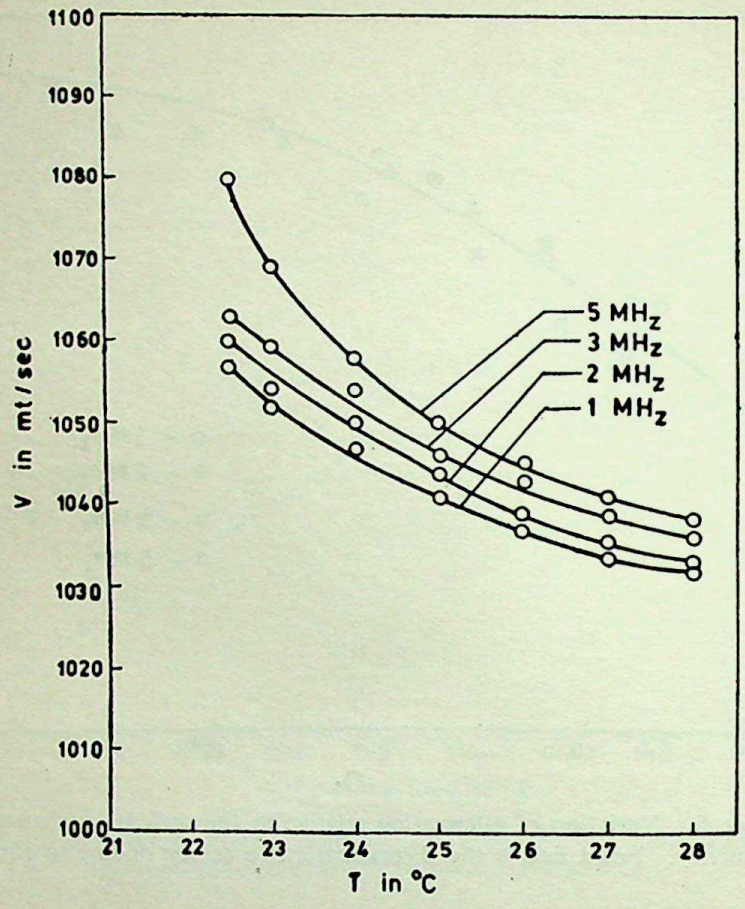

Figure 7. Temperature dependence of ultrasonic velocity at various frequencies.

Regarding velocity of ultrasonic waves in a binary system in the vicinity of T_c, it can be stated that there is no critical temperature dependence and this is contrary to the behaviour observed in the single-component fluids (Barmatz 1970; Garland and Williams 1974). FB developed a theory establishing quantitatively the existence of critical behaviour of sound velocity in binary liquids at sufficiently low but experimentally accessible frequencies. We have adopted a similar velocity analysis. Figure 8 indicates the frequency dependence of the real and imaginary parts of the fractional critical ultrasonic velocity at the critical point. The lower straight line in figure 8 is drawn by considering the critical variation given by

$$-2\pi\frac{u_2}{u_c} = a_c\,\lambda_c = 0{\cdot}0158\,f^{-0{\cdot}06}. \tag{8}$$

The coefficient 0·0158 is the computed value after substitution of values in (2). The experimental data on attenuation per wavelength at various frequencies have also been plotted in figure 8. The upper line is drawn by considering the real part of the complex velocity $(u_1 + iu_2)$ and is given by

$$\frac{u_1}{u_c} = -\frac{g^2\,u_c^2\,A}{2T_c\,B^2}\,(\gamma_0/2\pi)^{0{\cdot}06}\cos(0{\cdot}03\pi)\,f^{-0{\cdot}06}. \tag{9}$$

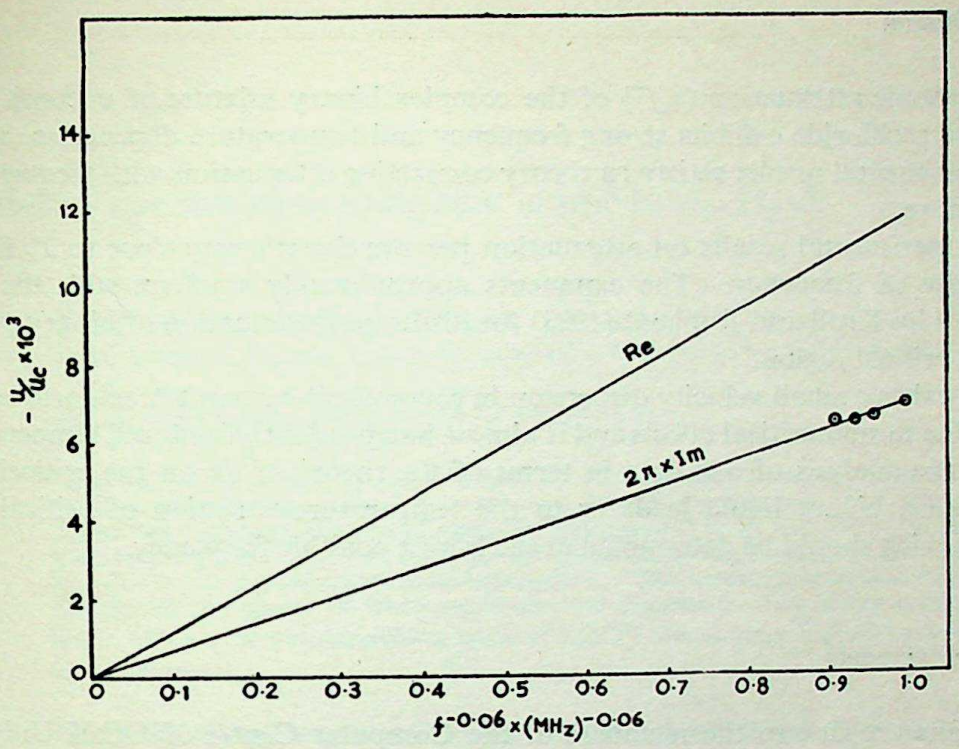

Figure 8. Frequency dependence of the real and imaginary parts of the fractional critical velocity at T_c with the data of coconut oil-carbon tetrachloride system.

Substituting the values in (9) we obtain

$$u_1/u_c = -\,0{\cdot}0266\, f^{-0{\cdot}06}. \tag{10}$$

Replacing ω by γ to convert the upper line in figure 8 into the thermodynamic relation, we obtain

$$u_1/u_c = -\,0{\cdot}0266\,(\gamma_0/2\pi\,\epsilon^2)^{-0{\cdot}06} = -\,0{\cdot}00763\,\epsilon^{-0{\cdot}12} \tag{11}$$

or

$$u_1/u_c \approx \text{constant} + 0{\cdot}00091\,\ln\,\epsilon. \tag{12}$$

Here u_c=1095 mt/sec as determined earlier. u_c represents the large non-critical velocity at T_c. It is observed that the critical temperature variation of velocity in the MHz region is absent. In the MHz region the velocity variation at the critical point is independent of ΔT or ϵ. Further, the critical temperature variation of sound velocity should be determined at the lowest possible frequency. The coefficient of $\log_e \epsilon$ in (5) is given by

$$a_0\, g^2\, A\, u_c^2/2T_c\, B^2 = a_0\, D/2T_c = 0{\cdot}00092.$$

This closely agrees with the coefficient of (12) which is obtained phenomenologically. The agreement of our measurements with the theories of FB is quite satisfactory.

4. Conclusion

The ultrasonic attenuation (α/f^2) of the complex binary mixture of coconut oil and carbon tetrachloride exhibits strong frequency and temperature dependence near T_c. The experimental results satisfy FB theory connecting attenuation with frequency and temperature.

Our experimental results on attenuation per wavelength very close to T_c follow a power law of frequency. The exponents approximately conform with the model developed by Kroll and Ruhland (1981) for ultrasonic attenuation of binary mixtures near the critical region.

There exists a small velocity dispersion in coconut oil-carbon tetrachloride system. This is due to non-critical effects and is almost independent of reduced temperature ϵ. Further the analysis of our data in terms of the theory of FB on the critical sound velocity in a binary liquid leads us to the temperature variation of critical sound velocity which should be determined at the lowest possible frequency.

Acknowledgements

Our thanks are due to the members of the Computer Centre of Utkal University, for the use of IBM 1130 computer for computation. This work has been supported in part by UGC, New Delhi.

References

Barmatz M 1970 *Phys. Rev. Lett.* **24** 651
Bhattacharya A C 1980 *Solid state physics*, Silver Jubilee Symposium, (Bombay: BARC) **C24** 345
Bhattacharya A C 1981 *J. Pure Appl. Ultra.* **3** 7
Bhattacharya A C and Deo B B 1981 *Indian J. Pure Appl. Phys.* **19** 1172
Bhattacharjee J K and Ferrell F A 1981 *Phys. Rev.* **A24** 1643
Burstyn H C, Sengers J V and Esfandiari P 1980 *Phys. Rev.* **A22** 282
Ferrell R A and Bhattacharjee J K 1981 *Phys. Rev.* **B24** 4095
Fenner D B 1981 *Phys. Rev.* **A23** 1931
Fixman M 1962 *J. Chem. Phys.* **36** 1961
Flecher and Powell 1963 *Comp. J.* **6** 163
Garland C W and Williams R D 1974 *Phys. Rev.* **A10** 1328
Harada Y, Suzuki Y and Ishida Y 1980 *J. Phys. Soc. Jpn.* **48** 703
ISI 1973 Indian Standard Specification for coconut oil (New Delhi: ISI) IS:542-1968
Kawasaki K 1970 *Phys. Rev.* **A1** 1750
Kroll D M and Ruhland J M 1981 *Phys. Rev.* **A23** 371
Mistura L 1971 *Critical phenomena* (ed.) M S Green (New York: Academic Press)p. 563
Mistura L 1972 *J. Chem. Phys.* **57** 2311

Pramāṇa, Vol. 21, No. 4, October 1983, pp. 283–291. © Printed in India.

Vibrational spectra of α-molybdic acid-$MoO_3 \cdot H_2O$

S SHEIK SALEEM and G ARULDHAS
Department of Physics, University of Kerala, Kariavattom 695 581, India

MS received 9 April 1983; revised 23 August 1983

Abstract. The IR and Raman spectra of molybdenum trioxide—monohydrate are studied assuming an effective tetrahedral Mo-O coordination and isolated water molecules, although the crystallographic coordination is six-fold with two long Mo-O distances. Based on C_i symmetry, the group theoretical analysis has been carried out and a vibrational assignment is proposed. The nature of hydrogen bonding and the librational modes of water molecules are discussed. The factor group splitting for ν_3, the asymmetric stretching mode of $MoO_4^=$ ion, is large indicating strong inter-chain coupling.

Keywords. Raman spectra; molybdic acid; librational modes; infrared spectra.

1. Introduction

The structural investigation of the different forms of molybdic acids (molybdenum trioxide-hydrates) was started by Lindqvist (1950, 1956). Recent investigations (Guntur 1972; Oswald *et al* 1975) revealed three different forms of $MoO_3 \cdot H_2O$—a white α-form, a white β-form and an yellow form. It has been established that the α-form has the oxygens 6-fold coordinated around molybdenum, of which the oxygen of the water molecule being the one, forming octahedral double chains (Oswald *et al* 1975). Further, from the O..O distances of the water oxygen there is evidence for hydrogen bonding between the octahedral double chains.

Guntur (1972) recorded the infrared spectra of $MoO_3 \cdot 2H_2O$ and $MoO_3 \cdot H_2O$ (yellow form) to study the coordination of water molecules. Maricic and Smith (1958) reported the infrared spectra of $MoO_3 \cdot 2H_2O$ and $MoO_3 \cdot H_2O$ and Krauss and Huber (1961) reported the spectrum of $MoO_3 \cdot 2H_2O$. However, no mention about the forms was made. The infrared and Raman spectra studies of the α-form of molybdenum trioxide-monohydrate could throw light on the nature and strength of hydrogen bonding, the librational modes of water molecules and the wide range of molybdenum-oxygen distances present in it.

2. Experimental

White molybdic acid (Analar grade) was used for the investigation. The far infrared spectrum (10-400 cm^{-1}) (figure 1) was recorded in an FIR 30 Polytec. The infrared spectrum (400–4000 cm^{-1}) using KBr pellet was recorded using spectrophotometer (Perkin Elmer).

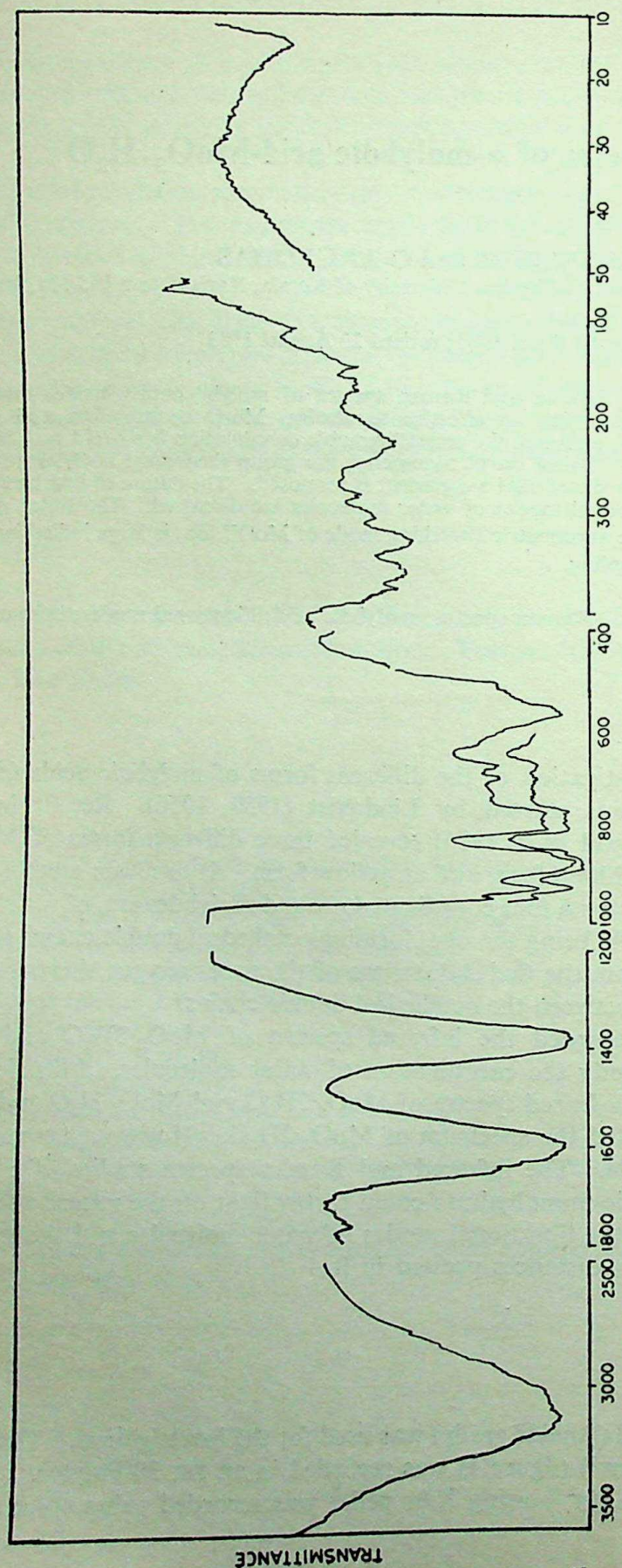

Figure 1. Far IR and IR spectra of α-molybdic acid.

The Raman spectrum (figure 2) was recorded using double monochromator, (Cary 82 and Spex Ramalog), both equipped with argon ion laser (Spectra Physics) operating at 4880 Å. The sample was placed in a metal cone of diameter 4-5 mm and a capillary tube of diameter 1.1 mm for Spex Ramalog.

3. Factor group analysis

The α-form molybdenum trioxide-monohydrate belonged to the triclinic system with the space group $P\bar{1}$ (C_i^1) (Oswald *et al* 1975). The oxygens are 6-fold coordinated around molybdenum forming an infinite double chain of edge-linked $[MoO_5(H_2O)]$ octahedra perpendicular to the *b*-axis. The Mo-O distances range between 1·66 and 2·37 Å. Hence as an approximation, if the two ligands with the largest Mo-O distances are neglected, the structure may be alternatively described as built up from chains (perpendicular to *b*-axis) of corner-linked distorted MoO_4-tetrahedra and isolated water molecules. This approximation is similar to the one by Kihlborg (1963) to characterize the structure of MoO_3 as a transitional state between octahedral and tetrahedral coordination. Using a similar approximation Blasse (1975) succeeded in explaining the vibrational spectra and the luminiscent properties of $HgMoO_4$.

The crystal has two formula units per unit cell and all atoms are located on the general positions. The symmetry of a free molybdate ion is T_d. However, in the crystal, it occupies a general site of C_1 symmetry. The anisotropic crystal field lifts the degeneracies of the normal modes. For such a configuration, the number of internals to be expected can be derived as indicated in table 1. Coupling between the vibrating ions produces further splitting of each crystal mode into components equal to the number of ions in the primitive unit cell (Davydov 1969).

4. Assignments

The internal modes of the molybdate ion are expected to occur in the region 775–950 cm^{-1} (stretching) 275–425 cm^{-1} (bending) irrespective of its environment. For the external modes, the frequency strongly depends on the type of motion (translation or rotation) and on the nature of the cation. Further, interactions could occur between rotational, translational and low-lying internal modes. It is difficult to explain the observed spectra of powdered samples due to the complex nature of the metal-oxygen

Table 1. Correlation table for the normal modes of the MoO_4 group with site symmetry C_1.

T_d symmetry[a]	Site symmetry	Two groups under C_i symmetry[b]
ν_1 A (R)	A	$A_g + A_u$
ν_2 E (R)	$2A$	$2A_g + 2A_u$
ν_3, ν_4 F_2 (i. r, R)	$3A$	$3A_g + 3A_u$

[a] (*R*) — Raman active; (i. r.) — infrared active
[b] *g* modes Raman active; *u* modes infrared active

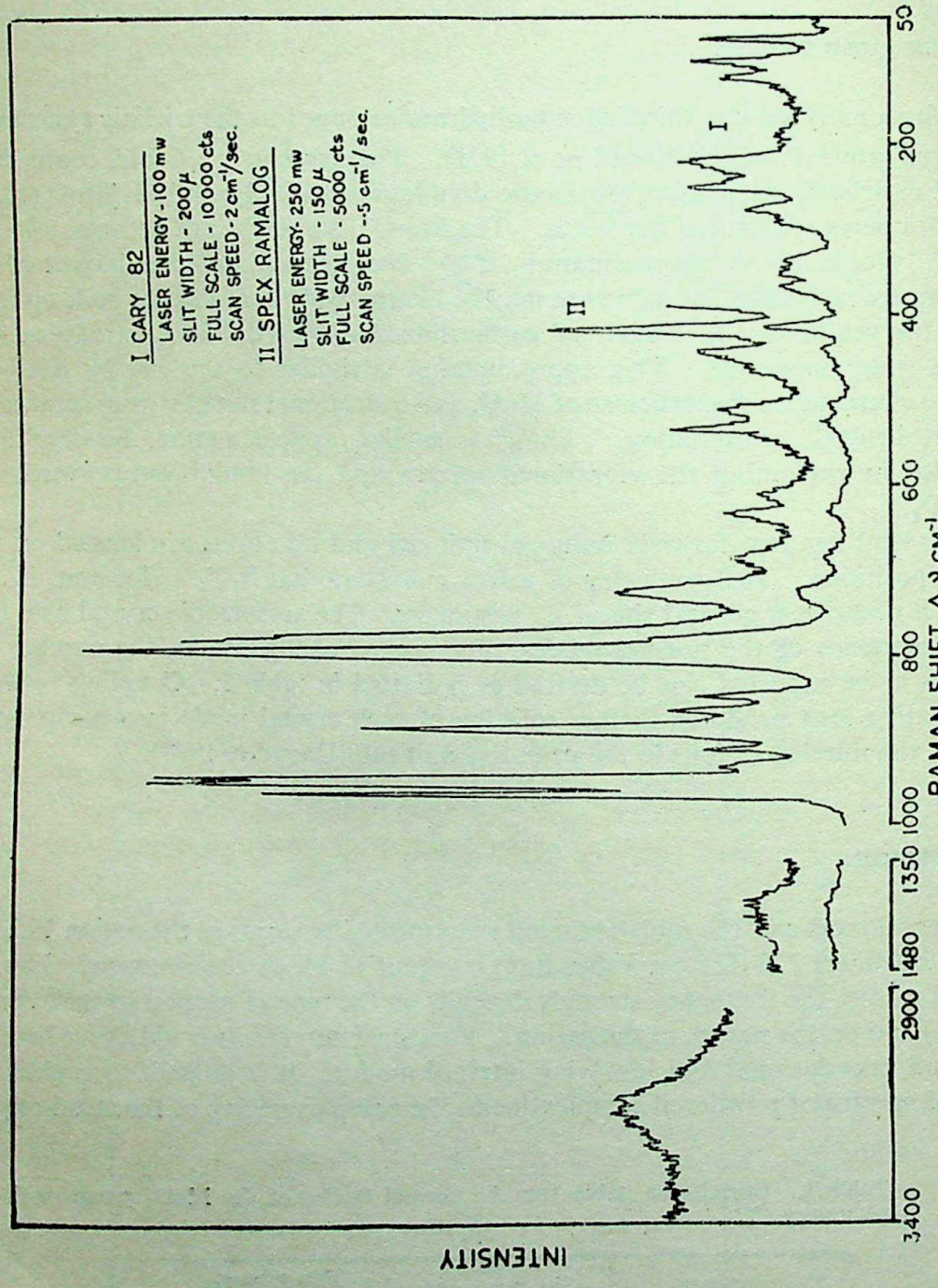

Figure 2. Raman spectra of α-molybdic acid

linkages and the distortions present in the metal-oxygen polyhedra. However, it is possible to make symmetry assignments by comparison with the normal modes of free molecules.

4.1 *O-H vibrations*

The octahedral double chains are linked through possible hydrogen bonds. The distances from the water oxygen O(4) to oxygen atoms $O(1^{iv})$, $O(3^{i})$, $O(3^{vii})$ of neighbouring octahedral double chain are respectively 2.76, 2.85 and 3.14Å. These values indicate medium and weak strength for the hydrogen bonding. Oswald *et al* (1975) have assumed that if $O(1^{iv})$ is definitely bonded it remains open which of the other two [$O(3^{i})$, $O(3^{vii})$] contacts represents the second water hydrogen bridge and the most probable hydrogen bonds are indicated by them (figure 3).

The strong bands at 3215, 3185, 3172 and 3155 cm^{-1} in Raman, and the strong broad band centred around 3140 cm^{-1} in infrared indicate hydrogen bonding of medium strength. Since the site symmetry of the water molecule is C_1, the two O-H bonds should be of unequal strength and the presence of four lines in Raman indicates this. These are the symmetric and asymmetric stretching of the hydrogens bonded to the $O(1^{iv})$ and $O(3^{i})$ with O(4)–$O(1^{iv})$ and O(4)–$O(3^{i})$ distance of 2·76 and 2.85 Å respectively. These O-H frequencies fall in the region of intermediate hydrogen bond strength (Novak 1979) and this clearly excludes the possibility of the hydrogen bonding with the $O(3^{vii})$ with an O(4)-$O(3^{vii})$ distance of 3.14 Å which is a distance indicative of a weak hydrogen bond.

The HOH deformation (ν_2) of a free water molecule occurs around 1600 cm^{-1} and will be strong in infrared and very weak in Raman. Usually the bending mode (ν_2) of water increases in wavenumber with increased strength of hydrogen bonding. However, this correlation does not always hold (Scherer 1978). Pezerat (1979) reported the bending vibration at low frequencies from a study of hydrogen bonded biological systems. In yellow molybdic acid ($MoO_3.2H_2O$) Sreenivasan (1979)

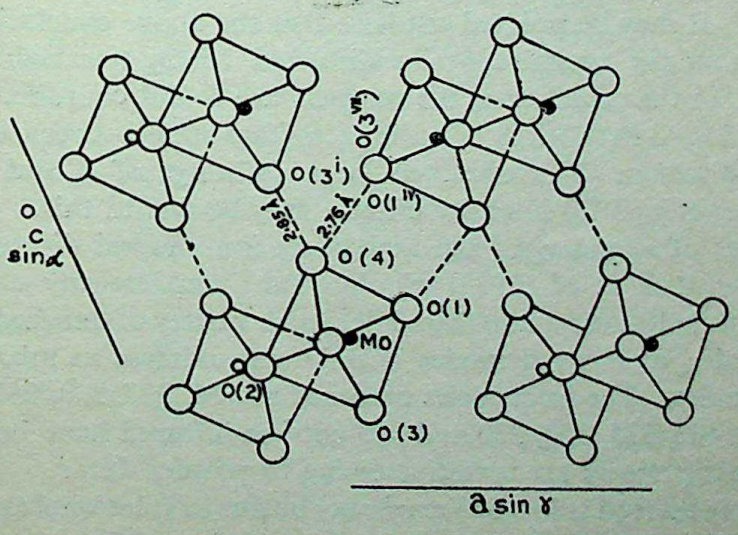

Figure 3. Projection of crystal structure parallel to [010]. Dotted lines indicate probable hydrogen bonds (after Oswald *et al* 1975).

observed the bending frequency around 1400 cm^{-1} which shifts to $\sim$ 1100 cm^{-1} on partial deuteration. In the present investigation, the infrared spectrum presents strong broad bands centred at 1600 and 1385 cm^{-1}. In Raman spectrum there is only a weak band in the region 1390-1445 cm^{-1} with distinct peaks at 1406 and 1436 cm^{-1} and no band could be observed around 1600 cm^{-1}. These observed frequencies are perhaps not HOH modes but OHO ones, one of a strongly bonded and the other that of a weakly bonded.

4.2 *Molybdate ion*

The molybdate ions are in a crystal field of low symmetry. Hence a large splitting of the degenerate vibrational modes is expected. Table 1 predicts four Raman active A_g modes and four infrared active A_u modes for the Mo-O stretchings. The frequency observed at 960 cm^{-1} in Raman and at 950 cm^{-1} in infrared is assigned to the symmetric stretching ν_1 of the molybdate ion. Such a high frequency for an Mo-O stretching is due to the Mo-O bond of 1·654 Å which is the shortest ever found in molybdenum-oxygen compounds. The frequencies 883 and 792 cm^{-1} correspond to two of the three predicted asymmetric frequencies of the molybdate ion. The third has split into a doublet (940 and 948 cm^{-1}) due to vibrational interaction with the neighbouring ions. The shoulder at 778 cm^{-1} may also be due to this interaction. The splitting of about 150 cm^{-1} for the triply degenerate ν_3 mode is unusually large. The complementary infrared frequencies are found at 927, 875 cm^{-1} and a broad band centred at 790 cm^{-1} with peaks at 770 and 805 cm^{-1}. Here again, the large splitting is maintained ($\sim$ 150 cm^{-1}). A similar type of splitting observed in $MgMoO_4$ (Miller 1971) and $HgMoO_4$ (Blasse 1975) is attributed to the strong interactions between the stretching motions of the tetrahedra and Mg-O, Hg-O interactions. The wide range of Mo-O distances present in the crystal can also give rise to such large splittings. Another possibility seems to be a strong interchain coupling.

The intensity of the symmetric stretching ν_1 is strong in Raman and weak in infrared whereas ν_3 is strong in both. Also the intensity ratio of ν_1/ν_3 is < 1 in both infrared and Raman. For tetrahedral ions Wienstock *et al* (1973) have established that ν_1 is strong in Raman and weak in infrared whereas ν_3 is strong in infrared and weak in Raman. It may be pointed out here that the above conclusion is based on the assumption that the crystal contains distorted MoO_4 tetrahedra and isolated water molecules. In the actual case, the oxygens are 6-fold coordinated with molybdenum and the Mo-O network is in an intermediate state between octahedral and tetrahedral coordination. The observed large splittings of ν_3 and the departure from Wienstock *et al's* (1973) intensity criteria may be due to this.

The assignments of ν_2 and ν_4 of the molybdate ion showed discrepancies before the work of Wienstock *et al* (1973) who proved from intensity calculations that $\nu_4 > \nu_2$ along with the Raman and infrared data of a variety of tetrahedral ions. The labelling of ν_2 and ν_4 as internal modes is only approximate as mixing is expected with the lattice modes. The frequencies observed at 414, 367, 350, 342 and 335 cm^{-1} in Raman and at 400, 375, 360, 350 and 325 cm^{-1} in infrared have been assigned to ν_4 and ν_2. The assignments are tentative owing to powder data.

The frequencies observed below 300 cm^{-1} may be due to rotational and translational modes. The possibility that some of the lines are lattice modes cannot be excluded. Further, it is difficult to distinguish between translational and rotational modes,

Table 2. Vibrational assignments of α-molybdic acid.

Infrared frequencies in cm^{-1} A_u symmetry	Raman frequencies in cm^{-1} A_g symmetry	Assignments
	3215	
3140	3185	OH stretching
	3172	
	3155	
1765		
1655		Combinations
1440–1360	1436	OHO bending
(broad band)	1406	
950	960	ν_1 MoO_4
927	948	ν_3 MoO_4
	940	
	908	Combination
875	883	ν_3 MoO_4
855	861	Combination
	846	Combination
805	792	ν_3 MoO_4
770	778	
	727·5	$R_y H_2O$
700		$R_y H_2O$
	689	$R_y H_2O$
675		$R_y H_2O$
	631	a
	610	a
570		$R_t H_2O$
	530	$R_t H_2O$
510	510	$R_t H_2O$
	461	$R_r H_2O$
	441	$R_r H_2O$
400	414	$\nu_4 MoO_4$
375	367	$\nu_4 MoO_4$
360	350	$\nu_4 MoO_4$
350	342	$\nu_2 MoO_4$
325	335	$\nu_2 MoO_4$
300	290	
280	274	
	246	R MoO_4
225	216	
165	188	
148	150	T MoO_4
114	120	
	116	
87	99	
78	74	
60		
50	52	Lattice modes
13		

a, coupled librations of H_2O; R_y, R_t, R_r, wag, twist and rock libration;
R, Rotation; T, Translation

However, rotational modes in general have higher wavenumber and intensity than translational modes. A tentative assignment is shown in table 2.

4.3 *Librational modes of H_2O*

The three librational movements of H_2O are the wagging, twisting and rocking. Lutz *et al* (1979) tried to assign the librational modes of H_2O molecules which are in an asymmetric force field and the sequence of $\nu_{wag} > \nu_{twist} > \nu_{rock}$ within the region 300–775 cm^{-1} was preferred. The different librational modes have recently been studied by Singh *et al* (1980). They assigned the bands in the region 900–500 cm^{-1} to these modes in the order $\nu_{rock} > \nu_{wag} > \nu_{twist}$. All these studies show that the assignments of the librational modes are ambiguous. However, the frequencies observed in the region 750–450 cm^{-1} have been tentatively assigned. In infrared, the frequencies at 700 and 675 cm^{-1} have been assigned to the wagging vibration. The strong band at 570 cm^{-1} with a shoulder at 510 cm^{-1} has been assigned to the twisting vibration. The very high intensity for this band is suggestive of the coupling of some other vibrational modes. In infrared it is reasonable to assume that the rocking vibrations are mixed up with ν_2 and ν_4 of the molybdate ion. The weak broad line observed at 727·5 and 689 cm^{-1} and 441, 461 cm^{-1} in Raman, assigned to the wagging and rocking vibrations respectively. The lines at 530 and 510 cm^{-1} can be assigned to the twisting, since it has a higher intensity (Lutz 1979).

The proposed vibrational assignments are shown in table 2.

5. Conclusions

The approximation that molybdenum trioxide-monohydrate contains distorted MoO_4 tetrahedra and isolated water molecules can fairly explain the observed vibrational spectra. The number of modes predicted by group theoretical analysis and mutual exclusion of frequencies to be obeyed under C_i point group have been observed (table 2). The large splitting of the Mo-O asymmetric stretching and the failure to obey the intensity criteria indicate that the molybdenum-oxygen coordination is in an intermediate state between tetrahedral and octahedral. The splitting of about 150 cm^{-1} for the ν_3 asymmetric stretching vibrations is indicative of strong interchain coupling. The observed OH stretching frequency falls in the region of intermediate strength hydrogen bonding and hence it may be said that the hydrogen bridge is formed between O(4) and $O(1^{iv})$, $O(3^{i})$. Hence one can rule out the possibility of the hydrogen bonding with $O(3^{vii})$.

Acknowledgement

The authors thank Prof. P S Narayanan for making available the Spex Ramalog for recording the spectrum and for hospitality to one of us (sss) during his stay at the Indian Institute of Science, Bangalore. sss is also grateful to CSIR New Delhi for a fellowship.

References

Blasse G 1975 *J. Inorg. Nucl. Chem.* **37** 97
Davydov A S 1969 *Theory of molecular excitons* (New York: McGraw-Hill)
Guntur J R 1972 *J. Solid State Chem.* **5** 354
Kihlborg L 1963 *Arkiv. Kemi* **21** 357
Krauss H L and Huber W 1961 *Chem. Ber.* **94** 2868
Lindqvist I 1950 *Acta Chem. Scand.* **4** 650
Lindqvist I 1956 *Acta Chem. Scand.* **10** 1362
Lutz H D, Pobischka W, Christan H and Becker R H 1979 *J. Raman Spectrosc.* **7** 130
Maricic S and Smith J A S 1958 *J. Chem. Soc.* **886**
Miller P J 1971 *Spectrochim. Acta* **A27** 957
Novak A 1979 *Mathematical and physical sciences* NATO advanced study institute series C (ed.). T M Theophanides (Holland, D Reidel Publishing Company), p. 279
Oswald H R, Guntur J R and Dubler E 1975 *J. Solid State Chem.* **13** 330
Pezerat H 1979 *J. Chim. Phys. & Phys. Chim. Biol.* **73** 104
Scherer J R 1978 *Advances in infrared and Raman spectroscopy* (eds.) R J H Clark and R Hester. (London: Heydon & Son) Vol. 5, p. 149
Singh B, Gupta S P and Khanna B N 1980 *Pramana* **14** 509
Sreenivasan S 1979 *Analysis of the infrared internal vibrations of certain crystals* Ph.D., University of Kerala
Wienstock N, Schulze H and Müller A 1973 *J. Chem. Phys.* **59** 5063

Pramāṇa, Vol. 21, No. 5, November 1983, pp. 293–299. © Printed in India.

e^-–H(2S) elastic scattering in the two-potential eikonal approximation

C N CHANDRA PRABHA and H S DESAI
Physics Department, Faculty of Science, M S University of Baroda, Baroda 390 002, India

MS received 5 March 1983; revised 25 July 1983

Abstract. The differential scattering cross-sections for $e^- - H(2S)$ elastic scattering are calculated at intermediate energies by using the two-potential eikonal approximation. The results are compared with the recent theoretical data and the conventional Glauber cross-sections.

Keywords. Elastic scattering; electrons; hydrogen (2S state).

1. Introduction

The study of electron scattering from the excited states of atoms has important applications in various branches of physics, besides the intrinsic theoretical interest associated with it. Very little work has been reported on the electron scattering from the excited states of atoms as compared to the large amount of calculations involving the ground states. Motivated by the recent successful application of the two-potential eikonal approximation (Ishihara and Chen 1975) in various scattering phenomena (Tayal *et al* 1980), we have made a generalized application of the above approximation to study the electron scattering from any of the excited states of hydrogen atom. As a special case, we study the scattering from H(2S)—a fundamental process for which it is reasonable to expect that experimental data will become available in the near future.

The Glauber approximation is known to be in appreciable error at all angles when applied to the elastic electron-atom scattering at medium and lower energies. Ishihara and Chen (1975) have shown that this is mainly due to the inadequate semiclassical treatment of close-encounter collisions. The two-potential eikonal approximation provides an effective method to treat such collisions properly.

2. Theory

The basic idea underlying this approximation is to pull out an arbitrary potential V_1 from the interaction potential V such that the rest of the interaction potential *i.e.* $V_0 = V - V_1$ satisfies the semiclassical conditions. V_0 is treated in the Glauber approximation and the contribution of V_1 is calculated quantum-mechanically by

taking a few partial waves. For the scattering of an electron from a Z-electron atom, the interaction potential is given by

$$V(\bar{r}, \bar{r}_1, \ldots, \bar{r}_Z) = \frac{-Z}{r} + \sum_{j=1}^{Z} \frac{1}{|\mathbf{r} - \mathbf{r}_j|}, \tag{1}$$

where $\bar{r}, \bar{r}_1, \ldots, \bar{r}_Z$ are the incident and target electron co-ordinates. A short range central potential V_{st}, which is the static potential of the target atom, is chosen for V_1.

Now $$V_0(\bar{r}, \bar{r}_1, \ldots, \bar{r}_Z) = V(\bar{r}, \bar{r}_1, \ldots, \bar{r}_Z) - V_{st}(r). \tag{2}$$

In the two-potential eikonal approximation, the transition amplitude from the initial state $|i\rangle$ of the target to the final state $|f\rangle$ is given by (Ishihara and Chen 1975).

$$F_{fi}(\theta) = \frac{K_i}{2\pi i} \int \mathrm{d}^2 b \exp(iq \cdot b) [\Gamma_{fi}(\bar{b}) - 1]$$

$$+ \frac{1}{K_i} \sum_l (2l+1) P_l(\cos\theta) \exp(i\delta_l^{(1)}) \sin \delta_l^{(1)} \int \frac{\mathrm{d}\phi}{2\pi} \Gamma_{fi}(\bar{b_l}). \tag{3}$$

The notations are same as in Ishihara and Chen (1975).

Here, $$\Gamma_{fi}(b) = \langle f | \exp(i\chi) | i \rangle \tag{4}$$

where $$\chi = \chi_0 + \Delta\chi,$$

with $$\chi_0 = -\frac{1}{K_i} \int_{-\infty}^{\infty} \mathrm{d}Z\, V_0. \tag{5}$$

The correction $\Delta\chi$ to the Glauber phase function contributes very little for energies greater than 100 eV and hence can be neglected.

To make use of (3) to study the electron-scattering from any of the excited states (nlm) of hydrogen, it is necessary to have the V_{st} and χ_0 corresponding to those states. The general form of V_{st} for elastic scattering is given by

$$V_{st}^{nlm} = \int \mathrm{d}\, v_1\, \psi_{nlm}^*\, \psi_{nlm} (-1/r + 1/|\mathbf{r} - \mathbf{r}_1|), \tag{6}$$

where the standard form of the wavefunction is given by

$$\psi_{nlm} = 2/n^2 \{(n-l-1)!/[(n+l)!]^3\}^{1/2} (2r_1/n)^l \exp(-r_1/n)$$

$$L_{n-l-1}^{2l+1}(2r_1/n)\, Y_{lm}(\theta, \phi). \tag{7}$$

Using (6) and (7)

$$V_{st}^{nlm} = -\frac{1}{r} + \sum_{p=0}^{\infty} \sum_{m=0}^{n-l-1} \sum_{j=0}^{n-l-1} (-1)^{m+j} (4\pi/(2p+1))^{1/2}$$

$$\binom{n+l}{n-l-1-m} \binom{n+l}{n-l-1-j} \frac{(2/n)^{m+j+2l}}{m!\, j!} \times 4/n^4$$

$$(n-l-1)! \,/\, [(n+l)!] \times [(2l+1)^2 (2p+1)/4\pi]^{1/2}$$

$$\begin{pmatrix} l & p & l \\ o & o & o \end{pmatrix} \begin{pmatrix} l & p & l \\ m & o & m \end{pmatrix} \left\{ \frac{1}{r^{p+1}} \left[S_1! \,/\, (2/n)^{s_1+1} \right.\right.$$

$$\left. - \exp(-2r/n) \sum_{k=0}^{s_1} \frac{s_1!}{k!} \frac{r^k}{(2/n)^{s_1-k+1}} \right] + r^p \exp(-2r/n)$$

$$\left. \sum_{k=0}^{s_2} \frac{S_2!}{k!} \frac{r^k}{(2/n)^{s_2-k+1}} \right\}, \tag{8}$$

where $S_1 = p + 2 + m + j + 2l$ and

$S_2 = 1 + m + j + 2l - p$

$\begin{pmatrix} l & p & l \\ o & o & o \end{pmatrix}$ are the usual Wigner notations.

The general form of χ_0^{nlm}

is $$\chi_0^{nlm} = \frac{-1}{k_l} \int_{-\infty}^{\infty} V \, dz + \frac{1}{k_l} \int_{-\infty}^{\infty} V_{st}^{nlm} \, dz. \tag{9}$$

For all states of H, the interaction potential

$V(b, z, b_1, z_1) = -(1/r) + (1/|\mathbf{r} - \mathbf{r}_1|)$, so that

$$-\frac{1}{k_l} \int_{-\infty}^{\infty} V \, dz = \frac{2}{k_l} \ln \frac{|b - b_1|}{b}. \tag{10}$$

Now $\int_{-\infty}^{\infty} V_{st}^{nlm}\,dz$ may be calculated from (8) using standard integration techniques. Since this is a very lengthy expression, we take up the (ns) states.

$$\int_{-\infty}^{\infty} V_{st}^{ns}\,dz = \frac{8}{n^4}\,\frac{(n-1)!}{(n!)}\sum_{m=0}^{n-1}\sum_{j=0}^{n-1}(-1)^{m+j}$$

$$\binom{n}{n-1-m}\binom{n}{n-1-j}(2/n)^{m+j}\,\frac{1}{m!\,j!}\left\{\sum_{k=0}^{S_3}\right.$$

$$\frac{S_3!}{k!\,(2/n)^{S_3-k+1}}(-1)^{k+1}\left(\frac{\partial^{k+1}}{\partial\lambda^{k+1}}\right)K_0(b\lambda)$$

$$\left.-\sum_{k=0}^{S_3+1}\frac{(S_3+1)!}{k!\,(2/n)^{s_3+2-k}}(-1)^k\frac{\partial^k}{\partial\lambda^k}K_0(b\lambda)\right\}, \tag{11}$$

where $S_3 = m + j + 1$ and $\lambda = 2/n$. Using (10) and (11) we can find the general expression for χ_0^{ns} for any (ns) state.

As a special case, we find Ψ, V_{st} and χ_0 for $H\,(2S)$ from (7), (8) and (10)

$$\Psi_{2s} = \frac{1}{4\sqrt{2\pi}}(2 - r_1)\exp(-r_1/2) \tag{12}$$

$$V_{st} = -\left(\frac{1}{r} + \frac{3}{4} + \frac{r}{4} + \frac{r^2}{8}\right)e^{-r} \tag{13}$$

and
$$\chi_0 = +\frac{2}{k_i}\ln|b - b_1/b| - \frac{2}{k_i}\left[1 - \frac{3}{4}\frac{\partial}{\partial\lambda} + \frac{1}{4}\frac{\partial^2}{\partial\lambda^2} - \frac{1}{8}\frac{\partial^3}{\partial\lambda^3}\right]K_0(\lambda b), \tag{14}$$

where $\lambda = 1$.

$\Gamma(b)$ given by (4) may be easily evaluated now.

The summation of partial waves is done similar to the procedure adopted by Jhanwar *et al* (1978). The exact and Born phase shifts are calculated for the potential V_{st} and the l value is so chosen that beyond this l value, the phase shifts differ by less than 3%. The rest of the partial wave contribution is taken as described by Jhanwar *et al* (1978). Now the scattering amplitude and hence the DCS may be evaluated using (3).

3. Results and discussion

The e⁻–H (2S) elastic differential cross-sections are calculated at 200 eV and 400 eV when data are available for comparison (figures 1 and 2). The results are compared with eikonal-Born series (EBS), optical model (OM) and the Glauber (G) results along with the most recently reported two-potential results (Pundir *et al* 1982) and high energy higher order Born (HHOB) results (Rao and Desai 1983). In the absence of any experimental data at present, it is rather difficult to comment on the accuracy of the various approaches. In the study of electron-scattering from H, He and Li, two-potential eikonal approximation is in good agreement with the experimental data and the other sophisticated theories. The HHOB results are always overestimating, especially in the large angle region (Rao and Desai 1981, 1983). Glauber approximation is well-known for its shortcomings—appreciable under estimation of the cross-section except at small angles where it logarithmically diverges. The present results lie between the above two results and nearer the EBS results and are in good agreement with experiments in other scattering processes.

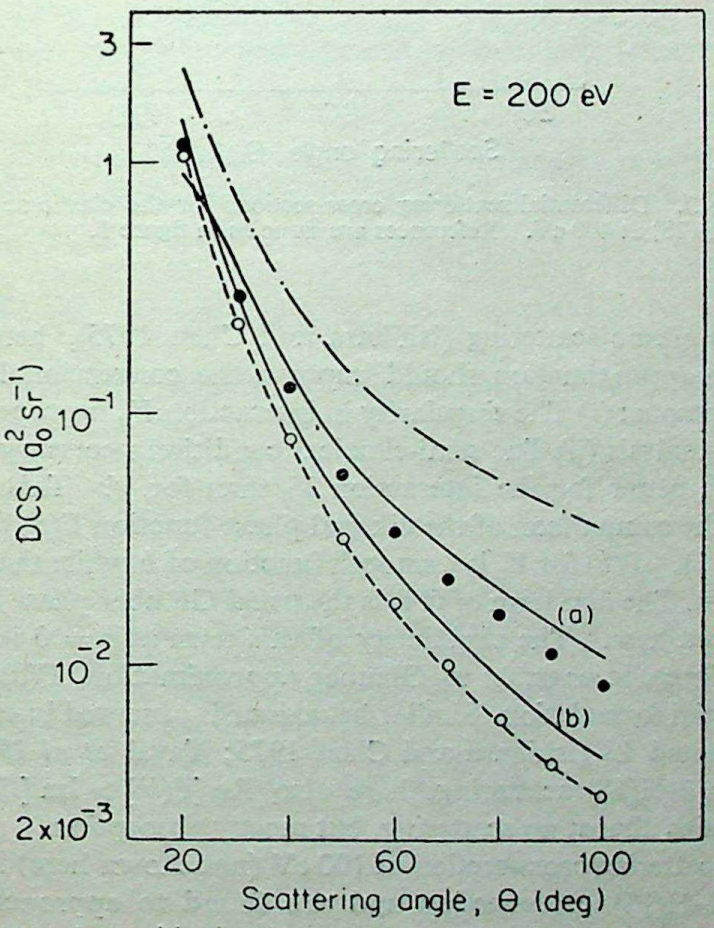

Figure 1. Differential scattering cross-sections for the elastic scattering of electrons from H(2S) at 200 eV.
Solid curve a.—present calculations, broken curve—present calculation in the Glauber approximation. Solid curve b—data of Pundir *et al* (1982). dash—dot curve HHOB results (Rao and Desai 1983). + — EBS results (Joachain *et al* 1977). . — OM results (Joachain and Winters 1980).

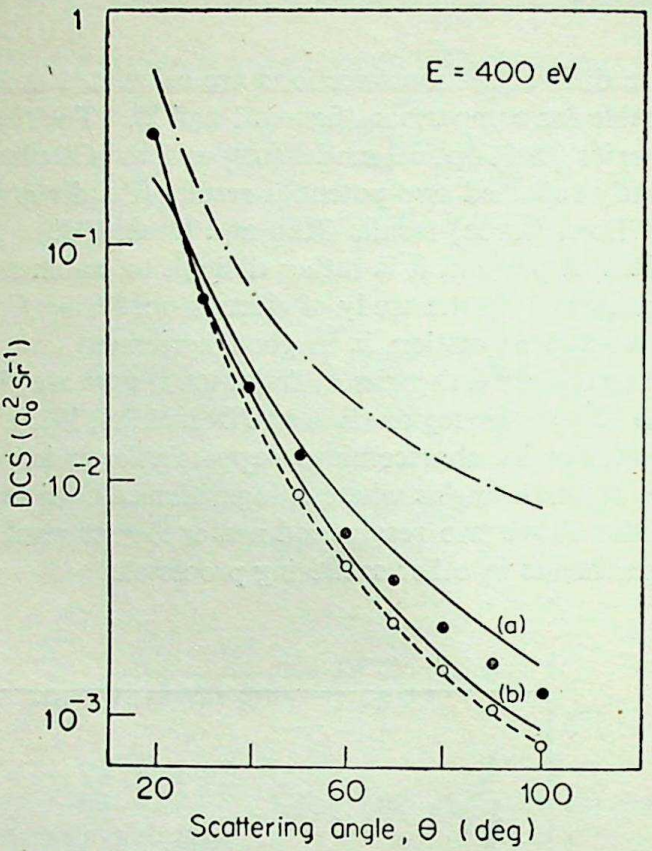

Figure 2. Differential scattering cross-sections for the elastic scattering of electrons from H(2S) at 400 eV. References are same as in figure 1.

As in $\bar{e}$–H(1S) elastic scattering (Ishihara and Chen 1975), here also the two-potential eikonal approximation should improve the conventional Glauber results because of two reasons: (*i*) The singularity in interaction V_{st} is properly taken care of by partial wave analysis (ii) The semi-classical condition necessary for the Glauber approximation is better for the interaction V_0 than for V. This aspect is clearly brought out by the comparison of the eikonal phase function $\Gamma(b)$ for the potentials V and V_0 (figure 3). $\Gamma(b)$ for V_0 is a smooth function of b while that for V oscillates for small b values. The first term of (14) is the usual Glauber phase for the scattering process considered here. The singularity of this term at $b = 0$ is cancelled by the second term. Hence, in contrast to Glauber approximation, $\Gamma(b)$ varies smoothly in the two-potential formulation. Similar behaviour is observed in electron scattering from H(1S), He and Li (Ishihara and Chen 1975; Tayal *et al* 1980). It may be noted that as in $\bar{e}$–H(1S) scattering, here also Re $[\Gamma(b)] \gg$ Im $[\Gamma(b)]$ everywhere. Hence $\Gamma(b)$ contains almost no scattering, but mostly absorption.

The $\bar{e}$–H(2S) scattering cross-section at 100 eV (not shown here) is compared with corresponding $\bar{e}$–H(1S) cross-section and are found to approach each other for larger angles where the interaction between the incident electron and the target nucleus progressively dominates the scattering. Similar type of behaviour was observed in the EBS (Joachain *et al* 1977) and two-potential (Pundir *et al* 1982) calculations. The present approximation is good for lower energies also whereas others like HHOB are good for $E > 200$ eV only. In view of the simplicity of the

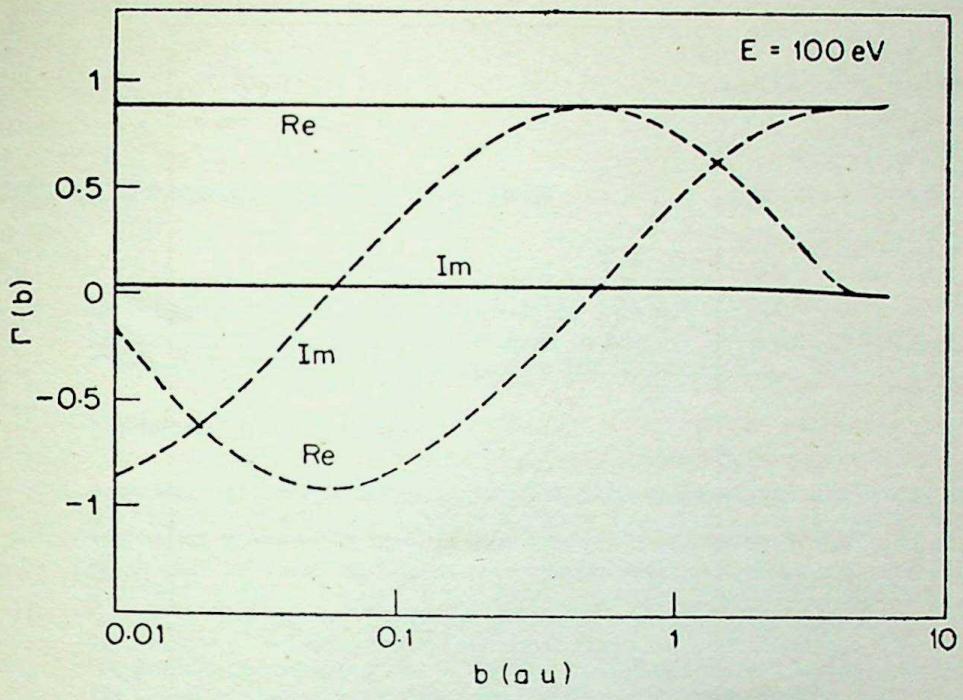

Figure 3. Real and imaginary parts of $\Gamma(b)$ for the potential V_0 (solid curve) and for the total interaction V (dashed curve) for elastic $\bar{e}$–H(2S) scattering at 100 eV.

present approach, we expect that it would provide reasonable description of the scattering process from the excited metastable states of hydrogen atom.

Acknowledgement

One of the authors (CNCP) is thankful to the NCERT for the science talent scholarship.

References

Ishihara T and Chen J C Y 1975 *Phys. Rev.* **A12** 370
Jhanwar B L, Khare S P and Kumar A 1978 *J. Phys.* **B11** 887
Joachain C J, Winters K H, Cartiaux L and Mendez-Moreno R M 1977 *J. Phys.* **B10** 1277
Joachain C J and Winters K H 1980 *J. Phys.* **B13** 1451
Pundir R S, Sharma R K and Mathur K C 1982 *Phys. Lett.* **A91** 15
Rao N S and Desai H S 1981 *Pramana* **17** 309
Rao N S and Desai H S 1983 *J. Phys.* **B**
Tayal S S, Tripathi A N and Srivastava M K 1980 *Phys. Rev.* **A22** 782

Pramāṇa, Vol. 21, No. 5, November 1983, pp. 301–309. © Printed in India.

Theory of divalent ions in crystals

G RAGHURAMA and RAMESH NARAYAN*
Department of Physics, Indian Institute of Science, Bangalore 560 012, India
*Raman Research Institute, Bangalore 560 080, India

MS received 26 July 1983

Abstract. The divalent ions in alkaline earth chalcogenides are viewed as compressible objects and are treated within a purely ionic model. As in earlier studies on the alkali and ammonium halides, the ions are taken to be in the form of space-filling polyhedral cells and the compression energy, which is the source of repulsion, is written as a surface integral over the cell faces. A simple method of computing the repulsion energy in any crystal lattice of arbitrary symmetry is proposed and the repulsion parameters B and σ are refined for the divalent ions under study. The theory explains the predominant occurrence of the NaCl structure in the alkaline earth chalcogenides. Hard sphere radii are estimated for the tetravalent cations Ti^{4+}, Sn^{4+} and Pb^{4+} using the repulsion parameters of O^{2-} ion and the data on the corresponding rutile structure oxides. These radii are seen to be consistent with the measured interionic distances in several compounds occurring in the perovskite structure. The free transfer of repulsion parameters among several structures, which is a key feature of the present approach to repulsion, is confirmed to be valid by the present study.

Keywords. Divalent ions; compressible ion theory; repulsion parameters; hard sphere radii.

1. Introduction

In a series of papers, Narayan and Ramaseshan (1976, 1978, 1979a, b) developed a compressible ion model of repulsion in ionic crystals. The theory treats compressibility as an ionic property and associates the repulsion energy between two ions with the compression energies of the individual ions. An early version (Narayan and Ramaseshan 1976, 1978), where the compression energy per bond was represented by a simple exponential function of the ionic radius, was later modified (Narayan and Ramaseshan 1979a, b) to empirically include many-body interactions. In this latter approach the ions are viewed as polyhedral, space-filling cells with the repulsion arising from the increased compression at the cell faces. This theory explained for the first time the structures of all the alkali halides and has, more recently, worked well in the ammonium halides (Raghurama and Narayan 1983b).

In view of its successes, it appeared worthwhile to extend the theory to other ions and crystals. In the present paper we study the alkaline earth chalcogenides, which are generally considered to be amenable to an ionic theory. At room temperature and pressure these compounds crystallize in the NaCl-type structure, except MgTe which occurs in the wurtzite structure. With a view to later extending the theory to more complicated structures, it was felt that a simpler formulation of the compressible polyhedral cell theory would be welcome. Section 2 presents such a formulation which is then used in § 3 to derive the repulsion parameters, B and σ, for the

divalent ions. A study of the structural stability of alkaline earth chalcogenides is carried out in § 4, where the theory is found to correctly predict the predominant occurrence of the NaCl structure. In § 5, the theory is extended to the noncubic rutile structure and hard sphere radii for tetravalent ions are derived. The radius of Ti^{4+} ion is found to be consistent with the experimental electron density map. Also, the radii of Ti^{4+} and Sn^{4+} fit the lattice spacings of several perovskite type crystals.

2. Simplified area theory

In the compressible ion model (Narayan and Ramaseshan 1979 a, b) a radius is associated with an ion in the direction of each of its nearest and next nearest neighbours. The ion is then pictured to be in the form of a polyhedron whose faces are perpendicular to the interionic bonds at distances from the ion centre equal to the corresponding radii. For each bond the sum of the radii of the ions is taken to be equal to the bond length and so the whole crystal is made up of space-filling polyhedra. The compression energy at the face i of an ion of polyhedral shape is assumed to be of the form

$$W_{\text{rep}} = \frac{B}{2\pi} \int \int \exp\left(- r'(s)/\sigma\right) \mathrm{d}s, \tag{1}$$

where $r'(s)$ is the distance from the centre of the cell to an area element $\mathrm{d}s$ on the face and the integral is over the face area. B and σ are the repulsion parameters for the ion under consideration. The cell face can be approximated to a circle of equal area (Narayan and Ramaseshan 1979b) and we can then write the compression energy of the ith face as

$$W_{\text{rep},\,i} = B\sigma\left[(r_i + \sigma)\exp\left(- r_i/\sigma\right) - (l_i + \sigma)\exp\left(- l_i/\sigma\right)\right], \tag{2}$$

where r_i is the distance to the ith face from the ion centre (referred to as the ' radius ' of the ion) and l_i is the distance to the circumference of the corresponding circular cell face. The l_i's depend on the interionic distance r as well as the crystal structure. Detailed formulae are given by Narayan and Ramaseshan (1979b) for the NaCl, CsCl and ZnS structures. However, the labour involved in deriving exact formulae for the different l_i can become quite excessive when one deals with other lower symmetry structures and this would defeat the very purpose of the present approach which seeks to develop a simple semi-empirical theory of repulsion. We present here an alternative simplified approach, where l_i is computed in terms of only the co-ordination number and ionic radii.

If there are n faces symmetrically disposed at equal distances from the ion centre, the solid angle subtended by each face at the centre is $\phi = 4\pi/n$. If the n faces are at different distances r_i from the centre, we may define a weighted average distance r_{av} as

$$r_{\text{av}} = \frac{1}{n}\sum_i r_i. \tag{3}$$

If $r_i < r_{av}$, the solid angle subtended by such a face will be greater than $4\pi/n$ while the reverse will be true when $r_i > r_{av}$. Motivated by this we approximately write

$$\phi_i = 4\pi \{1/n + K/2\ [1 - (r_i/r_{av})]\}, \tag{4}$$

where we have written ϕ_i in a form which ensures that $\sum_i \phi_i = 4\pi$. K is a suitable constant which has to be determined. It can be easily shown that (4) leads to the following relation for l_i

$$l_i = \frac{r_i}{1 - 2/n + K(r_i/r_{av} - 1)}. \tag{5}$$

The constant K has been estimated to be 0·85 by a least squares fit to the known exact values of the l_i's (Narayan and Ramaseshan 1979b) in the NaCl, CsCl and ZnS structures.

The main advantage of relation (5) is that the only inputs required for the calculation of l_i are the number of nearest and next nearest neighbours and the corresponding radii. This formula, when applied to the alkali halides, reproduces the interionic distances and compressibilities with RMS deviations of only 0·23% and 0·47% respectively from the exact results of Narayan and Ramaseshan (1979b).

3. Repulsion parameters for divalent ions

Using the experimental data on the lattice spacings and compressibilities of the alkaline earth chalcogenides as a function of pressure, we have refined the parameters B and σ for all the constituent ions.

The free energy per molecule of the crystal is given by

$$W_L = -\frac{Ae^2}{r} - \frac{C}{r^6} - \frac{D}{r^8} + W_{rep} + PV, \tag{6}$$

where r is the nearest neighbour distance, P the pressure and V the volume per molecule. The Madelung constant A is known for the structures of interest (Tosi 1964). The van der Waal's coefficients C and D can be calculated (Narayan and Ramaseshan 1978) in terms of the polarisabilities of the ions and the effective number of participating electrons (Kim and Gordon 1974). However, we have recently shown (Raghurama and Narayan 1983a) that the polarisabilities of the chalcogen ions cannot be considered to be constants but must be taken to vary in the form

$$\alpha_{anion} = \alpha_0\ (r/3)^n, \tag{7}$$

where the n value is 0·9. The effect is quite considerable and has to be taken into account.

In our calculations on the alkaline earth chalcogenides, the repulsion energy was computed using the simplified formulae (5). The actual procedure of optimising

the repulsion parameters B and σ is explained elsewhere (Narayan and Ramaseshan 1976, 1979b). In table 1 we give the refined parameters of the divalent ions. During the refinement, we included data on Pb, Sm, Eu and Yb chalcogenides and the parameters of these ions are also given. The RMS error between the calculated and observed interionic distances r in all the crystals included in the refinement is 0·76% while for $d^2 W_L/dr^2$ it is $\sim 17\%$. The comparatively large error in the second differential (which is essentially proportional to the bulk modulus) could perhaps imply that our purely ionic model of these crystals is an over simplification.

Using the repulsive parameters of the chalcogen ions, we can determine repulsion parameters for other divalent cations. However, considering the low compressibility of cations compared to anions, we can assume the cations to be hard spheres to a first approximation. Then we have only one parameter per ion, the hard sphere radius, which can be fitted to reproduce the experimental interionic distances of the corresponding chalcogenides. The results for Fe^{2+}, CO^{2+}, Ni^{2+}, Mn^{2+} and Cd^{2+} are given in table 2.

4. Structural stability studies

The compressible ion theory has been shown to satisfactorily explain the structures of the alkali and ammonium halides as well as the pressure and thermal transitions

Table 1. Repulsion parameters of divalent ions.

Ion	B (ergs/cm^2)	σ (Å)
Mg^{2+}	$9{\cdot}832 \times 10^{10}$	0·0750
Ca^{2+}	$6{\cdot}827 \times 10^{11}$	0·0784
Sr^{2+}	$2{\cdot}271 \times 10^{11}$	0·0900
Ba^{2+}	$9{\cdot}110 \times 10^{10}$	0·1050
Pb^{2+}	$5{\cdot}176 \times 10^{10}$	0·1060
Sm^{2+}	$5{\cdot}985 \times 10^{12}$	0·0769
Eu^{2+}	$1{\cdot}432 \times 10^{14}$	0·0662
Yb^{2+}	$3{\cdot}840 \times 10^{15}$	0·0556
O^{2-}	$9{\cdot}672 \times 10^{6}$	0·2179
S^{2-}	$9{\cdot}445 \times 10^{6}$	0·2646
Se^{2-}	$7{\cdot}959 \times 10^{6}$	0·2867
Te^{2-}	$9{\cdot}865 \times 10^{6}$	0·2933

Table 2. Hard sphere radii of some divalent ions.

Ion	Hard sphere radius (Å)
Cd^{2+}	1·297
Mn^{2+}	1·127
Fe^{2+}	1·075
Co^{2+}	1·064
Ni^{2+}	1·033

in these crystals, (Narayan and Ramaseshan 1979a, b; Raghurama and Narayan 1983b). We have carried out a similar study on the alkaline earth chalcogenides.

Experimentally, the most stable structure here happens to be the NaCl type, except for MgTe which exhibits a wurtzite type structure. The calculated free energies at 0°K of the various dichalcogenides were compared with the NaCl, CsCl and ZnS structures. The results showed that all the chalcogenides prefer the NaCl structure —even MgTe is predicted to occur in this phase. Thus, while the theory correctly identifies the NaCl structure as being the most likely, it appears to overestimate the stability of this phase. We note that the energy differences between the three structures is only about 1% of the total lattice energy. Apart from the Coulomb interaction, the other contributions to the free energy have been calculated through empirical models which could be in error. For instance, an error in the evaluation of the van der Waal's interaction cannot be ruled out. Also, we have completely neglected any possible covalency. At this stage, it is difficult to identify the precise source of the trouble.

5. Extension to rutile structure

One of the attractive features of the compressible ion theory is that the repulsion parameters are structure-independent and depend only on the ions concerned. Once the parameters B and σ of an ion have been determined from any set of experimental data the same parameters can be used for that ion in any other crystal in which it occurs. Thus, having obtained the parameters of the O^{2-} ion, we are now in a position to use them in other oxides. An interesting class of crystals are dioxides in the rutile structure. Calculations with these crystals would be an ideal opportunity to test the theory in a non-cubic structure.

Rutile has a tetragonal lattice with two molecules per cell (Wyckoff 1963). The atomic positions are (see figure 1)

$$\begin{aligned} Ti^{4+}: &\quad (0, 0, 0) \\ &\quad (0{\cdot}5, 0{\cdot}5, 0{\cdot}5) \\ O^{2-}: &\quad \pm (x, x, o) \\ &\quad \pm(0{\cdot}5 + x, \quad 0{\cdot}5 - x, \quad 0{\cdot}5) \end{aligned} \tag{8}$$

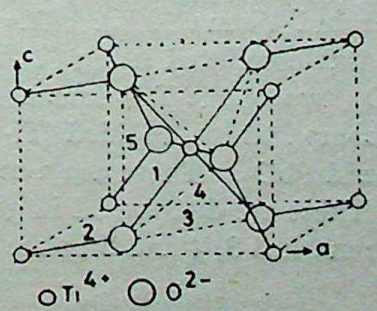

Figure 1. The unit cell of the tetragonal crystal rutile. The numbers refer to the bond types referred to in the text.

The x value is $\sim 0{\cdot}305$ in the oxides of interest to us. Each cation is held in a distorted oxygen octahedron, two oxygens being at a slightly different distance compared to the other four. The anion sites are non-centrosymmetric and thus the electric fields at these locations are non-zero. This leads to induced dipoles on the oxygen ions and thereby an additional polarisation energy. Though this contribution is not very significant (Bertaut 1978), for completeness we have included it in the free energy. Hence, we have per molecule

$$W_L(r) = -\frac{Ae^2}{r} - \frac{C}{r^6} - \frac{D}{r^8} + 2\,[W_{\text{rep}} - \tfrac{1}{2}\,\alpha\,E^2], \tag{9}$$

where the first term is the Coulomb attraction which we have calculated by the method of non-overlapping charges (Bertaut 1978), the second and third terms represent the van der Waal's attraction, and W_{rep} is the compression energy per anion. We take the cation to be a hard sphere and hence there is no corresponding contribution to W_{rep}. The last term in (9) represents the polarisation energy, where α is the anion polarisability [see equation (7)] and E is the magnitude of the electric field at the oxygen site. The factor of 2 accounts for two anions per molecule. The magnitude of the electric field at the anion site can be written as

$$E = S_E\, e/r^2,$$

where S_E is a lattice sum which we have evaluated using the method of Bertaut (1978). To make the treatment simple, the position parameter x in (8) is fixed at $0{\cdot}305$ and the c/a ratios in the various crystals are taken to be the experimentally observed values. The coefficients C and D are given in terms of the appropriate lattices sums S_{ij} and T_{ij} as

$$C = c_{+-}\,S_{+-} + c_{++}\,S_{++} + c_{--}\,S_{--},$$

$$D = d_{+-}\,T_{+-} + d_{++}\,T_{++} + d_{--}\,T_{--}, \tag{10}$$

where c_{ij} and d_{ij} are ion-dependent coefficients. The lattice sums of interest could not be found in the literature and were computed by summing in direct space (table 3).

We have studied three oxides *viz* TiO_2, PbO_2 and SnO_2. The polarisabilities of the cations Ti^{4+}, Pb^{4+} and Sn^{4+} were taken to be $0{\cdot}185$, $1{\cdot}12$ and $3{\cdot}4$ Å^3 respectively (Tessman *et al* 1953; Shanker and Verma 1976). The repulsion energy associated with the anion compression was computed using (2) and (5). Each anion has 3 surrounding cations. In TiO_2, two of the Ti^{4+} ions are at a shorter distance (Ti-O bonds marked 1 in figure 1) compared to the third (Ti-O bond, 2 in figure 1). The situation is reversed in SnO_2 and PbO_2. There are a total of 11 next nearest neighbours around each O^{2-} ion. These are distributed in groups of 1, 8 and 2 ions (the corresponding O-O bonds are marked 3, 4 and 5 in the figure). Thus the compression energy of each anion is

$$W_{\text{rep}} = 2W_{-+}^{(1)} + W_{-+}^{(2)} + W_{--}^{(3)} + 8\,W_{--}^{(4)} + 2\,W_{--}^{(5)}, \tag{11}$$

Table 3. Calculations on oxides in the rutile structure.

	TiO_2	SnO_2	PbO_2
Input Data			
a (Å)	4·593	4·737	4·946
c (Å)	2·959	3·186	3·379
r (Å)	1·948	2·060	2·171
A	19·099	19·129	19·025
S_E	0·736	0·428	0·320
S_{+-}	6·318	6·657	6·788
S_{++}	0·230	0·238	0·241
S_{--}	1·655	1·780	1·828
T_{+-}	5·861	6·272	6·435
T_{++}	0·072	0·073	0·073
T_{--}	0·725	0·804	0·835
Results			
Cation radius r_+ (Å)	1·196	1·340	1·348
$d^2 W_L/dr^2$ (10^6 erg/cm^2)			
Calculated	2·350	2·213	2·072
Experimental	2·18	...	...

where the superscripts describe which type of contact is involved (figure 1 gives the code). Each term in (11) can be written in terms of B_- and σ_- using (2) and (5). The total free energy (9) is minimised with respect to the shortest interionic distance r. The equilibrium condition at temperature T is given by (Hildebrand 1931),

$$\frac{dW_L(r)}{dr} = \frac{3V}{r}(T\beta/K), \tag{12}$$

where β is the coefficient of thermal expansion and K is the compressibility. The experimental values of β and K were taken from Krishna Rao (1973), Ming and Manghnani (1979) and Hazen and Finger (1981).

The radius of the tetravalent cation was optimised in each of the three dioxides studied so as to fit the experimentally observed interionic distance. The input data are given in table 4 along with the results. The calculated radii are much larger than the standard values. For example, we obtain a radius of 1·2 Å for Ti^{4+} ion which is almost double the value (0.76 Å) quoted by Shannon (1976). From the available electron density map of TiO_2 (Baur 1956), we deduce the 'experimental' radius of Ti^{4+} to be $\sim$ 1·15 Å. We consider this a strong experimental confirmation of our calculated radii. Moreover, our predicted compressibility of TiO_2 is within 8% of the measured value, again establishing the validity of our theory.

Another way to check the tetravalent cation radii is to predict the interionic distances in other structures where these ions may occur; *e.g.* the perovskite family. The results in table 4 show that the RMS error in the predicted cell dimensions in a

Table 4. Predictions on crystals in the perovskite structure.

Crystal	Cubic cell parameter (Å)			$d^2 W_L/dr^2$ (10^5 ergs/cm^2)		
	Calculated	Experimental	% error	Calculated	Experimental	% error
$BaTiO_3$*	4·049	4·012	0·92	7·63	5·99	27·4
$CaTiO_3$	3·908	3·840	1·77	7·69	...	...
$SrTiO_3$	3·958	3·904	1·38	7·75	6·34	22·0
$BaSnO_3$	4·155	4·117	0·92	6·99	...	...
$SrSnO_3$	4·089	4·033	1·39	6·81	...	...

*at $T = 474$ K; other data are at 300 K.

number of ABO_3 perovskites is only $\sim 1{\cdot}3\%$. This again confirms that the radii of the tetravalent ions as well as the B, σ values of the divalent ions are reliable and meaningful parameters describing the properties of these ions quite adequately. The bulk modulus agrees to within $\sim 25\%$ in $BaTiO_3$ and $SrTiO_3$, for which values could be traced (Huibregtse *et al* 1959; Okai and Yoshimoto 1975). This must be considered satisfactory in view of the long chain of calculations from the alkaline earth chalcogenides to rutile to the perovskites.

6. Conclusion

The compressible ion theory of repulsion has been applied to the alkaline earth chalcogenides using a simplified formulation of the polyhedral cell approach. The theory correctly shows that most of the crystals should occur in the NaCl structure. The repulsion parameters of the chalcogen ions have been used to derive hard sphere radii for a few divalent ions. Also, the theory has been extended to the rutile and perovskite structures where the interionic distances and compressibilities are satisfactorily predicted. These results indicate that the theory, which is based on a purely ionic picture, is quite valid for divalent ions in crystals. However, there is a mild discrepancy in the matter of the relative stability of different crystal structures. The present approach appears to overestimate the stability of the NaCl structure and underestimate the binding energies of the competing ZnO (or ZnS) and CsCl structures. The presence of covalency might possibly explain the discrepancy.

Acknowledgement

The authors thank Prof. S Ramaseshan for many discussions and for pointing out that a simplified formulation of the compressible polyhedral cell theory is a crucial prerequisite for future calculations on more complicated structures.

References

Baur W H 1956 *Acta Crystallogr.* **9** 515
Bertaut E F 1978 *J. Phys.* **39** 1331
Hazen R M and Finger L W 1981 *J. Phys. Chem. Solids.* **42** 143

Hildebrand J H 1931 *Z. Phys.* **67** 127
Huibregtse E J, Bessey W H and Drougard M E 1959 *J. Appl. Phys.* **30** 899
Kim Y S and Gordon R G 1974 *J. Chem. Phys.* **61** 1
Krishna Rao K V 1973 *AIP-Conf. Proc.* (*USA*) **17** 219
Ming L C and Manghnani M H 1979 *J. Geophys. Res.* **84** 4775
Narayan R and Ramaseshan S 1976 *J. Phys. Chem. Solids* **37** 395
Narayan R and Ramaseshan S 1978 *J. Phys. Chem. Solids* **39** 1287
Narayan R and Ramaseshan S 1979a *Phys. Rev. Lett.* **42** 992
Narayan R and Ramaseshan S 1979b *Pramana* **13** 581
Okai B and Yoshimoto J 1975 *J. Phys. Soc. Jpn.* **39** 162
Raghurama G and Narayan R 1983a *Curr. Sci.* **52** 210
Raghurama G and Narayan R 1983b *J. Phys. Chem. Solids* **44** 633
Shanker J and Verma M P 1976 *J. Phys. Chem. Solids* **37** 639
Shannon R D 1976 *Acta Crystallogr.* **A32** 751
Tessman J R, Kahn A H and Shockley W 1953 *Phys. Rev.* **92** 890
Tosi M P 1964 in *Solid state physics* (eds.) F Seitz and D Turnbull (New York: Academic Press) **16** 1
Wyckoff R W G 1963 *Crystal structures* (New York: Interscience) Vol. 1.

Pramāṇa, Vol. 21, No. 5, November 1983, pp. 311–322. © Printed in India.

Effect of minute's-scale aging on refractive index of chopped and non-chopped optical films

R K PURI, K VIJAYA and R N KAREKAR
Department of Physics, University of Poona, Poona 411 007, India

MS received 20 July 1983; revised 28 September 1983

Abstract. The refractive indices of non-chopped and chopped films of cryolite, MgF_2 and mixed cryolite-MgF_2, which is higher than the bulk value, measured using spectrophotometer, ellipsometer and Abelès method are observed to be higher than corresponding bulk values. Chopped films show a higher refractive index than non-chopped films. The electron diffraction study shows a more amorphous structure for the chopped films. The major part played by chop-time seems to be in increasing the initial minute's-scale aging rather than settling of ad-atoms during chop-time. The observed dispersion curve shows that some unknown material other than water gives an important aging effect.

Keywords. Non-chopped optical films; chopped optical films; refractive index; aging.

1. Introduction

Several workers have found the refractive index (Shklyarevskii *et al* 1972; Kinosita and Nishibori 1969; Heavens 1960) and studied the aging (Ogura *et al* 1975; Koch 1965; Ritter *et al* 1969; Koppelmann *et al* 1961) of optical films and there exists a large variation in the values obtained by them. The technique of chopping the vapour flow during deposition is seen to help in day-scale aging reduction (Vijaya *et al* 1980) as seen from ellipsometer Δ, ψ changes and spectrophotometer transmission coefficient (T) changes.

In this paper we report the refractive index values of both non-chopped and chopped films of cryolite, MgF_2 and mixed cryolite-MgF_2 as measured by spectrophotometer, ellipsometer and Abelès method. The knowledge about the refractive index, rather than Δ, ψ, T, of non-chopped and chopped films will be of great importance in the basic understanding of the aging phenomenon in these films.

2. Experimental details

The films both non-chopped and chopped cryolite, MgF_2 and mixed cryolite-MgF_2 were prepared by vacuum evaporation, using the method reported earlier with alternate chopping (Vijaya *et al* 1980), at a rate of 5 Hz using a circular chopper with a V-shaped cutout (of angle 155°). This gave thickness of about 2 Å during each cycle ensuring sufficient homogeneity in the film for ellipsometric and spectrophotometric measurements. For the mixed co-deposited film study, the two single films (cryolite,

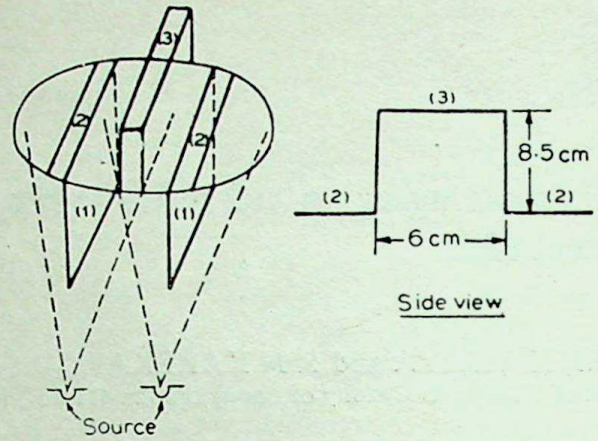

Figure 1. Schematic diagram of the shadowing arrangement for deposition of single and mixed films. (1) Projection for shadowing, (2) Side slots, (3) Central slot.

MgF_2) were deposited at one height and the mixed cryolite-MgF_2 film at a higher level so that the three films were simultaneously obtained and of roughly the same thickness (figure 1). The two sources were kept 22 cm from the substrate holder and were 4 cm apart, suitably shielded from each other. The position of the substrate holder was adjusted such that from the central slot both the filaments could be seen and from the side slots only one filament was seen.

The films were deposited on Belgian glass substrates of suitable size at room temperature. Unground glass was used for spectrophotometric measurements (Type VSU-2P) in the spectral range 4000–6500 Å, whereas glass with one side ground was used for ellipsometer (at 6328 Å) and Abelès method (at 5893 Å) measurements. The transmission data and Δ, ψ ellipsometric data were converted to refractive index using value fitting method by proper computer programs. The films studied were in the thickness range 300–1400 Å in general. The thickness was measured using the Fizeau fringe method and ellipsometer. All the measurements were carried out after removing the film from the vacuum chamber. The error in measurement of refractive index for the spectrophotometer is about $\pm$ 0·1 as compared to $\pm$ 0·002 for the ellipsometer and $\pm$ 0·0001 for Abelès method.

3. Results and discussion

The wavelength dependence of the average (of about 100 films each) initial refractive indices of non-chopped and chopped films, obtained spectrophotometrically, is given in figure 2. Figure 3 gives the average (average of about 140 films each) experimental values of refractive indices and thickness as measured by ellipsometer along with the values of refractive index as obtained by Abelès method. It is evident from these figures that, in general, the values obtained by all the three methods are in sufficiently good agreement with each other for both non-chopped and chopped films. For comparison these data are given in figure 4 along with data obtained by other workers. There are of course many other spot readings (at certain λ) available. It is observed in general that there is a spread in the reported values of refractive index

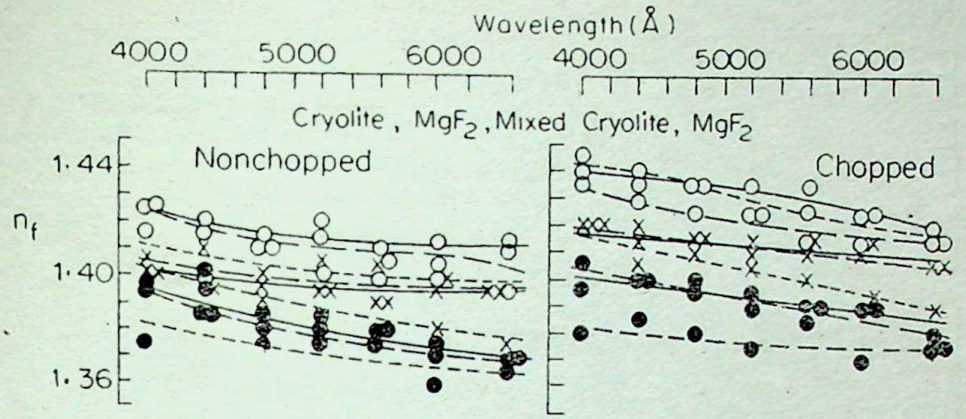

Figure 2. Wavelength dependance of the average, initial refractive index. ● cryolite, ○ MgF_2, × Mixed cryolite-MgF_2, Thickness: —— ~ 700 Å, — — ~ 900 Å, - - - - ~ 1100 Å Temperature of substrate: Room temperature (27°C).

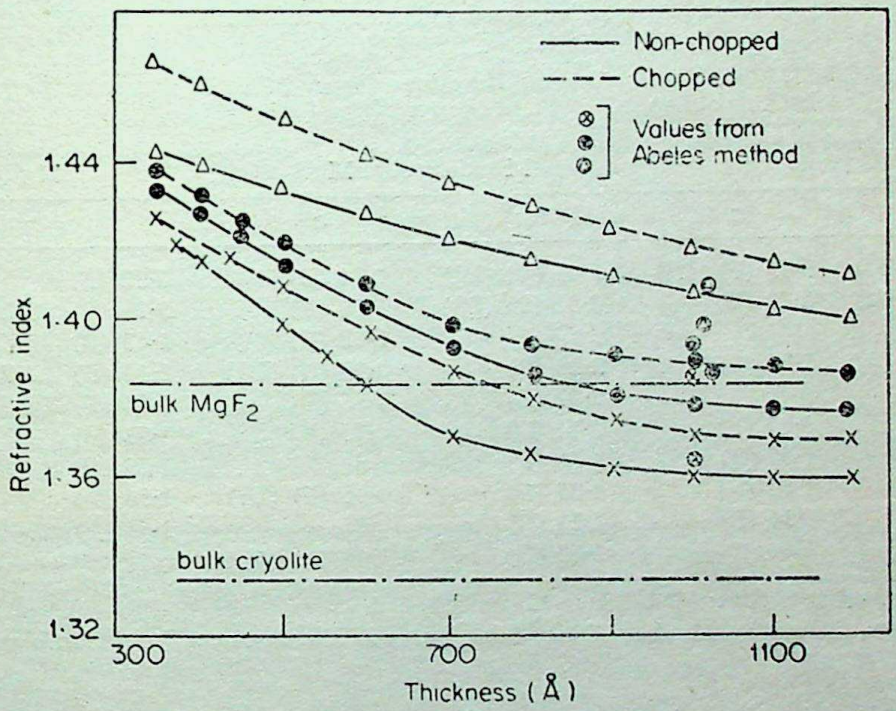

Figure 3. Average initial refractive index versus thickness as measured by ellipsometer at $\lambda = 6328$ Å, × cryolite, Δ MgF_2, ● mixed cryolite-MgF_2. Temperature of substrate: Room temperature (27°C).

(a) from 1·40 to 1·31 for cryolite, (b) 1·41 to 1·34 for MgF_2 at λ of about 6000 Å. Our values lie in the same range.

3.1 *Electron diffraction studies*

The electron diffraction studies (figure 5) show full Debye rings for cryolite, MgF_2 and mixed cryolite-MgF_2 films indicating the polycrystalline nature of the films. It is seen that the rings of non-chopped films are sharper than chopped films. The measured interplanar distance (d_0)-values of non-chopped and chopped films are given in table 1. These were compared with ASTM data for bulk cryolite and MgF_2. All

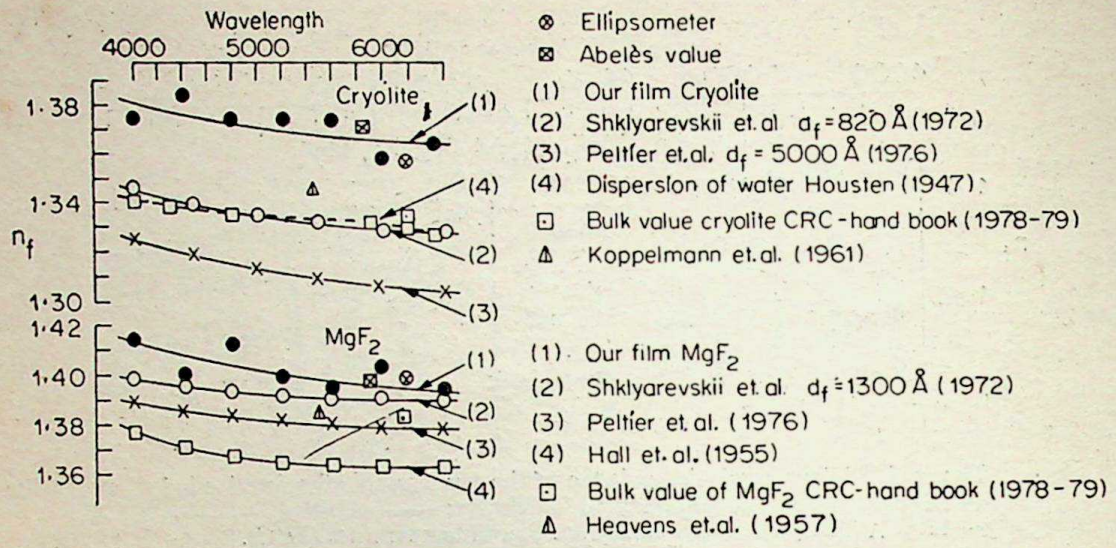

Figure 4. Comparison of reported and our refractive index values.

Table 1. Interplanar distance d_0 values for cryolite, MgF_2, mixed cryolite-MgF_2 films both non-chopped (NC) and chopped (C).

Cryolite		Mixed cryolite-MgF_2		MgF_2	
NC	C	NC	C	NC	C
4·29 (F) (UI)	3·83 (F) (UI)	3·45 (B) (UI)	1·34 (B)	3·32 (F)	...
3·66 (F) (UI)	2·70 (B)	2·52 (B) (UI)	1·14 (F)	3·29 (B)	2·21 (B)
2·74 (B)			1·02 (F)	2·42 (B)	1·82 (F) (UI)
2·28 (F)	2·26 (B)	2·28 (B)	0·93 (B) (UI)	2·10 (F)	1·75 (B)
		2·07 (F)	0·86 (B)	1·84 (F)	1·49 (F)
1·94 (B)	1·87 (F)	1·74 (B)	0·75 (B)	1·73 (B)	1·18 (F)
1·72 (F)	1·68 (F)	1·50 (F)		1·69 (F)	0·99 (F)
1·56 (B)	1·50 (F)	1·35 (F)	0·66 (F) (UI)	1·54 (F)	
1·22 (F)	1·34 (F)	1·23 (F)		1·43 (F)	
		1·13 (F)			

Error ± 0·04 Å; F-faint; B-bright; UI-unidentified.
Besides these, there are a number of very faint lines which are not easily measurable by optical methods.

the bright rings (both chopped and non-chopped) match with the corresponding bulk values indicating that the stoichiometry of the films is being maintained. The table also shows that the mixed cryolite MgF_2 film contains both cryolite and MgF_2 as would be expected. The single and mixed films were deposited in the same cycle. The rings are greater in number in mixed films as compared to single material films. In both single and mixed films there are some very faint lines which are not measurable as well as some lines which are not identifiable with the bulk data (denoted as UI in table 1).

An interesting feature observed in the diffraction pattern is that the d_0-values of non-chopped and chopped films are more often not the same although the film materials deposited are the same. This is shown more drastically in the chopped mixed film where none of the chopped mixed film rings coincide with either chopped or non-chopped single films.

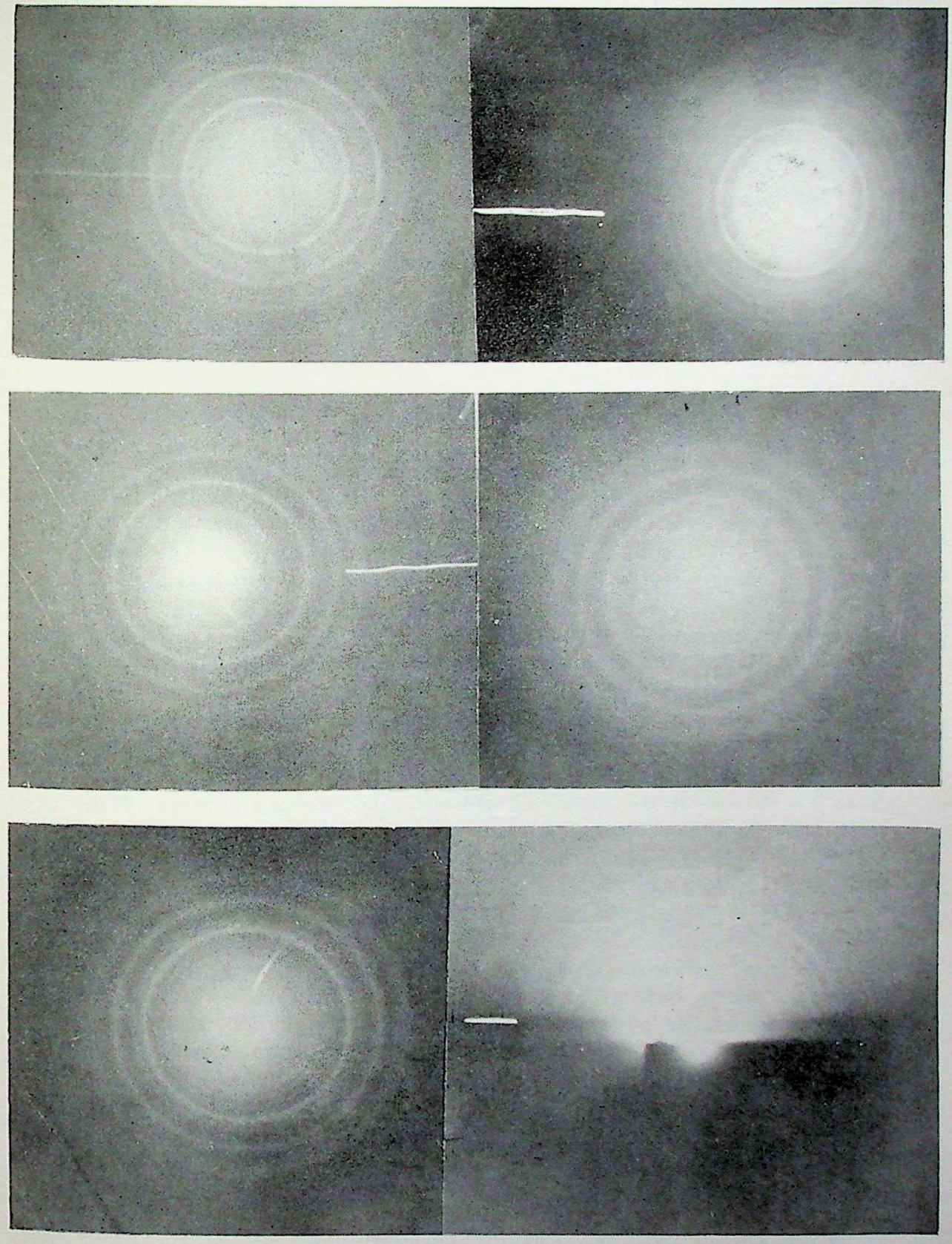

Figure 5. Electron diffraction pattern. a1, b1, c1 Non-chopped cryolite, MgF_2 and mixed cryolite-MgF_2 respectively. a2, b2, c2 chopped cryolite, MgF_2 and mixed cryolite-MgF_2 respectively.

The fact that the diffraction rings of non-chopped films are sharper than those of chopped films suggest a more amorphous (*i.e.* less polycrystalline) film growth for chopped films. But the absence of some of the rings in chopped films as compared to non-chopped films might indicate some reorientation of crystallite due to chopping, whereby the diffraction intensity is reduced, sometimes even to the extent that they are not visible. This effect is seen to be highly predominant in mixed chopped films.

3.2 *Single material films*

From figures 2 and 3, it is evident that the refractive indices of films of single cryolite and MgF_2 taken separately are greater than the corresponding bulk values. It is also seen that for films of cryolite and MgF_2, chopped films have higher refractive index than non-chopped films.

The refractive index of material proper should not change, really, even if its thickness is low (down upto 300 Å). But the film consists of a combination of known and unknown materials, as is reported (Koch 1965; Oliver 1970; Pulkar and Jung 1969; Pulkar and Zaminer 1970) and also as seen from our electron diffraction rings (UI). These materials have their own refractive indices and their own dispersion curves, which will affect the resultant refractive index and dispersion of the film. As the law to be followed is Lorentz-Lorenz theory only, there are three possible major factors (reactions) which may produce the changes in refractive index. (i) replacement *e.g.* vacuum (voids) to H_2O; (ii) conversion *e.g.* MgF_2 to MgO; (iii) addition *e.g.* H_2O layer added. Since the films studied are taken out of vacuum and then measured in air, the *in situ* aging (minute's-scale) is possible which might make the measured refractive index different from bulk values.

The refractive indices of single cryolite and MgF_2 films (see figures 2 and 3) are greater than the bulk values (1·338 and 1·384 respectively) (CRC Handbook 1978–79). This can be due to the presence of oxide material due to conversion reaction taking place, an oxide with higher refractive index than the film being formed due to the reaction with water vapour, present in the vacuum chamber. Another conversion reaction possible is the formation of boundary layer as reported by Oliver (1970). Our single film index is midway between the reported boundary layer and the main film value. Also, as reported by many workers (Kinosita and Nishibori 1969; Ritter and Hoffmann 1969; Ogura *et al* 1975; Macleod and Richmond 1976), moisture absorption increases the refractive index of the film. This sort of replacement and addition reactions can occur during deposition even at the 10^{-5} torr vacuum used by us and also during air inlet into the vacuum chamber.

All these effects seem to be more prominent in thinner films as seen from figure 3 which shows that the refractive index approaches the bulk value for higher thickness films. One would expect such thickness effects, if ' the conversion reaction ' takes place predominantly during deposition and/or during air inlet. These ellipsometric results do give larger spread in measurement at lower thicknesses. This is indicated by the scatter diagram plot (Vijaya 1982) and the values given in table 2 which show more scatter at lower thickness. The chopped films show the same trend and with reduced scatter, indicating reliability of the trends observed in measurements. This, in a way, indicates similarity in 'inhomogeneity' in non-chopped and chopped films (later being more homogeneous as 2 Å layers are produced).

Table 2. Scatter values of refractive index at three thickness for non-chopped (NC) and chopped (C) films.

Thickness Å	Cryolite		Mixed cryolite-MgF_2		MgF_2	
	NC	C	NC	C	NC	C
300	1·46-1·35	1·44-1·38	1·45-1·37	1·46-1·41	1·47-1·40	1·48-1·44
800	1·38-1·34	1·39-1·36	1·41-1·36	1-42-1·37	1·46-1·41	1·46-1·43
1100	1·37-1·35	1·38-1·37	1·39-1·36	1·40-1·38	1·42-1·40	1·42-1·41

The spectral response curve (figure 2) shows that due to the above types of reaction, the effective dispersion of the films is modified, the refractive index being higher throughout the spectral range. In addition, there are some small changes in relative spectral response.

3.3 *Packing fraction analysis*

The packing fraction analysis is the most convenient method for studying the single films. As suggested by many authors (Pulkar and Jung 1969; Guenther and Jung 1976) the films of cryolite and MgF_2 possess columnar crystal growth in a more or less closely packed structure. This means that the films are composed of relatively well-developed crystalline aggregates, grain boundaries and vacant places such as intermediate gaps and pores. Due to the process of chopping these long columnar growth may be quenched during crystal growth, whereby a denser (less-void) structure may be formed leading to the higher refractive index of chopped films as compared to non-chopped films. In our case the non-chopped and chopped films are two extreme limits of chopping speeds giving change in refractive index of about 0·01. The intermediate chopping speeds would show intermediate effects. This quenched crystal growth can be seen as more diffuse rings in the electron diffraction pattern. The growth can still be polycrystalline and somewhat columnar but more randomised (tending towards amorphous) and probably more closely packed due to the chop-time allowing for settling and aging.

Using the columnar model of crystal growth (vertical cylinders) the theoretically predicted packing density as calculated by Pulkar and Jung (1969) is 0·9069. According to Harris *et al* (1979) there exist situations in the columnar model where the packing density can be greater than 0·9069. This can be due to the columns expanding.

Now as the refractive index of the chopped films is higher than non-chopped films, we expect the packing density of the film to be higher than non-chopped films. During chopping of the films, the quenching of crystal growth may tend to produce randomised but somewhat expanding types of columns. This, it is felt, is a possible situation because chop-time aging effects give rise to more sites for adatoms as the film grows. Since we do not have any cross-sectional electron microscope data, we cannot exactly calculate the theoretical packing density of the chopped films. For simplicity, and as a comparison with non-chopped films we have assumed the packing density as 0·9069, also for chopped films. It may be noted that our films are sufficiently homogeneous whether chopped or non-chopped as chopping give 3Å layer if at all.

Assuming this to be the ultimate attainable packing density under ideal conditions, we have tried to calculate the different fractions of the various materials that may be present in our films. The packing density formula given by Koch (1965) can be modified to include the unknown material as follows:

$$\frac{n_f^2 - 1}{n_f^2 + 2} = P_m \frac{n_m^2 - 1}{n_m^2 + 2} + P_u \frac{n_u^2 - 1}{n_u^2 + 2} + P_{H_2O} \frac{n_{H_2O}^2 - 1}{n_{H_2O}^2 + 2}, \quad (1)$$

where, n_f, n_m, n_u, n_{H_2O} are the refractive indices of film, bulk material, unknown material and water respectively, P_m, P_u, P_{H_2O} are the respective packing fractions and $P_m + P_u + P_{H_2O} = 1$.

Due to the growth geometry the films are porous and the pores (1 — 0·9069) can be filled either with vacuum, air or water. We assume that the pores (0·0931) are filled with water and the remaining 0·9069 to be made up of *m* and *u*. Under this assumption we have calculated the different packing densities using data from our single films, which are given in table 3 along with the reported values. We have used the available data of oxides (CRC handbook 1978–79) and boundary layers (Oliver 1970) as the unknown materials. Besides, there are possibilities of other materials like $Mg(OH)_2$ being present, but its refractive index is not known. The fraction of the unknown material indicates to what extent the effective refractive index can change from the bulk value.

Table 3. Value for packing densities obtained from equation (1) for non-chopped (NC) and chopped (C) films of cryolite and MgF_2.

Film	Refractive index			Packing densities		
	n_f^* (observed)	n_m (bulk CRC handbook 1978-79)	n_u (assumed)	P_m	P_u	P_m date obtained by others
Cryolite	NC 1·360	1·335	1·46 (boundary layer, Oliver 1970)	0·697	0·209	0·84 (Shklyarevskii *et al* 1972)
	C 1·370			0·615	0·291	0·89 (Koppel Mann *et a* 1961, Pulkar *et al* 1969)
MgF_2	NC 1·405	1·385	1·47 (boundary layer, Oliver 1970)	0·606	0·300	0·80 (Ritter *et al* 1969)
	C 1·425			0·366	0·540	0·85 (Koch 1965)
						0·73 (Pulkar *et al* 1969)
	NC 1·405	1·385	1·70 (MgO CRC handbook 1978-79)	0·818	0·088	
	C 1·425			0·748	0·158	

*The refractive index n_f is an average of spectrophotometric, ellipsometer and Abelès values, which are very near each other; $P_{H_2O} = 0·0931$; $n_{H_2O} = 1·332$.

It is seen from table 3 that the percentage of the unknown material increases, in all the cases, in chopped films. The increase is about 9% for cryolite with reported boundary layer (Oliver 1970). But for MgF_2 the increase with the reported boundary layer (Oliver 1970) is about 24%, much higher than one would expect. It is also *not* shown by the electron diffraction pattern. But assuming MgO as the unknown gives an increase of just 7% which is within the expected limits.

If packing were to be more dense for chopped films reducing P_{H_2O} (0·0931), then the $(m + u)$ fraction will increase, slightly reducing the percentage of u (as refractive index of water is less than the material (m) used). The results thus indicate that chopping may reduce the reported ' day '—scale aging (Vijaya *et al* 1980) by increasing the initial ' minute's '—scale aging (increasing ' surface layer ' packing fraction). The major part played by chop-time seems to be this, rather than settling of adatoms during the chop-time. During the process of chopping about 3 Å of film gets deposited per cycle. Due to the presence of residual gases in the chamber even at 10^{-5} torr vacuum, there is a possibility of some chemisorption/oxidation type of reaction occurring at the individual layers thereby increasing the surface layer packing fraction. Of course the percentage of this type of conversion is very low since it is not noticeable as a strong ring in the electron diffraction pattern.

3.4 *Spectral response tilt comparison*

Though in general the dispersion curve ($n - \lambda$) can have any shape, for our materials and in the range of λ we have used, the n-values fall practically linearly with λ. Hence, as a simple ' measure ' of dispersion, we have defined here a quantity called the ' tilt ', as $\Delta n_f/\Delta\lambda\ A^{-1}$ where $\Delta\lambda = (6500 - 4000)$ Å, and Δn_f is change in n_f over this $\Delta\lambda$. As seen from figure 4 the dispersion curve obtained by us are quite similar to those by other workers, though there are some variations in the tilts. For convenience we consider MgF_2 films both non-chopped and chopped for discussion. The tilts of our MgF_2 films are: non-chopped 6×10^{-6} (with $\Delta n_f = 0{\cdot}015$), chopped 10×10^{-6} (with $\Delta n_f = 0{\cdot}025$). These are to be compared with that of water with a tilt 4×10^{-6} with $\Delta n_f = 0{\cdot}01$ (The dispersion curve of water is also given in figure 4).

It is seen that the tilts of non-chopped and chopped films are more than that of water and tilt of chopped films is higher than non-chopped films. This difference in tilt indicates that water is not the only additional material in the films. There are unknown materials also present in the films, which gives support to our packing density calculations using equation (1). The tilt of chopped films being higher than that of non-chopped films indicates that the chop-time aging effect which enhances the production of unknown material as seen from table 3.

3.5 *Co-deposited mixed cryolite-MgF_2 films*

As seen in figures 2 and 3, mixed cryolite-MgF_2 films for all thicknesses show a refractive index intermediate to our experimental single cryolite and MgF_2 films and as expected the refractive index of these co-deposited mixed films obeys the Lorentz-Lorenz relation as can be seen from data presented in table 4 for both non-chopped and chopped films. Apparently we can extend the assumption of minute's scale-pre-aging to the mixed films without much harm. There are definite indications of

Table 4. Refractive index of mixed cryolite-MgF_2 films both non-chopped (NC) and chopped (C). Thickness of film 1000 Å.

Method	Type	Refractive index as measured		Mixed cryolite-MgF_2	Mixed value from formula (Yadava *et al* 1973)
		Single cryolite	Single MgF_2		
Spectro-photometer	NC	1·370	1·405	1·395	1·388
6200 Å	C	1·385	1·415	1·405	1·400
Ellipsometer	NC	1·368	1·404	1·378	1·382
6328 Å	C	1·380	1·416	1·401	1·400
Abelès	NC	1·373	1·408	1·378	1·390
5893 Å	C	1·387	1·419	1·397	1·403

additional and different mixed phase boundary layers being formed, which are not observed in single films as indicated by electron diffraction (The d_0 values of chopped mixed films being very much different). The spectral responses of the mixed films show that these films follow the Lorentz-Lorenz relation at all wavelengths (figure 2) for both non-chopped and chopped films indicating that this type of co-deposition technique is successful in producing homogeneous mixed film.

4. Conclusions

This paper reports a special chopping and mixing effects on refractive index of optical coatings. For both chopped and non-chopped films there seems to be a few specific unknown materials present other than the original material which change the effective refractive index and dispersion curve of the films. This change in refractive index as compared to bulk is greater for the thinner films.

The effect of chopping, *i.e.* increase in the refractive index of the chopped film as compared to non-chopped film, tends to increase the initial minute's-scale aging along with the settling of adatoms during the chop-time.

The spectral tilts indicate that water is not the major constituent responsible for minute's-scale aging of the optical films. Identification of such unknown material (whose spectral and other data are not available for comparison) and that too in small quantity, in the matrix of the original material seems to be difficult. Further, the unknown material may decompose easily. Probably IR spectra analysis may lead to some identification.

The refractive index of mixed cryolite-MgF_2 films follow the Lorentz-Lorenz relation at all wavelengths, for both non-chopped and chopped films even using the co-deposition method, indicating homogeneity.

The electron diffraction patterns of non-chopped and chopped cryolite, MgF_2 and mixed cryolite-MgF_2 (obtained by co-deposition) suggest a more amorphous (less polycrystalline) film growth for chopped films and a crystallite reorientation.

Acknowledgement

One of the authors (KV) gratefully acknowledges the fellowship awarded by CSIR, India.

References

CRC 1978-79 *Handbook of chemistry and physics*, 59th ed., (Florida, USA: CRC Press)
Guenther H K and Jung E 1976 *Thin Solid Films* **4** 219
Hall J F and Fergusson W F C 1955 *J. Opt. Soc. Am.* **45** 75
Harris M, Macleod H A, Ogura S, Pelletier E and Vidal B 1979 **57** Thin Solid Films 173
Heavens O S and Smith S D 1957 *J. Opt. Soc. Am.* **47** 471
Heavens O S 1960 *Rep. Prog. Phys.* **23** 1
Housten R A 1947 *A treatise on light* (London: Longmans Green) 7th ed., p. 465
Kinosita K and Nishibori M 1969 *J. Vac. Sci. Technol.* **6** 730
Koch H 1965 *Phys. Status Solidi* **12** 533
Koppelmann G, Krebs K and Leyendecker H 1961 *Z. Phys.* **163** 557
Macleod H A and Richmond D 1976 *Thin Solid Films* **37** 1964
Ogura S, Sugawara N and Hiraga R 1975 *Thin Solid Films* **30** 3
Oliver W R 1970 *Philos. Mag.* **21** 1229
Pelletier E, Roche P and Vidal B 1976 *Nuovo. Rep. Opt.* **7** 353
Pulkar H K and Jung E 1969 *Thin Solid Films* **4** 219
Pulkar H K and Zaminer C 1970 *Thin Solid Films* **5** 421
Ritter E and Hoffmann R 1969 *J. Vac. Sci. Technol.* **6** 733
Shklyarevskii I N, Shazli A F A El and Govoruskehenko A I 1972 *Opt. Spectrosc.* **32** 40
Vijaya K 1982 Ellipsometric study of the changes in optical properties (aging) of non-chopped and chopped films of cryolite, MgF_2, ZnS and their co-deposited mixtures in various ambients Ph.D. thesis, Pune University, Pune
Vijaya K, Puri R K and Karekar R N 1980 *Thin Solid Films* **70** 105
Yadava V N, Sharma S K and Chopra K L 1973 *Thin Solid Films* **17** 243

Pramāṇa, Vol. 21, No. 5, November 1983, pp. 323-328. © Printed in India.

Study of $^{40}_{18}$Ar ion tracks in cellulose nitrate

SUBHASH CHANDER*, SHYAM KUMAR, J S YADAV and A P SHARMA
Department of Physics, Kurukshetra University, Kurukshetra 132 119, India
*Department of Physics, Dayanand College, Hissar 125 001, India

MS received 15 June 1983; revised 26 September 1983

Abstract. Sample of cellulose nitrate (Russian) is exposed to $^{40}_{18}$Ar ions. The bulk etch rate has been studied at different etching temperatures and the activation energy for bulk etch rate has been calculated. The etched track lengths are measured for different etching times. The energy loss rate and range of $^{40}_{18}$Ar ions in CN(R) is also calculated. The critical threshold value for etchable track in CN(R) is determined by comparing the theoretical and experimental values of track length. The response curve of CN(R) is also presented.

Keywords. Cellulose nitrate; chemical etching; activation energy; track length; response curve.

1. Introduction

In recent years, solid state nuclear track detectors (SSNTDs) have been used increasingly in various branches of science and technology (Fleischer *et al* 1975; Fleischer 1977). Track etching technique has successfully been employed in many insulating materials for revealing the path of charged particles and for their identification. SSNTDs are currently being used in the study of heavy particles, search of super heavy elements, fission fragments studies, cosmic ray studies etc. The cellulose nitrate (Russian) (CN(R)) is one of the most sensitive plastic track detectors available. The various track parameters, which can be measured experimentally, can be used for particle identification.

In this paper the tracks of $^{40}_{18}$Ar ion of energy 7·5 MeV/N and 4·22 MeV/N at an angle of 10° with respect to detector surface in CN(R) are studied. The bulk etch rate has been measured at different etching temperatures and the activation energy for bulk etch rate is calculated. We have also measured the track etch rate V_t and the range of this ion in CN(R). We have calculated the total energy loss dE/dX and range of $^{40}_{18}$Ar ions in CN(R) using the relations of Mukherji and Nayak (1979) and the value of critical threshold for track etching $(dE/dX)_c$ for this plastic has been estimated. The response of this plastic is also studied.

2. Experimental details

Samples of CN(R) with composition $C_6H_8O_9N_2$ and thickness 1000μm were exposed at JINR, Dubna, USSR to $^{40}_{18}$Ar ions with energies 7·5 MeV/N and 4·22 MeV/N at angles

90° and 10° to the plane of the samples. The exposed samples were etched in stirred 6·25 N sodium hydroxide solution at (60 ± 1)°C. The thickness difference method was preferred for measuring bulk etch rate V_b over the weight-loss method. This was because the latter method is not applicable since water absorption by the plastic ($\simeq$ 4% by weight at 70°C, Blandford *et al* 1969) makes it difficult to measure the dissolved weight accurately. We have also measured bulk etch rate V_b by the diameter measurement technique using fission fragment of ^{252}Cf (Rao *et al* 1981). For $V_t \gg V_b$, the average diameter D of fission fragment is obtained by the relation.

$$D = 2\, V_b\, t, \tag{1}$$

where V_b is the bulk etch rate and t is the etching time.

The etch pit diameter and length were measured with a transmitted light microscope 'Olympus' BH(Japan) having an eyepiece micrometer whose least count = 0·215 μm at a magnification of 900 X. The V_t value was calculated on the assumption that it remains constant for very small etching time during which a small segment of particle trajectory is etched (Fleischer *et al* 1975). The correlation between the V_t and the track length for an etching time t, is given by relation

$$L = \int_0^t V_t\, \mathrm{d}t, \tag{2}$$

or

$$V_t = \delta L/\delta t, \tag{3}$$

where δL is the small change of track length in small etching time δt.

3. Results and discussion

Figure 1 shows the variation of log V_b against $1/T$, where T is the etching temperature in °K, to find out the activation energy E_b for bulk etching which is found to be

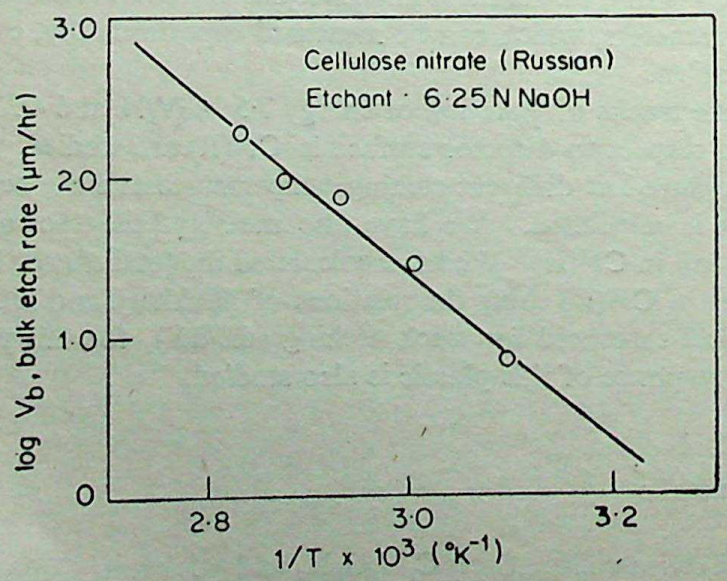

Figure 1. Plot of log V_b vs $1/T \times 10^3$ (°K^{-1}).

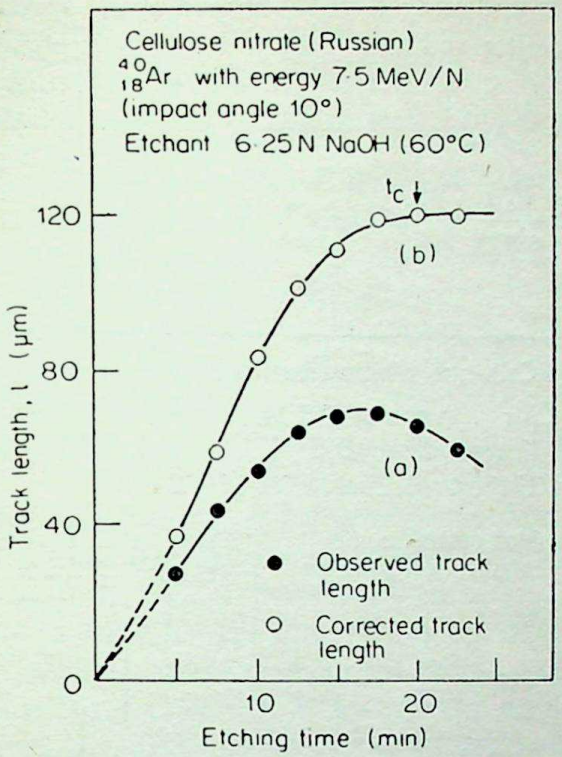

Figure 2. Variation of a observed track length with etching time; b corrected track length with etching time; for $^{40}_{18}$Ar having the energy 7·5 MeV/N at an angle 10°.

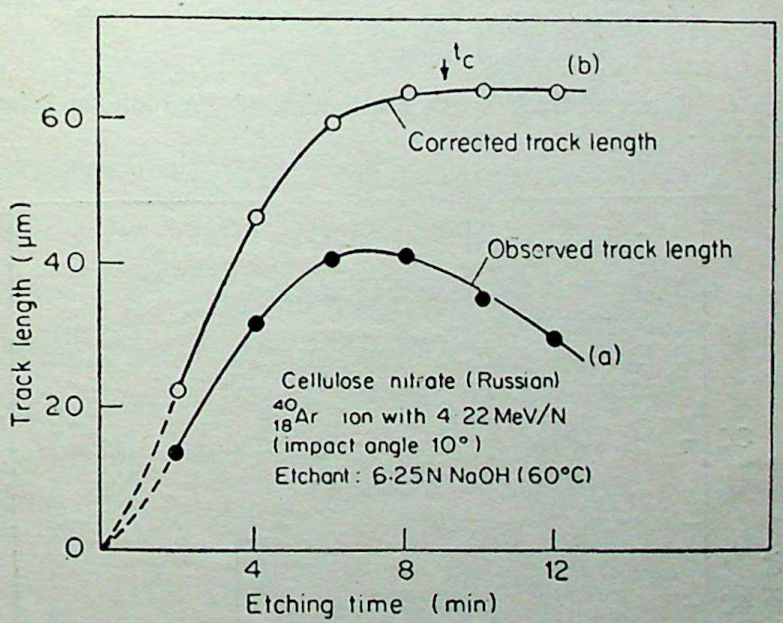

Figure 3. Variation of a observed track length with etching time; b corrected track length with etching time; for $^{40}_{18}$Ar having the energy 4·22 MeV/N at an angle 10°.

(0·86 ± 0·02) eV. Figures 2a and 3a show the variation of observed length of $^{40}_{18}$Ar tracks for energies 7·5 MeV/N and 4·22 MeV/N. It is seen that the observed track length first increases and then starts decreasing after a certain etching time, t_c which is required to etch the tracks completely. The observed track length first increases with etching time due to V_t along the track till the end point is reached. Beyond

this point the material is undamaged and is etched at the speed V_b. Further etching causes a decrease in the observed track length due to over etching. Figures 2b and 3b show the variation of corrected track length with etching time for both the energies. The corrected track length (L) is determined by using the relation

$$L = \frac{l}{\cos\phi} + \frac{V_b\, t}{\sin\phi} - V_b\,(t - t_c), \tag{4}$$

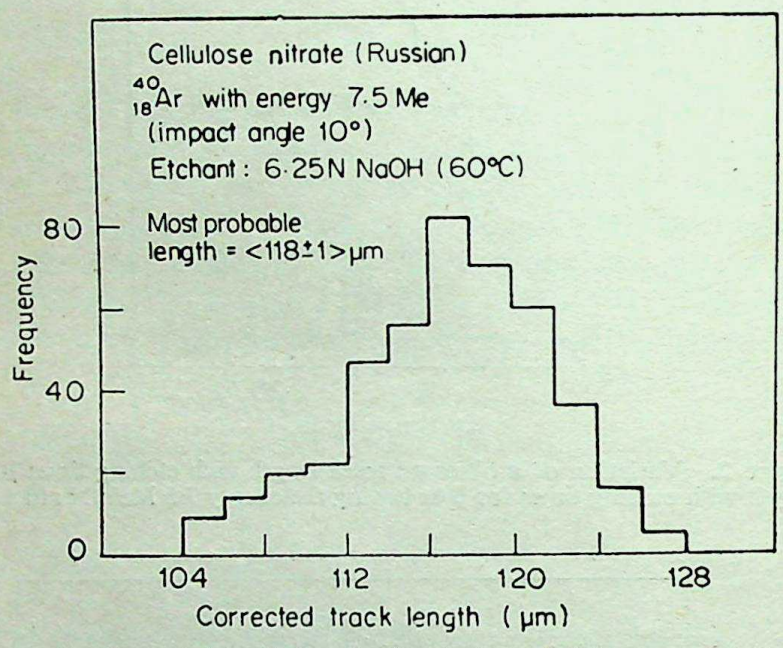

Figure 4. Corrected track length distribution of $^{40}_{18}$Ar ion track having the energy 7·5 MeV/N.

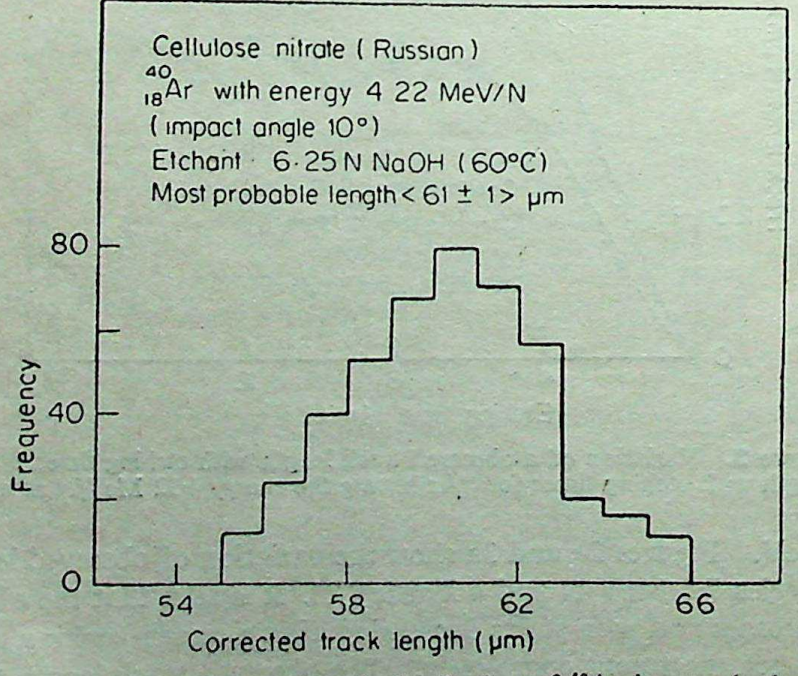

Figure 5. Corrected track length distribution of $^{40}_{18}$Ar ion tracks having the energy 4·22 MeV/N.

where l is the observed length and ϕ the angle of incidence to the detector surface. It is clear that the corrected track length first increases and then becomes constant beyond t_c.

The corrected track length distribution was observed by plotting the frequency against the corrected track length as shown in figures 4 and 5 for an angle of 10° with energies 7·5 MeV/N and 4·22 MeV/N respectively. From these histograms the most probable track length come out as (118 ± 1) μm and (61 ± 1) μm for $^{40}_{18}$Ar ions of energy 7·5 MeV/N and 4·22 MeV/N respectively.

Assuming the validity of Bragg's additive rule and using the Mukherji and Nayak (1979) range energy equations, we have calculated the energy loss rate dE/dX and range of $^{40}_{18}$Ar ions in CN(R), using the computer TDC 316. The value of range for this ion is found to be 121·4 μm and 64·4 μm for energies 7·5 MeV/N and 4·22 MeV/N respectively.

By comparing the theoretical values of range with the total etchable track length, we have calculated the critical threshold value $(dE/dX)_c$ for CN(R). The $(dE/dX)_c$ value for $^{40}_{18}$Ar comes out to be (3 ± 1) MeV mg^{-1} cm^2.

The V_t values were obtained from the values of corrected track length at different etching times. A plot of the track etch rate versus corresponding energy loss dE/dX in cellulose nitrate (Russian) is shown in figure 6. The dE/dX at which V_t equals the V_b is taken as the critical energy loss for etchable track and below this energy loss no 'etchable track' is produced. From this plot the value of critical energy loss $(dE/dX)_c$ was found to be (2·8 ± 0·5) MeV mg^{-1} cm^2 for $^{40}_{18}$Ar ion tracks in cellulose nitrate (Russian).

Acknowledgement

Authors are grateful to JINR, (USSR) authorities for providing the exposed samples.

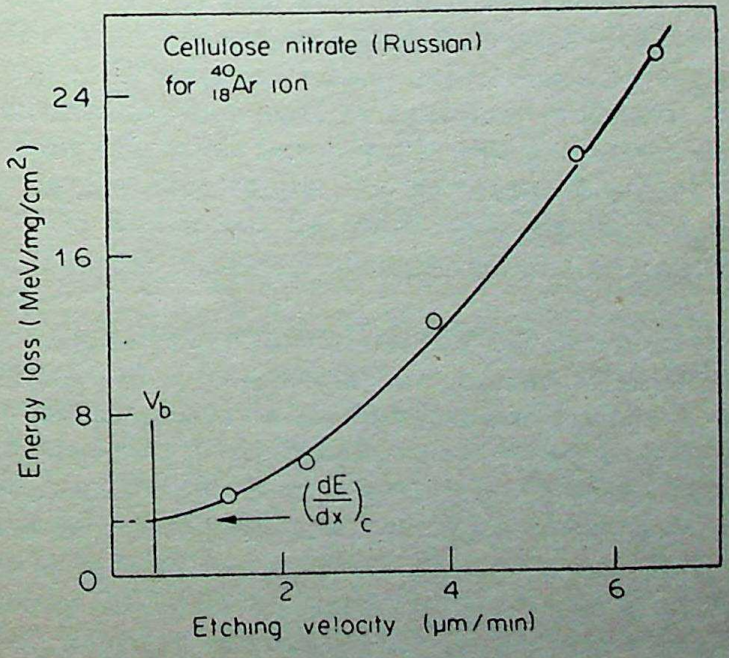

Figure 6. Plot of energy loss vs etching velocity.

References

Blandford G E, Walker R M and Wafer I P 1969 Proc. Int. Topical Conf. on Nuclear registration Clerment Ferrand Vol. 1, p. III-27

Fleischer R L, Price P B and Walker R M 1975 *Nuclear tracks in solids* (Berkeley: University of California Press)

Fleischer R L 1977 *Nucl. Instrum. Method.* **147** 1

Mukherji S and Nayak A K 1979 *Nucl. Instrum. Method.* **159** 421

Rao Y V, Davis A, Spencer T and Filz R C 1981 *Nucl. Instrum. Method.* **180** 153

Pramāṇa, Vol. 21, No. 5, November 1983, pp. 329–337. © Printed in India.

Mesonic decays of τ^- lepton: Effects of neutrino mass and mass mixing

R R L SHARMA* and N K SHARMA
Department of Physics, University of Rajasthan, Jaipur 302 004, India
*On leave from Government College, Dholpur 328 001, India

MS received 23 October 1982; revised 21 July 1983

Abstract. Experimentally established mesonic decays of τ^- lepton have been re-examined with the inclusion of the effects of finite neutrino mass and the associated mass mixing in the form of Kobayashi-Maskawa mixing matrix. A comparison with the experimentally predicted decay probabilities provides limits for the ν_τ mass which are finite in all decays except for the lower limit in mass mixing case of the decay $\tau^- \to K^{*-}(892) + \nu_\tau$ for which $m_{\nu_\tau} = (420 \pm 610)$ MeV. The large error in this value is because of (i) large errors in the experimental values of life time and branching ratio for this decay and (ii) the KM mixing used in the calculations. The ratio of parity-violating to parity-conserving terms in the differential decay probabilities of various decays differs slightly from their values corresponding to those with vanishing ν_τ mass.

Keywords. τ^- lepton; Kobayashi-Maskawa mixing matrix; Tau neutrino; neutrino mass; mass mixing.

1. Introduction

Massive neutrinos, their mixing and oscillations (Maki *et al* 1962; Bilenky and Pontecorvo 1978; Lyubimov and De Rujula 1981 and De Rujula and Lusignoli 1982) have become a field of immense current importance especially after the reporting of the finite electron neutrino mass by Lyubimov *et al* 1980. Effects of inclusion of these have been calculated theoretically with predictions that could be tested in experiments in the near future. In particular, processes involving β-decays (Bergkvist 1972; De Rujula and Lusignoli 1982) and muon decay (Kalyaniak and Ng 1981) have attracted maximum attention because of their obvious importance and accessibility.

In this paper we report the results of our calculations on the experimentally established mesonic decays of τ^- lepton in the lowest order. The effects of finite neutrino mass and their associated mixing are included with the use of mixing mass matrix (Kobayashi and Maskawa 1973). Bilenky and Pontecorvo (1978), and Shrock (1980) have emphasized that the effects of finite neutrino mass should be much more pronounced and detectable in two body mesonic decays involving a neutrino as compared with those from three body decays like β-decays. Further, very recently Divakaran and Ramachandran (1982) have argued extensively that it is sufficient to take into consideration the effects of dominant mass mixing term without oscillations while considering the effects of finite neutrino mass and mass-mixing. As such, in these

Table 1. ν_τ mass values and the ratio (R) of parity non-conserving to parity-conserving terms in mesonic angular distribution of τ^- lepton decays.

Decay mode	ν_τ mass (MeV) (without mass mixing)	ν_τ mass (MeV) (with mass mixing)	R_0 (with $m_{\nu_\tau} = 0$)	R (without mass mixing but m_{ν_τ} finite)	R (with mass mixing m_{ν_τ} finite)
1. $\tau^- \to \pi^- + \nu_\tau$	610 ± 240	660 ± 260	1	0·97 ± 0·06	0·96 ± 0·09
2. $\tau^- \to K^- + \nu_\tau$	570 ± 210	570 ± 270	1	0·99 ± 0·03	0·99 ± 0·05
3. $\tau^- \to \rho^- + \nu_\tau$	700 ± 150	760 ± 170	0·04	0·09 ± 0·00	0·08 ± 0·02
4. $\tau^- \to K^{*-}(892) + \nu_\tau$	460 ± 440	420 ± 610	0·64	0·62 + 0·02	0·62 ± 0·01

For the calculation of the parameters listed in this table, the values of physical constants have been used from Particle Data Group (1982), Sources for parameters not given in this booklet are referred to appropriately in the manuscript. Results, in the table, are of two-figure accuracy.

calculations we have not given any consideration to time dependent oscillation terms. The decays considered are $\tau^- \to \pi^- + \nu_\tau$; $\tau^- \to K^- + \nu_\tau$; $\tau^- \to \rho^- + \nu_\tau$ and $\tau^- \to K^{*-}(892) + \nu_\tau$. The mass limits obtained for ν_τ mass are found to vary for various decays (table 1). The inclusion of experimental errors in various quantities involved in the decay probabilities contribute substantially to the statistical errors in the mass of the Tau neutrino. The theoretical predictions are not in agreement with the experimental upper limit $m_{\nu_\tau} < 250$ MeV (perhaps favoured) provided by DELCO group (Kirkby 1979; Flügge 1979). This does not require any serious consideration at this stage as the experimental values including the errors are expected to undergo changes with future improvement in experimental techniques and statistics.

2. Calculations of decay probability and R

2.1 *The decay* $\tau^- \to \pi^- + \nu_\tau$

Following the procedure of Tsai (1971), and with the inclusion of the contribution due to neutrino mass mixing (Barger *et al* 1980) treated as Dirac neutrino, we write the matrix element as (figure 1)

$$M = -i\frac{G}{\sqrt{2}}\cos\theta_1 |f_\pi| \sum_{i=1}^{3} U_{\tau i}\, \bar{u}_{\nu i}\, \gamma^u (1 - \gamma 5)\, u_\tau\, q_\mu, \tag{1}$$

where $U_{\tau i}$ are the elements of the Kobayashi-Maskawa (1973) mixing mass matrix for lepton and θ_1 is the mixing angle in U_{kM} for quarks (Shrock and Wang 1978),

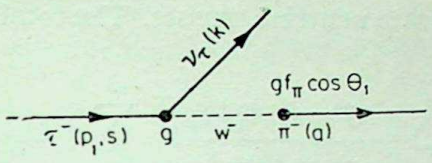

Fig 1

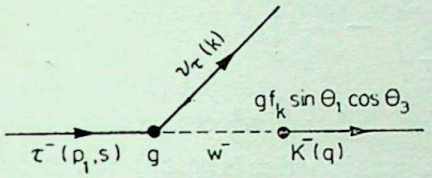

Fig. 2

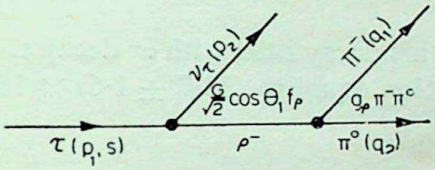

Fig. 3

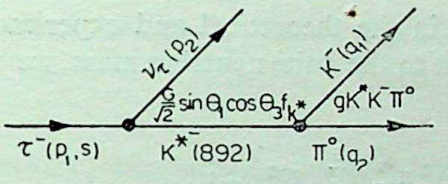

Fig. 4

Figures 1-4. **1.** Decay of the τ^- into Tau neutrino (ν_τ) and π^- meson. W^- is the intermediate boson, θ_1 is the mixing angle in U_{km}. **2.** Decay of the τ^- into Tau Neutrino and K^- meson with the intermediate boson W^-. θ_1 and θ_3 are mixing angles in U_{km}. **3.** Decay mode $\tau^- \to \nu_\tau + \rho^-$

$\rho^- \to \pi^- + \pi^o$.

4. Decay mode $\tau^- \to \nu_\tau + K^{*-}(892)$

$K^{*-} \to K^- + \pi^o$.

in u_τ the subscript τ merely denotes the τ lepton spinor, and no summation over τ is implied. The differential decay probability for the polarised τ^- decay is given as

$$dW = \frac{G^2 |f_\tau|^2 \sum_{i=i}^{3} |U_{\tau i}|^2 m_\tau^3}{16\pi} \left[\left(1 - \frac{m_{\pi^-}^2}{m_\tau^2}\right)^2 + \frac{m_i^2}{m_\tau^2}\left(\frac{7}{2}\frac{m_i^2}{m_\tau^2} + \frac{m_{i-}^2}{m_\tau^2} - 3\right) \right.$$

$$\left. + \hat{S}\cdot\hat{q} \left\{ \left(1 - \frac{m_{\pi^-}^2}{m_\tau^2}\right)^2 + \frac{m^2}{m_\tau^2}\left(\frac{2m_i^2}{m_\tau^2} + \frac{2m_{\pi^-}^2}{m_\tau^2} - 3\right) \right\} \right] \frac{d\Omega}{4\pi} \cos^2\theta_1, \quad (2)$$

where m_i denote non-degenerate neutrino masses. The total decay rate is obtained as

$$W(\tau^- \to \pi^- + \nu_\tau) = \frac{G^2 \cos^2 \theta_1 |f_\pi|^2}{16\pi} \sum_{i=1}^{3} |U_{\tau i}|^2 m_\tau^3 \times \left[\left(1 - \frac{m_{\pi^-}^2}{m_\tau^2}\right)^2 - \frac{3m_i^2}{m_\tau^2}\right], \tag{3}$$

where terms of the order of $m_{\pi^-}^4/m_\tau^4$, m_i^4/m_τ^4 etc. are neglected. The theoretical decay rate with zero neutrino mass in this order is calculated to be

$$W(\tau^- \to \pi^- + \nu_\tau) = 3{\cdot}6155 \times 10^{11}/\text{sec}. \tag{4}$$

The experimental value of this decay rate, with τ^- decay time as $(4{\cdot}6 \pm 1{\cdot}9) \times 10^{-13}$ sec and the branching fraction equal to $(10{\cdot}7 \pm 1{\cdot}6) \times 10^{-2}$, (Particle Data Group 1982) is found to be

$$W_{\text{exp}}(\tau^- \to \pi^- + \nu_\tau) = (2{\cdot}3 \pm 0{\cdot}98) \times 10^{11}/\text{sec}. \tag{5}$$

Attributing the difference in the theoretical and experimental values of the decay rate to the contribution due to the finite neutrino mass, we equate it to the theoretical expression

$$\frac{3G^2 \cos^2 \theta_1 |f_\pi|^2 m_\tau^3 \sum_{i=1}^{3} U_{\tau i}^2 \frac{m_i^2}{m_\tau^2}}{16\pi}.$$

We use the solution (A) of Barger (1980) in terms of the mixing mass matrix

$$U_{\nu_l} = \begin{bmatrix} 0{\cdot}64 & 0{\cdot}66 & 0{\cdot}38 \\ -0{\cdot}72 & 0{\cdot}69 & 0{\cdot}01 \\ -0{\cdot}26 & -0{\cdot}28 & 0{\cdot}92 \end{bmatrix}, \tag{6}$$

where ν denotes e, μ, τ in our approximations.
Assuming that $m_{\nu_e} = m_1$, $m_{\nu_\mu} = m_2$ and $m_{\nu_\tau} = m_3$, we retain only $m_{\nu_\tau}^2/m_\tau^2$ term as dominant contributing term because the contribution due to $m_{\nu_e}^2/m_\tau^2$ and $m_{\nu_\mu}^2/m_\tau^2$ will be negligible (Kalyniak and Ng 1981). This enables us to determine limits on ν_τ mass which are given in table 1.

Further the ratio (R) of parity-violating to parity-conserving terms, in (2), for this process is given by

$$R = \frac{\left(1 - \frac{m_{\pi^-}^2}{m_\tau^2}\right)^2 + \frac{m_i^2}{m_\tau^2}\left(\frac{2m_i^2}{m_\tau^2} + \frac{2m_{\pi^-}^2}{m_\tau^2} - 3\right)}{\left(1 - \frac{m_{\pi^-}^2}{m_\tau^2}\right)^2 + \frac{m_i^2}{m_\tau^2}\left(\frac{7}{2}\frac{m_i^2}{m_\tau^2} + \frac{m_{\pi^-}^2}{m_\tau^2} - 3\right)}. \tag{7}$$

Using the ν_τ mass as obtained earlier, the R value for finite neutrino mass without and with mass-mixing are calculated and are given in table 1.

2.2 *The decay* $\tau^- \to K^- + \nu_\tau$

The process of calculations follow the same path as that for $\tau^- \to \pi^- + \nu_\tau$, with $f_\pi \to f_k$, $m_{\pi^-} \to m_{k^-}$ and $\cos\theta_1 \to \sin\theta_1 \cos\theta_3$ (figure 2), θ_3 is the mixing angle in U_{kM} (Shrock and Wang 1978).

The differential decay probability is given by

$$dW = \frac{G^2 |f_k|^2 \sin^2\theta_1 \cos^2\theta_3}{16\pi} \sum_{i=1}^{3} |U_{\tau_i}|^2 m_\tau^3 \left[\left(1 - \frac{m_{k^-}^2}{m_\tau^2}\right)^2 + \frac{m_i^2}{m_\tau^2} \right.$$

$$\left. \left(\frac{7}{2}\frac{m_i^2}{m_\tau^2} + \frac{m_{k^-}^2}{m_\tau^2} - 3\right) + \hat{s}\cdot\hat{q} \left\{ \left(1 - \frac{m_{k^-}^2}{m_\tau^2}\right)^2 + \frac{m_i^2}{m_\tau^2}\left(\frac{2m_i^2}{m_\tau^2} + \frac{2m_{k^-}^2}{m_\tau^2} - 3\right)\right\}\right] \frac{d\Omega}{4\pi}, \quad (8)$$

and the total decay rate as

$$W = \frac{G^2 |f_k|^2 \sin^2\theta_1 \cos^2\theta_3}{16\pi} \sum_{i=1}^{3} |U_{\tau_i}|^2 \left[m_\tau^3 \left(1 - \frac{m_{k^-}^2}{m_\tau^2}\right)^2 - 3m_i^2 m_\tau \right]. \quad (9)$$

Following the procedure of (2.1) with the use of experimental value for the τ^- decay time (Feldman *et al* 1981) $T = (4{\cdot}6 \pm 1{\cdot}9) \times 10^{-13}$ sec and the branching ratio $\approx 0{\cdot}5\%$ (Perl 1979), the limits on ν_τ mass and the ratio R have been calculated and tabulated in table 1. The values obtained for ν_τ mass for this case are valid to the extent of the validity of the aforesaid value of branching ratio which is not yet well established (Particle Data Group 1982).

2.3 *The decay* $\tau^- \to \nu_\tau + \rho^-$

$\rho^- \to \pi^0 + \pi^-$

The calculations for this decay are slightly complicated. We follow the procedure due to Tsai (1971) with the inclusion of finite neutrino mass and mass-mixing. We write for the matrix element the expression (figure 3).

$$M = g_{\tau\rho\nu}\, g_{\rho\pi^-\pi^0} \sum_{i=1}^{3} U_{\tau i}\, \bar{u}_{\nu i}\, \gamma^\lambda (1 - \gamma^5)\, u_\tau \frac{1}{(q_1 + q_2)^2 - m_\rho^2 + i\Gamma_\rho m_\rho} Q_\lambda, \quad (10)$$

with $$Q = q_1 - q_2 \text{ and } \Gamma_\rho = \frac{g_{\rho\pi^-\pi^0}^2}{48\pi^2} m_\rho \left\{1 - \frac{2(m_{\pi^-}^2 + m_{\pi^0}^2)}{m_\rho^2}\right\}^{3/2}. \quad (11)$$

Taking τ^- to be polarised and replacing the Breit-Wigner factor by a delta function, *i.e.*,

$$\left|\frac{1}{(q_1+q_2)^2 - m_\rho^2 + i\,\Gamma_\rho m_\rho}\right|^2 = \frac{\pi}{\Gamma_\rho m_\rho}\,\delta\{(q_1+q_2)^2 - m_\rho^2\}, \tag{12}$$

we get the following expression for the angular distribution of π^-:

$$\frac{dW}{d\Omega} = \frac{3g_{\tau\rho\nu}^2 \sum_{i=1}^{3} |U_{\tau i}|^2}{(4\pi)^2 m_\tau^2 m_\rho^2 \left(1 - 2\frac{m_{\pi^-}^2 + m_{\pi^0}^2}{m_\rho^2}\right)^{3/2}} \Bigg[\frac{16}{3} m_\tau^2 (w_1 - A)^3 - 4m_\tau (w_1 - A)^2 D$$

$$+ (m_\tau^2 - m_\rho^2 + m_i^2)\, CW_1 + (\hat{s}\cdot\hat{q}_1)\, 4m_\tau \Bigg\{\Bigg(\frac{4}{3} m_\tau W_1^2 - 4m_\tau w_1 A$$

$$+ 4m_\tau A^2 + \frac{8}{3} m_{\pi^-}^2 m_\tau + Bm_\tau - AC - D(w_1 - 2A)\Bigg) E - \Bigg(4m_\tau m_{\pi^-}^2 A$$

$$+ m_\tau AB + m_{\pi^-}^2 D + \frac{DB}{2} - \frac{C}{4}(m_\rho^2 + D)\Bigg) \log (w_1 + E)\Bigg\}\Bigg]_{w_1 \min.}^{w_1 \max.}, \tag{13}$$

where

$$A = m_\tau^2 + m_\rho^2 - m_i^2/4m_\tau; \quad B = m_\rho^2 - 3m_{\pi^-}^2 - m_{\pi^0}^2;$$

$$C = m_\rho^2 - 2(m_{\pi^-}^2 + m_{\pi^0}^2); \quad D = m_{\pi^-}^2 - m_{\pi^0}^2; \quad E = (w_1^2 - m_\rho^2)^{1/2}; \tag{14}$$

$$w_{1\max.} = A\left(\frac{D}{m_\rho^2} + 1\right) + \left(A^2 - \frac{m_\rho^2}{4}\right)^{1/2}\left(1 - 2\frac{m_{\pi^-}^2 + m_{\pi^0}^2}{m_\rho^2}\right)^{1/2};$$

and

$$w_{1\min.} = A\left(\frac{D}{m_\rho^2} + 1\right) - \left(A^2 - \frac{m_\rho^2}{4}\right)^{1/2}\left(1 - 2\frac{m_{\pi^-}^2 + m_{\pi^0}^2}{m_\rho^2}\right)^{1/2}.$$

The decay rate is given by

$$W(\tau^- \to \rho^- + \nu_\tau) = \frac{G^2 \cos^2\theta_1\, m_\rho^2}{64\pi^2} \sum_{i=1}^{3} |U_{\tau_i}|^2$$

$$\times [m_\tau^3 (1 - m_\rho^2/m_\tau^2)^2 (1 + 2m_\rho^2/m_\tau^2) - 3 m_i^2 m_\tau], \tag{15}$$

where $g_{\tau\rho\nu} = \dfrac{G}{\sqrt{2}} \cos\theta_1 f_\rho$,

and f_ρ (Tsai 1971) $= m_\rho^2/2\sqrt{\pi}$) have been used. Using the experimental τ^- decay time $T = (4{\cdot}6 \pm 1{\cdot}9) \times 10^{-13}$ sec and the branching ratio equal to $(21{\cdot}6 \pm 3{\cdot}6)\%$ (Particle Data Group 1982), we calculate ν_τ mass and the ratio R for the process following the procedure given in § 2.1. The results are given in table 1.

2.4 *The decay* $\tau^- \to K^{*-}(892) + \nu_\tau$

$$\Big\lfloor\!\!\longrightarrow K^- + \pi^0$$

For this process calculations follow the same path as that for $\tau^- \to \rho^- + \nu_\tau$, with the following replacements:

$$g_{\tau\rho\nu} \to g_{\tau k^*\nu};\ g_{\rho\pi^-\pi^0} \to g_{k^*k^-\pi^0};\ m_\rho \to m_{k^*};\ m_{\pi^-} \to m_{k^-};$$

$$f_\rho \to f_{k^*} \text{ and } \cos\theta_1 \to \sin\theta_1 \cos\theta_3 \text{ (figure 4).} \tag{16}$$

We obtain for the angular distribution of K^-, the expression

$$\frac{dW}{d\Omega} = \frac{3\, g_{\tau k^*\nu}^2 \sum_{i=1}^{3} |U_{\tau_i}|^2}{(4\pi)^2\, m_\tau^2\, m_{k^*}^2 \{1 - 2(m_{k^-}^2 + m_{\pi^0}^2)/m_{k^*}^2\}^{3/2}}$$

$$\times \Bigg[\frac{16}{3} m_\tau^2 (w_1 - A)^3 - 4\, m_\tau (w_1 - A)^2\, D$$

$$+ (m_\tau^2 - m_{k^*}^2 + m_i^2)\, CW_1 + (\hat{s}\,.\,\hat{q}_1)\, 4m_\tau \Bigg\{\Bigg(\frac{4}{3} m_\tau\, w_1^2 - 4m_\tau\, w_1\, A$$

$$+ 4m_\tau\, A^2 + \frac{8}{3} m_{k^-}^2\, m_\tau + Bm_\tau - AC - D(w_1 - 2A)\Bigg) E$$

$$- \Bigg(4m_\tau\, m_{k^-}^2\, A + m_\tau\, AB + m_{k^-}^2\, D + \frac{DB}{2} - \frac{c}{4}(m_{k^*}^2 + D)\Bigg)$$

$$\times \log(w_1 + E)\Bigg\}\Bigg]_{w_1 \text{ min.}}^{w_1 \text{ max.}}, \tag{17}$$

where A, B, C, D, E, $w_{1\,\text{max.}}$ and $w_{1\,\text{min.}}$ are identical to those given in (14) with the use of the replacement (16). The decay rate is given by

$$W(\tau^- \to \nu_\tau + K^*(892)) = \frac{G^2\, m_\rho^2 \sin^2\theta_1 \cos^2\theta_3}{64\,\pi^2} \sum_{i=1}^{3} |U_{\tau_i}|^2 \Bigg[m_\tau^3 \Bigg(1 - \frac{m_{k^*}^2}{m_\tau^2}\Bigg)^2$$

$$\times \Bigg(1 + \frac{2m_{k^*}^2}{m_\tau^2}\Bigg) - 3m_i^2\, m_\tau\Bigg], \tag{18}$$

where $g^2_{\tau\, k^*\, \nu}$ (Tsai 1971) $= \dfrac{G^2\, m_\rho^2\, m_{k^*}^2 \sin^2\theta_1 \cos^2\theta_3}{8\pi}$.

Using the experimental τ^- decay time $T = (4{\cdot}6 \pm 1{\cdot}9) \times 10^{-13}$ sec and the branching ratio equal to $(1{\cdot}7 \pm 0{\cdot}7) \times 10^{-2}$ (Particle Data Group 1982), we calculate the ν_τ mass and the ratio R for this process following the procedure given in § 2·1. The results are given in table 1.

The values of ν_τ mass obtained from this decay involve large errors so much so that when mixing is included, the lower limit becomes negative. This is because of (i) large errors in the experimental values of decay time and the branching ratio for this decay and (ii) type of mixing used. The values quoted in table 1 are with the use of KM mixing. Instead, if the hierarchical mixing is used (Kalyanik and Ng 1981), the ν_τ mass limits are found to be (400 ± 580) MeV. Further if one replaces $\cos\theta_1$ by $\cos\theta_c$ and $\sin\theta_1 \cos\theta_3$ by $\sin\theta_c$, θ_c being the Cabibbo angle (Cabibbo 1963), one finds these mass-limits as (500 ± 480) MeV and (470 ± 460) MeV for KM mixing and hierarchical mixing respectively.

3. Conclusion

The ν_τ mass limits calculated for the four decays are not consistent with the experimental upper bound < 250 MeV (perhaps favoured) provided by DELCO group (Flügge 1979 and Kirkby 1979). But with the exclusion of errors, the finite masses are nearly consistent with the SLAC-LBL limit of 600 MeV (Perl *et al* 1977b) and PLUTO limit of 540 MeV (Knies 1977). The large errors in ν_τ mass values calculated are because of the large errors in the experimental parameters used in the calculations. In particular, the errors in lifetime, branching ratio and the mixing angles contribute substantially. These errors used along with KM mixing in the decay $\tau^- \to K^{*-}(892) + \nu_\tau$, renders the lower ν_τ mass limit unphysical. The discussion following relation (18) shows that in this case the type of mixing used also plays a significant role.

In view of the large uncertainties of the experimentally measured parameters, the agreement of the ν_τ mass limit with the experimental upper bound may be considered fortuitous. As such, the lack of agreement with the experimental upper bound of ν_τ mass < 250 MeV, is no disaster for the theory. With the availability of more reliable experimental data and improved statistics, these limits will undergo changes. The main result of this work is essentially an upper limit on the mass of ν_τ, of the order of 700 MeV.

The R values ≈ 1, for the decays $\tau^- \to \pi^- + \nu_\tau$, and $\tau^- \to K^- + \nu_\tau$, show that these decays are purely of weak origin with maximal parity violation, the contribution from mass mixing being insignificant. For the decay $\tau^- \to K^{*-}(892) + \nu_\tau$, reduction in the R value from one may be because of contribution from the strong decay $K^{*-}(892) \to K^- + \pi^0$. The value $R \approx 0$ for the decay $\tau^- \to \rho^- + \nu_\tau$ is because of the kinematical factors, namely, the near zero difference in π^- and π^0 masses which is not the case with K^- and π^0 masses involved in the decay $\tau^- \to K^{*-}(892) + \nu_\tau$.

Acknowledgements

The authors wish to express their sincere thanks to Prof. S Lokanathan for useful discussions. One of them (RRLS) was profitted from discussions with Mr M L Sharma. He is also grateful to the University Grants Commission for providing him financial assistance.

References

Barger V 1980 in *Proc. XX Int. Conf. High Energy Phys.* Univ. of Wisconsin, Madison, W153706
Barger V, Whisnant K and Phillips R J N 1980 *Phys. Rev.* **D22** 1636
Bergkvist K E 1972 *Nucl. Phys.* **B39** 317
Bilenky S M and Pontecorvo B 1978 *Phys. Rep.* **C41** 225
Cabibbo N 1963 *Phys. Rev. Lett.* **10** 531
De Rujula A 1981 talk given at the *IX Int. Conf. on High Energy Physics and Nuclear Structures, Varsailles*
De Rujula A and Lusignoli 1982 Ref. TH 3377-CERN Geneva
Diwakaran P P and Ramachandran R 1982 Preprint TIFR/TH/82-7
Feldman J *et al* 1981 SLAC-PUB 2819
Flügge Günter 1979 in invited talk presented at the International Conference on High Energy Physics, Geneva (Switzerland)
Kalyniak P and Ng J 1981 *Phys. Rev.* **D24** 1874
Kirkby J 1979 in *Proc. Int. Symp. on lepton and photon interactions at High Energy*, Fermi National Lab., Batavia, Illinois
Knies G 1977 *Proc. Int. Symp. on lepton and photon interactions at High Energies*, Ductsches Electronen-Synchrotron, Hamburg, Germany
Kobayashi M and Maskawa T 1973 *Prog. Theor. Phys.* **49** 652
Lyubimov V A, Novikov E G, Nozik V Z, Tretyakov E F and Kosik V S 1980 *Phys. Lett.* **B94** 226
Maki Z, Nakagawa and Sakata S 1962 *Prog. Theor. Phys.* **28** 870
Particle Data Group 1982 Review of Particle Properties *Phys. Lett.* Vol. **B111** April 1982
Perl M L *et al* 1977b *Phys. Lett.* **B70** 487
Perl M L 1979 SLAC-PUB 2446
Shrock R E and Wang L-L 1978 *Phys. Rev. Lett.* **41** 1692
Shrock R E 1980 *Phys. Lett.* **B96** 159
Tsai Y S 1971 *Phys. Rev.* **D4** 2821

Pramāṇa, Vol. 21, No. 5, November 1983, pp. 339–345. © Printed in India.

Response of Makrofol polycarbonate plastic track detector to 1.1 MeV/N $^{132}_{54}$Xe-ion

S M FARID and A P SHARMA
Department of Physics, Kurukshetra University, Kurukshetra 132 119, India

MS received 25 November 1982; revised 7 May 1983

Abstract. Makrofol polycarbonate plastic track detectors have been exposed to $^{132}_{54}$Xe -ions of energy 1·1 MeV/N from the cyclotron beam. The bulk etch rate and track etch rate are measured for different temperatures and the activation energies are calculated. The maximum etched track length is compared with the theoretically computed range. The critical energy loss is $(dE/dx)_c = 5$ MeV cm^2 mg^{-1} for this detector material.

Keywords. Solid state nuclear track detector; activation energy; track registration sensitivity; response curve; critical energy loss.

1. Introduction

In recent years solid state nuclear track detectors (SSNTDS) have found widespread applications (Fleischer *et al* 1975). In these detectors paths of individual heavily ionizing charged particles are revealed by selective chemical etching of the radiation damaged material along the particle's trajectory. The maximum etched track length provides the particle range and its energy. The length is also a measure of the mass A and charge Z of the incident particles (Price and Fleischer 1971; Fleischer *et al* 1965). In the present work we have tried to measure the range of $^{132}_{54}$Xe-ion by determining the maximum etched track length. Theoretical relations are used to compute the range of $^{132}_{54}$Xe-ion in Makrofol and the range is compared with maximum etched track length. The response curve is plotted and the critical energy loss $(dE/dx)_c$ is determined. The bulk and track etch rate are measured for different temperatures and the activation energy is calculated.

2. Experimental details

In the present study the bulk etch rate has been measured by the track diameter method (Enge *et al* 1975). In this method small areas of detectors are irradiated vertically in vacuum with fission fragments from ^{252}Cf source and then etched in NaOH solution at a constant temperature. The bulk etch rate V_b is calculated by

$$D = 2V_b\, t, \tag{1}$$

where D is the diameter of fission fragment tracks and t is the etching time.

Samples of Makrofol-E (200 μm thick) have been irradiated with $^{132}_{54}$Xe-ions of energy 1·1 MeV/N at an angle of 30° with respect to the detector surface from the cyclotron beam at the Joint Institute for Nuclear Research, Dubna, USSR. Conical tracks are observed after etching for a short time in the NaOH solution. The major and minor axis diameters are measured. The projected track length is measured from the centre of track ellipse at the etched surface to the end of the track tip. At least 50 tracks are measured each time. The corrected projection length l_p is determined by taking the geometry of tracks (Benton 1968). The true track length L (the length from the original surface to the terminal end of the track) is calculated by the relation (Dwivedi 1977; Dwivedi and Mukherji 1979).

$$L = \frac{l_p}{\cos \delta} + \frac{V_b\, t}{\sin \delta} - V_b\,(t - t_c), \tag{2}$$

where δ is the dip angle and t_c is the etching time required to etch the tracks upto the point where they stop. The track etch rate V_t is calculated using the relation (Dwivedi 1977; Dwivedi and Mukherji 1979)

$$V_t = \Delta L/\Delta t, \tag{3}$$

where ΔL is the track length increase in etching time Δt.

After exposure the plastic samples are developed for convenient times in a NaOH (6 $\pm$ 0·05) N stirred solution at a constant temperature of $\pm$ 0·5°C. All measurements are made with an Olympus microscope having an eyepiece micrometer (least count = 0·215 μm) at a total magnification of 900×.

3. Results and discussion

3.1 *Effect of temperature on bulk etch rate*

The bulk etch rate V_b is determined at 50, 60, 70, 80 and 90°C for NaOH solution. New solutions are used so that the etchant concentration remains constant throughout the experiment. The results are shown in figure 1a. It is obvious that in the temperature range applied in our experiments, the data can be well described by the Arrhenius correlation of the form

$$V_b = A \exp(-E_b/kT), \tag{4}$$

where A is a constant, k is the Boltzmann constant, E_b is the activation energy for the bulk etching and T is the temperature of etchant in °K. The activation energy is found to be $E_b = (0{\cdot}72 \pm 0{\cdot}06)$ eV which agrees with that reported by Enge *et al* (1975).

3.2 *Effect of temperature on track etch rate*

The variation of l_p with etching time when etched in 6N NaOH at 70°C is shown in

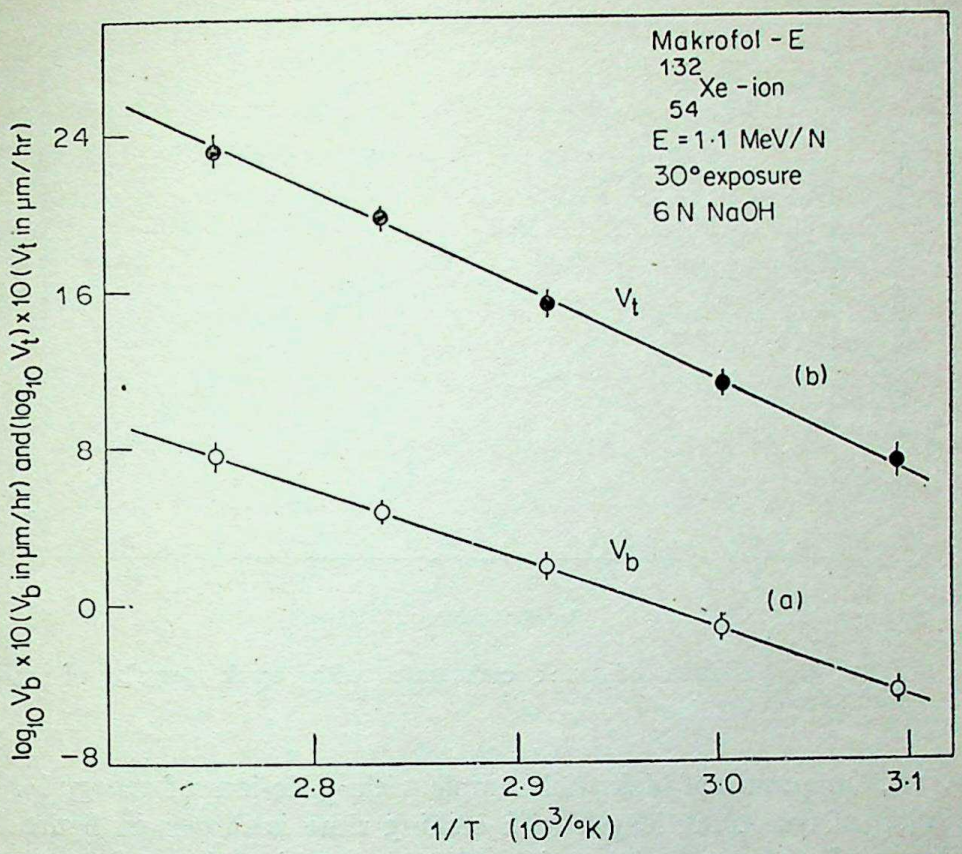

Figure 1. Variation of (a) bulk etch rate and (b) track etch rate with etching temperature for Makrofol-E exposed to 1·1 MeV/N $^{132}_{54}$Xe-ions.

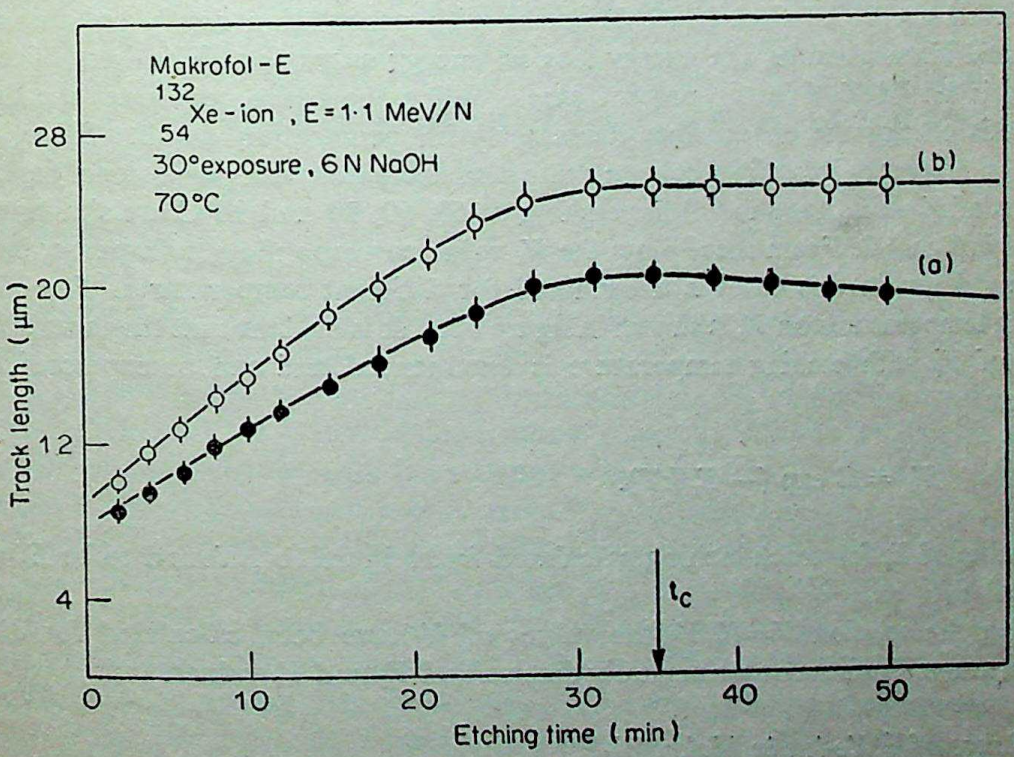

Figure 2. Variation of (a) projected track length and (b) true track length of $^{132}_{54}$Xe-ion in Makrofol-E with etching time.

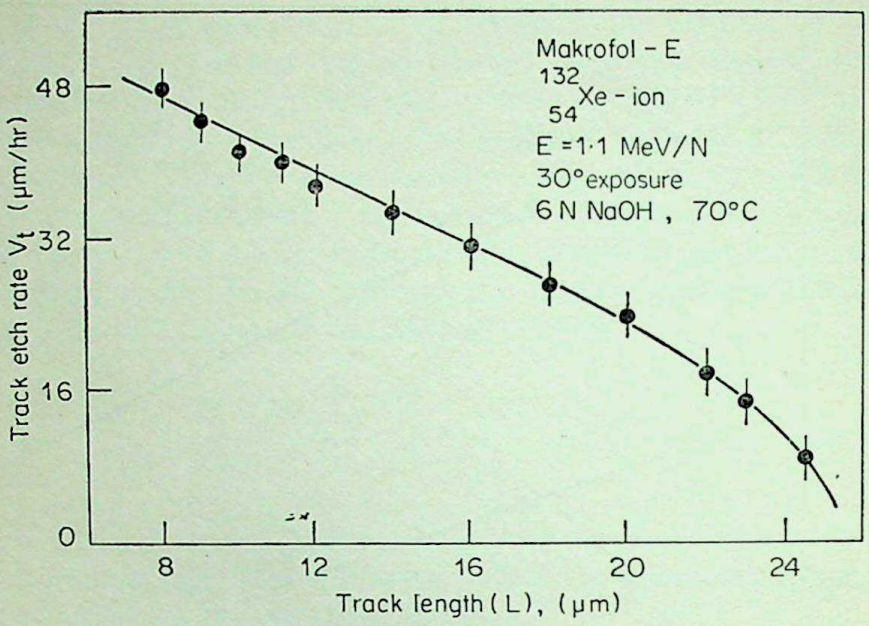

Figure 3. Variation of track etch rate with track length of $^{132}_{54}$Xe-ions in Makrofol-E.

figure 2a for 30° exposure of Makrofol sample with $^{132}_{54}$Xe-ion of energy 1·1 MeV/N. The variation of true track length with etching time is shown in figure 2b. The projected track length starts decreasing after the etching time t_c because the bulk etching shortens the completely developed track after t_c. When the bulk etching and over etching corrections are made (see equation (2)), the true track length remains constant beyond t_c (figure 2b). Figure 3 shows the variation of V_t with L for 6N NaOH at 70°C. Clearly V_t decreases with penetration depth and this can be explained if we consider the energy loss *vs* energy curve for $^{132}_{54}$Xe-ion. The beam energy is 1·1 MeV/N in the present case. When the beam penetrates the detector with this energy the energy loss decreases with penetration depth. Since V_t is a function of energy loss, the track etch rate also decreases with penetration depth.

Plots of V_t *vs* L (not shown) for etching at 50, 60, 80 and 90°C are similar to that shown in figure 3. From these plots the V_t value corresponding to a particular track length (14 μm in this case) is determined for different temperatures. The effect of etching temperatures on V_t is shown in figure 1b. It is evident that the increase in the value of V_t with etching temperature is exponential and can be expressed by the relation

$$V_t = B \exp(-E_t/kT). \tag{5}$$

The value of E_t for track etching calculated from figure 1b is found to be $E_t = (0{\cdot}70 \pm 0{\cdot}04)$ eV.

Using the relation $V = V_t/V_b$ the values of V have been calculated for different temperatures from the experimentally determined V_b and V_t values.

3.3 *Range of $^{132}_{54}$Xe-ion in Makrofol-E*

Recently, Mukherji and Nayak (1979) have given a set of equations to calculate the

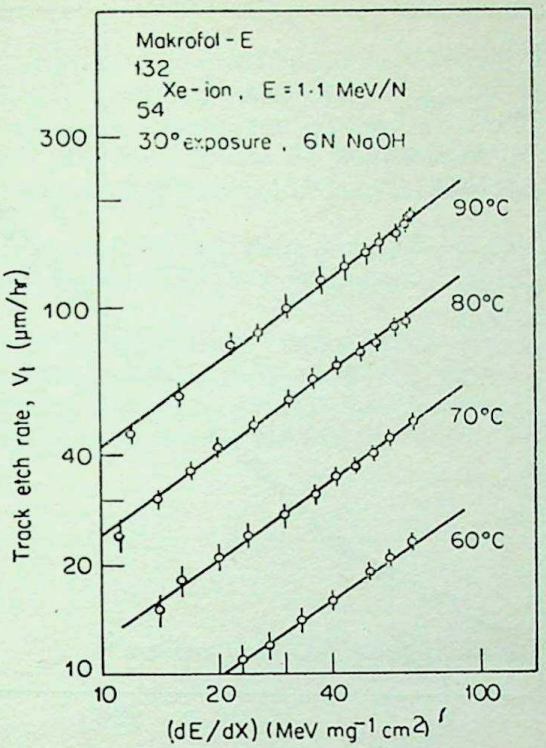

Figure 4. Variation of track etch rate with energy loss for $^{132}_{54}$Xe-ion tracks in Makrofol-E.

energy loss rate and range of heavy ions in complex media. The same procedure is followed by us to compute the range and energy loss of $^{132}_{54}$Xe-ion in Makrofol-E ($C_{16}H_{14}O_3$ and $\rho = 1{\cdot}2$ g/cm^3). The theoretical range of 1·1 MeV/N $^{132}_{54}$Xe-ion in Makrofol-E is found to be $R = 27{\cdot}27$ μm. The average length of etched tracks is calculated using (2). About 300 tracks are measured to calculate the average value. The average value of maximum etched track length with its standard deviation is $L = (25{\cdot}75 \pm 1{\cdot}02)$ μm.

3.4 *The response curve*

Using computer output, the plot of energy loss dE/dx *vs* penetration depth *i.e.* track length has been drawn (not shown). The variation of V_t with track length is shown in figure 3. Combining these two figures, the response curve [(dE/dx) *vs* V_t] for etching at 70°C is plotted on a double-logarithmic paper as shown in figure 4. The response curves for different etch bath temperatures are also presented in figure 4 and it is clear that V_t depends on dE/dx as well as on etch bath temperature.

The experimental data are transformed into the normalized track etch rate (V_t/V_b) and in figure 5 these are plotted against (dE/dx) on a linear diagram for four different temperatures. It can be seen that all our data normalized in this way belong to the same curve within the accuracy of the measurements. Thus the normalized track etch rate depends only on energy loss dE/dx and not on the etching temperatures. The solid curve is the best fit to the experimental points. This is done with the use of computer program which fits the curve of nth degree based on the principle of least-square polynomial approximation. The curve is extrapolated for the predicted values

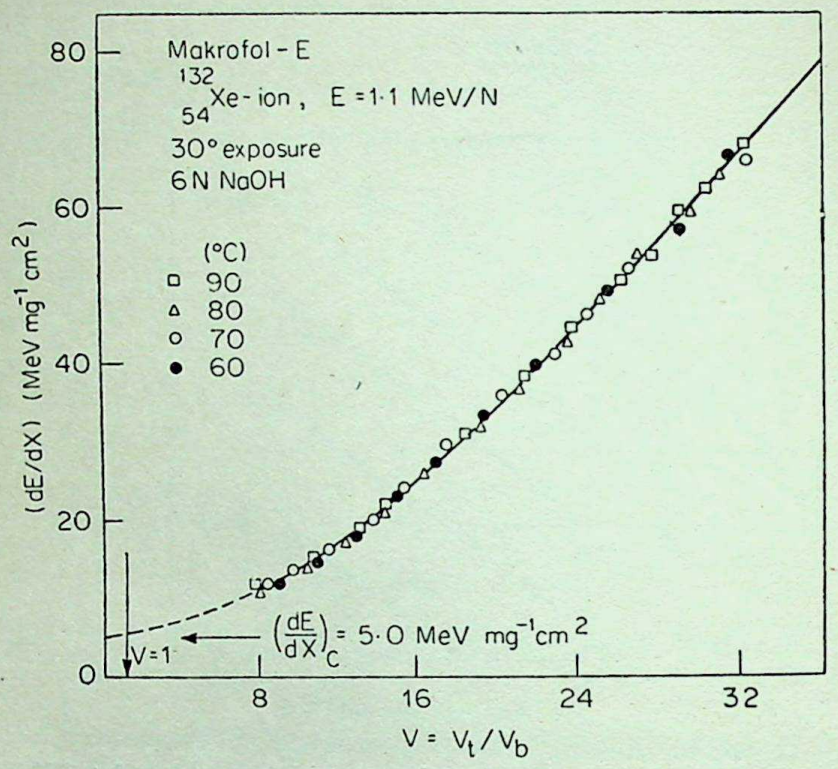

Figure 5. Variation of normalized track etch rate with energy loss for $^{132}_{54}$Xe-ion tracks in Makrofol-E.

of (dE/dx) against V. The dE/dx at which the V_t equals V_b (*i.e* $V_t/V_b=1$) is taken as the critical energy loss $(dE/dx)_c$ for track etching below which no etchable track can be produced (Tanti-Wipawin 1975). The present value of $(dE/dx)_c=5$ MeV cm^2 mg^{-1} agrees with that reported in literature (Debeauvais *et al* 1967; Fleischer *et al* 1965).

The relation between V and (dE/dx) can be expressed by the relation (Somogyi *et al* 1976; Enge *et al* 1975).

$$V = 1 + A(dE/dx)^B, \tag{6}$$

where A and B are fitting parameters. Using the computer program the A and B values are found to be $A = 0{\cdot}016$ and $B = 2{\cdot}78$. These values agree with those reported earlier (Somogyi *et al* 1976; Enge *et al* 1975).

4. Concluding remarks

The dependence of both V_b and V_t on etching temperature is exponential. The maximum etched track length can be regarded as the range of $^{132}_{54}$Xe-ion in Makrofol. The normalized track etch rate is independent of etching temperature. The critical energy loss for this detector material is relatively high as compared to other plastic detectors like CN and CR-39.

References

Benton E V 1968 Study of charged particle tracks in cellulose nitrate, USNRDL-TR-68-14

Debeauvais M, Stein R, Ralarosy J and Cure P 1967 *Nucl. Phys.* **A90** 186

Dwivedi K K 1977 *Studies of heavy ion tracks in solid dielectrics* Ph. D. Thesis, IIT, Kanpur

Dwivedi K K and Mukherji S 1979 *Nucl. Instrum. Method* **159** 433

Enge W, Grabisch K, Dallmoyer L, Bartholoma K P and Beaujean R 1975 *Nucl. Instrum. Method* **127** 125

Fleischer R L, Price P B and Walker R M 1965 *Annu. Rev. Nucl. Sci.* **15** 1

Fleischer R L, Price P B and Walker R M 1975 *Nuclear tracks in solids* (Berkeley: University of California Press)

Mukherji S and Nayak A K 1979 *Nucl. Instrum. Method* **159** 421

Price P B and Fleischer R L 1971 *Annu. Rev. Nucl. Sci.* **21** 295

Somogyi G, Grabisch K, Scherzer R and Enge W 1976 *Nucl. Instrum. Method* **134** 129

Tanti-Wipawin W 1975 *Nucl. Instrum. Method* **126** 597

Pramāṇa, Vol. 21, No. 6, December 1983, pp. 347–355. © Printed in India.

Infrared intensity analysis of $CHCl_3$ and $CDCl_3$

L D WAHEGOANKAR and N RAJESWARA RAO*
Department of Physics, Osmania University, Hyderabad 500 007, India
*3-6-416/2, Himayatnagar, Hyderabad 500 029, India

MS received 22 June 1982; revised 19 October 1983

Abstract. IR intensity formulae can be derived in the form $I = L' A$; I being square root of intensity I^2, has sign ambiguity. Equations like $I' I = A' LL' A = A' GA$ have been used to solve the sign ambiguity. There is only one equation for each species. This position has now been improved by introducing a new concept about this sign ambiguity and solved for electro-optical parameters taking a pair of molecules $CHCl_3$ and $CDCl_3$ for demonstration. This incidentally solves the sign ambiguity problem of polar tensors which are calculated for these molecules.

Keywords. Infrared intensities; polar tensors.

1. Introduction

It is well-known that $\partial P\sigma/\partial Q$, change in the σ component of dipole moment of a molecule during any oscillation Q, obtained from IR intensities can be related to electro-optical parameters by a formula

$$I = L' A, \tag{1}$$

I is written for $\partial P/\partial Q$, L' is transpose of L matrix which connects the symmetry and normal coordinates and A contains the electro-optical parameters. Since I is the square root of the intensities I^2, it has a sign ambiguity. This leads to 2^n sets, n being the number of frequencies in any species, and correspondingly so many sets of A elements. The L matrix elements derived from force constants are not generally reliable. Moreover the intensities cannot be determined with sufficient accuracy. The intensities of the strong lines can be obtained within an accuracy of 5%, and those of medium intensities to about 10%. But there is no limit to the inaccuracy of weak lines.

According to Naik and Rajeswara Rao (1979) equation (1) can be written as

$$I' I = A'LL'A = A'GA \tag{2}$$

thus eliminating all the three defects mentioned above. But this gives only one equation for each species. Therefore, we have taken similar equations from an isotopic molecule to have sufficient number of equations to solve for the eop's (Naik and Rajeswara Rao 1979). We have to admit, however, that the analysis is defective and requires improvement; we now demonstrate how it can be improved and in the

process try to throw light on the sign ambiguity problems. We shall take up a pair of molecules $CHCl_3$ and $CDCl_3$.

2. Intensity formulae

The derivation of the intensity formulae was discussed at length in our earlier papers (Naik and Rajeswara Rao 1979). We shall only give them in the forms (1) and (2). In deriving these formulae we have used terms involving change in the dipole moment of a bond with the change in the length of the other bonds also. This is called the first order approximation. However, the dipole moment of a bond is assumed to be independent of angle changes.

$\underline{A_1}$

$$I_i = A_1 L_{1i} + A_2 L_{2i} + A_3 L_{3i}; \; i = 1, 2, 3. \tag{3}$$

$\underline{E}$

$$I_i = A_4 L_{4i} + A_5 L_{5i} + A_6 L_{6i}; \; i = 4, 5, 6. \tag{4}$$

Here,

$$A_1 = \partial P_z / \partial D = \epsilon_1; \tag{5a}$$

$$A_2 = \frac{1}{3}\left(\frac{P_z}{d_1} + \frac{P_z}{d_2} + \frac{P_z}{d_3}\right) = \frac{\epsilon_2}{\sqrt{3}} \tag{5b}$$

$$A_3 = \frac{2}{\sqrt{3}}\mu_1; \tag{5c}$$

$$A_4 = \left(\frac{\epsilon_3}{\sqrt{6}} - p\right); \tag{5d}$$

$$A_5 = \left(\frac{2}{\sqrt{6}}\mu_1 + q\right); \tag{5e}$$

$$A_6 = \left(\frac{2}{\sqrt{6}}\mu_1 + r\right); \tag{5f}$$

$$\epsilon_3 = \left(2\frac{\partial P_x}{\partial d_1} - \frac{\partial P_x}{\partial d_2} - \frac{\partial P_x}{\partial d_3}\right);$$

p, q, r in (5) are given by

$$p = \frac{P_z}{\Delta}\left(-\frac{3\sqrt{3}}{2} a^3 b\,(a\,\mu_{Cl} - b\,\mu_H)\,\mu_{Cl},\right.$$

$$q = \frac{P_z}{\Delta}\left[15/(2\sqrt{6})\, a^2 b^2 \mu^2_{Cl}\,(\mu_C + \mu_H) + \frac{9}{2\sqrt{6}}\, a^2 b\, \mu_C \mu_{Cl}\,(a\,\mu_{Cl} + 4b\,\mu_H)\right],$$

$$r = \frac{P_z}{\Delta}\left[-\frac{3}{2\sqrt{6}}\, a^2\, b^2\, \mu^2_{Cl}\,(3\,a\,\mu_C + b\,\mu_C + b\,\mu_H)\right]\Big).$$

Here Δ is the determinant of the G matrix and P_z dipole moment of the molecule.

$$a = 1/d; \quad b = 1/D$$

where d and D are the C-Cl and C-H bond lengths respectively. For the two molecules we can write the following equations in the form of (2). The I_i values $= \partial P/\partial Q_i$ are taken from table 1.

A_1

$CHCl_3$

$$\Sigma I_i^2 = 0{\cdot}0744 = 0{\cdot}6525\, A_1^2 + 0{\cdot}03373\, A_2^2 + 0{\cdot}09664\, A_3^2 + 2[-0{\cdot}029\, A_1 A_2 + 0{\cdot}0656\, A_1 A_3 - 0{\cdot}0379\, A_2 A_3] \quad (6)$$

E

$$\Sigma I_i^2 = 1{\cdot}8362 = 0{\cdot}01398\, \epsilon_3^2 + 0{\cdot}8165\,(0{\cdot}0547\,\mu_1 + 0{\cdot}053\,\mu_4)\,\epsilon_3 + 30{\cdot}7879\,(0{\cdot}0547\,\mu_1 + 0{\cdot}053\,\mu_4)^2 + 45{\cdot}1754\,(0{\cdot}0526\,\mu_1 + 0{\cdot}0424\,\mu_4)^2 + 1{\cdot}2891\,(0{\cdot}066\,\mu_1 + 0{\cdot}6795\,\mu_4)^2 + 2\,[-28{\cdot}3174\,(0{\cdot}0547\,\mu_1 + 0{\cdot}053\,\mu_4)\,(0{\cdot}0526\,\mu_1 + 0{\cdot}0424\,\mu_4) - 0{\cdot}8359\,(0{\cdot}0547\,\mu_1 + 0{\cdot}053\,\mu_4)\,(0{\cdot}0662\,\mu_1 + 0{\cdot}6795\,\mu_4) - 0{\cdot}5777\,(0{\cdot}0526\,\mu_1 + 0{\cdot}0424\,\mu_4)\,(0{\cdot}0662\,\mu_1 + 0{\cdot}6795\,\mu_4)] \quad (7)$$

$CDCl_3$

A_1

$$\Sigma I_i^2 = 0{\cdot}0793 = 0{\cdot}3514\, A_1^2 + 0{\cdot}03373\, A_2^2 + 0{\cdot}0664\, A_3^2 + 2\,[-0{\cdot}029\, A_1 A_2 + 0{\cdot}0656\, A_1 A_3 - 0{\cdot}0379\, A_2 A_3] \quad (8)$$

E

$$\Sigma I_i^2 = 1{\cdot}7441 = 0{\cdot}01398\, \epsilon_3^2 + 0{\cdot}8165\,(0{\cdot}0547\,\mu_1 + 0{\cdot}053\,\mu_4)\,\epsilon_3 + 31{\cdot}3072\,(0{\cdot}0547\,\mu_1 + 0{\cdot}053\,\mu_4)^2 + 45{\cdot}4298\,(0{\cdot}0526\,\mu_1 + 0{\cdot}0424\,\mu_4)^2 + 2{\cdot}5138\,(0{\cdot}0662\,\mu_1 + 0{\cdot}3709\,\mu_4)^2 + 2\,[-27{\cdot}973\,(0{\cdot}0547\,\mu_1 + 0{\cdot}053\,\mu_4)\,(0{\cdot}0526\,\mu_1 + 0{\cdot}0424\,\mu_4) - 1{\cdot}6261\,(0{\cdot}0547\,\mu_1 + 0{\cdot}053\,\mu_4)\,(0{\cdot}0662\,\mu_1 + 0{\cdot}3709\,\mu_4) - 1{\cdot}1250\,(0{\cdot}0526\,\mu_1 + 0{\cdot}0424\,\mu_4)\,(0{\cdot}0662\,\mu_1 + 0{\cdot}3709\,\mu_4)]. \quad (9)$$

The above equations contain 5 electro-optical parameters.

$$\epsilon_1 = \partial P_z/\partial D$$

$$\epsilon_2 = \left(\frac{\partial P_z}{\partial d_1} + \frac{\partial P_z}{\partial d_2} + \frac{\partial P_z}{\partial d_3}\right);\ \epsilon_3 = \left(2\frac{\partial P_x}{\partial d_1} - \frac{\partial P_x}{\partial d_2} - \frac{\partial P_x}{\partial d_3}\right)$$

μ_1 (dipole moment of C-Cl) and μ_4 (dipole moment of CH or CD). We can take the dipole moment of the whole molecule as derived from dielectric constant measurements as the fifth equation.

$$P_z = \mu_1\, 1z + \mu_2\, 2z + \mu_3\, 3z + \mu_4\, 4z. \tag{10}$$

This makes $-1{\cdot}01 = -\mu_1 + \mu_4$. Here P_z is the dipole moment of the molecule along z (CH or CD) direction. Since $P_x = P_y = 0$, P_z is the value for the whole molecule (Weast 1969). We take $\mu_1 = \mu_2 = \mu_3$. $1z$, $2z$ and $3z$ are direction cosines of d's and $4z$ of D. We can write equations similar to (10) for P_x and P_y also. Now,

$$\frac{\partial P_z}{\partial D} = 1z\frac{\partial \mu_1}{\partial D} + 2z\frac{\partial \mu_2}{\partial D} + 3z\frac{\partial \mu_3}{\partial D} + 4z\frac{\partial \mu_4}{\partial D}$$

$$= \frac{\partial \mu_1}{\partial D}(1z + 2z + 3z) + 4z\frac{\partial \mu_4}{\partial D} \tag{11}$$

Here, $\partial\mu_4/\partial D$ is dipole moment of CH (or CD) with respect to D. This is called the zero order term and $\partial\mu_1/\partial D$ the first order term. The *eop*'s we have to determine are groups like this.

I_i in equations (6)—(9) are taken from Morcillo *et al* (1969) and are given in table 1.

3. Intensity analysis

In equations (6) and (8) all terms except ϵ_1^2 are common. Also, ΣI_i^2 is almost the

Table 1. Frequencies and IR intensities.

Species	Frequency (cm^{-1})		$\frac{\partial P}{\partial Q}$	
	$CHCl_3$	$CDCl_3$	$CHCl_3$	$CDCl_3$
A_1	3034	2259	0·0676	0·0293
	681	655	0·2505	0·2723
	366	362	0·0844	0·0654
E	1221	914	0·4732	0·7899
	769	744	1·2696	1·0582
	258	258	0·0189	0·0189

same, so that we have $\epsilon_1 = 0$. In the E type equations, substituting for μ_1 from (10) and subtracting (9) from (7) results in

$$0{\cdot}2414\ \mu_4^2 + 0{\cdot}3371\ \mu_4 + 0{\cdot}04006 = -\ 0{\cdot}09207, \tag{12}$$

(four figures are used here for computational consistency).

This makes μ_4 imaginary and the analysis defective. The left side of (12) is mostly the contribution of the wagging mode to the intensity which is small. While the sum of the intensities is large, in both (7) and (9), the difference is very small and is of the same order of magnitude as error in their determination. Since the intensity of the wagging mode is small, the accuracy of its determination is very low. Hence, the right side of (12) can be very different from the value shown. This defect shows itself whenever difference equations like (12) are to be used for evaluation of *eop's*. Now, we propose to solve the problem by trying to understand the sign ambiguity of I. One of the equations of (1) can be written as

$$I_1 = A_1L_{11} + A_2L_{21} + A_3L_{31} = A{\cdot}L_1. \tag{13}$$

The vector ($L_{11}\ L_{21}\ L_{31}$) which is obtained from force constants, can have a positive or a negative sign. If the sign of L_{11} changes, the sign of the other elements also have to change. Therefore, since A_1, A_2, A_3 are constants, the sign of I_1 is dependent on the sign of L_1 only. Table 2 gives the L matrices of A_1 species of $CHCl_3$ and $CDCl_3$ obtained by us from Raman intensity analysis.

It can be easily seen that the G elements are independent of the signs of the L vectors (column triplets referring to frequencies). But we have arranged these vectors so that they have the same sign for the two molecules. Since we are assuming that the A's are the same for the two molecules (as they have the same electronic configuration) for any frequency, if we take the L vectors of the same sign, the I's also will be of the same sign, though the exact sign cannot be judged.

Now, in A_1 species, I_2 is large in the two molecules, compared to I_1 or I_3. Therefore, we shall take it that it is determined with reasonable accuracy. Writing these equations, we have

$$\pm\ 0{\cdot}2505 = A_2L_{22} + A_3L_{32} \text{ for } CHCl_3, \tag{14}$$

$$\pm\ 0{\cdot}2723 = A_2L'_{22} + A_3L'_{32} \text{ for } CDCl_3. \tag{15}$$

Table 2. L matrices of A_1 species.

	L		
$CHCl_3$	0·8708	0·0045	0
	− 0·0367	0·1553	0·092
	0·0820	− 0·2803	0·0983
$CDCl_3$	0·5928	0·0021	0
	− 0·0483	0·1539	0·0891
	0·1087	− 0·2693	0·1031

Since $A_1 = 0$, it does not occur in these equations. Primes on L_{22} and L_{32} indicate that they are for $CDCl_3$. In these equations the signs on the left are both positive or both negative. It is now possible to eliminate the intensities and get an eliminant equation

$$0 = A_2 (0{\cdot}2723\, L_{22} - 0{\cdot}2505\, L'_{22}) + A_3 (0{\cdot}2723\, L_{32} - 0{\cdot}2505\, L'_{32}). \quad (16)$$

This provides the third equation for A_1 species, and A_2 and A_3 can be evaluated. But often when we deal with isotopic molecules that are similar and have nearly equal L vectors also, so that the coefficients of A_2 and A_3 in (16), are very small, the equation becomes unreliable. This is particularly so because, the L vectors cannot be determined with great accuracy in spite of one using Coriolis interaction constants and rotation distortion constants.

But (14) or (15) can be individually used with some advantage. Now using (14) and the eliminant of A_1 from (6) and (8), one can calculate

$$\mu_1 = \pm 0{\cdot}6984;\ \mu_4 = 0{\cdot}3116, \quad (17)$$

using (15)

$$\mu_1 = \pm 0{\cdot}7786;\ \mu_4 = 0{\cdot}2314. \quad (18)$$

A negligibly small negative sign under square root in the evaluation of these values is neglected, as it is attributable to small errors in I_2 or L's.

Now, in (10) since μ_4 (μ_{C-H}) is much smaller than μ_1 (μ_{C-Cl}), μ_1 has to be positive which means it is in the C—Cl direction. Considering that there is some error in the determination of I_2 as well as L's the closeness of the μ_1 values is good. This enables us to determine A_2.

In the expanded forms,

$$\epsilon_1 = \frac{\partial \mu_4}{\partial D} - \frac{\partial \mu_1}{\partial D} = 0,$$

$$\epsilon_2 = \frac{\partial \mu_1}{\partial d_1} + \frac{2\partial \mu_2}{\partial d_1} - 3\frac{\partial \mu_4}{\partial d_1} = -5{\cdot}32 \text{ or } -5{\cdot}79,$$

$$\epsilon_3 = \frac{\partial \mu_1}{\partial d_1} - \frac{\partial \mu_2}{\partial d_1} = -4{\cdot}22.$$

In the expressions for ϵ_2 and ϵ_3, $\partial\mu_2/\partial d_1$ is the first order term. Seeing the closeness of ϵ_2 and ϵ_3 the first order terms are perhaps small. In ϵ_1, this is not to be regarded as an equation between $\partial\mu_4/\partial D$ and $\partial\mu_1/\partial D$ since both of them are small and negligible.

Another point of interest is that it is not possible to separately evaluate $\partial\mu_1/\partial d_1$ and $\partial\mu_2/\partial d_1$, the zero order and first order terms.

4. Polar tensors

IR intensity is analysed in another way. In the above method, we have started with a model. We have assumed that the dipole moment of a molecule is the vectorial sum of dipole moments of its bonds. Also, we have taken the dipole moment to be along the bond. It is not obvious that the electronic distribution should be symmetrical with respect to a bond. In fact, Sverdlov (1961, 1963) referred to by Allen Rupprecht (1981) has shown that the dipole moment need not be along the bond and it can have components perpendicular to it. Therefore, bond dipole moment theory may be too much of a simplification.

Biarge *et al* (1961), referred to by Newton and Person (1976), have suggested a method of avoiding a specific model. They defined a tensor

$$P_x(a) = \begin{vmatrix} \frac{\partial P_x}{\partial x_a} & \frac{\partial P_x}{\partial y_a} & \frac{\partial P_x}{\partial z_a} \\ \frac{\partial P_y}{\partial x_a} & \frac{\partial P_y}{\partial y_a} & \frac{\partial P_y}{\partial z_a} \\ \frac{\partial P_z}{\partial x_a} & \frac{\partial P_z}{\partial y_a} & \frac{\partial P_z}{\partial z_a} \end{vmatrix}$$

for each atom a. The elements show how the dipole moment of the whole molecule changes as the atoms move in various directions. This can be obtained from

$$P_X = (\partial P/\partial X) = (\partial P/\partial Q)\,(\partial Q/\partial S)\,(\partial S/\partial R)\,(\partial R/\partial X)$$

$$= I'\,L^{-1}\,UB \tag{19}$$

$$= A'\,UB \tag{19a}$$

Table 4. Polar tensors.

Molecule	Cl_1			H			C		
	X	Y	Z	X	Y	Z	X	Y	Z
$CHCl_3$									
P_x	0	0·1670	0	0	−0·6553	0	0	−4·8983	0
P_y	3·5354	0	1·5973	−0·6553	0	0	−4·8983	0	0
P_z	−1·7955	0	−0·2425	0	0	0	0	0	0·7274
$CDCl_3$									
P_x	0	0·1923	0	0	−0·6594	0	0	−4·9339	0
P_y	3·5366	0	1·6084	−0·6594	0	0	−4·9339	0	0
P_z	−1·7955	0	−0·2425	0	0	0	0	0	0·7274

Table 3. Expressions for polar tensors.

	Cl_1			H			C		
	x	y	z	x	y	z	x	y	z
$\frac{\partial P_x}{\partial \sigma}\frac{\partial P_x}{\partial Q_i}$	—	$\frac{-\sqrt{3}a}{\sqrt{2}}A_5$	—	—	$\frac{\sqrt{3}b}{\sqrt{2}}A_6$	—	—	$\left\{\frac{2}{\sqrt{3}}A_4+\frac{2\sqrt{2}a}{\sqrt{3}}A_5-\frac{\sqrt{3}}{\sqrt{2}}(a/3+b)A_6\right\}$	—
$\frac{\partial P_y}{\partial \sigma}\frac{\partial P_y}{\partial Q_i}$	$\left\{\frac{-4}{3\sqrt{3}}A_4+\frac{a}{3\sqrt{6}}A_5+\frac{2a}{3\sqrt{6}}A_6\right\}$	—	$\left\{\frac{-2}{3\sqrt{6}}A_4-\frac{2a}{3\sqrt{3}}A_5-\frac{4a}{3\sqrt{3}}A_6\right\}$	$\frac{\sqrt{3}b}{\sqrt{2}}A_6$	—	—	$\left\{\frac{2}{\sqrt{3}}A_4+\frac{2\sqrt{2}a}{\sqrt{3}}A_5-\frac{\sqrt{3}}{\sqrt{2}}(a/3+b)A_6\right\}$	—	—
$\frac{\partial P_z}{\partial \sigma}\frac{\partial P_z}{\partial Q_i}$	$\left\{\frac{-2\sqrt{2}}{3\sqrt{3}}A_2-\frac{2a}{3\sqrt{6}}A_3\right\}$	—	$\left\{\frac{-1}{3\sqrt{3}}A_2+\frac{4a}{3\sqrt{3}}A_3\right\}$	—	—	A_1	—	—	$\left\{-A_1+\frac{A_2}{\sqrt{3}}-\frac{4a}{\sqrt{3}}A_3\right\}$

σ indicates x_a, y_a and z_a.

I' is transpose of I and using (1), L and L^{-1} cancel off. Newton and Person (1976) have however used (19) and obtained P_x for various atoms. Their procedure suffers from all the defects that the earlier workers experienced in evaluating the *eop*'s. (i) I, having sign ambiguity, means that we can have 2^n sets of the row vector I'. (ii) Evaluation of L^{-1} matrix from force constants which are uncertain and (iii) Inaccuracy in the determination of I elements will affect these results also.

Our suggestion of using (19a) takes away all these defects, but we need a model. Therefore, we look at the polar tensor problem as a check on the model, so that one can improve the theory to make the polar tensors obtained by (19) and (19a) to be equal. In any case, this method dispenses with sign ambiguity trouble once for all. While choosing the signs of I's and L^{-1} vectors, one can look for the values obtained from (19a). Then, the differences in the numerical values can be discussed to improve either the model or the methods of determining L^{-1} elements.

We now give the polar tensors of $CHCl_3$ and $CDCl_3$ using (19a) both in the form of expressions and in numbers.

We are now not discussing a rotation correction that is necessary to get P_X. This comes about because the B matrix is rectangular and rotation and translation of the molecule have to be added to make it, a square. These corrections have been worked out by Newton and Person (1976). They have to be added to (19) as well as (19a) to get the correct P_X. But, for the purpose we have suggested, rotation correction need not be considered.

In table 3, we have given expressions only for Cl_1 as those for Cl_2 and Cl_3 can be obtained by symmetry operations. Similarly in table 4, columns under Cl_2 and Cl_3 can be obtained by symmetry operation on Cl_1.

References

Allan Rupprecht 1981 *J. Mol. Spectrosc.* **89** 356
Biarge J F, Herrans J and Morcillo J 1961 *Ann. R. Soc. ESP. Fis. Quim.* **A57** 81
Morcillo J, Biarge J F, Heredin J M V and Medina A 1969 *J. Mol. Struct.* **3** 77
Newton J H and Person W B 1976 *J. Chem. Phys.* **64** 3036
Pratibha Naik and Rajeswara Rao N 1979 *Pramana* **12** 505
Sverdlov L M 1961 *Opt. Spectrosc.* **10** 76, 371
Sverdlov L M 1963 *Opt. Spectrosc.* **15** 72
Weast C R 1968 *Hand book of Chemistry and Physics* (Cleveland Chicago: Chemical Rubber Co.) 49th edn.

Pramāṇa, Vol. 21, No. 6, December 1983, pp. 357–367. © Printed in India.

Lattice sum of electric field gradients in tetragonal crystals

D P VERMA*, A YADAV and H C VERMA
Department of Physics, *Department of Mathematics, Science College, Patna 800 005, India

MS received 29 June 1983; revised 20 October 1983.

Abstract. A new method to calculate the lattice contribution to electric field gradients at a nuclear site in tetragonal crystals is developed. The crystal is regarded as an assembly of positive ions at lattice points embedded in a uniform background of negative charge (point charge model). The method uses Euler-Maclaurin formula and makes the plane-wise summation in the direct crystal space unlike most of the previous methods utilising Fourier transform to reciprocal space. The numerical values obtained using the above approach agree well with previous results.

Keywords. Electric field gradient; lattice sum; convergence; tetragonal crystals; Euler-Maclaurin formula.

1. Introduction

Electric field gradients (EFG) have played an important role in providing insight of the electric charge distribution surrounding a nuclear site, shielding-antishielding mechanism, electron-phonon interactions etc. This quantity can be experimentally measured using Mössbauer effect, NQR, PAC etc techniques. A large number of such measurements were made during recent years and interesting systematic trends of EFG were pointed out (Christiansen *et al* 1976; Raghavan *et al* 1976). An excellent review on the subject has been presented by Kaufman and Vianden (1979).

The EFG in a metal is conventionally separated into ionic and electronic parts, the former being due to the positive ions of the lattice outside the atom containing the nucleus of interest and the latter due to conduction electrons. The distortion of the otherwise spherical atomic core due to the electric field of lattice ions is taken into account by multiplying the lattice EFG by the 'Sternheimer antishielding factor' (Sternheimer 1954, 1954a) $(1 - \gamma_\infty)$. The total EFG is thus written as

$$eq = eq_{\text{latt}}\,(1 - \gamma_\infty) + eq_{\text{electron}}. \tag{1}$$

The lattice contribution eq_{latt} is represented by a sum over lattice points

$$eq_{\text{latt}} = \sum_{\alpha}{}' \frac{Ze}{4\pi\,\epsilon_0}\,\frac{3\,z_\alpha^2 - r_\alpha^2}{r_\alpha^5}, \tag{2}$$

where z_α is the z-coordinate and r_α the distance of αth lattice point from the origin situated at the nucleus of interest. The summation runs through all the lattice points

except the one containing origin and this is indicated by a ' prime ' over the summation.

The interest in the lattice EFG has been greatly enhanced after the identification of the so called ' universal correlation ' (Raghavan *et al* 1976) between the lattice and electronic parts of EFG. This correlation may be expressed as

$$eq = eq_{\text{latt}}\ (1 - \gamma_\infty)\ (1 - K), \tag{3}$$

where $K = 2 \sim 5$. Thus the complicated electronic contributions may be estimated from the knowledge of (2). This offers a great simplification as the first principle calculation of the electronic part needs a knowledge of electronic wavefunctions and crystal potentials, which are available for only relatively few metals.

The sum in (2) is known to converge extremely slowly. Techniques have been developed to improve the convergence. The basic idea of the method developed by Simmons and Slichter (1961) is to divide the crystal into electrically neutral polyhedra and sum the contributions from the multipole moments of each external cell. Another rapidly converging procedure involving transformation to reciprocal lattice space was introduced by Ewald (1921) and was further developed by Nijboer and de Wette (1957, 1958). This method has since been widely applied to get the lattice EFG (de Wette 1961; Das and Pomerantz 1961; de Wette and Schacher 1965; Dickmann and Schacher 1967; etc.). We here report a new method to evaluate the sum in (2) in the direct lattice space itself for a simple tetragonal lattice. The results match with those given by de Wette (1961) employing the Fourier transform methods.

2. Theoretical formulation

The sum in (2) is conditionally convergent. It means that its value depends on the shape of the boundary of the infinite crystal (de Wette 1961). The EFG at a lattice point which receives contributions from positive charges as well as from negative background, however, is not an ambiguous quantity and is independent of the shape. This EFG may be written as

$$eq = \int \frac{\rho(\mathbf{r})}{4\pi\,\epsilon_0}\,\frac{3z^2 - r^2}{r^5}\,\mathrm{d}^3\,\mathbf{r} + \frac{Ze}{4\pi\,\epsilon_0}\sum_a{}' \frac{3z_a^2 - r_a^2}{r_a^5}. \tag{4}$$

Assuming a uniform negative background making the crystal electrically neutral, $\rho(\mathbf{r}) = Ze/v$, where v is the volume of the unit cell. Both the terms are conditionally convergent and the values of the terms depend on the order of summation inside Σ' and the boundary shape of crystal in the integration. We can choose the order of summation that is most advantageous, but the integration has to be done accordingly. We follow the order used by de Wette (1961), *i.e.* we choose the z axis along the c axis of the tetragonal crystal and make summation in the planes $z = 0, \pm c, \pm 2c$, etc. and then add these partial sums. This summation order means that we take the shape of the crystal to be a slab of infinite thickness with faces perpendicular to the c axis.

The integration in (4) is

$$\int \frac{3z^2 - r^2}{r^5} \, \mathrm{d}^3 \mathbf{r} = -8\pi/3 \tag{5}$$

for such a slab-shaped crystal (de Wette 1961). The sum over the lattice is

$$S_0 = \frac{Ze}{4\pi\epsilon_0 a^3} \sum_{n_3=-\infty}^{\infty} \sum_{n_2=-\infty}^{\infty} \sum_{n_1=-\infty}^{\infty} \frac{2n_3^2 \alpha^2 - n_1^2 - n_2^2}{\{n_1^2 + n_2^2 + n_3^2 \alpha^2\}^{5/2}} \tag{6}$$
(except origin)

for a tetragonal crystal where $\alpha = c/a$. The summations over n_1 and n_2 are to be carried out before summation over n_3.

2.1 *Contribution of baseplane* ($z = 0$)

The contribution to

$$\left(\frac{4\pi\epsilon_0 a^3}{Ze} S_0\right)$$

from the baseplane is

$$A_0 = \sum_{n_2=-\infty}^{\infty} \sum_{n_1=-\infty}^{\infty} \frac{-1}{(n_1^2 + n_2^2)^{3/2}}, \tag{7}$$
(except origin)

$$= -4 \sum_{n_2=1}^{\infty} \sum_{n_1=0}^{\infty} \frac{1}{(n_1^2 + n_2^2)^{3/2}}.$$

The Euler-Maclaurin (EM) formula (Hildebrand 1956) is

$$\sum_{n=M}^{N} f(n) = \int_M^N f(x)\,\mathrm{d}x + \tfrac{1}{2}\{f(N) + f(M)\} + \int_M^N P_1(x) \frac{\mathrm{d}f(x)}{\mathrm{d}x}\,\mathrm{d}x$$

where $P_1(x) = x - 1/2$ for $0 < x < 1$ and is defined outside this region by $P_1(x+1) = P_1(x)$.

Applying this to summation over n_1 and replacing the dummy index n_2 by n, we get

$$\sum_{n_1=0}^{\infty} \frac{1}{(n_1^2+n_2^2)^{3/2}} = \int_0^{\infty} \frac{dx}{(x^2+n^2)^{3/2}} + \frac{1}{2n^3} + \int_0^{\infty} P_1(x) \frac{-3x\,dx}{(x^2+n^2)^{5/2}}$$

$$= \frac{1}{n^2} + \frac{1}{2n^3} - \int_0^{\infty} \frac{3\,P_1(x)\,x\,dx}{(x^2+n^2)^{5/2}}$$

Hence $$A_0 = -4\sum_{n=1}^{\infty}\frac{1}{n^2} - 2\sum_{n=1}^{\infty}\frac{1}{n^3} + 12\sum_{n=1}^{\infty}\int_0^{\infty}\frac{P_1(x)\,x\,dx}{(x^2+n^2)^{5/2}}$$

$$= -4\zeta(2) - 2\zeta(3) + 12\sum_{n=1}^{\infty}\int_0^{\infty}\frac{P_1(x)\,x\,dx}{(x^2+n^2)^{5/2}}$$

$$= -8{\cdot}9838500 + \epsilon(\infty), \tag{8}$$

where $\zeta(2) = \pi^2/6$ and $\zeta(3) = 1{\cdot}20205690\ldots$ are Riemann zeta functions at 2 and 3 respectively and $\epsilon(\infty)$ is the term involving integral in the expression of A_0. To estimate $\epsilon(\infty)$ we apply the above procedure to the finite sum

$$A_0(N) = \sum_{n_2=-N}^{N}\sum_{n_1=-N}^{N}\frac{-1}{(n_1^2+n_2^2)^{3/2}},$$
(except origin)

and get

$$A_0(N) = \sum_{n=1}^{N}\frac{-4N}{n^2(N^2+n^2)^{1/2}} - 2\sum_{n=1}^{N}\frac{1}{n^3}$$

$$-2\sum_{n=1}^{N}\frac{1}{(N^2+n^2)^{3/2}} + 12\sum_{n=1}^{N}\int_0^{N}\frac{P_1(x)\,x\,dx}{(x^2+n^2)^{5/2}}$$

or $$\epsilon(N) = 12\sum_{n=1}^{N}\int_0^{N}\frac{P_1(x)\,x\,dx}{(x^2+n^2)^{5/2}}$$

$$= -4\sum_{n_2=1}^{N}\sum_{n_1=0}^{N}\frac{1}{(n_1^2+n_2^2)^{3/2}} + 4N\sum_{n=1}^{N}\frac{1}{n^2(N^2+n^2)^{1/2}}$$

$$+2\sum_{n=1}^{N}\frac{1}{n^3} + 2\sum_{n=1}^{N}\frac{1}{(N^2+n^2)^{3/2}}. \tag{9}$$

As will be discussed later, our results are expected to have an accuracy up to the fifth decimal place. The quantity $|\epsilon(\infty)-\epsilon(N)|$ is discussed in the appendix and it is shown that $\epsilon(80)$ gives a good enough approximation of $\epsilon(\infty)$ for the present calculations. Evaluating the right side of (9) with $N = 80$ we get $\epsilon(80) = -0{\cdot}04976934$ and using this for $\epsilon(\infty)$ in (8) we get

$$A_0 = -9{\cdot}033619, \tag{10}$$

which compares well with the corresponding value ($-9{\cdot}033621$) obtained by de Wette (1961).

2.2 *Contribution of plane* $z = n_3 a = k$

The contribution of plane $z = n_3 a = k$ to $\left(\frac{4\pi\epsilon_0 a^3}{Ze} S_0\right)$ is

$$A_k = \sum_{n_1=-\infty}^{\infty} \sum_{n_2=-\infty}^{\infty} \frac{2k^2 - (n_1^2 + n_2^2)}{(k^2 + n_1^2 + n_2^2)^{5/2}}$$

$$= 4 \sum_{n_1=0}^{\infty} \sum_{n_2=0}^{\infty} \frac{2k^2 - (n_1^2 + n_2^2)}{(k^2 + n_1^2 + n_2^2)^{5/2}}$$

$$- 4 \sum_{n=0}^{\infty} \frac{2k^2 - n^2}{(k^2 + n^2)^{5/2}} + \frac{2}{k^3}. \tag{11}$$

Using EM formula we have

$$\sum_{n=0}^{\infty} \frac{3k^2 - A^2 - n^2}{(A^2 + n^2)^{5/2}} = \frac{2k^2 - A^2}{A^4} + \frac{3k^2 - A^2}{2A^5}$$

$$+ \int_0^{\infty} \frac{3P_1(x)\, x\, (x^2 + A^2 - 5k^2)}{(A^2 + x^2)^{7/2}} \mathrm{d}x. \tag{12}$$

Making use of this result in the summation over n_2 in the double summation in (11) and replacing the dummy index n_1 by n, we have,

$$A_k = 4 \sum_{n=0}^{\infty} \left\{ \frac{2k^2}{(k^2 + n^2)^2} - \frac{1}{k^2 + n^2} \right\} - 2 \sum_{n=0}^{\infty} \frac{3k^2 - k^2 - n^2}{(k^2 + n^2)^{5/2}}$$

$$+ \frac{2}{k^3} + 12 \sum_{n=0}^{\infty} \int_0^{\infty} \frac{P_1(x)\, x\, (x^2 + n^2 - 4k^2)}{(x^2 + n^2 + k^2)^{7/2}} \mathrm{d}x. \tag{13}$$

The first and second series in this equation can be exactly summed using Cauchy formulae for contour integration

$$\sum_{n=0}^{\infty} \frac{1}{(k^2+n^2)^2} = \frac{\pi}{4}\left\{\frac{\coth(\pi k)}{k^3} + \frac{\pi \operatorname{cosech}^2(\pi k)}{k^2}\right\} + \frac{1}{2k^4}$$

and,
$$\sum_{n=0}^{\infty} \frac{1}{k^2+n^2} = \frac{1+\pi k \coth(\pi k)}{2k^2}.$$

The third series of (13) can be expanded using the result (12) and then A_k becomes

$$A_k = 2\pi^2 \operatorname{cosech}^2(\pi k) + \epsilon_k(\infty) \tag{14}$$

where
$$\epsilon_k(\infty) = -6\int_0^{\infty} \frac{P_1(x)\, x\,(x^2-4k^2)}{(k^2+x^2)^{7/2}}\,dx$$

$$+12\sum_{n=0}^{\infty}\int_0^{\infty} \frac{P_1(x)\, x\,(x^2+n^2-4k^2)}{(x^2+n^2+k^2)^{7/2}}\,dx.$$

Again to evaluate $\epsilon_k(\infty)$ we apply the above procedure to the finite sum:

$$A_k(N) = \sum_{n_1=-N}^{N}\sum_{n_2=-N}^{N} \frac{2k^2-n_1^2-n_2^2}{(k^2+n_1^2+n_2^2)^{5/2}}$$

and get,

$$\epsilon_k(N) = -6\int_0^{N} \frac{P_1(x)\, x\,(x^2-4k^2)}{(k^2+x^2)^{7/2}}\,dx$$

$$+12\sum_{n=0}^{N}\int_0^{N} \frac{P_1(x)\, x\,(x^2+n^2-4k^2)}{(k^2+n^2+x^2)^{7/2}}\,dx$$

$$=4\sum_{n_1=0}^{N}\sum_{n_2=0}^{N} \frac{2k^2-n_1^2-n_2^2}{(k^2+n_1^2+n_2^2)^{5/2}} - 4\sum_{n=0}^{N} \frac{2k^2-n^2}{(k^2+n^2)^{5/2}}$$

$$+\frac{2}{k^3} - \left\{4\sum_{n=0}^{N} \frac{k^2 N(2N^2+3k^2+3n^2)}{(N^2+k^2+n^2)^{3/2}(k^2+n^2)^2}\right.$$

$$+\frac{1}{2}\frac{2k^2-n^2-N^2}{(k^2+n^2+N^2)^{5/2}}-\frac{N}{(k^2+n^2+N^2)^{1/2}(k^2+n^2)}\Bigg\}$$

$$+\frac{2k^2-N^2}{(k^2+N^2)^{5/2}}+\frac{2N(2N^2+3k^2)}{k^2(k^2+N^2)^{3/2}}-\frac{2N}{k^2(k^2+N^2)^{1/2}}. \qquad (15)$$

We evaluate $\epsilon_k(N)$ for $N = 80$ and substitute it for $\epsilon_k(\infty)$ in (4) as we did to calculate the contribution due to base plane.

3. Results and discussion

The different terms in (15) have different orders of magnitude. The largest order is for the third series of (15) and its value for $k = 1$ is $-10{\cdot}46462$ as given by computer in an eight digit mantissa calculation. Thus the accuracy of this term is 10^{-5}. As the absolute errors add in addition or subtraction the values of $\epsilon(k)$ thus obtained may be accurate only up to the fifth decimal place. We made calculations for three crystals with $c/a = 1$, 1·1 and 1·5. Contributions due to planes $|z| > 4$ are found to ' zero ' within the mentioned error limits.

Table 1. Lattice EFG in tetragonal crystals in units of $Ze/(4\pi\,\epsilon_0\,a^3)$.

c/a	$k = n_3\,c/a$	$2\pi^2$ cosec h$^2\,\pi k$	ϵ_k	$\epsilon_k + 2\pi^2$ cosech$^2\,\pi k$
1	1	0·14800	0·17947	0·32747
	2	0·00028	0·00028	0·00056
	3	0·00000	0·00000	0·00000
	4	0·00000	0·00000	0·00000
	$B_0 = 0{\cdot}32803$		$2B_0 = 0{\cdot}65606$	$A_0 + 2B_0 = -8{\cdot}37756$
1·1	1·1	0·07882	0·09166	0·17048
	2·2	0·00008	0·00008	0·00016
	3·3	0·00000	0·00000	0·00000
	4·4	0·00000	0·00000	0·00000
	$B_0 = 0{\cdot}17064$		$2B_0 = 0{\cdot}34128$	$A_0 + 2B_0 = -8{\cdot}69234$
1·5	1·5	0·00637	0·00674	0·01311
	3·0	0·00000	0·00000	0·00000
	4·5	0·00000	0·00000	0·00000
	6·0	0·00000	0·00000	0·00000
	$B_0 = 0{\cdot}01311$		$2B_0 = 0{\cdot}02622$	$A_0 + 2B_0 = -9{\cdot}00740$

Values from de Wette (1961) for the three cases are $-8{\cdot}37758$, $-8{\cdot}69234$ and $-9{\cdot}00740$ respectively.

The contribution to $(4\pi\epsilon_0 a^3/Ze)\ S_0$ from baseplane is $A_0 = -9{\cdot}03362$ (equation (10)) and from other planes is $2\,B_0$ where B_0 is the sum of contribution from the plane $z = c$, $2c$, $3c$ and $4c$. These values are given in table 1 together with the values of de Wette (1961) for comparison. It is seen that the present values are in excellent agreement with the previous calculations.

The EFG in point change model eq_{ion} is obtained by adding the contribution of negative background to $(A_0 + 2B_0)$. For $c/a = 1$, this EFG is zero. This is expected from symmetry as the crystal reduces to a simple cubic for this value of c/a.

4. Conclusion

Euler Maclaurin summation formula is used to sum the extremely slowly convergent lattice sum of electric field gradient at a nuclear site in simple tetragonal lattice. The summation is carried out in the direct lattice space itself, contrary to the popular methods employing Fourier transforms to work in reciprocal space. To reproduce the known results up to five decimal places it is sufficient to make numerical summation of certain series up to $N = 80$.

Acknowledgement

The authors are thankful to the authorities of IIT, Kanpur for computation facilities.

Appendix

Estimation of $\epsilon(\infty) - \epsilon(N)$

The contribution from baseplane to the EFG is given by(8) containing $\epsilon(\infty)$. For computations, $\epsilon(\infty)$ was replaced by $\epsilon(N)$. In this appendix, we estimate the error introduced by using a finite N and show that to get an accuracy up to the fifth decimal place, it is sufficient to take $N = 80$.

Let $f(x) = x/(n^2 + x^2)^{5/2}$ and the prime denote differentiation with respect to x. Then,

$$\epsilon(\infty) - \epsilon(N) = 12\left\{\sum_{n=1}^{\infty}\int_0^{\infty} P_1(x)f(x)\,dx - \sum_{n=1}^{N}\int_0^{N} P_1(x)\,f(x)\,dx.\right\} \quad \text{(A1)}$$

The Bernaulli's polynomials $P_k(x)$ have the following properties,

$$P_k'(x) = P_{k-1}(x)\ ; \quad P_{2k}(0) = \frac{B_{2k}}{(2k)!},$$

$$P_{2k+1}(0) = 0; \qquad |P_k(x)| \leqslant \frac{2\,\zeta(k)}{(2\pi)^k},$$

$$P_k(x) = P_k(x+1)\,,$$

where B_{2k} are the Bernoulli's numbers and $\zeta(x)$ is the Riemann zeta function. In particular $P_2(0) = 1/12$ and $|P_3(x)| < 1/100$. Using these properties, we have for α and β integers,

$$\int_\alpha^\beta P_1(x)\ f(x)\ \mathrm{d}x = [P_2(x)\ f(x)]_\alpha^\beta - \int_\alpha^\beta P_2(x)\, f'(x)\, \mathrm{d}x$$

$$= \frac{1}{12}\,[f(\beta) - f(\alpha)] + \int_\alpha^\beta P_3(x)\, f''(x)\, \mathrm{d}x$$

Also $f(0) = f(\infty) = 0$.

Hence,

$$\epsilon(\infty) - \epsilon(N)$$

$$= -\sum_{n=1}^{N} \frac{N}{(n^2 + N^2)^{5/2}} + 12 \sum_{n=1}^{\infty} \int_0^\infty P_3(x) f''(x)\, \mathrm{d}x$$

$$- 12 \sum_{n=1}^{N} \int_0^N P_3(x)\, f''(x)\, \mathrm{d}x$$

$$= -N \sum_{n=1}^{N} \frac{1}{(n^2 + N^2)^{5/2}} + 12 \sum_{n=1}^{N} \int_N^\infty P_3(x)\, f''(x)\, \mathrm{d}x$$

$$+ 12 \sum_{n=N+1}^{\infty} \int_0^\infty P_3(x)\, f''(x)\, \mathrm{d}x$$

$$= -N\,\Sigma_1 + 12\,\Sigma_2 + 12\,\Sigma_3. \qquad \text{(A2)}$$

In Σ_1, the terms decrease as n increases. Hence

$$\int_1^{N+1} \frac{\mathrm{d}x}{(x^2 + N^2)^{5/2}} < \Sigma_1 < \int_0^N \frac{\mathrm{d}x}{(x^2 + N^2)^{5/2}},$$

or,
$$\Sigma_1 = \int_0^N \frac{\mathrm{d}x}{(x^2 + N^2)^{5/2}} - q_1$$

$$= \frac{5}{6\sqrt{2}\,N^4} - q_1 \text{ with } 0 < q_1 < \frac{1}{N^5} \qquad \text{(A3)}$$

In $\Sigma_2, f''(x)$ is always positive. Hence,

$$|\Sigma_2| \leqslant \sum_{n=1}^{N} \int_{N}^{\infty} |P_3(x)| f''(x)\, dx \leqslant \frac{1}{100} \sum_{n=1}^{N} \frac{4N^2 - n^2}{(n^2 + N^2)^{7/2}}$$

$$= \frac{N^2}{20} \sum_{n=1}^{N} \frac{1}{(n^2 + N^2)^{7/2}} - \frac{1}{100} \sum_{n=1}^{N} \frac{1}{(n^2 + N^2)^{5/2}}.$$

Using method same as that to estimate Σ_1, we get,

$$|\Sigma_2| \leqslant \frac{1}{20N^4} \cdot \frac{43}{60\sqrt{2}} - \frac{1}{100N} \cdot \frac{5}{6\sqrt{2}N^3} - q_2 + \frac{q_1}{100N},$$

$$= \frac{11}{400\sqrt{2}N^4} - q_2 + \frac{q_1}{100N} \text{ with } 0 < q_2 < \frac{1}{20N^5}. \tag{A4}$$

In $\Sigma_3, f''(x)$ is negative for $0 < x < \sqrt{3}\, n/2$ and is positive for $\sqrt{3}\, n/2 < x < \infty$. Hence,

$$|\Sigma_3| \leqslant \frac{1}{100} \sum_{n=N+1}^{\infty} \left\{ \int_{\sqrt{3}\, n/2}^{\infty} f''(x)\, dx - \int_{0}^{\sqrt{3}\, n/2} f''(x)\, dx \right\}$$

$$= \frac{1}{100} \left\{ 1 + \frac{512}{343\sqrt{7}} \right\} \sum_{n=N+1}^{\infty} \frac{1}{n^5} \leqslant \frac{0{\cdot}004}{N^4}. \tag{A5}$$

Using (A3), (A4) and (A5) in (A2),

$$\epsilon(\infty) - \epsilon(N) = -\frac{5}{6\sqrt{2}N^3} + q \text{ with } |q| < \frac{2}{N^4}$$

or,

$$|\epsilon(\infty) - \epsilon(80)| \leqslant 1{\cdot}15 \times 10^{-6} + 4{\cdot}9 \times 10^{-8}$$

$$< 1{\cdot}2 \times 10^{-6}$$

Thus for calculations up to the fifth decimal place it is sufficient to take $N = 80$. The nature of expressions $\epsilon_k(\infty) - \epsilon_k(N)$ are also similar and in view of the small contributions A_k from planes $n_3 > 0$, $N = 80$ will set an appropriate limit for the present calculations.

References

Christiansen J, Heubes P, Keitel R, Klinger W, Loeffler W, Sandner W and Witthuhn W 1976 *Z. Phys.* **B24** 177
Das T P and Pomerantz M 1961 *Phys. Rev.* **123** 2070
de Wette F W 1961 *Phys. Rev.* **123** 103
de Wette F W and Schacher G E 1965 *Phys. Rev.* **137** A78 and A92
Dickmann D B and Schacher G E 1967 *J. Comput. Phys.* **2** 87
Ewald P P 1921 *Ann. Phys. (Leipz).* **64** 253
Hildebrand F B 1956 *Introduction to numerical analysis* (New Delhi: Tata McGraw-Hill) p. 152
Kaufman E N and Vianden R J 1979 *Rev. Mod. Phys.* **51** 161
Nijboer B R A and de Wette F W 1957 *Physica* **23** 309
Nijboer B R A and de Wette F W 1958 *Physica* **24** 422
Raghavan P, Kaufman E N, Raghavan R S, Ansaldo E J and Naumahn R A 1976 *Phys. Rev.* **B13** 2835
Simmons W W and Slichter C P 1961 *Phys. Rev.* **121** 1580
Sternheimer R M 1954 *Phys. Rev.* **95** 736
Sternheimer R M 1954a *Phys. Rev.* **96** 951

Pramāṇa, Vol. 21, No. 6, December 1983, pp. 369-373. © Printed in India.

Electrical conductivity in undoped and Mn^{2+}-doped $NaNO_2$ single crystals

S K GUPTA and S D PANDEY
Physics Department, P P N College, Kanpur 208 001, India

MS received 1 January 1983; revised 7 October 1983

Abstract. Electrical conductivity studies in $NaNO_2$ single crystals with inherent impurities and also in crystals with added Mn^{2+} impurities have been reported. The heating conductivity runs of undoped and doped $NaNO_2$ crystals have been compared. The decrease in conductivity in cooling following a heating run has been attributed to the oxidation during heating leading to the bulk precipitation of impurities in the host. Above 170°C however the intrinsic defects are responsible for conduction. An anomaly is noticed in both the heating and cooling conductivity runs of the sample at about the Curie temperatures and has been found to show thermal hysteresis.

Keywords. Electrical conductivity; $NaNO_2$ single crystals; intrinsic defects; thermal hysteresis.

1. Introduction

Various physical properties of $NaNO_2$ have been extensively studied since its ferroelectricity was discovered by Sawada *et al* (1958). $NaNO_2$ undergoes a phase transition of first order from the ferroelectric to the sinusoidal-anti-ferroelectric or incommensurate phase at 164°C (T_c: called the Curie temperature) followed by a second order phase transition to the paraelectric phase at $\sim$ 165°C (T_N: called the Néel temperature), the phase transitions being of an order-disorder type.

The electrical resistivity in pure sodium nitrite single crystals has been measured by Asao *et al* (1962) and Takagi and Gesi (1967). Their studies, however, did not throw any light on the nature of defects responsible for the observed conduction in this system. The electrical conductivity measurements in undoped and doped alkali halides and some low symmetry crystals (Barr and Lidiard 1970; Ramasastry and Murti 1968; Radhakrishna and Pande 1973) have nevertheless been proved to be fruitful in establishing the defect nature in corresponding crystal systems. To the best of our knowledge such measurements have not been reported in $NaNO_2$ crystals containing aliovalent impurities, though some EPR studies have been made in Mn^{2+}-doped $NaNO_2$ single crystals (Pandey and Upreti 1970 a, b; 1971). In this paper, we report the electrical conductivity measurements in undoped and Mn^{2+}-doped $NaNO_2$ single crystals.

2. Experimental

Single crystals of undoped $NaNO_2$ were grown from melt while those of Mn^{2+}-doped $NaNO_2$ by a solution method (Jain 1977) using GR grade (M/s Sarabhai M. Chemi-

cals, India) sodium nitrite as the starting material. It was not possible to grow crystals of Mn^{2+}-doped $NaNO_2$ from melt as no stable dopant suitable for this purpose was available. The manganese concentration in our doped samples as determined by atomic absorption analysis was 140 ppm. The crystals were cut into platelets of approximate size $5 \times 5 \times 2$ mm. The smallest dimension of the platelet was along the crystal *b*-axis so that conductivity measurements could be made for current flow along this axis.

The DC conductivity was measured in the temperature range 85–253°C with an electrometer amplifier (ECIL EA 815). In order to get a good electrical contact, the opposite faces of the crystal specimen were coated with a thin layer of silver paint. A chromel/alumel thermocouple was kept just touching the crystal specimen to measure the temperature of the crystal for each observation. During observations, the heating/cooling rate was kept as small as half a degree per minute to allow the specimen to attain thermal equilibrium at any temperature. All the conductivity measurements were made in air and the maximum error in the measurement of temperature was $\pm 0{\cdot}5$°C. The polarization effects inherent in the DC conductivity measurements of ionic crystals were avoided by applying the electric field across the crystal only for a short duration of time (less than 20 sec) and noting the temporary pause of the meter needle.

3. Results

The results of the electrical conductivity measurements in single crystals of undoped and Mn^{2+}-doped $NaNO_2$ have been presented in figure 1 where the logarithm of conductivity σ is plotted as a function of reciprocal temperature in the temperature range 85–253°C. The graphs show conductivity results during heating and cooling runs for both types of crystals. The figure also shows the corresponding heating run plot obtained by using the data of Takagi and Gesi (1967) for their melt grown $NaNO_2$ single crystal. This plot is henceforth referred to as the "TG plot".

4. Discussion

The conduction process in sodium nitrite is evidently ionic (Zheludev 1971) and could thus occur either *via* vacancy jumps and/or through interstitial jumps of Na^+ ions. In the ferroelectric phase (below the Curie temperature) the conductivity values in the heating run of Mn^{2+}-doped $NaNO_2$ crystal are large as compared to those in the corresponding plot of undoped $NaNO_2$. This increase of conductivity shows that additional charge carriers participate towards conductivity in Mn^{2+}-doped $NaNO_2$. To derive such a conclusion by comparing the conductivity values in the heating run plots of undoped and doped crystals, grown by two different techniques (melt and solution) may normally appear ambiguous. The conductivity in a solution-grown crystal of an undoped material has been reported to be less than that of the corresponding melt-grown crystal (Ramasastry and Murti 1968; Mansingh and Smith 1971). But in the present case the situation is reversed because the solution grown Mn^{2+}-doped $NaNO_2$ crystal has a higher conductivity compared to the melt-grown crystal of undoped $NaNO_2$. Thus in our doped $NaNO_2$ crystals the role of Mn^{2+}

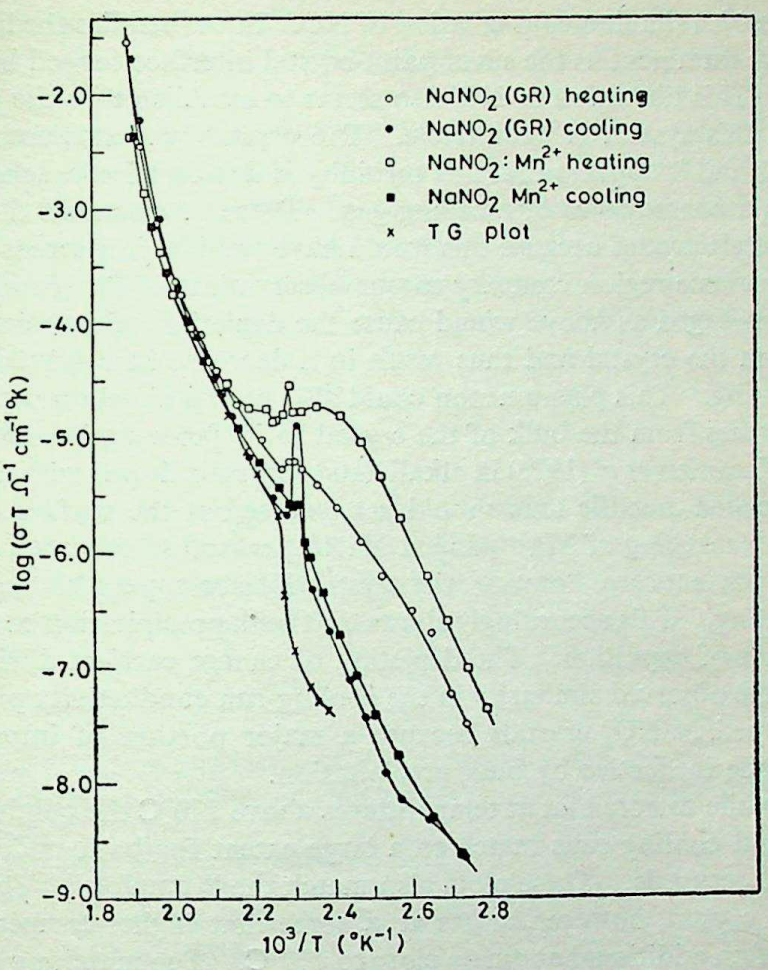

Figure 1. The temperature dependence of electrical conductivity σ for the undoped and Mn^{2+}-doped $NaNO_2$ single crystals in heating and cooling runs.

impurities towards increased electrical conduction is quite evident. Through EPR studies, it has been reported (Jain 1977) that when a divalent cation impurity (Mn^{2+}) is introduced in sodium nitrite, it replaces the sodium ion and a sodium ion vacancy is created to fulfil the charge neutrality requirement. Thus the additional charge carriers (extrinsic conduction) responsible for electrical conduction in Mn^{2+}-doped $NaNO_2$, are the sodium ion vacancies which move through the lattice with Na^+ ion jumps.

A comparison of the conductivity values in the heating run plot of undoped $NaNO_2$ with the TG plot, similarly shows that even in undoped $NaNO_2$ crystal there are appreciable number of charge carriers similar to those in Mn^{2+}-doped $NaNO_2$. This may be understood if it is considered that the starting host material has been reported to contain some aliovalent impurities: (Ca $\sim$35 ppm), (Fe $\sim$12 ppm), (Pb $\sim$ 3 ppm) and (SO_4 $\sim$ 36 ppm). Thus the undoped $NaNO_2$ crystal may consist of divalent and trivalent impurities.

The appreciably large values of conductivity in the heating runs below 170°C for both undoped and Mn^{2+}-doped $NaNO_2$, as compared to the corresponding cooling run values, may further be explained if it is presumed that divalent cation impurities imbedded in the crystal get oxidized and thus precipitated during the heating process (above 164°C). The oxygen for such an oxidation may probably be made available

by nitrite ions with simultaneous creation of NO. In our studies the liberation of NO appeared quite imminent as the silver paint-crystal interface turned brown after each heating run. This liberation of NO also seems to establish that the precipitation of impurities in this system is irreversible. The crystal was also found turbid after measurements and it appears that this turbidity is due to microcracks created within the crystal as a consequence of escaping gas. These microcracks do not cause any detachment of electrodes because this would have resulted in decreased conductivity even in the intrinsic region contrary to our observations. The precipitation of impurity ions envisaged as above would cause the depletion of associated sodium ion vacancies from the crystal and thus result in a decrease in conductivity in cooling following heating. This phenomenon could also be explained on the basis of expulsion of impurities from the bulk of the crystal to its faces similar to what has been reported by Yacaman *et al* (1976) in alkali halide crystals doped with divalent impurities. The expelled metallic ions should get oxidized at the surface and one would thus observe blackening of Mn^{2+} -doped $NaNO_2$ crystal surface due to MnO formation. In the present case, however, the crystal did not appear blackened at the surface after heating. This accordingly shows that bulk precipitation mechanism dominates over that of expulsion. The depletion of charge carriers during heating can also explain the observed similarity in the cooling-run conductivity plots of undoped and Mn^{2+}-doped $NaNO_2$ crystals because a major portion of impurities in these crystals is made ineffective by bulk precipitation.

It is worthwhile to note that at temperatures above 170°C the conductivity plots in the heating and cooling runs match to a large extent for both undoped and Mn^{2+} -doped $NaNO_2$ crystals. These plots also match the " TG plot ". The matching for Mn^{2+} -doped crystal, however, starts at a somewhat higher temperature with the observation of an additional anomaly close to 177°C. The matching of all conductivity plots at temperatures exceeding 170°C indicates that the impurity ions are no longer responsible for conduction and that the conduction in this region may be due to the dominant intrinsic defects. The prominent intrinsic defects in this system are probably the interstitial sodium ions (Frenkel defects) because NO_2^- cannot be easily moved from their lattice sites due to their bigger size. The predominance of Frenkel defects over the Schottky defects in a similar system ($NaNO_3$) has been established by Murti (1967) through his theoretical investigation. The conduction in the paraelectric phase of $NaNO_2$ may thus be due to the motion of interstitial sodium ions and vacancies. The mobilities of these high temperature defects may not be equal and further vary differently with temperature explaining the high temperature curvature in the conductivity plots.

Finally, the cooling run plots of the two crystals do not exactly match the 'TG plot' indicating that some impurities with associated vacancies do remain in these crystals even after heating. The sharp fall in conductivity in the TG plot at low temperatures is further due to the fact that interstitials are eliminated at such temperatures leaving only a few impurity-generated vacancies.

In the cooling runs of both undoped and Mn^{2+}-doped $NaNO_2$ an anomalous peak in the conductivity plot is observed at 159·5°C. In the heating run of undoped $NaNO_2$, however, the anomaly is indicated at 162°C and for the sample with added Mn^{2+} impurities it is at 164°C. An anomaly is thus observed in the heating and cooling runs of both the samples at about the Curie temperature. The observed thermal hysteresis of 2·5°C in undoped $NaNO_2$ crystals and of 4·5°C in the corresponding

doped crystal probably reflects the first order nature of the phase transition in $NaNO_2$ in concurrence with Sawada *et al* (1961), Hamano (1964) and Bohm and Hoffmann (1978).

A second anomaly has been observed at 177°C in Mn^{2+}-doped $NaNO_2$ crystal in its heating run. However, this has not been found in the undoped crystal with less impurities. It thus seems that the impurities have a role to make the anomalous behaviour detectable at 177°C. It would, however, be worthwhile to report that an anomaly at 178°C was for the first time reported by Hoshino and Shibuya (1961) and later by a number of other workers (Takagi and Gesi 1967; Sawada *et al* 1961).

Acknowledgements

This work was supported under an equipment grant from UGC India. One of the authors (SKG) is thankful to the CSIR, New Delhi for the award of a research fellowship. It was pleasure to have discussions with Dr Akhilesh Kumar Jain, ISM, Dhanbad.

References

Asao Y, Yoshida I, Ando R and Sawada S 1962 *J. Phys. Soc. Jpn.* **17** 442
Barr L W and Lidiard A B 1970 in *Physical chemistry* (ed) W Jost (New York: Academic Press) Vol. 10 Chap. 3
Bohm H and Hoffmann W 1978 *Ferroelectrics* **19** 19
Hamano K 1964 *J. Phys. Soc. Jpn* **19** 945
Hosino S and Shibuya I 1961 *J. Phys. Soc. Jpn* **16** 1254
Jain A K 1977 Ph.D. Thesis, IIT Kanpur
Mansingh A and Smith A M 1971 *J. Phys.* **D4** 560
Murti Y V G S 1967 Ph.D. Thesis, IIT Madras
Pandey S D and Upreti G C 1970a *Phys. Status Solidi* **1** K69
Pandey S D and Upreti G C 1970b *Phys. Status Solidi* **2** K207
Pandey S D and Upreti G C 1971 *Ferroelectrics* **2** 155
Radhakrishna S and Pande K P 1973 *Phys. Status Solidi* **16** 433
Ramasastry C and Murti Y V G S 1968 *Proc. R. Soc.* **A305** 441
Sawada S, Nomura S, Fujii S and Yoshida I 1958 *Phys. Rev. Lett.* **1** 320
Sawada S, Nomura S and Asao Y 1961 *J. Phys. Soc. Jpn* **16** 2207
Takagi Y and Gesi K 1967 *J. Phys. Soc. Jpn* **22** 979
Yacaman M J, Gomez A and Bassett G A 1976 *Thin Solid Films* **35** 37
Zheludev I S 1971 *Physics of crystalline dielectrics* (New York: Plenum Press) Vol. 2 Chap. 8

Pramāṇa, Vol. 21, No. 6, December 1983, pp. 375–384. © Printed in India.

Temperature dependence of the linewidth of the first-order Raman spectra for MnF_2 crystal

TSUTOMU SATO
Department of Physics, Faculty of Science, Hirosaki University, Hirosaki 036, Japan

MS received 19 July 1983; revised 24 October 1983

Abstract. The first-order Raman spectra of E_g and A_{1g} modes in MnF_2 crystal were measured at temperatures from 4·2 to 563 K, and the values of the linewidths obtained. The temperature dependence of the linewidths was analyzed by the phonon dispersion curves based on the rigid ion model, and the result showed that it was caused approximately by the cubic anharmonic term in crystal potential energy.

Keywords. Raman spectra; linewidth; temperature dependence; anharmonic term; phonon dispersion curves; two phonon density of states; rigid ion model.

1. Introduction

Measurements in regard to the temperature dependence of linewidths and frequencies of normal vibrations of a lattice have been carried out for a long time. Early investigations in this branch were carried out mainly for alkali halides with simple crystal structure (Heilmann 1958; Hass 1960) and for ionic crystals (Jones *et al* 1961; Jasperse *et al* 1966). Since 1970, investigations have been carried out not only for crystals (Borer *et al* 1971; Change and Mitra 1972; Skryabinskii and Ukhanov 1973; Stolen 1975; Bairamov *et al* 1975) with a simple structure but also for more complex molecular crystals (Sakurai and Sato 1971; Gervais *et al* 1972, 1975b; Sood *et al* 1981). In these investigations, the temperature dependence of linewidth and frequency has been discussed by considering the cubic and quartic anharmonic terms of the crystal potential energy.

On the other hand, a theoretical investigation of crystal dynamics on the basis of anharmonicity of the lattice was first carried out by Born and Huang (1954). Later Ipatova *et al* (1967) performed detailed theoretical calculations in regard to the linewidth and frequency of the lattice vibration of NaCl and LiF considering the cubic and quartic anharmonic terms and a fair agreement with the experimental data was obtained (Heilmann 1958; Hass 1960). Furthermore, the theoretical calculations for various crystals with CaF_2 structure have been performed by Elliott *et al* (1978) and are in good agreement with experimental results. More recently, Sato and Tateyama (1982a, b) performed the theoretical calculations and experiments for two crystals with CaF_2 structure. However, theoretical calculations of the temperature dependence of the linewidth and frequency for crystals with more complex structure have been hardly performed. While experimental investigation has shown that linewidth of GaSb (Skryabinskii and Ukhanov 1973) with the ZnS structure is caused only by the

cubic anharmonic term, the linewidth of GaP (Bairamov *et al* 1975) with the same structure is caused by the cubic and quartic terms. The same result has been found for crystals MgO (Jasperse *et al* 1966), LiF (Heilmann 1958), and NaF (Chang and Mitra 1972) with the NaCl structure. Furthermore, in many experimental investigations (Jasperse *et al* 1966; Borer *et al* 1971; Chang and Mitra 1972; Skryabinskii and Ukhanov 1973; Stolen 1975; Bairamov *et al* 1975; Gervais *et al* 1972; Gervais and Piriou 1974, 1975a; Sakurai and Sato (1971); Ohsaka 1980; Sood *et al* 1981) the frequencies used to analyze the linewidth do not relate to the phonon dispersion curves and have almost no physical foundation. No clear conclusion is presently available regarding the relative importance of the contribution to linewidth arising from cubic and quartic terms. As seen from the calculations of the linewidths for relatively simple crystals (Ipatova *et al* 1967; Monga *et al* 1979; Elliott *et al* 1978; Sato and Tateyama (1982a, b) until now, those for more complex crystals would be very complex and tedious. Recently Gervais *et al* (1975b) investigated the temperature dependence of the linewidth of TO and LO A_2 modes in quartz and reported that the dependence of the linewidth has been interpreted by considering the actual effect of temperature on the one-phonon density of state. Also the linewidth of phonons in TiO_2 was measured by Gervais and Piriou (1974). They showed that the phonon lifetimes in TiO_2 are limited by the cubic anharmonic term. From the above standpoint, the purpose of the present work is to study the temperature dependence of the Raman linewidth for MnF_2 crystal belonging to the TiO_2 structure, (which until now has not been investigated in detail, Sauvajol *et al* 1977), in order to confirm if it can be explained only by the cubic anharmonic term as indicated by Gervais and Piriou (1974) and by the phonon density of state as indicated by Gervais *et al* (1975b).

2. Experiment

As already mentioned MnF_2 belongs to the space group D_{4h}^{14} of which the normal lattice vibration at the Γ point of the Brillouin zone is given on the basis of group theory (Porto *et al* 1967)

$$1A_{1g} + 1A_{2g} + 1A_{2u} + 1B_{1g} + 1B_{2g} + 2B_{1u} + 1E_g + 3E_u.$$

Among these, the active Raman modes are B_{1g} (Γ_3^+), E_g(Γ_5^-), A_{1g} (Γ_1^+) and B_{2g} (Γ_4^+). Consequently, four first-order Raman spectra are to be observed, but Raman intensities for B_{1g} and B_{2g} modes are weak. In the present work, the E_g and A_{1g} modes were measured.

The specimens used in the present work were partly transparent light red crystal (prepared by Murakami Engineering Co.), cut perpendicularly to the *a*, *b* and *c* axes, optically polished and measured 4 × 4 × 2 (*c* axis) and 5 × 5 × 6 (*c* axis) mm^3. The polarized and unpolarized Raman spectra were measured using a laser Raman spectrophotometer (Nihon Denshi Ul-UV) equipped with a photon counting system. The values of the linewidths obtained by both the measurements were consistent within the limits of experimental error. For temperatures above 300 K the specimens were heated in a nichrome furnace, and the temperatures controlled to within ± 1 K. When MnF_2 crystal is heated up to

about 600 K in air, it changes to black colour from surface and becomes opaque. Hence, the measurements were performed at a temperature below 563 K. For the measurements at 120 K the temperature of the specimen was determined by the ratio of the intensity of Stokes and anti-Stokes. At 4·2 K the specimen was placed in liquid helium. The beam of an Ar ion laser 4880 and 5145 Å was used as the light source for Raman excitation. A resolution of about 1 $\sim$ 4 cm^{-1} was used in the experiment. The accuracy of the wavelength was $\pm$ 0·5 Å ($\approx$ 2 cm^{-1}). The Raman frequency and linewidth were obtained by deconvoluting the recorded spectrum using the instrument function.

3. Results and discussion

Typical first-order Raman spectrum recorded for two different temperatures in E_g mode of MnF_2 crystal is shown in figure 1. With increasing temperature the Raman line of E_g mode shifts to lower frequencies and becomes broadened. In order to

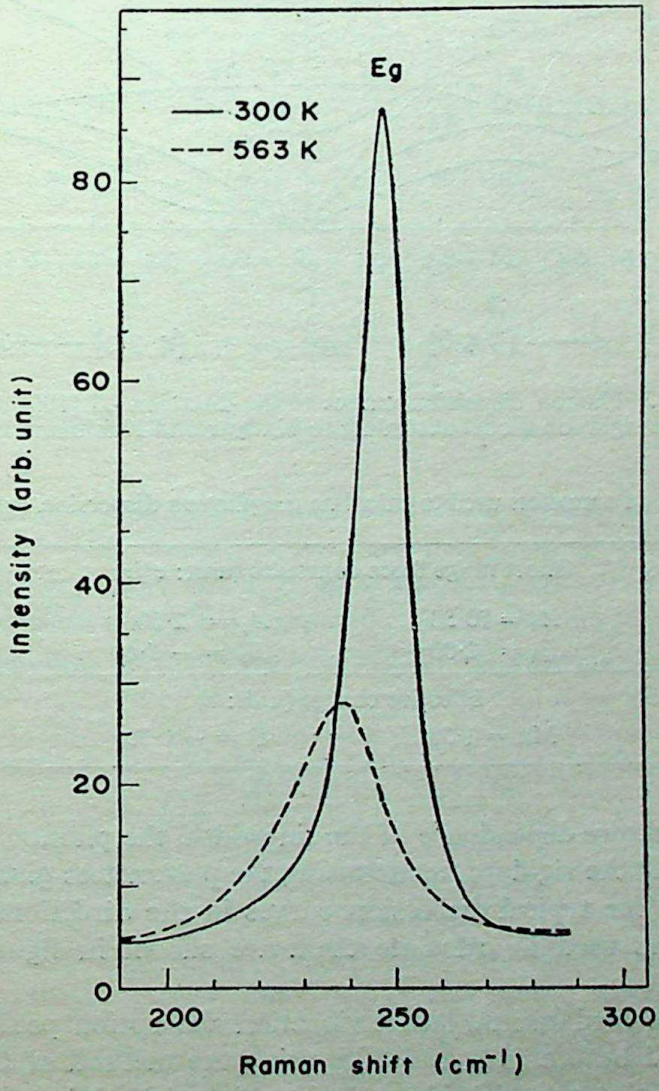

Figure 1. The Raman spectra at 300 and 563 K with wavenumbers (cm^{-1}).

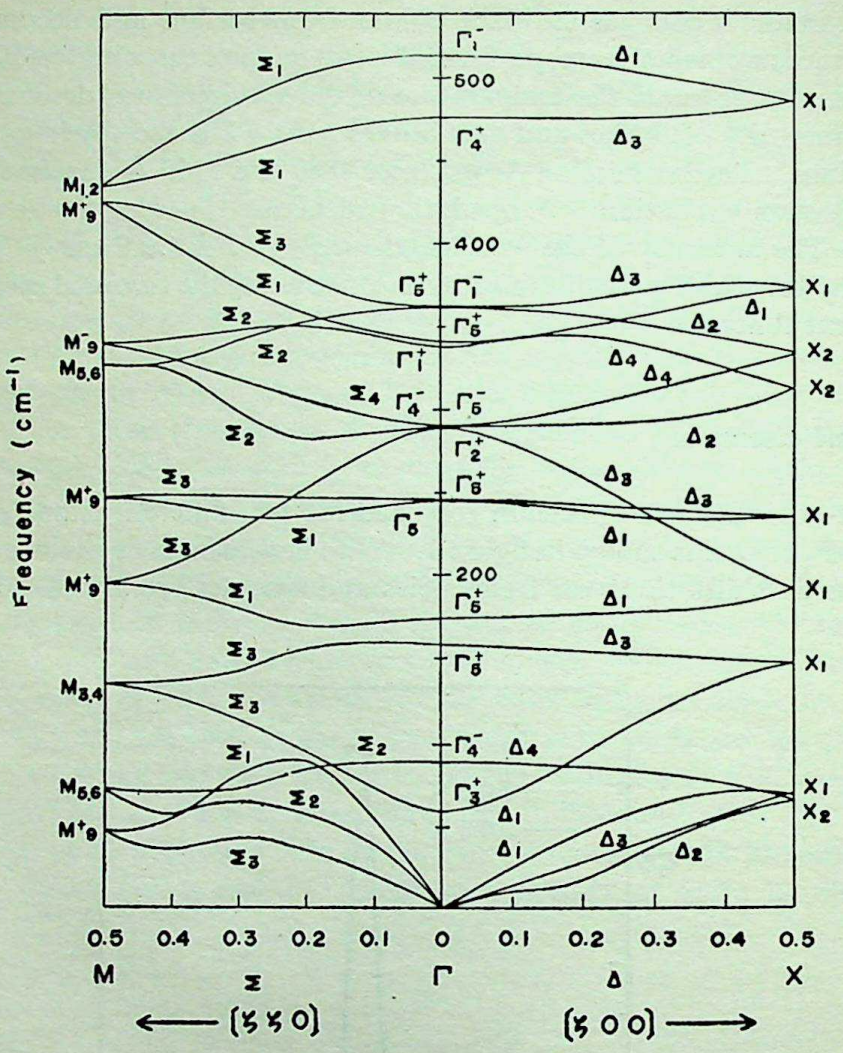

Figure 2. Phonon dispersion curves in the direction of [100] and [110], calculated using the rigid ion model according to Katiyar and Krishnan (1969).

Table 1. Parameters used to calculate the phonon dispersion curves.

Short range force constants (unit: e^2/v)			
$A_1 = 77{\cdot}60$	$A_2 = 70{\cdot}50$	$A_3 = 2{\cdot}00$	$A_4 = 22{\cdot}40$
$B_1 = 2{\cdot}30$	$B_2 = 2{\cdot}00$	$B_3 = -5{\cdot}40$	$B_4 = 4{\cdot}00$
Effective charge (unit: e)			
Mn $= 1{\cdot}58$		F $= -0{\cdot}79$	

analyse the temperature dependence of the linewidth, the phonon dispersion curves were calculated with the rigid ion model using the parameters given by Katiyar and Krishnan (1969). The typical dispersion curves in the directions [100] and [110], and the parameters used to calculate them are shown in figure 2 and table 1, respectively.

The width of the fundamental lattice vibration absorption peak in ionic crystals has been calculated by Wallis *et al* (1966) using the method of Green's functions. According to Wallis *et al* (1966), if the Raman linewidth $2\Gamma_j(\omega)$ is caused by only

the cubic anharmonic term in crystal potential energy, the linewidth $2\Gamma_j^{(3)}(\omega)$ due to the cubic term can be expressed as follows

$$\Gamma_j^{(3)}(\omega) = -18\frac{\pi}{\hbar^2}\sum_{\mathbf{q}_1}\sum_{j_1 j_2}|V(\mathbf{O}j;\mathbf{q}_1 j_1;-\mathbf{q}_1 j_2)|^2\{(n_{j_1}(\mathbf{q}_1)+n_{j_2}(-\mathbf{q}_1)+1)$$

$$\times[\delta(\omega+\omega_{j_1}(\mathbf{q}_1)+\omega_{j_2}(-\mathbf{q}_1))-\delta(\omega-\omega_{j_1}(\mathbf{q}_1)-\omega_{j_2}(-\mathbf{q}_1))]$$

$$+2(n_{j_1}(\mathbf{q}_1)-n_{j_2}(-\mathbf{q}_1))\,\delta(\omega-\omega_{j_1}(\mathbf{q}_1)+\omega_{j_2}(-\mathbf{q}_1))\}. \quad (1)$$

Here, $n_j(\mathbf{q}) = [\exp(\hbar\omega_j(\mathbf{q})/kT)-1]^{-1}$ is the phonon occupation number, $V(\mathbf{O}j;\mathbf{q}_1 j_1;-\mathbf{q}_1 j_2)$ is the cubic anharmonic coefficient of the crystal potential. Similarly, the linewidth $2\Gamma_j^{(4)}(\omega)$ caused by the quartic term can be expressed as follows

$$\Gamma_j^{(4)}(\omega) = -\frac{96\pi}{\hbar^2}\sum_{\mathbf{q}_1,\mathbf{q}_2,\mathbf{q}_3}\sum_{j_1,j_2,j_3}|V(\mathbf{O}j;\mathbf{q}_1 j_1;\mathbf{q}_2 j_2;\mathbf{q}_3 j_3)|^2\{[(n_{j_1}(\mathbf{q}_1)+1)$$

$$\times(n_{j_2}(\mathbf{q}_2)+1)(n_{j_3}(\mathbf{q}_3)+1)-n_{j_1}(\mathbf{q}_1)n_{j_2}(\mathbf{q}_2)n_{j_3}(\mathbf{q}_3)]\,[\delta(\omega+\omega_{j_1}(\mathbf{q}_1)$$

$$+\omega_{j_2}(\mathbf{q}_2)+\omega_{j_3}(\mathbf{q}_3))-\delta(\omega-\omega_{j_1}(\mathbf{q}_1)-\omega_{j_2}(\mathbf{q}_2)-\omega_{j_3}(\mathbf{q}_3))]$$

$$+3[n_{j_1}(\mathbf{q}_1)(n_{j_2}(\mathbf{q}_2)+1)\times(n_{j_3}(\mathbf{q}_3)+1)-(n_{j_1}(\mathbf{q}_1)+1)n_{j_2}(\mathbf{q}_2)n_{j_3}(\mathbf{q}_3)]$$

$$[\delta(\omega-\omega_{j_1}(\mathbf{q}_1)+\omega_{j_2}(\mathbf{q}_2)+\omega_{j_3}(\mathbf{q}_3))$$

$$-\delta(\omega+\omega_{j_1}(\mathbf{q}_1)-\omega_{j_2}(\mathbf{q}_2)-\omega_{j_3}(\mathbf{q}_3))]\}. \quad (2)$$

As these calculations would be very complex and enormous, the anharmonic coefficients $V(\mathbf{O}j;\mathbf{q}_1 J_1;-\mathbf{q}_1 j_2)$ and $V(\mathbf{O}j;\mathbf{q}_1 j_1;\mathbf{q}_2 j_2;\mathbf{q}_3 j_3)$ are considered to be independent of the variables $\mathbf{O}j$, $\mathbf{q}_1 j_1$, $\mathbf{q}_2 j_2$ and $\mathbf{q}_3 j_3$, and treated as an adjustable parameter to fit the data by a similar method given by Gervais *et al* (1975). Therefore, $\Gamma_j^{(3)}(\omega)$ and $\Gamma_j^{(4)}(\omega)$ may be rewritten in the following equations, respectively

$$\Gamma_j^{(3)}(\omega) = A\sum_{\mathbf{q}_1}\sum_{j_1,j_2}\frac{1}{\omega_j(\mathbf{O})\,\omega_{j_1}(\mathbf{q}_1)\,\omega_{j_2}(-\mathbf{q}_1)}\{(n_{j_1}(\mathbf{q}_1)+n_{j_2}(-\mathbf{q}_1)+1)\,[\delta(\omega$$

$$+\omega_{j_1}(\mathbf{q}_1)+\omega_{j_2}(-\mathbf{q}_1))-\delta(\omega-\omega_{j_1}(\mathbf{q}_1)-\omega_{j_2}(-\mathbf{q}_1))]$$

$$+2(n_{j_1}(\mathbf{q}_1)-n_{j_2}(-\mathbf{q}_1))\times\delta(\omega-\omega_{j_1}(\mathbf{q}_1)+\omega_{j_2}(-\mathbf{q}_1))\}, \quad (3)$$

$$\Gamma_j^{(4)}(\omega) = B\sum_{\mathbf{q}_1 j_1}\sum_{\mathbf{q}_2 j_2}\sum_{\mathbf{q}_3 j_3}\frac{\Delta(\mathbf{q}_1+\mathbf{q}_2+\mathbf{q}_3)}{\omega_j(\mathbf{O})\,\omega_{j_1}(\mathbf{q}_1)\,\omega_{j_2}(\mathbf{q}_2)\,\omega_{j_3}(\mathbf{q}_3)}\{[(n_{j_1}(\mathbf{q}_1)+1)$$

$$\times (n_{j_2}(\mathbf{q}_2)+1)(n_{j_3}(\mathbf{q}_3)+1) - n_{j_1}(\mathbf{q}_1)\, n_{j_2}(\mathbf{q}_2)\, n_{j_3}(\mathbf{q}_3)]\,[\delta(\omega+\omega_{j_1}(\mathbf{q}_1)$$

$$+\omega_{j_2}(\mathbf{q}_2)+\omega_{j_3}(\mathbf{q}_3)) - \delta(\omega-\omega_{j_1}(\mathbf{q}_1)-\omega_{j_2}(\mathbf{q}_2)-\omega_{j_3}(\mathbf{q}_3))]$$

$$+3\,[n_{j_1}(\mathbf{q}_1)(n_{j_2}(\mathbf{q}_2)+1)\times(n_{j_3}(\mathbf{q}_3)+1) - (n_{j_1}(\mathbf{q}_1)+1)\, n_{j_2}(\mathbf{q}_2)$$

$$\times n_{j_3}(\mathbf{q}_3)]\,[\delta(\omega-\omega_{j_1}(\mathbf{q}_1)+\omega_{j_2}(\mathbf{q}_2)+\omega_{j_3}(\mathbf{q}_3)) - \delta(\omega+\omega_{j_1}(\mathbf{q}_1)$$

$$-\omega_{j_2}(\mathbf{q}_2)-\omega_{j_3}(\mathbf{q}_3)]\}, \tag{4}$$

where $\Delta(\mathbf{q}_1+\mathbf{q}_2+\mathbf{q}_3)$ in (4) states wavevector conservation. The summation terms except the constant A in (3) can be identified as two-phonon density of states. Thus two-phonon density of states is expressed as follows

$$\sum_{q_1}\sum_{j_1\,j_2}\frac{1}{\omega_j(\mathbf{O})\,\omega_{j_1}(\mathbf{q}_1)\,\omega_{j_2}(-\mathbf{q}_1)}\{(n_{j_1}(\mathbf{q}_1)+n_{j_2}(-\mathbf{q}_1)+1)\,[\delta(\omega+\omega_{j_1}(\mathbf{q}_1)$$

$$+\omega_{j_2}(-\mathbf{q}_1))-\delta(\omega-\omega_{j_1}(\mathbf{q}_1)+\omega_{j_2}(-\mathbf{q}_1))]+2\,(n_{j_1}(\mathbf{q}_1)-n_{j_2}(-\mathbf{q}_1))$$

$$\times\delta(\omega-\omega_{j_1}(\mathbf{q}_1)+\omega_{j_2}(-\mathbf{q}_1))\}. \tag{5}$$

Similarly, the summation terms except B in (4) can be identified as three-phonon density of states. The equation is explicit from (5) and abbreviated. With the aid of the phonon dispersion curves, two- and three-phonon densities of states were calculated. In the calculations of the two-phonon density of states the summations over wavevector $\mathbf{q}$ were taken over about 9000 points in the Brillouin zone, and in the three-phonon density of states the summations were taken over about 1800 points. The δ function was approximated as follows

$$\delta(x) = \lim_{\epsilon\to+0}\frac{1}{\pi}\frac{\epsilon}{x^2+\epsilon^2}, \tag{6}$$

where ϵ was taken as 5 and the δ function affected the region within about 10 cm^{-1}. The two-phonon density of states with wavenumbers at 300 and 563 K is shown in figure 3 (the values less than 10^{-6} order are not shown). Therefore, the values of wavenumbers above 500 cm^{-1} are less than 10^{-6} order. Also the three-phonon density of states as a function of temperatures for the E_g and A_{1g} modes is shown in figure 4. As calculation of the density for all wavenumbers is very laborious, results are presented only for the frequencies 247 and 341 cm^{-1}. As seen from figure 4, the three-phonon density with temperatures shows conspicuous change. For both the modes the values at 563 K are about 22 times those at 120 K. The observed linewidths $2\Gamma_j(\omega)$ show slow change with temperatures, and show approximately linear variation except those temperatures below 100 K. Therefore, $\Gamma_j^{(3)}(\omega)$ due to the cubic anharmonic term only is considered for comparison with the observed linewidths. The constant A for E_g mode was taken as $3{\cdot}92\times10^3$ cm^{-1} and for A_{1g} mode as $2{\cdot}7\times10^4$ cm^{-1}. As seen in figure 5, the calculated linewidth is in agreement with

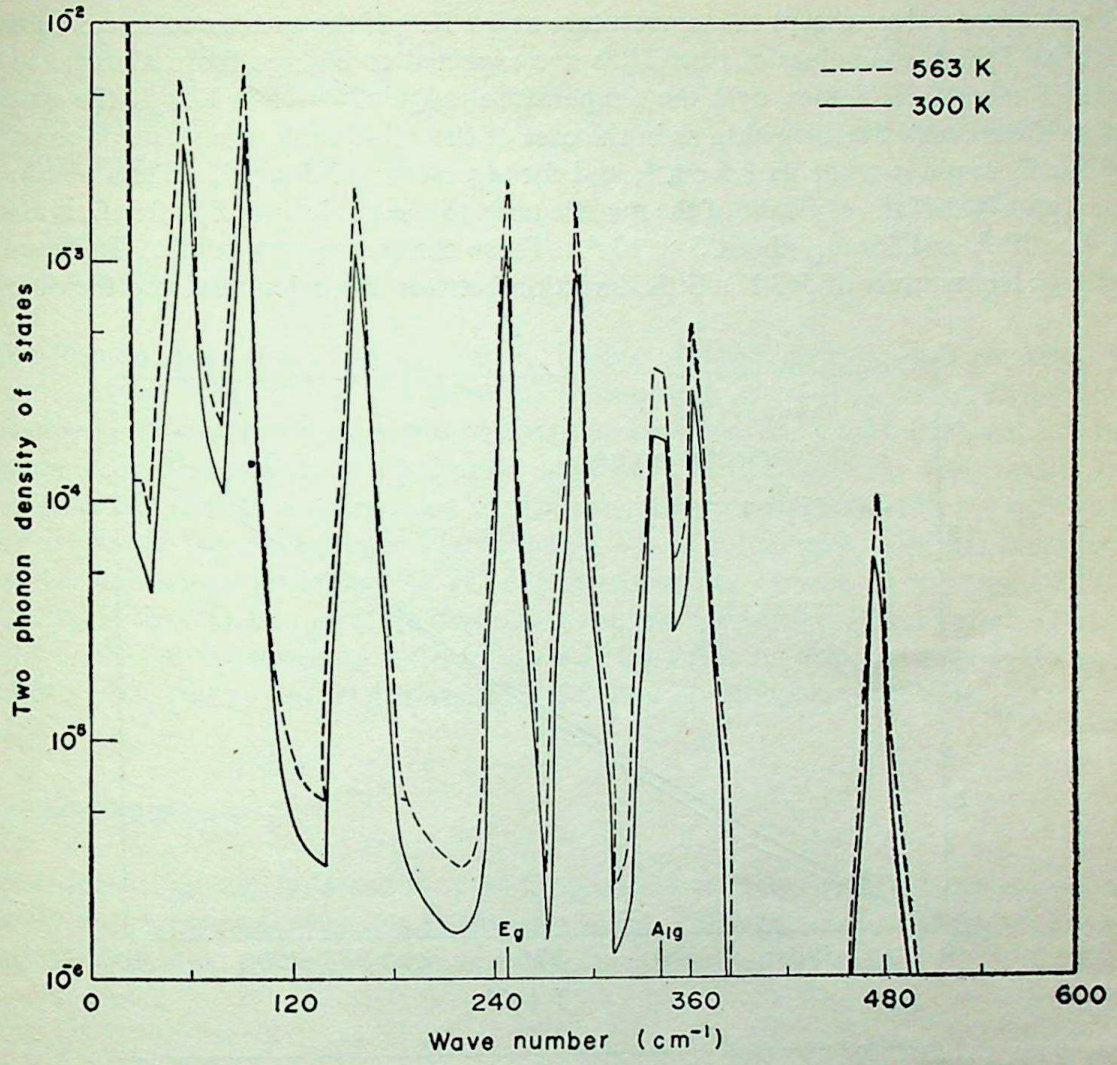

Figure 3. The two-phonon density of states with wavenumbers.

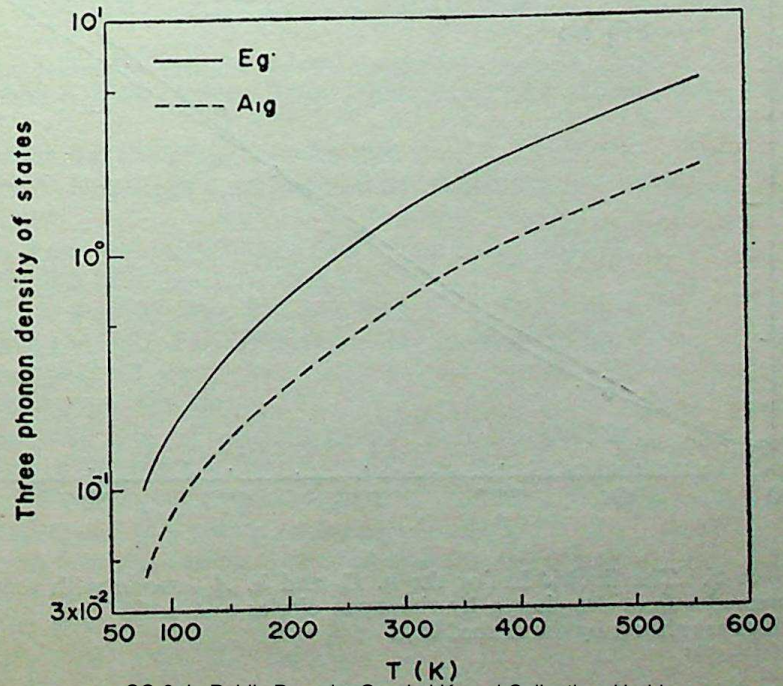

Figure 4. The three-phonon density of states with temperatures.

the observed values except the temperature at 4·2 K. If the quartic term contributes only to $\Gamma_j(\omega)$, the values of linewidths are expected to change from about 3 to 60 cm^{-1} for both the modes, over the temperature range 120 — 560 K. If the quartic term affects only the linewidth, as in the case of the cubic term, the value of constant B for E_g mode is taken as 5·5 cm^{-1}, and for A_{1g} about 13·5 cm^{-1}. Thus obtaining the ratio B/A of the constant of the quartic term to the cubic one, B/A for E_g is about $1{\cdot}4 \times 10^{-3}$, and for A_{1g} about 5×10^{-4}. These ratios are very small. In figure 5, at high temperature of 563 K a little deviation between the calculated and the observ-

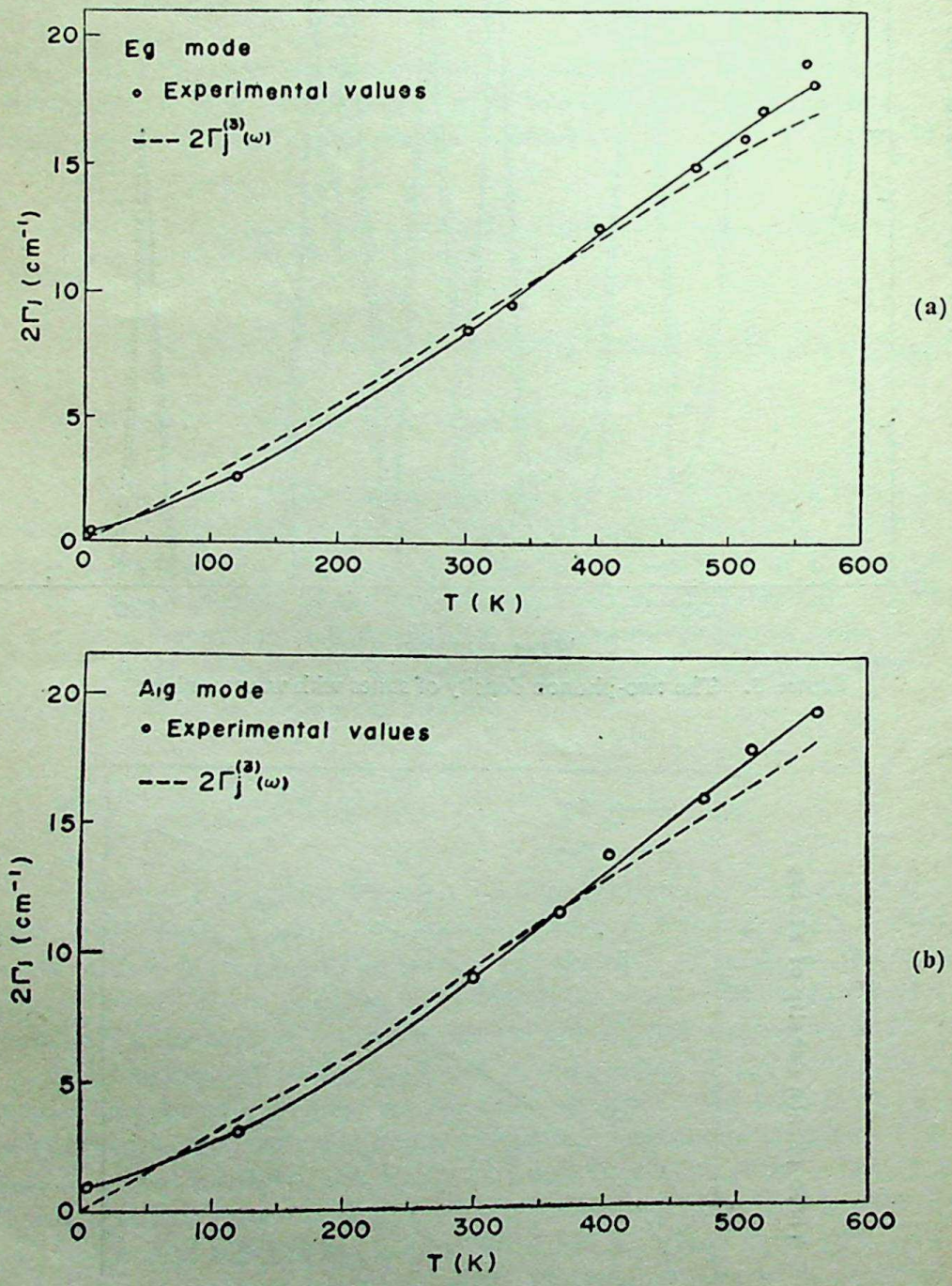

Figure 5. The linewidths for the **a.** E_g and **b.** A_{1g} mode with temperatures. The observed values are shown by the open circles and solid line, and the calculated values are shown by the dashed line.

ed values is about 1 cm^{-1}. If the value of linewidth 1 cm^{-1} is existed by the quartic term, this value will be less than 2% of one of $2\Gamma_j^{(4)}(\omega)$. However, the deviation is within the limits of experimental error, and not due to the quartic term from the calculations for CeO_2, and CdF_2.

4. Conclusion

The Raman spectra for the E_g and A_{1g} modes of MnF_2 crystal were measured at temperatures 4·2 to 563 K. The values of linewidths at various temperatures were obtained. The phonon dispersion curves for MnF_2 crystal were calculated, and the temperature dependence of the Raman linewidths was analyzed by considering the two-phonon density of states due to the cubic anharmonic term and three-phonon density due to the quartic one. The values of A for $\Gamma_j^{(3)}(\omega)$ were taken and the experimental and calculated values for $2\Gamma_j(\omega)$ show good agreement. From this fact it is concluded that the temperature dependence of the linewidth for MnF_2 crystal can be explained approximately by considering only the cubic anharmonic term of the crystal potential energy and is governed by the phonon occupation number.

Acknowledgements

The author is greatly indebted Prof. M Ishigame for making the Raman spectrophotoi meter and instrument available for present work. Thanks are due to Mrs T Okazak- and Mr Y Sohma for their assistance with the analysis of linewidth.

References

Bairamov B Kh, Kitaev Yu É, Negoduiko V K and Khashkhozhev Z M 1975 *Sov. Phys. Solid State* **16** 1323

Borer W J,Mitra S S and Namjoshi K V 1971 *Solid State Commun.* **9** 1377

Born M and Huang K 1954 *Dynamical theory of crystal lattice* (Oxford: Oxford University Press). p. 363

Chang I F and Mitra S S 1972 *Phys. Rev.* **B5** 4049

Elliott R J, Hayes W, Kleppman W G, Rushworth A J and Ryan J F 1978 *Proc. R. Soc. London Ser* **A360** 317

Gervais F, Piriou B and Cabannes F 1972 *Phys. Status Solidi.* **B51** 701

Gervais F and Piriou B 1974 *Phys. Rev.* **B10** 1642

Gervais F and Piriou B 1975a *Phys. Rev.* **B11** 3944

Gervais F, Piriou B and Billard D 1975b *Solid State Commun.* **17** 861

Hass M 1960 *Phys. Rev.* **117** 1497

Heilmann G 1958 *Z. Phys.* **152** 368

Ipatova I P, Maradudin A A and Wallis R F 1967 *Phys. Rev.* **155** 882

Jasperse J R, Kahn A, Plendle J N and Mitra S S 1966 *Phys. Rev.* **146** 526

Jones G O, Martin P H, Mawer P A and Perry C H 1961 *Proc. R. Soc. London* **A261** 10

Katiyar R S and Krishnan R S 1969 *J. Indian Inst. Sci.* **51** 121

Monga M R, Jindal V K and Pathak K N 1979 *Phys. Rev.* **B19** 1230

Ohsaka T 1980 *J. Phys. Soc. Jpn.* **48** 1661

Porto S P S, Fleury P A and Damen T C 1967 *Phys. Rev.* **154** 522

Sakurai T and Sato T 1971 *Phys. Rev.* **B4** 583

Sato T and Tateyama S 1982a *Phys. Rev.* **B26** 2257
Sato T and Tateyama S 1982b *Phys. Status Solidi* **b113** 291
Sauvajol J, Almairac R, Benoit C and Bon A M 1977 *Proc. Int. Conf. Lattice Dyn.* (ed) M Balkanski (Paris: Flammarion Science), p. 199
Skryabinskii I V and Ukhanov Yu I 1973 *Sov. Phys. Solid State* **15** 886
Sood A K, Arora A K, Umadevi V and Venkataraman G 1981 *Pramana* **16** 1
Stolen R H 1975 *Phys. Rev.* **B11** 767
Wallis R F, Ipatova I P and Maradudin A A 1966 *Sov. Phys. Solid State* **8** 850

Pramāṇa, Vol. 21, No. 6, December 1983, pp. 385–391. © Printed in India.

Factorisation in large-N limit of lattice gauge theories revisited

A CHATTERJEE and D GANGOPADHYAY
Saha Institute of Nuclear Physics, 92, Acharya Prafulla Chandra Road, Calcutta 700 009, India

MS received 26 August 1983

Abstract. We prove using the Schwinger-Dyson equations that the factorisation property holds for all gauge-invariant Green's function in the large-N limit of a Wilson-Polyakov lattice gauge theory.

Keywords. Large-N limit; factorisation; Schwinger-Dyson equations; lattice gauge theory.

1. Introduction

The dynamics of a gauge theory simplifies to a great extent in the limit of large number of gauge degrees of freedom. This simplification leads to some of the recent remarkable results like the closed form of equations for the Wilson loop average (Makeenko and Migdal 1979; Wadia 1981) and the reduction in the number of effective space-time degrees of freedom (Eguchi and Kawai 1982; Gross and Kitazawa 1982; Das and Wadia 1982; Parisi 1982; Bhanot *et al* 1982).

As in spin models where it results in complete solution, this simplification in gauge theories is ultimately related to the factorisation property exhibited by the gauge-invariant Green's functions. This implies that the fluctuations in the gauge-invariant observables become negligible and the Hartree-Fock approximation is exact.

However, this factorisation property though a *fait accompli*, we feel, is not all that obvious. In the present paper we make a modest investigation of the factorisation property in the $U(N)$ Wilson-Polyakov lattice gauge theories based on the study of the Schwinger-Dyson equations and prove that it indeed is satisfied by all gauge invariant Green's functions in the large-N limit.

In § 2 we introduce the loop space Green's functions. In § 3 we review the derivation of Schwinger-Dyson (SD) equation and write down its general form for $U(N)$ lattice gauge theory. In § 4 we discuss the single loop Green's function and write down the corresponding SD equation. In § 5 we derive the SD equation satisfied by the multiloop Green's functions and prove the factorisation property.

2. Loop space Green's functions

The gauge-invariant physical content of a lattice gauge theory is described by the multiloop Green's functions

$$W(C_1, C_2, \ldots) = \left\langle \frac{1}{N} \mathrm{Tr}\, U(C_1) \frac{1}{N} \mathrm{Tr}\, U(C_2) \ldots \right\rangle, \tag{1}$$

where $C_1, C_2, \ldots$ are closed contours on the lattice and

$$U(C) = \prod_{l \in c} U_l, \tag{2}$$

with the product being path-ordered and U_l the $U(N)$ (or $SU(N)$) matrix in the fundamental representation corresponding to the link l. N is the number of internal (" colour ") degrees of freedom.

In particular for a single closed loop, the Wilson loop average

$$W(C) = \left\langle \frac{1}{N} \mathrm{Tr}\, U(C) \right\rangle,$$

determines the static inter-quark potential.

The aim of the present paper is to show that in the limit $N \to \infty$, with $g^2 N$ fixed where g is a coupling constant, the multiloop Green's functions defined above (equation (1)) factorise *i.e.*:

$$W(C_1, C_2, \ldots) \simeq W(C_1)\, W(C_2) \ldots + O(N^{-2}). \tag{3}$$

Thus, for $N \to \infty$ we have a class of non-fluctuating operators characterising the configuration space of the theory. One then has the appealing interpretation: large N gauge theory is a string theory where the relevant operators are the non-fluctuating loop operators that create bare strings of (" colour ") flux from the vacuum.

3. Schwinger-Dyson equations

We first briefly review the derivation of the SD equations for $U(N)$ gauge theory defined on a hypercubical lattice. The action is

$$S = \frac{1}{g^2} \sum_p \mathrm{Tr}\, U(p), \tag{4}$$

with the sum over all oriented plaquettes p; g is the coupling and the plaquette variable

$$U(p) = \prod_{l \in p} U_l, \tag{5}$$

where U_l is the $U(N)$ matrix in the fundamental representation ($N \times N$) corresponding to the link l. Explicitly

$$U_l = U_{x,\mu} = U^{-1}_{x+\hat{\mu},-\mu} = U^{+}_{x+\hat{\mu},-\mu}, \tag{6}$$

x denoting a site and μ the direction.

The average of any function f of the U's is defined by

$$\langle f \rangle = Z^{-1} \int \prod_l \mathrm{d}U_l \, e^S f, \tag{7}$$

where $$Z = \int \prod_l \mathrm{d}U_l \, e^S, \tag{8}$$

is the partition function and $\mathrm{d}U_l$ is the invariant Haar measure over $U(N)$.

We now make an infinitesimal transformation:

$$U_{x,\mu} \to \exp(i\epsilon T_j)\, U_{x,\mu} = (1 + i\epsilon T_j)\, U_{x,\mu} + O(\epsilon^2), \tag{9}$$

in the numerator of (7) and compute the corresponding change in $\langle f \rangle$. This being a unitary transformation the measure $\mathrm{d}U_{x,\mu}$ is invariant and f changes according to

$$f \to f + \epsilon D^{x,\mu} f + O(\epsilon^2), \tag{10}$$

where the linear differential operator $D_j^{x,\mu}$ at the link (x, μ) is defined by

$$D_j^{x,\mu} f = \lim_{\epsilon \to 0} \frac{1}{\epsilon} [f(\ldots, (1 + i\epsilon T)\, U_{x,\mu}, \ldots) - f(\ldots, U_{x,\mu}, \ldots)], \tag{11}$$

T_j's are hermitian generators of $U(N)$ in the fundamental representation normalised according to

$$\sum_j (T_j)_{ab} (T_j)_{cd} = \delta_{ad} \delta_{bc}. \tag{12}$$

Equating the first order change in $\langle f \rangle$ to zero we obtain

$$\langle D_j^{x,\mu} f \rangle + \langle f (D_j^{x,\mu} S) \rangle = 0. \tag{13}$$

Now replacing f by f_j and summing over the possible values of j corresponding to the mutually orthogonal directions of a local tangent plane in the group manifold we get

$$\sum_j \langle D_j^{x,\mu} f_j \rangle + \sum_j \langle f_j (D^{x,\mu} S) \rangle = 0. \tag{14}$$

The action S according to (4) is given by a sum over oriented plaquettes and the differential operator $D_j^{x,\mu}$ acts only on the plaquettes containing either the link (x, μ) or the oppositely oriented link $(x + \hat{\mu}, -\mu)$.

Thus

$$D_j^{x,\mu} S = \frac{1}{g^2} \Big\{ \sum_{\substack{p \\ (x,\mu) \in \partial p}} \mathrm{Tr} \{ i T_j U(p) \} - \sum_{\substack{p \\ (x,\mu) \in \partial p^{-1}}} \mathrm{Tr} \{ i T_j U(p) \} \Big\},$$

where the first (second) sum is over all plaquettes p such that the link (x, μ) is contained in the boundary ∂p of p (the boundary ∂p^{-1} of the oppositely oriented plaquette p^{-1}).

Finally from (14)

$$\sum_j \langle D_j^{x,\mu} f_j \rangle + \frac{1}{g^2} \sum_j \Big\{ \sum_{\substack{p \\ (x,\mu)\in\partial p}} \langle f_j \operatorname{Tr} (i T_j U(p)) \rangle - \sum_{\substack{p \\ (x,\mu)\in\partial p^{-1}}} \langle f_j \operatorname{Tr} (i T_j U(p)) \rangle \Big\} = 0. \tag{15}$$

This is the general form of the SD equations. In what follows we apply it to the case of single loop as well as multiloop Greens' functions.

4. Single loop Green function

In writing down the SD equations the local variations of the contour are of paramount importance as stressed by Makeenko and Migdal (1979) and Wadia (1981). In this context we introduce the loop deformation operator (Wadia 1981) for the unitary group in loop space, in the $\nu \neq \mu$ direction at the link $(x, x + \hat{\mu})$ as:

$$d_\nu (x, x+\hat{\mu}) \; [\ldots\!\rightarrow\!\ldots] \quad (x,\ \hat{\mu},\ x+\hat{\mu})$$

$$= \quad \nu \quad - \quad \mu$$

Defining

$$\sum_{\nu \neq \mu} d_\nu (x, x+\hat{\mu}) \equiv d(x, x+\mu),$$

one has

$$\mathrm{d}(x, x+\mu)\, U(C) = \sum_{\substack{p \\ (x,\mu)\,\in\,\partial p}} U(C \cup \partial p) - \sum_{\substack{p \\ (x,\mu)\,\in\,\partial p^{-1}}} U(C \cup \partial p), \tag{16}$$

where $C \cup \partial p$ is the loop obtained by adding the boundary ∂p of the plaquette p to C.

The SD equation corresponding to a single loop is obtained from (15) by making the choice

$$f_j = \frac{1}{N} \operatorname{Tr} [i T_j U(C)],$$

and using the identities

$$\text{Tr I} = N, \tag{17}$$

$$\sum_j \text{Tr}\,(T_j\, A)\ \text{Tr}\,(T_j\, B) = \text{Tr}\,(AB), \tag{18}$$

$$\sum_j \text{Tr}\,(T_j\, A\ T_j\, B) = \text{Tr}\, A\ \text{Tr}\, B, \tag{19}$$

which follow from (12). Since this equation is already available in the literature (Foerster 1979; Eguchi 1979; Weingarten 1979; Wadia 1981) we omit details and write down its final form

$$\frac{1}{g^2 N}\,\text{d}\,(x, x+\mu)\ W(C)$$

$$+ \sum_{(y,\nu)\,\epsilon\, C} [\delta\,(x, x+\mu\,|\,y, y+\nu)\ W(C_{xy}, C_{yx}) - \delta\,(x, x+\mu\,|\,y+\nu, y)$$

$$\times\ W(C_{x,\,y+\nu},\ C_{y+\nu,\,x})] = 0. \tag{20}$$

Here C_{xy} represents part of the loop C from the point x to the point y. The first δ-function always contributes when $C_{xy} = C$. It also contributes when there is multiple traversal of the link $(x, x+\hat{\mu})$ in the same direction leading to string rearrangement. The second δ-function contributes only when the link $(x, x+\hat{\mu})$ is multiply-traversed in opposite directions and leads to string splitting.

5. Multiloop Green functions

We first consider the case of two loops C_1 and C_2 and make the choice

$$f_j = \frac{1}{N}\text{Tr}\,[iT_j\, U(C_1)]\ \frac{1}{N}\text{Tr}\ U(C_2)$$

in (15).

If C_1 and C_2 are completely disjoint *i.e.* have no link in common the SD equation is obtained by simply replacing $W(C)$ in (20) by $W(C_1, C_2)$.

Next we consider the case where the loops have a single link $(x, x+\hat{\mu})$ in common and the common link is traversed only once in both C_1 and C_2.

In this case a new term appears in the SD equation because the operator $D_j^{x,\,\mu}$ can now act on C_2 producing a new term in $D_j^{x,\,\mu} f_j$:

$$\frac{1}{N}\text{Tr}\,[iT_j\, U(C_1)]\ \frac{1}{N}\text{Tr}\,[iT_j\, U(C_2)] = -\frac{1}{N^2}\text{Tr}\ U(C_1 \cup C_2),$$

where we have used the identity (18). Thus the SD equation in this case is

$$\frac{1}{g^2N}\Big[\sum_{\substack{p\\(x,\mu)\in\partial p}} W(C_1\cup\partial p, C_2) - \sum_{\substack{p\\(x,\mu)\in\partial p^{-1}}} W(C_1\cup\partial p, C_2)\Big]$$

$$+ W(C_1, C_2) - \frac{1}{N^2} W(C_1\cup C_2) = 0. \tag{21}$$

If the common link $(x, x+\hat{\mu})$ is traversed more than once in one of the loops say C_1, then we get the usual string rearrangement and splitting terms and the SD equation becomes

$$\frac{1}{g^2N} W[d(x, x+\mu) C_1, C_2]$$

$$+ \sum_{(y,\nu)\in C_1} [\delta(x, x+\mu \,|\, y, y+\nu)\, W(C^1_{xy}, C^1_{yx}; C_2)$$

$$- \delta(x, x+\mu \,|\, y+\nu, y)\, W(C^1_{x,\,y+\nu}, C^1_{y+\nu,x}; C_2)]$$

$$- \frac{1}{N^2} W(C_1\cup C_2) = 0, \tag{22}$$

where

$$d(x, x+\mu) C_1 = \sum_{\substack{p\\(x,\mu)\in\partial p}} (C_1\cup\partial p) - \sum_{\substack{p\\(x,\mu)\in\partial p^{-1}}} (C_1\cup\partial p),$$

gives the effect of loop deformation.

If in the second loop C_2, the common link $(x, x+\hat{\mu})$ occurs more than once then C_1 may be connected to it in various ways and $W(C_1\cup C_2)$ would be replaced by an algebraic sum over the various possibilities.

The SD equation for a general n-loop Green function is obtained by an obvious generalisation of the process outlined in the two loop case and some straightforward algebra. Thus we take

$$f_j = \frac{1}{N}\mathrm{Tr}\,[i T_j U(C_1)]\,\frac{1}{N}\mathrm{Tr}\,U(C_2)\,\ldots\,\frac{1}{N}\mathrm{Tr}\,U(C_n)$$

in (15) and the SD equation becomes

$$\frac{1}{g^2 N} W[\mathrm{d}(x, x+\mu) C_1, C_2, \ldots, C_n]$$

$$+ \sum_{(y,\nu)\in C_1} [\delta(x, x+\mu \,|\, y, y+\nu)\, W(C^1_{xy}, C^1_{yx}; C_2; \ldots, C_n)$$

$$- \delta(x, x+\mu \,|\, y+\nu, y)\, W(C^1_{x,y+\nu}, C^1_{y+\nu,x}; C_2, \ldots. C_n)]$$

$$-\frac{1}{N^2}\Big\{ \sum_{\substack{k \neq 1 \\ (x,\mu) \in C_k}} W(C_1 \cup C_k, C_2, \ldots., C_{k-1}, C_{k+1}, \ldots. C_n)$$

$$- \sum_{\substack{k \neq 1 \\ (x,\mu) \in C_k^{-1}}} W(C_1 \cup C_k, C_2, \ldots., C_{k-1}, C_{k+1}, \ldots. C_n)\Big\} = 0. \quad (23)$$

We are now ready to prove the factorisation property stated in (3).

We note that because of (20)

$$W(C_1, C_2, \ldots., C_n) = W(C_1)\, W(C_2) \ldots. W(C_n)$$

satisfies (23) with the last $O(N^{-2})$ term on the left side omitted. However this $O(N^{-2})$ term is negligible in the limit $N \to \infty$ with g^2N fixed. Thus assuming the uniqueness of the solution of the SD equation (23) we immediately arrive at the factorisation property (3).

6. Conclusion

In this paper we have proved that the factorisation property holds for all gauge invariant Green's functions in the large-N limit of a Wilson-Polyakov lattive gauge theory. Even though our discussions are based on the gauge group $U(N)$ it may be easily extended to other gauge groups like $SU(N)$ and $O(N)$. In our proof the lattice with its intrinsic short distance cut-off provides a convenient framework and we believe that the same method would work in the continuum case as well, though some of the steps may require careful definition.

Before we end, we hasten to add that the correctness of our proof depends of course on the validity of the currently accepted philosophy that the Schwinger-Dyson equations describe a theory completely.

References

Bhanot G, Heller U and Neuberger H 1982 *Phys. Lett.* **B113** 47
Das S and Wadia S 1982 *Phys. Lett.* **B117** 228
Eguchi T 1979 *Phys. Lett.* **B87** 91
Eguchi T and Kawai H 1982 *Phys. Rev. Lett.* **48** 1063
Foerster D 1979 *Phys. Lett.* **B87** 87
Gross D J and Kitazawa Y 1982 *Nucl. Phys.* **B206** 440
Makeenko Y M and Migdal A A 1979 *Phys. Lett.* **B88** 135
Parisi G 1982 *Phys. Lett.* **B112** 463
Wadia S 1981 *Phys. Rev.* **D24** 970
Weingarten D 1979 *Phys. Lett.* **B87** 97

Pramāṇa, Vol. 21, No. 6, December 1983, pp. 393–399. © Printed in India.

Nature of wave front of light radiations from a tachyon

G ALAGAR RAMANUJAM, G A SAVARIRAJ* and
T S SHANKARA**
P G Department of Physics, N G M College, Pollachi 642 001, India
*P G Department of Physics, St. Joseph's College, Tiruchirapalli 620 002, India
**Department of Mathematics, Indian Institute of Technology, Madras 600 036, India

MS received 5 December 1981; revised 24 October 1983

Abstract. The nature of wave front of light radiations from a tachyon is studied from the first principles. The elementary approach employed here yields many novel and interesting results. These results, specially the conical envelope of radiation, bear an excellent analogy to the case of Cerenkov radiation. Finally a possible astrophysical method of searching for the existence of tachyonic celestial objects is discussed.

Keywords. Tachyon splitting; conical wave front; radiation envelope; moving objects; Cerenkov radiation.

1. Introduction

The study of the nature of light radiations from a source with tachyonic velocity has received considerable attention in recent years (Gron 1978; Lemke 1975; Recami 1978, 1981). A close examination of the approaches employed in the above studies not only reveals the limitations of some of the approaches but also leads to certain interesting questions. For example, the approach employed by Lemke (1975), has the following limitations: (a) The invariance of the light velocity has been given up. This means that light pulses from subluminal sources travel at speed c in all directions, but the light pulses emitted from a superluminally moving source travel at different speeds in different directions. This leads to a concept of two types of massless particles. (b) The opening angle of the cone remains fixed ($\pi/2$) and is independent of the velocity of the moving superluminal source. This deviates from an analogous situation in supersonic motion of a point source in a medium. There, the pressure disturbances in the medium are confined to a Mach Cone and the angle of the cone is a function of the velocity of the supersonic motion.

The results obtained by Recami (1978) and Gron (1978) through their investigations of the radiations from a superluminal source have much similarity with the corresponding results in supersonic motion. In view of their possible application in astrophysics, the approach of Recami and Gron assume a special significance. However, there arise many questions. For example, Gron deals with a tachyon moving along a line and existing at all times from $-\infty$ to $+\infty$. If one considers a tachyon created at a finite time, say at a time $t = 0$, what will be the nature of the appearance of that tachyon for an observer?

Such questions are discussed in detail in this paper. In § 2, by employing an elementary approach, many interesting results are derived and their applicability to the study of Cerenkov radiation is discussed. It is assumed that the tachyons are moving from infinite past into the infinite future. However, with an eye on a possible laboratory experiment, the study of tachyons created at $t = 0$ is taken up in § 3. Finally, in § 4 we briefly discuss a possible astrophysical search for tachyons in the background of a speculation (Schulman 1971) that the source of the gravitational radiations claimed to have been detected by Weber (1970) might be a dense aggregate of tachyonic objects.

2. Wave front due to a moving light source

2.1 *The conical wavefront*

The wave front due to a static source of light, as we all know, is spherical in shape. The shape of the wavefront due to a moving source is studied here. This study leads to certain interesting results when the velocity of the source exceeds the velocity of light (c) itself. Let u be the velocity of the source and A its position at the time $t = 0$ (figure 1). P and Q are two points to which light rays emitted at A, reach at a time $t = T$. Since the source is moving, by the time the ray from A reaches, say, Q, the source may move to B and a ray emitted at B also may reach Q. Thus, there is a possibility of Q receiving two light rays at a given time. In such a case, we will have

$$\frac{AQ}{c} = \frac{AB}{u} + \frac{BQ}{c}. \tag{1}$$

By invoking the triangle inequality, we can show that (1) can be satisfied only when $u > c$. Or in other words, the possibility of a single point, (here Q) receiving two light rays at a given time, exists only when the velocity of the source exceeds the velocity of light itself. In what follows, unless otherwise specified, we take u to be greater than c.

If τ_1, is the time taken by the tachyonic source to travel from A to B, then we have from figure 1,

$$(u\tau_1 - x)^2 + y^2 + z^2 = c^2 (T - \tau_1)^2, \tag{2}$$

$$\tau_1 < T, \tag{3}$$

$$x^2 + y^2 + z^2 = c^2 T^2, \tag{4}$$

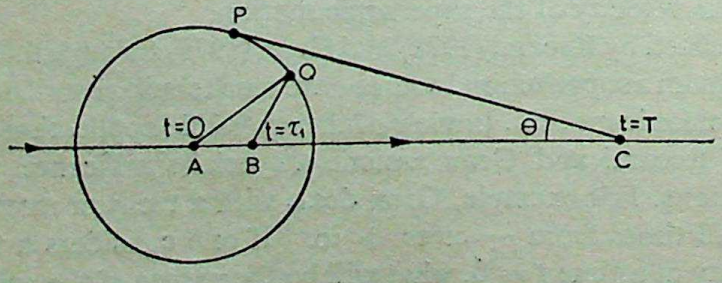

Figure 1. Wave front due to a tachyonic light source.

where x, y and z are the coordinates of the point Q in the frame whose origin is at A. To locate the position of B, we solve (2) for τ_1 and get

$$\tau_1 = 0 \text{ or } 2(ux - c^2 T)/(u^2 - c^2)\,. \tag{5}$$

(Incidentally, it may be noted here that for $u < c$, the second solution for τ_1 becomes greater than T and hence is unphysical. This only confirms our earlier assertion that the possibility of a single point receiving two rays simultaneously does not exist when $u < c$).

For $u > c$, τ_1 has two values and hence Q will receive two rays at time $t = T$. However, if we choose an observer P with coordinates x_0, y_0 and z_0 such that

$$ux_0 = c^2 T \tag{6}$$

and

$$x_0^2 + y_0^2 + z_0^2 = c^2 T^2 \tag{7}$$

then, τ_1 has only one value *i.e.* 0 and hence P will receive only one ray at $t = T$. Equation (6) shows that the locus of all points which receive a single ray at $t = T$ lie on the surface of a cone of semivertex angle given by $\theta = \sin^{-1}(c/u)$. The vertex of the cone lies at c at a distance of uT from A. Thus, at the time $t = T$, the light energy emitted by the source is confined inside this cone. We call the space inside the cone ' Zone of illumination ' and the space outside it ' Zone of darkness '.

At any time $t = \tau > T$, the observations of $P(x_0, y_0, z_0)$ have some interesting features which are discussed in the rest of this section. When $t = \tau > T$, (2) and (4) become

$$(u\tau_2 - x_0)^2 + y_0^2 + z_0^2 = c^2(\tau - \tau_2)^2, \tag{8}$$

$$x_0^2 + y_0^2 + z_0^2 = c^2 T^2. \tag{9}$$

Here τ_2 is the time taken by the tachyon to travel from A to a point from where a light ray reaches P at the time τ. From (8) and (9), we get

$$\tau_2 = \{-c^2(\tau - T) \pm c\,[c^2(\tau - T)^2 + (u^2 - c^2)(\tau^2 - T^2)]^{1/2}\}\,(u^2 - c^2)^{-1} \tag{10}$$

The existence of two values for τ_2 means that there are two different positions of the source from where light rays reach the observer P at time τ. Thus a single tachyon *ic* (i.e. $u > c$) light source gives rise to two moving light sources, S_1 and S_2 (figure 2).

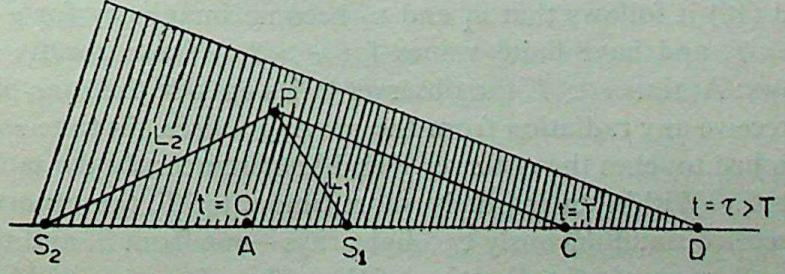

Figure 2. An observer inside the zone of illumination.

To locate the positions of these two light sources, let us examine the nature of the two τ_2 in detail. By virtue of the facts that $\tau > T$ and $u > c$, it is clear that of the two τ_2 values, one is positive and the other is negative. Let σ denote the positive value and ρ the negative value. In figure 2, the position S_1 corresponds to the positive value σ and S_2 corresponds to the negative value ρ. Let us now find the velocities of the apparent sources S_1 and S_2 with respect to the observer P.

2.2 *Velocities of S_1 and S_2*

If L_1 and L_2 are the distances of S_1 and S_2 from the observer, then from figure 2, we have

$$L_1 = c(\tau - \sigma), \tag{11}$$

$$L_2 = c(\tau - \rho). \tag{12}$$

Obtaining the values of σ and ρ from (10) and using (11) and (12), we get

$$L_1 = [(u\tau - x_0)\beta - R]/(\beta^2 - 1), \tag{13}$$

$$L_2 = [(u\tau - x_0)\beta + R]/(\beta^2 - 1), \tag{14}$$

$$\beta = u/c;\ R = [(u\tau - x_0)^2 - (uT - x_0)^2]^{1/2}. \tag{15}$$

Let us consider a coordinate system with P as its origin and x-axis parallel to the direction of motion of the source. The x-coordinate (x_1) of the apparent source S_1 in this system is given as

$$x_1 = [L_1^2 - (y_0^2 + z_0^2)]^{1/2}. \tag{16}$$

Hence, the x-component (u_1) of the phase velocity of the apparent source S_1 is given as

$$u_1 = dx_1/dt = (L_1/x_1)\,[u\beta - R^{-1}(u\tau - x_0)\,u]\,(\beta^2 - 1)^{-1}. \tag{17}$$

Similarly, for the x-component (u_2) of the phase velocity of the apparent source S_2, we obtain

$$u_2 = -(L_2/x_2)\,[u\beta + R^{-1}(u\tau - x_0)\,u]\,(\beta^2 - 1)^{-1}. \tag{18}$$

From (17) and (18) it follows that u_1 and u_2 become imaginary for $\tau < T$, become infinite for $\tau = T$, and have finite values for $\tau > T$. These results can be interpreted as follows: At time $\tau < T$, the observer P lies outside the zone of illumination and does not receive any radiation from the moving source. At time $\tau = T$, the zone of illumination just touches the observer P and instantaneously the tachyonic source is observed at A. Within an infinitely short time after T, the observer lies inside the zone and receive simultaneously two light rays—one from S_1 and the other from S_2. The source S_1 moves in the direction of the tachyonic source and S_2 moves in the

opposite direction. Finally, in the limit $\tau \to \infty$, the two sources move with constant velocities given by

$$u_1 = \beta c/(\beta + 1), \tag{19}$$

$$u_2 = -\beta c/(\beta - 1). \tag{20}$$

2.3 *Cerenkov radiation*

The theory developed in §§ 2.1 and 2.2 is applicable to any situation where the source of disturbance travels with a velocity greater than the velocity of the disturbance itself. Cerenkov radiation (Bethe 1949) is one such situation which is emitted when a very fast charged particle passes through a transparent solid medium whose characteristic velocity of light C' (c/n where n is the index of refraction) is less than the velocity of the particle in that medium. A detailed theory of this effect has been worked out by Blatt and Jackson (1949). The theory indicates that the radiation is confined to a cone whose half angle is given by $\sin\theta = c/nu = C'/u$. This cone is similar to the zone of illumination discussed in this paper. Other features such as the splitting of a single particle into two sources may be shown to exist for the particle emitting Cerenkov radiation also. However, one point must be borne in mind. The treatment given in §§ 2.1 and 2.2 assumes the medium to be of infinite length. But in the actual Cerenkov radiation experiments in the laboratory, the charged particle travels only a short, finite distance inside the medium. The finiteness of the medium, when taken into account, is likely to modify the results of §§ 2.1 and 2.2. Only such modified results would be exhibited by the particle emitting Cerenkov radiation. Work in this direction is in progress.

3. Radiations from tachyons created at a finite time

In the discussions so far, the point A was considered to be the position of the tachyon (*i.e.* the tachyonic source) at a time $t = 0$, in the observer's frame, where the tachyon is assumed to exist at all times *i.e.* $-\infty < \tau < \infty$. If, on the other hand, the tachyon is created at a space point O at a time $t = 0$, then the time at which that tachyon is observed by P lies between 0 and ∞. This change in the boundary values of τ is likely to introduce certain modifications in the results obtained so far. We investigate here such modifications, and then discuss their possible astrophysical applications.

It can be seen from figure 3 that all the observers lying on the surface of the cone PP_1P_2 will simultaneously receive the right radiations from the tachyon, say, at a time T. At the same time the radiations emitted by the tachyon at O would have reached the observers P_3, P_4 and P_5 lying on the spherical surface of radius OP. Thus at time T, the radiation from the tachyon is confined inside an envelope $PP_1P_2P_3P_4P_5$ of parachute-like shape.

Between the observation of the observers on the spherical surface and that of the observers on the conical surface, there is a striking difference. While all the observers on the spherical surface see the source of disturbances at O, the observers on the cone will see the source of disturbance at different points on the line of motion

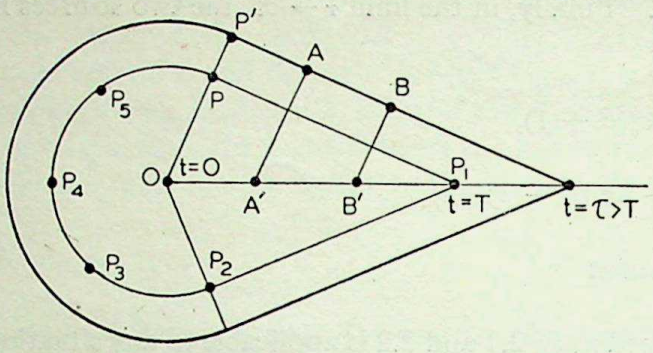

Figure 3. Parachute-like wave front.

of the tachyon. For example, an observer A on the cone will observe the tachyon at A′ and an observer B will observe the same at B′ (*cf.* figure 3).

Apart from this difference, there is also a subtle difference between the observations of different observers on the cone itself. To see this, let us consider the observers P′ and A. At time τ, P′ observes the tachyon at O and A observes the tachyon at A′. At any time $t > \tau$, for P′, the observed tachyon at O splits into two sources (S_2 and S_1). Since there is no source of disturbance to the left of O (the tachyon is created at O and proceeds towards P_1) the source S_2 does not exist for P′. Consequently, the observer P′ always observes only one source, that is, S_1. Now, let us discuss the case with observer A. For him, the observed tachyon at A′ will split into two sources. The source S_2 exists for him over the distance A′O. This means that A first observes the tachyon at A′, then observes two sources for some time interval, and after that observes only one source. Such subtle and novel features do not seem to have been noticed earlier.

4. Astrophysical search for tachyonic motions

There is a speculation (Schulman 1971) that the source of the gravitational radiations claimed to have been observed by Weber (1970) might be a dense aggregate of tachyonic matter. If such tachyonic celestial objects exist then it is quite possible that radio signals from such objects might be reaching the earth. In this connection, the following observation by Feynman (1969) is quite interesting: "....once the object is moving faster than the speed of sound, it will make sound. That is, it is not necessary that it have certain tone vibrational character. Any object moving through a medium faster than the speed at which the medium carries waves, will generate waves on each side, automatically, just from the motion itself. This is simple in the case of sound, but it also occurs in the case of light...."

If one can develop certain guidelines to distinguish between the nature of radio signals from a superluminal object and that from a subluminal object, then by using these guidelines, the possible presence of tachyonic celestial objects could be established. The discussion given in §§ 2 and 3 enables us to propose one such guideline. If one receives the radio signals from a cosmological source S, and exactly in the following order, one can conclude that S has a superluminal velocity.

(i) One receives a radio signal from a single source S.

(ii) Immediately after that, he receives radio signals from two sources (S_1 and S_2).
(iii) Either he continues to receive the radio signals from the two sources or after an interval of time, the signal from one source (S_2) ceases.

A similar method proposed by Recami (1981) took into account only the points (i) and (ii), and hence the above method proposed by us should be considered as a more general one.

5. Conclusion

Starting with the simple requirement that light radiations from a tachyon travel at speed c, we have detected many interesting and novel features associated with the radiations from a tachyon. The theory presented here has given us not only the results of Gron, but also certain additional new results, such as the parachute-like wave envelope. Recently, the nature of image of a rapidly moving object has been discussed in detail by Sala (1979). It has been shown by Sala that under certain conditions a rapidly moving object gives rise to two images simultaneously. A detailed study of Sala's work shows that these two images have properties similar to those of the sources S_1 and S_2 discussed in this paper. In a future publication, we will demonstrate that the theory developed in this paper for the radiations from a tachyon can be used to obtain not only Sala's equations but also certain additional features regarding the nature of image of a rapidly moving object. This demonstration confirms our basic approach to tachyons and expresses the usefulness of our theory.

Acknowledgement

The authors are extremely grateful to the referee of this paper for his critical remarks and very many, useful suggestions. Thanks are due to Profs. P M Mathews and N Mukunda for many useful discussions, Prof. E Recami for having critically gone through the original manuscript and to Prof. N Namasivayam, Dr K A Gundu Rao and Rev. Fr. C K Swamy for their kind help and encouragement. One of them GAR is grateful to the UGC for a major research grant.

References

Bethe H A 1949 *Phys. Rev.* **76** 38
Blatt J D and Jackson J M 1949 *Phys. Rev.* **76** 18
Feynman R P, Leighton B and Mathew Sands 1969 *The Feyman lectures on physics* (Addition-Wesley—B I Publications), Vol. I, p. 51–1
Gron O 1978 *Lett. Nuovo Cimento* **23** 97
Lenke H 1975 *Lett. Nuovo Cimento* **12** 342
Recami E (ed) 1978 *Tachyons, Monopoles and related topics* (Amsterdam: North Holland Pub. Co,)
Recami E 1981 *Proc. of the Einstein Centenary Symposium*, Nagpur
Sala K 1979 *Phys. Rev.* **A19** 2377
Schulman L S 1971 *Nuovo Cimento* **B2** 38
Weber J 1970 *Phys. Rev. Lett.* **24** 276

Pramāṇa, Vol. 21, No. 6, December 1983, pp. 401–402. © Printed in India.

Comment on: Bag like potential and quarkonium

K R BROWNSTEIN
Department of Physics and Astronomy, University of Maine, Orono, Maine 04469 USA

MS received 13 June 1983

Abstract. Some errors in a recent article by Zadoo and Sofi are discussed.

Keywords. Bag like potential; charmonium spectra; upsilon spectra.

A recent article by Zadoo and Sofi* (1982) attempts to fit the spectra of charmonium and upsilon by means of the energy eigenvalues associated with a simple central potential $V(r)$. Unfortunately, their work appears to be marred by several algebraic errors. Some of these are, undoubtedly, of a typographical nature and will be merely mentioned in passing. Others, however, are of a more substantive nature and cannot be so easily rectified.

Zadoo and Sofi seek to solve the radial Schrödinger equation

$$\left[\frac{\mathrm{d}^2}{\mathrm{d}r^2} - \frac{l(l+1)}{r^2} + \frac{2}{r}\frac{\mathrm{d}}{\mathrm{d}r} - \frac{2\mu}{\hbar^2}\{V(r) - E\}\right] R = 0. \tag{1}$$

Here μ is the reduced mass, E is the energy eigenvalue and $R(r)$ is the radial wave function. (The negative sign in front of the $\{\ \}$ bracketed term has been inserted to correct a typographical error.) The potential energy function chosen by Zadoo and Sofi is

$$V(r) = (r - r_0)\{B(r - r_0) - C/r\} \tag{2}$$

where B, C and r_0 are parameters. It is asserted that the following dimensionless form of (1)

$$\left[\frac{\mathrm{d}^2}{\mathrm{d}\rho^2} - \frac{l(l+1)}{\rho^2} + \frac{2}{\rho}\frac{\mathrm{d}}{\mathrm{d}\rho} - \frac{2}{\rho} - \epsilon\right] R = 0 \tag{3}$$

is obtained under the change of variables

$$\epsilon = \frac{2\mu r}{\rho^2\hbar^2}(C - E) \tag{4}$$

and

$$\rho = \frac{\mu}{\hbar^2} r^2 \{B(r - r_0)^2 - Cr_0/r\}. \tag{5}$$

*The article by Zadoo and Sofi appeared in Pramāṇa **18** 291

(Here the exponent " 2 " in the denominator of the centrifugal term and the negative sign in front of the $2/\rho$ term in (3) and the " r " in the denominator of the last term in (5) have been inserted to correct typographical errors).

However, when (2), (4) and (5) are substituted into (1) the result is

$$\left[\frac{r^2}{\rho^2}\left\{\frac{d^2}{dr^2}+\frac{2}{r}\frac{d}{dr}\right\}-\frac{l(l+1)}{\rho^2}-\frac{2}{\rho}-\epsilon\right]R=0. \tag{6}$$

The following two points are to be noted:

(i) Equation (6) is structurally different from (3). Thus the dimensionless Schrödinger equation (3) does not arise from the indicated changes of variable.

(ii) The quantity ϵ is a function of location (r or ρ) as may be seen by inspection of (4) and (5). The (implied) use of ϵ as an eigenvalue in (3) is then untenable.

Because of the above two points, the validity of the numerical results reported by Zadoo and Sofi would appear to be in doubt.

The author acknowledges the encouragement from E F Carr regarding the submission of this comment.

Pramāṇa

a journal of Physics

Volume 21, July–December 1983

INDEX

The Indian Academy of Sciences
Bangalore 560 080

Pramāṇa
a journal of Physics

Volume 21, July–December 1983

SUBJECT INDEX

AUTHOR INDEX